polymers

Advances in Plasma Processes for Polymers

Edited by

Choon-Sang Park

MDPI

Advances in Plasma Processes for Polymers

Advances in Plasma Processes for Polymers

Editor

Choon-Sang Park

MDPI • Basel • Beijing • Wuhan • Barcelona • Belgrade • Manchester • Tokyo • Cluj • Tianjin

MDPI

Editor
Choon-Sang Park
Electrical Engineering
Milligan University
Johnson City
United States

This is a reprint of articles from the Special Issue published online in the open access journal *Polymers* (ISSN 2073-4360) (available at: www.mdpi.com/journal/polymers/special_issues/adv_plasma_processes_polym).

For citation purposes, cite each article independently as indicated on the article page online and as indicated below:

LastName, A.A.; LastName, B.B.; LastName, C.C. Article Title. *Journal Name* **Year**, *Volume Number*, Page Range.

Contents

A Review of Plasma Synthesis Methods for Polymer Films and Nanoparticles under Atmospheric Pressure Conditions

Hyo Jun Jang [1,†], Eun Young Jung [1,†], Travis Parsons [2], Heung-Sik Tae [1,3,*] and Choon-Sang Park [4,*]

[1] School of Electronic and Electrical Engineering, College of IT Engineering, Kyungpook National University, Daegu 41566, Korea; bs00201@knu.ac.kr (H.J.J.); eyjung@knu.ac.kr (E.Y.J.)
[2] GBS (Global Business Services) IT, The Procter & Gamble Company, Cincinnati, OH 45202, USA; trav.parson@gmail.com
[3] School of Electronics Engineering, College of IT Engineering, Kyungpook National University, Daegu 41566, Korea
[4] Department of Electronics and Computer Engineering, College of Engineering, Kansas State University, Manhattan, KS 66506, USA
* Correspondence: hstae@ee.knu.ac.kr (H.-S.T.); purplepcs@ksu.edu (C.-S.P.)
† These authors contributed equally to this work.

Abstract: In this paper, we present an overview of recent approaches in the gas/aerosol-through-plasma (GATP) and liquid plasma methods for synthesizing polymer films and nanoparticles (NPs) using an atmospheric-pressure plasma (APP) technique. We hope to aid students and researchers starting out in the polymerization field by compiling the most commonly utilized simple plasma synthesis methods, so that they can readily select a method that best suits their needs. Although APP methods are widely employed for polymer synthesis, and there are many related papers for specific applications, reviews that provide comprehensive coverage of the variations of APP methods for polymer synthesis are rarely reported. We introduce and compile over 50 recent papers on various APP polymerization methods that allow us to discuss the existing challenges and future direction of GATP and solution plasma methods under ambient air conditions for large-area and mass nanoparticle production.

Keywords: atmospheric-pressure plasma; solution plasma; plasma polymerization; polymer films; room temperature growth; nanoparticles

1. Introduction

In previous years, many of the papers and studies on polymer synthesis using the atmospheric-pressure plasma (APP) method have focused on specific application processes. However, there are very few review papers that provide a comprehensive view of the polymer synthesis methods using APP, which makes it difficult for new researchers in the field who want to try APP polymer synthesis. Beginning in the 1790s, the report written by N. Bondt et al. on polymer synthesis using electrical discharge [1] is seen as one of the first documented studies on plasma polymerization. In the 19th century, arc synthesis of hydrocarbons was studied by chemists such as de Wilde et al. [2], Berthelot et al. [3,4], and P. and A. Thenard [5]. Studies on the synthesis of various organics using glow discharge were first published by German scientists in the 1960s [6–9]. Afterwards, the first applications using these plasma polymers were reported by Goodman [10], and subsequent studies on the property improvements of materials using plasma polymers were actively conducted, with a focus on the interaction between plasma and various substances [11–16]. Today, plasma synthesis is selected for various applications, such as layer deposition for electrical devices [17–20], antibio- or bio-material applications [21–24], and surface modification [25–28], among others.

Plasmas are well known as ionized quasi-neutral gases consisting of photons, neutral particles, metastable particles, ions, radicals, and electrons. Plasmas with the same den-

sity of positive-charged particles (ions) and negative-charged particles (electrons) behave macroscopically neutrally in free space [29,30]. These plasmas can be artificially generated by waves, lasers, combustion, flames, and even nuclear reactions, though the most common approach for plasma generation is electrical discharge from electric power sources in the laboratory [31,32]. The plasma generated by electric power is called 'non-equilibrium plasma' because the temperature (or kinetic energy) of heavy particles, including ions, is different from that of the electrons. Only the electrons receive energy from the electric field generated by applied electric power; thus, the electron temperature (several thousand K) is relatively higher than the heavy particles' temperature (around room temperature). This fact is responsible for the definition of such plasma generated by electric power as 'cold plasma' or 'non-thermal plasma' [32]. In the case of polymer synthesis, the non-thermal plasma method (or non-thermal plasma polymerization) can avoid thermal damage to substrates or substances due to the relatively low temperatures of the heavy particles. In addition, the energetic electrons with high energy supplied from plasma can produce high concentrations of reactive species or free radicals from precursors [32–34]. This method not only has the degree of freedom for material selectivity without insolubility problems, but also reduces or eliminates the need for an oxidant or reductant [35–38]. Overall, plasma polymerization presents several advantages, such as simple installation, high reactivity, high throughput, fast processing, low cost, low temperature, and green synthesis [39–42].

The non-thermal plasmas are roughly classified into vacuum plasma and APP, depending on the plasma working pressure required—of which APP has substantial potential for process enlargement because it does not require a high-quality vacuum system, which significantly reduces the overall setup and operating costs. Such APP can be obtained under atmospheric pressure conditions, avoiding extreme handling conditions [43]. For these reasons, polymer synthesis methods using APP have attracted growing attention in recent years, owing to their high potential for polymer deposition and nanoparticle (NP) synthesis for various applications [17–28]. Accordingly, attempts to generate plasma under atmospheric pressure have been successful, and various structures of plasma devices have been proposed [44–48]. Many reports have described the conditions needed to generate plasma, and the properties of plasma-synthesized polymers have been thoroughly investigated [25,39,42,45,49,50]. These studies may lead to further active investigations into methods and applications of this new plasma equipment in the near future.

We divide these APP polymer synthesis techniques into two types, depending on the phase of employed precursors: the first is APP polymerization, using a gas- or aerosol-type precursor [21,39,41], while the second is when the solution itself is supplied as a precursor [38,43,44], as shown Figure 1. In this review, the former is referred to as the gas/aerosol-through-plasma (GATP) method, and the latter is denominated as the solution plasma method. For students and researchers starting out in the APP polymerization field, the aim of this review is to introduce an overview of recent studies on these polymer synthesis methods employed by various APP techniques for the formation of polymer films and NPs. Additionally, the methodological classification of APP polymer synthesis according to the precursor phase employed, using various kinds of plasma equipment, is included. The main purpose of this review paper is to provide a reference for recent APP devices for polymerization, while briefly discussing APP polymerization. We hope that students and researchers trying to synthesize plasma polymers can then select the best suited methods for their experiments.

(**a**)

(**b**)
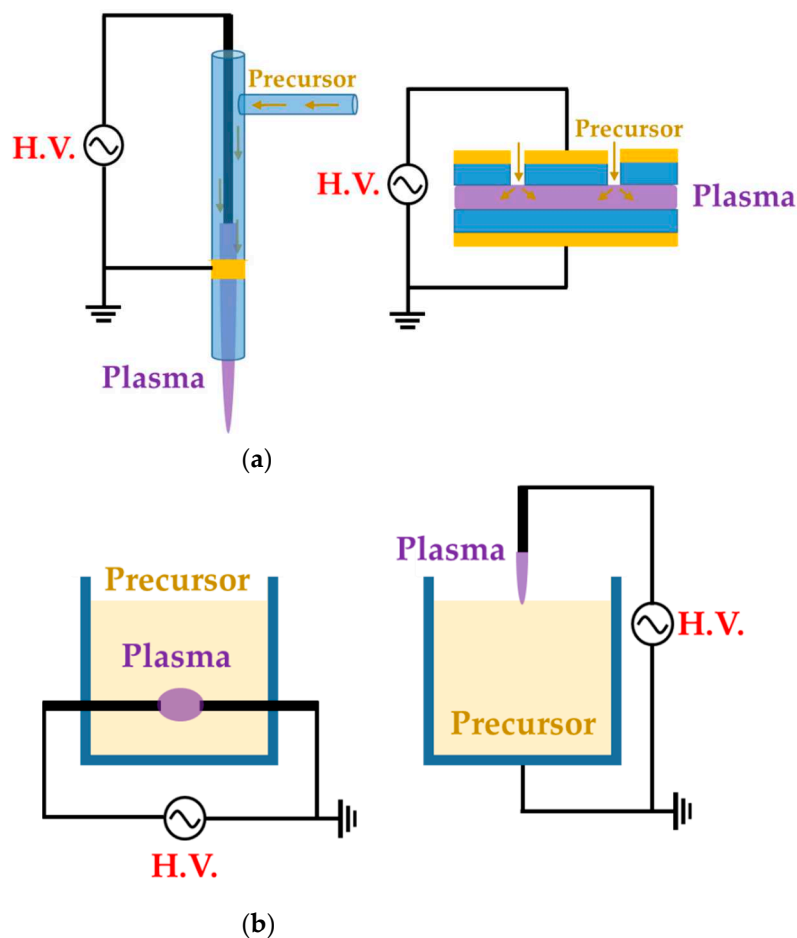
Figure 1. Representative configuration of (**a**) gas/aerosol-through-plasma (GATP) methods (left: jet type, right: dielectric-barrier discharge (DBD) type) and (**b**) solution plasma methods (left: in-solution plasma, right: on-solution plasma).

2. Synthesis Method Using Gas/Aerosol-Type Precursors (GATP)

GATP methods use a discharge gas for generating the APP, and floated precursors that are in aerosol or gaseous form. Materials in a gaseous state at room temperature are themselves applied as precursors, whereas materials that exist as liquids are mainly introduced to a plasma region as an aerosol via atomizing or bubbling with gas. GATP methods are commonly used for the deposition of polymer films [51–85], as this method allows in-line processing by moving either the APP devices or the substrates [39].

2.1. Atmospheric-Pressure Plasma Jet (APPJ) Method

An atmospheric-pressure plasma jet (APPJ) is a device for polymerization that generates directional plasma from a narrow nozzle and a gas flow with high input energy. Polymerization with APPJ devices enables local processing, because the process area is limited to the jet plasma plume size [51,59]. A gas/aerosol precursor becomes activated (or fragmented) by passing through the plasma generation region, and then the fragments become neutral passive (or recombine) beyond the plasma stream end, and are deposited onto a substrate that lies outside the plasma region [86,87].

Zhang et al. [51], Ricci Castro et al. [52], Van Vrekhem et al. [53], and Pandiyaraj et al. [54] reported an APPJ with pin–ring electrodes. The pin electrode and the ring electrode are used as high-voltage (HV) and ground electrodes, respectively. Zhang et al. reported an APPJ for poly(methyl methacrylate) (PMMA) coating on a bumpy surface. This APPJ consists of a T-shaped quartz glass body and pin–ring electrodes; the pin electrode is a copper (Cu) rod covered with a quartz glass tube (Figure 2a). Both the plasma discharge

gas and monomer bubbler gas are argon (Ar). In this method, the methyl methacrylate (MMA) monomer liquid is housed in a bottle within an oil bath held at 40 °C, and is bubbled with Ar gas introduced through the branch of the quartz body in an aerosol state. The power generation uses an alternating current (AC) source from 10 kHz to 60 kHz with a maximum voltage of 17 kV supplied through the pin electrode [51].
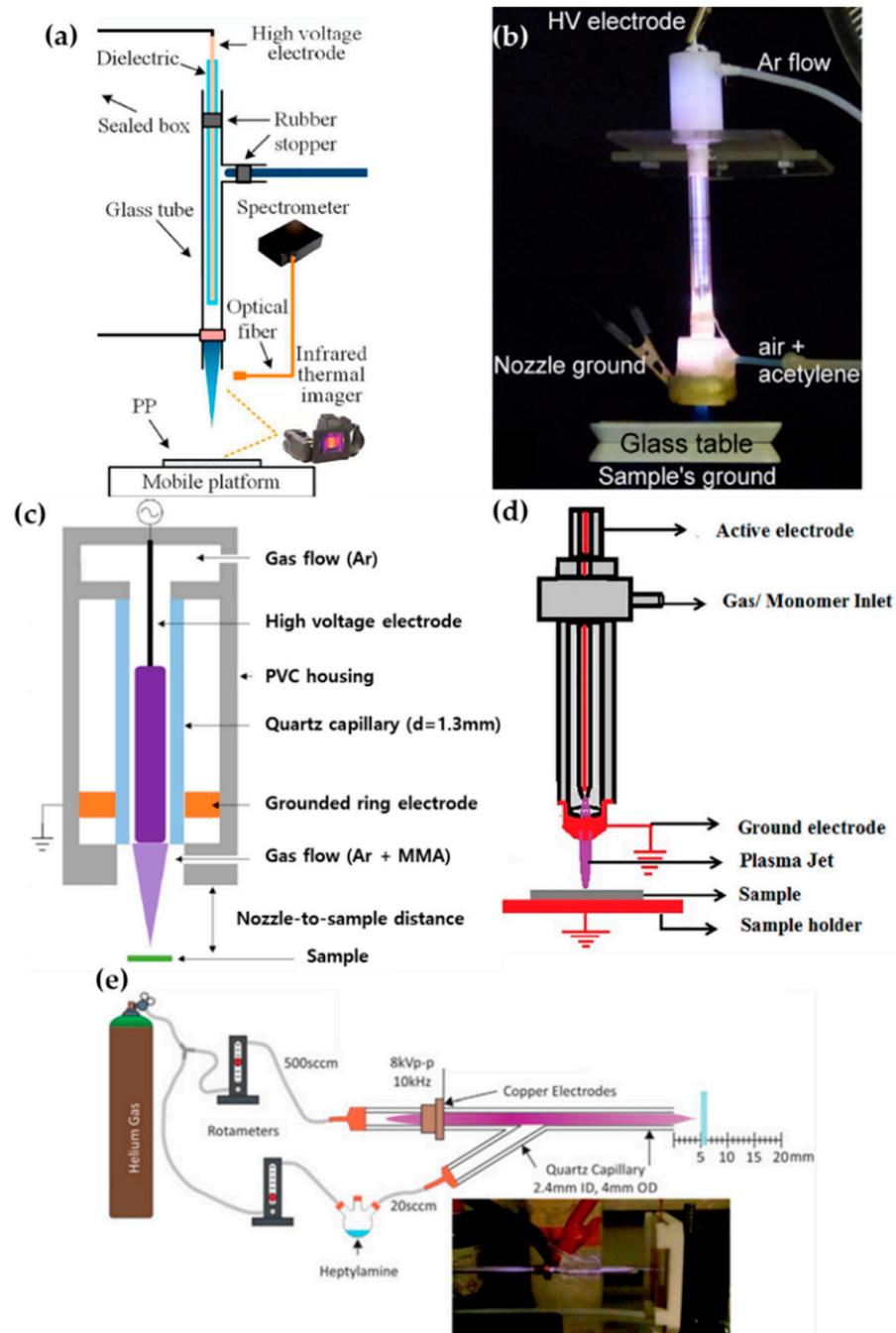
Figure 2. Structures of pin–ring-electrode-type APPJs from (**a**) Zhang et al. [51], (**b**) Ricci Castro et al. [52], (**c**) Van Vrekhem et al. [53], and (**d**) Pandiyaraj et al. [54], and (**e**) schematic of experiment using a y-shaped APPJ with a ring powered electrode, by Doherty et al. [55].

Ricci Castro et al. and Van Vrekhem et al. used a similar configuration of the APPJ for synthesizing plasma polymers: Two APPJs were utilized that both had tungsten pin electrodes; however, aluminum (Al) and copper (Cu) were used as grounded ring electrodes. As shown in Figure 2b,c, these APPJ devices consisted of three parts: the head of the

device had an HV electrode and a discharge gas inlet; the body was constructed of a glass tube; and the final component was a plasma nozzle with a grounded ring electrode and precursor inlet. In the paper by Ricci Castro et al., Ar was supplied for discharging, and an air/acetylene mixture gas was supplied as a precursor. The power source was at 19 kHz frequency and 17 kVp–p (peak-to-peak) voltage, consisting of two sinusoidal waves with disparate amplitudes to avoid overheating issues [52]. In the paper by Van Vrekhem et al., Ar gas was also used as the discharge gas, while aerosol MMA was bubbled by the Ar gas and input into the plasma afterglow region; this utilized power generation from a 23-kHz AC HV source to activate the APP [53].

The APPJ of Pandiyaraj et al. was fed the discharge gas, with the monomer in the same path. Both the pin and ring electrodes were made of Cu; the pin Cu electrode was encapsulated by a quartz tube (Figure 2d). Triisopropyl phosphate (TIP) was vaporized by heating to a maximum temperature of up to 500 °C, and the Ar discharge gas carried the TIP vapor into the inlet. Here, the AC power (maximum voltage = 40 kV; current = 30 mA; and frequency = 50 kHz) was supplied to generate the APP [54].

Doherty et al. synthesized the plasma polymer of heptylamine onto polystyrene. They used a y-shaped quartz capillary as the APPJ body, with a single powered ring electrode. Helium gas (He) used for plasma discharge was introduced in the downstream flow, and heptylamine aerosol was bubbled by the He introduced into the stream via a branch off the quartz body (Figure 2e). The supplied power was a sinusoidal current with a voltage of 8 kVp–p and a frequency of 10 kHz [55].

Kodaira et al. [56], Hossain et al. [57], and Malinowski et al. [58] proposed an APPJ with only pin-type electrodes for generating the APP, as shown in Figure 3. Kodaira et al. investigated the characterization of APP-polymerized hexamethyldisilazane (HMDSN); they used the same device as the studies from Ricci Castro et al. [52], but without a grounded ring electrode (Figure 3a). The power was also the same waveform, with 12 kVp–p. Both the discharge gas and HMDSN monomer carrier gas were Ar, which was introduced through the upper side and nozzle of the APPJ, respectively [56].
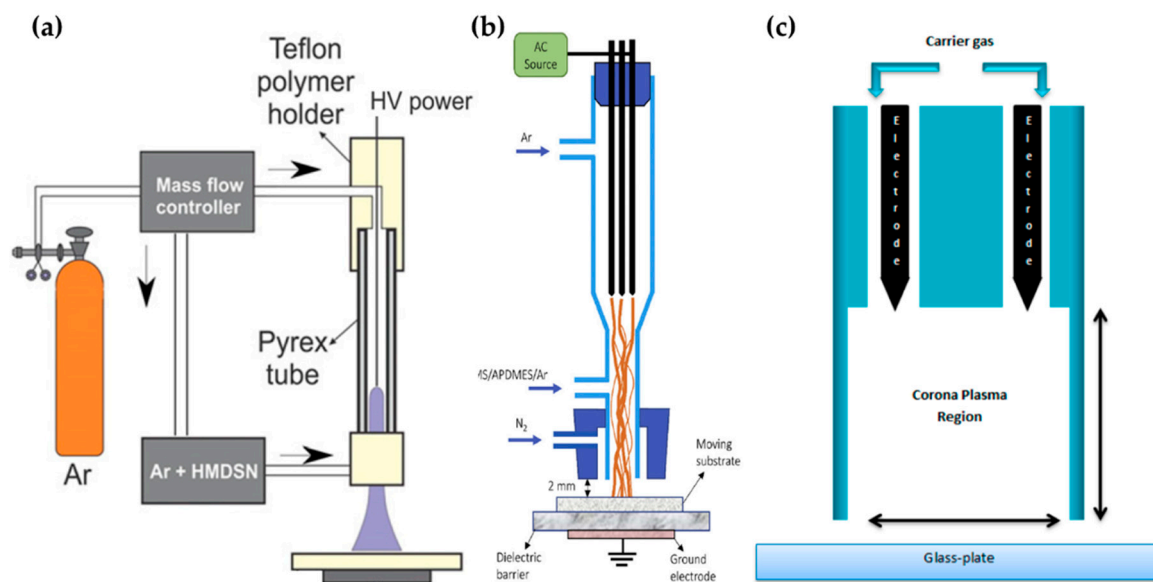
Figure 3. Structures of pin electrode type in the APPJs of (**a**) Kodaira et al. [56], (**b**) Hossain et al. [57], and (**c**) Malinowski et al. [58].

Hossain et al. reported the APP polymerization of tetramethylsilane (TMS) and 3-aminopropyl(diethoxy)methylsilane (APDMES) for superhydrophobic coatings on glass. The APP was generated from three pin electrodes, which were stainless steel needles arranged at 120° intervals in a DBD glass reactor. This glass had two branches as a gas inlet—the upper branch was the main Ar gas inlet for discharge, while the lower branch

guided the precursor flow. A cap was attached to the nozzle component, and nitrogen gas (N$_2$) was injected to shield the stream from interaction with the ambient air. A mixed liquid of TMS and APDMES was prepared as the precursor, and was bubbled with Ar (Figure 3b). This plasma reactor was served with AC power at a frequency of 11.5 kHz to generate the APP discharge [57].

A sinusoidal AC HV power source with a peak voltage of 2–6 kV and a frequency of 20 kHz was applied through two pin electrodes to generate He corona plasma for the deposition of laccase by Malinowski et al. (Figure 3c). The solution of laccase with 10% ethyl alcohol was then atomized by a nebulizer for precursor injection to the plasma region [58].

The research groups of Jang et al., Park et al., and Kim et al. [59–62] proposed an APPJ with three array jets and a unique shielding system. This system is called the guide-tube and bluff-body (GB) system. The guide tube that blocks the plasma reactor from ambient air is attached to the tip of the array jets, and the bluff body serves to introduce a substrate into the guide tube. The three jets are wrapped with Cu tape as HV electrodes (Figure 4a). Thanks to the ambient air blocking and special internal flow of the GB system, it is possible to expand the area of high-density plasma by more than 60 times (Figure 4b) [62]. They synthesized the copolymer [59], pin-hole-free polymer [60], conducting polymer [61], and single-crystalline polymer [62] using this APPJ device.
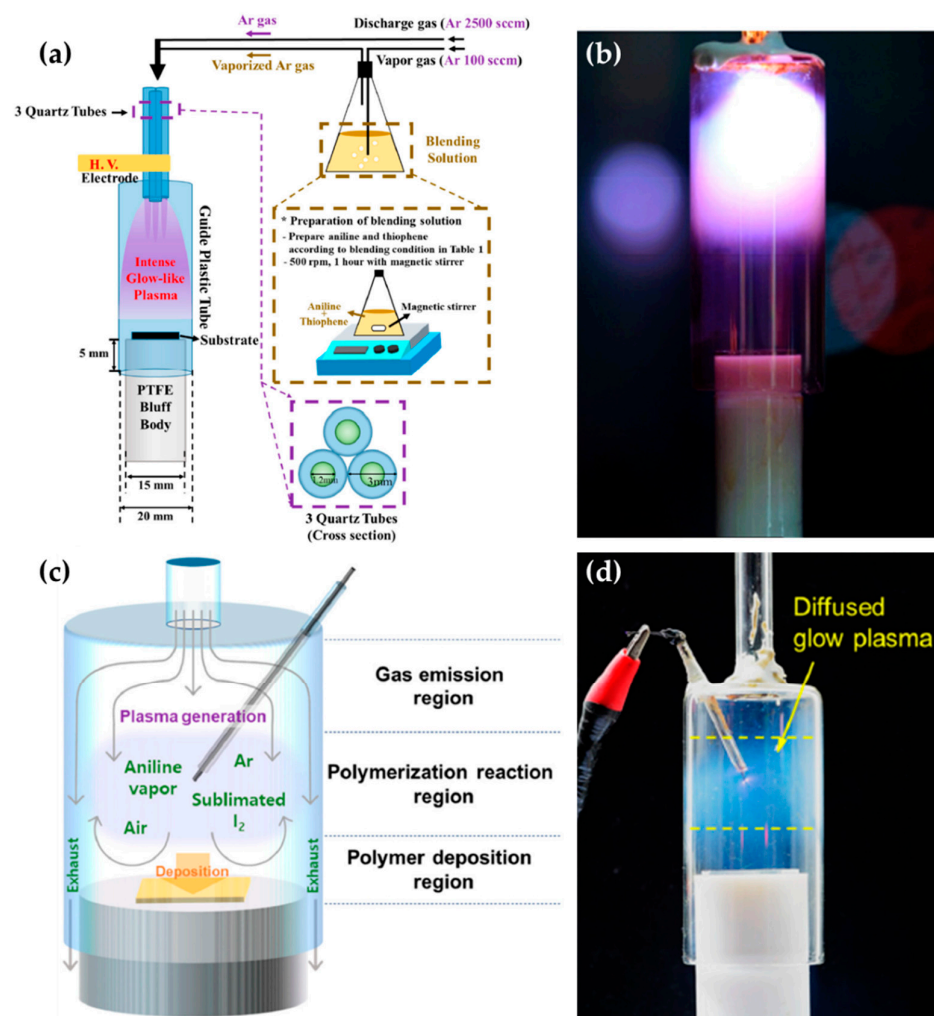
Figure 4. (**a**) Setup [59] and (**b**) photo image [62] of the APPJ with three array jets and a GB system. (**c**) Configuration [63] and (**d**) photo image [64] of the pin-type APPJ with a GB system.

Kim et al. report a pin-type APPJ with the GB system for synthesizing a conducting polymer [63] and a transparent polymer [64]. As shown in Figure 4c, this device consists of four components: a narrow glass for gas inlet, a wide glass tube as the guide tube, a polytetrafluoroethylene stand as the bluff body, and a tungsten wire electrode to generate plasma. The tungsten wire electrode is covered with a glass capillary, with just the 2-mm tip of the wire remaining exposed. A discharge gas and a precursor are introduced into the guide tube via the gas inlet. A sinusoidal power with a peak voltage of 4–5 kV and a frequency of 30 kHz is applied through the tungsten wire electrode, forming a diffused-glow plasma for polymerization (Figure 4d).

There are also studies using commercial APPJ devices; Karl et al. [65], Yan et al. [66], and Yang et al. [67] used a commercial plasma jet instrument (Plasmatreat AS400 with the single-nozzle-type PFW10, Figure 5a) to apply a superhydrophobic property to a target substrate by polymerizing hexamethyldisiloxane (HMDSO). A frequency of 19 kHz and a plasma voltage of 285 V were supplied to generate the plasma. The discharge gas (air, N_2, oxygen (O_2)) was introduced into this device, while the vapored precursor was transported to the nozzle component by the carrier gas (Ar, N_2). Yan et al. and Yang et al. put the plasma jet instrument onto a moving system (Figure 5b), and Moosburger-Will et al. demonstrated that this APPJ method is advantageous for in-line processing [68]. They also used the same plasma jet (PFW10) for the deposition of methyltrimethoxysilane onto 1200 m of carbon fiber (Figure 5c). Table 1 presents a summary of this subsection.
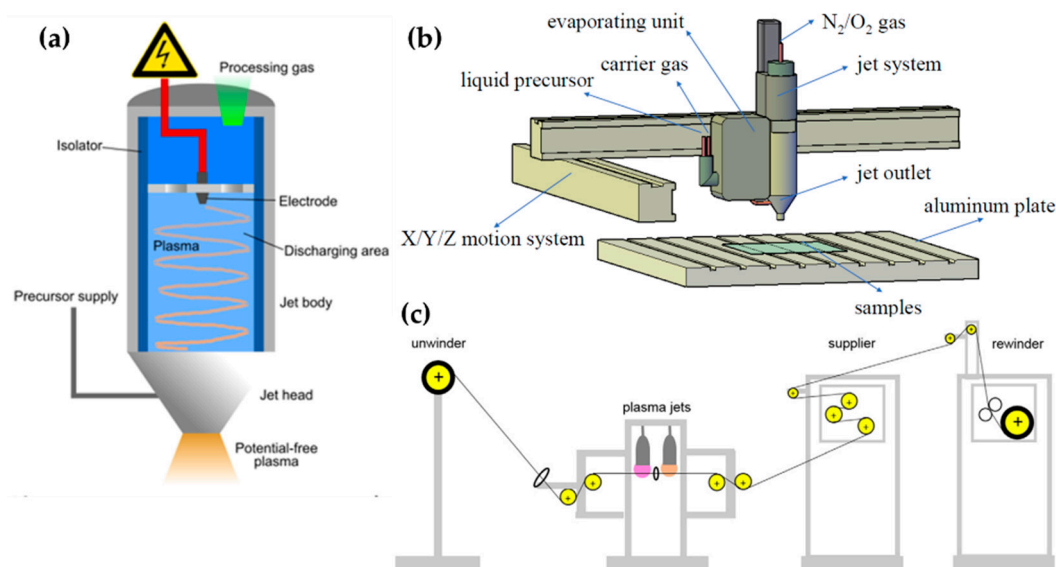
Figure 5. (**a**) The plasma jet instrument schematic (Plasmatreat AS400 with the single-nozzle-type PFW10) [65], and setup of (**b**) polymerization of HMDSO [67] and (**c**) in-line processing of carbon fiber [68].

2.2. Planar Dielectric-Barrier Discharge (DBD) Method

A planar DBD generator is typically a structure in which one or both planar electrodes are covered by dielectric material in order to avoid arc formation while facing one another [69,70]. When an HV current is applied to one side, a glow plasma is created between the electrodes. Since the size of the plasma area depends on the size of the electrodes, it is easier to cover a wider area with this method than with the APPJ method.

Table 1. Summary of the synthesis of polymers using APPJ methods.

No	Object	Precursor	Power	Year	Author Reference
1	Improvement of flashover performance of polypropylene surface	methyl-methacrylate (MMA)	Ar gas RF power (17 kV, 10~60 kHz)	2020	Zhang et al. [51]
2	Deposition of polymer film from Ar/air/acetylene	Acetylene	Air, Ar gas AC Pulse (Sine) (12 kV, 19 kHz, 2.8 W)	2017	Ricci Castro et al. [52]
3	Deposition of PMMA film	MMA	Ar gas AC Pulse power (23 kHz, 2 W)	2018	Vrekhem et al. [53]
4	Deposition of phosphorous containing functional coatings	Triisopropyl phosphate (TIP)	Ar gas (1 kPa) AC Pulse power (40 kV, 50 kHz)	2019	Pandiyaraj et al. [54]
5	Polymerization of heptylamine	Heptylamine	He gas AC Pulse (Sine) (8 kV, 10 kHz)	2019	Doherty et al. [55]
6	Polymerization of HMDSN	Hexamethyldisilazane (HMDSN)	Air, Ar gas AC Pulse (Sine) (12 kV, 19 kHz, 2.8 W)	2017	Kodaira et al. [56]
7	Superhydrophobic coating	Tetramethylsilane (TMS), 3-aminopropyl(diethoxy)methylsilane (APDMES)	Ar gas RF power (7.5 kV, 11.5 kHz)	2019	Hossain et al. [57]
8	Durable bioactive coating	Laccase	He gas AC Pulse (2~6 kV, 20 kHz)	2018	Malinowski et al. [58]
9	Copolymerization	Mixture of thiophene and Aniline	Ar gas AC Pulse (Sine) (23 kV, 26 kHz)	2020	Jang et al. [59]
10	Polymerization of PMMA	MMA	Ar gas AC Pulse (Sine) (12 kV, 30 kHz)	2019	Park et al. [60]
11	Humidity-independent conducting polymer	aniline	Ar gas AC Pulse (Sine) (8 kV, 26 kHz)	2017	Park et al. [61]
12	Single-crystalline polymer film	Pyrrole	Ar gas AC Pulse (Sine)(12 kV, 30 kHz)	2017	Kim et al. [62]
13	Conducting polymer film	aniline	Ar gas AC Pulse (Sine) (5 kV, 30 kHz)	2021	Kim et al. [63]
14	Transparent thin film	aniline	Ar gas AC Pulse (Sine) (4 kV, 30 kHz)	2021	Kim et al. [64]
15	Deposition from organosilicon	HMDSO, Tetraethyl orthosilicate (TEOS)	Air, N_2 gas Pulse power (19 kHz, 1 kW)	2020	Karl et al. [65]
16	Preservation of paper-based relics	HMDSO	Air, Ar gas Pulse power	2019	Yan et al. [66]
17	Superhydrophobic cotton fabrics	HMDSO	O_2, N_2 gas RF power (19 kHz)	2018	Yang et al. [67]
18	Reinforcement of carbon fiber	Methyltrimethoxysilane (MTMS)	Ar gas AC Pulse (252 V, 21 kHz, 600 W)	2017	Moosburger-Will et al. [68]

Pandivaraj et al. [69], Ramkumar et al. [70], Mertens et al. [71], Getnet et al. [72], and Dvorˇáková et al. [73] report polymer deposition by using planar DBD with fixed electrodes, as shown in Figure 6. Pandivaraj et al. used a plasma generator with a typical DBD structure to increase the antifouling properties of low-density polyethylene (LDPE) films by copolymerizing. This plasma generator consisted of two square electrodes covered by a dielectric material sheet (polypropylene with a thickness of 3 mm) and a chamber. Two electrodes were placed in the chamber with a separation distance of 7 mm. The LDPE film was placed on the lower electrode (grounded electrode), and the plasma was generated by AC power with a voltage of 40 kV and a frequency of 50 Hz through the

upper electrode (powered electrode) (Figure 6a). Thereafter, a mixture vapor of acrylic acid and polyethylene glycol (PEG) produced by heat (80 °C and 220 °C respectively) was fed into the chamber [69]. Ramkumar et al. used the same device and procedure as Pandivaraj et al.; however, they employed PEG methyl ether methacrylate (PEGMA) as a precursor to enhance the biocompatibility of LDPE films. The gap between the electrodes was 5 mm and the PEGMA vapor was prepared at 60 °C [70].

Mertens et al. employed two electrodes covered with different dielectric materials for hydrophilic and hydrophobic coatings for about 11 substances. The upper Cu electrode (powered electrode) and the lower Cu electrode (grounded electrode) were covered by a 3-mm-thick α-alumina and a 2-mm-thick borosilicate, respectively. The gap between the two electrodes was 4 mm. This plasma generation system was placed in a Pyrex glass cylinder chamber. The inside of the chamber was pumped down to 270 Pa and filled to atmospheric pressure with Ar. The precursor bubbled by a secondary flow was introduced into the plasma region by diluting it with the primary flow (Figure 6b) [71].

Getnet et al. conducted the deposition of carvacrol thin film on a stainless steel substrate using a DBD generator with only the lower-side electrode (grounded electrode) covered with a polyester sheet as a dielectric layer. Two parallel circular brass electrodes were fixed at 3 mm. A sinusoidal AC pulse with a frequency of 60 Hz and a maximum voltage of 15 kV was applied to the upper electrode (powered electrode). Ar at a flow of 5 L/min was used for the plasma discharge and vaporizing the carvacrol (Figure 6c) [72].

Dvořáková et al. used diffuse coplanar surface barrier discharge (DCSBD) methods for fast surface hydrophilization. The DCSBD device was described as a set of parallel, strip-like molybdenum electrodes embedded in alumina as a dielectric material [88]. The thin-layer plasma was generated on the DCSBD surfaces when a high-voltage sine wave was applied to DCSBD electrodes. The substrate holder was fixed at 0.1 mm from the DCSBD surface. A gas mixture of propane, butane, and N_2 was supplied via a gas inlet in the middle of the substrate holder (Figure 6d) [73].

Bardon et al. [74], Manakhov et al. [75], Obrusník et al. [76], and St'ahel et al. [77] used a movable upper electrode with a gas inlet for improving the deposition uniformity [75], as shown in Figure 7. Bardon et al. improved the coating's mechanical properties by using DBD plasma and mixtures of dodecyl acrylate (DOCA) with 1,6-hexanediol diacrylate (HdiA) or 1,6-hexanediol dimethacrylate (HdiMA) as precursors. The DBD generator consisted of an earthed-bottom aluminum plate and two powered aluminum top plates covered with a 3.25 mm-thick glass plate. The gap between the bottom electrode and the glass plate was set to 2 mm. The bottom electrode had a slot as a sample holder to set the surface of the samples and the electrode at the same level (Figure 7a) [89]. The precursor mixture was atomized to an aerosol state using He, entering the space between the top electrodes. For the plasma generation, an AC power of 110 W with a peak-to-peak voltage of 11 kV was used [74].

Manakhov et al. utilized a DBD plasma system to copolymerize maleic anhydride (MA) and C_2H_2 for carboxyl-rich coatings in a metallic cube chamber. The two rectangular pieces were separated to provide room for the gas feed, while the top electrode was covered with Al_2O_3 ceramics with a thickness of 1 mm, and the bottom metallic electrode (grounded electrode) was also covered with the ceramic. The gap between the top and bottom ceramics was set at 1.6 mm (Figure 7b). This chamber was pumped down, and then filled up to 96 kPa with Ar, MA, and C_2H_2 as a deposition gas mixture. The plasma was ignited by a sinusoidal wave with a frequency of 5–6.6 kHz and a power of 8 W [75]. Obrusník et al. and St'ahel et al. used a plasma-generating system with the same electrode configuration as Manakhov et al., albeit in open air; the gas was supplied through the inlet in the middle of the top electrode connected to a 4-cm-long rectangular duct (Figure 7c) [76]. In the work of St'ahel et al., a heating spiral was added to the bottom electrode along with a thermocouple to increase the substrate temperature, and the gap between the electrodes was changed to 1.0 mm (Figure 7d) [77].
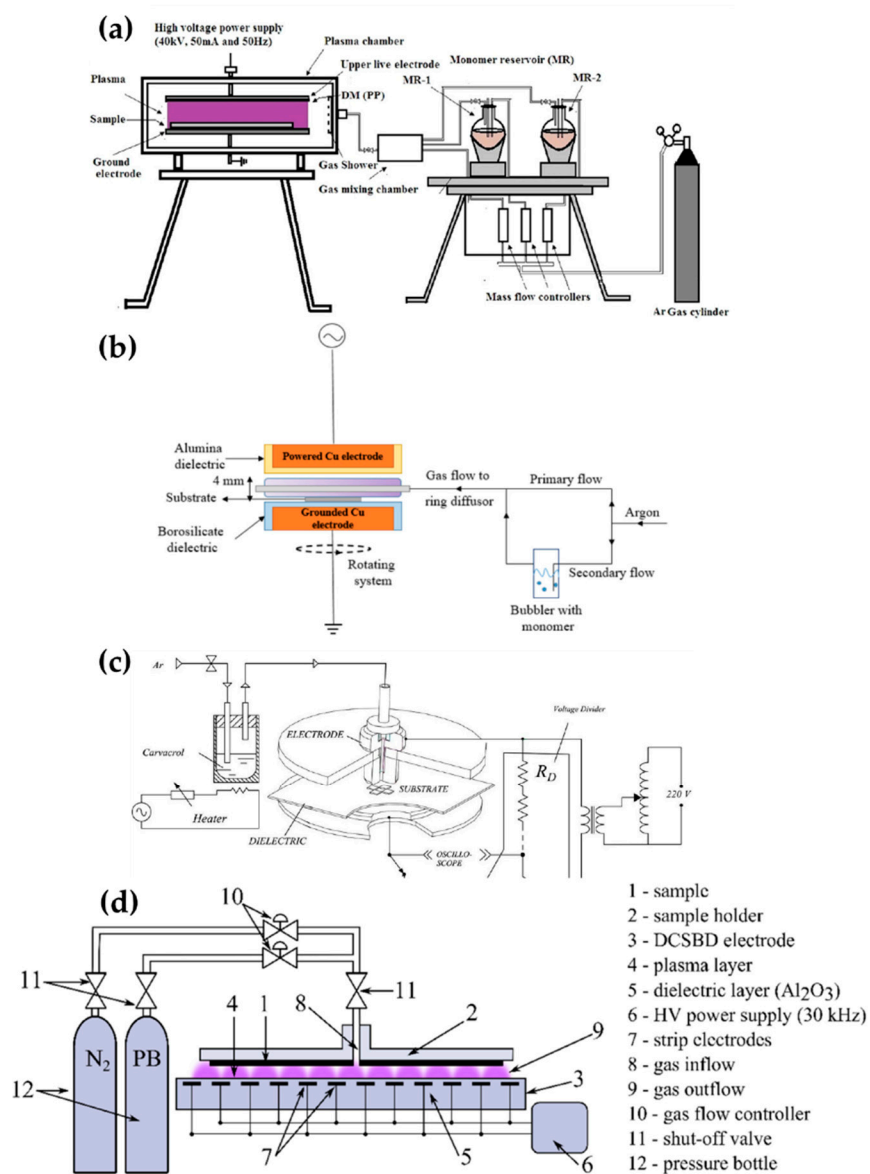
Figure 6. The polymerization systems using planar DBD of (**a**) Pandivaraj et al. [69], (**b**) Mertens et al. [71], (**c**) Getnet et al. [72], and (**d**) Dvorˇáková et al. [73].

Demaude et al. [78], Nisol et al. [79], Jalaber et al. [80], Ma et al. [81], Ondo et al. [82], and Loyer et al. [83–85] employed a DBD plasma generator with a moving substrate stage (bottom electrode) for homogeneous coverage and scale-up [79,81], as shown in Figure 8. Demaude et al. and Nisol et al. synthesized a polymer for hydrophilic/phobic patter coating [78] and age-resistant coating [79], respectively. In this DBD plasma device, a long aluminum strip covered with a 4-mm-thick borosilicate glass plate was used as a movable lower electrode, while the upper electrode consisted of two Cu plates, with a separation between the plates for a gas/precursor inlet. Both the discharge gas and precursor bubbling/carrier gas were Ar (Figure 8a) [78,79].
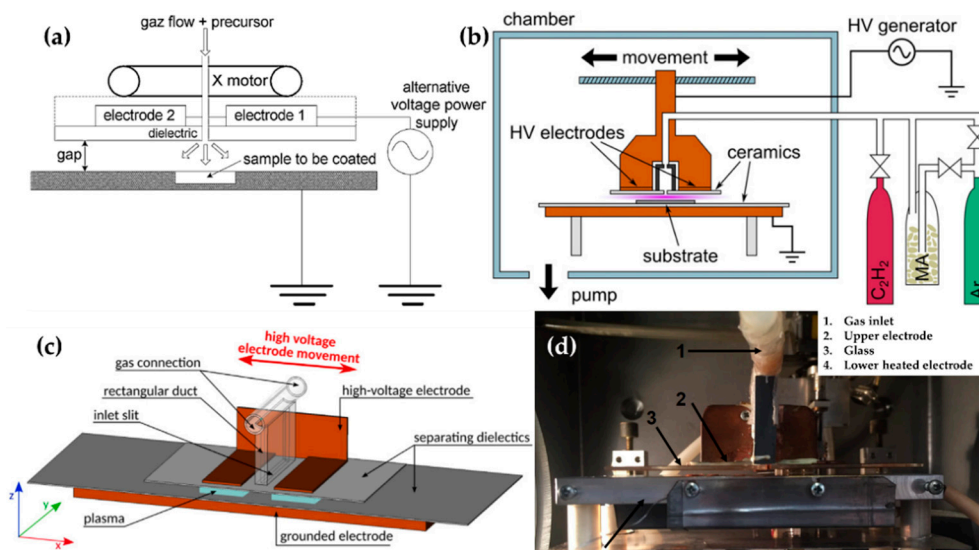
Figure 7. The polymerization systems using planar DBD with a movable top electrode (powered electrode) of (**a**) Bardon et al. [74,89], (**b**) Manakhov et al. [75], and (**c**) Obrusník et al. [76], and the image of the DBD system of (**d**) St'ahel et al. [77].
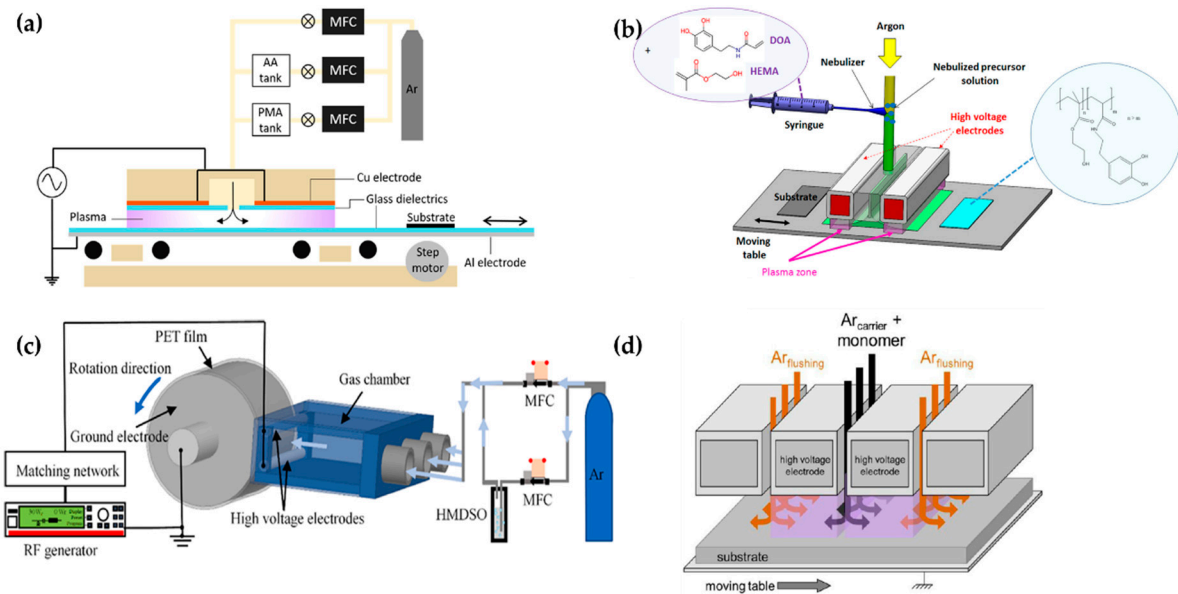
Figure 8. The polymerization systems using planar DBD with a movable substrate stage (bottom electrode) of (**a**) Demaude et al. [78], (**b**) Jalaber et al. [80], (**c**) Ma et al. [81], and (**d**) Loyer et al. [83].

Jalaber et al. used DBD plasma polymerization for eco-friendly and catalyst-free polymer synthesis. Their device ignited the DBD plasma from between two plane-parallel HV electrodes covered with alumina and a movable substrate stage as a grounded electrode. The distance between the HV electrodes and the substrate stage was 1 mm. A 10 kHz sinusoidal voltage was applied through two plane-parallel electrodes to generate the plasma. Dopamine acrylamide as the precursor was atomized using a nebulizer, and its flow was controlled with a syringe pump (Figure 8b) [80].

Ma et al. utilized a plasma device with a rolling electrode system; two cylindrical HV electrodes (Φ = 4 mm; length = 100 mm) were fixed at a distance of 7 mm from the top layer and the bottom layer of the outlet of the gas chamber. The cylindrical ground electrode (Φ = 60 mm; length = 100 mm) was made of stainless steel and controlled by a motor. Within the triple-inlet gas chamber, some glass wool pieces were placed inside to provide gas flow homogeneity. The ground electrode was wrapped in the PET substrate

(Figure 8c). A 13.56 MHz RF power source with 30 W applied through the HV electrodes ignited the plasma in open-air conditions [81].

Ondo et al. and Loyer et al. used a polymerization method called plasma-initiated chemical vapor deposition (PiCVD). This method is characterized by the usage of an ultra-short square-wave pulse power to ignite the DBD plasma for the deposition of a polymer film with a high degree of polymerization [82–85]. This plasma generator consisted of two parallel HV electrodes made of alumina and a movable stage as the ground electrode [90]. The gap between the parallel electrodes and the ground electrode was maintained at 1 mm (Figure 8d). An ultra-short square-wave pulse was employed to generate the plasma with an extremely low plasma duty cycle ($t_{on}/(t_{on} + t_{off})$); a very low duty cycle plasma (0.1~0.001%) was employed for their studies [82–85]. Table 2 shows a summary of this subsection.

Table 2. Summary of the synthesis of polymer films using planar DBD plasma.

No	Object	Precursor	Plasma Source	Year	Author Reference
1	Improvement of antifouling properties	mixture of acrylic acid (AAC) and poly (ethylene glycol) (PEG)	Ar gas AC Pulse (14 kV, 44 kHz)	2019	Pandiyaraj et al. [69]
2	Enhancement of biocompatibility	poly (ethylene glycol) methylether methacrylate (PEGMA)	Ar gas AC Pulse (14 kV, 44 kHz)	2017	Ramkumar et al. [70]
3	Hydrophilic and hydrophobic coatings	11 precursors for hydrophilic and hydrophobic coatings	Ar gas AC Pulse (17.1 kHz)	2020	Mertens et al. [71]
4	Inhibition of bacteria adhesion and proliferation	Carvacrol (5-Isopropyl-2-methylphenol, $(CH_3)_2CHC_6H_3(CH_3)OH$)	Ar gas AC Pulse (15 kV, 60 Hz)	2020	Getnet et al. [72]
5	Surface hydrophilization	propane-butane (PB) gas	N2 gas AC Pulse (30 kHz)	2019	Dvořáková et al. [73]
6	Reinforcement of mechanical properties of DOCA film	Dodecyl acrylate (DOCA), 1,6-hexanediol diacrylate (HdiA), 1,6-hexanediol dimethacrylate (HdiMA)	He gas AC Pulse (11 kV, 10 kHz, 110 W)	2018	Bardon et al. [74]
7	Carboxyl-rich coatings	maleic anhydride (MA), acetylene	Ar gas AC Pulse (Sine) (4 kV, 5~6.6 kHz, 8 W)	2016	Manakhov et al. [75]
8	Copolymerization	MA, acetylene	Ar gas AC Pulse (4 kV, 4 kHz, 3.3 W)	2017	Obrusník et al. [76]
9	Antibacterial properties and cytocompatibility performance	2-methyl-2-oxzoline, polyoxazoline (POx)	Ar gas AC Pulse (6 kHz, 55 W)	2019	Sťahel et al. [77]
10	Hydrophilic/phobic patterns	acrylic acid (AA) propargyl methacrylate (PMA)	Ar, O_2 gas AC Pulse (Sine) (16.2 kHz, 90 W)	2019	Demaude et al. [78]
11	Age-resistant coatings with tunable wettability	AA, PMA	Ar gas AC Pulse (Sine) (15.64 kHz, 30 to 90 W)	2016	Nisol et al. [79]
12	Preparation of tunable catechol-bearing thin films	dopamine acrylamide (DOA) 2-hydroxyethyl methacrylate monomer (HEMA)	Ar, O_2 gas AC Pulse (Sine) (10 kHz)	2019	Jalaber et al. [80]
13	Hydrophilicity	HMDSO	Ar gas 13.56 MHz RF (30 W)	2020	Ma et al. [81]
14	Low-k Polymer Insulating Layers	4 cyclic organosilicon monomers	N2 gas AC square Pulse (6 kV, 100 Hz)	2019	Ondo et al. [82]
15	Comparison of polymer properties according to applied duty cycle	3 methacrylate monomers (MMA, BMA, GMA)	Ar gasAC square Pulse (6.5 kV, 10 kHz)	2017	Loyer et al. [83]

Table 2. *Cont.*

No	Object	Precursor	Plasma Source	Year	Author Reference
16	Comparison of polymer properties according to applied duty cycle	2 methacrylate monomers (MMA, GMA)	Ar gas AC square Pulse (6.5 kV, 10 kHz)	2018	Loyer et al. [84]
17	Deposition of NVCL with water-stable and thermo-responsive properties	*N*-vinyl caprolactam (NVCL) ethylene glycol dimethacrylate (EGDMA)	Ar gas AC square Pulse (6.5 kV, 10 kHz)	2019	Loyer et al. [85]

3. Synthesis Method Using Liquid-Type Precursors

APP synthesis methods using liquid-type precursors leverage the interaction between APP and a bulk liquid precursor. The complicated chemical and physical reactions at the plasma–liquid interface cause reduction, oxidation, and sputtering. In most cases, NPs are synthesized from the various radicals generated by the plasma–liquid reactions [43,91]. This method is classified into two types, depending on the location of the APP generation.

3.1. Atmospheric-Pressure Plasma (APP) Generated by Outside Bulk Liquid Precursors

APP generated on the outside of bulk liquid precursors—so-called (on-solution plasma)—is affected by natural air components. Therefore, chemical and physical reactions at the plasma–liquid interface take place with various species caused by the interaction between the APP and air components such as O_3, N_2O_5, N_2O, NHO_3, H_2, NO_3, H_2O_2, HNO_2, and NO_2 [38]. Complex reactions that are not well understood due to various radicals can produce unusual results [92].

Tan et al. [93,94], Schäfer [95] et al., Zhang et al. [96], and Gamaleev et al. [97] used on-solution plasma generated by various methods, as shown in Figure 9. Tan et al. employed an APPJ with a cross-shaped borosilicate glass body with five nozzles as a plasma outlet, two inlets for Ar flow as a discharge gas, and two side tubes for the electrodes. The power and ground electrodes were made of tungsten, with a separation of 5 mm (Figure 9a). An AC power source with a voltage of 15 kV and a frequency of 60 Hz was applied from a neon sign transformer to ignite the APP. This APP treats the surface of styrene [93] and MMA [94] as bulk liquid precursors (Figure 9b).

Schäfer et al. synthesized three liquid organosilicon compounds (HMDSO, octamethyl-tetrasiloxane, and tetrakis(trimethylsilyloxy)silane) as precursors using a commercial APPJ (kINPen 11; neoplas tools, Greifswald, Germany). This commercial APPJ consisted of a powered pin electrode centered in a ceramic capillary and a grounded outer ring electrode. Ar gas was introduced as a discharge gas through the ceramic capillary (Figure 9c). A power source of 5 W with a frequency of 1.1 MHz was needed to generate the APP. Liquid precursors were applied to the surface of the substrate, and these were synthesized by exposure to the APP (Figure 9d) [95].

Zhang et al. utilized the discharge between a stainless steel capillary and a liquid bulk surface to synthesize the metallic NPs embedded in a conducting polymer. In this research, the liquid precursor was $HAuCl_4$ aqueous solution added to poly(3,4-ethylenedioxy thio-phene) polystyrene sulfonate (PEDOT:PSS). This APP generator system used a stainless steel capillary as the powered electrode and a carbon rod as the grounded electrode. The stainless steel capillary also acted on the APPJ generating the He plasma. The distance between the tip of the capillary and the surface of the liquid precursor was 0.9 mm (Figure 9e). The APP was ignited by direct current (DC) with a voltage of 2 kV, and maintained by a voltage of 0.8 kV [96].

Gamaleev et al. employed a pin-type electrode for the generation of on-solution plasma to produce nanographene. First, 100 mL of ethanol liquid precursor was placed in a beaker. A Cu plate grounded electrode was immersed in the ethanol, and a Cu rod powered electrode was placed in the air. The beaker was filled in at a flow rate of 5 slm (Figure 9f) [97]. Table 3 contains a summary of this subsection.
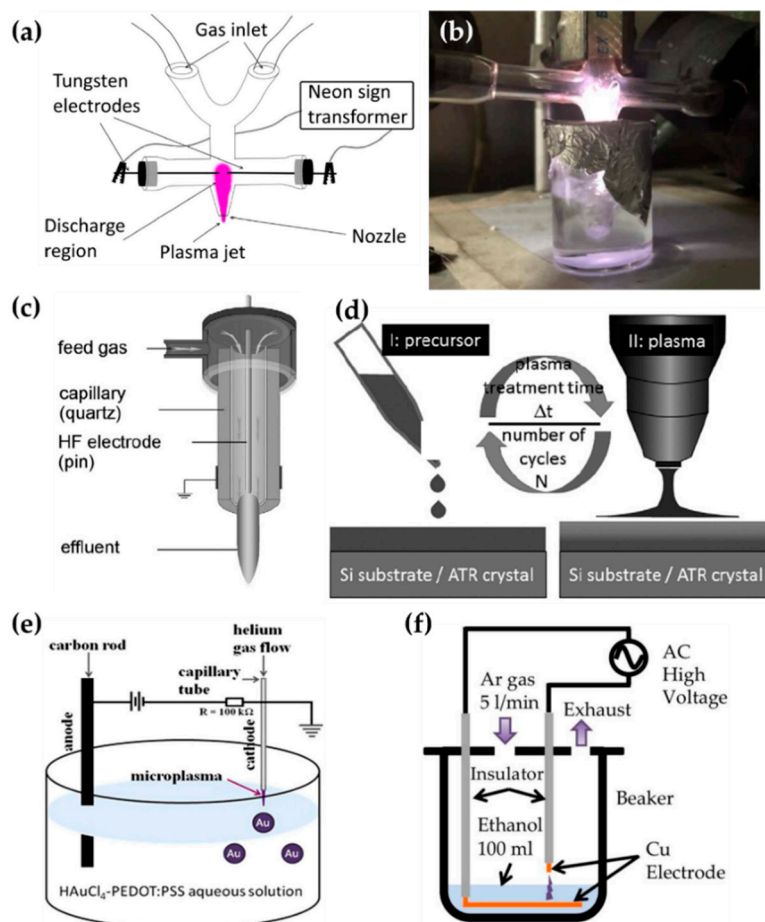
Figure 9. Schematics of generation of the on-solution plasma systems of (**a**,**b**) Tan et al. [93,94], (**c**,**d**) Schäfer [95] et al., (**e**) Zhang et al. [96], and (**f**) Gamaleev et al. [97].

Table 3. Summary of syntheses using on-solution plasma methods.

No	Object	Precursor	Plasma Source	Year	Author Reference
1	Plasma-treated styrene	Styrene	Ar gas AC Pulse (15 kV, 60 Hz, 450 W)	2018	Tan et al. [93]
2	Plasma-treated MMA	MMA	Ar gas AC Pulse (15 kV, 60 Hz, 450 W)	2020	Tan et al. [94]
3	Thin, solid SiO_x film	HMDSO, octamethyltetrasiloxane (OMCTS), tetrakis(trimethylsilyloxy)silane (TTMS)	Ar gas AC Pulse (1.1 MHz, 5 W)	2017	Schäfer et al. [95]
4	Metallic NPs embedded in a conducting polymer	HAuCl4 aqueous solution, poly(3,4-ethylenedioxy thiophene) polystyrene sulfonate (PEDOT:PSS)	He gas DC Pulse (ignition 2 kV, maintain 0.8 kV)	2017	Zhang et al. [96]
5	Nanographene	Ethanol	AC high voltage	2018	Gamaleev et al. [97]

3.2. Atmospheric-Pressure Plasma (APP) Generated by Inside Bulk Liquid Precursors

In this section, in-solution plasma is defined as generating the APP in liquid precursors. In-solution plasma is mostly generated between tungsten pin-to-pin electrodes. One of the structurally critical points of the in-solution plasma system is the gap between electrodes; the gap can induce a breakdown of plasma in liquid media [98–100]; therefore, tungsten is commonly chosen for synthesis using an in-solution plasma due to its high melting point,

corrosion resistance, high stability, and good electrical conductivity [101,102]. Since the in-solution plasma is immersed in the solution, only reactions between the plasma and the solution occur in their entirety. Many recent papers about synthesis methods using in-solution plasma have mostly been reported on the formation of NPs [103–112].

Hyun et al. [103,104], Panomsuwan et al. [105], Morishita et al. [106], Lee et al. [107], Li et al. [108], Tipplook et al. [109], and Lee et al. [91] used in-solution plasma systems generated by the plasma discharge between tungsten pin-to-pin electrodes, and Alsaeedi et al. [110] chose carbon rods as the electrodes, as shown in Figures 10–12. Hyun et al. used a pair of tungsten electrodes 1 mm in diameter to generate the in-solution plasma; these electrodes were located at a distance of 1.5 mm from the glass reactor. A bipolar HV pulse of 2 kV with a repetition frequency of 25–200 kHz and a pulse width of 1 μs was applied via the electrodes. Liquid precursors such as *N*-methyl-2-pyrrolidone, 2-pyrrolidone, pyrrolidine, 1-methylpyrrolidine, pyrrole, cyclopentanone, and cyclohexanone were used for the synthesis of nitrogen–carbon nanosheets (Figure 10a) [103,104].
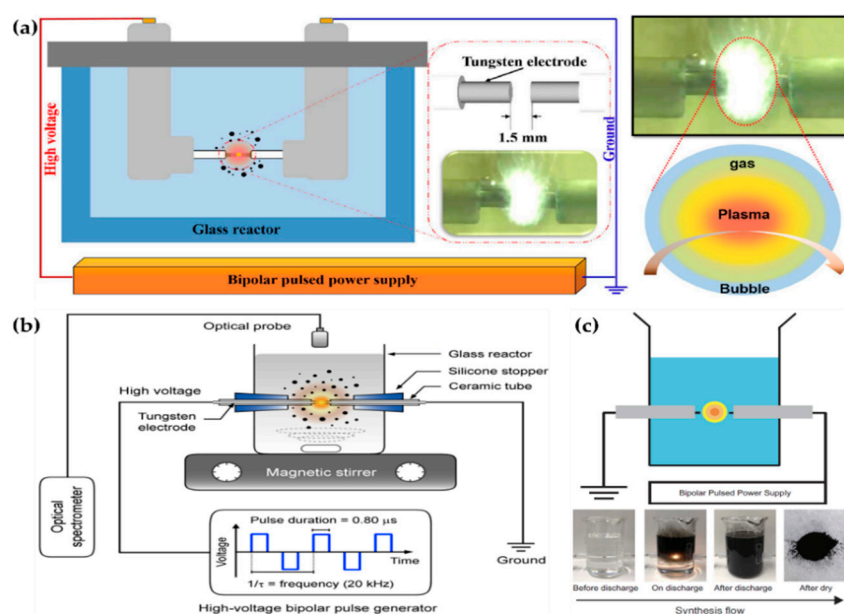
Figure 10. Representative figures on the generation of the in-solution plasma systems of (**a**) Hyun et al. [104], (**b**) Panomsuwan et al. [105], and (**c**) Morishita et al. [106].

Panomsuwan et al. also used a pair of tungsten electrodes 1 mm in diameter. The electrodes were covered with an insulating ceramic tube, and had a gap of 1 mm. The bipolar power source used had a pulse duration of 0.80 μs and a frequency of 20 kHz. In-solution plasma was initiated and stably maintained inside 100 mL of liquid precursor under vigorous stirring (Figure 10b). Cyano-aromatic molecules (2-cyanopyridine, cyanopyrazine) were used as liquid precursors for the synthesis of nitrogen-doped carbon NPs (NCNPs) [105].

Morishita et al. also employed tungsten electrodes 1 mm in diameter for in-solution plasma. The electrodes were covered with a ceramic segment, and the distance between them was set to 0.5 mm. The applied voltage was about 1.7 kV, the repetition frequency was 15 kHz, and the pulse width was 1.0 μs. The precursors for the fast formation of nanocarbons were hexane, hexadecane, cyclohexane, and benzene. For the extraction of nanocarbons, plasma-treated precursors were dried at 100 °C in an oven (Figure 10c) [106].
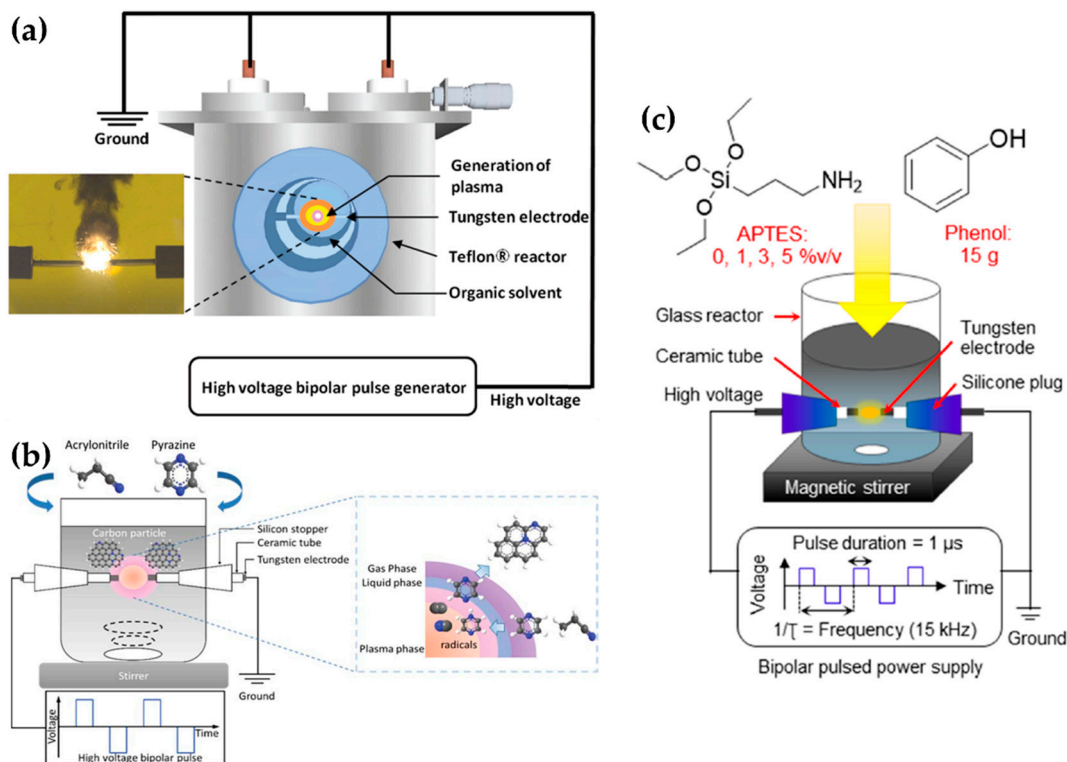
Figure 11. Schematics of generation of the in-solution plasma systems of (**a**) Lee et al. [107], (**b**) Li et al. [108], and (**c**) Tipplook et al. [109].
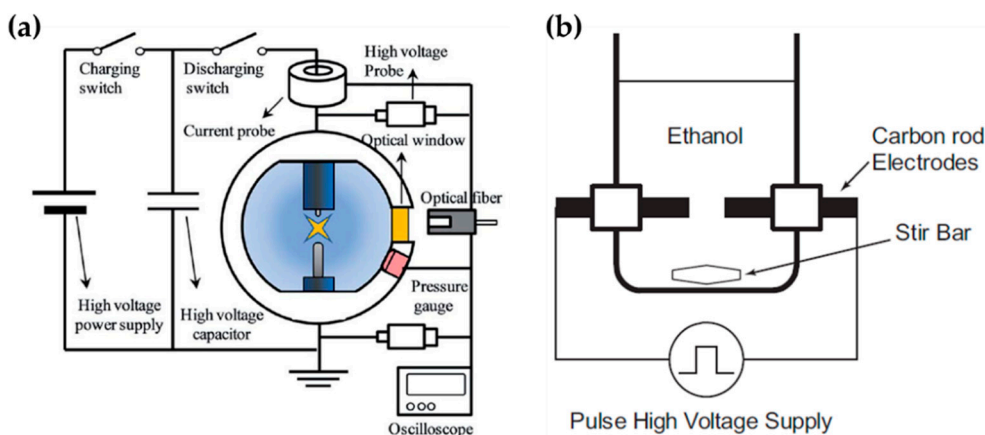
Figure 12. Schematic diagrams of the in-solution plasma systems proposed by (**a**) Lee et al. [91] and (**b**) Li et al. [110].

Lee et al. selected a pair of tungsten electrodes with a diameter of 0.8 mm, covered with an insulating ceramic tube. The electrodes were placed in the center of the Teflon reactor with a gap distance of 1.0 mm (Figure 11a). The optimized applied voltage conditions of in-solution plasma were found to be 0.5 μs, 100 kHz, and 2 kV for the pulse duration, pulse repetition frequency, and voltage, respectively. In-solution plasma was produced from various solvents—such as carbon, nitrogen, and boron precursors—for synthesizing boron–carbon–nitrogen nanoparticles [107].

Li et al. employed a pair of tungsten electrodes with a diameter of 1 mm as the powered electrode and grounded electrode. These electrodes were placed at the center of a glass reactor with a gap distance of 0.5 mm. To ignite the plasma discharge of the in-solution plasma system, power was applied by using a bipolar pulse with a voltage of

2.0 kV. The pulse duration and repetition frequency were 1 µs and 20 kHz, respectively (Figure 11b). NCNPs were synthesized from pyrazine and acrylonitrile [108].

Tipplook et al. used in-solution plasma as an in situ system for the synthesis of amino-rich nanocarbons. This system had a pair of tungsten rods with a diameter of 1 mm as the powered and grounded electrodes. The electrodes were covered with an insulating tube, inserted into a silicone stopper, and placed at the center of the glass reactor, 1 mm apart. The glass reactor (Figure 11c) contained 100 mL of a liquid precursor (phenol, (3-aminopropyl)triethoxysilane, and ethanol). Then, a HV bipolar pulse power with a voltage of 4kV, a pulse duration of 1 µs, and a repetition frequency of 15 kHz was applied through the electrodes to generate the in-solution plasma [109].

Lee et al. chose an in-solution plasma system with an asymmetrical pair of tungsten needle electrodes. The diameter of the anode was 1.5 mm, and the gap between the electrodes was 5 mm. Five capacitors with a capacitance of 0.1 µF were connected in parallel, and the capacitors with equivalent capacitance of 0.5 µF were charged by a positive-polarity DC power supply with a maximum charging voltage of 19 kV (Figure 12a). Titanium tetraisopropoxide dissolved in ethanol (Ti-contained solution) was used as a liquid precursor to synthesize carbon-incorporated titanium oxide nanocrystals [91].

Alsaeedi et al. reported that nanocarbons were successfully synthesized by using in-solution plasma. In this paper, the in-solution plasma was generated between two carbon electrodes. The carbon rod electrodes each had a diameter of 3 mm, and were separated by a gap of 1 mm. The electrodes were immersed in 50 mL of ethanol (Figure 12b), and the pulse voltage, frequency, and pulse width were 4 kV, 30 kHz, and 4 µs, respectively [110].

Shin et al. [111,112] added a gas bubble to the in-solution plasma system. The gas bubble was often used as a plasma channel to enhance in-solution plasma performance in pulsed discharge systems [111]. In a cylindrical glass reactor, the two tungsten electrodes were oriented 1 mm apart, and were positioned in the capillary glass tube for the Ar gas channel. The Ar gas was introduced along with two electrodes in parallel [111], thus forming a gas bubble channel between the electrodes. The gap between the glass capillaries was 3 mm. The plasma discharge was generated in a gas bubble between the electrodes in an aniline monomer acting as the liquid precursor (Figure 13a). A bipolar pulse with an amplitude of 16.4 kV and a frequency of 5 kHz was used to generate the in-solution plasma within the Ar bubble channel, and the bipolar pulse duty ratio was 60 µs [111].

Additionally, Shin et al. [112] also used an asymmetrical electrode structure: the tungsten electrode was placed in a quartz tube for the Ar gas inlet, where its diameter was 0.5 mm and its exact position extruded 1 mm from the end of the capillary quartz tube. On the other hand, a cylindrical copper electrode with a 5 mm width was wrapped around the outside surface of the quartz tube. The copper electrode was positioned 3 mm away from the end of the capillary quartz tube. There were two capillary tubes, with a separation distance of 2 mm. The plasma channel was formed from Ar gas with a flow rate of 100 sccm. A bipolar pulse with a voltage of 16 kV, a frequency of 5 kHz, and a pulse width of 100 µs was employed to generate the in-solution plasma (Figure 13b) [112]. Table 4 displays a summary of this subsection.
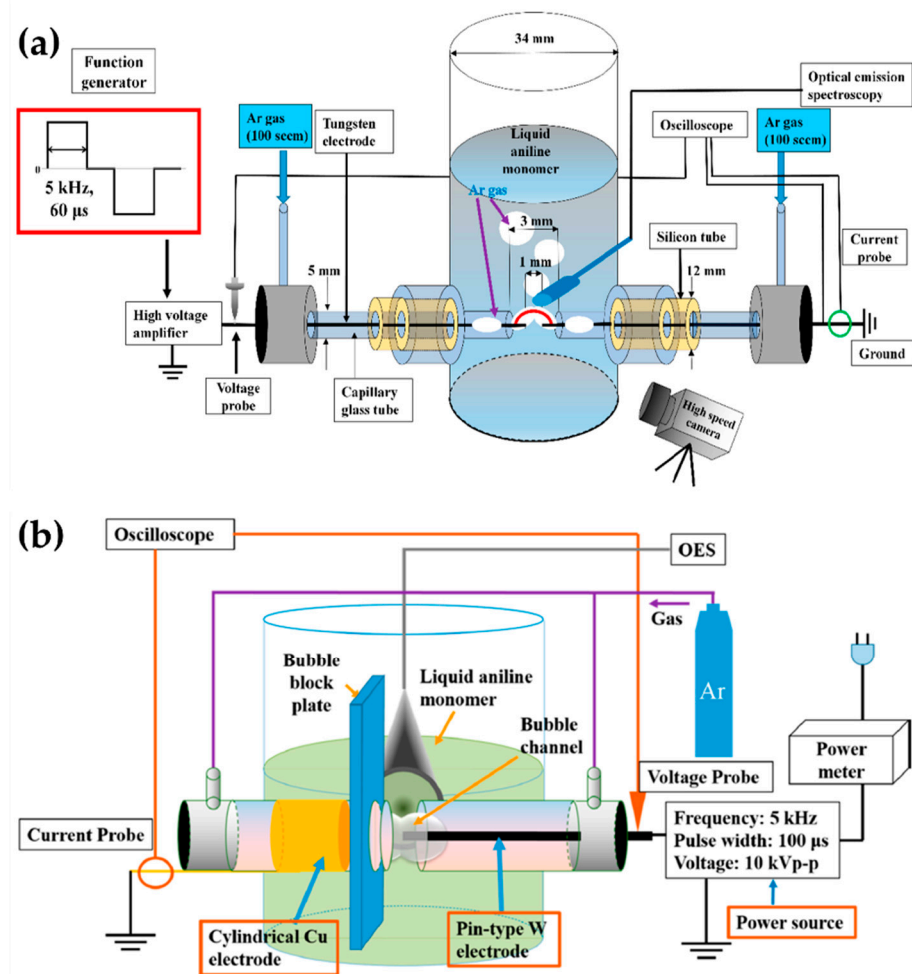
Figure 13. Schematic diagrams of the in-solution plasma system with a gas channel proposed by (**a**,**b**) Shin et al. [111,112].

Table 4. Summary of syntheses using in-solution plasma methods.

No	NPs	Electrode (Gap)	Precursor	Plasma Source	Year	Author Reference
1	Nitrogen–carbon nanosheets (NCNS)	Tungsten (1 mm)	*N*-methyl-2-pyrrolidone	Bipolar Pulse (2 kV, 25–200 kHz, 1 μs)	2016	Hyun et al. [103]
2	NCNS	Tungsten (1 mm)	2-Pyrrolidone, 1-methylpyrrolidine, pyrrolidine, pyrrole, cyclopentanone, and cyclohexanone	Bipolar Pulse (2 kV, 200 kHz, 1 μs)	2017	Hyun et al. [104]
3	Nitrogen-doped carbon nanoparticles (NCNPs)	Tungsten (1 mm)	Cyanopyridine, cyanopyrazine	Bipolar Pulse (20 kHz, 0.8 μs)	2016	Panomsuwan et al. [105]
4	Nanocarbons	Tungsten (0.5 mm)	Hexane, hexadecane, cyclohexane, benzene	Bipolar Pulse (1.7 kV, 15 kHz, 1 μs)	2016	Morishita et al. [106]
5	Boron–carbon–nitrogen nanocarbons	Tungsten (1 mm)	Pyridine, B-tribromoborazine, boric acid	Bipolar Pulse (2 kV, 100 kHz, 0.5 μs)	2017	Lee et al. [107]
6	Carbon	Tungsten (0.5 mm)	Pyrazine, acrylonitrile	Bipolar Pulse (2 kV, 20 kHz, 1 μs)	2016	Li et al. [108]
7	Amino-modified nanocarbon	Tungsten (1 mm)	Phenol (3-aminopropyl)triethoxysilane (APTES)	Bipolar Pulse (4 kV, 15 kHz, 1 μs)	2020	Tipplook et al. [109]
8	Carbon TiOX/carbon composite nanosheets	Tungsten (5 mm)	Ti-contained solution	DC (19 kV)	2015	Lee et al. [91]

Table 4. *Cont.*

No	NPs	Electrode (Gap)	Precursor	Plasma Source	Year	Author Reference
9	Carbon, Pt–carbon	Carbon (1 mm)	Ethanol	Pulse (4 kV, 30 kHz, 4 μs)	2019	Alsaeedi et al. [110]
10	Polyaniline	Tungsten (1 mm)	Aniline	Bipolar Pulse (16.4 kV, 5 kHz, 60 μs)		Shin et al. [111]
11	Polyaniline	Tungsten–copper (4 mm)	Aniline	Bipolar Pulse (16 kV, 5 kHz, 100 μs)		Shin et al. [112]

4. Plasma Polymerization

4.1. Synthesis of Polymers Using Plasma Techniques

Plasma polymerization accompanies complex physicochemical reactions that are very different from conventional chemical polymerization methods. In plasma polymerization, monomer molecules are broken into electrons, ions, radicals, and excited molecules through collisions with energetic electrons. A resulting polymer then grows by random recombination among these particles. Figure 14a shows the mechanisms of plasma polymerization [113]; Figure 14b is a scheme of a general plasma polymerization system with these mechanism stages [114]. A polymer is synthesized onto a solid phase through recombination, where single or divalent reactive species generated by plasma are polymerized (recombination) by the reactions between reactive species and monomers (Reactions (1) and (4)) or between the reactive species (Reactions (2), (3), and (5)) [113,114]. Indeed, plasma polymerization is a competitive process between formation by synthesis of polymer-forming species and ablation of the polymer film itself [115]. Unlike conventional chemical polymerization methods—such as self-assembly, layer-by-layer, or spin coating— a continuous fragmentation and random recombination easily creates the high cross-linking property that is characteristic of plasma polymers, as shown in Figure 14c [116]. The high cross-linking property of plasma polymers is responsible for providing better mechanical stability and less morphological changes [74,114,117].

4.2. Characterization and Chemical Structure of the Polymerized Films Obtained Using APP Techniques

In general, the reaction mechanism of plasma polymerization is mainly established in a vacuum state or low-pressure conditions. In APP methods, the reaction scheme of plasma polymerization is not yet verified, and the related underlying mechanisms are under-studied. Nevertheless, the detailed reaction mechanism of APP polymerization can be confirmed by clearly identifying the chemical structures of polymerized films via characterization methods such as Fourier transform infrared spectroscopy (FT-IR), nuclear magnetic resonance (NMR), and X-ray photoelectron spectroscopy (XPS). The results of this analysis can be seen in Figure 15, where Asandulesa et al. reported a polymerization mechanism by identifying the chemical structures of the polymer films through the characterization of APP-polymerized films synthesized from various monomers [118]. In the case of the benzaldehyde-based polymer films, the polymerized films showed two different types of chemical structures, depending on the plasma conditions: The first type was where the aromatic ring was preserved during the APP polymerization; in this case, reactions of benzaldehyde were initiated by breaking the π bonds from aldehyde, which was confirmed by the presence of C–O bonds in the polymeric film through FT-IR and XPS spectra, as shown in Figure 15a. The second type was where the aromatic ring was broken during the APP polymerization; in this case, aliphatic functional groups were likely obtained from the aromatic ring breakage during plasma polymerization, and aliphatic hydrocarbons (CH_2 and CH_3 protons) were also produced by hydrogenation reactions—which was confirmed through FT-IR and NMR spectra, as shown in Figure 15b,c. Finally, the reactive species were shown to randomly recombine, and the polymeric film was obtained via the reactions between radical species during the APP polymerization, as shown in Figure 15d. The reactive species could also be oxidized during film growth, producing functional

groups such as ethers, alcohols, and esters—which was confirmed by the presence of ethers, alcohol, esters, and carbonate units in the chemical composition of the polymeric film identified from FT-IR and XPS data, as shown in Figure 15e [118]. In summary, the APP polymerization mechanism, from a chemical point of view, is related to the formation of benzaldehyde-based polymer films, as illustrated in Figure 16.
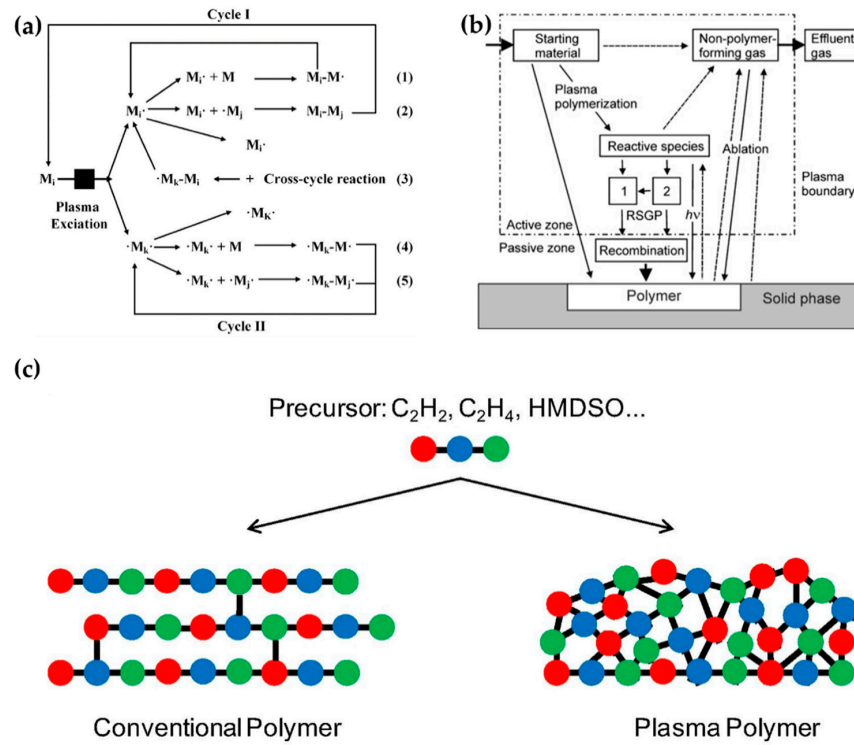
Figure 14. (**a**) Mechanisms of plasma polymerization [113]. (**b**) A scheme of a general plasma polymerization system [114]. (**c**) Comparison of a conventional polymer (left) and plasma polymer (right), derived from equivalent monomers [116].
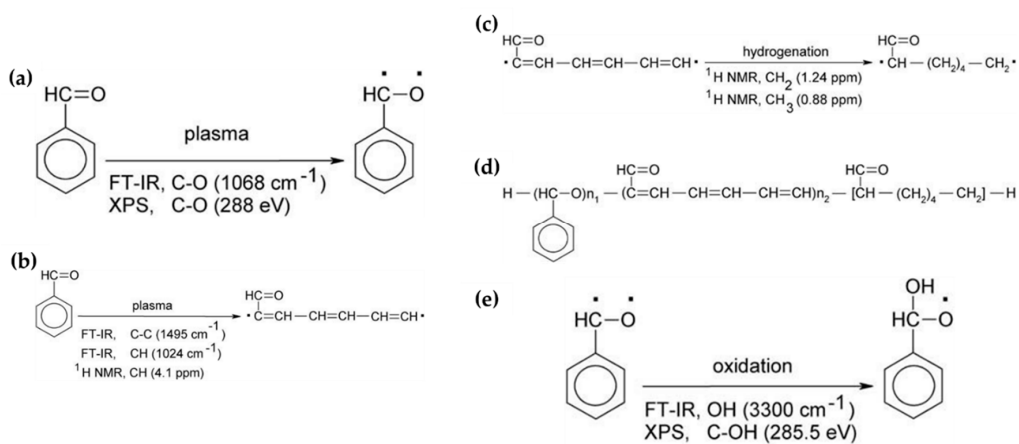
Figure 15. Chemical structures identified via characterization of benzaldehyde-based polymer films using APP techniques, where (**a**) depicts benzaldehyde radical generation by π bond breakage from aldehyde, (**b**) depicts aliphatic chain production by aromatic ring breakage, (**c**) depicts hydrogenation of the aliphatic chain, (**d**) depicts the recombination process between benzaldehyde radicals and aliphatic chains, and (**e**) depicts benzaldehyde radical oxidation under plasma conditions [118].
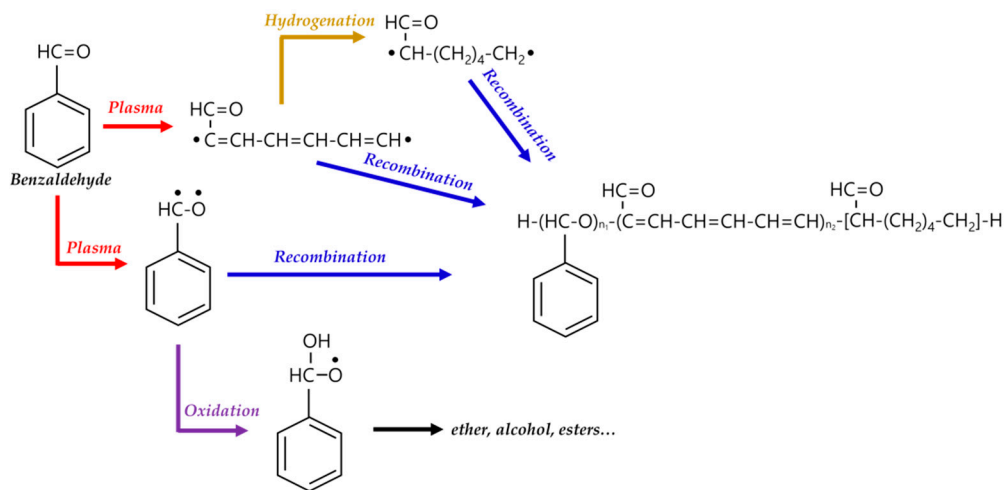
Figure 16. APP polymerization mechanisms, from a chemical point of view, related to the formation of benzaldehyde-based polymer films.

5. Main Properties and Current Applications of the Polymers Obtained via APP Polymerization

The technical state of APP polymerization is sufficiently enhanced to synthesize a conducting polymer film with single- and polycrystalline properties (Figure 17a,b) [62]. These advanced APP polymerization techniques are actively investigated for various applications; functional coatings are one such representative application of APP polymerization. Plasma polymerization can change the wettability of any surface to demonstrate hydrophobic/philic characteristics, depending on the amount of polar or nonpolar functional groups on the coating's surface [78,81]. Therefore, the properties of functional coatings are commonly determined from the kinds of materials used. For example, TMS, APDMES, HMDSO, AA, and PMA are utilized for wettable coatings (hydrophilic/phobic) (Figure 17c,d) [57,67,71,73,78,81]. In a biological application, Getnet et al. [72] and St'ahel et al. [77] investigated whether polymer films synthesized via APP polymerization could be applied for antibacterial properties (Figure 18a,b) [72,77]. As shown in Figure 14c [116], the plasma polymers have the high cross-linking property resulting from continuous fragmentation and random recombination during plasma polymerization; that is, the polymers obtained using plasma techniques show better mechanical stability and fewer morphological changes [74,114,117]. Bardon et al. [74] reported that the DOCA polymer coatings were modified by adding HdiA or HdiMA to the DOCA precursor, and the related mechanical reinforcement was examined (Figure 18c) [74]. Abessolo et al. [82] also reported that the dielectric constant of polymer films deposited by APP could be lowered by varying the monomer precursors used—i.e., siloxane and silazane—as well as by varying their ring size (Figure 18d) [82]. Additionally, the surface morphology of the polymers obtained using APP polymerization shows rough or porous films, thereby enhancing their sensing capability as gas sensors. A porous polythiophene prepared via APP polymerization showed outstanding response properties as a NO_2 gas sensor when compared to polythiophene synthesized via chemical methods (Figure 18e) [119].
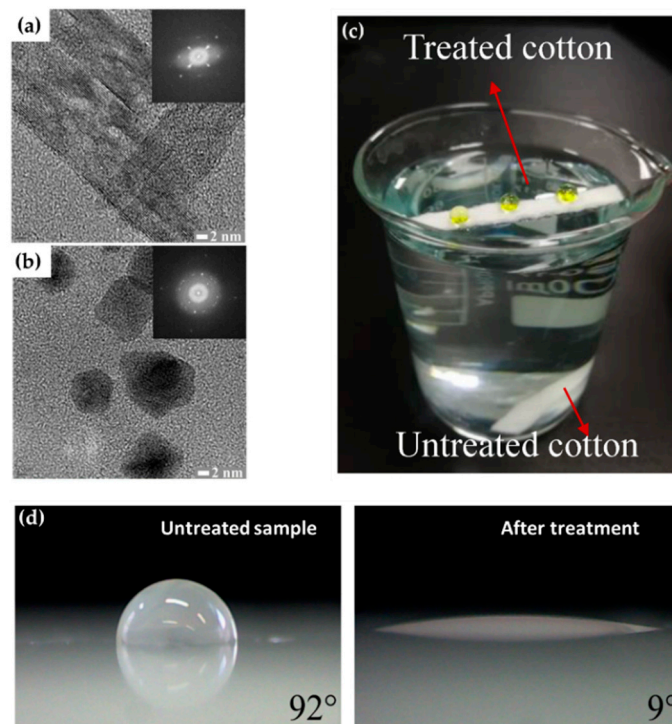
Figure 17. Transmission electron microscopy (TEM) images of polypyrrole NPs with (**a**) single-crystalline and (**b**) polycrystalline properties [62]. (**c**) Superhydrophobicity of the coated films on the cotton fabrics [67]. (**d**) Hydrophilization of the surface of polypropylene [73].
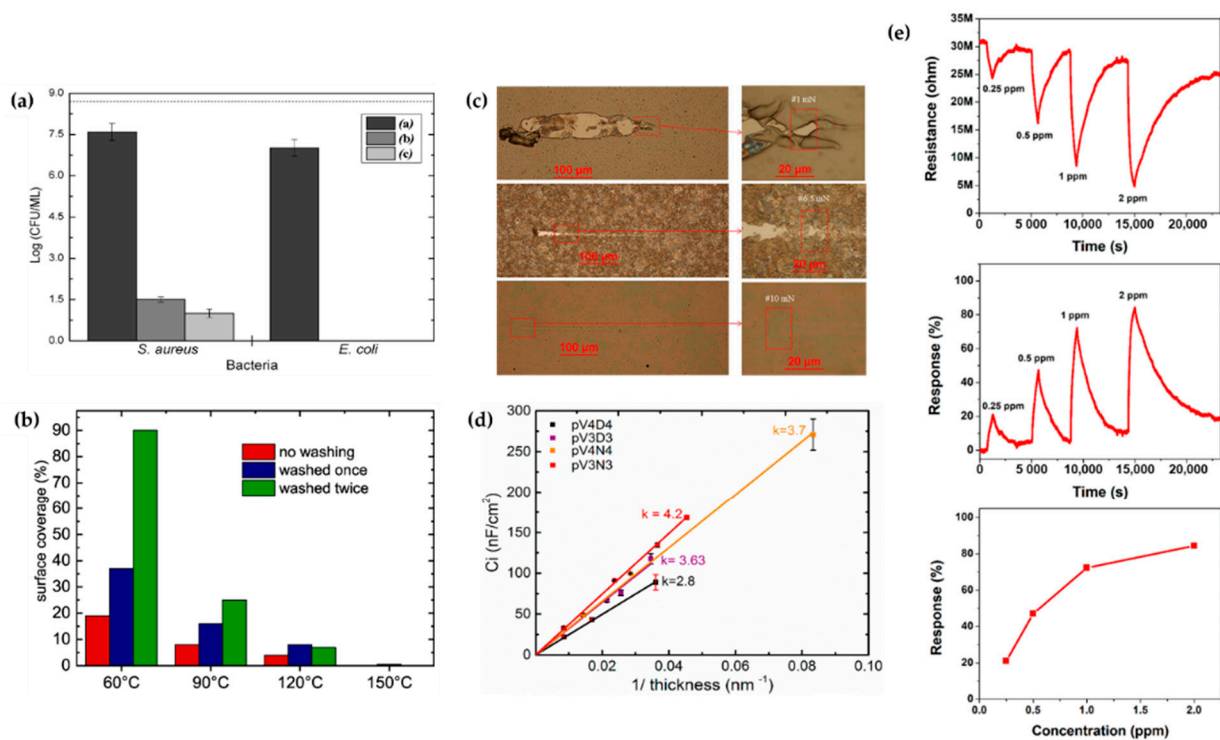
Figure 18. (**a**,**b**) Antibacterial properties created by APP polymerization [72,77]. (**c**) Scratch tracks for coatings of DOCA, HdiA and HdiMA films [74]. (**d**) Estimation of the dielectric constant of insulating layers made by cyclic organosilicons [82]. (**e**) NO_2-sensing properties of a polythiophene film prepared using the APPJ technique [119].

6. Conclusions and Future Perspectives

In summary, the plasma synthesis of polymer films and NPs under atmospheric pressure has become an advanced and replicated method, due to the various experimental advantages of this kind of synthesis, such as simplified equipment, faster processes, lower thermal temperatures, lower costs, and eco-friendly waste. In this review, we presented the recent studies on the synthesis of polymer films and NPs using the various APP methods. These methods are categorized into two types, depending on the state of the precursor: The APP methods using a gas/aerosol-phase precursor are almost always used for a polymer deposition or coating. The APP methods using liquid-type precursors are more favorable for the formation of NPs. First, we described and summarized various GATP methods that are employed as synthesis methods for polymer films. These methods all successfully form polymer films via variations in the specific GATP techniques by varying experimental parameters, such as the structure of the electrodes, types of precursors, types of discharge gas, and discharge power sources (frequency, voltage, duty cycle). Next, this review provided a summary and discussion of various liquid-plasma techniques used primarily for the formation of NPs via non-thermal plasma interactions with various liquids, including water or organic monomer solutions. Again, a wide range of NP synthesis can be successfully achieved using liquid-plasma systems with various configurations of electrodes, materials, and plasma power sources.

In the near future, various APP polymer synthesis methods will likely become ideal candidates for industrial applications due to their potential for scaling-up while retaining a practical and sustainable environment for synthesis. However, there remain some challenges for applications of these APP methods, i.e., the low plasma density of APP and the potential for using a large amount of the gas source in some cases. Thus, it is important to incentivize and support further investigations and research on novel APP polymerization and synthesis methods in order to continue to overcome these challenges and accomplish large-scale polymer film deposition or mass production of NPs with stable discharge under open-air conditions.

Author Contributions: H.J.J., E.Y.J., H.-S.T. and C.-S.P. contributed to the conception. H.J.J., E.Y.J., H.-S.T. and C.-S.P. reviewed references and wrote the draft of the manuscript. The authors contributed equally review and editing. All authors have read and agreed to the published version of the manuscript.

Institutional Review Board Statement: Not applicable.

Informed Consent Statement: Not applicable.

Data Availability Statement: Not applicable.

Conflicts of Interest: The authors declare no conflict of interest.

References

1. Plasma polymerization. In *The Plasma Chemistry of Polymer Surfaces: Advanced Techniques for Surface Design*, 1st ed.; Wiley-VCH: Weinheim, Germany, 2021; pp. 337–375.
2. de Wilde, P. Vermischte mittheilungen. *Berichte* **1876**, *7*, 352.
3. Berthelot, M. Formation de l'acétylène dans les combustions incomplètes. *Ann. Chim. Phys.* **1866**, *9*, 413.
4. Berthelot, M. Action Réciproque des carbures d'hydrogène. synthèse de styrolène, de la napthaline, de l'anthracéne. *Ann. Chim. Phys.* **1867**, *12*, 5–52.
5. Thenard, P.; Thenard, A. Acétylène liquéfié et solidifié sous l'influence de l'effluve électrique. *Comptes Rendus* **1874**, *78*, 219.
6. Schüler, H.; Reinebeck, L. Über neue spektren in der glimmentladung mit naphthalindampf. *Z. Nat. A* **1951**, *6a*, 270–275. [CrossRef]
7. Schüler, H.; Reinebeck, L. Über diacetylen in der glimmentladung. *Z. Nat. A* **1954**, *9a*, 350–354. [CrossRef]
8. Schüler, H.; Prchal, K.; Kloppenburg, E. Chemische reaktionen in der positiven säule einer glimmentladung reaktionsprodukte des benzols. *Z. Nat. A* **1960**, *15a*, 308–310. [CrossRef]

9. König, H.; Helwig, G. Über dünne aus kohlenwasserstoffen durch elektronen- oder ionenbeschuß gebildete schichten. *Z. Phys.* **1951**, *129*, 491–503. [CrossRef]

10. Goodman, J. The formation of thin polymer films in the gas discharge. *J. Polym. Sci.* **1960**, *44*, 551–552. [CrossRef]

11. Inagaki, N.; Ohkubo, J. Plasma polymerization of hexafluoropropene/methane mixtures and composite membranes for gas separations. *J. Memb. Sci.* **1986**, *27*, 63–75. [CrossRef]

12. Lawton, E.L. Adhesion improvement of tire cord induced by gas plasma. *J. Appl. Polym. Sci.* **1974**, *18*, 1557–1574. [CrossRef]

13. Stille, J.K.; Rix, C.E. The reaction of halobenzenes in a radiofrequency glow discharge. *J. Org. Chem.* **1966**, *31*, 1591–1594. [CrossRef]

14. Denaro, A.R.; Owens, P.A.; Crawshaw, A. Glow discharge polymerization-II α-methylstyrene, ω-methylstyrene and allylbenzene. *Eur. Polym. J.* **1969**, *5*, 471–482. [CrossRef]

15. Kobayashi, H.; Bell, A.T.; Shen, M. Formation of an amorphous powder during the polymerization of ethylene in a radio-frequency discharge. *J. Appl. Polym. Sci.* **1973**, *17*, 885–892. [CrossRef]

16. Yasuda, H. Plasma polymerization for protective coatings and composite membranes. *J. Memb. Sci.* **1984**, *18*, 273–284. [CrossRef]

17. Inagaki, N.; Tasaka, S.; Ikeda, Y. Plasma polymerization of copper phthalocyanines and application of the plasma polymer films to NO_2 gas sensor device. *J. Appl. Polym. Sci.* **1995**, *55*, 1451–1464. [CrossRef]

18. He, J.-H.; Singamaneni, S.; Ho, C.H.; Lin, Y.-H.; McConney, M.E.; Tsukruk, V.V. A thermal sensor and switch based on a plasma polymer/ZnO suspended nanobelt bimorph structure. *Nanotechnology* **2009**, *20*, 065502. [CrossRef]

19. Kim, M.; Kang, T.W.; Kim, S.H.; Jung, E.H.; Park, H.H.; Seo, J.; Lee, S.J. Antireflective, self-cleaning and protective film by continuous sputtering of a plasma polymer on inorganic multilayer for perovskite solar cells application. *Sol. Energy Mater. Sol. Cells* **2019**, *191*, 55–61. [CrossRef]

20. Seo, H.J.; Gil, Y.E.; Hwang, K.-H.; Ananth, A.; Boo, J.-H. Synthesis and characterization of plasma-polymer gate dielectric films for graphene field effect transistor devices. *Electron. Mater. Lett.* **2019**, *15*, 396–401. [CrossRef]

21. Truica-Marasescu, F.; Wertheimer, M.R. Nitrogen-rich plasma-polymer films for biomedical applications. *Plasma Process. Polym.* **2008**, *5*, 44–57. [CrossRef]

22. Vasani, R.B.; Szili, E.J.; Rajeev, G.; Voelcker, N.H. On-demand antimicrobial treatment with antibiotic-loaded porous silicon capped with a pH-responsive dual plasma polymer barrier. *Chem.-An Asian J.* **2017**, *12*, 1605–1614. [CrossRef]

23. Coad, B.R.; Scholz, T.; Vasilev, K.; Hayball, J.D.; Short, R.D.; Griesser, H.J. Functionality of proteins bound to plasma polymer surfaces. *ACS Appl. Mater. Interfaces* **2012**, *4*, 2455–2463. [CrossRef]

24. Vasilev, K. Nanoengineered plasma polymer films for biomaterial applications. *Plasma Chem. Plasma Process.* **2014**, *34*, 545–558. [CrossRef]

25. Bhatt, S.; Pulpytel, J.; Aref-Khonsari, F. Low and atmospheric plasma polymerisation of nanocoatings for bio-applications. *Surf. Innov.* **2015**, *3*, 63–83. [CrossRef]

26. Hegemann, D.; Lorusso, E.; Butron-Garcia, M.-I.; Blanchard, N.E.; Rupper, P.; Favia, P.; Heuberger, M.; Vandenbossche, M. Suppression of hydrophobic recovery by plasma polymer films with vertical chemical gradients. *Langmuir* **2016**, *32*, 651–654. [CrossRef] [PubMed]

27. Fan, Y.; Li, X.; Yang, R. The surface modification methods for constructing polymer-coated stents. *Int. J. Polym. Sci.* **2018**, *2018*, 3891686. [CrossRef]

28. Rao, J.; Bao, L.; Wang, B.; Fan, M.; Feo, L. Plasma surface modification and bonding enhancement for bamboo composites. *Compos. Part B Eng.* **2018**, *138*, 157–167. [CrossRef]

29. Langmuir, I. Oscillations in ionized gases. *Proc. Natl. Acad. Sci. USA* **1928**, *14*, 627–637. [CrossRef]

30. Khelifa, F.; Ershov, S.; Habibi, Y.; Snyders, R.; Dubois, P. Free-radical-induced grafting from plasma polymer surfaces. *Chem. Rev.* **2016**, *116*, 3975–4005. [CrossRef]

31. Ishijima, T.; Nosaka, K.; Tanaka, Y.; Uesugi, Y.; Goto, Y.; Horibe, H. A high-speed photoresist removal process using multibubble microwave plasma under a mixture of multiphase plasma environment. *Appl. Phys. Lett.* **2013**, *103*, 1–6. [CrossRef]

32. Bitar, R.; Cools, P.; Geyter, N.D.; Morent, R. Acrylic acid plasma polymerization for biomedical use. *Appl. Surf. Sci.* **2018**, *448*, 168–185. [CrossRef]

33. Moreau, M.; Orange, N.; Feuilloley, M.G.J. Non-thermal plasma technologies: New tools for bio-decontamination. *Biotechnol. Adv.* **2008**, *26*, 610–617. [CrossRef] [PubMed]

34. Mariotti, D.; Sankaran, R.M. Microplasmas for nanomaterials synthesis. *J. Phys. D Appl. Phys.* **2010**, *43*, 323001. [CrossRef]

35. Özçiçek, N.P.; Pekmez, K.; Holze, R.; Yildiz, A. Spectroelectrochemical investigations of aniline-thiophene copolymers in acetonitrile. *J. Appl. Polym. Sci.* **2003**, *90*, 3417–3423. [CrossRef]

36. Udum, Y.A.; Pekmez, K.; Yildiz, A. Electrochemical preparation of a soluble conducting aniline-thiophene copolymer. *Eur. Polym. J.* **2005**, *41*, 1136–1142. [CrossRef]

37. Xu, Y.; Dai, L.; Chen, J.; Gal, J.-Y.; Wu, H. Synthesis and characterization of aniline and aniline-o-sulfonic acid copolymers. *Eur. Polym. J.* **2007**, *43*, 2072–2079. [CrossRef]

38. Mun, M.K.; Lee, W.O.; Park, J.W.; Kim, D.S.; Yeom, G.Y.; Kim, D.W. Nanoparticles synthesis and modification using solution plasma process. *Appl. Sci. Converg. Technol.* **2017**, *26*, 164–173. [CrossRef]

39. Chou, W.-C.; Liu, W.-J. Study of dye sensitized solar cell application of TiO$_2$ films by atmospheric pressure plasma deposition method. In Proceedings of the International Conference on Electronics Packaging (ICEP), Sapporo, Japan, 20–22 April 2016; pp. 664–668.

40. Muzammil, I.; Li, Y.; Lei, M. Tunable wettability and pH-responsiveness of plasma copolymers of acrylic acid and octafluorocyclobutane. *Plasma Process. Polym.* **2017**, *14*, 1–10. [CrossRef]

41. Khoo, Y.S.; Lau, W.J.; Liang, Y.Y.; Karaman, M.; Gürsoy, M.; Lai, G.S.; Ismail, A.F. Rapid and eco-friendly technique for surface modification of TFC RO membrane for improved filtration performance. *J. Environ. Chem. Eng.* **2021**, *9*, 105227. [CrossRef]

42. Liu, T.; Yang, F.; Li, Y.; Ren, L.; Zhang, L.; Xu, K.; Wang, X.; Xu, C.; Gao, J. Plasma synthesis of carbon nanotube-gold nanohybrids: Efficient catalysts for green oxidation of silanes in water. *J. Mater. Chem. A* **2014**, *2*, 245–250. [CrossRef]

43. Rezaei, F.; Vanraes, P.; Nikiforov, A.; Morent, R.; Geyter, N.D. Applications of plasma-liquid systems: A review. *Mateials* **2019**, *12*, 2751. [CrossRef]

44. Saito, G.; Akiyama, T. Nanomaterial synthesis using plasma generation in liquid. *J. Nanomater.* **2015**, *2015*, 123696. [CrossRef]

45. Fauchais, P.; Etchart-Salas, R.; Rat, V.; Coudert, J.F.; Caron, N.; Wittmann-Ténèze, K. Parameters controlling liquid plasma spraying: Solutions, sols, or suspensions. *J. Therm. Spray Technol.* **2008**, *17*, 31–59. [CrossRef]

46. Nie, Q.Y.; Cao, Z.; Ren, C.S.; Wang, D.Z.; Kong, M.G. A two-dimensional cold atmospheric plasma jet array for uniform treatment of large-area surfaces for plasma medicine. *New J. Phys.* **2009**, *11*, 115015. [CrossRef]

47. Nie, Q.-Y.; Ren, C.-S.; Wang, D.-Z.; Zhang, J.-L. A simple cold Ar plasma jet generated with a floating electrode at atmospheric pressure. *Appl. Phys. Lett.* **2008**, *93*, 011503. [CrossRef]

48. Kim, H.; Brockhaus, A.; Engemann, J. Atmospheric pressure argon plasma jet using a cylindrical piezoelectric transformer. *Appl. Phys. Lett.* **2009**, *95*, 211501. [CrossRef]

49. Yang, P.; Zhang, J.; Guo, Y. Synthesis of intrinsic fluorescent polypyrrole nanoparticles by atmospheric pressure plasma polymerization. *Appl. Surf. Sci.* **2009**, *255*, 6924–6929. [CrossRef]

50. Teslaru, T.; Topala, I.; Dobromir, M.; Pohoata, V.; Curecheriu, L.; Dumitrascu, N. Polythiophene films obtained by polymerization under atmospheric pressure plasma conditions. *Mater. Chem. Phys.* **2016**, *169*, 120–127. [CrossRef]

51. Zhang, P.; Zhang, S.; Kong, F.; Zhang, C.; Dong, P.; Yan, P.; Cheng, X.; Ostrikov, K.K.; Shao, T. Atmospheric-pressure plasma jet deposition of bumpy coating improves polypropylene surface flashover performance in vacuum. *Surf. Coat. Technol.* **2020**, *387*, 125511. [CrossRef]

52. Ricci Castro, A.H.; Kodaira, F.V.P.; Prysiazhnyi, V.; Mota, R.P.; Kostov, K.G. Deposition of thin films using argon/acetylene atmospheric pressure plasma jet. *Surf. Coat. Technol.* **2017**, *312*, 13–18. [CrossRef]

53. Van Vrekhem, S.; Morent, R.; Geyter, N.D. Deposition of a PMMA coating with an atmospheric pressure plasma jet. *J. Coat. Technol. Res.* **2018**, *15*, 679–690. [CrossRef]

54. Pandiyaraj, K.N.; Ramkumar, M.C.; Kumar, A.A.; Vasu, D.; Padmanabhan, P.V.A.; Tabaei, P.S.E.; Cools, P.; Geyter, N.D.; Morent, R.; Jaganathan, S.K. Development of phosphor containing functional coatings via cold atmospheric pressure plasma jet—Study of various operating parameters. *Appl. Surf. Sci.* **2019**, *488*, 343–350. [CrossRef]

55. Doherty, K.G.; Oh, J.S.; Unsworth, P.; Sheridan, C.M.; Weightman, P.; Bradley, J.W.; Williams, R.L. Plasma polymerization using helium atmospheric-pressure plasma jet with heptylamine monomer. *Plasma Process. Polym.* **2019**, *16*, 1–10. [CrossRef]

56. Kodaira, F.V.P.; Ricci Castro, A.H.; Prysiazhnyi, V.; Mota, R.P.; Quade, A.; Kostov, K.G. Characterization of plasma polymerized HMDSN films deposited by atmospheric plasma jet. *Surf. Coat. Technol.* **2017**, *312*, 117–122. [CrossRef]

57. Hossain, M.M.; Trinh, Q.H.; Nguyen, D.B.; Sudhakaran, M.S.P.; Mok, Y.S. Formation of plasma-polymerized superhydrophobic coating using an atmospheric-pressure plasma jet. *Thin Solid Films* **2019**, *675*, 34–42. [CrossRef]

58. Malinowski, S.; Herbert, P.A.F.; Rogalski, J.; Jaroszyńska-Wolińska, J. Laccase enzyme polymerization by soft plasma jet for durable bioactive coatings. *Polymers* **2018**, *10*, 532. [CrossRef] [PubMed]

59. Jang, H.J.; Park, C.-S.; Jung, E.Y.; Bae, G.T.; Shin, B.J.; Tae, H.-S. Synthesis and properties of thiophene and aniline copolymer using atmospheric pressure plasma jets copolymerization technique. *Polymers* **2020**, *12*, 2225. [CrossRef] [PubMed]

60. Park, C.-S.; Jung, E.Y.; Jang, H.J.; Bae, G.T.; Shin, B.J.; Tae, H.-S. Synthesis and properties of plasma-polymerized methyl methacrylate via the atmospheric pressure plasma polymerization technique. *Polymers* **2019**, *11*, 396. [CrossRef]

61. Park, C.-S.; Kim, D.Y.; Kim, D.H.; Lee, H.-K.; Shin, B.J.; Tae, H.-S. Humidity-independent conducting polyaniline films synthesized using advanced atmospheric pressure plasma polymerization with in-situ iodine doping. *Appl. Phys. Lett.* **2017**, *110*, 033502. [CrossRef]

62. Kim, D.H.; Park, C.-S.; Kim, W.H.; Shin, B.J.; Hong, J.G.; Park, T.S.; Seo, J.H.; Tae, H.-S. Influences of guide-tube and bluff-body on advanced atmospheric pressure plasma source for single-crystalline polymer nanoparticle synthesis at low temperature. *Phys. Plasmas* **2017**, *24*, 023506. [CrossRef]

63. Kim, J.Y.; Iqbal, S.; Jang, H.J.; Jung, E.Y.; Bae, G.T.; Park, C.-S.; Tae, H.-S. In-situ iodine doping characteristics of conductive polyaniline film polymerized by low-voltage-driven atmospheric pressure plasma. *Polymers* **2021**, *13*, 418. [CrossRef] [PubMed]

64. Kim, J.Y.; Iqbal, S.; Jang, H.J.; Jung, E.Y.; Bae, G.T.; Park, C.-S.; Shin, B.J.; Tae, H.-S. Transparent polyaniline thin film synthesized using a low-voltage-driven atmospheric pressure plasma reactor. *Materials* **2021**, *14*, 1278. [CrossRef] [PubMed]

65. Karl, C.W.; Rahimi, W.; Kubowicz, S.; Lang, A.; Geisler, H.; Giese, U. Surface modification of ethylene propylene diene terpolymer rubber by plasma polymerization using organosilicon precursors. *ACS Appl. Polym. Mater.* **2020**, *2*, 3789–3796. [CrossRef]

66. Yan, X.; Liu, G.-S.; Yang, J.; Pu, Y.; Chen, S.; He, H.-W.; Wang, C.; Long, Y.-Z.; Jiang, S. In situ surface modification of paper-based relics with atmospheric pressure plasma treatment for preservation purposes. *Polymers* **2019**, *11*, 786. [CrossRef] [PubMed]

67. Yang, J.; Pu, Y.; Miao, D.; Ning, X. Fabrication of durably superhydrophobic cotton fabrics by atmospheric pressure plasma treatment with a siloxane precursor. *Polymers* **2018**, *10*, 460. [CrossRef]

68. Moosburger-Will, J.; Bauer, M.; Schubert, F.; Kunzmann, C.; Lachner, E.; Zeininger, H.; Maleika, M.; Hönisch, B.; Küpfer, J.; Zschoerper, N.; et al. Methyltrimethoxysilane plasma polymerization coating of carbon fiber surfaces. *Surf. Coat. Technol.* **2017**, *311*, 223–230. [CrossRef]

69. Pandiyaraj, K.N.; Ramkumar, M.C.; Arun Kumar, A.; Padmanabhan, P.V.A.; Pichumani, M.; Bendavid, A.; Cools, P.; Geyter, N.D.; Morent, R.; Kumar, V.; et al. Evaluation of surface properties of low density polyethylene (LDPE) films tailored by atmospheric pressure non-thermal plasma (APNTP) assisted co-polymerization and immobilization of chitosan for improvement of antifouling properties. *Mater. Sci. Eng. C* **2019**, *94*, 150–160. [CrossRef]

70. Ramkumar, M.C.; Navaneetha Pandiyaraj, K.; Arun Kumar, A.; Padmanabhan, P.V.A.; Cools, P.; Geyter, N.D.; Morent, R.; Uday Kumar, S.; Kumar, V.; Gopinath, P.; et al. Atmospheric pressure non-thermal plasma assisted polymerization of poly (ethylene glycol) methylether methacrylate (PEGMA) on low density polyethylene (LDPE) films for enhancement of biocompatibility. *Surf. Coat. Technol.* **2017**, *329*, 55–67. [CrossRef]

71. Mertens, J.; Nisol, B.; Hubert, J.; Reniers, F. Use of remote atmospheric mass spectrometry in atmospheric plasma polymerization of hydrophilic and hydrophobic coatings. *Plasma Process. Polym.* **2020**, *17*, 1900250. [CrossRef]

72. Getnet, T.G.; da Silva, G.F.; Duarte, I.S.; Kayama, M.E.; Rangel, E.C.; Cruz, N.C. Atmospheric pressure plasma chemical vapor deposition of carvacrol thin films on stainless steel to reduce the formation of *E. coli* and *S. aureus* biofilms. *Materials* **2020**, *13*, 3166.

73. Dvořáková, H.; Čech, J.; Stupavská, M.; Prokeš, L.; Jurmanová, J.; Buršíková, V.; Ráhel', J.; St'ahel, P. Fast surface hydrophilization via atmospheric pressure plasma polymerization for biological and technical applications. *Polymers* **2019**, *11*, 1613. [CrossRef]

74. Bardon, J.; Martin, A.; Fioux, P.; Amari, T.; Mertz, G.; Delmée, M.; Ruch, D.; Roucoules, V. Reinforcement of a dodecylacrylate plasma polymer by admixture of a diacrylate or a dimethacrylate cross-linker. *Plasma Process. Polym.* **2018**, *15*, 1800031. [CrossRef]

75. Manakhov, A.; Michlíček, M.; Nečas, D.; Polčák, J.; Makhneva, E.; Eliáš, M.; Zajíčková, L. Carboxyl-rich coatings deposited by atmospheric plasma co-polymerization of maleic anhydride and acetylene. *Surf. Coat. Technol.* **2016**, *295*, 37–45. [CrossRef]

76. Obrusník, A.; Jelínek, P.; Zajíčková, L. Modelling of the gas flow and plasma co-polymerization of two monomers in an atmospheric-pressure dielectric barrier discharge. *Surf. Coat. Technol.* **2017**, *314*, 139–147. [CrossRef]

77. St'ahel, P.; Mazánková, V.; Tomečková, K.; Matoušková, P.; Brablec, A.; Prokeš, L.; Jurmanová, J.; Buršíková, V.; Přibyl, R.; Lehocký, M.; et al. Atmospheric pressure plasma polymerized oxazoline-based thin films-antibacterial properties and cytocompatibility performance. *Polymers* **2019**, *11*, 2069. [CrossRef] [PubMed]

78. Demaude, A.; Poleunis, C.; Goormaghtigh, E.; Viville, P.; Lazzaroni, R.; Delcorte, A.; Gordon, M.; Reniers, F. Atmospheric pressure plasma deposition of hydrophilic/phobic patterns and thin film laminates on any surface. *Langmuir* **2019**, *35*, 9677–9683. [CrossRef]

79. Nisol, B.; Ghesquière, J.; Reniers, F. Easy synthesis of ageing-resistant coatings with tunable wettability by atmospheric pressure plasma. *Plasma Chem. Plasma Process* **2016**, *36*, 1239–1252. [CrossRef]

80. Jalaber, V.; Del Frari, D.; De Winter, J.; Mehennaoui, K.; Planchon, S.; Choquet, P.; Detrembleur, C.; Moreno-Couranjou, M. Atmospheric aerosol assisted pulsed plasma polymerization: An environmentally friendly technique for tunable catechol-bearing thin films. *Front. Chem.* **2019**, *7*, 183. [CrossRef]

81. Ma, C.; Wang, L.; Nikiforov, A.; Onyshchenko, Y.; Cools, P.; Ostrikov, K.; Geyter, N.D.; Morent, R. Atmospheric-pressure plasma assisted engineering of polymer surfaces: From high hydrophobicity to superhydrophilicity. *Appl. Surf. Sci.* **2021**, *535*, 147032.

82. Abessolo Ondo, D.; Loyer, F.; Werner, F.; Leturcq, R.; Dale, P.J.; Boscher, N.D. Atmospheric-pressure synthesis of atomically smooth, conformal, and ultrathin low-k polymer insulating layers by plasma-initiated chemical vapor deposition. *ACS Appl. Polym. Mater.* **2019**, *1*, 3304–3312. [CrossRef]

83. Loyer, F.; Frache, G.; Choquet, P.; Boscher, N.D. Atmospheric pressure plasma-initiated chemical vapor deposition (AP-PiCVD) of poly(alkyl acrylates): An experimental study. *Macromolecules* **2017**, *50*, 4351–4362. [CrossRef]

84. Loyer, F.; Bengasi, G.; Frache, G.; Choquet, P.; Boscher, N.D. Insights in the initiation and termination of poly(alkyl acrylates) synthesized by atmospheric pressure plasma-initiated chemical vapor deposition (AP-PiCVD). *Plasma Process. Polym.* **2018**, *15*, 1800027. [CrossRef]

85. Loyer, F.; Combrisson, A.; Omer, K.; Moreno-Couranjou, M.; Choquet, P.; Boscher, N.D. Thermoresponsive water-soluble polymer layers and water-stable copolymer layers synthesized by atmospheric plasma initiated chemical vapor deposition. *ACS Appl. Mater. Interfaces* **2019**, *11*, 1335–1343. [CrossRef] [PubMed]

86. Cools, P.; Morent, R.; Geyter, N.D. Plasma modified textiles for biomedical applications. In *Advances in Bioengineering*; Serra, P.A., Ed.; IntechOpen: London, UK, 2015; pp. 117–148.

87. Kim, D.H.; Kim, H.J.; Park, C.-S.; Shin, B.J.; Seo, J.H.; Tae, H.-S. Atmospheric pressure plasma polymerization using double grounded electrodes with He/Ar mixture. *AIP Adv.* **2015**, *5*, 097137. [CrossRef]

88. Šimor, M.; Ráhel', J.; Vojtek, P.; Černák, M.; Brablec, A. Atmospheric-pressure diffuse coplanar surface discharge for surface treatments. *Appl. Phys. Lett.* **2002**, *81*, 2716–2718. [CrossRef]

89. Bour, J.; Bardon, J.; Aubriet, H.; Del Frari, D.; Verheyde, B.; Dams, R.; Vangeneugden, D.; Ruch, D. Different ways to plasma-polymerize HMDSO in DBD configuration at atmospheric pressure for corrosion protection. *Plasma Process. Polym.* **2008**, *5*, 788–796. [CrossRef]

90. Boscher, N.D.; Choquet, P.; Duday, D.; Verdier, S. Advantages of a pulsed electrical excitation mode on the corrosion performance of organosilicon thin films deposited on aluminum foil by atmospheric pressure dielectric barrier discharge. *Plasma Process. Polym.* **2010**, *7*, 163–171.

91. Lee, C.W.; Lee, S.-G.; Noh, J.H.; Jun, H.S.; Chung, K.-J.; Hong, K.S.; Kim, D.W.; Hwang, Y.S.; Kim, S.-W. Synthesis of carbon-incorporated titanium oxide nanocrystals by pulsed solution plasma: Electrical, optical investigation and nanocrystals analysis. *RSC Adv.* **2015**, *5*, 9497–9502. [CrossRef]

92. Senthilnathan, J.; Weng, C.-C.; Liao, J.-D.; Yoshimura, M. Submerged liquid plasma for the synthesis of unconventional nitrogen polymers. *Sci. Rep.* **2013**, *3*, 2414. [CrossRef]

93. Tan, P.E.C.; Mahinay, C.L.S.; Culaba, I.B.; Streeter, O.K.M.; Hilario, M.R.A. Plasma polymerization of styrene using an argon-fed atmospheric pressure plasma jet. *J. Vac. Sci. Technol. B* **2018**, *36*, 04I102. [CrossRef]

94. Tan, P.E.C.; Abalos, J.G.F.; Mahinay, C.L.S.; Culaba, I.B. Surface analysis and characterization of atmospheric pressure argon plasma jet treated methyl methacrylate monomer films. *Jpn. J. Appl. Phys.* **2020**, *59*, SAAB08. [CrossRef]

95. Schäfer, J.; Fricke, K.; Mika, F.; Pokorná, Z.; Zajíčková, L.; Foest, R. Liquid assisted plasma enhanced chemical vapour deposition with a non-thermal plasma jet at atmospheric pressure. *Thin Solid Film* **2017**, *630*, 71–78. [CrossRef]

96. Zhang, R.-C.; Sun, D.; Zhang, R.; Lin, W.-F.; Macias-Montero, M.; Patel, J.; Askari, S.; McDonald, C.; Mariotti, D.; Maguire, P. Gold nanoparticle-polymer nanocomposites synthesized by room temperature atmospheric pressure plasma and their potential for fuel cell electrocatalytic application. *Sci. Rep.* **2017**, *7*, 46682. [CrossRef]

97. Gamaleev, V.; Kajikawa, K.; Takeda, K.; Hiramatsu, M. Investigation of nanographene produced by in-liquid plasma for development of highly durable polymer electrolyte fuel cells. *J. Carbon Res.* **2018**, *4*, 65. [CrossRef]

98. Sano, N.; Wang, H.; Chhowalla, M.; Alexandrou, I.; Amaratunga, G.A.J. Synthesis of carbon 'onions' in water. *Nature* **2001**, *414*, 506–507. [CrossRef] [PubMed]

99. Pech, D.; Brunet, M.; Durou, H.; Huang, P.; Mochalin, V.; Gogotsi, Y.; Taberna, P.-L.; Simon, P. Ultrahigh-power micrometre-sized supercapacitors based on onion-like carbon. *Nat. Nanotechnol.* **2010**, *5*, 651–654. [CrossRef] [PubMed]

100. Omurzak, E.; Shimokawa, W.; Taniguchi, K.; Chen, L.; Okamoto, M.; Iwasaki, H.; Yamasaki, M.; Kawamura, Y.; Sulaimankulova, S.; Mashimo, T. Synthesis of wurtzite-type ZnMgS by the pulsed plasma in liquid. *Jpn. J. Appl. Phys.* **2011**, *50*, 01AB09. [CrossRef]

101. Miron, C.; Bratescu, M.A.; Saito, N.; Takai, O. Time-resolved optical emission spectroscopy in water electrical discharges. *Plasma Chem. Plasma Process* **2010**, *30*, 619–631. [CrossRef]

102. Horikoshi, S.; Serpone, N. In-liquid plasma: A novel tool in the fabrication of nanomaterials and in the treatment of wastewaters. *RSC Adv.* **2017**, *7*, 47196. [CrossRef]

103. Hyun, K.Y.; Ueno, T.; Li, O.L.; Saito, N. Synthesis of heteroatom-carbon nanosheets by solution plasma processing using *N*-methyl-2-pyrrolidone as precursor. *RSC Adv.* **2016**, *6*, 6990–6996. [CrossRef]

104. Hyun, K.Y.; Saito, N. The solution plasma process for heteroatom-carbon nanosheets: The role of precursors. *Sci. Rep.* **2017**, *7*, 3825. [CrossRef] [PubMed]

105. Panomsuwan, G.; Saito, N.; Ishizaki, T. Electrocatalytic oxygen reduction on nitrogen-doped carbon nanoparticles derived from cyano-aromatic molecules via a solution plasma approach. *Carbon* **2016**, *98*, 411–420. [CrossRef]

106. Morishita, T.; Ueno, T.; Panomsuwan, G.; Hieda, J.; Yoshida, A.; Bratescu, M.A.; Saito, N. Fastest formation routes of nanocarbons in solution plasma processes. *Sci. Rep.* **2016**, *6*, 36880. [CrossRef]

107. Lee, S.; Heo, Y.K.; Bratescu, M.A.; Ueno, T.; Saito, N. Solution plasma synthesis of a boron-carbon-nitrogen catalyst with a controllable bond structure. *Phys. Chem. Chem. Phys.* **2017**, *19*, 15264–15272. [CrossRef]

108. Li, O.L.; Chib, S.; Wad, Y.; Lee, H.S.; Ishizaki, T. Selective nitrogen bonding states in nitrogen doped carbon via a solution plasma process for advanced oxygen reduction reaction. *RSC Adv.* **2016**, *6*, 109354–109360. [CrossRef]

109. Tipplook, M.; Pornaroontham, P.; Watthanaphanit, A.; Saito, N. Liquid-phase plasma-assisted in situ synthesis of amino-rich nanocarbon for transition metal ion adsorption. *ACS Appl. Nano Mater.* **2020**, *3*, 218–228. [CrossRef]

110. Alsaeedi, A.; Show, Y. Synthesis of nano-carbon by in-liquid plasma method and its application to a support material of Pt catalyst for fuel cell. *Nanomater. Nanotechnol.* **2019**, *9*, 1–6. [CrossRef]

111. Shin, J.-G.; Park, C.-S.; Jung, E.Y.; Shin, B.J.; Tae, H.-S. Synthesis of a polyaniline nanoparticle using a solution plasma process with an Ar gas bubble channel. *Polymers* **2019**, *11*, 105. [CrossRef] [PubMed]

112. Shin, J.-G.; Shin, B.J.; Jung, E.Y.; Park, C.-S.; Kim, J.Y.; Tae, H.-S. Effects of a dielectric barrier discharge (DBD) on characteristics of polyaniline nanoparticles synthesized by a solution plasma process with an Ar gas bubble channel. *Polymers* **2020**, *12*, 1939. [CrossRef]

113. Iqbal, M.; Dinh, D.K.; Abbas, Q.; Imran, M.; Sattar, H.; Ahmad, A.U. Controlled Surface Wettability by Plasma Polymer Surface Modification. *Surfaces* **2019**, *2*, 349–371. [CrossRef]

114. Hegemann, D.; Hossain, M.M.; Ko¨rner, E.; Balazs, D.J. Macroscopic description of plasma polymerization. *Plasma Process. Polym.* **2007**, *4*, 229–238. [CrossRef]

115. Yasuda, H.K. *Plasma Polymerization*; Academic Press: Orlando, FL, USA, 1985.

116. Vandenbossche, M.; Hegemann, D. Recent approaches to reduce aging phenomena in oxygen- and nitrogen-containing plasma polymer films: An overview. *Curr. Opin. Solid State Mater. Sci.* **2018**, *22*, 26–38. [CrossRef]

117. Ligot, S.; Bousser, E.; Cossement, D.; Klemberg-Sapieha, J.; Viville, P.; Dubois, P.; Snyders, R. Correlation Between Mechanical Properties and Cross-Linking Degree of Ethyl Lactate Plasma Polymer Films. *Plasma Process. Polym.* **2015**, *12*, 508–518. [CrossRef]

118. Asandulesa, M.; Topala, I.; Pohoata, V.; Legrand, Y.M.; Dobromir, M.; Totolin, M.; Dumitrascu, N. Chemically polymerization mechanism of aromatic compounds under atmospheric pressure plasma conditions. *Plasma Chem. Plasma Process* **2013**, *10*, 469–480. [CrossRef]

119. Park, C.-S.; Kim, D.Y.; Jung, E.Y.; Jang, H.J.; Bae, G.T.; Kim, J.Y.; Shin, B.J.; Lee, H.K.; Tae, H.-S. Ultrafast Room Temperature Synthesis of Porous Polythiophene via Atmospheric Pressure Plasma Polymerization Technique and Its Application to NO$_2$ Gas Sensors. *Polymers* **2021**, *13*, 1783. [CrossRef] [PubMed]

Ultrafast Room Temperature Synthesis of Porous Polythiophene via Atmospheric Pressure Plasma Polymerization Technique and Its Application to NO₂ Gas Sensors

Choon-Sang Park [1,†], Do Yeob Kim [2,†], Eun Young Jung [3], Hyo Jun Jang [3], Gyu Tae Bae [3], Jae Young Kim [3], Bhum Jae Shin [4], Hyung-Kun Lee [2,*] and Heung-Sik Tae [3,5,*]

1   Department of Electronics and Computer Engineering, College of Engineering, Kansas State University, Manhattan, NY 66506, USA; purplepcs@ksu.edu
2   ICT Creative Research Laboratory, Electronics & Telecommunications Research Institute, Daejeon 34129, Korea; nanodykim@etri.re.kr
3   School of Electronic and Electrical Engineering, College of IT Engineering, Kyungpook National University, Daegu 41566, Korea; eyjung@knu.ac.kr (E.Y.J.); bs00201@knu.ac.kr (H.J.J.); doctor047@knu.ac.kr (G.T.B.); jyk@knu.ac.kr (J.Y.K.)
4   Department of Electronics Engineering, Sejong University, Seoul 05006, Korea; hahusbj@sejong.ac.kr
5   School of Electronics Engineering, College of IT Engineering, Kyungpook National University, Daegu 41566, Korea
*   Correspondence: hklee@etri.re.kr (H.-K.L.); hstae@ee.knu.ac.kr (H.-S.T.); Tel.: +82-53-950-6563 (H.-S.T.)
†   These authors contributed equally to this work.

Abstract: New nanostructured conducting porous polythiophene (PTh) films are directly deposited on substrates at room temperature (RT) by novel atmospheric pressure plasma jets (APPJs) polymerization technique. The proposed plasma polymerization synthesis technique can grow the PTh films with a very fast deposition rate of about 7.0 μm·min⁻¹ by improving the sufficient nucleation and fragment of the thiophene monomer. This study also compares pure and iodine (I₂)-doped PTh films to demonstrate the effects of I₂ doping. To check the feasibility as a sensing material, NO₂-sensing properties of the I₂-doped PTh films-based gas sensors are also investigated. As a result, the proposed APPJs device can produce the high density, porous and ultra-fast polymer films, and polymers-based gas sensors have high sensitivity to NO₂ at RT. Our approach enabled a series of processes from synthesis of sensing materials to fabrication of gas sensors to be carried out simultaneously.

Keywords: atmospheric pressure plasma; room temperature growth; plasma polymerization; porous polythiophene; conducting polymer; NO₂; gas sensors

1. Introduction

Recently, conducting polymers, such as polyaniline (PAni), polypyrrole (PPy), polythiophene (PTh), and their derivatives, have attracted attention to researchers as sensing materials of toxic gases [1–4]. In comparison with most of the commercial gas sensors, which are usually based on metal oxides and operated at high temperatures, the gas sensors made of conducting porous polymers have many advantages [5–7]. The advantages of conducting polymers compared to inorganic materials used until now are their diversity, their easy synthesis, and particularly, their sensitivity at room temperature. Conducting polymers can be synthesized by various techniques, such as chemical synthesis, electrochemical method, hard and soft templates, interfacial polymerization, and plasma polymerization [1]; however, some of conducting polymers are interactable and soluble in few kinds of solution [8]. Therefore, in-situ polymerization of conducting polymers on substrates with nanostructures, such as pore network or perpendicular pillar structure without external heat or association of other processes, is important for the preparation of gas sensor devices. Very recently, we have developed a nano-porous polymer synthesis

method with dry process using a novel atmospheric pressure plasma jets (APPJs) with additional guide tube and bluff body [9–16]. The nitrogen-containing polymer nanoparticles were successfully synthesized by using aniline and pyrrole monomers via an APPJs polymerization technique. The plasma polymerizations of aniline and pyrrole have been successfully implemented using intense and broad glow-like plasma [10–15]. However, there is no report on the synthesis of sulfur (S)-containing conjugated PTh through the novel APPJs polymerization technique. In addition, to the authors' knowledge, there have been no previous reports on the investigation of the gas sensors based on conducting nano-porous polymers prepared by APPJs polymerization.

Accordingly, this study uses field emission-scanning electron microscopy (FE-SEM), atomic force microscopy (AFM), Fourier transform-infrared spectroscopy (FT-IR), X-ray photoelectron spectroscopy (XPS), and time of flight-secondary ion mass spectrometry (ToF-SIMS) to analyze pure and iodine (I_2)-doped PTh films synthesized by APPJ polymerization. We also investigate the NO_2-sensing properties of the I_2-doped conducting porous PTh films in order to check the feasibility for sensing materials of gas sensors.

2. Experimental

2.1. Atmospheric Pressure Plasma Jets (APPJs) for Synthesis of Polythiophene

In the previous work, in order to produce intense glow-like plasma by using novel APPJs, we use a guide tube and polytetrafluoroethylene bluff body installed at the jet end to confine the jet flow and to minimize the quenching from ambient air. Consequently, the novel APPJs can expand farther downstream in nucleation region and can produce the broad and intense glow-like plasma during plasma polymerization (Figure S1 in the Supplementary Material). In the case of APPJs without the proposed guide and bluff body, the plasma was only produced within the area of the array jets due to the directional properties of the streamer-like plasma discharges. Whereas, in the case of the APPJs with proposed guide tube and bluff body (impinging jet) systems, the intense and broaden plasma was produced within the whole area of the impinging region, thereby increasing the plasma region about 60-fold and the deposition area. This APPJs with impinging technique can produce a broadened and intense plasma discharge with large area and homogeneous deposition of polymers. The detailed plasma polymerization method using a stationary APPJs with a guide tube and bluff body was previously described in detail [9–15]. During polymerization experiments by using APPJs, the plasma jet was not moved, and as such, experiments were conducted in a stationary deposition. Argon gas was employed as the discharge gas for plasma generation and its flow rate was fixed to 1700 standard cm^3/min (sccm). Liquid thiophene monomer was vaporized by means of a glass bubbler, which was supplied by argon gas with the flow rate of 170 standard cm^3/min. When the mass flow rate of the monomer was applied higher than the optimal condition (170 standard cm^3/min), the discharge was disturbed and becomes unstable even though the proposed guide tube and bluff body with impinging jet systems was used. Whereas, when the mass flow rate of the monomer was applied lower than the optimal condition, the deposition rate was decreased. The PTh films were obtained at a sinusoidal wave with a peak value of 8 kV and a frequency of 26 kHz under ambient air. The pure PTh films using APPJs without any proton donor doping has been an insulating state. Therefore, it is necessary to introduce charge carriers into the plasma polymerized structures to render them conductive by using I_2 doping method and require further examination for the formation of novel pure and I_2-doped PTh materials using a novel APPJs technique. For I_2 doping, PTh samples were placed in a sealed glass container containing 2 g of solid I_2 crystals for 30 sec at room temperature immediately after plasma polymerization.

2.2. Instruments

The field emission-scanning electron microscopy (FE-SEM; Hitachi SU8220, Hitachi, Tokyo, Japan) was employed to analyze the planar and cross-sectional morphologies of the synthesized PTh films with an accelerating voltage and current of 5 kV and 10 mA,

respectively. A conductive platinum coating was used when imaging the samples. The photographs of the device and plasmas were taken using a digital camera (D5300, Nikon, Tokyo, Japan) with a Macro 1:1 lens (SP AF 90 mm F2.8 Di, Tamron, Saitama, Japan). AFM (NX20, Park Systems) was used to monitor the surface roughness based on three-dimensional (3D) pure and I_2-doped PTh surface images. The scan rate was set at 0.5 Hz and the scanning area was 20 μm × 20 μm. AFM data was analyzed using the i-solution software (IMT i-solution Inc., Burnaby, BC, Canada) to obtain the distribution of granular sizes (granularity cumulation) in the deposited PTh film. The molecular structure of the PTh film on the glass was taken by using a Fourier transformation infrared spectroscopy (FT-IR; Vertex 70, Bruker, Berlin, Germany) at the Korea Basic Science Institute (KBSI; Daegu, Korea). FT-IR spectra were measured by averaging 128 scans at a wavenumber resolution of 0.6 cm^{-1} using attenuated total reflection (ATR) mode between 500 and 4000 cm^{-1} to determine the chemical difference in the pure and I_2-doped PTh films. The XPS was carried out on an ESCALAB 250XI surface analysis system (Thermo Fisher Scientific, Waltham, MA, USA), using monochromatic Al Kα X-ray source (hυ = 1486.71 eV) operated at 15 kV and 20 mA. The pressure in the analyzing chamber was maintained at 10^{-7} Pa or lower during analysis and the size of the analyzed area was 500 μm × 500 μm. Spectra were acquired with the angle between the direction of the emitted photoelectrons and the surface equal to 60°. The estimated analyzing depth of the used XPS set up was 8 to 10 nm. The high-resolution spectra were taken in the constant analyzer energy mode with a 200 eV for survey scan and a 50 eV pass energy for element scan, respectively. The value of 285.8 eV of the C 1s core level was used for calibration of the energy scale. To curve fit the high-resolution C 1s, S 2p, and O 1s peaks, the deconvolution of C 1s, S 2p, and O 1s peaks was analyzed by the Thermo Advantage software. The peaks were deconvoluted using Gaussian–Lorentzian peak shapes (constrained between 80% and 100% Gaussian) and the full-width at half maximum (FWHM) of each line shape was constrained between 2.0 and 3.0 eV. The ToF-SIMS data were obtained using a ToF-SIMS V instrument (ION-TOF GmbH, Münster, Germany) equipped with a reflectron analyzer, a bismuth primary-ion (Bi_3^+) source and a pulsed electron flood source for charge compensation. The pressure in the analysis chamber was maintained at less than 7.5 × 10^{-12} Pa. Bi_3^+ (0.5 pA) accelerated at 30 keV was used as the analysis (primary) gun. Negative-ion and positive-ion mass spectra were acquired from a 500 μm × 500 μm area using a Bi_3^+ primary-ion beam operating at 30 keV. The mass resolution was typically greater than 8000 at *m/z* = 29 Si. Secondary ions were detected in negative ion mode and a full spectrum from 1 to 2000 amu was acquired.

2.3. Sensor Fabrication and Measurement of Gas-Sensing Properties

The alumina substrates supplied with Pt interdigitated electrodes (IDEs) were ultrasonically cleaned in acetone and deionized water for 10 min, respectively. Au wires were bonded to two contact pads of the IDEs using an Au conducting paste and then heating at 500 °C for 30 min was conducted to enhance the adhesion between the Au wires and contact pads of the IDEs. The PTh films as a sensing material were directly deposited onto the alumina/IDEs substrates using APPJs polymerization. The fabricated sensor devices were located in a gas measurement chamber without any external heater. Air with 65% relative humidity was used as a balance gas at a flow rate of 1000 sccm, while 50 ppm of NO_2 gas was used as an analyte. The analyte was diluted with the balance gas to achieve the desired concentration of 0.25 to 2 ppm using mass flow controllers. The resistance of the PTh based gas sensors was recorded using a data acquisition system consisting of Agilent 34970A and BenchLink Data Logger software during the gas measurement.

3. Results and Discussion

Figure 1a shows the planar and cross-sectional SEM images of the PTh films deposited at RT for 60 s through novel APPJs polymerization technique. The pure (undoped) PTh films consisted of dense nanoparticles with porous networks and showed very fast deposition rates of about 7 μm·min^{-1} (inset of Figure 1a). Most of nanoparticles vanished after

I_2 doping for 30 sec as shown in Figure 1b and the thickness of the PTh films decreased to 3 μm (inset of Figure 1b). To further investigate the characteristics of the PTh films, roughness (R_{rms}) and grain diameter of PTh films were studied by the AFM measurement as can be seen in Figure 1c–f. The pure PTh surface showed relatively small-size protrusions and the surface R_{rms} was 370 nm. On the other hand, after I_2 doping for 30 sec, lots of large protrusions appeared on the PTh surface and the R_{rms} increased to 890 nm. In addition, as shown in the granularity cumulation distribution charts in Figure 1e,f, the diameter range for the pure PTh sample was between 0.4 and 1.8 μm. After I_2 doping, however, the diameter range became wider, between 0.3 and 2.3 μm due to particle aggregation, thereby increasing the grain size. The increase in the average grain diameter from 0.8 to 1.1 μm after I_2 doping means that I_2 doping decreases the number of grain boundaries. This decreased number of grain boundaries was mainly due to particle aggregation and disconnected networks between adjacent nanofibers from higher porosity. For this iodine doping process, the particles were aggregated due to the hydration and I_2 particles. The surface morphology of the doped PTh film was changed a more globular particle and rougher surface by an incorporation of iodine. The surface of the doped PTh film presents large grains separated by smooth areas. This type of topography can be attributed to the branched molecular geometry of the doped PTh film, which would facilitate the formation of granular agglomerates. These results are similar to the tendency of the APP polymerized polyaniline nanoparticles vanished and aggregated after I_2 doping [10]. Thereby, the surface morphology of the doped PTh film was changed into a more globular particle owing to the aggregated particles by an incorporation of iodine [10,17,18].
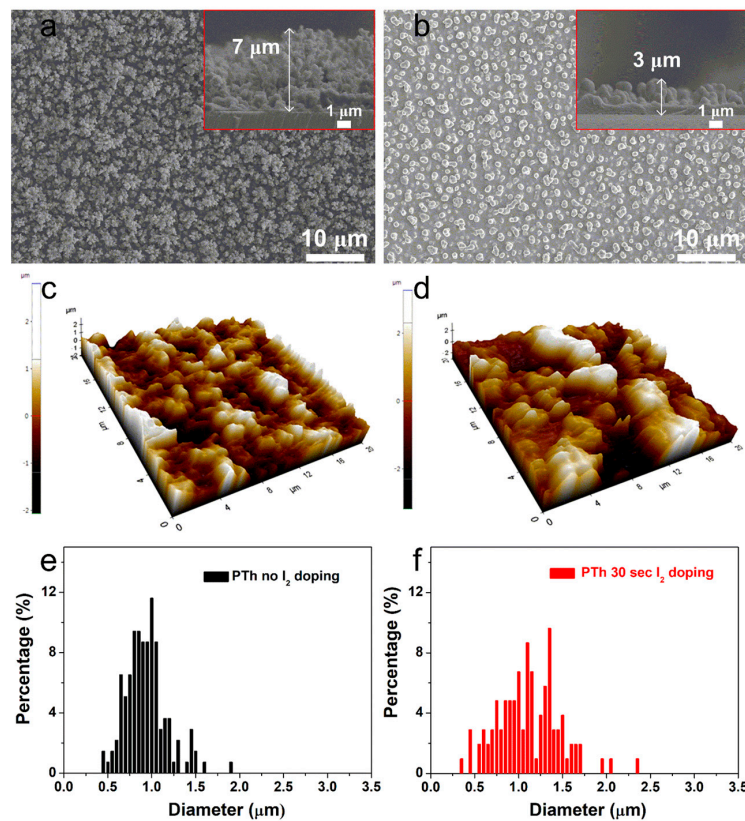
Figure 1. Planar and cross-sectional (insets) SEM images of the plasma polymerized thiophene (PTh) films (**a**) without and (**b**) with I_2 doping. AFM images of the PTh films (**c**) without and (**d**) with I_2 doping. Granularity cumulation distribution charts obtained from AFM images of the PTh films (**e**) without and (**f**) with I_2 doping.

In order to identify chemical composition of PTh films, we analyzed the films by using FT-IR and XPS techniques. Figure 2 shows the obtained FT-IR spectra of the PTh films synthesized by the novel APPJs polymerization technique. The small peak of the C–H stretching vibration of the alkyne bond was observed in the peak at 3282 cm^{-1}. Furthermore, the peak at about 2100 cm^{-1}, which in that case could be attributed to triple bond C≡C stretching of alkyne functions, seems to be present in pure PTh film [18–20]. The spectrum of polymer contains the peak at 3094 cm^{-1} that can be assigned to the C–H stretching of the aromatic proton bands within the thiophene ring. The two small peaks at 2977 and 2931 cm^{-1} can be also assigned to the C–H stretching vibration. A peak belonging to the C=O symmetric stretching vibration modes of thiophene ring was located at 1675 cm^{-1} [19]. This carbonyl group is formed due to the reaction of thiophene and oxygen in ambient air. This functional group provides the hydrophilic into the film. Therefore, water from the ambient air is absorbed, thus resulting in forming the O–H stretching bond at around 3500 cm^{-1} in the PTh film [19,20]. The peak at 1411 cm^{-1} is a characteristic of the aromatic C=C stretching vibration. A peak belonging to the C–O stretching bond was located at 1217 cm^{-1}. The peaks at 1039, 750, and 704 cm^{-1} are related to in-plane and out-of-plane C–H deformation vibration in the thiophene ring. The two peaks at 852 and 643 cm^{-1} can be assigned to the C–S bending [21–25]. Those results confirm the presence of thiophene ring in the PTh film structure. The absorption peaks at 1675 and 1217 cm^{-1} confirm the inclusion of small amounts of oxygen in the films, incorporated during plasma deposition [25]. These small amounts of oxygen could have originated in the oxidation of the PTh from ambient air [19,20]. After I$_2$ doping for 30 sec, most of the spectra peaks significantly diminished and became smooth, presumably due to the absorption of hydrogen in the PTh films via the I$_2$ doping. Iodine probably reacted with residual radicals in the PTh films by the doping. Iodine radicals can also be formed by the hemolytic dissociation of iodine. As iodine radicals can extract hydrogen atoms from the PTh structure, this could change the bonding characteristics of plasma polymerized films [18,20–27]. In particular, hydrogen iodide formed by reaction of iodine radicals and hydrogen atom can react with C≡C bond, thus causing the disappearance of C≡C bond after I$_2$ doping [20]. In addition, after I$_2$ doping process, the decrease of spectra intensities is presumably due to the decrease in the relative amounts of surface reflection, which is originated by film properties, such as particle size and surface roughness of the film [28].

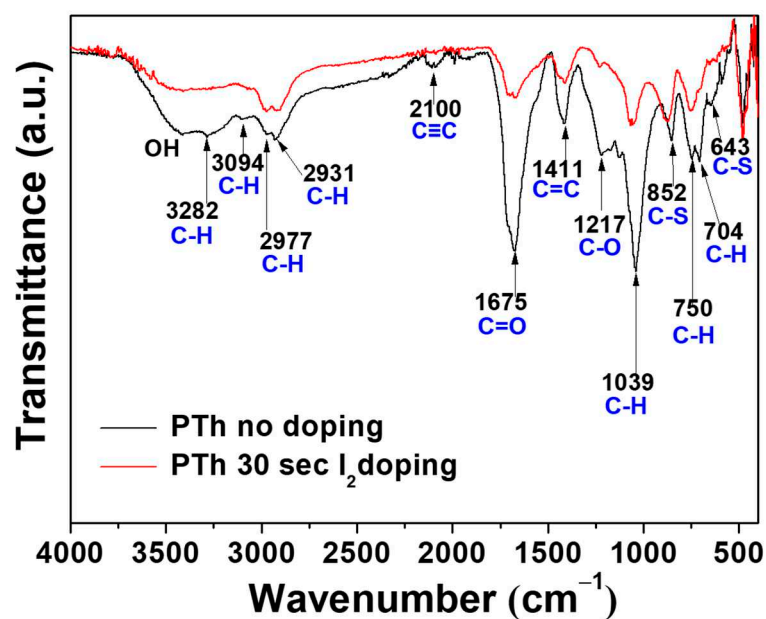**Figure 2.** FT-IR spectra of the plasma polymerized thiophene films without and with I$_2$ doping.

Chemical composition of the PTh films obtained by FT-IR spectra was analyzed by comparing the XPS results. In Table 1 and Figure 3a, the elemental concentration in atomic percentages and survey spectra identified from XPS are presented. The high-resolution C 1s, S 2p, O 1s, and I 3d peaks were analyzed in detail, as presented in Figure 3b–e and Figure S2 in the Supplementary Material. The peak assignments and envelope compositions of various C 1s, S 2p, and O 1s were summarized in Tables 2–4, respectively. The XPS survey spectra in Figure 3a show signals corresponding to C 1s (285.5 eV), S 2s (228.0 eV), S 2p (164.0 eV and 168.5 eV), O 1s (532.1 eV), I $3d_{3/2}$ (620.6 eV), I $3d_{5/2}$ (631.0 eV), and I 4d (53.0 eV) electronic orbitals. The presence of O atoms in the PTh plasma polymerized films is expected because we synthesized the PTh films under ambient air and the films obtained through APPJs polymerization technique are an oxidized state of polymer, which are in agreement with the FT-IR data. The C 1s peak could be divided into three distinctive component peaks (Figure 3b and Figure S2 in the Supplementary Material, and Table 2) attributed to C–C, C=C, C–H bonds (284.7 eV), C–S bond (287.5 eV), and C–O bond (290 eV) [25]. The S 2p peak could be split into three component peaks (Figure 3c and Figure S2 in the Supplementary Material, and Table 3) mainly contributed by aromatic sulfide (C–S–C, 163.6 eV), sulfoxide (C–SO–C, 166.38 eV), and sulfone (C–SO_2–C, 168.9 eV) [29]. The O 1s peak was decomposed in three peaks (Figure 3e and Figure S2 in the Supplementary Material, and Table 4). From the spectra of O 1s, it could be seen that S-doped carbon displays the same oxygen species of O–C–O (532.3 eV) and O=C–O (534.7 eV). In addition, it also had a characteristic peak at 531.1 eV, which was attributed to the S-containing group S=O [29,30]. The XPS spectra exhibited by I 3d core of the I_2-doped PTh are shown in Figure 3e, which shows the location of I $3d_{5/2}$ and I $3d_{3/2}$ peaks at the binding energy of 620.6 and 631.0 eV, respectively. The location of these peaks and the peak separation of 10.4 eV strongly suggest the I_2-doped polymer characteristics [30,31]. After I_2 doping for 30 sec, the carbons with oxidation, such as C–O and O–C–O, were remarkably decreased, which showed more hydrophobic characteristics [10,15]. The atomic percentage of C–C, C–H, and C=C bonds decreased from 39.9 to 31.7%, indicating some disruption to the conjugated framework of the films [31]. Whereas, S-containing groups with carbon and oxygen, such as C–S, C–SO–C, C–SO_2–C, and S=O except for C–S–C, increased when adopting the I_2 doping. Therefore, total amounts of oxygen decrease only slightly. In addition, since iodine could easily absorb hydrogen from materials, this reduced the C–H bond.

Table 1. Elemental concentration in atomic percentages of PTh films without and with I_2 doping observed in XPS spectra in Figure 3a.

Sample	Elemental Concentration			
	C 1s (at.%)	S 2p (at.%)	O 1s (at.%)	I 3d (at.%)
PTh without I_2 doping	67.8	20.9	11.3	0.0
PTh with I_2 doping	68.4	18.6	11.0	2.0

Table 2. Peak assignment (BE, eV) and envelope composition (%, total = 100) of various C 1s core level spectra of PTh films observed in XPS in Figure 3b.

Sample	C 1s Peaks Assignment and Envelope Composition		
	284.70 C–C, C–H, C=C	287.53 C–S	290.03 C–O
PTh without I_2 doping	39.9	43.5	16.6
PTh with I_2 doping	31.7	56.9	11.4
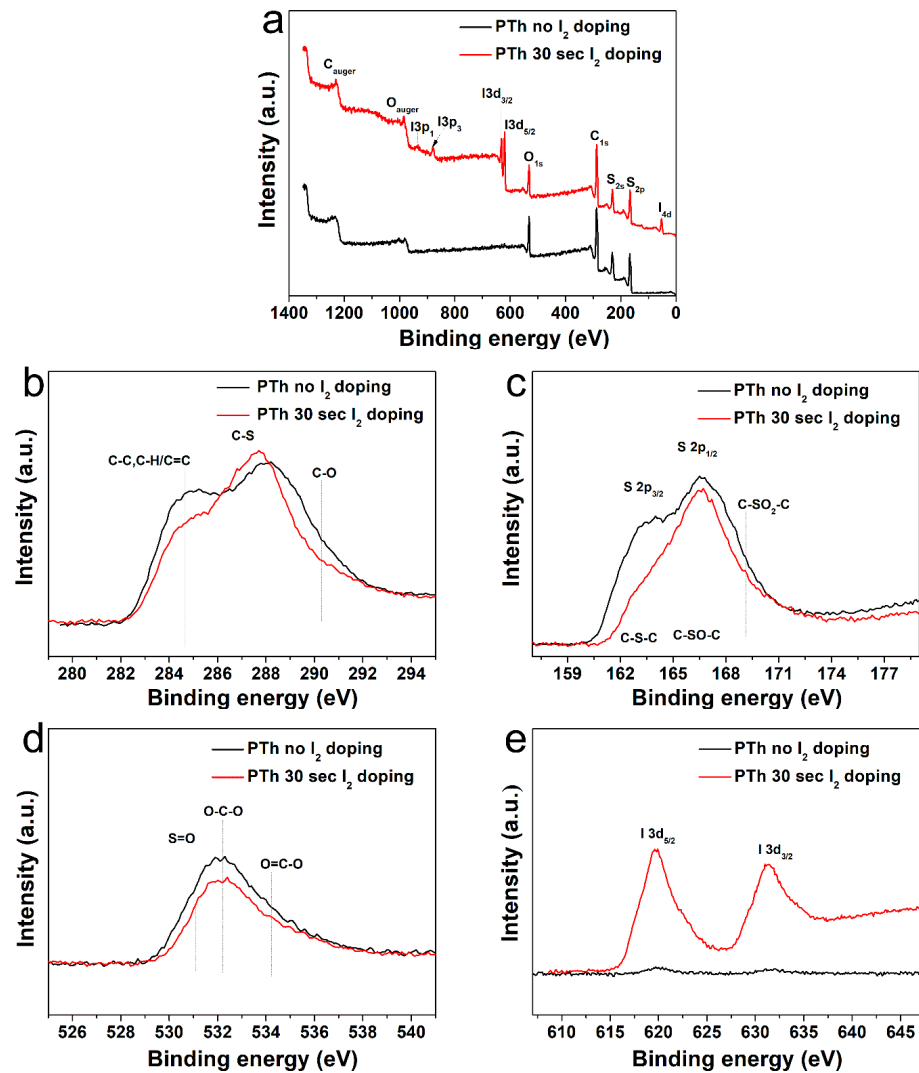
Figure 3. (**a**) XPS spectra of the plasma polymerized thiophene films without and with I_2 doping. High-resolution XPS spectra of (**b**) C 1s, (**c**) S 2p, (**d**) O 1s, and (**e**) I 3d.

Table 3. Peak assignment and envelope composition of various S 2p core level spectra of PTh films observed in XPS in Figure 3c.

Sample	S 2p Peaks Assignment and Envelope Composition		
	163.62 C–S–C	166.38 C–SO–C	168.99 C–SO$_2$–C
PTh without I_2 doping	39.7	46.8	13.5
PTh with I_2 doping	27.1	57.0	15.9

Table 4. Peak assignment and envelope composition of various O 1s core level spectra of PTh films observed in XPS in Figure 3d.

Sample	O 1s Peaks Assignment and Envelope Composition		
	531.12 S=O	532.38 O–C–O	534.74 O=C–O
PTh without I_2 doping	15.7	58.5	25.8
PTh with I_2 doping	18.4	52.7	28.9

35

In order to determine the specific chemical structures between the pure and I_2-doped PTh films after the APPJs polymerization, the PTh films were characterized in both the positive and negative ion modes using ToF-SIMS. In Figure 4 and Figure S3 in the Supplementary Material, the negatively and positively charged ions static mass spectra and normalized intensities of ToF-SIMS for the PTh films are presented. The assignments of the selected peaks of PTh detected in the negative and positive mode are shown in Tables S1 and S2 in the Supplementary Material. For the PTh features, several characteristic peaks from the polymer chain were detected. In Figure S3a,b in the Supplementary Material, many ion peaks of the S-containing group were detected at m/z = 32, 33, 44, 45, 48, 56, 57, 64, 80, 81, 83, 92, 93, 105, and 129 amu and attributed to S^-, HS^-, CS^-, CHS^-, SO^-, C_2S^-, C_2HS^-, SO_2^-, C_4HS^-, $C_4H_3S^-$, C_5S^-, C_5HS^-, C_6HS^-, and C_8HS^-, respectively, which were characteristics of PTh fragments. The negative ions were related with abundant secondary ions $C_{2n}HS^-$ (n = 0–4) which were the fragments of PTh backbones (with alkyl side chains). The $C_{2n}HS^-$ ions show that polythiophene backbones were easily accessed by ToF-SIMS. In addition, the secondary ion fragments $C_{2n}H^-$ (n = 0–4) of alkyl side chains (and S- from thiophene ring) were detected (Figure 4a) [15,32]. Figure S3c,d in the Supplementary Material show the series of hydrocarbon fragments arising from PTh, such as CH_3^+, $C_2H_3^+$, $C_2H_5^+$, $C_3H_3^+$, $C_3H_5^+$, $C_3H_7^+$, $C_4H_3^+$, $C_4H_5^+$, $C_4H_7^+$, $C_4H_9^+$, $C_5H_7^+$, $C_5H_9^+$, $C_6H_5^+$, $C_6H_9^+$, $C_7H_7^+$, $C_7H_9^+$, and $C_7H_{11}^+$. These clusters are typical aliphatic hydrocarbon fragments of the form C_nH_{2n-3}, C_nH_{2n-1}, and C_nH_{2n+1}, arising from the PTh chain (Figure 4b). After I_2 doping for 30 sec, almost all normalized intensities were decreased, presumably due to the absorption of hydrogen in the PTh films via the I_2 doping. In addition, few negative and positive ion peaks of the oxygen-containing group were detected, which was likely to originate from the oxidation of particles from atmospheric pressure during the APPJs polymerization. These results agreed well with the FT-IR and XPS analyses.
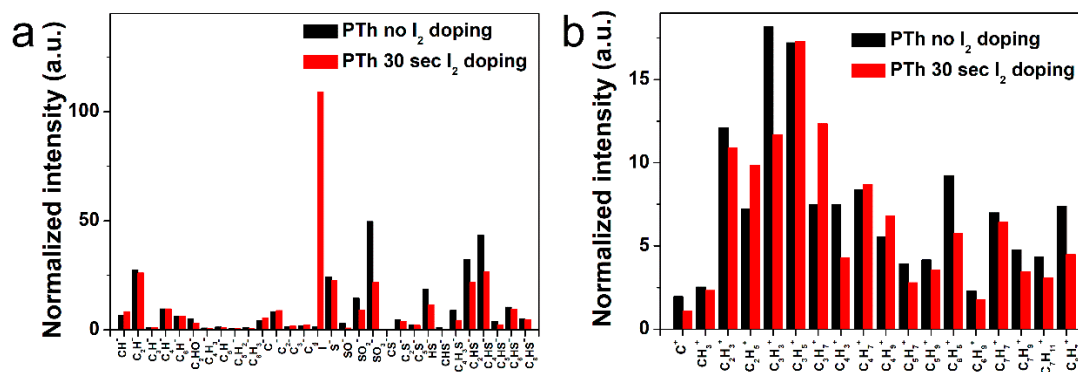
Figure 4. Normalized intensities of (**a**) negative-ion spectra and (**b**) positive-ion spectra of ToF-SIMS on surface of the plasma polymerized thiophene films without and with I_2 doping.

To check the feasibility as a sensing material for the detection of poisonous gas, we investigated NO_2 sensing characteristics of the I_2-doped PTh films at RT. The gas response is defined as follows. Response (%) = $(R_a - R_g)/R_a \times 100$, where R_a and R_g are resistances of the PTh films before and after exposure to NO_2 gas, respectively.

Figure 5a,b show the dynamic resistance and response of the gas sensors to various NO_2 concentrations ranging from 0.25 to 2 ppm, respectively. It is observed that the exposure of PTh films to NO_2 results in a decrease in value of resistance and the resistance of the PTh films gradually recover to its initial value when NO_2 gas is turned off. It is known that PTh is a *p*-type material and NO_2 is an oxidizing gas (electron acceptor). When PTh interacts with NO_2, the concentration of majority charge carriers (holes) increases, which implies that the conductivity of *p*-type PTh increases. The initial base resistance (~31 MΩ) shifts toward lower resistance (~28 MΩ right before exposure to 2 ppm) with an increase in the NO_2 concentration because the longer time is required for full recovery. Figure 5c

shows the response of PTh films as a function of NO_2 concentration. The gas response is increased with an increase in the NO_2 concentration and the response of the PTh films was 21, 47, 72, and 84% for the NO_2 concentration of 0.25, 0.5, 1, and 2 ppm, respectively. The gas sensors reported here exhibit highly sensitive behavior to NO_2 compared to PTh based sensors reported previously, as shown in Table 5 [33–35]. To examine the repeatability of the sensor based on I_2-doped PTh films, the NO_2-sensing measurement was repeated, as shown in Figure S4 in the Supplementary Material. The difference in response between the first and second measurements at each concentration was within 5%, indicating good repeatability of the sensor based on I_2-doped PTh films.
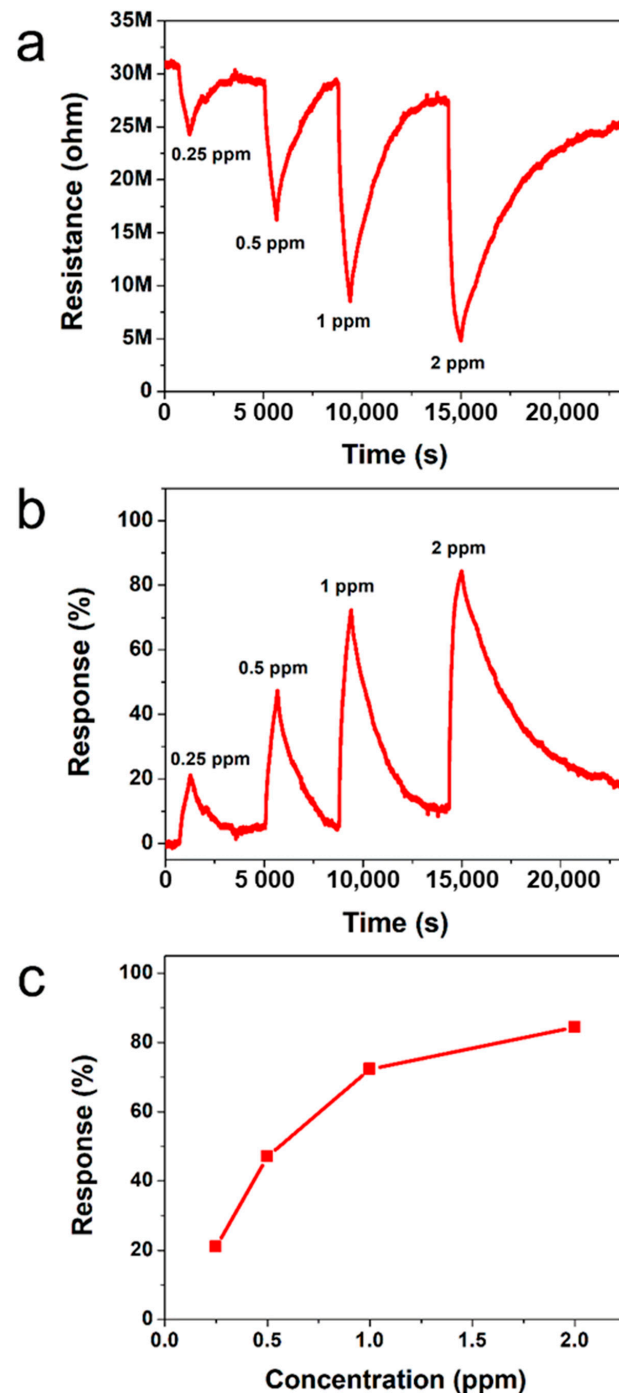
Figure 5. Transient (**a**) resistance and (**b**) response of sensors based on I_2-doped PTh films to different NO_2 concentrations at RT. (**c**) Responses as a function of NO_2 concentration.

Table 5. NO_2 responses of PTh based gas sensors.

Sensing Material	Concentration	Temperature	Response	Ref
PTh	1 ppm	RT	3%	1
PTh	10 ppm	RT	9%	2
PTh	10 ppm	RT	8%	3
Poly(3-hexylthiophene)	20 ppm	RT	10%	4
PTh	1 ppm	RT	72%	This work

We think that the high response of PTh through APPJs polymerization comes from porous structure of PTh resulting from in-situ polymerization on the substrate. Such a higly porous structure assists NO_2 in interacting with the surface of PTh films as well as the inside of porous network. As a result, new nanostructured conducting porous polymer sensor prepared using novel APPJs polymerization technique showed the excellent NO_2-sensing properties at RT. In addition, our approach enables a series of processes from synthesis of sensing materials to fabrication of gas sensors to be carried out simultaneously.

4. Conclusions

In this study, porous PTh films were successfully synthesized from liquid thiophene monomer by using novel APPJs polymerization technique and demonstrated as a sensing material for NO_2 detection. The PTh films consisted of dense nanoparticles with porous networks and had ultra-high fast deposition rates of about 7.0 $\mu m \cdot min^{-1}$. Spectroscopic analyses (FT-IR, XPS, and ToF-SIMS) reflect the retention of the aromatic ring and fragments of backbones in the structure of PTh films. As a result, new nanostructured conducting porous PTh sensor prepared using novel APPJs polymerization technique with I_2 doping showed the excellent NO_2-sensing properties at RT.

References

1. Bai, H.; Shi, G. Gas sensors based on conducting polymers. *Sensors* **2007**, *7*, 267–307. [CrossRef]
2. Bissell, R.A.; Persaud, K.C.; Travers, P. The influence of non-specific molecular partitioning of analytes on the electrical responses of conducting organic polymer gas sensors. *Phys. Chem. Chem. Phys.* **2002**, *4*, 3482–3490. [CrossRef]
3. Virji, S.; Huang, J.; Kaner, R.B.; Weiller, B.H. Polyaniline nanofiber gas sensors: Examination of response mechanisms. *Nano. Lett.* **2004**, *4*, 491–496. [CrossRef]
4. Nicolas-Debarnot, D.; Poncin-Epaillard, F. Polyaniline as a new sensitive layer for gas sensors. *Anal. Chim. Acta* **2003**, *475*, 1–15. [CrossRef]
5. Kim, D.Y.; Kang, H.; Choi, N.-J.; Park, K.H.; Lee, H.-K. A carbon dioxide gas sensor based on cobalt oxide containing barium carbonate. *Sens. Actuators B Chem.* **2017**, *248*, 987–992. [CrossRef]
6. Yang, F.; Su, H.; Zhu, Y.; Chen, J.; Lau, W.M.; Zhang, D. Bioinspired synthesis and gas-sensing performance of porous hierarchical α-Fe_2O_3/C nanocomposites. *Scr. Mater.* **2013**, *68*, 873–876. [CrossRef]
7. Sharma, A.; Bhojane, P.; Rana, A.K.; Kumar, Y.; Shirage, P.M. Mesoporous nickel cobalt hydroxide/oxide as an excellent room temperature ammonia sensor. *Scr. Mater.* **2017**, *128*, 65–68. [CrossRef]
8. Frommer, J.E. Conducting polymer solutions. *Acc. Chem. Res.* **1986**, *19*, 2–9. [CrossRef]
9. Kim, D.H.; Park, C.-S.; Kim, W.H.; Shin, B.J.; Hong, J.G.; Park, T.S.; Seo, J.H.; Tae, H.-S. Influences of guide-tube and bluff-body on advanced atmospheric pressure plasma source for single-crystalline polymer nanoparticle synthesis at low temperature. *Phys. Plasmas* **2017**, *24*, 023506. [CrossRef]
10. Park, C.-S.; Kim, D.Y.; Kim, D.H.; Lee, H.-K.; Shin, B.J.; Tae, H.-S. Humidity-independent conducting polyaniline films synthesized using advanced atmospheric pressure plasma polymerization with in-situ iodine doping. *Appl. Phys. Lett.* **2017**, *110*, 033502. [CrossRef]
11. Park, C.-S.; Jung, E.Y.; Jang, H.J.; Bae, G.T.; Shin, B.J.; Tae, H.S. Synthesis and properties of plasma-polymerized methyl methacrylate via the atmospheric pressure plasma polymerization technique. *Polymers* **2019**, *11*, 396. [CrossRef]
12. Jang, H.J.; Park, C.S.; Jung, E.Y.; Bae, G.T.; Shin, B.J.; Tae, H.S. Synthesis and properties of thiophene and aniline copolymer using atmospheric pressure plasma jets copolymerization technique. *Polymers* **2020**, *12*, 2225. [CrossRef] [PubMed]
13. Park, C.-S.; Kim, D.H.; Shin, B.J.; Kim, D.Y.; Lee, H.-K.; Tae, H.-S. Conductive polymer synthesis with single-crystallinity via a novel plasma polymerization technique for gas sensor applications. *Materials* **2016**, *9*, 812. [CrossRef] [PubMed]
14. Park, C.-S.; Kim, D.H.; Shin, B.J.; Tae, H.-S. Synthesis and characterization of nanofibrous polyaniline thin film prepared by novel atmospheric pressure plasma polymerization technique. *Materials* **2016**, *9*, 39. [CrossRef] [PubMed]
15. Park, C.-S.; Jung, E.Y.; Kim, D.H.; Kim, D.Y.; Lee, H.-K.; Shin, B.J.; Lee, D.H.; Tae, H.-S. Atmospheric pressure plasma polymerization synthesis and characterization of polyaniline films doped with and without iodine. *Materials* **2017**, *10*, 1272. [CrossRef] [PubMed]
16. Kim, D.H.; Kim, H.-J.; Park, C.-S.; Shin, B.J.; Seo, J.H.; Tae, H.-S. Atmospheric pressure plasma polymerization using double grounded electrodes with He/Ar mixture. *AIP Adv.* **2015**, *5*, 097137. [CrossRef]
17. Zhang, D.Y.; Porter, T.L. Surface morphology changes in polythiophene and polythiophene derivative films after being oxidized with iodine. A scanning probe. *Synth. Met.* **1995**, *74*, 55–58. [CrossRef]
18. Paosawatyanyong, B.; Kamphiranon, P.; Bannarakkul, W.; Srithana-anant, Y.; Bhanthumnavin, W. Doping of polythiophene by microwave plasma deposition. *Surf. Coat. Technol.* **2010**, *204*, 3053–3058. [CrossRef]
19. Dams, R.; Vangeneugden, D.; Vanderzande, D. Plasma Deposition of Thiophene Derivatives Under Atmospheric Pressure. *Chem. Vap. Depos.* **2006**, *12*, 719–727. [CrossRef]
20. Groenewoud, L.M.H.; Engbers, G.H.M.; White, R.; Feijen, J. On the iodine doping process of plasma polymerised thiophene layers. *Synth. Met.* **2002**, *125*, 429–440. [CrossRef]
21. Rassie, C.; Olowu, R.A.; Waryo, T.T.; Wilson, L.; Williams, A.; Baker, P.G.; Iwuoha, E.I. Dendritic 7T-polythiophene electro-catalytic sensor system for the determination of polycyclic aromatic hydrocarbons. *Int. J. Electrochem. Sci.* **2011**, *6*, 1949–1967.
22. Navale, S.T.; Mane, A.T.; Khuspe, G.D.; Chougule, M.A.; Patil, V.B. Room temperature NO_2 sensing properties of polythiophene films. *Synth. Met.* **2014**, *195*, 228–233. [CrossRef]
23. Liu, R.; Liu, Z. Polythiophene: Synthesis in aqueous medium and controllable morphology. *Chin. Sci. Bull.* **2009**, *54*, 2028–2032. [CrossRef]
24. Gnanakan, S.R.P.; Rajasekhar, M.; Subramania, A. Synthesis of polythiophene nanoparticles by surfactant-assisted dilute polymerization method for high performance redox supercapacitors. *Int. J. Electrochem. Sci.* **2009**, *4*, 1289–1301.
25. Teslaru, T.; Topala, I.; Dobromir, M.; Pohoata, V.; Curecheriu, L.; Dumitrascu, N. Polythiophene films obtained by polymerization under atmospheric pressure plasma conditions. *Mater. Chem. Phys.* **2016**, *169*, 120–127. [CrossRef]
26. Zoromba, M.S.; El-Ghamaz, N.A.; El-Sonbati, A.Z.; El-Bindary, A.A.; Diab, M.A.; El-Shahat, O. Conducting polymers. VII. Effect of doping with iodine on the dielectrical and electrical conduction properties of polyaniline. *Synth. React. Inorg. Met. Nano Metal. Chem.* **2016**, *46*, 1179–1188. [CrossRef]
27. Malkeshi, H.; Moghaddam, H.M. Ammonia gas-sensing based on polythiophene film prepared through electrophoretic deposition method. *J. Polym. Res.* **2016**, *13*, 108. [CrossRef]
28. Laroche, G.; Fitremann, J.; Gherardi, N. FTIR-ATR spectroscopy in thin film studies: The importance of sampling depth and deposition substrate. *Appl. Surf. Sci.* **2013**, *273*, 632–637. [CrossRef]

29. Ji, H.; Wang, T.; Liu, Y.; Lu, C.; Yang, G.; Ding, W.; Hou, W. A novel approach for sulfur-doped hierarchically porous carbon with excellent capacitance for electrochemical energy storage. *Chem. Commun.* **2016**, *52*, 12725–12728. [CrossRef]

30. Zhu, M.; Zhang, W.; Li, Y.; Gai, L.; Zhou, J.; Ma, W. Multishell structured magnetic nanocomposites carrying a copolymer of pyrrole–thiophene for highly selective Au(III) recovery. *J. Mater. Chem. A* **2016**, *4*, 19060–19069. [CrossRef]

31. Kantzas, T.T.; Byers, J.C.; Semenikhin, O.A. Photocurrent enhancement in polythiophene-based photoelectrodes through electrochemical anodic halogenation. *J. Electrochem. Soc.* **2012**, *159*, H885–H892. [CrossRef]

32. Awsiuk, K.; Budkowski, A.; Marzec, M.M.; Petrou, P.; Rysz, J.; Bernasik, A. Effects of polythiophene surface structure on adsorption and conformation of bovine serum albumin: A multivariate and multitechnique study. *Langmuir* **2014**, *30*, 13925–13933. [CrossRef] [PubMed]

33. Kamble, D.B.; Sharma, A.K.; Yadav, J.B.; Patil, V.B.; Devan, R.S.; Jatratkar, A.A.; Yewale, M.A.; Ganbavle, V.V.; Pawar, S.D. Facile chemical bath deposition method for interconnected nanofibrous polythiophene thin films and their use for highly efficient room temperature NO_2 sensor application. *Sens. Actuators B Chem.* **2017**, *244*, 522–530. [CrossRef]

34. Dua, V.; Surwade, S.P.; Ammu, S.; Zhang, X.; Jain, S.; Manohar, S.K. Chemical Vapor Detection Using Parent Polythiophene Nanofibers. *Macromolecules* **2009**, *42*, 5414–5415. [CrossRef]

35. Xie, T.; Xie, G.; Zhou, Y.; Huang, J.; Wu, M.; Jiang, Y.; Tai, H. Thin film transistors gas sensors based on reduced graphene oxide poly(3-hexylthiophene) bilayer film for nitrogen dioxide detection. *Chem. Phys. Lett.* **2014**, *614*, 275–281. [CrossRef]

Optimization of Atmospheric Pressure Plasma Jet with Single-Pin Electrode Configuration and Its Application in Polyaniline Thin Film Growth

Eun Young Jung [1,†] , Choon-Sang Park [2,†], Hyo Jun Jang [1], Shahzad Iqbal [1] , Tae Eun Hong [3], Bhum Jae Shin [4], Muhan Choi [1,5] and Heung-Sik Tae [1,6,*]

1   School of Electronic and Electrical Engineering, College of IT Engineering, Kyungpook National University, Daegu 41566, Korea; eyjung@knu.ac.kr (E.Y.J.); bs00201@knu.ac.kr (H.J.J.); shahzadiqbal@knu.ac.kr (S.I.); mhchoi@ee.knu.ac.kr (M.C.)
2   Department of Electrical Engineering, Milligan University, Johnson City, TN 37682, USA; cpark@milligan.edu
3   Division of High-Technology Materials Research, Korea Basic Science Institute, Busan 46742, Korea; tehong@kbsi.re.kr
4   Department of Electronics Engineering, Sejong University, Seoul 05006, Korea; hahusbj@sejong.ac.kr
5   Digital Technology Research Center, Kyungpook National University, Daegu 41566, Korea
6   School of Electronics Engineering, College of IT Engineering, Kyungpook National University, Daegu 41566, Korea
*   Correspondence: hstae@ee.knu.ac.kr
†   These authors contributed equally to this work.

Abstract: This study systematically investigated an atmospheric pressure plasma reactor with a centered single pin electrode inside a dielectric tube for depositing the polyaniline (PANI) thin film based on the experimental case studies relative to variations in pin electrode configurations (cases I, II, and III), bluff-body heights, and argon (Ar) gas flow rates. In these cases, the intensified charge-coupled device and optical emission spectroscopy were analyzed to investigate the factors affecting intensive glow-like plasma generation for deposition with a large area. Compared to case I, the intense glow-like plasma of the cases II and III generated abundant reactive nitrogen species (RNSs) and excited argon radical species for fragmentation and recombination of PANI. In case III, the film thickness and deposition rate of the PANI thin film were about 450 nm and 7.5 nm/min, respectively. This increase may imply that the increase in the excited radical species contributes to the fragmentation and recombination due to the increase in RNSs and excited argon radicals during the atmospheric pressure (AP) plasma polymerization to obtain the PANI thin film. This intense glow-like plasma generated broadly by the AP plasma reactor can uniformly deposit the PANI thin film, which is confirmed by field emission-scanning electron microscopy and Fourier transform infrared spectroscopy.

Keywords: atmospheric pressure plasmas; glow-like discharge; single pin electrode; plasma deposition; PANI thin film

1. Introduction

In recent decades, the atmospheric pressure plasma (APP) process has attracted much attention due to its many advantages, such as low cost and fast operation, low temperature, operation in air, and the ability to produce reactive chemistry at room temperature [1,2]. Thus, the APP process has enabled technology in several biological and industrial applications, such as thin-film deposition, nanomaterial synthesis, polymeric surface modification, and biomedical applications [1–6]. Numerous research groups have developed various kinds of plasma devices based on methods of plasma generation and studied using the discharge plasma based on different geometries using various electrode materials [1,7–15].

Our group has proposed a new plasma polymerization technique adopting an additional glass-tube and bluff-body system. Additionally, we have been researching the synthesis of polymers and copolymers using AP plasma processing [16]. Recently, a new AP plasma reactor (APPR) with a needle electrode has been proposed by J.Y. Kim et. al. [17,18]. However, no detailed experimental results exist for various electrode configurations in atmospheric plasma. Therefore, it is necessary to specifically investigate case studies on the various electrode configurations for a high deposition rate to overcome the localized area deposition. In particular, we focused on the various case studies of pin electrode configurations for overcoming the localized area deposition problem by supplying excited species formed within the gas-feeding tube into the nucleation (or fragmentation) region.

Accordingly, we systematically investigate the plasma properties of APPR with three pin electrode configurations, argon flow rates, and bluff-body heights. The plasma characteristics of APPR are investigated using an intensified charge-coupled device (ICCD) and optical emission spectroscopy (OES). Moreover, we investigated the characteristics of the deposited PANI thin film prepared by APPR with respect to three electrode configurations. The deposited polyaniline (PANI) thin films were characterized using field emission-scanning electron microscopy (FE-SEM), atomic force microscopy (AFM), stylus profiler, and Fourier transform infrared spectroscopy (FTIR).

2. Materials and Methods

2.1. Experimental Setup

Figure 1 shows the experimental setup and the configuration of the APPR used. Herein, we mainly focused on the three pin electrode configurations (cases I, II, and III) to generate glow-like discharge for depositing a large-area polymer thin film. For all cases, the APPR comprises a glass tube for feeding the gas (i.e., gas-feeding tube), a glass guide-tube for generating plasma, a bluff-body, a capillary glass tube, and a centered pin electrode made up of a 0.5 mm diameter tungsten needle. The tungsten wire electrode was covered with a capillary glass tube, and the tip of the tungsten wire was protruded at 2 mm from the end of the capillary glass tube. Additionally, the glass guide-tube has a length and an outer diameter of 7.5 cm and 34 mm, respectively. The gas injection glass tube has a length and inner diameter of 37 cm and 6.8 mm, respectively. The bluff-body was made of polytetrafluoroethylene insulating material, and the substrate was placed on the bluff-body inside the glass guide-tube. The bluff-body position with respect to the guide-tube significantly influences the production of intense and broadened plasma in the nucleation (or fragmentation) region.

Moreover, this APPR was used with a single pin electrode configuration with no grounded electrode. In particular, in case I, the pin electrode was vertically placed in the center of a glass guide-tube parallel to the gas-feeding tube. In case II, the pin electrode was titled at ~50° on the side of the glass guide-tube and was also separated from the gas-feeding tube. In case III, the pin electrode was vertically combined into the gas-feeding tube on top of the glass guide-tube in the APPR to form excited radical spaces at the gas-feeding tube for large-area plasma expansion. The case III structure is largely divided into two parts. Part 1 forms the free excited radical for injecting the excited radical spaces in the gas-feeding tube. Part 2 is the region where the nucleation (or fragmentation) reaction occurs by the injected free excited radical species for polymer thin-film deposition.

The aniline monomer solution was coated on glass and silicon wafer substrates by the proposed APPR with various pin electrodes. Accordingly, to produce the intense glow-like plasma, three case studies were systematically investigated using three electrode configurations, different argon flow rates, and bluff-body heights. The detailed case studies for generating plasma discharge are presented in Figure 1 and Table 1.
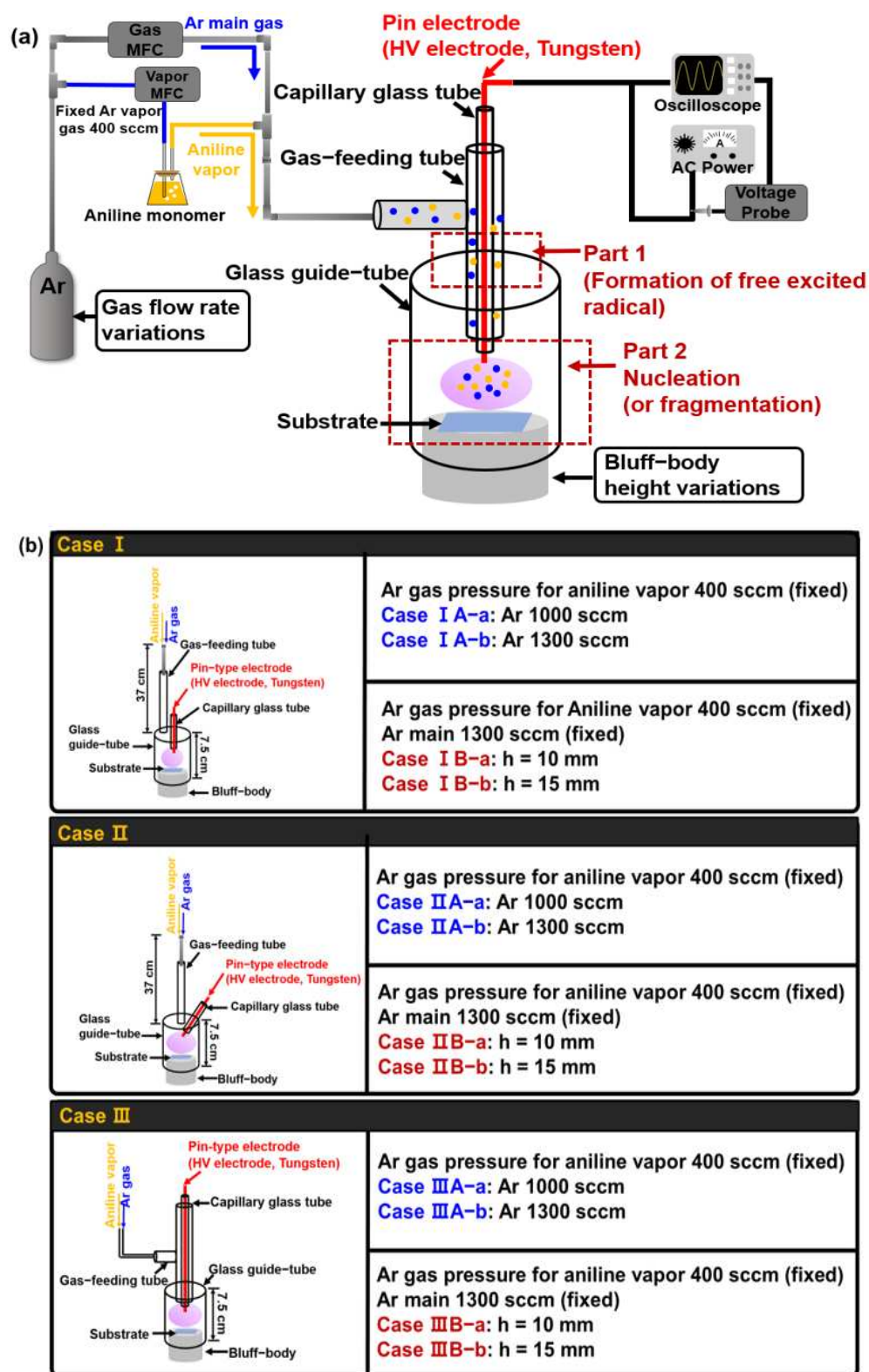
Figure 1. (**a**) Experimental setup, (**b**) schematic for three electrode configurations of APPR, and the detailed case studies used herein.

High-of argon (99.999%) was used as the main gas for producing the intense glow-like plasma. Aniline monomer (MW = 93 g·mol^{-1}, Sigma-Aldrich Co., St. Louis, MO, USA) solution was vaporized using a glass bubbler with a 40-mL amount, which was supplied by argon flowing at 400 standard cubic centimeters per minute (sccm). A bipolar sinusoidal

voltage wave pulse with a peak-to-peak (V_{p-p}) value of 8 kV and a frequency of 30 kHz was applied to the powdered pin electrode to produce the plasma. The characteristics of the plasma produced by the APPR strongly depend on the system configuration, gas flow rate, and bluff-body height.

Table 1. Detailed case studies for generating the intense glow-like discharge using APPR with pin electrode used herein.

Electrode Configuration	Case I: Vertically Parallel Pin Electrode
	Case II: Titled Pin Electrode
	Case III: Vertically Combined Pin Electrode
Precursor liquid solution	Aniline monomer
Driving power source	AC sinusoidal
Plasma driving voltage (V_{p-p})	8 kV (Fixed)
Frequency	30 kHz (Fixed)
Argon pressure for aniline vapor	400 sccm (Fixed)
Argon main gas pressure	1000 sccm and 1300 sccm (controllable)
Bluff-body height	10 mm and 15 mm (controllable)

2.2. Intensified Charge-Coupled Device (ICCD)

The generated plasma investigations were conducted using an ICCD camera (PI-MAX 2, Princeton Instruments, Trenton, NJ, USA) in both shutter modes with 100 ms exposure time to identify the spatial distribution of the generated glow plasma.

2.3. Discharge Voltage and Current Waveform Analysis

The applied voltage and discharge current were obtained using a high-voltage probe (P6015A, Tektronix Inc., Beaverton, OR, USA) and a current monitor (Pearson 4100, Pearson Electronics Inc., Palo Alto, CA, USA), respectively. The electrical signals were monitored and stored through a digital oscilloscope (WaveRunner 64Xi, Teledyne LeCroy Inc., Chestnut Ridge, NY, USA). The discharge current was obtained by subtracting the current waveform obtained when the plasma was turned off by stopping the argon supply from the current waveform, measured when the plasma was turned on.

2.4. Optical Emission Spectroscopy

To investigate the excited radical species present in the generated plasma discharge due to the interaction between the aniline monomer and argon plasma, OES techniques were used to measure and analyze the optical intensities and spectra of the excited nitrogen and argon peaks, using a fiber optic spectrometer (Ocean Optics Inc., USB-4000, Dunedin, FL, USA) associated with a 1 mm diameter optical fiber and a collimating lens. The spectral resolution of the instrument was 0.06 nm.

2.5. Field Emission-Scanning Electron Microscopy

The surface morphology images of the PANI thin films were examined using FE-SEM (Hitachi SU8220, Hitachi High-Technologies, Tokyo, Japan) with accelerated electrons at a voltage and current of 3 kV and 10 μA, respectively. The samples for FE-SEM were made conductive by coating them with platinum before loading into the chamber.

2.6. Stylus Profiler

The film thicknesses of the PANI thin films were obtained using a stylus profiler (KLA Tencor, P-7, KLA Tencor Corp., Milpitas, CA, USA) at the Korea Basic Science Institute (KBSI; Busan, Korea). Measurements were performed while moving the stylus in contact with the PANI film surface at a scan speed of 200 μm/s.

2.7. Atomic Force Microscopy

The surface roughness characteristics of the PANI thin films were investigated in a on a noncontact mode by AFM (NanoWizard II, Brucker, Berlin, Germany) at the Korea Basic Science Institute (KBSI; Busan, Korea). All measurements were obtained under controlled room temperature. Moreover, the scanning area was 20 μm × 20 μm, and the scan rate was set at 1 Hz. Bruker NanoWizard software was used for image processing and interpretation.

2.8. Fourier Transform Infrared Spectroscopy

The main functional groups and crystalline phases of the PANI thin films were measured by FTIR (Vertex 70, Bruker, Ettlingen, Germany) at the KBSI (Daegu, Korea). The FTIR spectra were measured by averaging 128 scans at a wavenumber resolution of 0.6 cm^{-1} ranging from 650–4000 cm^{-1} in the attenuated total reflection (ATR) mode.

3. Results

Figure 2 shows the ICCD images of plasma discharge generated by the proposed APPR with various case studies such as three electrode configurations, argon flow rates, and bluff-body heights. To optimize the geometry of the proposed APPR for large-area deposition, we investigated the various cases, namely, three different electrode configurations (cases I–III), two different gas flow rates, and two different bluff-body heights inside the guide-tube. The detailed case studies for generating plasma discharge are presented in Figures 1 and 2.

For all three cases, the plasma intensity increased when the main gas (argon) flow rate increased from 1000 to 1300 sccm (Figure 2). This result implies that the higher argon flow is essential in generating the glow discharge with highly intense cloud-like glow plasma [19–22]. Additionally, for all cases, when changing the bluff-body height from 10 (cases IB-a, IIB-a, and IIIB-a) to 15 mm (cases IB-b, IIB-b, and IIIB-b), with other conditions kept constant, the produced plasma discharge was highly intense.

Moreover, the ICCD images show that the intense plasma is generated at the vicinity of the needle electrode applied by high voltage [23–26]. In particular, the produced plasma in case III was spatially expanded into the horizontal space inside the guide-tube of the APPR due to the nucleation and fragmentation reactions through the injected free excited radical species. These results confirmed that optimal conditions were required to generate the glow discharge with intense glow-like plasma for PANI thin film deposition. Based on the experimental results of Figure 2, the optimal conditions were obtained for producing highly intense plasma and synthesizing PANI thin film. The optimal conditions are argon flow rate and bluff-body height of 1300 sccm and 15 mm, respectively.

To identify the discharge behavior of the APPR at an optimal condition for the three-pin electrode configurations (cases I, II, and III), the applied voltage, total current in plasma ON state, and instantaneous power were each measured as a function of time, and the results are indicated in Figure 3.

For all cases, the average power, P_a in the APPR was calculated from Equation (1).

$$P_a = \frac{1}{T} \int_0^T V(t) \times I(t) dt \tag{1}$$

where T is the applied voltage period, V(t) is the voltage signal, I(t) is the acquired current, and t is the time. The average power during 1 period was calculated through the integrated value of the power waveform during 1 period. Consequently, the average power values of the plasma reactors in cases I, II, and III are 0.8, 1.5, and 1.6 W, respectively. Table 2 summarizes the detailed experimental results of the APPR under optimal conditions with three electrode configurations. Thus, it was confirmed that case III exhibited the highest dissipated power, mainly because excited radical species were produced within the gas-feeding tube.
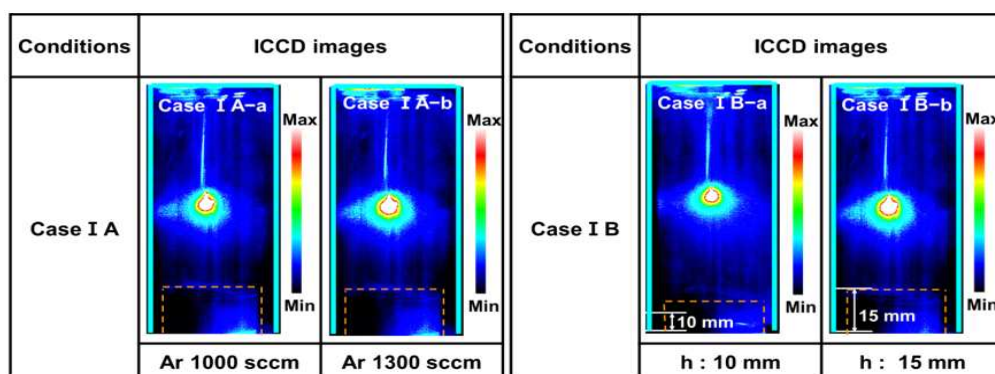
(**a**)
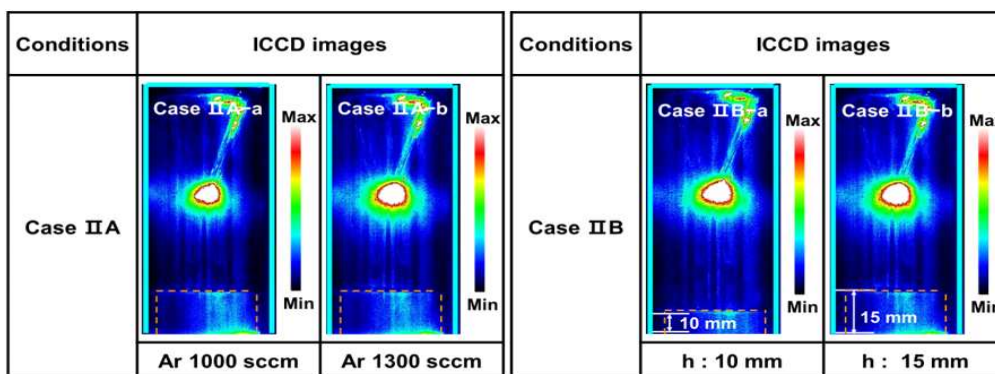
(**b**)
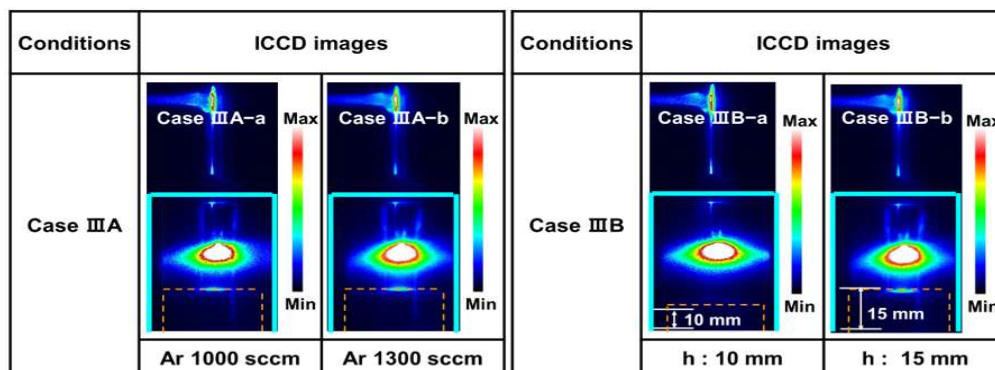
(**c**)

Figure 2. ICCD images of plasma produced in the APPR with pin electrode with respect to three different electrode configurations of cases (**a**) I, (**b**) II, and (**c**) III.

Table 2. Summary of experimental results of the applied voltage and average power during plasma polymerization in APPR with three-pin electrodes used herein.

Electrode Configuration	Case I	Case II	Case III
Driving type	AC	AC	AC
Voltage waveform	Sinusoidal	Sinusoidal	Sinusoidal
Plasm a driving voltage (V_{P-P})	8 kV	8 kV	8 kV
Average power	0.8 W	1.5 W	1.6 W

(**a**)

(**b**)

(**c**)
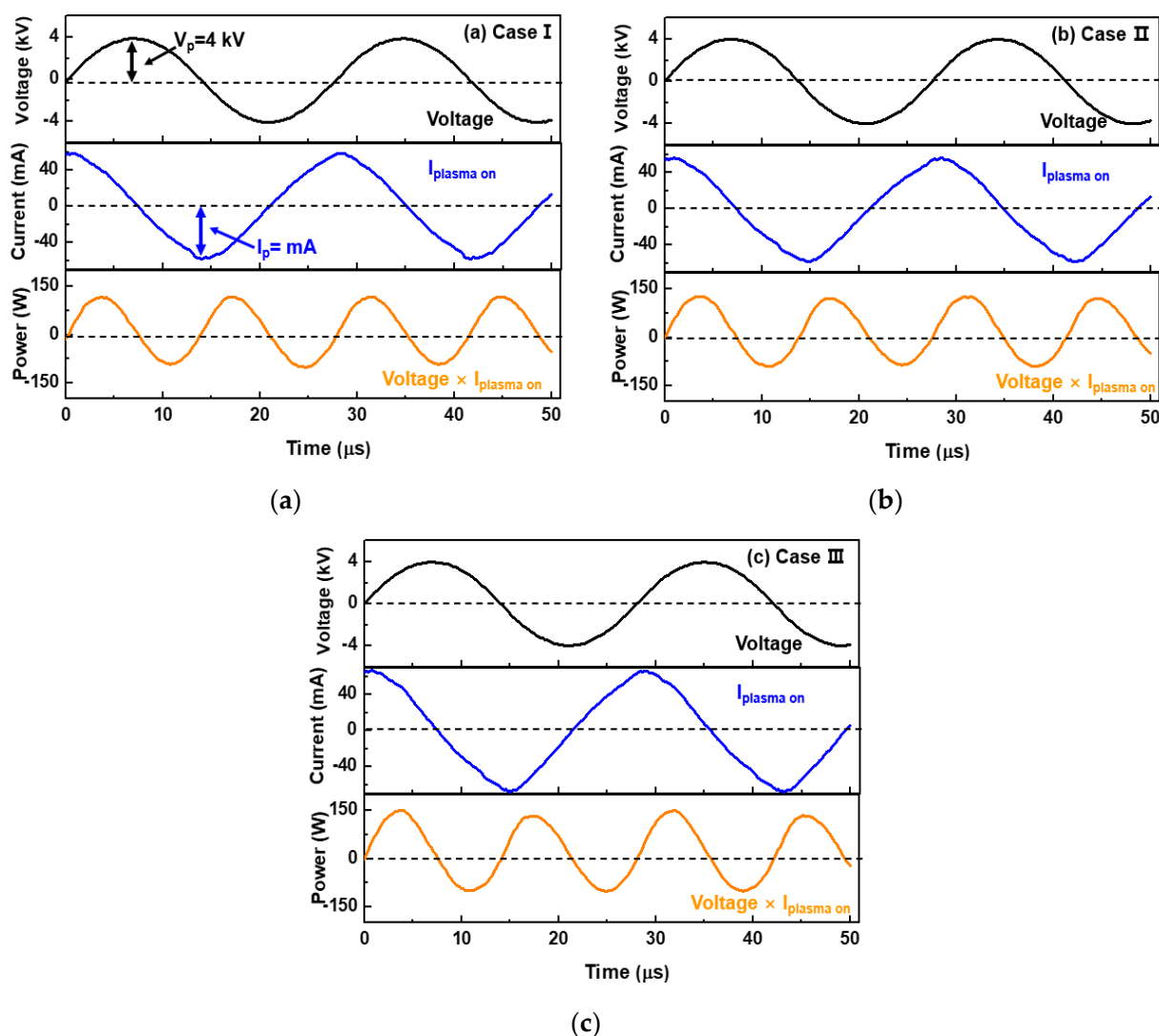
Figure 3. Characteristics of applied voltage, total current in plasma ON state, and instantaneous power of the APPR under optimal conditions (argon flow rate = 1300 sccm and bluff − body height = 15 mm) with respect to three electrode configurations of cases (**a**) I, (**b**) II, and (**c**) III.

To investigate the mechanism of the produced plasma with an intense glow-like discharge and the effect of the excited reactive radical species produced by the APPR with a single-pin electrode using argon discharge, OES measurements were conducted to investigate the excited reactive radical species, such as nitrogen, oxygen, and argon radical species in the APPR with single-pin electrode for three different electrode configurations (cases I, II, and III) under optimal conditions. Figure 4 shows the OES spectra measured in the plasma plumes of the APPR. Consequently, several peaks of excited nitrogen (N_2; 337.1, 357.7, and 388 nm), oxygen (OH radicals), and argon peaks were observed at the wavelength ranging from 300–900 nm [19–22]. In particular, when compared to case I, case III's peak intensities of the excited N_2 and Ar radical species increased, resulting from a frequent collision reaction between gas mixtures. Herein, these N_2 peaks indicate a higher concentration of reactive nitrogen species (RNSs), which are essential in depositing PANI polymer films [16]. Based on these results, the increase in excited radical species in case III could contribute to nucleation and fragmentation reactions through the injected free excited radical species for depositing PANI thin films.
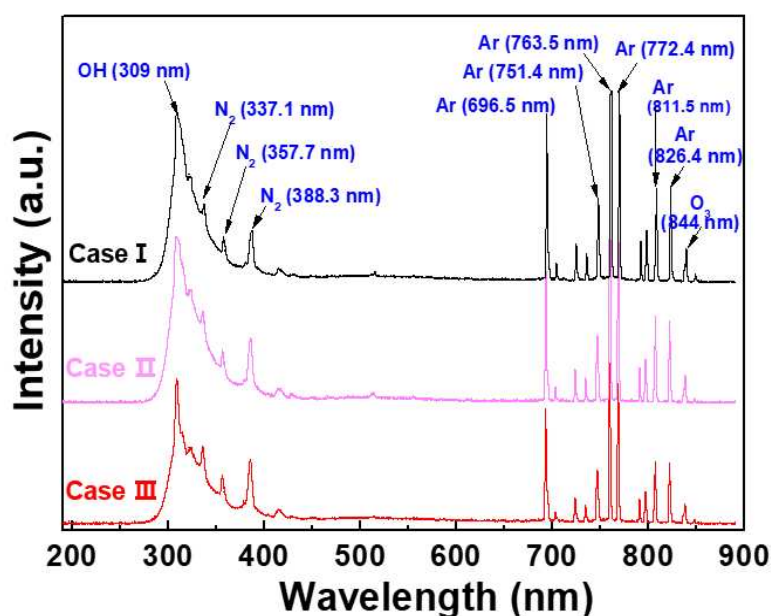
Figure 4. OES spectra of APPR under optimal conditions with respect to three electrode configurations of cases I, II, and III.

To compare the OES analysis quantitatively among the RNS and excited argon radicals, the total emission intensities were calculated from each emission intensity. Figure 5a,b show the total peak intensities of RNS and excited argon radicals calculated from the OES spectra of Figure 4, respectively. The total peak intensities of RNS in Figure 5a,b are the sum of the peak intensities of several RNS obtained from the OES spectra of Figure 4, where the wavelengths of several RNS are 337.1, 357.7 and 388.3 nm. The total peak intensities of exited argon radicals in Figure 5b are the sum of the peak intensities of several exited argon radicals obtained from the OES spectra of Figure 4, where the wavelengths of several exited argon radicals are 696.5, 751.4, 763.5, 772.4, 811.5 and 826.4 nm. The increase in the total peak intensities of RNS and excited argon radicals is related to the argon flow rate, including the bluff-body position in which the substrate is placed. In particular, in case III, it was confirmed that the higher density plasma could expand in the horizontal direction inside the glass guided-tube due to the formation of excited radical spaces within the gas-feeding tube. Based on the experimental results of Figures 2–5, the optimal deposition conditions were chosen for depositing the PANI thin films.
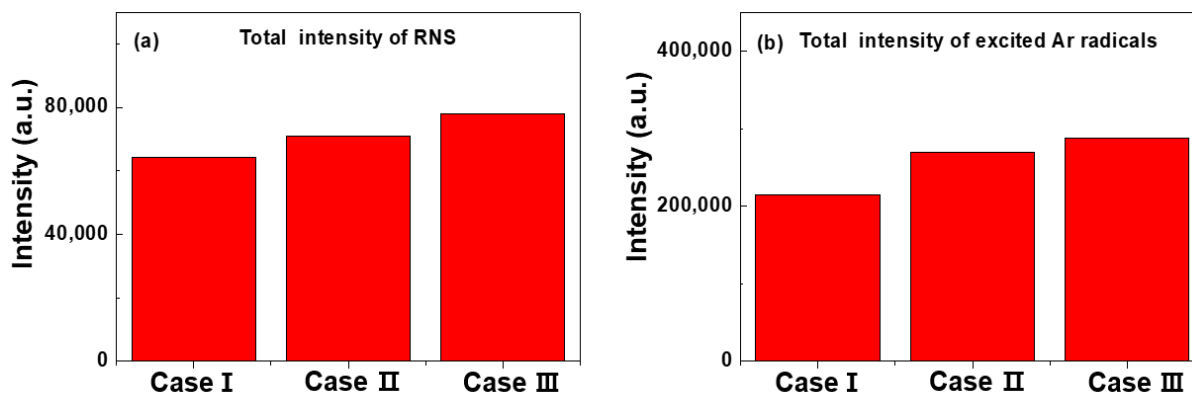
Figure 5. Total peak intensity of (**a**) excited RNS and (**b**) argon radicals from OES spectra under optimal conditions with respect to three electrode configurations of cases I, II, and III.

The morphologies of the deposited PANI thin films were investigated under the optimal conditions with respect to three electrode configurations. Figure 6 shows the SEM

images of the deposited PANI thin films under the optimal conditions using the APPR with respect to three electrode configurations. For case I, spherical particles were observed on the surface of the deposited PANI thin film (Figure 6a). However, for cases II and III, the surface of the deposited PANI thin film was homogeneous and smooth (Figure 6b,c). Thus, these results show that the surface morphologies of PANI thin films are strongly affected by the pin electrode configurations of APPR.

Figure 6. FE-SEM images of PANI thin films prepared using APPR with pin electrode under optimal conditions with respect to three electrode configurations of (**a**) cases I, (**b**) II, and (**c**) III.

Figure 7a,b show the film thicknesses and deposition rate variations for PANI thin films deposited by the APPR with the pin electrode on glass substrates under optimal conditions for 1 h with respect to three electrode configurations. For case III, the film thickness and deposition rate of the PANI thin film were about 450 nm and 7.5 nm/min, respectively. For case III, the PANI thin film with the highest film thickness and deposition rate was obtained. This trend may be mainly due to the supply of excited species, such as RNS and argon radicals, formed within the gas-feeding tube into the nucleation or fragmentation region. The additional increase in RNS and argon radicals within the gas-feeding tube requires additional power consumption, which is confirmed by a higher dissipated power during AP polymerization for case III (Table 2).
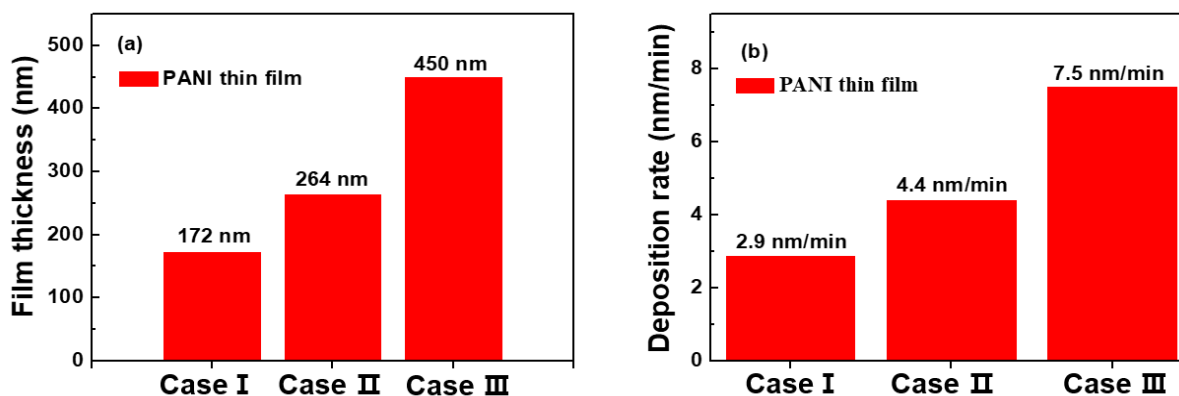
Figure 7. (**a**) Film thickness and (**b**) deposition rate of PANI thin film prepared by APPR with pin electrode under optimal conditions when using three electrode configurations (cases I, II, and III).

Figure 8 shows the changes in two- and three-dimensional AFM images of PANI thin films deposited on glass substrates for 1 h. The root means' square roughness (R_{rms}) and average roughness (R_a) obtained from the AFM images of PANI thin film surfaces of Figure 8 are summarized in Table 3. First, for case I, the surface R_a and R_{rms} values are 0.22 and 0.75 nm, respectively. Second, for case II, the surface R_a and R_{rms} values are 1.03 and 1.31 nm, respectively. Finally, for case III, the surface R_a and R_{rms} are 0.61 and 0.85 nm, respectively. Thus, these results show that the surface roughness characteristics of the PANI thin films are significantly affected by the pin electrode configurations of the APPR.
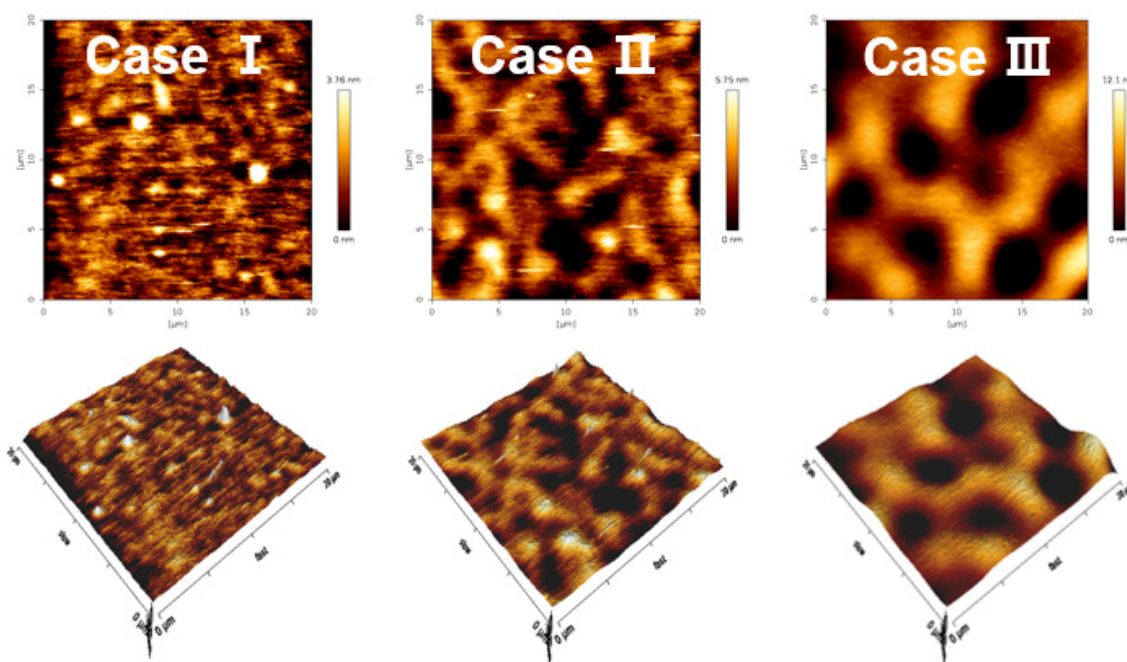
Figure 8. Two- and three-dimensional AFM images of PANI thin films prepared by APPR with pin electrode under optimal conditions with respect to three electrode configurations (cases I, II, and III).

Table 3. Root mean square roughness (R_{rms}) and average roughness (R_a) of PANI thin films obtained from AFM images in Figure 8.

Sample Conditions	Case I	Case II	Case III
R_a	2.22 nm	1.03 nm	0.61 nm
R_{rms}	2.75 nm	1.31 nm	0.85 nm

Figure 9 shows the FTIR absorption spectrum of the PANI thin films deposited on silicon wafer substrates for 1 h by APPR under optimal conditions with respect to three electrode configurations (cases I, II, and III). Herein, all spectra show the characteristic peaks of the PANI polymer at 2959, 2844, 1601, 1501, 1313, 1250, and 763 cm^{-1}. The peaks at 1501 and 1601 cm^{-1} are attributed to benzenoid and quinoid ring stretching vibrations, respectively. The band at 763 cm^{-1} is ascribed to the C–H out-of-plane deformation from the aromatic ring, and the peak at 1313 cm^{-1} is attributed to the C–N stretching vibration [17,27]. In addition, the assigned peaks at 2844 and 2959 cm^{-1} are attributed to the stretching within the polymer chains [17,27]. From the FTIR spectra, the peak assignments of the PANI thin films deposited by APPR are represented in Table 4. In particular, the FTIR peak intensities of the π-conjugated bonds (1501 and 1601 cm^{-1}) and the C–N bond (1313 cm^{-1}) increased for cases (cases II) when compared to case I. The enhancement of the C–N peak is related to the electrical conductivity due to the nitrogen atom of the quinone ring [28,29]. Moreover, the increase in π-conjugated bonds is expected to enhance the π–π stacking of intermolecular polymer chains, thereby resulting in good carrier mobility and improved electrical conductivity [28,29]. Hence, the proposed APPR with pin electrode configuration (case III) can inject the excited radical species formed within the gas-feeding tube into the nucleation or fragmentation region. The PANI thin film grown in the proposed APPR exhibited the highest film thickness, deposition rate, and lowest roughness. Thus, the proposed APPR device is applicable to various PANI-based gas sensors [16] by overcoming the low deposition rate of conventional PANI films.
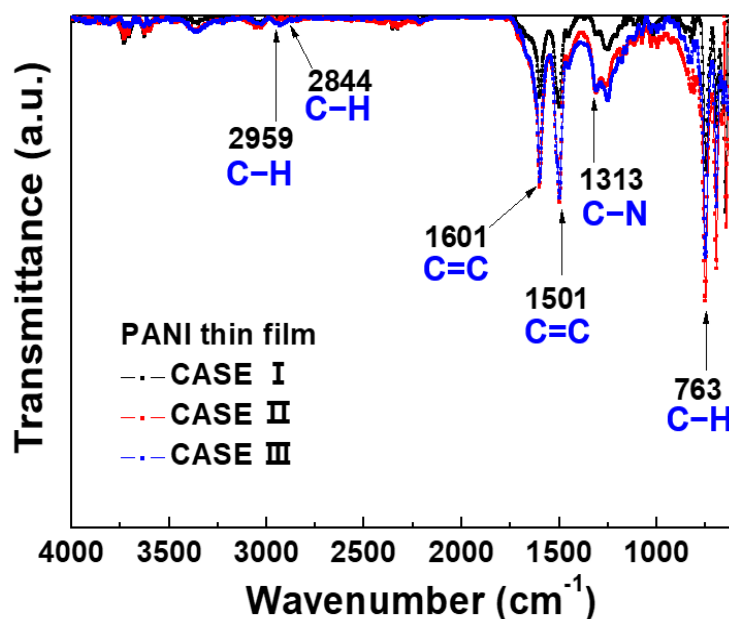
Figure 9. FTIR spectra of PANI thin films prepared by APPR with pin electrode under optimal conditions with respect to three electrode configurations (cases I, II, and III).
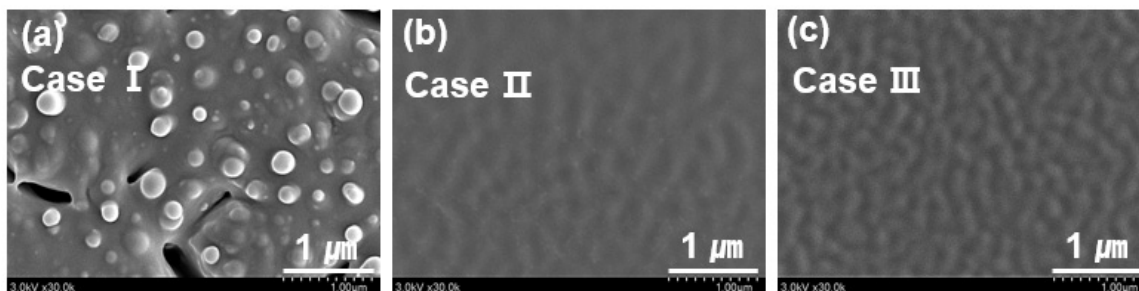
Table 4. Comparison of FTIR spectra of PANI thin films deposited by APPR with pin electrode under optimal conditions with respect to three electrode configurations (cases I, II, and III) obtained from FTIR spectra of PANI thin films in Figure 9.

Wavenumber	Peak Assignment
763 cm^{-1}	C–H out-of-plane bending
1313 cm^{-1}	C–N stretching vibration
1501 cm^{-1}	C=C stretching vibrations of the benzenoid rings
1601 cm^{-1}	C=C stretching vibrations of quinoid rings
2844 cm^{-1}	C–H stretching vibration
2959 cm^{-1}	C–H stretching vibration

4. Conclusions

To broadly generate a glow-like intense plasma for depositing PANI thin films, we evaluated various case studies in detail, depending on the variations of the APPR, such as pin electrode configurations (cases I, II, and III), bluff-body heights, and argon flow rates. The morphologies, structures, and deposition rates of the PANI thin films strongly depend on pin electrode configurations. For case III, the PANI thin films show the maximum film thickness (about 450 nm) and the highest deposition rate (7.5 nm/min). The PANI thin films show homogeneous, flat, and smooth surfaces with roughness characteristics below a few nanometers, as revealed by SEM and AFM. The PANI thin films show the structural feature increasing the π-conjugated bonds (1501 and 1601 cm^{-1}) and C–N bond (1313 cm^{-1}), as confirmed by FTIR. This growth of high-quality PANI thin films is due to the increased excited radical species contributing to the fragmentation and recombination for obtaining the PANI thin film during plasma deposition. Therefore, it is expected that the APPR with the pin electrode in case III deposits large-area PANI thin films with a high deposition rate by overcoming the localized area deposition problem of conventional AP plasma devices.

Author Contributions: E.Y.J., C.-S.P., H.J.J., S.I. and H.-S.T. conceived and designed the study; E.Y.J., H.J.J. and S.I. performed the experiments; E.Y.J. and T.E.H. contributed the analytical tools; E.Y.J., H.J.J., S.I., C.-S.P. and H.-S.T. analyzed the data; E.Y.J., C.-S.P., H.J.J., S.I., B.J.S., M.C. and H.-S.T. wrote most of the paper. All authors have read and agreed to the published version of the manuscript.

References

1. Nur, M.; Kinandana, A.W.; Winarto, P.; Muhlisin, Z.; Nasrudin. Study of an atmospheric pressure plasma jet of argon generated by column dielectric barrier discharge. *J. Phys. Conf. Ser.* **2016**, *776*, 012102. [CrossRef]

2. Chauvet, L.; Therese, L.; Caillier, B.; Guillot, P. Characterization of an asymmetric DBD plasma jet source at atmospheric pressure. *J. Anal. At. Spectrom.* **2014**, *29*, 2050–2057. [CrossRef]

3. Nastuta, A.V.; Gerling, T. Cold atmospheric pressure plasma jet operated in Ar and He: From basic plasma properties to vacuum ultraviolet, electric field and safety thresholds measurements in plasma medicine. *Appl. Sci.* **2022**, *12*, 644. [CrossRef]

4. Deng, S.; Cheng, C.; Ni, G.; Meng, Y.; Chen, H. Bacterial inactivation by atmospheric pressure dielectric barrier discharge plasma jet. *Jpn. J. Appl. Phys.* **2008**, *48*, 7009–7012. [CrossRef]

5. Kuzminova, A.; Kretková, T.; Kylián, O.; Hanuš, J.; Khalakhan, I.; Prukner, V.; Doležalová, E.; Šimek, M.; Biederman, H. Etching of polymers, proteins, and bacterial spores by atmospheric pressure DBD plasma in air. *J. Phys. D Appl. Phys.* **2017**, *50*, 135201. [CrossRef]

6. Dimitrakellis, P.; Travlos, A.; Psycharis, V.P.; Gogolides, E. Superhydrophobic paper by facile and fast atmospheric pressure plasma etching. *Plasma Process Polym.* **2017**, *14*, 1600069. [CrossRef]

7. Prakash, C.V.; Behera, N.; Patel, K.; Kumar, A. Concise characterization of cold atmospheric pressure helium plasma jet. *AIP Adv.* **2021**, *11*, 085329. [CrossRef]

8. Zhou, Y.-J.; Yuan, Q.-H.; Li, F.; Wang, X.-M.; Yin, G.-Q.; Dong, C.-Z. Nonequilibrium atmospheric pressure plasma jet using a combination of 50 kHz/2MHz dual-frequency power sources. *Phys. Plasmas* **2013**, *20*, 113502. [CrossRef]

9. Mohamed, A.-A.H.; Aljuhani, M.M.; Almarashi, J.Q.M.; Alhazime, A.A. The effect of a second grounded electrode on the atmospheric pressure argon plasma jet. *Plasma Res. Express* **2020**, *2*, 015011. [CrossRef]

10. Kang, H.R.; Chung, T.H.; Joh, H.M.; Kim, S.J. Effects of dielectric tube shape and pin-electrode diameter on the plasma plume in atmospheric pressure helium plasma jets. *IEEE Trans. Plasma Sci.* **2017**, *45*, 691–697. [CrossRef]

11. Deepak, G.D.; Joshi, N.K.; Prakash, R. Model analysis and electrical characterization of atmospheric pressure cold plasma jet in pin electrode configuration. *AIP Adv.* **2018**, *8*, 055321. [CrossRef]

12. Lietz, A.M.; Kushner, M.J. Electrode configurations in atmospheric pressure plasma jets: Production of reactive species. *Plasma Sources Sci. Technol.* **2018**, *27*, 105020. [CrossRef]

13. Nguyen, D.B.; Mok, Y.S.; Lee, W.G. Enhanced atmospheric pressure plasma jet performance by an alternative dielectric barrier discharge configuration. *IEEE Trans. Plasma Sci.* **2019**, *47*, 4795–4801. [CrossRef]

14. Lommatzsch, U.; Ihde, J. Plasma polymerization of HMDSO with an atmospheric pressure plasma jet for corrosion protection of aluminum and low-adhesion surfaces. *Plasma Processes Polym.* **2009**, *6*, 642–648. [CrossRef]

15. Jiang, N.; Ji, A.; Cao, Z. Atmospheric pressure plasma jet: Effect of electrode configuration, discharge behavior, and its formation mechanism. *J. Appl. Phys.* **2009**, *106*, 013308. [CrossRef]

16. Park, C.-S.; Kim, D.Y.; Kim, D.H.; Lee, H.-K.; Shin, B.J.; Tae, H.-S. Humidity-independent conducting polyaniline films synthesized using advanced atmospheric pressure plasma polymerization with in-situ iodine doping. *Appl. Phys. Lett.* **2017**, *110*, 033502. [CrossRef]

17. Kim, J.Y.; Iqbal, S.; Jang, H.J.; Jung, E.Y.; Bae, G.T.; Park, C.-S.; Shin, B.J.; Tae, H.-S. Transparent polyaniline thin film synthesized using a low-voltage-driven atmospheric pressure plasma reactor. *Materials* **2021**, *14*, 1278. [CrossRef]

18. Kim, J.Y.; Iqbal, S.; Jang, H.J.; Jung, E.Y.; Bae, G.T.; Park, C.-S.; Tae, H.-S. In-situ iodine doping characteristics of conductive polyaniline film polymerized by low-voltage-driven atmospheric pressure plasma. *Polymers* **2021**, *13*, 418. [CrossRef]

19. Kim, D.H.; Park, C.-S.; Kim, W.H.; Shin, B.J.; Hong, J.G.; Park, T.S.; Seo, J.H.; Tae, T.-S. Influences of guide-tube and bluff-body on advanced atmospheric pressure plasma source for single-crystalline polymer nanoparticle synthesis at low temperature. *Phys. Plasmas* **2017**, *24*, 023506. [CrossRef]

20. Lotfy, K. The impact of the carrier gas composition of non-thermal atmospheric pressure plasma jet for bacteria sterilization. *AIP Adv.* **2020**, *10*, 015303. [CrossRef]

21. Xiao, D.; Cheng, C.; Lan, Y.; Ni, G.H.; Shen, J.; Meng, Y.D.; Chu, P.K. Effects of atmospheric-pressure nonthermal nitrogen and air plasma on bacteria inactivation. *IEEE Trans. Plasma Sci.* **2016**, *44*, 2699–2707. [CrossRef]

22. Bae, G.T.; Park, C.-S.; Jung, E.Y.; Kim, D.; Jang, H.J.; Shin, B.J.; Tae, T.-S. Atmospheric synthesis of polyvinylidene fluoride film using novel atmospheric pressure plasma deposition with direct injection nozzle. *Mol. Cryst. Liq. Cryst.* **2021**, 1972207. [CrossRef]

23. Zhang, J.; Wang, Y.; Wang, D. Computational simulation of atmospheric pressure discharges with the needle-array electrode. *Phys. Plasmas* **2018**, *25*, 072101. [CrossRef]

24. Liu, T.; Timoshkin, I.; Wilson, M.P.; Given, M.J.; MacGregor, S.J. The nanosecond impulsive breakdown characteristics of air, N_2, and CO_2 in a sub-mm gap. *Plasma* **2022**, *5*, 12–29. [CrossRef]
25. Liu, D.; Zhang, Z.; Liu, Z.; Wang, B.; Li, Q.; Wang, X.; Kong, M.G. Plasma jets with needle–ring electrodes: The insulated sealing of the needle and its effect on the plasma characteristics. *IEEE Trans. Plasma Sci.* **2018**, *46*, 2942–2948. [CrossRef]
26. Sato, Y.; Ishikawa, K.; Tsutsumi, T.; Ui, A.; Akita, M.; Oka, S.; Hori, M. Numerical simulations of stable, high-electron-density atmospheric pressure argon plasma under pin-to-plane electrode geometry: Effects of applied voltage polarity. *J. Phys. D Appl. Phys.* **2020**, *53*, 265204. [CrossRef]
27. Botewad, S.N.; Pahurkar, V.G.; Muley, G.G. Fabrication and evaluation of evanescent wave absorption based polyaniline-cladding modified fiber optic urea biosensor. *Opt. Fiber Technol.* **2018**, *40*, 8–12. [CrossRef]
28. Wang, S.; Zhou, Y.; Liu, Y.; Wang, L.; Gao, C. Enhanced thermoelectric properties of polyaniline/polypyrrole/carbon nanotube ternary composites by treatment with a secondary dopant using ferric chloride. *J. Mater. Chem. C* **2020**, *8*, 528–535. [CrossRef]
29. Su, N. Improving electrical conductivity, thermal stability, and solubility of polyaniline-polypyrrole nanocomposite by doping with anionic spherical polyelectrolyte brushes. *Nanoscale Res. Lett.* **2015**, *10*, 301. [CrossRef]

Article

Changes in Surface Characteristics of BOPP Foil after Treatment by Ambient Air Plasma Generated by Coplanar and Volume Dielectric Barrier Discharge

Petra Šrámková [1] [iD]**, Zlata Kelar Tučeková** [1] [iD]**, Michal Fleischer** [1]**, Jakub Kelar** [1] **and Dušan Kováčik** [1,2,*] [iD]

[1] Department of Physical Electronics, CEPLANT—R&D Centre for Plasma and Nanotechnology Surface Modifications, Faculty of Science, Masaryk University, Kotlářská 2, 611 37 Brno, Czech Republic; petra.sramkova@mail.muni.cz (P.Š.); zlata.tucekova@mail.muni.cz (Z.K.T.); michal.fleischer@mail.muni.cz (M.F.); jakub.kelar@mail.muni.cz (J.K.)

[2] Department of Experimental Physics, Faculty of Mathematics, Physics and Informatics, Comenius University in Bratislava, Mlynská dolina, 842 48 Bratislava, Slovakia

* Correspondence: dusan.kovacik@mail.muni.cz or kovacik@fmph.uniba.sk

Abstract: Biaxially oriented polypropylene (BOPP) is a highly transparent polymer defined by excellent mechanical and barrier properties applicable in the food packaging industry. However, its low surface free energy restricts its use in many industrial processes and needs to be improved. The presented study modifies a BOPP surface using two different atmospheric-pressure plasma sources operating in ambient air and capable of inline processing. The volume dielectric barrier discharge (VDBD) and diffuse coplanar surface barrier discharge (DCSBD) were applied to improve the wettability and adhesion of the 1–10 s treated surface. The changes in morphology and surface chemistry were analyzed by SEM, AFM, WCA/SFE, and XPS, and adhesion was evaluated by a peel force test. Comparing both plasma sources revealed their similar effect on surface wettability and incorporation of polar functional groups. Additionally, higher surface roughness in the case of VDBD treatment contributed to slightly more efficient adhesion in comparison to DCSBD. Although we achieved comparable results for both plasma sources in the term of enhanced surface wettability, degree of oxidation, and stability of induced changes, DCSBD had less effect on the surface deterioration than VDBD, where surface structuring caused an undesirable haze.

Keywords: BOPP foil; DCSBD; VDBD; surface wettability; adhesion; ageing; surface functionalization

1. Introduction

Biaxially oriented polypropylene (BOPP) is produced from melted polypropylene stretched in both transverse directions, producing molecular chains oriented in cross directions. Stretching into both directions ensures the significant improvement of its properties including enhanced barrier properties, increased toughness, and stiffness [1]. These properties, along with high transparency, make BOPP an excellent and cost-effective material in food [2,3] and tobacco packaging, but also in high energy density applications, e.g., capacitor production [4]. The BOPP's low surface free energy, however, hinders processes where good printability, adhesion, or improved wettability are required. The treatment by cold atmospheric-pressure plasma provides a popular solution for the surface activation of polymers and other thermally sensitive materials. However, the overturning and migration of these surface functional groups into a volume of material result in so-called hydrophobic recovery. This phenomenon often appears within days, and a loss of improved properties can be observed within a month on most BOPP substrates [5,6]. Thus, stable surface functionalization and adhesion improvement are required for industrially produced BOPP, often stored before further processing.

Dielectric barrier discharges (DBD) of various geometries are often used as the atmospheric-pressure nonequilibrium plasma sources for inline industrial applications.

Volume DBD (VDBD), so-called "industrial corona", and diffuse coplanar surface barrier discharge (DCSBD) with a concavely curved electrode system suitable for roll-to-roll arrangement are often used for flexible large-area material treatment such as foils [7], paper, [8] and nonwoven textiles [9]. The treatment by atmospheric-pressure air DBD introduces polar functional groups providing hydrophilicity and an increase of surface free energy of the polymer surface. Industrial corona represents the most widely used plasma source in commercial use due to its simple operation in ambient air at the atmospheric pressure, fast speed, as well as short treatment times sufficient for material activation. However, corona discharge comprises hot filamentary microdischarges, which often cause thermally sensitive polymers' deterioration due to the perpendicular orientation of randomly distributed microdischarges towards the treated surface. In contrast to industrial corona, DCSBD enables generation of plasma consisting of microdischarges, where diffuse parts are intensified, while the filamentary elements are suppressed and parallel to the treated surface. The resulting diffuse plasma is thin, homogeneous, more effective, and less harmful to sensitive polymer materials.

Until now, the efficiency of surface activation of DCSBD plasma has been investigated on several polymer substrates. The high power density of such plasma ensured the improved wettability in the case of polyesters such as PEN [10], PET [11], PLA [12], or polycarbonate [13], as well as PMMA [14], even after 1 s of treatment. Moreover, our recent study considering the surface changes of PA 6 after DCSBD plasma treatment demonstrated the high potential of this technology to be part of industrial systems due to its very fast surface activation (0.25 s) and long-term preservation of the achieved properties [7]. The largest group of produced polymers worldwide represented by polyolefins were subjected to DCSBD plasma treatment in several studies [15–17]. However, the used exposure times were often too long (30–60 s) to meet industrial demand. Moreover, these studies were focused on changes in viscoelastic and tribological properties after plasma treatment. Despite BOPP being one of the most abundant polymers utilized in the packaging industry, plasma activation by DCSBD for a shorter treatment time (1–5 s) has only been reported once [18]. However, the achieved results were discussed very briefly, and the operation parameters of the DCSBD plasma source have been upgraded since the publishing of these data. There is lack of systematic study of the DCSBD plasma effect on the surface properties of BOPP substrate.

Here, we investigate and compare the efficiency of routinely used VDBD plasma represented by industrial corona systems and its possible alternative, namely DCSBD, for standard industrial roll-to-roll BOPP foil processing. The DCSBD in a concavely curved configuration of the electrode system is used for surface activation of BOPP foil, and changes in surface characteristics are compared with those achieved after treatment by VDBD. Morphological changes, surface wettability, adhesion, chemical composition, and the stability of the achieved properties are investigated.

2. Materials and Methods

2.1. Material

Biaxially oriented polypropylene (BOPP) cigarette foil used for the experiments was provided by Chemosvit folie s.r.o., Svit, Slovakia. BOPP foil with a thickness of 25 μm and a square weight of 22.8 g m^{-2} was delivered in the form of a roll. BOPP foil of a width of 25 cm was treated by plasma and cut to the required size for a particular analysis.

2.2. Plasma Treatment

The plasma treatment was carried out by two different dielectric barrier discharges generating nonequilibrium "cold" atmospheric plasma. Diffuse coplanar surface barrier discharge (DCSBD) in concavely curved configuration of the electrode system operating at atmospheric pressure in ambient air produces particularly diffuse "cold" plasma, while volume dielectric barrier discharge (VDBD) generates "cold" plasma solely in filamentary mode. A schematic description of both electrode systems is depicted in Figure 1. Detailed

technical specifications of both plasma sources were discussed elsewhere [7]. Regarding DCSBD, the sample was attached to the roller at a distance of 0.3 mm from the electrode system. Input power was adjusted at a value of 400 W (the frequency of ~15 kHz), and the treatment speed was set at a constant value of 4.8 m min^{-1} corresponding to a treatment time of 1 s. Samples were exposed to plasma for 1, 3, 5, and 10 s applying the corresponding rotation cycles. VDBD operated in the following conditions: the input power was set to the value of 380 W, corresponding to the same square power density of 2.5 W cm^{-2} as the plasma produced by DCSBD. The average speed of cylinder rotation was 18 m min^{-1}, and the distance between the sample and high-voltage electrodes was set to the value of 1 mm. Treated samples were stored in Petri dishes under the following laboratory conditions: temperature = 23 °C and humidity = 40%.
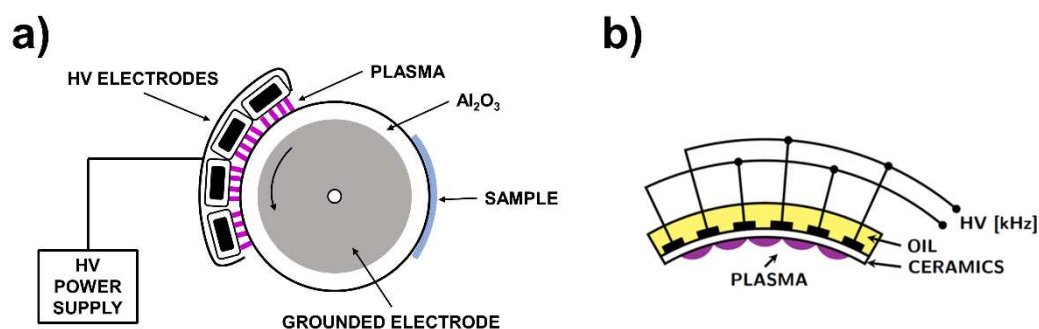
Figure 1. Schematic representation of used plasma sources: (**a**) VDBD electrode system and (**b**) concavely curved DCSBD electrode system.

2.3. Analytical Methods

Imaging of surface morphology was performed using a Scanning Electron Microscope Mira3 (Tescan, Brno, Czech Republic) with a maximum resolution of 1 nm and a maximum magnification of 1,000,000. The detector of secondary electrons and accelerating voltage of 15 kV was used. The surface morphology analysis was conducted with magnification up to 50,000. To prevent charging of the sample, the BOPP foil surface was coated with 20 nm of the Au/Pd layer by sputter coater Quorum Q150R-ES (Quorum Technologies, Lewes, United Kingdom). The changes in surface roughness were measured using Atomic Force Microscope NTEGRA Prima (NT-MDT, Moscow, Russia) in a semi-contact mode. The Root Mean Square (RMS) roughness was estimated from the area 5 × 5 mm^2 with resolution 512 × 512 px^2 and scanning frequency of 1 Hz.

The contact angles (CA) of water, diiodomethane, and ethylene glycol were measured by a See (Surface Energy Evaluation) System analyzer (Advex Instruments, Brno, Czech Republic) using sessile droplets with volume 1 μL. The resulting values of CA were calculated as an average value from at least ten droplets taken at the BOPP surface exposed to plasma at different treatment conditions. Surface free energy (SFE) values were calculated using the Owens-Wendt regression model [19].

XPS analysis was performed by the spectrometer Axis Supra (Kratos Analytical Ltd., Manchester, United Kingdom) using monochromated AlKα radiation of energy of 1486.6 eV. Emitted photoelectrons were collected by an analyzer from a sample area of size 300 × 700 μm^2 perpendicular to the sample surface. Because the samples are insulators, it was necessary to use a charge neutralizer electron source to compensate for sample charging during analysis. All spectra obtained under such conditions are shifted from the base position by a few eV to the lower binding energies. Therefore, it was necessary to perform energy calibration by shifting spectra according to a reference peak. Survey spectra were collected using an analyzer pass energy of 80 eV and high-resolution spectra for pass energy of 20 eV. The step size of the high-resolution spectra was 0.1 eV. Spectra calibration, processing, and fitting routines were completed using CASA software (trial version CasaXPS 2.3.16, CASA international nv, Olen, Belgium).

Static material testing machine Texture Analyser TA.XT *plusC* (Stable Micro Systems, Surrey, United Kingdom) was used for peel force measurements [20,21]. The 90° tape peel test for evaluating adhesion on plasma-treated BOPP foils was carried out using a peel fixture called "Rotating German Wheel" for continuous peeling off of the adhesive tape from the sample. Measurement was performed according to the FINAT test method no. 2. (a 90° peel adhesion test). The loading speed was set to the value of 10 mm min^{-1}, and the load cell with a 50 N range was used for adhesion measurements. The sample was prepared by sticking a 19 mm wide -Scotch™ Magic™ adhesive tape (3M, St. Paul, MN, USA) on the BOPP foil sample and ensuring 10 passes over a taped area with a rolling pin. The evaluation of measured peel force was in a range from 20 mm to 70 mm, whereas measurement values for the initial length of 20 mm were discarded. The average peel force was calculated from 3 to 5 tests of samples treated in the same conditions [7].

3. Results

3.1. Surface Morphology

Physicochemical interactions at the plasma–polymer interface can induce the etching of the polymer surface, which primarily affects the morphology of the surface. Therefore, morphological changes were monitored by scanning electron microscopy (SEM) and atomic force microscopy (AFM). The SEM image of the untreated BOPP foil surface (REF) depicted in Figure 2 demonstrates its very smooth and homogeneous nature at the micrometer scale. Lower plasma exposure times (1 and 3 s) in the case of DCSBD did not affect the surface morphology. After 5 s as well as 10 s of plasma treatment, we observed the formation of droplet-like structures with a diameter around 50–100 nm. Compared to the moderate effect of DCSBD on surface roughening, VDBD had a much more pronounced effect on the surface morphology. One second of plasma treatment showed mild structuring (Figure 2e) of surface, but a longer treatment time induced formation of droplet-like structures. However, the formed droplets had a size of around 200 nm (3 and 5 s in Figure 2f,g) or even larger (10 s in Figure 2h). Our results from SEM were quite different from other studies. Shekargoftar et al. [11] treated the PP/Al/PET-based laminated foil by DCSBD as well as the VDBD plasma source. The authors achieved the droplet-like structure at the PP side of the foil, after 3 s of plasma treatment by both plasma sources. Additionally, the droplets were enlarged due to merging after DCSBD treatment (up to 5 μm in diameter) in comparison to VDBD. A recent study by Janík et al. [16] demonstrated the formation of very similar structures after the treatment of PP specimens by coplanar DCSBD. However, in both mentioned studies, the size of droplets formed after treatment by DCSBD plasma was around 1–5 μm, which is much higher than our droplets possessing size in nanometers. In the case of PP/Al/PET-based laminated foil [11], these differences could be caused by the presence of a conductive Al layer, causing the parasitic microfilaments to burn perpendicular to the foil during DCSBD treatment, and also by the different nature of the used PP substrate, which relates to the manufacturing process as well as to the ratio of amorphous and crystalline regions on the surface. The degree of crystallinity and arrangement of crystalline and amorphous segments in polymer determine the resulting structuring of the surface after plasma treatment [22]. Plasma etching leads to the faster degradation of the amorphous phase in the BOPP structure, while crystalline regions become revealed, which defines the resulting roughening.

The AFM images are depicted in Figure 3 with inserted values of RMS roughness. The results from the AFM measurement revealed the low degree of roughness of raw BOPP foil with a value of 5.0 nm comparable to other papers. Strobel et al. [23] observed RMS roughness values in the range 2.3–4.3 nm for various types of BOPP differing in orientation. Another paper by Chen et al. [24] measured RMS roughness of 3.8 nm, and Darvish et al. [25] published roughness of BOPP film with a value of 6.8 nm. Exposure to DCSBD only slightly influenced the RMS values, but the AFM images show negligible surface topography changes. Plasma treatment during the first 3 s (Figure 3a,b) induced the formation of hole-like structures even though the roughness seemingly did not change

in comparison to reference. However, the formed holes possessed very low depth, which supported small differences in roughness. Longer treatment times (Figure 3c,d) resulted in a decrease in roughness, but values varied in the range of 4–4.6 nm, which represented a negligible change. In accordance with the SEM images, plasma treatment by VDBD induced more pronounced changes in topography and roughness. With increasing plasma exposure times, roughness gradually increased (Figure 3e–h) to the highest value of 24.9 nm after 10 s of VDBD plasma treatment. Wang et al. [26] used atmospheric-pressure dielectric barrier discharge to generate the air plasma for PP treatment and achieved roughness values from 15.3 nm to 55.3 nm depending on different treatment conditions. Oravcová et al. [18] monitored the effect of atmospheric-pressure plasma generated by DCSBD on surface characteristics of monoaxially oriented PP. They achieved a roughness increase to value 24 nm after 5 s of plasma treatment. However, the BOPP in our case cannot be directly compared with other PP substrates, because the manufacturing by stretching in two directions provides different properties than other types of PP. BOPP was treated by DBD in the study of Chen et al. [24], where they observed a change in roughness from the initial 3.8 nm to 7.2 nm after 3 s of treatment which corresponds to our value after 1 s of VDBD treatment.
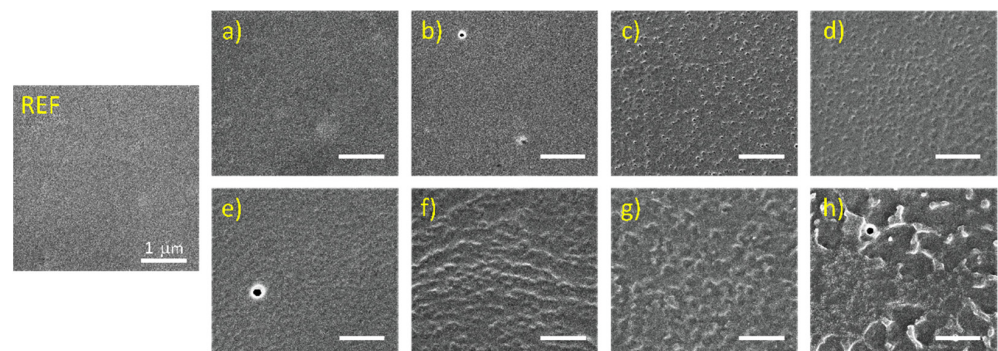
Figure 2. SEM images of BOPP foil treated by plasma at the different experimental conditions: (**a–d**) DCSBD at 1 s, 3 s, 5 s, and 10 s and (**e–h**) VDBD at 1 s, 3 s, 5 s, and 10 s.
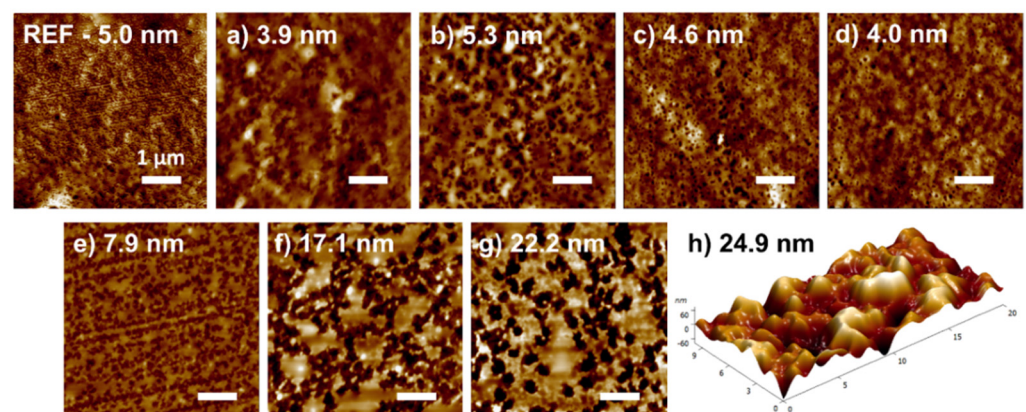
Figure 3. AFM images of BOPP foil treated by plasma at the different experimental conditions: (**a–d**) DCSBD at 1 s, 3 s, 5 s, and 10 s and (**e–h**) VDBD at 1 s, 3 s, 5 s, and 10 s. Values of roughness are inserted in the appropriate pictures.

Moreover, morphological changes monitored on the BOPP surface treated by VDBD induced changes in the optical properties of BOPP foil. The fully transparent foil lost its transparency after 3 s of exposure, and we monitored the formed haze, which intensified with the plasma treatment time. Haze is caused by light scattering, which can originate from the bulk of the material as well as from its surface. Since the DCBSD treated samples did not change their optical properties, the haze visible on VDBD treated samples is

probably connected to the creation of hole-like structures (Figure 3f–h), which can cause light scattering. The most probable explanation for such structures is the penetration of filamentary plasma through the upper layer of the surface. Moreover, the generated droplet-like structures with sizes between 0.2 and 1 μm corroborated these findings. Surface structures possessing dimensions similar to the visible light wavelength induce Mie scattering resulting in the milky appearance of the plasma treated foil [27].

3.2. Wettability and Ageing Study

Regarding the hydrophobic nature of polypropylene, the wettability of pristine BOPP film is very low, which agrees with the water contact angle (WCA) value of $104.8 \pm 0.4°$ and surface free energy (SFE) value of 26.8 mJ m^{-2}. The development of WCA after plasma treatment is depicted in Figure 4a, and changes in SFE are shown in Figure 4b. The treatment of BOPP surface by both plasma sources, coplanar and volume DBD, improved the wettability already after 1 s of plasma exposure. In the case of DCSBD, increased plasma exposure time resulted in gradually decreased WCA until achieving the lowest value ($52.1 \pm 0.5°$) after 10 s of treatment. In comparison, VDBD resulted in decreasing WCA to $68.9 \pm 0.8°$ already after 1 s. The lowest WCA was observed after 3 s of treatment ($66.5 \pm 3.5°$), followed by an increase in WCA with prolonged plasma exposure time. The rising of WCA after high plasma exposure times (10 s) can be explained by roughening of the surface after the VDBD treatment caused by etching. Although, etching usually occurs at higher exposure times (order of minutes), in the case of destructive VDBD filamentary plasma, it is possible that 10 s is sufficient for surface roughening and undesirable hydrophobization. The study on the plasma treatment of selected polyolefins revealed how an appropriate combination of microscale features on the surface with plasma-etched nanoscale roughness can regulate the wettability of the substrate [28].
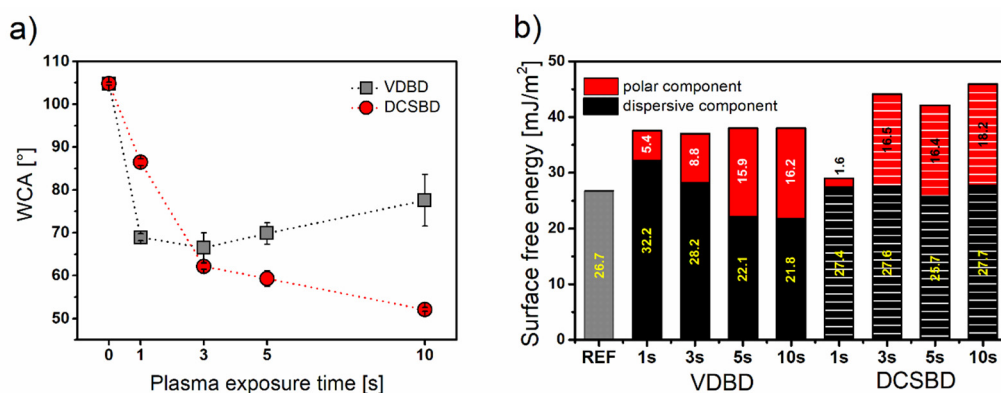
Figure 4. Graphs of WCA and SFE measurements: (**a**) WCA values measured immediately after plasma exposure of BOPP foil by VDBD (grey square) and DCSBD (red circle) for different plasma treatment times (1, 3, 5, and 10 s); (**b**) comparison of surface free energy (SFE) of BOPP foil treated by VDBD and DCSBD with inserted values of polar and dispersive component of SFE.

The SFE of pristine BOPP mainly comprised a dispersive component representing 26.7 mJ m^{-2} from 26.8 mJ m^{-2} of total SFE value. The absence of a polar component corresponds to the fully hydrocarbon structure of BOPP. Oxidation of the BOPP surface induced by plasma treatment resulted in an increase in SFE for both plasma sources (Figure 4b). Treatment by VDBD in all exposure times led to similar SFE values of 37–38 mJ m^{-2}. Additionally, the polar component gradually rose with the increased plasma exposure time from 5.4 mJ m^{-2} to 16.2 mJ m^{-2} proving the high effect of atmospheric cold plasma on the polar part of SFE. The increasing polar component represents the formation of polar functional groups on treated BOPP due to the presence of oxygen and nitrogen in air. The air humidity and hydrogen abstraction from the polymer chain allows the formation of hydroxyl radicals in the gas phase and causes the formation of free radicals [29]. The free radicals provide further reaction of the activated surface with reactive oxygen and nitrogen species present in air plasma. The change in dispersive component is related mostly to the

presence of nonpolar functional groups. Furthermore, the changes in surface morphology also contribute to the dispersive component. The increase in the dispersive component of SFE after the short VDBD plasma treatment was observed on PP in Shekargoftar et al. [11], followed by a decrease to the reference value after 5 s.

In comparison, DCSBD was more efficient in surface activation showing higher values of SFE (42–45.9 mJ m^{-2}) except for the exposure time of 1 s where only 29 mJ m^{-2} was achieved. Moreover, atmospheric plasma generated by DCSBD had a more pronounced impact on the polar part of SFE, which reached values in the range of 16.4–18.2 mJ m^{-2}. The polar component of surface energy represents the highest contribution to the total value of SFE. The increase in and further stabilization of the polar component of SFE were achieved after 3 s of DCSBD treatment. The dispersive component altered negligibly after the DCSBD treatment reflecting the small changes in surface morphology.

Enhancement of surface wettability after the plasma treatment is not fully permanent. The rate of hydrophobic recovery of the activated surface depends on many factors, such as the chemical nature of the substrate, storage conditions, as well as the used plasma source. Monitoring the WCA changes over time represents a great tool for investigating the stability of plasma-induced changes. WCA development during the 30 days of storage under laboratory conditions is illustrated in Figure 5. Surprisingly, the ageing effect for the samples treated by VDBD was very slow. WCAs measured on BOPP sample exposed to VDBD plasma for 1 s maintained the stable contact angle during the whole monitoring time. Similar behavior was observed by Borcia et al. [30] for HDPE treated by filamentary type of DBD. Compared to other hydrocarbon polymers (polystyrene and polymethylpentene), the HDPE surface stayed stable for two weeks. On the contrary, the BOPP sample exposed to DCSBD for 1 s recovered to the reference WCA value within the first 24 h. Further, VDBD samples treated for 3 s and longer experienced slight hydrophobic recovery during the first 3 days of storage. After a month of storage, all VDBD samples remained hydrophilic. Similar effects were observed in the case of 3–10 s DCSBD treated samples. However, after the month of storage, the WCA values were lower for DCSBD than for VDBD treated samples.
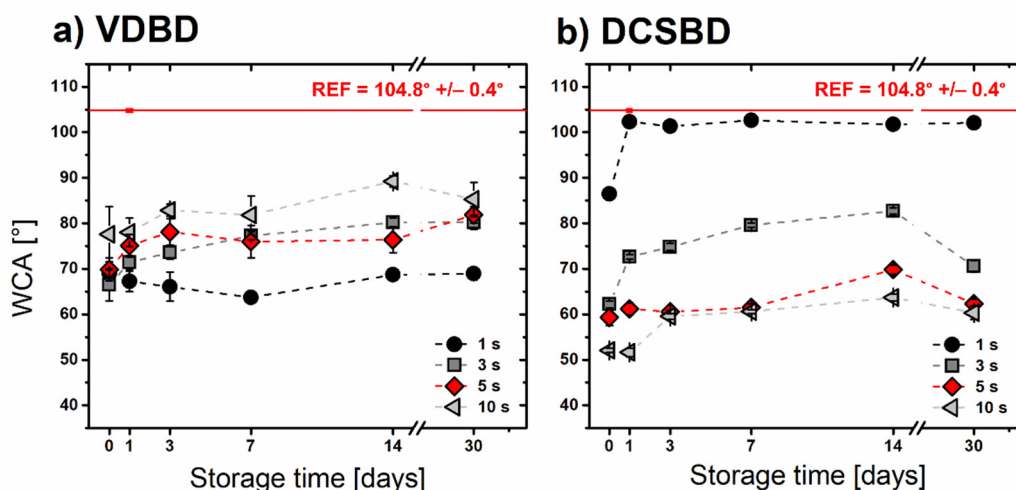
Figure 5. WCA development during the storage of BOPP foils under laboratory conditions: WCA values dependent on storage time after the plasma treatment by (**a**) VDBD and (**b**) DCSBD.

3.3. Peel Force

The peel force improvement of the BOPP surface was observed after the treatment by both plasma sources (Figure 6). The reference value of 0.75 N cm^{-1} almost tripled after 1 s of VDBD and rose with increased treatment time. The high error values of peel force are often related to the nonuniform treatment of large-area surfaces by VDBD [31]. In our case, these variations could be the results of surface topography and roughness changes, which

also contributed to higher peel force values for VDBD compared to less invasive diffuse plasma generated by DCSBD. However, the adhesion improvement of the BOPP surface corresponds with the polar component increase after VDBD plasma treatment, which was also observed for DCSBD treated samples. After 3 s of treatment by DCSBD, the peel force value stabilized, and it did not change with prolonged treatment. In contrast, Bhat et al. [32] observed a decrease in peel force during the first 60 s of RF plasma exposure. The expected increase occurred after plasma exposure time on the order of minutes. The postponed effect of plasma treatment was explained as plasma cleaning of commercially manufactured and contaminated BOPP surface prior to surface modification. As a result, the time needed for BOPP adhesion improvement in the case of RF plasma was significantly longer than in our case. These results indicate the relation of BOPP adhesive properties with the formation of polar functional groups and surface roughness [5,32,33].
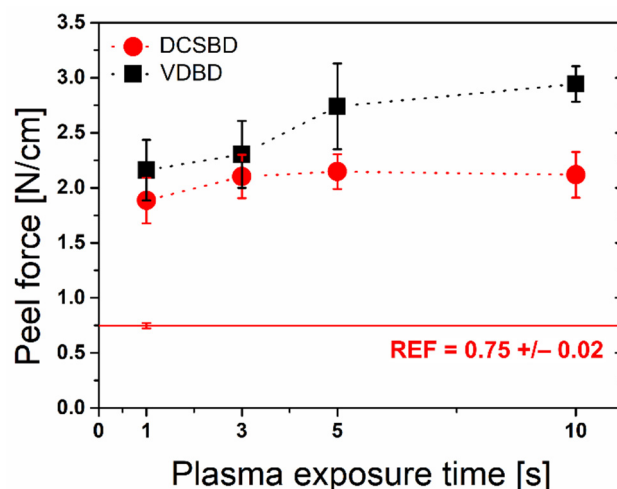
Figure 6. Development of the peel force of the BOPP surface after plasma treatment.

3.4. Surface Chemical Analysis

Improved wettability after plasma treatment indicates increased hydrophilicity of the BOPP surface related to the formation of polar functional groups. Chemical changes on the plasma-treated samples were monitored by X-ray photoelectron spectroscopy (XPS). The atomic composition of untreated and plasma-treated BOPP foil observed by XPS is summarized in Table 1. The untreated BOPP foil contained 95% carbon and 5% oxygen, which is in good accordance with other studies using various PP substrates [15,26,34,35]. The presence of oxygen on the raw BOPP surface suggests organic contamination or low-level surface oxidation. The treatment by both plasma sources induced an increase in oxygen concentration to 20% after 1 s. Further increasing plasma exposure time led to the higher oxygen content with the highest level at 28% for the sample treated by VDBD at 10 s. Otherwise, achieved oxygen contents were comparable for both plasma sources, reflecting the similar level of surface oxidation for diffuse and filamentary plasma. Compared to the study of Saranko et al. [15], where they observed 23.6% of oxygen content after 60 s of plasma treatment by DCSBD (pristine ~5.3%), we proved that a few seconds of plasma treatment were sufficient for surface activation of hydrophobic polymers. Despite the use of ambient air as a working gas for experiments, nitrogen atoms appeared at the BOPP surface in a negligible concentration (1–2.2%). A similar outcome was also monitored in other studies [29,36,37]. Dorai and Kushner explained the poor incorporation of *N*-based functional groups due to the low reactivity of N atoms towards the plasma-treated PP surface. They described in detail the mechanism of PP surface functionalization under the industrial corona treatment in humid air resulting in the formation of alcohol, carbonyl, carboxy, and peroxy groups.

Table 1. The atomic concentration and relative area of C1s chemical bonds of the BOPP surface analyzed by XPS measurement after treatment by DCSBD and VDBD plasma sources.

		Atomic Concentration [%] [1]			O/C Ratio	Functional Groups Concentration [%] [2]			
		C	O	N		C–C/C-H 284.8 eV	C–O 285.9 eV	C=O 287.5 eV	O–C=O 289.3 eV
	REF	95	5	-	0.05	94.2	5.8	-	-
DCSBD	1 s	80	20	<1	0.25	76.5	15.1	6.7	1.7
	3 s	74	24	1.8	0.33	71.5	14.3	8.1	6.1
	5 s	73	24	2.2	0.33	69.2	14.2	9.1	7.5
	10 s	72	26	1.7	0.36	65.8	15.9	9.8	8.6
VDBD	1 s	79	20	<1	0.26	73.7	14.0	7.1	5.3
	3 s	74	25	1.0	0.33	66.5	15.3	9.3	8.9
	5 s	73	26	1.1	0.35	65.7	15.2	9.1	10.0
	10 s	71	28	1.2	0.39	62.3	15.3	9.6	12.9

[1] Estimated from survey spectra. [2] Estimated by deconvolution of C1s high-resolution spectra.

The deconvolution of C1s high-resolution spectrum of the reference sample consisted dominantly of C–C/C–H bonds typical for a BOPP structure. Further, the residual quantity of the C–O bonds originating from the manufacturing process was revealed. After the air plasma treatment, the concentration of C–O bonds increased from an initial 6% and saturated at a value of approx. 15% for all used plasma treatment conditions. This can be explained by quenching of alkoxy radicals formed at the PP backbone after H-abstraction, which results in the formation of C–O groups. Other alkoxy radicals undergo the β-scission to yield C=O groups. In our study, the C=O and O–C=O bonds were formed right after the short plasma treatment by both plasma sources, and their concentrations increased with time. The level of C=O bonds was slightly higher for samples treated by VDBD as well as the amount of O–C=O groups. The O–C=O groups achieved higher values for all plasma exposure times in the case of VDBD treatment. The air humidity also plays a great role in the concentration of formed functional groups [29]. However, investigating the influence of relative humidity on chemical changes after plasma treatment of BOPP surface was outside of the scope of this study. Borcia et al. [30] observed comparable chemical changes on the surface of hydrocarbon polymers after treatment by air VDBD plasma having similar operating conditions as our experiment. Oxidation of poly(ethylene) (PE) was more efficient than in the case of branched poly(methylpentene) (PMP) in terms of functional groups concentration. In our case, after the corresponding treatment time, we observed 14–15.3% of alcohol groups presenting the lower level compared to 18–19.2% for PE and PMP in the mentioned study. However, the achieved concentrations of carbonyl and carboxyl functionalities in our experiment were between PE and PMP. Considering the structure of monomer units in particular polymers (PE, PMP and PP), oxidation of PE consisting fully of –CH$_2$– bonds was faster than in the case of branched PMP and PP. According to the proposed mechanism for hydrocarbon oxidation in plasma [29], initial H-abstraction from the surface depends on its position in the polymer backbone. Although the probability of abstractions follows the order: H$_{tert}$ > H$_{sec}$ > H$_{pri}$, the most reactive tertiary H present in PP and PMP is hindered by less reactive H from –CH$_3$ groups. This could be the reason for the more rapid oxidation of PE consisting solely of secondary H.

The polar functional groups contribute to the polar component of SFE and increased wettability of the BOPP surface. However, the respective XPS data do not reflect the corresponding WCA results. The similar behavior monitored by Borcia et al. [30] explains the discrepancies between WCA and XPS results based on the different effective depths analyzed by these two techniques.

Additionally, XPS analysis was employed to monitor the stability of surface oxidation during the storage of samples under laboratory conditions. In Figure 7, the O/C ratio is plotted against the storage time. Ageing curves of BOPP samples treated by DCSBD for

3–10 s follow a similar decreasing trend and end up around value 0.22. In general, the O/C ratio values achieved right after the treatment decreased by 31–39% after 28 days of storage. In comparison to these samples, the sample treated for 1 s possessing the lowest oxidation exhibited a less steep trend of ageing (20%). The O/C ratio of VDBD treated samples after 28 days of storage were very similar to those achieved in the case of DCSBD (the decrease by 30–34%). Leroux et al. [36] investigated the development of the O/C ratio on the PP surface treated by DBD plasma during the 30 days of ageing. Surprisingly the ageing process was slower than in our case (17–23%); however, they observed much lower values of O/C ratios (0.12–0.16). A similar trend of O/C ratio decrease during ageing was also observed for oxygen containing functional groups proportional to C-C bonds.
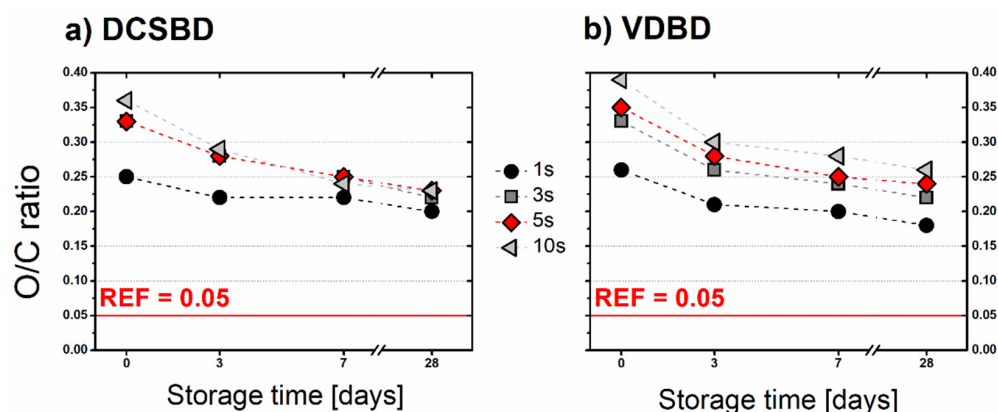
Figure 7. Development of the O/C ratio during the storage of BOPP foils under laboratory conditions: O/C ratio plotted against the storage time for (**a**) DCSBD and (**b**) VDBD for all plasma treatment conditions.

4. Conclusions

In the present work, we investigated the impact of VDBD and DCSBD plasma treatment on the surface characteristics of BOPP foil. Considering the surface morphology, the filamentary plasma produced by VDBD had a more destructive effect than the diffuse plasma generated by DCSBD. The smooth nature of BOPP foil remained unchanged during the first 3 s of DCSBD plasma treatment, whereas VDBD caused surface roughening after 1 s of treatment. Moreover, plasma exposure time higher than 1 s in the case of VDBD induced undesirable haze. Although DCSBD treatment at 5–10 s resulted in the formation of droplet-like structures, the foil remained transparent. Improvement in wettability was achieved for both plasma sources. However, exposure to VDBD plasma longer than 3 s led to a WCA increase perhaps due to surface roughening. Increased roughness after VDBD treatment also contributed to enhanced adhesion, where longer treatment time (5–10 s) caused an increase in peel force. Nevertheless, adhesion improved after 1 s of treatment by both plasma sources, indicating the direct relation of BOPP adhesive properties with the formation of polar functional groups. Surface oxidation was achieved after 1 s of plasma exposure and increased with the plasma treatment time. Observed oxygen contents were comparable for both plasma sources reflecting the similar level of surface oxidation for diffuse and filamentary plasma. Considering the WCA values as well as the O/C ratio development during the month of storage, the acquired surface properties slightly recovered without achieving initial characteristics. BOPP foil remained hydrophilic after the treatment by both plasma sources; however, the WCA after a month in the case of DCSBD were lower than for VDBD treated samples. These data show that BOPP foil requires treatment by diffuse plasma of DCSBD longer than 1 s for sufficient surface oxidation. BOPP treated at 3 s by both plasma sources achieved similar surface activation. However, considering the surface morphology, VDBD treatment longer than 3 s induced structural changes in the microscale which led to optical haze, whereas DCSBD treatment retained the transparency of the foil. Although these results prove a similar efficiency of diffuse and

filamentary plasma on BOPP surface activation, it supports the high potential of DCSBD technology to be part of industrial systems as it is gentler to sensitive polymeric surfaces.

References

1. Calafut, T. Polypropylene Films. In *Plastic Films in Food Packaging*; Elsevier: Amsterdam, The Netherlands, 1998; pp. 17–20.
2. Ščetar, M.; Kurek, M.; Režek Jambrak, A.; Debeaufort, F.; Galić, K. Effect of high power ultrasound on physical–chemical properties of polypropylene films aimed for food packaging: Structure and surface features. *Polym. Bull.* **2019**, *76*, 1007–1021. [CrossRef]
3. Gull, A.; Prasad, K.; Kumar, P. Quality Changes in Functional Pasta During Storage in Two Different Packaging Materials: LDPE and BOPP. *J. Food Process. Preserv.* **2017**, *41*, 1–7. [CrossRef]
4. Huan, T.D.; Boggs, S.; Teyssedre, G.; Laurent, C.; Cakmak, M.; Kumar, S.; Ramprasad, R. Advanced polymeric dielectrics for high energy density applications. *Prog. Mater. Sci.* **2016**, *83*, 236–269. [CrossRef]
5. Guimond, S.; Radu, I.; Czeremuszkin, G.; Carlsson, D.J.; Wertheimer, M.R. Biaxially Oriented Polypropylene (BOPP) Surface Modification by Nitrogen Atmospheric Pressure Glow Discharge (APGD) and by Air Corona. *Plasmas Polym.* **2002**, *7*, 71–88. [CrossRef]
6. Novák, I.; Florián, Š. Investigation of long-term hydrophobic recovery of plasma modified polypropylene. *J. Mater. Sci.* **2004**, *39*, 2033–2036. [CrossRef]
7. Štěpánová, V.; Šrámková, P.; Sihelník, S.; Stupavská, M.; Jurmanová, J.; Kováčik, D. The effect of ambient air plasma generated by coplanar and volume dielectric barrier discharge on the surface characteristics of polyamide foils. *Vacuum* **2021**, *183*, 109887. [CrossRef]
8. Galmiz, O.; Kelar Tučeková, Z.; Kelar, J.; Zemánek, M.; Stupavská, M.; Kováčik, D.; Černák, M. Effect of atmospheric pressure plasma on surface modification of paper. *AIP Adv.* **2019**, *9*, 105013. [CrossRef]
9. Černák, M.; Kováčik, D.; Ráhel', J.; Sťahel, P.; Zahoranová, A.; Kubincová, J.; Tóth, A.; Černáková, L. Generation of a high-density highly non-equilibrium air plasma for high-speed large-area flat surface processing. *Plasma Phys. Control. Fusion* **2011**, *53*, 124031. [CrossRef]
10. Kormunda, M.; Homola, T.; Matoušek, J.; Kováčik, D.; Černák, M.; Pavlik, J. Surface analysis of poly(ethylene naphthalate) (PEN) films treated at atmospheric pressure using diffuse coplanar surface barrier discharge in air and in nitrogen. *Polym. Degrad. Stab.* **2012**, *97*, 547–553. [CrossRef]
11. Shekargoftar, M.; Kelar, J.; Krumpolec, R.; Jurmanová, J.; Homola, T. A Comparison of the Effects of Ambient Air Plasma Generated by Volume and by Coplanar DBDs on the Surfaces of PP/Al/PET Laminated Foil. *IEEE Trans. Plasma Sci.* **2018**, *46*, 3653–3661. [CrossRef]
12. Hergelová, B.; Zahoranová, A.; Kováčik, D.; Stupavská, M.; Černák, M. Polylactic acid surface activation by atmospheric pressure dielectric barrier discharge plasma. *Open Chem.* **2015**, *13*, 564–569. [CrossRef]
13. Kelar, J.; Shekargoftar, M.; Krumpolec, R.; Homola, T. Activation of polycarbonate (PC) surfaces by atmospheric pressure plasma in ambient air. *Polym. Test.* **2018**, *67*, 428–434. [CrossRef]
14. Homola, T.; Matoušek, J.; Hergelová, B.; Kormunda, M.; Wu, L.Y.L.; Černák, M. Activation of poly(methyl methacrylate) surfaces by atmospheric pressure plasma. *Polym. Degrad. Stab.* **2012**, *97*, 886–892. [CrossRef]
15. Saranko, A.; Szakal, Z.; Kalacska, G.; Samyn, P.; Sukumaran, J.; Klebert, S.; Karoly, Z. Adhesion and sliding tribological properties of polyolefins treated by diffuse coplanar surface barrier discharges. *Express Polym. Lett.* **2018**, *12*, 972–985. [CrossRef]
16. Janík, R.; Kohutiar, M.; Pajtášová, M.; Dubec, A.; Pagáčová, J.; Šulcová, J. The impact of DCSBD plasma discharge on polypropylene. *IOP Conf. Ser. Mater. Sci. Eng.* **2020**, *776*, 012090. [CrossRef]

17. Kohutiar, M.; Janík, R.; Pajtášová, M.; Ondrušová, D.; Labaj, I.; Zvoláneková Mezencevová, V. Study of structural changes in thermoplastics using dynamic mechanical analysis. *IOP Conf. Ser. Mater. Sci. Eng.* **2020**, *776*, 012092. [CrossRef]

18. Oravcová, A.; Hudec, I. The influence of atmospheric pressure plasma treatment on surface properties of polypropylene films. *Acta Chim. Slovaca* **2010**, *3*, 57–62.

19. Owens, D.K.; Wendt, R.C. Estimation of the surface free energy of polymers. *J. Appl. Polym. Sci.* **1969**, *13*, 1741–1747. [CrossRef]

20. Wokovich, A.M.; Brown, S.A.; McMaster, F.J.; Doub, W.H.; Cai, B.; Sadrieh, N.; Mei, L.C.; Machado, S.; Shen, M.; Buhse, L.F. Evaluation of substrates for 90° peel adhesion—A collaborative study: I. Medical tapes. *J. Biomed. Mater. Res. Part B Appl. Biomater.* **2008**, *87*, 105–113. [CrossRef]

21. McGuiggan, P.M.; Chiche, A.; Filliben, J.J.; Yarusso, D.J. Peel of an adhesive tape from a temperature-gradient surface. *Int. J. Adhes. Adhes.* **2008**, *28*, 185–191. [CrossRef]

22. Junkar, I.; Cvelbar, U.; Vesel, A.; Hauptman, N.; Mozetič, M. The role of crystallinity on polymer interaction with oxygen plasma. *Plasma Process. Polym.* **2009**, *6*, 667–675. [CrossRef]

23. Strobel, M.; Strobel, J.M.; Jones, V.; Lechuga, H.; Lyons, C.S. Effect on wettability of the topography and oxidation state of biaxially oriented poly(propylene) film. *J. Adhes. Sci. Technol.* **2019**, *33*, 1644–1657. [CrossRef]

24. Chen, W.X.; Yu, J.S.; Chen, G.L.; Qiu, X.P.; Hu, W.; Bai, H.Y.; Shao, J.Z. Development of a novel protocol for the permanent hydrophilic modification of a BOPP film for high quality printing with water-based ink. *RSC Adv.* **2015**, *5*, 87963–87970. [CrossRef]

25. Darvish, F.; Mostofi Sarkari, N.; Khani, M.; Eslami, E.; Shokri, B.; Mohseni, M.; Ebrahimi, M.; Alizadeh, M.; Dee, C.F. Direct plasma treatment approach based on non-thermal gliding arc for surface modification of biaxially-oriented polypropylene with post-exposure hydrophilicity improvement and minus aging effects. *Appl. Surf. Sci.* **2020**, *509*, 144815. [CrossRef]

26. Wang, C.; He, X. Polypropylene surface modification model in atmospheric pressure dielectric barrier discharge. *Surf. Coat. Technol.* **2006**, *201*, 3377–3384. [CrossRef]

27. Gim, S.; Lee, I.; Park, J.Y.; Lee, J.L. Spontaneously Embedded Scattering Structures in a Flexible Substrate for Light Extraction. *Small* **2017**, *13*, 1–8. [CrossRef] [PubMed]

28. Cortese, B.; Morgan, H. Controlling the Wettability of Hierarchically Structured Thermoplastics. *Langmuir* **2012**, *28*, 896–904. [CrossRef] [PubMed]

29. Dorai, R.; Kushner, M.J. A model for plasma modification of polypropylene using atmospheric pressure discharges. *J. Phys. D Appl. Phys.* **2003**, *36*, 666–685. [CrossRef]

30. Borcia, G.; Anderson, C.A.; Brown, N.M.D. The surface oxidation of selected polymers using an atmospheric pressure air dielectric barrier discharge: Part I. *Appl. Surf. Sci.* **2004**, *221*, 203–214. [CrossRef]

31. Hanusová, J.; Kováčik, D.; Stupavská, M.; Černák, M.; Novák, I. Atmospheric pressure plasma treatment of polyamide-12 foils. *Open Chem.* **2015**, *13*, 382–388. [CrossRef]

32. Bhat, N.V.; Upadhyay, D.J. Plasma-induced surface modification and adhesion enhancement of polypropylene surface. *J. Appl. Polym. Sci.* **2002**, *86*, 925–936. [CrossRef]

33. Mirabedini, S.M.; Arabi, H.; Salem, A.; Asiaban, S. Effect of low-pressure O_2 and Ar plasma treatments on the wettability and morphology of biaxial-oriented polypropylene (BOPP) film. *Prog. Org. Coat.* **2007**, *60*, 105–111. [CrossRef]

34. Morent, R.; De Geyter, N.; Leys, C.; Gengembre, L.; Payen, E. Comparison between XPS- And FTIR-analysis of plasma-treated polypropylene film surfaces. *Surf. Interface Anal.* **2008**, *40*, 597–600. [CrossRef]

35. Navaneetha Pandiyaraj, K.; Selvarajan, V.; Deshmukh, R.R.; Gao, C. Adhesive properties of polypropylene (PP) and polyethylene terephthalate (PET) film surfaces treated by DC glow discharge plasma. *Vacuum* **2008**, *83*, 332–339. [CrossRef]

36. Leroux, F.; Campagne, C.; Perwuelz, A.; Gengembre, L. Polypropylene film chemical and physical modifications by dielectric barrier discharge plasma treatment at atmospheric pressure. *J. Colloid Interface Sci.* **2008**, *328*, 412–420. [CrossRef] [PubMed]

37. Ding, L.; Zhang, X.; Wang, Y. Study on the Behavior of BOPP Film Treated by Corona Discharge. *Coatings* **2020**, *10*, 1195. [CrossRef]

Article

Surface Modification of Poly(lactic acid) Film via Cold Plasma Assisted Grafting of Fumaric and Ascorbic Acid

Asma Abdulkareem [1], Peter Kasak [1,*], Mohammed G. Nassr [1,2], Abdelrahman A. Mahmoud [1,2], Mahmoud Khatib A. A. Al-Ruweidi [1,2], Khalid J. Mohamoud [1,2], Mohammed K. Hussein [1,2] and Anton Popelka [1,*]

1   Center for Advanced Materials, Qatar University, Doha P.O. Box 2713, Qatar;
     asma.alkareem@qu.edu.qa (A.A.); mn1402336@student.qu.edu.qa (M.G.N.); am1306019@qu.edu.qa (A.A.M.);
     ma1207471@qu.edu.qa (M.K.A.A.A.-R.); km1306840@student.qu.edu.qa (K.J.M.);
     mh1300782@student.qu.edu.qa (M.K.H.)
2   Department of Chemistry and Earth Sciences, College of Arts & Sciences (CAS) Qatar University,
     Doha P.O. Box 2713, Qatar
*   Correspondence: peter.kasak@qu.edu.qa (P.K.); anton.popelka@qu.edu.qa (A.P.); Tel.: +974-4403-5676 (A.P.)

Abstract: Plant-based materials have found their application in the packaging with a yearly growing production rate. These naturally biodegradable polymers are obtained from renewable and sustainable natural resources with reduced environmental impact and affordable cost. These materials have found their utilization in fully-renewable plant-based packaging products, such as Tetra Pak®-like containers, by replacing commonly-used polyethylene as the polymer component. Poly(lactic acid) (PLA) is one of the representative plant-based polymers because of its eco-friendliness and excellent chemical and mechanical properties. In this work, a PLA surface was modified by various food additives, namely ascorbic acid (ASA) and fumaric acid (FA), using plasma-initiated grafting reactions in order to improve the surface and adhesion properties of PLA. Various analytical and microscopic techniques were employed to prove the grafting process. Moreover, the improved adhesion of the modified PLA foil to aluminum (Al) foil in a laminate configuration was proven by peel resistance measurements. The peel resistance of modified PLA increased by 74% and 184% for samples modified by ASA and FA, respectively, compared with untreated PLA.

Keywords: poly(lactic acid); PLA; ascorbic acid; fumaric acid; plasma treatment; grafting; wettability; adhesion

1. Introduction

Global environmental policy and market knowledge of the use and consumption of materials with low environmental effects are the first guiding factors in the production and investigation of new biodegradable or organic products. The packaging industry is one of the most critical waste generators [1]. Current consumption patterns in our society are producing a great deal of waste that needs to be carefully handled to generate the least environmental effects. Plastic, apparently, constitutes a significant part of this form of waste, and it is challenging and costly to recycle due to its petrochemical origin [2], primarily due to the current problem of separation. Accordingly, polymeric materials occupy core study lines because of the importance that polymers obtained from sustainable sources (plant-based polymers) substitute petroleum-based polymers [3–7]. Poly(lactic acid) (PLA) is currently the most promising biodegradable, compostable and renewable polymer in synthetic form that can be completely degraded [8,9]. PLA is a linear thermoplastic aliphatic polyester that can be produced by the ring opening polymerization of lactide. Lactide, as a cyclic dimer, is made from the controlled depolymerization of lactic acid oligomers, which is are obtained from sugar feedstock fermentation, corn fermentation, and other sources [10–12]. PLA has excellent mechanical properties, high stiffness, biodegradabil-

ity [13], biocompatibility [13], bio-absorbency [13], transparency [14], gas permeability [14], low toxicity [15], ease of processing [15], and UV resistance [15]. Due to these facts, PLA also has found a wide range of applications such as in the agricultural, biomedical, and packaging industries (specifically food packaging applications) [16–18]. Nevertheless, neat PLA possesses low surface free energy (wettability) resulting in weak adhesion and thus, limits the wider usage of PLA in the packaging industry. In recent years, many research studies have been reported about improving PLA properties by fusion with different additives such as lubricants, plasticizers or other polymers [19–21]. However, this approach is not recommended for food packaging applications because it can generate waste that may have the potential to harm the environment and health [3]. Consequently, treatments that overcome such issue waste are of increasingly high importance. As a response to this issue, surface modification is a safe, simple, and affordable option [22–24]. Surface modification methods can be physical or chemical, and there are a variety of treatments available. Over the last few decades, these modification methods have been established with an emphasis on the surface incorporation of extra functionalities responsible for the growing increase of surface free energy (wettability) and tailored applications [25–27]. Such modifications should only affect the top surface area (tens of nm), which is essential for functional strength and at the same time to maintain integrity of the material. For this reason, plasma technology has become the preferable choice as a representative technique used for physical treatment. As the fourth state of matter, plasma is an ionized gas representing a mixture of electrons, ions, metastatic ions, and free radicals with enough energy to modify a treated surface [23,28–30]. During plasma treatment, the activated species reach the surface of the substrate and break up the molecular chain, forming new functional groups (mostly containing oxygen). Furthermore, surface activation can be induced by atom substitution and/or recombination, which is the most important mechanism [31]. This leads to improved roughness, adhesion, wettability and protection of material [32]. In food packaging applications, antibacterial packaging materials are used to keep food from being vulnerable to microorganisms and to extend the shelf life of food [33–35]. To create biomaterials, some antibacterial procedures include combining antibacterial agents inside the polymeric content [36,37]. Nevertheless, this method is not ideal for all packaging materials because it alters the materials' key physical and mechanical properties and reduces their stability. Therefore, the development of PLA based films with enhanced antimicrobial properties is highly demanded. For this purpose, the PLA surface can be modified with antimicrobial agents using the plasma technique as an effective radical initiator for the grafting processes [38]. Due to their nontoxicity, biocompatibility, and antimicrobial properties, ascorbic acid (ASA) and fumaric acid (FA) are promising materials for this modification [39,40]. These material compounds are components of organic biosynthesis in humans, essential bioactive species, and conservant, and they are often used in medicinal applications [41]. Therefore, for enhancement of the adhesion of PLA to Al as a component towards packaging applications, a rapid fabrication process is required combining cold plasma treatment as a simple, scalable and physical surface modification technique together with a surface modification by addition of cost effective, sustainable and biocompatible molecules.

Thus, in this research study, commonly used food additives such as ASA and FA were grafted on the surface of PLA film using low-temperature plasma acting as an initiator of radical grafting reactions. Furthermore, the effect of non-thermal plasma treatment and grafting on the adhesion improvement of PLA film was investigated.

2. Materials and Methods

2.1. Materials

Commercial poly(lactic acid) (PLA) with a D-isomer content of 4.3%, Mw of 2.53×10^5 g/mol, melt flow index of 6 g/10 min (190 °C/2.16 kg), and density of 1.24 g/cm^3 was supplied in pellets from (NatureWorks, Minnetonka, MN, USA), which was used for the PLA film preparation. Ethylene glycol (>98% FLUKA, Overijse, Belgium), ultra-pure water (prepared

by Purification System Direct Q3, Rue de Luzais, France), and formamide (>98% FLUKA, Overijse, Belgium) were utilized as testing liquids to study wettability. Aluminum foil (Al) (GLAD, Qingdao, Shandong, China) was used to prepare the adhesive joint with PLA. Fumaric acid (FA) $C_4H_4O_4$, with an average Mw of 116.07 g/mol was purchased from Merck KGaA, (Darmstadt, Germany) and L-ascorbic acid (>99.0% Research-Lab, Uran Islampur, India), molecular weight = 176.14 g/mol and sodium iodide: extra pure, MW 197.89 g/mol purchases from Research-Lab, Uran Islampur (India) were used for the PLA modification. Glacial acetic acid (CH_3COOH) supplied from VWR International (BDH) CHEMICALS (Radnor, PA, USA), anhydrous ($\geq$99.9% purity) and sodium thio-sulfate pentahydrate $Na_2S_2O_3.5H_2O$: extra pure (crystals), MW 248.17 g/mol, purchased from Research-lab Fine Chem Industries (Mumbai, India) were used for hydroperoxides determination. All the chemicals were used without further treatment.

2.2. Preparation of PLA Films and PLA/Al Laminate

A hot mounting press machine AutoFour/3012-PL,H (Carver, Wabash, IN, USA)was used to fabricate thin, homogeneous PLA films with a thickness of around 0.3 mm. The PLA pellets were melted and pressed with a force of two tones for two minutes at 180 °C in order to achieve a smooth surface in the film. Then the PLA samples were cooled down using a water medium to room temperature and subsequently were washed thoroughly with ethanol to remove any chemicals, residuals, or possible contaminants from the molding process that could affect the surface properties, and dried for 20 min at room temperature under ambient air. Finally, the film samples were sliced into narrow strips (5 cm × 1 cm) and used directly for surface treatment and analysis. Furthermore, 10 cm × 10 cm samples were placed between two steel plates covered by Al foil and molded into a thin film at 160 °C via the hot mounting press machine AutoFour/3012-PL,H (Carver, Wabash, IN, USA) for 2 min at a force of 1 ton. The film was allowed to cool down until it reached 30 °C and was then cut into 2 × 10 cm strips in order to be used for a peel test.

2.3. Surface Modification of PLA Using Plasma Treatment

PLA films were treated with a low-temperature plasma at vacuum pressure using the RF plasma equipment Venus75-HF (Plasma Etch Inc, Carson, CA, USA). The plasma discharge was generated at radiofrequency (RF) powered electrodes with a capacitive parallel plate design operating at a frequency of 13.56 MHz. A cylindrical chamber made of an Al chamber containing PLA samples was vacuumed to 0.2 Torr, and the plasma treatment was applied for 30 to 180 s at 80 W nominal power. The PLA samples were treated from both sides.

2.4. Grafting Process

The prepared PLA films were subsequently modified by an antimicrobial agent using plasma treatment as an initiator for a radical grafting mechanism. Then, the antimicrobial agents ASA and FA were grafted to the surface of the prepared PLA films using low-temperature plasma as initiator for radical grafting. Grafting was carried out for 24 h on plasma-treated PLA samples immersed in ASA 10% *w/v* aqueous solution and in FA 5% *w/v* ethanol solution. Subsequently, the samples were thoroughly washed and dried. The graft yield was obtained gravimetrically to prove the grafting of ASA and FA on the PLA surface using three different samples. The graft yield (GY) was calculated by Equation (1):

$$GY\,[\%] = ((W_2 - W_1)/W_1) \times 100\% \tag{1}$$

where, W_1 and W_2 represent the weights of the PLA samples before and after the modification, respectively.

2.5. Wettability Analysis

Static contact angle measurements were used to assess the changes in wettability of the plasma-treated and grafting modified PLA surface. For this study, an OCA35 optical

contact-angle measurement device (DataPhysics, Filderstadt, Germany) was used, which was equipped with a high-resolution CCD camera. As testing liquids, ultra-pure water, ethylene glycol, and formamide were used. To eliminate the gravitational effect, a 3 μL droplet was dispensed on the sample in ambient air. The contact angle was recorded approximately after 3 s (attainment of thermodynamic consistency between the sample interfaces and the liquid). The average value of testing contact angle value was calculated using five independent measurements in various positions. The total surface-free energy, as well as its polar and dispersive components, were calculated using the Owens, Wendt, Rabel and Kaelble model.

2.6. Hydroperoxides Determination

To detect hydroperoxides created on the PLA surface after plasma treatment, a modified iodometric method based on Wagner et al. [31] was conducted. The reactions are described in following equations. The first is a reaction of hydroperoxides with sodium iodide in a presence of acetic acid ($1H_2O_2$:$1I_2$) (Equation (2)):

$$H_2O_2 + 2NaI + 2CH_3COOH \rightarrow 2CH_3COONa + I_2 + 2H_2O \tag{2}$$
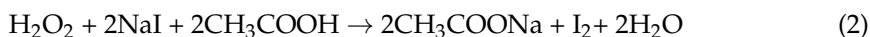
The next step involves reactions of iodine with thiosulfate to determine the hydroperoxide concentration through a quantification of reduced iodine ($1I_2$:2I-) (Equations (3) and (4)):

$$Na_2S_2O_3 + H_2O \rightarrow S_2O_3{}^{2-} + Na^+ + H^+ + OH^- \tag{3}$$

$$2S_2O_3{}^{2-} + I_2 \rightarrow S_4O_6{}^{2-} + 2I \tag{4}$$
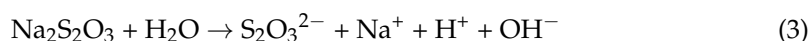
PLA samples were immersed into 50 mL of glacial acetic inside an Erlenmeyer flask. Then, 1 g of sodium iodide was added to the flask. Due to the light sensitivity of sodium iodide, the flask was covered with Al foil. Reactions were carried out in an inert (argon gas) atmosphere and away from light to ensure that only the created hydroperoxides were used to oxidize the iodide. The color of the mixture changed to yellow after the iodide was oxidized to iodine. After reaching the titration threshold, a subsequent titration with sodium thiosulfate (0.0005 M) solution resulted in a colorless solution, and the concentration of hydroperoxides per treated area was calculated.

2.7. Surface Morphology Analysis

The surface topography for plasma-treated PLA films was analyzed using a confocal method for optical surface metrology using a Leica DCM8 profilometer (Leica microsystems, Wetzlar, Germany). A high-precision surface profiling optical system was used to measure the influence of polymer concentration on nano-fibre morphology. Images were sizes 160×130 μm^2 using $100\times$ objective lens. The mean of arithmetic height (Sa), which was estimated over the entire measured area, was used to quantify the roughness of the surface.

The surface morphology of the PLA samples was investigated by scanning electron microscopy (SEM). Two-dimensional (2D) images of the examined surfaces were taken using the Nova NanoSEM 450 SEM microscope (FEI, Hillsboro, OR, USA). Thin Au layers a few nanometers thick were sputtered onto PLA samples to obtain high-resolution SEM images and to prevent electron accumulation in the measured substance.

Atomic force microscopy (AFM) was used to examine the surface topography/morphology of PLA samples using an MFP-3D system (Oxford Instruments Asylum research, Abingdon, Oxford, UK) equipped with an AC160TS cantilever with tip (Al reflex coated Veeco model-OLTESPA, Olympus, Tokyo, Japan). Under atmospheric conditions, scanning was conducted using air tapping mode (AC mode) from a surface area of 5×5 μm^2. Alternatively, the value of the roughness parameter (Ra–arithmetic mean height of line) and line profile were evaluated from images collected from the AFM Z-sensor.

2.8. Chemical Composition Investigation

Fourier transformed infrared spectroscopy with attenuated accessory (FTIR-ATR) was used to examine the chemical composition changes in the plasma-treated and modified PLA samples. The Spectrum 400 (Perkin Elmer, Waltham, MA, USA) was used to characterize the chemical composition of the PLA samples and identify the functional groups introduced after the plasma treatment and grafting reactions. After background (air) subtraction, all measurements were obtained using eight scans with a resolution of four. Qualitative data were gathered about the absorption of chemical groups in the middle infrared region $(4400–500 \text{ cm}^{-1})$.

X-ray photoelectron spectroscopy (XPS) was used to quantify the changes in chemical structure caused by plasma treatment and modification of the PLA surface. The device used for this analysis was an AXIS XPS (Kratos Empirical, Manchester, UK). A spherical mirror analyzer and a delay detector are included in the XPS device, which provide good spectral resolution and flexibility for rapid chemical composition screening. Data can be collected at a depth of 1–10 nm using this system.

2.9. The Evaluation of Nano-Mechanical Properties

The surface nano-mechanical properties of the PLA samples were determined by a MFP-3D AFM system (Oxford Instruments Asylum research, Abingdon, Oxford, UK) using an amplitude modulation–frequency modulation (AM–FM) mode. The probe was simultaneously excited at its specific resonant frequency and another eigenmode in this approach. The topographical/morphological features of the PLA samples were determined using the fundamental resonance, while the nano-mechanical properties were assessed using the frequency and amplitude shift of other eigenmodes. The interaction stiffness (ΔkFM) was estimated using the frequency shift (Δf) according to the Equation (5):

$$\Delta k^{FM} \approx 2k_c \times \Delta f/f_c \tag{5}$$

where kc denotes the cantilever's spring constant and fc denotes the frequency of the cantilever eigenmode. A general Hertz model describing the contact mechanics between the tip and the analyzed sample was used to calculate the sample's Young's modulus. The cantilever elasticity $(590.41 \times 10^3 \text{ Pa/Hz})$ was first determined using polystyrene standard with a known Young's modulus (3.3 GPa). The absolute values of Young's modulus of the analyzed PLA samples were then calculated using this cantilever elasticity.

2.10. Peel Test Analysis

A peel test was carried out to analyze the adhesion characteristics of the PLA/Al adhesion joints under a 90° peeling angle of the PLA foil from the Al foil. Peeling resistance (peeling force per width) was obtained by these measurements. The tests were performed by means of a Lloyd LS 1K Plus (LLOYD Instruments Ltd., Bognor Regis, UK) friction/peel tester machine. The sample width and length were 2×10 cm, and the sample was under peeling for 360 s at a peeling rate of 10 mm/min. To obtain average values of the peeling resistance, five separate readings were carried out.

3. Results

3.1. Surface Wettability Analysis

The ability of a liquid surface to bind to a solid surface is characterized by surface free energy and wettability. It means that the lower the contact angle of a sample, the more wettable it is. The effect of RF plasma treatment on the wettability changes of prepared PLA films was investigated using contact angle measurements. The changes in the surface wettability of the modified samples are summarized in Figure 1 and Table 1. Surface-free energy and its components were determined using water (relatively high surface tension ~72.1 mN/m, polar component = 52.2 mN/m and disperse component = 19.9 mN/m) [41], formamide (surface free tension = 56.9 mN/m, polar component = 33.4 mN/m, and dis-

persive component = 23.5 mN/m) [40], ethylene glycol (surface free tension = 48.0 mN/m, polar component = 19.0 mN/m, and dispersive component = 29.0 mN/m) [42]. For the untreated PLA, the contact angles obtained with the three test liquids: water, formamide, and glycerol were 70.2°, 61.5°, and 47.2°, respectively. A hydrophobic surface is defined by contact angles greater than 90 degrees [39]. As a result, the untreated PLA surface has a hydrophilic behavior with a low total surface free energy (33.3 mJ/m^2), and a relatively high polar component (15.2 mJ/m^2). The polar functional groups present on the surface increase surface wettability. Therefore, it was observed that 30 s of RF the plasma treatment of PLA films led to the improvement of wettability, confirmed by the decrease of contact angles as result of the incorporation of new polar functionalities (mainly containing oxygen), etching and ablation processes. The addition of new oxygen-containing functional groups resulted in a 45.0 mJ/m^2 and 26.8 mJ/m^2 increase in total surface free energy and polar components, respectively, while the contact angle of water was reduced to 55.1°. Plasma treatment modified only the topmost layers (tens nm) of the material, leaving the bulk of the material unchanged. In order to improve wettability and therefore adhesion characteristics, grafting of the PLA surface by antibacterial agents was performed. The grafting of the polymer surface by polar compounds enhanced the polarity due to the defined structure attachment [24]. Therefore, ASA and FA acid were grafted on the surface of the prepared PLA film a using low-temperature plasma acting as an initiator for radical grafting reactions. The effect of ASA or FA grafting on the PLA surface was demonstrated in terms of its surface wettability and adhesion properties. The graft yield was 5.3% and 3.6% for the PLA surface modified by ASA and FA, respectively, indicating a multilayer formation of both ASA and FA. Moreover, the total surface free energy increased significantly for the PLA surface modified by ASA and FA to 46.4 mJ/m^2 and 49.0 mJ/m^2, respectively, as result of increased polar component (34.9 mJ/m^2 for ASA and 36.3 mJ/m^2 for FA). It can be concluded that grafting of FA and ASA resulted in significant improvement to the wettability of the PLA surface represented by the polar component of the surface free energy.
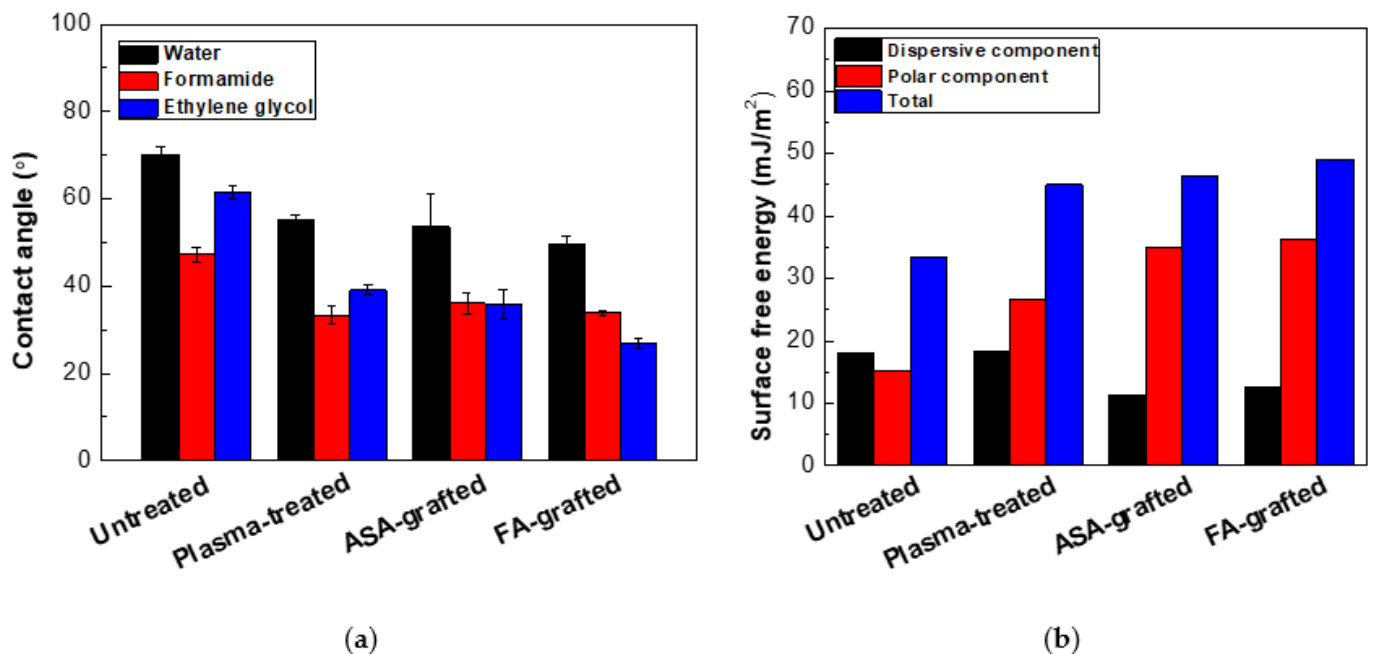
Figure 1. (**a**) The contact angles of the testing liquids on the PLA samples, (**b**) The surface free energy of the PLA samples.

Table 1. The contact angles, surface free energy and graft yields of the PLA samples.

PLA Samples	Water (○)	Ethylene Glycol (○)	Formamide (○)	Total Surface Free Energy (mJ/m^2)	Dispersive (mJ/m^2)	Polar (mJ/m^2)	GY (%)
Untreated	70.2 (±1.6)	47.2 (±1.7)	61.5 (±1.3)	33.3	18.1	15.2	-
Plasma-treated	55.1 (±1.2)	33.4 (±2.0)	39.0 (±1.2)	45.0	18.3	26.8	-
ASA-grafted	53.7 (±7.5)	36.0 (±3.3)	36.1 (±2.4)	46.4	11.4	34.9	5.3
FA-grafted	49.6 (±1.9)	26.8 (±1.2)	33.8 (±0.4)	49.0	12.6	36.3	3.6

3.2. Hydroperoxides Determination

As plasma treatment incorporates functionalities on the treated polymer surface, various forms of functional groups can be identified (mostly oxygen-containing). Nonetheless, the majority of free radicals are transformed into peroxides through air exposure before and after plasma treatment [43], and the quantity of peroxide content in either the infrared FTIR or XPS change spectra is difficult to discern. Therefore, an iodometric titration represents a suitable quantification approach according to Wagner et al. [44], which can be used to quantify the concentration of the created hydroperoxides after the plasma treatment process. Grafting reactions by FA or ASA occur with alkoxy radicals, which are created by the decomposition of hydroperoxides [45,46]. Moreover, water-soluble ASA acts as free radical scavenger [47,48] forming ascorbate radicals by electron transfer to alkoxy radicals, and therefore these ascorbate radicals are able to interact with other radicals or unsaturated carbons formed by plasma treatment. Figure 2 depicts the results obtained from the iodometric titration of plasma-treated PLA samples. Plasma treatment took place at different treatment times. The application of iodometric titration indicated that the level of hydroperoxides slightly increased with the time of treatment, rising from 2.4×10^{-7} mol/cm^2 to 2.7×10^{-7} mol/cm^2 for 30 s and 120 s, respectively. This shows that the longer exposure times of the polymer samples do not significantly increase hydroperoxide formation, and thus that the surface is saturated with a certain amount of peroxides at this optimum time [49]. Therefore, 30 s of treatment time was chosen for subsequent grafting reactions and to avoid potential degradation processes, which could occur using longer treatment times.
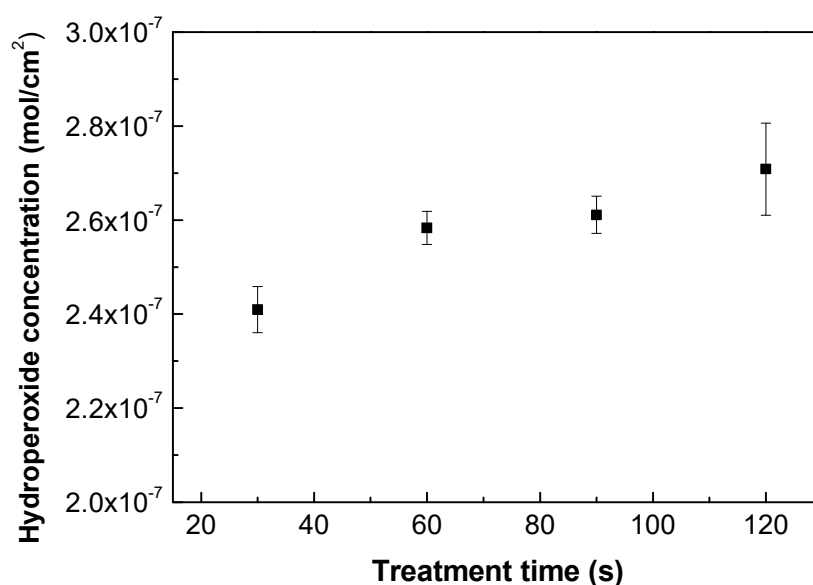
Figure 2. Hydroperoxide concentration vs. treatment time of plasma-treated PLA samples.

3.3. Chemical Composition Investigation

The chemical composition of the PLA samples was examined using FTIR-ATR spectroscopy after a modification step and surface oxidation caused by plasma treatment [31]. The data of the FTIR-ATR study show that there are structural changes in the molecu-

lar chains of PLA after the RF plasma treatment represented by slight changes in the peak intensities of the groups containing oxygen (Figure 3). The important regions of the PLA absorbance bands in the FTIR-ATR spectrum are at maximum of the wavenumbers 1750 cm^{-1} for the C=O stretching of the ester group, 3650–3000 cm^{-1} for the –OH stretching, 2993 cm^{-1} and 2943 cm^{-1} for –CH stretching, 1450 cm^{-1} for C–H bending, and 1180 cm^{-1} and 1085 cm^{-1} belonging to the C–O. Plasma treatment of PLA film resulted in slightly decreased intensity of –OH (3650 cm^{-1} for free and 3500 cm^{-1} for H bonded bonding) indicating chain scissoring in the PLA structure that resulted in subsequent functionalization by other functional groups such as C=O. Therefore, C=O and C–O (secondary alcohol) increased after plasma treatment. Moreover, in the PLA films modified by ASA and FA, a new absorption band at 1680 cm^{-1} developed that was attributed to C=O stretching of the acid group from the grafted ASA and FA species. These observed changes in the FTIR-ATR spectra of the prepared PLA films proved the functionalization processes occurred during the plasma treatment process. The FTIR spectra of modified PLA films by ASA and FA are illustrated in Figure 3.
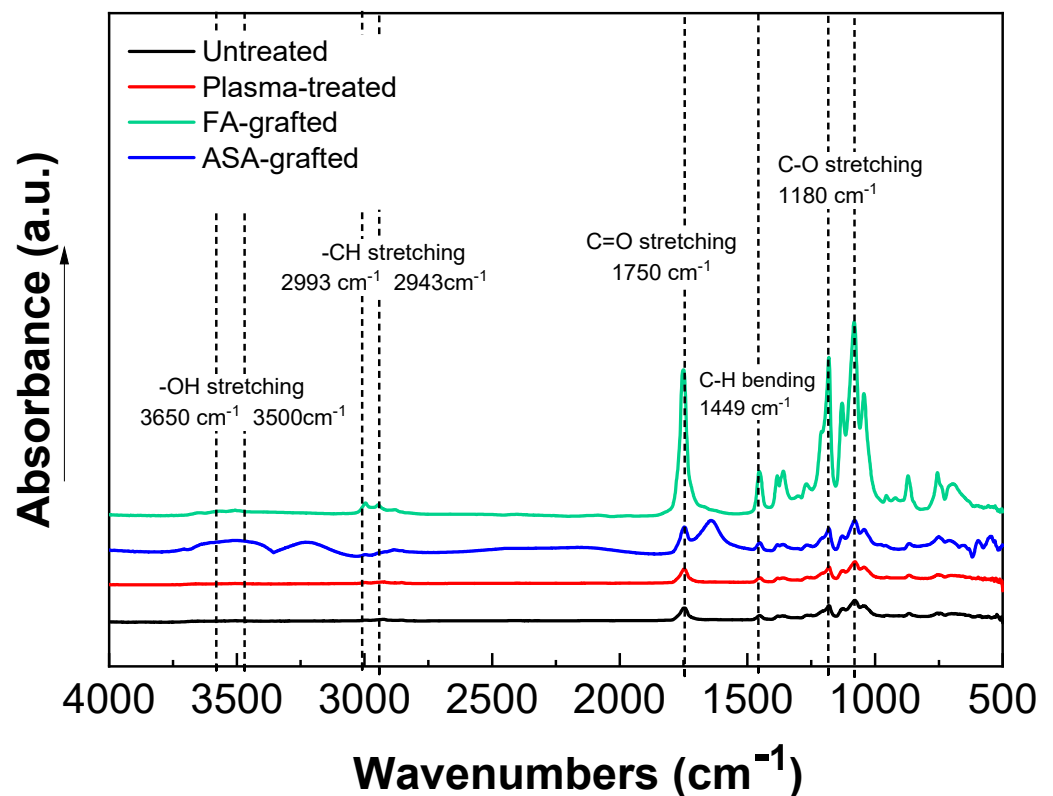
Figure 3. Fourier transform infrared spectroscopy (FTIR) spectra of PLA samples.

The XPS technique was used to determine the chemical composition of PLA samples. Figure 4 shows the XPS spectra of the PLA samples after the plasma treatment and modification step. The XPS spectrum for the untreated PLA reveals two main contributions corresponding to C1s at ~285 eV and O1s at ~530 eV, attributable to the PLA's chemical composition, distinguished by the existence of oxygen in the polymer chain [3,23,37]. The incorporation of new functional groups in the PLA surface was caused by plasma treatment. This functionalization is primary generated by oxygen-rich species because of their high reactivity and, to a lesser extent, nitrogen-rich species [50]. As a result, the peak intensity corresponding to the O1s transition increased significantly, while the peak C1 contribution decreased significantly. The etching process and the formation of radical and oxygen-containing groups led to reduction of the intensity of the C1 peak to 67.3 at.% [23]. The oxygen-containing groups in ASA and FA were primarily responsible for the increase

in at.% of the O1 peak caused by the antimicrobial agent grafting on the PLA surface. The O1 peak in the ASA-grafted PLA samples was 32.5 at.%, while the C1 peak intensity was 65.8 at.%. Furthermore, due to probably the presence of nitrogen-containing impurities, the N1 intensity increased slightly to 1.8 at.% when compared to the plasma-treated PLA sample. In contrast, a significant increase in the intensity of the maximum O1 peak, achieving a value of 37.6 at.% indicated the incorporation of the FA grafted to the PLA surface.
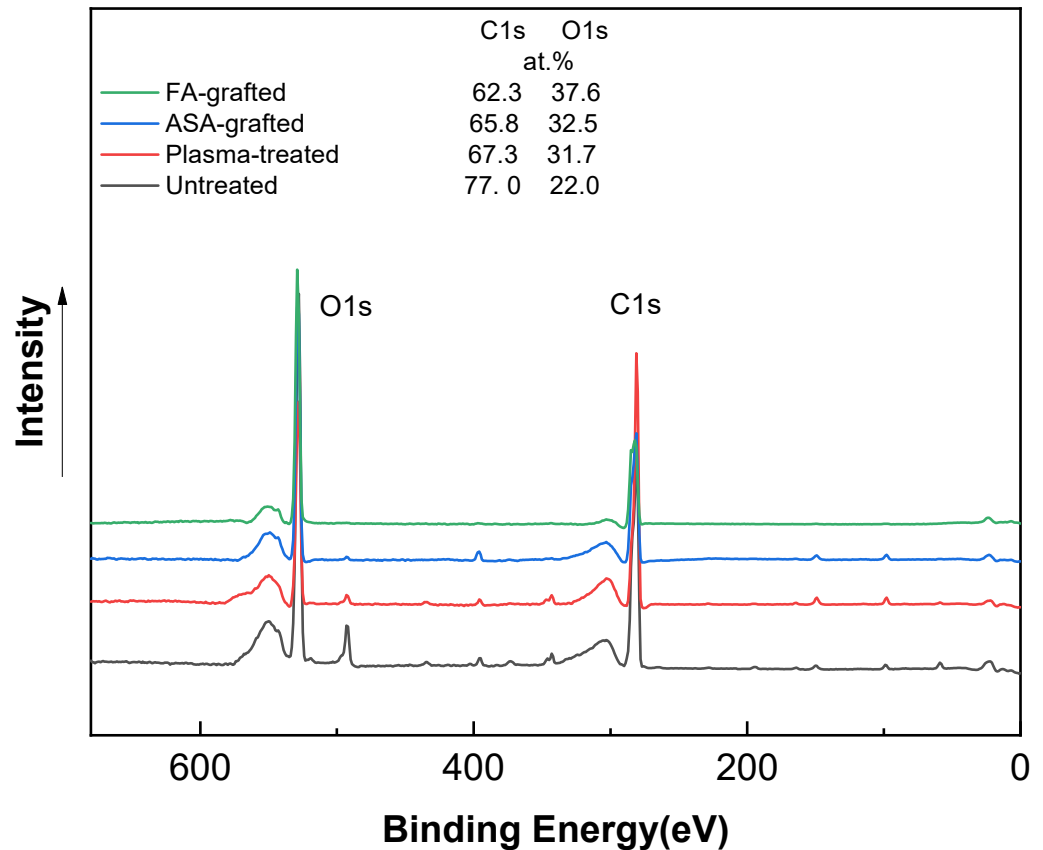
Figure 4. X-ray photoelectron spectroscopy (XPS) spectra of PLA samples.

3.4. Surface Morphology/Topography

SEM (Figure 5) was uses to analyze the surface morphological changes of the PLA samples after the plasma treatment and modification steps. The SEM image of the untreated PLA (Figure 5a) shows a homogeneous surface with a relatively smooth and uniform appearance. The PLA surface treated with plasma discharge (Figure 5b) reveals an entirely different surface morphology compared to the untreated surface. Small spots, grooves and cavities were observed on the substrate where some removal occurred and some roughness changes were produced. This phenomenon was aided by the physical bombardment of the surface with high-energy particles generated during plasma generation [31,43]. The PLA samples grafted with ASA and FA experienced clear surface morphological changes that demonstrated areas on the surface as grafting occurred. PLA films modified by ASA (Figure 5c) and FA (Figure 5d) were coated by specific layers on the film surface, which confirmed the presence of an antimicrobial agent after the modification process. It can be concluded that modification of PLA by ASA and FA led to an overall roughness increase as the films were coated with antimicrobial agents.
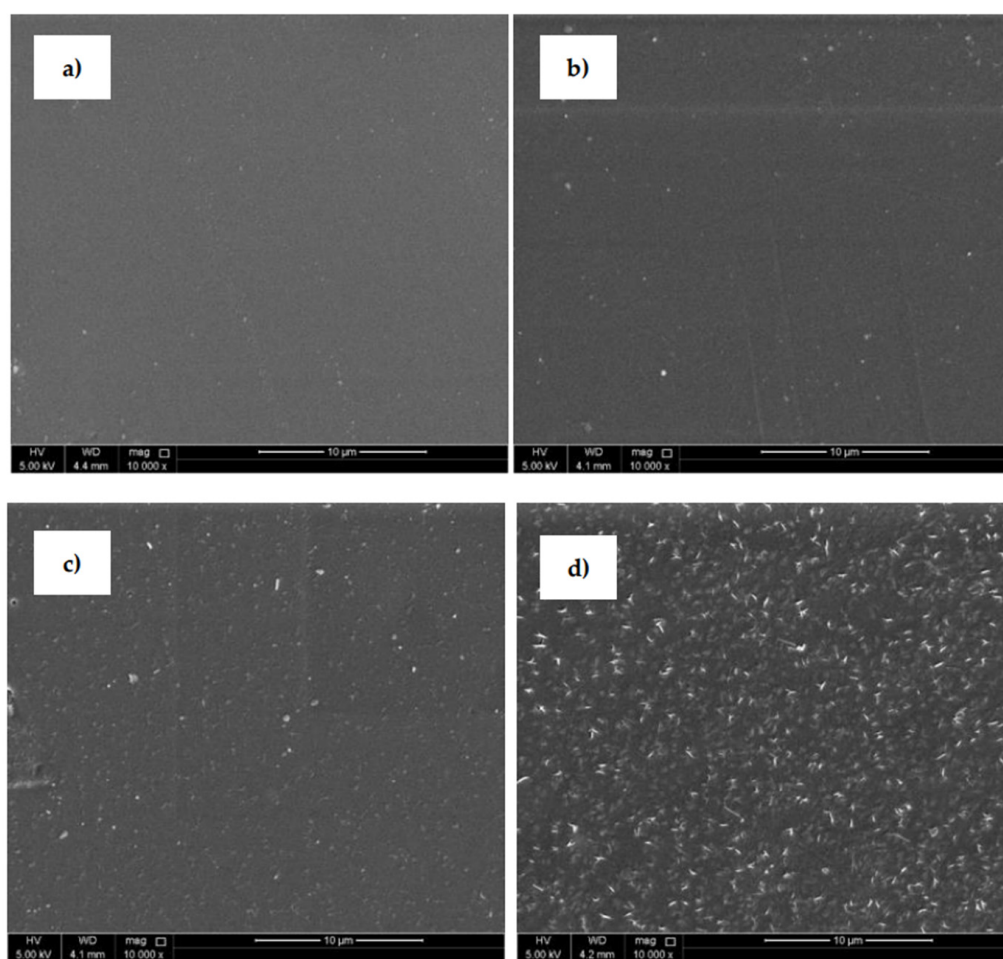
Figure 5. Scanning electron microscopy (SEM), images of PLA: (**a**) untreated, (**b**) plasma-treated, (**c**) ASA-grafted, and (**d**) FA-grafted.

The detailed surface topography and morphology of PLA samples was obtained by AFM from 5×5 μm^2 surface area. The AFM images (Figure 6) provide information about the roughness of the PLA surface after each modification step. The surface of the untreated PLA had a characteristic texture and uniform topography/morphology originating from the preparation process, while Ra (arithmetical mean height of line) was 17.0 nm (Figure 6a). Plasma treatment led to noticeable changes in the surface area of PLA and the surface roughness increased as result of the bombarding action of plasma reactive species with the polymer surface responsible for etching reactions. The Ra parameter of the plasma-treated PLA sample increased to 31.2 nm (Figure 6b). Modification of PLA by ASA and FA led to a formation of specific layers, while Ra was 30.2 nm and 16.3 nm, respectively.
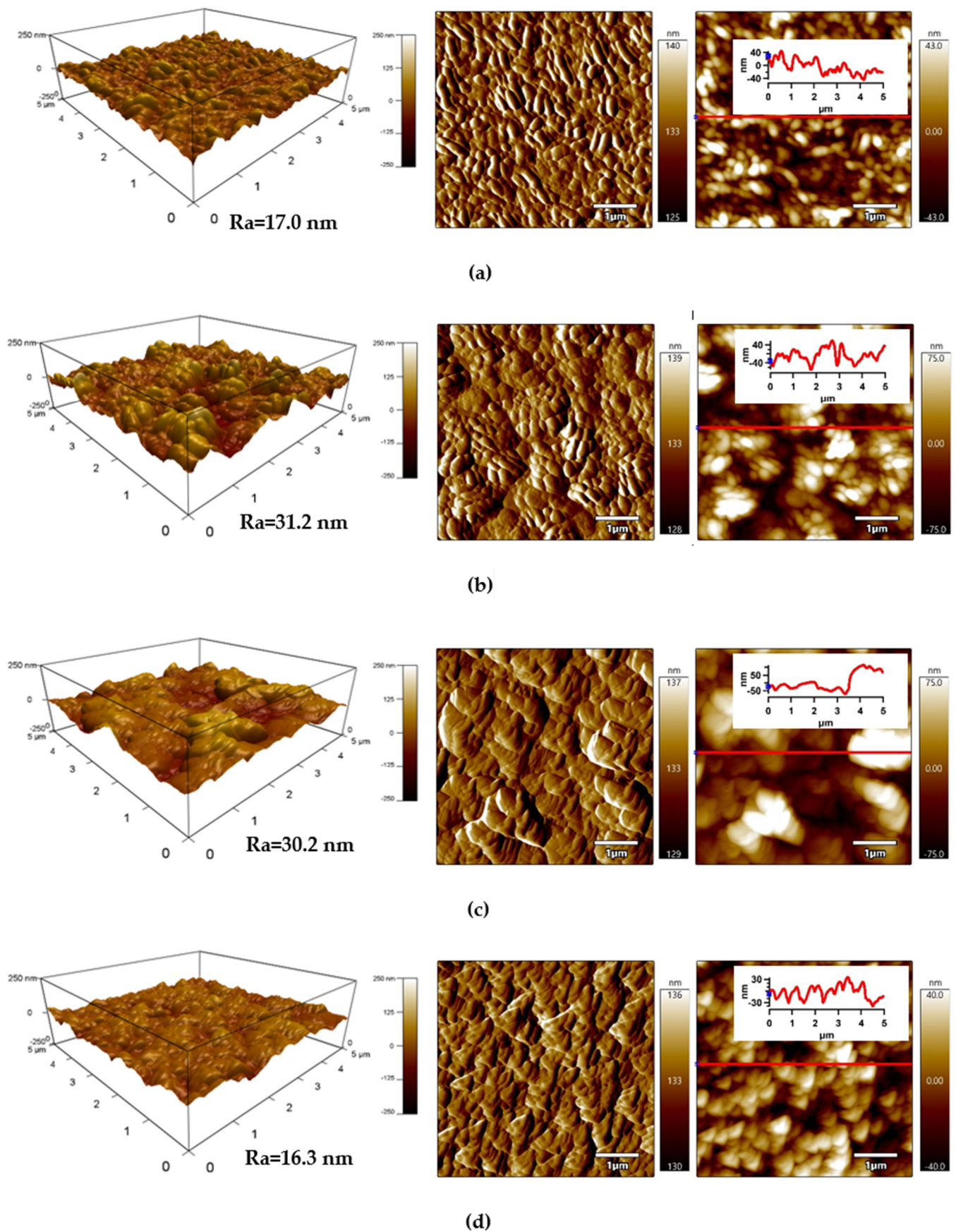
Figure 6. Atomic force microscopy (AFM) images (from left to right: 3D Height, Amplitude, ZSensor including line profile) of PLA: (**a**) untreated, (**b**) plasma-treated, (**c**) ASA-grafted, and (**d**) FA-grafted.

3.5. Mechanical Properties

The nano-mechanical properties of the PLA surfaces were analyzed using an advanced AM–FM mode of AFM in parallel with topography/morphology measurements [50]. The AM–FM AFM images representing the stiffness and Young's modulus distribution in the entire surface are shown in Figure 7. In addition, a mean value of stiffness and Young's modulus was calculated as an arithmetic mean value of the measured distribution using Gaussian related histograms [51], which are summarized in Table 2. The untreated PLA surface exceled in uniform distribution of stiffness and Young's modulus in the entire $5 \times 5 \ \mu m^2$ surface area. The mean of stiffness and Young's modulus were 48.4 mN/m and 2.7 GPa, respectively. Plasma treatment was responsible for slightly increasing the nano-mechanical properties of the PLA surface due to structural reorganization caused by ablation, etching, functionalization or crosslinking processes [52], while the stiffness and Young's modulus increased to 54.6 mN/m and 3.0 GPa. Modification of the PLA samples by ascorbic acid and fumaric acid was responsible for a slight enhancement of the nano-mechanical properties in the surface area due to the formation of compact grafted layers covalently bonded on the PLA surface [53,54]. The stiffness and Young's modulus increased to 64.1 mN/m and 3.5 GPa for the PLA modified by ASA and to 70.7 mN/m and 3.9 GPa for the PLA modified by FA.

(a)

(b)

(c)
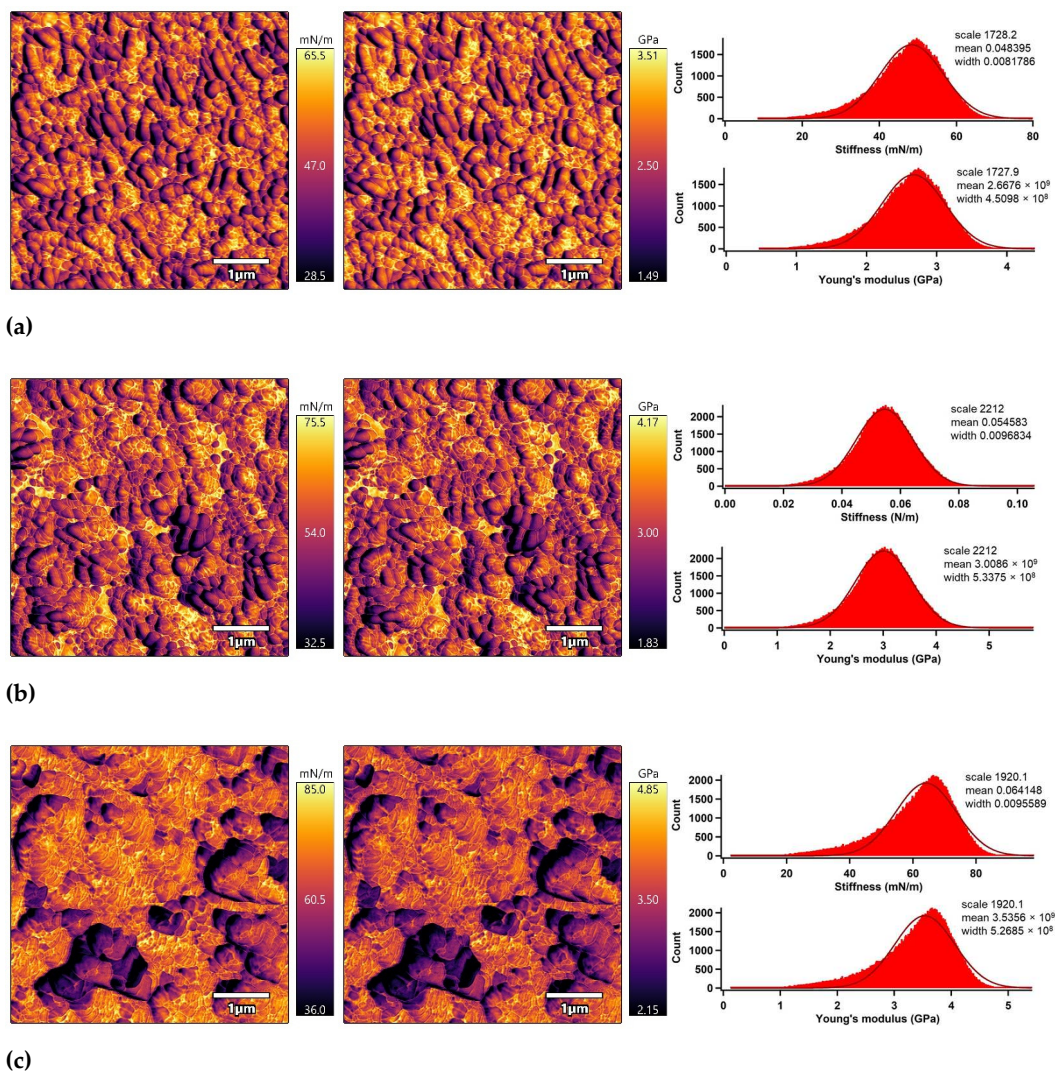
Figure 7. *Cont.*
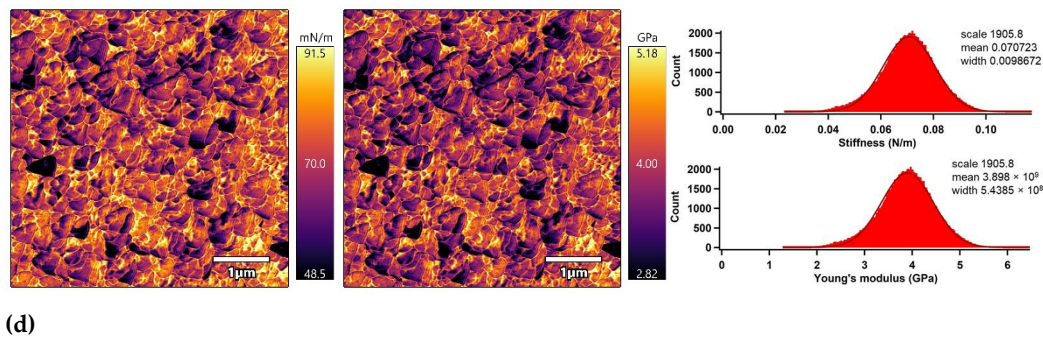
Figure 7. AM–FM AFM images (left: stiffness, right: Young's modulus) and related histograms of PLA: (**a**) untreated, (**b**) plasma-treated, (**c**) ASA-grafted, and (**d**) FA-grafted.

Table 2. Nano-mechanical properties of the PLA surfaces.

Sample Code	Stiffness (mN/m)		Young's Modulus (GPa)	
	Mean	Peak Width	Mean	Peak Width
Untreated	48.4	8.2	2.7	0.5
Plasma-treated	54.6	9.7	3.0	0.5
ASA-grafted	64.1	9.6	3.5	0.5
FA-grafted	70.7	9.9	3.9	0.5

3.6. Adhesion Analysis

The peel resistance measurements were carried out to evaluate the adhesion properties of the PLA/Al laminate. Higher peel resistance is associated with good adhesion and vice versa, as the result of improved wettability. Figure 8 depicts the changes in the peel resistance of the PLA/Al laminate after plasma treatment and FA and ASA grafting of the PLA surface. Due to the smooth surface and the lowest wettability, the untreated PLA surface had poor adhesion, while peel resistance was 74.4 N/m. On the contrary, the adhesion of the PLA surface was improved after plasma treatment, and peel resistance increased to 107 N/m. This improvement in peel resistance was mainly caused by improvements in wettability and surface roughness, which were due to the incorporation of polar functional groups and the etching reactions in the PLA surface. As illustrated in Figure 8, ASA grafting on the PLA surface resulted in an additional increase in peel resistance (130 N/m) compared with only the plasma-treated PLA samples. The highest wettability was attained by grafting FA onto the PLA surface, the peel resistance increased to 211 N/m (Figure 8). Furthermore, both ASA and FA were subjected to PLA modification without prior plasma pre-treatment (blind test). It was observed that the peel resistance of the untreated PLA modified with ASA and FA had a similar value to that of the untreated PLA sample (73.3 N/m and 87.2 N/m, respectively), indicating that the ASA and FA were not covalently bonded to PLA surface without plasma pre-treatment.

3.7. Adhesion Analysis

The peel resistance measurements were carried out to evaluate the adhesion properties of the PLA/Al laminate. Higher peel resistance is associated with good adhesion and vice versa, as the result of improved wettability. Figure 8 depicts the changes in the peel resistance of the PLA/Al laminate after plasma treatment and FA and ASA grafting of the PLA surface. Due to the smooth surface and the lowest wettability, the untreated PLA surface had poor adhesion, while peel resistance was 74.4 N/m. On the contrary, the adhesion of the PLA surface was improved after plasma treatment, and peel resistance increased to 107 N/m. This improvement in peel resistance was mainly caused by improvements in wettability and surface roughness, which were due to the incorporation of polar functional groups and the etching reactions in the PLA surface. As illustrated in Figure 8, ASA grafting on the PLA surface resulted in an additional increase in peel

resistance (130 N/m) compared with only the plasma-treated PLA samples. The highest wettability was attained by grafting FA onto the PLA surface, the peel resistance increased to 211 N/m (Figure 8). Furthermore, both ASA and FA were subjected to PLA modification without prior plasma pre-treatment (blind test). It was observed that the peel resistance of the untreated PLA modified with ASA and FA had a similar value to that of the untreated PLA sample (73.3 N/m and 87.2 N/m, respectively), indicating that the ASA and FA were not covalently bonded to PLA surface without plasma pre-treatment.

Figure 8. Peel resistance of PLA/Al laminate.

4. Conclusions

In summary, the effect of plasma treatment and ASA or FA modification on the surface and adhesion properties of the PLA surface was analyzed by various analytical and microscopic techniques. Due to the incorporation of new polar functional species on the PLA films surfaces, wettability was improved after plasma treatment. Following surface modification of the PLA film with ASA or FA, it was discovered that plasma treatment was successful in grafting ASA and FA on the surface of the PLA film. The plasma treatment and modification of the PLA surface by ASA or FA was proven by various techniques and methods such as profilometry, SEM, AFM, peel tests, contact angle measurements, XPS and FTIR. This modification led to enhanced wettability and therefore improved adhesion characteristics. The peel test of PLA/Al laminate revealed enhancement of the peel resistance of the PLA modified samples, while the peel resistance of PLA modified by ASA and FA increased by 74% and 184%, respectively, compared to untreated PLA. Modification of PLA with plasma technology and subsequent grafting of active species opens an avenue to such tailored properties as biofouling, antibacterial and antiviral activities. It should be pointed out that plasma treatment is not limited to PLA only and can be applied generally to different polymeric surfaces, which makes this approach attractive as well.

Institutional Review Board Statement: Not applicable.

Informed Consent Statement: Not applicable.

Data Availability Statement: MDPI Research Data Policies.

Conflicts of Interest: The authors declare no conflict of interest.

References

1. Owens, K.A.; Conlon, K. Mopping up or turning off the tap? Environmental injustice and the ethics of plastic pollution. *Front. Mar. Sci.* **2021**, *8*, 1227. [CrossRef]
2. Geyer, R.; Jambeck, J.R.; Law, K.L. Production, use, and fate of all plastics ever made. *Sci. Adv.* **2017**, *3*, e1700782. [CrossRef]
3. Avérous, L. Biodegradable multiphase systems based on plasticized starch: A review. *J. Macromol. Sci. Part C* **2004**, *44*, 231–274. [CrossRef]
4. Bélard, L.; Poncin-Epaillard, F.; Dole, P.; Avérous, L. Plasma-polymer coatings onto different biodegradable polyesters surfaces. *Eur. Polym. J.* **2013**, *49*, 882–892. [CrossRef]
5. Nampoothiri, K.M.; Nair, N.R.; John, R.P. An overview of the recent developments in polylactide (PLA) research. *Bioresour. Technol.* **2010**, *101*, 8493–8501. [CrossRef]
6. Masutani, K.; Kimura, Y. Chapter 1 PLA synthesis. from the monomer to the polymer. In *Poly(Lactic Acid) Science and Technology: Processing, Properties, Additives and Applications*; The Royal Society of Chemistry: London, UK, 2015; pp. 1–36. [CrossRef]
7. Ou, X.; Cakmak, M. Comparative study on development of structural hierarchy in constrained annealed simultaneous and sequential biaxially stretched polylactic acid films. *Polymer* **2010**, *51*, 783–792. [CrossRef]
8. Farah, S.; Anderson, D.G.; Langer, R. Physical and mechanical properties of PLA, and their functions in widespread applications—A comprehensive review. *Adv. Drug Deliv. Rev.* **2016**, *107*, 367–392. [CrossRef] [PubMed]
9. Hamad, K.; Kaseem, M.; Ayyoob, M.; Joo, J.; Deri, F. Polylactic acid blends: The future of green, light and tough. *Prog. Polym. Sci.* **2018**, *85*, 83–127. [CrossRef]
10. Södergård, A.; Stolt, M. Properties of lactic acid based polymers and their correlation with composition. *Prog. Polym. Sci.* **2002**, *27*, 1123–1163. [CrossRef]
11. Wang, S.; Cui, W.; Bei, J. Bulk and surface modifications of polylactide. *Anal. Bioanal. Chem.* **2005**, *381*, 547–556. [CrossRef]
12. Botvin, V.; Karaseva, S.; Khasanov, V. Depolymerization of lactic acid oligomers into lactide: Epimerization, stereocomplex formation, and nature of interactions of oligomers. *Polym. Degrad. Stab.* **2020**, *182*, 109382. [CrossRef]
13. Casalini, T.; Rossi, F.; Castrovinci, A.; Perale, G. A perspective on polylactic acid-based polymers use for nanoparticles synthesis and applications. *Front. Bioeng. Biotechnol.* **2019**, *7*, 259. [CrossRef]
14. George, A.; Shah, P.A.; Shrivastav, P.S. Natural biodegradable polymers based nano-formulations for drug delivery: A review. *Int. J. Pharm.* **2019**, *561*, 244–264. [CrossRef]
15. Nagarajan, V.; Mohanty, A.K.; Misra, M. Perspective on polylactic acid (PLA) based sustainable materials for durable applications: Focus on toughness and heat resistance. *ACS Sustain. Chem. Eng.* **2016**, *4*, 2899–2916. [CrossRef]
16. Okamoto, M.; John, B. Synthetic biopolymer nanocomposites for tissue engineering scaffolds. *Prog. Polym. Sci.* **2013**, *38*, 1487–1503. [CrossRef]
17. Saeidlou, S.; Huneault, M.A.; Li, H.; Park, C.B. Poly(lactic acid) crystallization. *Prog. Polym. Sci.* **2012**, *37*, 1657–1677. [CrossRef]
18. Zhao, Q.; Ding, Y.; Yang, B.; Ning, N.; Fu, Q. Highly efficient toughening effect of ultrafine full-vulcanized powdered rubber on poly(lactic acid)(PLA). *Polym. Test.* **2013**, *32*, 299–305. [CrossRef]
19. Baiardo, M.; Frisoni, G.; Scandola, M.; Rimelen, M.; Lips, D.; Ruffieux, K.; Wintermantel, E. Thermal and mechanical properties of plasticized poly(L-lactic acid). *J. Appl. Polym. Sci.* **2003**, *90*, 1731–1738. [CrossRef]
20. Ljungberg, N.; Wesslén, B. The effects of plasticizers on the dynamic mechanical and thermal properties of poly(lactic acid). *J. Appl. Polym. Sci.* **2002**, *86*, 1227–1234. [CrossRef]
21. Ljungberg, N.; Andersson, T.; Wesslén, B. Film extrusion and film weldability of poly(lactic acid) plasticized with triacetine and tributyl citrate. *J. Appl. Polym. Sci.* **2003**, *88*, 3239–3247. [CrossRef]
22. Kavc, T.; Kern, W.; Ebel, M.F.; Svagera, R.; Pölt, P. Surface modification of polyethylene by photochemical introduction of sulfonic acid groups. *Chem. Mater.* **2000**, *12*, 1053–1059. [CrossRef]
23. Habib, S.; Lehocky, M.; Vesela, D.; Humpolíček, P.; Krupa, I.; Popelka, A. Preparation of progressive antibacterial LDPE surface via active biomolecule deposition approach. *Polymers* **2019**, *11*, 1704. [CrossRef]

24. Chanunpanich, N.; Ulman, A.; Strzhemechny, Y.M.; Schwarz, S.A.; Janke, A.; Braun, H.G.; Kraztmuller, T. Surface modification of polyethylene through bromination. *Langmuir* **1999**, *15*, 2089–2094. [CrossRef]

25. Yuan, W.; Xia, D.; Wu, S.; Zheng, Y.; Guan, Z.; Rau, J.V. A review on current research status of the surface modification of Zn-based biodegradable metals. *Bioact. Mater.* **2022**, *7*, 192–216. [CrossRef]

26. Kosareva, E.K.; Zharkov, M.N.; Meerov, D.B.; Gainutdinov, R.V.; Fomenkov, I.V.; Zlotin, S.G.; Pivkina, A.N.; Kuchurov, I.V.; Muravyev, N.V. HMX surface modification with polymers via sc-CO2 antisolvent process: A way to safe and easy-to-handle energetic materials. *Chem. Eng. J.* **2022**, *428*, 131363. [CrossRef]

27. Wu, W.; Zhao, W.; Gong, X.; Sun, Q.; Cao, X.; Su, Y.; Yu, B.; Li, R.K.Y.; Vellaisamy, R.A.L. Surface decoration of Halloysite nanotubes with POSS for fire-safe thermoplastic polyurethane nanocomposites. *J. Mater. Sci. Technol.* **2022**, *101*, 107–117. [CrossRef]

28. Biederman, H. *Plasma Polymer Films*; World Scientific: Singapore, 2004.

29. Pascual, M.; Balart, R.; Sánchez, L.; Fenollar, O.; Calvo, O. Study of the aging process of corona discharge plasma effects on low density polyethylene film surface. *J. Mater. Sci.* **2008**, *43*, 4901–4909. [CrossRef]

30. Popelka, A.; Novák, I.; Lehocký, M.; Junkar, I.; Mozetič, M.; Kleinová, A.; Janigová, I.; Šlouf, M.; Bílek, F.; Chodák, I. A new route for chitosan immobilization onto polyethylene surface. *Carbohydr. Polym.* **2012**, *90*, 1501–1508. [CrossRef]

31. Jordá-Vilaplana, A.; Fombuena, V.; García-García, D.; Samper, M.D.; Sánchez-Nácher, L. Surface modification of polylactic acid (PLA) by air atmospheric plasma treatment. *Eur. Polym. J.* **2014**, *58*, 23–33. [CrossRef]

32. Popelka, A.; Krupa, I.; Novák, I.; Al-Maadeed, M.A.S.A.; Ouederni, M. Improvement of aluminum/polyethylene adhesion through corona discharge. *J. Phys. D Appl. Phys.* **2016**, *50*, 035204. [CrossRef]

33. Han, J.H.; Floros, J.D. Casting antimicrobial packaging films and measuring their physical properties and antimicrobial activity. *J. Plast. Film. Sheeting* **1997**, *13*, 287–298. [CrossRef]

34. Bazaka, K.; Jacob, M.V.; Chrzanowski, W.; Ostrikov, K. Anti-bacterial surfaces: Natural agents, mechanisms of action, and plasma surface modification. *RSC Adv.* **2015**, *5*, 48739–48759. [CrossRef]

35. Weng, Y.-M.; Chen, M.-J.; Chen, W. Antimicrobial food packaging materials from poly(ethylene-co-methacrylic acid). *LWT-Food Sci. Technol.* **1999**, *32*, 191–195. [CrossRef]

36. Ahmed, I.; Ready, D.; Wilson, M.; Knowles, J.C. Antimicrobial effect of silver-doped phosphate-based glasses. *J. Biomed. Mater. Res. Part A* **2006**, *79A*, 618–626. [CrossRef] [PubMed]

37. Valappil, S.P.; Pickup, D.M.; Carroll, D.L.; Hope, C.K.; Pratten, J.; Newport, R.J.; Smith, M.E.; Wilson, M.; Knowles, J.C. Effect of silver content on the structure and antibacterial activity of silver-doped phosphate-based glasses. *Antimicrob. Agents Chemother.* **2007**, *51*, 4453–4461. [CrossRef] [PubMed]

38. Popelka, A.; Abdulkareem, A.; Mahmoud, A.A.; Nassr, M.G.; Al-Ruweidi, M.K.A.A.; Mohamoud, K.J.; Hussein, M.K.; Lehocky, M.; Vesela, D.; Humpolíček, P.; et al. Antimicrobial modification of PLA scaffolds with ascorbic and fumaric acids via plasma treatment. *Surf. Coat. Technol.* **2020**, *400*, 126216. [CrossRef]

39. Houglum, K.P.; Brenner, D.A.; Chojkier, M. Ascorbic acid stimulation of collagen biosynthesis independent of hydroxylation. *Am. J. Clin. Nutr.* **1991**, *54*, 1141s–1143s. [CrossRef]

40. Busscher, H.J.; van Pelt, A.W.J.; de Boer, P.; de Jong, H.P.; Arends, J. The effect of surface roughening of polymers on measured contact angles of liquids. *Colloids Surf.* **1984**, *9*, 319–331. [CrossRef]

41. Wei, Q.; Haag, R. Universal polymer coatings and their representative biomedical applications. *Mater. Horiz.* **2015**, *2*, 567–577. [CrossRef]

42. Bradley, J.-C. *Handbook of Surface and Colloid Chemistry*; Birdi, K.S., Ed.; CRC Press: Boca Raton, FL, USA, 1998; ISBN 0-8493-9459-7.

43. E Abusrafa, A.; Habib, S.; Krupa, I.; Ouederni, M.; Popelka, A. Modification of polyethylene by rf plasma in different/mixture gases. *Coatings* **2019**, *9*, 145. [CrossRef]

44. Wagner, C.D.; Smith, R.H.; Peters, E.D. Evaluation of modified iodometric method. *Anal. Chem.* **1947**, *19*, 976–979. [CrossRef]

45. Niki, E. Action of ascorbic acid as a scavenger of active and stable oxygen radicals. *Am. J. Clin. Nutr.* **1991**, *54*, 1119S–1124S. [CrossRef]

46. Ardjani, T.E.A.; Alvarez-Idaboy, J.R. Radical scavenging activity of ascorbic acid analogs: Kinetics and mechanisms. *Theor. Chem. Acc.* **2018**, *137*, 69. [CrossRef]

47. Casasola, R.; Thomas, N.L.; Trybala, A.; Georgiadou, S. Electrospun poly lactic acid (PLA) fibres: Effect of different solvent systems on fibre morphology and diameter. *Polymer* **2014**, *55*, 4728–4737. [CrossRef]

48. Cassie, A.B.D.; Baxter, S. Wettability of porous surfaces. *Trans. Faraday Soc.* **1944**, *40*, 546–551. [CrossRef]

49. Suzuki, M.; Kishida, A.; Iwata, H.; Ikada, Y. Graft copolymerization of acrylamide onto a polyethylene surface pretreated with glow discharge. *Macromolecules* **1986**, *19*, 1804–1808. [CrossRef]

50. Borris, J.; Dohse, A.; Hinze, A.; Thomas, M.; Klages, C.-P.; Möbius, A.; Elbick, D.; Weidlich, E.-R. Improvement of the adhesion of a galvanic metallization of polymers by surface functionalization using dielectric barrier discharges at atmospheric pressure. *Plasma Process. Polym.* **2009**, *6*, S258–S263. [CrossRef]

51. Kutnyanszky, E.; Vancso, G.J. Nanomechanical properties of polymer brushes by colloidal AFM probes. *Eur. Polym. J.* **2012**, *48*, 8–15. [CrossRef]

52. Vesel, A.; Primc, G.; Zaplotnik, R.; Mozetič, M. Applications of highly non-equilibrium low-pressure oxygen plasma for treatment of polymers and polymer composites on an industrial scale. *Plasma Phys. Control. Fusion* **2020**, *62*, 024008. [CrossRef]

53. Abudonia, K.S.; Saad, G.R.; Naguib, H.F.; Eweis, M.; Zahran, D.; Elsabee, M.Z. Surface modification of polypropylene film by grafting with vinyl monomers for the attachment of chitosan. *J. Polym. Res.* **2018**, *25*, 125. [CrossRef]

54. Wang, S.; Wang, Z.; Li, J.; Li, L.; Hu, W. Surface-grafting polymers: From chemistry to organic electronics. *Mater. Chem. Front.* **2020**, *4*, 692–714. [CrossRef]

Hydrophobic Leather Coating for Footwear Applications by a Low-Pressure Plasma Polymerisation Process

Carlos Ruzafa Silvestre *[ID]**, María Pilar Carbonell Blasco, Saray Ricote López, Henoc Pérez Aguilar, María Ángeles Pérez Limiñana, Elena Bañón Gil, Elena Orgilés Calpena and Francisca Arán Ais**[ID]

Footwear Technology Centre, Campo Alto Campground, 03600 Alicante, Spain; pcarbonell@inescop.es (M.P.C.B.); sricote@inescop.es (S.R.L.); hperez@inescop.es (H.P.A.); maperez@inescop.es (M.Á.P.L.); elenab@inescop.es (E.B.G.); eorgiles@inescop.es (E.O.C.); aran@inescop.es (F.A.A.)
* Correspondence: cruzafa@inescop.es; Tel.: +34-965-395-213

Abstract: The aim of this work is to develop hydrophobic coatings on leather materials by plasma polymerisation with a low-pressure plasma system using an organosilicon compound, such as hexamethyldisiloxane (HMDSO), as chemical precursor. The hydrophobic coatings obtained by this plasma process were evaluated with different experimental techniques such as Fourier transform infrared spectroscopy (FTIR), X-ray photoelectron spectroscopy (XPS), scanning electron microscopy (SEM) and standardised tests including colour measurements of the samples, surface coating thickness and water contact angle (WCA) measurements. The results obtained indicated that the monomer had polymerised correctly and completely on the leather surface creating an ultra-thin layer based on polysiloxane. The surface modification produced a water repellent effect on the leather that does not alter the visual appearance and haptic properties. Therefore, the application of the plasma deposition process showed promising results that makes it a more sustainable alternative to conventional functional coatings, thus helping to reduce the use of hazardous chemicals in the finishing process of footwear manufacturing.

Keywords: low-pressure plasma; plasma process; plasma polymerisation; surface modification; plasma deposition

1. Introduction

Leather is a natural material commonly used to produce a wide range of footwear. Depending on the type of footwear and its intended use, a different type of leather with specific features is required. For such purpose during post-tanning operations, numerous finishing additives and treatments are used to improve certain leather properties, such as water resistance, oleophobicity, perspirability, flame retardancy, antimicrobial properties and abrasion resistance or antistatic properties [1].

Specifically, leather is a hydrophilic material due to the polar groups of the collagen fibers' amino acid residues that promote their interaction with water molecules. However, this property is not desirable in certain applications where water-resistant leather is required. This repellence can be achieved by a combination of the material's structure and finish with specific chemicals such as fluorocarbons, wax emulsions, metallic soaps and surface-active agents [2–4].

More durable waterproofing treatments are mainly based on halocarbons compounds, including chlorofluorocarbons (CFCs), perfluorocarbons (PFCs), hydrofluorocarbons (HFCs) and hydrochlorofluorocarbons (HCFCs), which are considered as greenhouse gases (GHGs), since they absorb infrared radiation emitted by the Earth in a spectral range where the energy is not removed by CO_2 or water vapour [5].

For instance, HCFCs have been used to replace CFCs in several applications because they have a shorter atmospheric lifetime, and consequently, cause less ozone depletion. HFCs and PFCs have also been identified as potential replacements for ozone depleting

substances (ODS) in the long term since they do not contain bromine or chlorine and do not cause significant ozone depletion. However, all these substances are also GHGs, and contribute thus to varying degrees to climate change [5]. For this reason, there is a high concern about the continued release of these persistent organic pollutants (POPs) into the environment [6], being also bioacumulative chemicals. That is why most companies are looking for alternatives to replace not only the compounds used for waterproofing but also the chemical process used to do so [7–11], to reduce not only the input of materials into the process but also the production of waste, contributing thus to reduce environmental footprint of the process [12].

Some alternative processes to traditional ones are currently based on plasma technologies as they are more resource-efficient and sustainable processes. These technologies might imply a significant reduction in the environmental impacts of traditional coating processes in terms of greenhouse gas emissions, reduction of hazardous chemicals and waste, and water and energy consumption [13].

Specifically, the plasma polymerisation technology can infuse monomers into plasma and coat surfaces with ultra-thin layers, such as polymer coatings, by formation of gas-phase free radicals and their recombination at radical sites during film growth resulting in stable and durable structures [14] able to impart functional properties to a great variety of materials. Many monomers can be used for the deposition of ultra-thin films by plasma polymerisation, among which the most widely used is hexamethyldisiloxane (HMDSO) [9–11,15,16].

Different studies focused on plasma polymerisation of HMDSO to obtain super hydrophobic and water repellency properties to different materials. They reported that the achieved film properties depend on the plasma composition [6,7] and the polymerisation process conditions, such as plasma power and monomer flux [8–17]. Nevertheless, little work has been carried out on plasma deposition on natural leathers.

In addition, Thomas Gengenbach and Hans Griesser conducted extensive studies on the generation of hydrophobic coatings by low-pressure plasma for various polymer, glass and silicon substrates, and also in the electronics sector. The aforementioned studies have been summarised by Siow et al., which includes the works from the 1980s as well as those from electronic sectors [18]. The role of surface restructuring in the ageing behaviour of siloxane plasma polymer was discussed by Gengenbach and Griesser in their study of HMDSO and hexamethyldisilazane (HMDSN) plasma polymers [19]. In another study, they concluded that the perfluoro-1,3-dimethylcyclohexane (PFDMCH) plasma polymers were therefore well deposited and suited for applications that require long-term stability and predictable, stable interfacial properties [20].

In this sense, a previous work carried out by the authors was based on the use of Multiple Laser Surface Enhancement (MLSE) technology in the framework of the European Life Textileather project [13], to provide leathers and textiles with functional properties such as water, fire and stain resistances, as well as antimicrobial properties. MLSE technology combines atmospheric plasma and laser treatments in the presence of non-toxic gases, such as nitrogen (N_2) and oxygen (O_2), allowing the surface modification of materials [21]. This treatment produces nanometric scale modifications, which enables the functionalisation of the material without noticeably affecting its appearance. In addition, Kayaoglu et al. reported surface modifications of natural leather samples through plasma polymerisation of different HMDSO/toluene compositions at low pressure that showed promising results towards improving the easy clean property of natural leather in upholstery applications [14]. Gaidau et al. also reported the use of cold plasma generated by dielectric barrier discharge (DBD) at atmospheric pressure and room temperature as a promising technique for dry reactivation and physical modification of collagen and keratin-based materials to improve complex characteristics, such as water repellence and flame retardancy [22]. Finally, a concise overview on plasma treatment for application on textile and leather materials was provided recently by Tudoran et al. [23].

In the present study, a low-pressure plasma system was used for the development of hydrophobic coating by plasma polymerisation on natural leather for footwear applications. For the coating treatments, the chemical precursor 100% hexamethyldisiloxane (HMDSO) was selected because it contains silicon groups, which can be favourable for improving the hydrophobic properties of the materials. For this purpose, a plasma process involving consecutive activation and etching using oxygen as the reactive gas, and HMDSO polymerisation using argon as the inert gas, has been carried out. The properties of the thin film deposited on the leather surface were characterised by different experimental techniques, in terms of water repellence, surface modifications, thickness and colour and appearance changes. The aim of this research is to use plasma treatment as an environmentally friendly finishing method to impart hydrophobicity to the surface of natural leather, which can be used in the footwear and leather industries as well as in the textile industry [24–32].

2. Experimental

2.1. Materials

In this work, hexamethyldisiloxane (HMDSO, $(CH_3)_3$-Si-O-Si-$(CH_3)_3$, 98% purity) provided by Merck Life Science S.L.U. (Madrid, Spain) was used as a hydrophobic monomeric precursor, as received. For plasma polymerisation processes, a blue chrome-tanned cow leather with aniline finishing supplied by the company Pies Cuadrados Leather S.L. (Aspe, Spain) was used as representative upper material for footwear applications. Table 1 includes the main physical and mechanical properties of the used leather.

Table 1. Physical and mechanical properties of leather.

Material	Tensile Strength (MPa)	Elongation (%)	Dichloromethane Extractable Matter (wt %)	Ash Content at 950 °C (wt %)
Leather	16.2	57	5.85	4.3

Argon (Ar) and oxygen (O_2) were used as carrier gases, both with 99.995% purity and supplied by Carburos Metálicos S.A. (Barcelona, Spain).

2.2. Plasma Treatment

Plasma polymerised HMDSO films on leather samples were prepared in a nano low-pressure plasma equipment (Diener Electronic Vertriebs GmbH, Germany), of modular configuration, with a chamber volume of 24 L, in stainless steel and with a tray for sample support. The plasma reactor was operating at a fixed frequency of 13.56 MHz and 300 W of maximum power. All the samples in this work were treated at the plasma power of 150 W. A composition of 100% HMDSO was injected by a micro-dossing pump during plasma polymerisation on natural leather samples.

This low-pressure plasma system is equipped with two gas supply channels. Oxygen (O_2) and argon (Ar) were used as working gases with flows at 500 mL/min and 685 mL/min, respectively. A micro-dosing pump introduces the monomer into the reactor at 0.5 µL/s. The thermostatised treatment chamber allows the temperature to be raised during the plasma process, which increases the effectiveness of the deposition process [23,33]. (Table 2).

The treatment comprises different and consecutive stages: activation, polymerisation and etching.

Firstly, activation with plasma was carried out to create radical sites in which HMDSO reacts, and greatly facilitated thus the adhesion of non-reactive or non-wettable surfaces. The type of mechanisms that primarily contribute to the activation effect depend on the material to be treated and the nature of the plasma gas. As a working gas, oxygen was used to provide leather with new surface functionalities that completely reverse the polarity of leather samples increasing its surface wettability to improve the HMDSO deposition. In addition to these factors, the working pressure, the power of the plasma and the activation time of the gas used are also crucial.

Table 2. Plasma operating conditions of the plasma deposition process.

Plasma Stages	Gas	Time (s)	Power (W)	Pressure (Pa)	Monomer	Dossing Pump (µL/s)
Activation	O_2	300	150	300	-	-
Polymerisation	Ar	300	150	300	HMDSO	0.5
Etching	O_2	12	150	300	-	-
Polymerisation	Ar	300	150	300	HMDSO	0.5
Etching	O_2	12	150	300	-	-
Polymerisation	Ar	300	150	300	HMDSO	0.5

Secondly, HMDSO was added to produce its polymerisation by plasma. This monomer is in a liquid state under ambient conditions, and when subjected to vacuum conditions, it becomes gaseous. This causes it to be susceptible to being excited by an energy source, which gives rise to silicon radicals and atoms of silicon, hydrogen, carbon and oxygen that interact on the surface of the treated material. Consequently, an ultra-thin coating layer is deposited onto leather surface permanently. For this stage, argon was selected as conductive gas because it is an inert gas and does not react with the monomeric precursor. It has a large mechanical effect since it continuously removes individual atoms from the surface contributing to a suitable layer anchorage. The properties provided by the newly deposited layer will depend on both the nature of the monomer used and the different conditions used during the process. The parameters that greatly influence the surface finish and therefore determine the water repellence obtained are the pump flow, the conductive gas, the selected prepolymer, the coating time and the number of coats applied, among others [34].

After the polymerisation stage, a fast-etching process was conducted with oxygen gas to strengthen the polymerised HMDSO layer anchorage and achieve coatings with a considerable and effective thickness.

Finally, three HMDSO layers were deposited onto leather samples surface with argon gas according to the operating conditions described in Table 2, which were previously optimised in the framework of the COATPLAS project [35,36]. In addition, Figure 1 summarises the process conducted in this work.
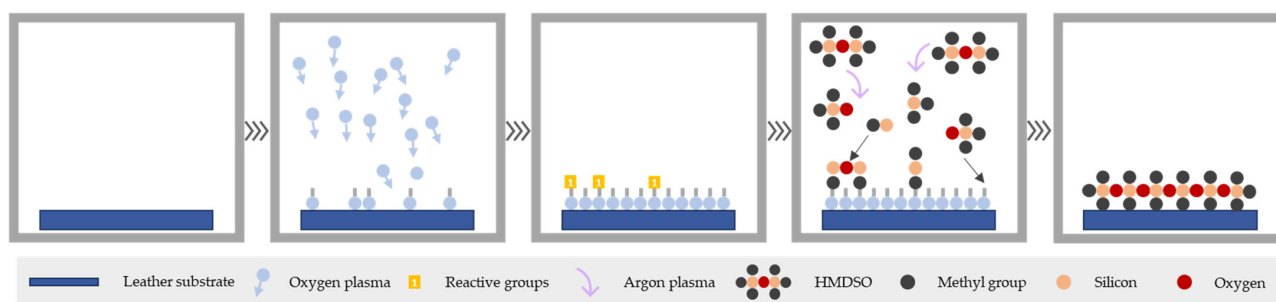
Figure 1. Surface activation and plasma polymerisation phases of the treatment.

Samples with and without plasma treatment will be referenced as "plasma coated leather" and "untreated leather", respectively.

2.3. Fourier Transform Infrared Spectroscopy (FTIR)

The surface chemical modifications of the coated leather were determined using a Varian 660-IR infrared spectrophotometer (VARIAN Australia PTY LTD; Mulgrave, Australia). Attenuated total reflectance (ATR) mode with 16 scans at a resolution of $4 \, cm^{-1}$ was used as the FTIR sampling technique. This ATR accessory works by measuring changes in the infrared beam when the beam comes into contact with the sample.

2.4. X-Ray Photoelectron Spectroscopy (XPS)

An X-ray Photoelectron Spectroscopy (XPS, K-ALPHA, Thermo Scientific) was used to analyse the chemical compositions of the surface of the siloxane polymer film obtained by plasma. Due to these films being extremely thin, XPS is the most suitable technique to determine their chemical properties. This analysis was conducted by the Technical Research Services (SSTTI) of the University of Alicante (UA). XPS measurements were collected with K-ALPHA (Al-K) radiation (1486.6 eV), monochromatised by a double crystal monochromator and yielding a focused X-ray spot (elliptical in shape with a major axis length of 400 μm) were generated at 3 mA × 12 kV. The alpha hemispherical analyser operated in constant energy mode, scanning through the 200 eV energy to measure the entire energy band, and used 50 eV in a narrow scan to selectively measure specific elements. Avantage software was used to analyse the XPS data, and the smart background function was used to approximate the experimental background and calculate the elemental composition of the surface based on the peak area subtracted from the background. Charge compensation was achieved using the systems flood gun, which provides low-energy electrons and low-energy argon ions from a single source.

2.5. Scanning Electron Microscopy (SEM)

The surface modifications and morphological analysis were conducted with a Phenom ProX scanning electron microscope (Phenom World, Eindhoven, Netherlands). Samples were cut into square specimens of 2 mm x 2 mm. The microscope operates under high vacuum, using an electron beam at a potential of 5–15 keV, so that there is greater resolution of the image, going from micrometric to nanometric scale.

2.6. Sample Colour Measurements

The measurement of the colour difference of plasma treated leathers was carried out with the spectrophotometer CM-600d according to the standard EN ISO 22700:2020 [37]. This portable spectrophotometer is designed to assess the colour and appearance of samples of different sizes, including the surfaces of flat, shaped or curved objects. It has a fixed aperture of 8 mm and two measurement modes to suit the surface conditions of each sample: Specular Reflectance Included (SPINC) and Specular Reflectance Excluded (SPEX), the latter being used for measurement as it considers the surface finish of the sample. Measurements were made at three spots in the central part of the sample.

2.7. Surface Coating Thickness

The thickness of layer deposited onto the leather surface was determined according to the standard EN ISO 17186-method A [38]. A macm 1 rotary microtome (model 2030, Leica Reichert-Jung Biocut, Germany) was used with an optical microscope (model STD-18, Zeiss, Germany) equipped with a x 10 ocular with a graduated scale including a range of 2.6–261.9 μm and a x 16 magnification lens.

2.8. Water Contact Angles (WCA) Measurements

The hydrophobicity of the plasma coating was evaluated by determining the water contact angles. An optical contact angle measurement goniometer (Muver, Petrel, Spain) was used. This equipment has a thermostatised chamber that allows working in a saturated atmosphere, with an exhaustive control of the temperature at 25 °C. The equipment is provided with a vision system on a camera with a telecentric lens, which is backlit by a matrix of LEDs, and was used for droplet images captures. Deionised water was used as test liquid with a controlled volume of 4 μL by a syringe. Three drops were placed and measured at different points of the samples. Measurement procedure was performed as described in the standard EN 828-2013 [39]. The measurements were carried out at various times: 0 min, 5 min, 15 min, 25 min, 60 min and 90 min after plasma treatment to follow the wettability of the leather samples as a function of the time.

3. Results and Discussion

This section will provide a concise and precise description of the experimental results, their interpretation, as well as the experimental conclusions that can be drawn.

3.1. FTIR Analysis

FTIR was performed to further analyse the surface modifications of the plasma-coated leather samples with the non-polar 100% HMDSO, as well as to identify which functional groups contribute to the hydrophobic layer deposited. Figure 2 shows the FTIR spectra of the treated and untreated leather, as well as the spectrum corresponding to the HMDSO as precursor.
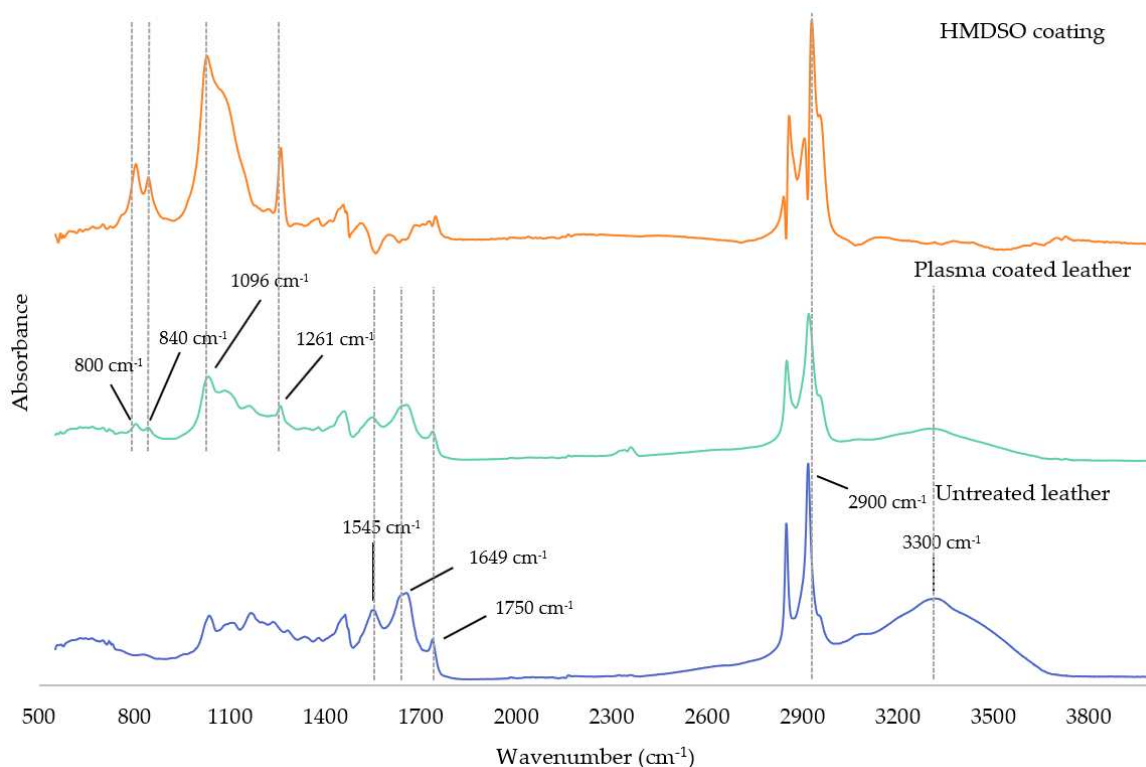
Figure 2. FTIR spectra of untreated leather sample, plasma coated leather and HMDSO plasma polymerised onto the leather surface.

On the one hand, the FTIR spectrum of the natural leather as untreated sample showed sharp absorption peaks located at 1633 and 1649 cm^{-1} associated with the C=O amide in the peptide band (Amide I). The peak at 1545 cm^{-1} represented the N-H of Amide II and the peak at 1750 cm^{-1} corresponded to the C=O stretching due to the ester fatty acids. The absorption band between 2800 and 3000 cm^{-1} was related to -CH *stretching vibration mode (st)*. which was usually quite stable on the leather surface. In addition, amide A band appeared around 3300 cm^{-1} due to the stretching vibration of -NH groups and the conformation of the backbone, which was very sensitive to the strength of the hydrogen bonds [40].

On the other hand, the FTIR spectrum of the plasma-coated leather after activation, and subsequently, of the HMDSO polymerisation with oxygen and argon as carrier gases, respectively, showed the characteristic bands of the natural leather in addition to new bands corresponding to the deposited coating on the surface. Specifically, the bands between 2800–3000 cm^{-1} and 1261 cm^{-1} corresponded to C-H *st* and Si-(CH$_3$) bending symmetric vibration (δ_{sy}), respectively. The peak attributed to the Si-O-Si bonds appeared around 1096 cm^{-1}, while the band at 840 and 800 cm^{-1} corresponded to the Si-C *st*and Si-(CH$_3$) out-of-plane bending vibration (γ). The spectrum of the plasma-polymerised HMDSO layer deposited onto the leather surface was obtained by spectral subtraction, which

confirmed the formation of a polysiloxane based layer on the leather surface [41–43]. Table 3 summarises the main characteristic bands observed in the mentioned samples [44–46]. In addition, the FTIR results were complemented with XPS analysis to comprehensively analyse the chemical groups created in the plasma-coated leather.

Table 3. Assignments of the main FTIR absorption bands observed for the spectra in Figure 2.

Wavenumber	Assignment
800 cm^{-1}	(Si-)CH$_3$ γ
840 cm^{-1}	Si-C γ
1096 cm^{-1}	Si-O-Si
1261 cm^{-1}	(Si-)CH$_3$ δ_{sy}
1545 cm^{-1}	N-H (Amide II)
1633–1649 cm^{-1}	C=O (Amide I)
1750 cm^{-1}	C=O ester
2800–3000 cm^{-1}	-CH *st*
3300 cm^{-1}	-NH (Amide A)

3.2. XPS Analysis

An XPS analysis was necessary to comprehensively analyse the chemical modifications on the outermost surface The surface chemistry of the untreated and plasma coated leather was analysed by X-ray photoelectron spectroscopy (XPS) to confirm the formation of silicon compounds, such as polysiloxanes, as a layer deposited on leather surface. Figure 3 shows the results of the XPS-survey of untreated leather and plasma coated leather. The leather surface was mainly composed of oxygen (O 1s), nitrogen (N 1s), carbon (C 1s) and low percentage of silicon (Si 2s and Si 2p), whose peaks were positioned at about 532, 400, 285, 154 and 103 eV. In the survey of plasma polymerised leather, the peaks appeared in the same positions for C, O, N and Si peaks, which highlights a considerable increase of oxygen and silicon peaks and a decrease of carbon and nitrogen, more noticeable in the latter, due to the plasma deposition of HMDSO [47,48].
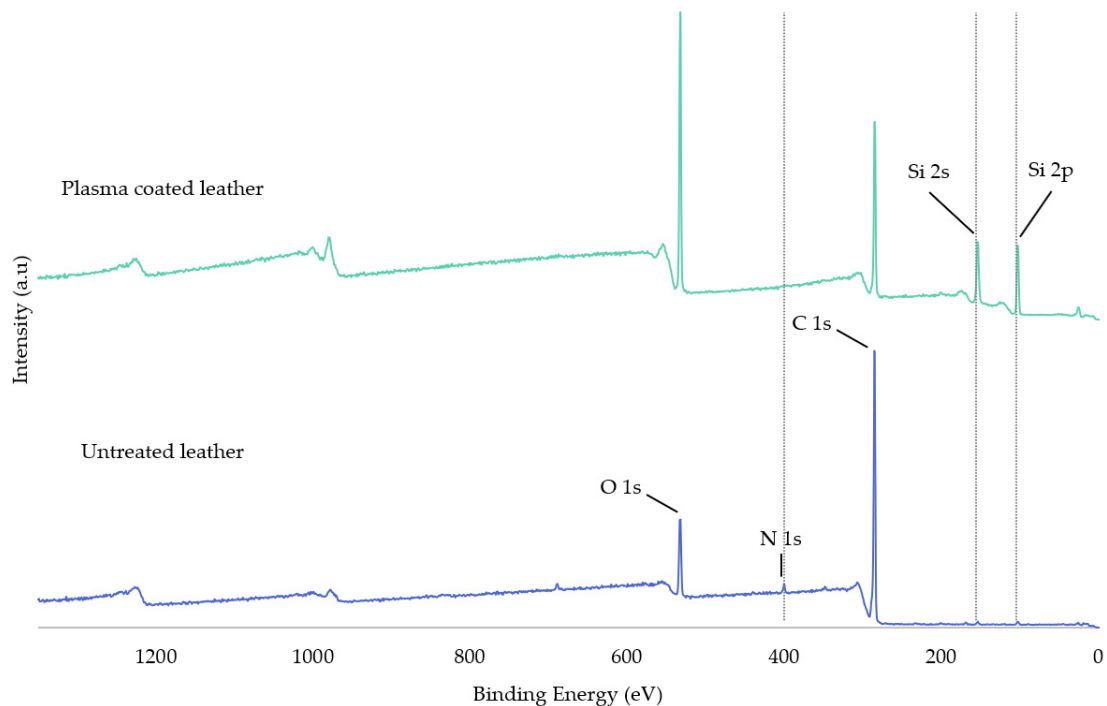
Figure 3. XPS-survey of untreated leather and plasma coated leather with HMDSO.

For such purpose, the atomic percentages of the carbon, oxygen, nitrogen, and silicon components were determined and included in Table 4. It should be noted that in the deconvolution of the Si 2p spectrum, four contributions were shown in all samples corresponding to Si 2p3/2 and Si 2p1. Since they are doublet pair, to quantify only the most sensitive one, Si 2p3/2 was used. There was 1.12% silicon on the surface of the untreated sample, which may come from the manufacturing of leather or may be due to silicon existing in the analysis XPS chamber. Compared to the untreated sample, the atomic percentage of silicon in the HMDSO plasma treated sample increased up from 1.12 to 22.39% due to a high deposition of monomer which is composed of silicon components. Moreover, the atomic percentage of C decreased due to the removal and oxidation of organic compounds by the oxygen plasma used in the etching stage, and O increased after plasma treatment due to the introduction of new oxygenated by etching and siliconised molecules deposited on the leather surface, and because of their presence in the polysiloxane composition. The nitrogen (1.33%) that appeared in the untreated leather is due to the proteins that constitute the original leather. However, in the HMDSO treated sample, 0.25% of nitrogen was observed. The detection of this small amount of several nitrogenous functional groups in the plasma coated leather could be due to contamination because of the 3–7 nm depth the XPS reaches and the thickness of the deposited HMDSO layer being greatly higher, as can be seen in Section 3.5. Therefore, the amount of nitrogen obtained in the coated sample can be considered negligible, indicating that no signal from the XPS-based substrate has been obtained and uniform coverage has been made on the substrate during plasma deposition. Furthermore, the atomic ratios showed an increase in the percentage of oxygen and silicon and a decrease in the atomic percentage of carbon due to the named chemical modifications [14,15,49].

Table 4. Elemental compositions of untreated and HMDSO plasma deposited leather sample.

Sample	Atomic Percentages (%)				Atomic ratio	
	C	O	N	Si	Si/C	Si/O
Untreated leather	84.87	12.44	1.33	1.12	0.01	0.09
Plasma coated leather	48.81	27.70	0.25	22.39	0.45	0.80

Figure 4 shows the deconvoluted C1s and Si 2p peak spectra of the leather with and without plasma deposition, and Table 5 includes the functional group contents of carbon and silicon. The decomposed bands were assigned to the appropriate functional groups. The resolution of the C 1s peak curve of the untreated leather was fitted with four peaks: one large peak was located at about 284.64 eV, due to the C-H or C=C bond; the other peak was found at about 286.05 eV corresponding to the C-O or C-N bond; and two small peaks were about 287.77 eV, due to the C-O=O, and about 288.78 eV the C=O bond appeared. In the plasma coated samples, the C 1s peak was also the same as in the untreated leather, but the intensity was lower due to the HMDSO coating, and a new contribution appeared at 286.42 eV corresponding to the C-Si bond which was due to the methyl groups present in the decomposed HMDSO. It was also possible to perform curve resolution of the Si 2p peaks to obtain more information about the chemical bonds in the samples. The deconvolution of Si 2p spectra of the untreated leather showed low content of silicon oxides (SiO) at 101.90 and 102.76 eV, silicon oxycarbide (Si-O-C) at 102.76 eV and silicon dioxide (SiO_2) at 101.90, 103.75 and 104.28 eV. The silicon oxides could have formed on the surface of the leather due to its manufacture and the XPS chamber. The Si 2p peaks of the plasma coated leather showed $SiO_2(CH_3)_2$, SiO_4, $SiO(CH_3)_3$ and SiO_2 units at approximately 102.27, 103.00, 103.27 and 104.00 eV, respectively. This result was due to the formation of a new layer of silicon compound on the surface by HMDSO plasma deposition. The high portion of $SiO_2(CH_3)_3$ indicates that the film had a structure like polydimethylsiloxane (PDMS). The presence of $SiO(CH_3)_3$ is the oxidation product of PDMS. The inorganic structures SiO_2 and SiO_4 represent complete oxidation at the deconvolution peak. These results support

the formation of a $SiO_xC_yH_z$ film with an organic structure using Ar as a carrier gas, as well as an inorganic structure through the O_2 etching stage [15,17,49–51].
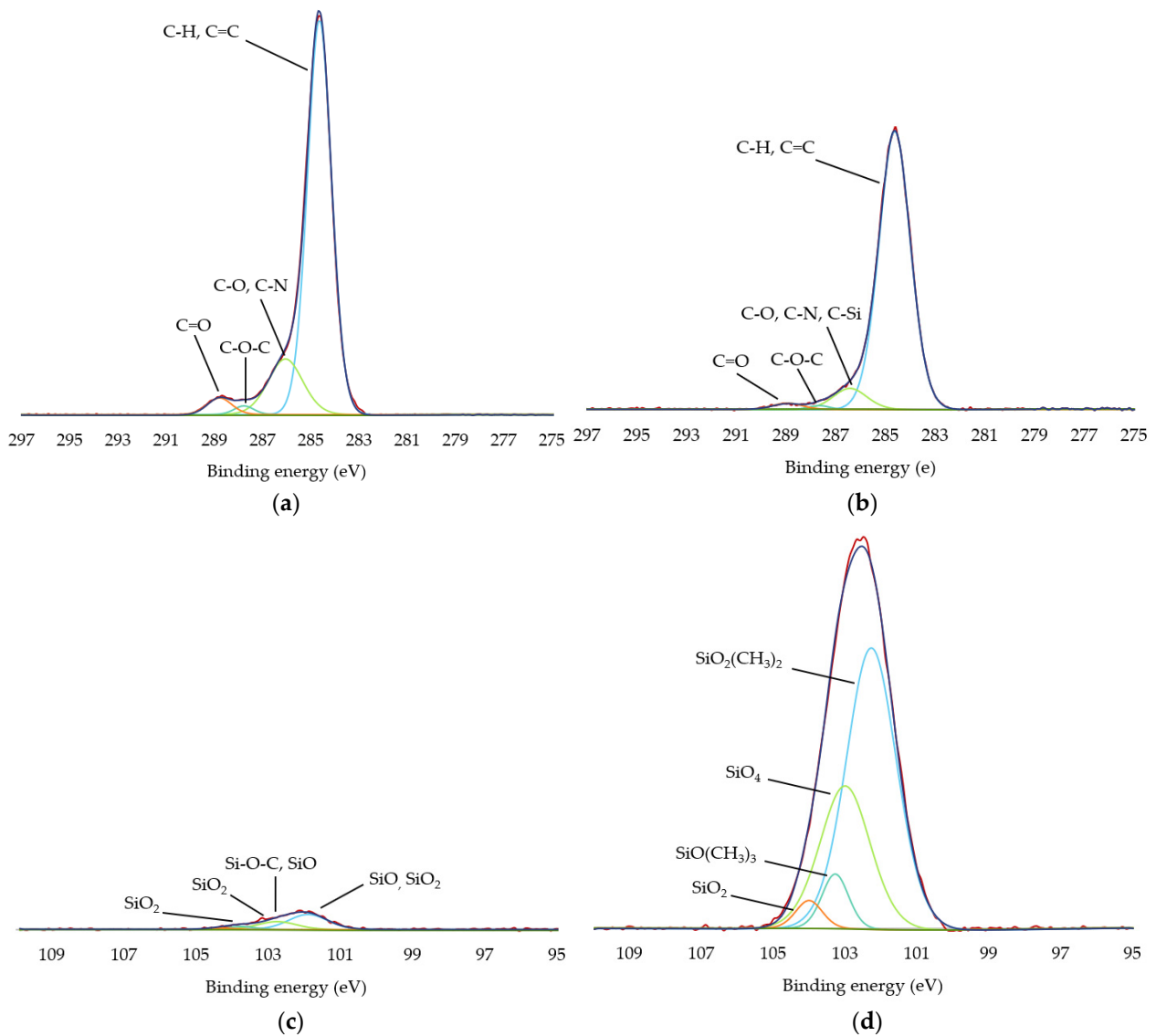
Figure 4. High-resolution peaks of HMDSO film deposited on leather. (**a**) C 1s of untreated sample; (**b**) C 1s of plasma coated leather; (**c**) Si 2p of untreated sample; (**d**) Si 2p of plasma coated leather.

Table 5. Atomic percentages (at. %) of chemical species at C 1s and Si 2p peaks of the untreated and plasma coated leather determined by XPS.

	Untreated Leather				Plasma Coated Leather		
Element	Chemical State	Binding Energy (eV)	At. (%)	Element	Chemical State	Binding Energy (eV)	At. (%)
C 1s	C-H, C=C	284.64	67.05	C 1s	C-H, C=C	284.62	44.77
	C-O, C-N	286.05	13.63		C-O, C-N, C-Si	286.42	3.67
	C-O-C	287.77	1.21		C-O-C	287.66	0.35
	C=O	288.78	2.98		C=O	288.94	0.86

Table 5. *Cont.*

	Untreated Leather				Plasma Coated Leather		
Element	Chemical State	Binding Energy (eV)	At. (%)	Element	Chemical State	Binding Energy (eV)	At. (%)
Si 2p	SiO or SiO$_2$	101.90	0.98	Si 2p	SiO$_2$(CH$_3$)$_2$	102.27	20.29
	Si-O-C, SiO	102.76	-		SiO$_4$	103.00	-
	SiO$_2$	103.75	0.14		SiO (CH$_3$)$_3$	103.27	2.10
	SiO$_2$	104.28	-		SiO$_2$	104.00	-

3.3. SEM Analysis

The morphology of the leather surface before and after HMDSO plasma deposition was analysed by means of scanning electron microscopy according to the images shown in Figure 5. The untreated sample appears with small cracks and some white spots; such surface irregularities are typical in materials of natural origin such as leather, and the dark, rough pores of the leather are also visible. In the plasma deposited material, the gaps or pinholes caused by the animal hair follicles were partially covered by the plasma coating making them smaller. It was observed that a smooth, clean, thin film was formed on the remaining parts of the substrate, which covered the cracks. These modifications to the surface of the HMDSO plasma deposition treated material resulted in the coating being uniformly deposited creating an ultra-thin hydrophobic layer on the leather [52].

(**a**)   (**b**)
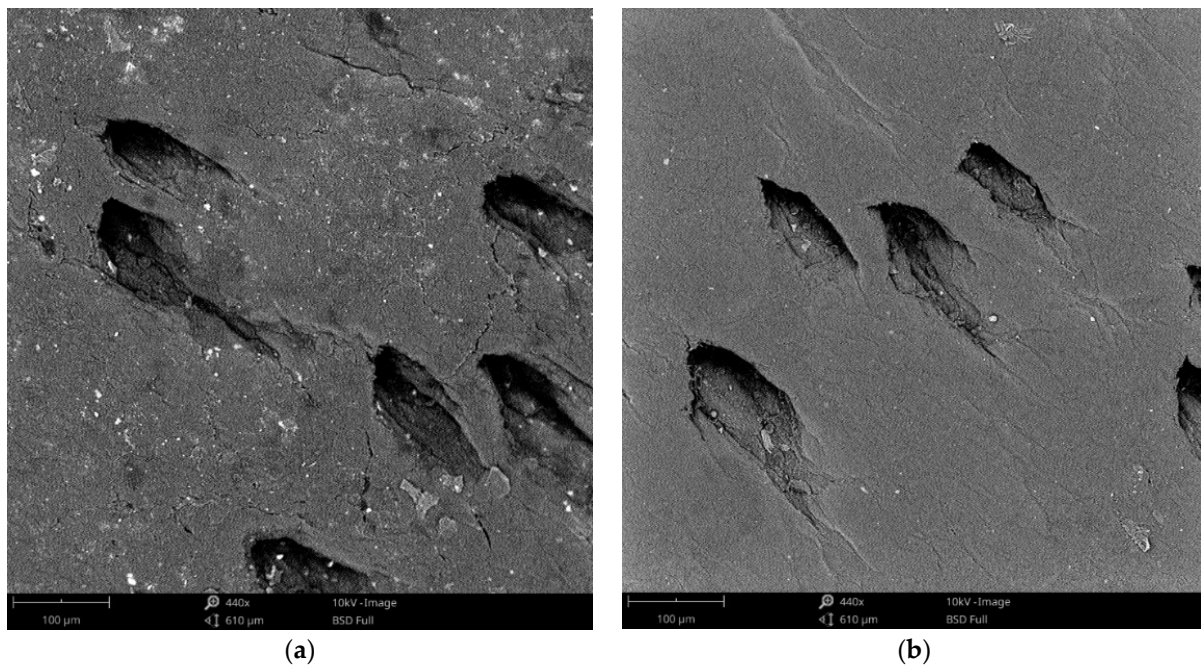
Figure 5. SEM images obtained before and after plasma polimerisation (440×). (**a**) Untreated leather; (**b**) Plasma coated leather.

3.4. Colour Change Measurements

The influence of the plasma treatment on the colour was measured in CIELAB L*, b* and a* values, as shown in Figure 6. The CIELAB colour system quantifies the relationship of the colours on three axes: L* indicates the lightness, and a* and b* are chromatic coordinates corresponding to the colours red/green and yellow/blue, respectively. In the component values obtained, no significant changes were observed depending on the plasma treatment and the untreated sample. It can be highlighted that the HMDSO coating deposited by plasma polymerisation on the leather sample does not affect neither the

colour nor the surface appearance of the original pigment of the leather, as can be seen in Figure 7, according to the requirement that there must be a difference between the values ≤ 2.5 established by INESCOP's upper materials laboratory based on its experience [53].
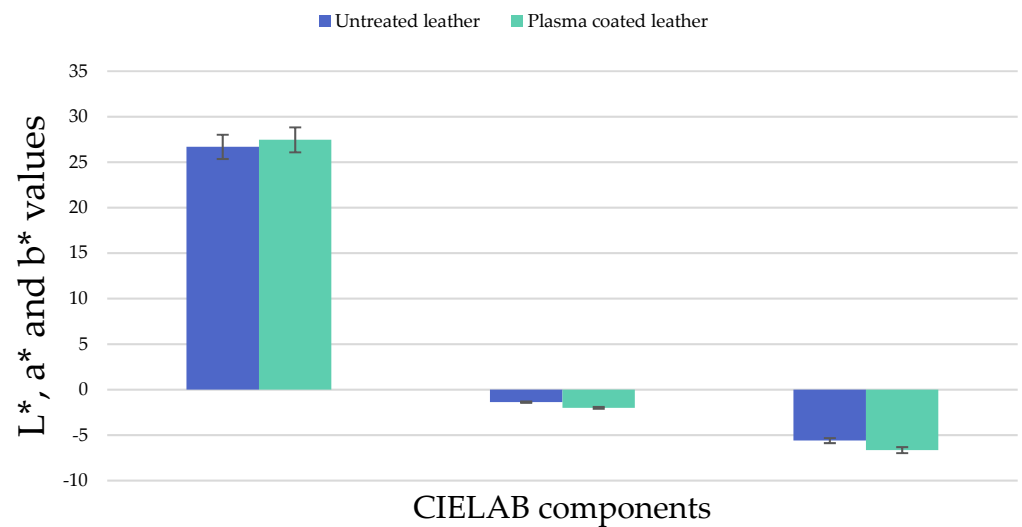
Figure 6. L*, a* and b* values for both untreated and plasma treated leather.
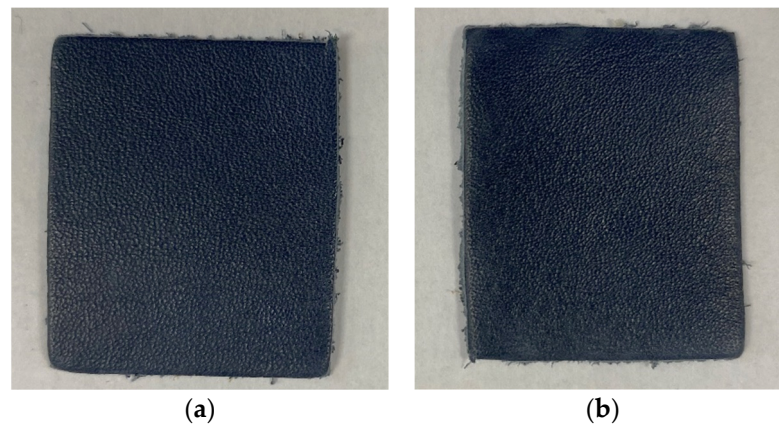
Figure 7. Pictures of (**a**) untreated and (**b**) plasma coated leather samples.

3.5. Surface Coating Thickness

The thickness of the HDMSO film deposited by plasma on the leather samples was measured by a manual rotary microtome coupled to an optical microscope according to the standard EN ISO 17186-method A. Table 6 includes the different thickness values determined, which have been obtained from three cuts of leather and, in each cut, 3 measurements have been made. The result is the average of the nine measurements. The thickness of the untreated leather was less than that of the plasma coated leather films. The HMDSO coating formed was 600 nm (see Figure 8), which is considered very small compared to a coating thickness on the aniline finish leather [15]. In addition, it can still be considered leather as the coating limit is 150,000 nm according to European regulations and standards [54–56].

Table 6. Thickness values of untreated, plasma treated samples and plasma polymerised HMDSO coating.
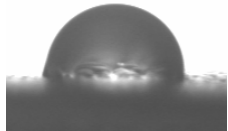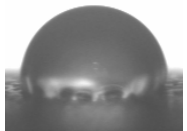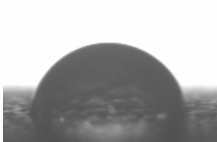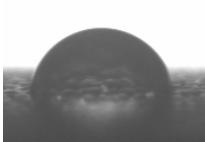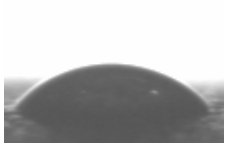
Sample	Thickness (nm)
Untreated leather	3700
Plasma coated leather	4300
HMDSO coating	600

(a)

(b)
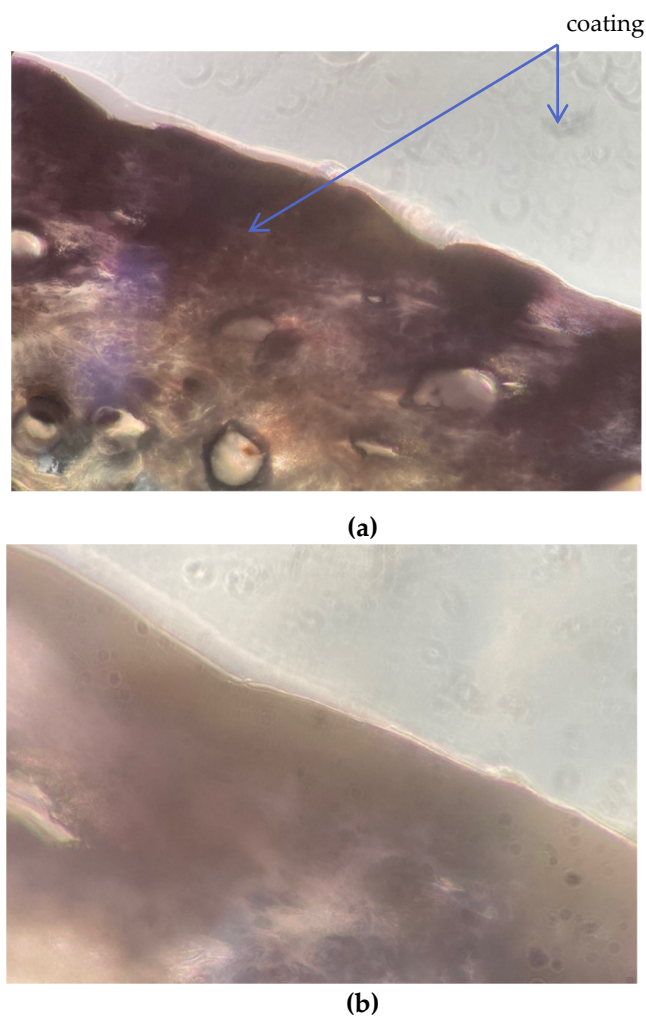
Figure 8. Cross-section images of plasma coated leather of HMDSO at 16× (**a**) and magnified at 40× (**b**).

3.6. Water Contact Angle (WCA) Measurements

The results of contact angle measurements with distilled water and absorption times of the plasma-treated and untreated leather are shown in Table 7. In addition, the evolution of wettability of untreated and plasma-treated samples over time has been represented in Figure 9.

Table 7. Absorption time and contact angle in plasma treated and untreated leather samples.

Absorption Time (min)	Water Contact Angle (WCA)	
	Untreated Leather	**Plasma Coated Leather**
t = 0 min		
t = 5 min		
	66.41° ± 2.66	83.43° ± 0.77
t = 15 min		
	0.33° ± 0.29	78.25° ± 0.72
t = 25 min		
	0.00° ± 0.00	76.97° ± 2.38
t = 60 min		
	0.00° ± 0.00	51.52° ± 0.46
t = 90 min		
	0.00° ± 0.00	0.00° ± 0.00
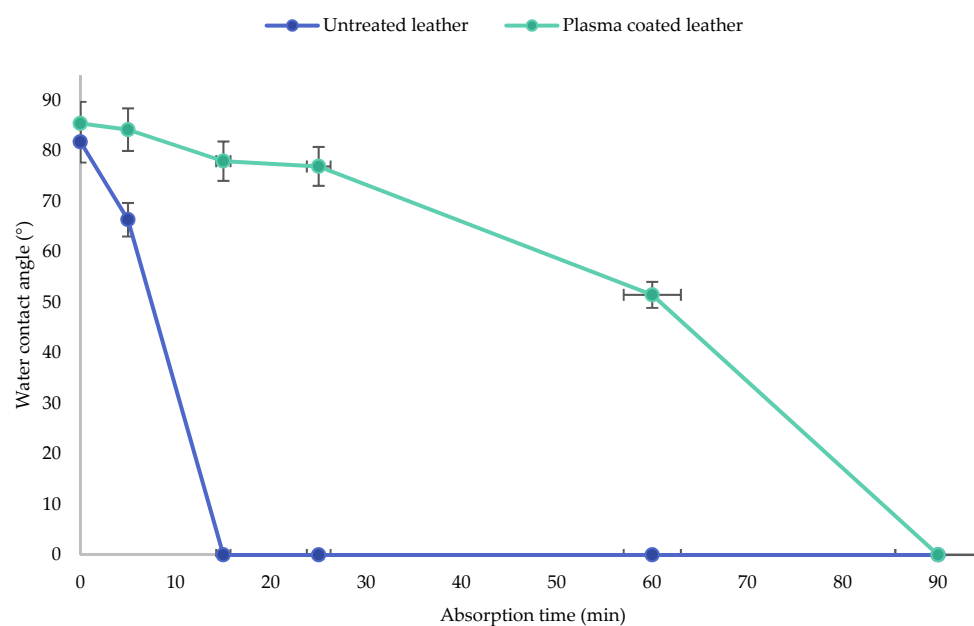
Figure 9. Evolution of wettability of untreated and plasma treated samples over time.

For natural leather as untreated sample, the water contact angle decreased from 81.83° to 0.33° within the first 15 min, time in which the water droplets had already been completely absorbed and entirely spread on the sample due to the hydrophilic nature of the natural leather. However, in the treated sample, the evolution of the contact angle as a function of time was quite different. Within the first 15 min, the water contact angle slightly decreased from 85.48° to 78.25°. After 25 min, the water droplets remained again on the surface with a similar contact angle of 76.97°. After 90 min, the contact angle reached 0.00° because the evaporation and contraction of the droplets occurred. Therefore, it can be said that the HMDSO plasma polymerised coating on leather provided high hydrophobic performance to leather, which exceeded the absorption time of 60 min [57].

The results of the wettability study showed that the surface hydrophobicity of the leather samples is significantly improved. This result can be attributed to the hydrophobic surface formed by plasma deposition of the silicon compound of polysiloxane. Plasma polymerisation of HMDSO with the application of 150 W plasma power with an initial surface activation process of 300 s with oxygen and alternating treatments of 12 s oxygen etching and 300 s argon coating resulted in a noticeable hydrophobic film coating on the leather surface [58,59]

4. Conclusions

In this study, the surface modifications of natural leather samples, a material commonly used for footwear applications, by plasma polymerisation with a 100% HMDSO composition have been evaluated by means of different experimental techniques. According to the results, the combination of optimised plasma activation and etching pre-treatment, both with O_2 and coating treatment with HMDSO/Ar, improved the hydrophobicity of the surface due to the introduction and deposition of silane groups on the leather surface. More specifically, the formation of an ultra-thin hydrophobic layer of polysiloxane nature and completely deposited by low-pressure plasma led to high water contact angles and absorption times compared to the natural and untreated leather. Most importantly, the HMDSO plasma coating deposited on the leather samples does not affect the original pigment of the leather, neither the colour nor the surface appearance and feel.

It can be concluded that plasma deposition of HMDSO at low pressure showed promising results to provide natural leather with water repellence for footwear applications. Plasma hydrophobic coatings may be used as a more sustainable alternative to replace conventional treatments currently used based on halocarbons and organic solvents.

Finally, it should be noted that this study contributes greatly to the three pillars of the Sustainable Development Goals (SDGs): the economic, social and environmental objectives set by the European Green Deal and its Circular Economy Plan, enabling thus the footwear sector to move increasingly towards a production model based on sustainability and automation, and contributing to the flexibility of processes and the modernisation of the industry by increasing its resilience [60].

References

1. Williams, J. (Ed.) *Waterproof and Water Repellent Textiles and Clothing*; The Textile Institute book series; Elsevier Science: Manchester, UK; Duxford, UK; Cambridge, MA, USA, 2017; ISBN 9780081012123.
2. Luo, Z.; Fan, H.; Lu, Y.; Shi, B. Fluorine-containing aqueous copolymer emulsion for waterproof leather. *J. Soc. Leather Technol. Chem.* **2008**, *92*, 107–113.
3. Serenko, O.; Nizamova, Z.; Kalinin, M.; Ostrovsky, Y.; Polukhina, L.; Muzafarov, A. Effect of the Morphology of Leather Surface on the Hydrophobic-Hydrophilic Properties. *Adv. Mater. Phys. Chem.* **2014**, *4*, 13–19. [CrossRef]
4. Ma, J.; Zhang, X.; Bao, Y.; Liu, J. A facile spraying method for fabricating superhydrophobic leather coating. *Colloids Surf. A Physicochem. Eng. Asp.* **2015**, *472*, 21. [CrossRef]
5. de Redacción, E.P.; Pachauri, R.K.; Meyer, L. (Eds.) *IPCC, 2014: Cambio Climático 2014: Informe de Síntesis. Contribución de los Grupos de Trabajo I, II y III al Quinto Informe de Evaluación del Grupo Intergubernamental de Expertos Sobre el Cambio Climático*; IPCC: Ginebra, Switzerland, 2014.
6. Synthesis Paper on Per and Polyfluorinated Chemicals-OECD. Available online: https://www.oecd.org/chemicalsafety/risk-management/synthesis-paper-on-per-and-polyfluorinated-chemicals.htm (accessed on 28 July 2021).
7. EUR-Lex—02019R1021-20210315—EN. *Regulation (EU) 2019/1021 of the European Parliament and of the Council of 20 June 2019 on Persistent Organic Pollutants*; EUR-Lex: Luxembourg, 2019.
8. Akovali, G.; Banerjee, B.; Sen, A.K.; Setua, D.K. *Advances in Polymer Coated Textiles*; Smithers Rapra Technology Ltd.: Shrewsbury, UK, 2012; ISBN 9781847354976.
9. Whittaker, M.H.; Heine, L. Toxicological and environmental issues associated with waterproofing and water repellent formulations. In *Waterproof and Water Repellent Textiles and Clothing*; Woodhead Publishing: Sawston, UK, 2018; pp. 89–120. [CrossRef]
10. Van der Veen, I.; Hanning, A.-C.; Stare, A.; Leonards, P.E.G.; De Boer, J.; Weiss, J.M. The effect of weathering on per- and polyfluoroalkyl substances (PFASs) from durable water repellent (DWR) clothing. *Chemosphere* **2020**, *249*, 126100. [CrossRef] [PubMed]
11. Holmquist, H.; Schellenberger, S.; Van der Veen, I.; Peters, G.M.; Leonards, P.E.G.; Cousins, I.T. Properties, performance and associated hazards of state-of-the-art durable water repellent (DWR) chemistry for textile finishing. *Environ. Int.* **2016**, *91*, 251–264. [CrossRef] [PubMed]
12. Institute for Prospective Technological Studies (Joint Research Centre); Rydin, S.; Delgado Sancho, L.; Canova, M.; Black, M.; Roudier, S.; Scalet, B.M. *Best Available Techniques (BAT) Reference Document for the Tanning of Hides and Skins: Industrial Emissions Directive 2010/75/EU (Integrated Pollution Prevention and Control)*; Publications Office of the European Union: Luxembourg, 2013; ISBN 9789279329470.
13. Sánchez Navarro, M.M.; Escoto Palacios, M.J.; Arán Ais, F.; Roig Orts, M.; Orgilés Barceló, C.; Puche Albert, C. Leather functionalisation by means of MLSE technology. *J. AQEIC* **2016**, *67*, 85.
14. Kayaoğlu, B.K.; Öztürk, E. Imparting hydrophobicity to natural leather through plasma polymerisation for easy care effect. *Fibers Polym* **2013**, *14*, 1706–1713. [CrossRef]

15. West, J.O.F.; Critchlow, G.W.; Lake, D.R.; Banks, R. Development of a superhydrophobic polyurethane-based coating from a two-step plasma-fluoroalkyl silane treatment. *Int. J. Adhes. Adhes.* **2016**, *68*, 195–204. [CrossRef]

16. Waters, L.J.; Finch, C.V.; Mehedi, H.; Bhuiyan, A.K.M.; Hemming, K.; Mitchell, J.C. Effect of plasma surface treatment of poly(dimethylsiloxane) on the permeation of pharmaceutical compounds. *J. Pharm. Anal.* **2017**, *7*, 338–342. [CrossRef]

17. Dakroub, G.; Duguet, T.; Esvan, J.; Lacaze-Dufaure, C.; Roualdes, S.; Rouessac, V. Comparative study of bulk and surface compositions of plasma polymerized organosilicon thin films. *Surf. Interfaces* **2021**, *25*, 101256. [CrossRef]

18. Siow, K.S. Low pressure plasma modifications for the generation of hydrophobic coatings for biomaterials applications. *Plasma Process. Polym.* **2018**, *15*, 1800059. [CrossRef]

19. Gengenbach, T.R.; Griesser, H.J. Post-deposition ageing reactions differ markedly between plasma polymers deposited from siloxane and silazane monomers. *Polymer* **1999**, *40*, 5079–5094. [CrossRef]

20. Gengenbach, T.R.; Griesser, H.J. Compositional changes in plasma-deposited fluorocarbon films during ageing. *Surf. Interface Anal.* **1998**, *26*, 498–511. [CrossRef]

21. Mistry, P.; Jahr, T. Method and Apparatus for Surface Treatment of Materials Utilizing Multiple Combined Energy Sources. U.S. 9,309,619, 12 April 2016.

22. Gaidau, C.; Nicolescu, M.D.; Vladkova, T.G.; Surdu, L.; Barbu, I.; Dineff, P. Research on cold plasma treatment of leather and fur based materials as ecological alternative. *Industria Textila* **2017**, *68*, 350. [CrossRef]

23. Tudoran, C.; Roşu, M.-C.; Coroş, M. A concise overview on plasma treatment for application on textile and leather materials. *Plasma Process. Polym.* **2020**, *17*, 2000046. [CrossRef]

24. Štěpánová, V.; Kelar, J.; Slavíček, P.; Chlupová, S.; Stupavská, M.; Jurmanová, J.; Černák, M. Surface modification of natural leather using diffuse ambient air plasma. *Int. J. Adhes. Adhes.* **2017**, *77*, 198–203. [CrossRef]

25. Choi, J.H.; Lee, E.S.; Baik, H.K.; Lee, S.-J.; Song, K.M.; Hwang, M.K.; Huh, C.S. Surface modification of natural leather using low-pressure parallel plate plasma. *Surf. Coatings Technol.* **2003**, *171*, 257–263. [CrossRef]

26. Bian, D.; Wu, Y. Enduring and Stable Surface Dielectric Barrier Discharge (SDBD) Plasma Using Fluorinated Multi-Layered Polyimide. *Polymers* **2018**, *10*, 606. [CrossRef]

27. Krtouš, Z.; Hanyková, L.; Krakovský, I.; Nikitin, D.; Pleskunov, P.; Kylián, O.; Sedlaříková, J.; Kousal, J. Structure of Plasma (re)Polymerized Polylactic Acid Films Fabricated by Plasma-Assisted Vapour Thermal Deposition. *Materials* **2021**, *14*, 459. [CrossRef]

28. Godeau, G.; Amigoni, S.; Darmanin, T.; Guittard, F. Post-functionalization of plasma treated polycarbonate substrates: An efficient way to hydrophobic, oleophobic plastics. *Appl. Surf. Sci.* **2016**, *387*, 28–35. [CrossRef]

29. Fu, X.; Jenkins, M.J.; Sun, G.; Bertoti, I.; Dong, H. Characterization of active screen plasma modified polyurethane surfaces. *Surf. Coat. Technol.* **2012**, *206*, 4799–4807. [CrossRef]

30. Ting, J.A.S.; Rosario, L.M.D.; Lee Jr, H.V.; Ramos, H.J.; Tumlos, R.B. Hydrophobic coating on glass surfaces via application of silicone oil and activated using a microwave atmospheric plasma jet. *Surf. Coat. Technol.* **2014**, *259*, 7–11. [CrossRef]

31. Abdul Moktadir, M.; Badri Ahmadi, H.; Sultana, R.; Zohra, F.-T.; James, J.H.L.; Rezaei, J. Circular economy practices in the leather industry: A practical step towards sustainable development. *J. Clean. Prod.* **2020**, *251*, 119737. [CrossRef]

32. Palop Arroyo, R.; Sabaté Rojas, D. *Química de la Fabricación del Cuero*; Delta: Madrid, Spain, 2021; ISBN 9788417526917.

33. *Plasma Technology*, 4th ed.; Diener electronic GmbH + Co. KG: Ebhausen, Germany, 2011.

34. Kaygusuz, M.; Meyer, M.; Junghans, F.; Aslan, A. Modification of Leather Surface with Atmospheric Pressure Plasma and Nanofinishing. *Polym.-Plast. Technol. Eng.* **2018**, *57*, 260–268. [CrossRef]

35. Footwear Technology Centre. IVACE R&D&I Projects-INESCOP. Centre for Technology and Innovation. Available online: https://www.inescop.es/en/inescop/activities/r-d-i-projects/ivace-r-d-i-projects (accessed on 26 August 2021).

36. Mitschker, F. *Influence of Plasma Parameters in Pulsed Microwave and Radio Frequency Plasmas on the Properties of Gas Barrier Films on Plastics*; Ruhr-Universität Bochum, Fakultät für Elektrotechnik und Informationstechnik: Bochum, Germany, 2019. [CrossRef]

37. ISO 22700:2019. *Leather-Measuring the Colour and Colour Difference of Finished Leather*; ISO: Geneva, Switzerland, 2019.

38. ISO 17186:2011. *Leather-Physical and Mechanical Tests-Determination of Surface Coating Thickness*; ISO: Geneva, Switzerland, 2011.

39. EN 828-2013. *Adhesives. Wettability-Determination by Measurement of Contact Angle and Surface Free Energy of Solid Surface*; European Committee for Standardization: Brussels, Belgium, 2013.

40. You, X.; Gou, L.; Tong, X. Improvement in surface hydrophilicity and resistance to deformation of natural leather through O_2/H_2O low-temperature plasma treatment. *Appl. Surf. Sci.* **2016**, *360*, 398–402. [CrossRef]

41. Kurosawa, S.; Choi, B.-G.; Park, J.-W.; Aizawa, H.; Shim, K.-B.; Yamamoto, K. Synthesis and characterization of plasma-polymerized hexamethyldisiloxane films. *Thin Solid Film.* **2006**, *506*, 176–179. [CrossRef]

42. Yang, J.; Pu, Y.; Miao, D.; Ning, X. Fabrication of Durably Superhydrophobic Cotton Fabrics by Atmospheric Pressure Plasma Treatment with a Siloxane Precursor. *Polymers* **2018**, *10*, 460. [CrossRef] [PubMed]

43. Li, H.; Yang, L.; Wang, Z.; Liu, Z.; Chen, Q. Pre-grafted Group on PE Surface by DBD Plasma and Its Influence on the Oxygen Permeation with Coated SiOx. *Molecules* **2019**, *24*, 780. [CrossRef] [PubMed]

44. Mitschker, F.; Dietrich, J.; Ozkaya, B.; de los Arcos, T.; Giner, I.; Awakowicz, P.; Grundmeier, G. Spectroscopic and Microscopic Investigations of Degradation Processes in Polymer Surface-Near Regions During the Deposition of SiOx Films. *Plasma Process. Polym.* **2015**, *12*, 1002–1009. [CrossRef]

45. Ozkaya, B.; Mitschker, F.; Ozcan, O.; Awakowicz, P.; Grundmeier, G. Inhibition of Interfacial Oxidative Degradation During SiOx Plasma Polymer Barrier Film Deposition on Model Organic Substrates. *Plasma Process. Polym.* **2015**, *12*, 392–397. [CrossRef]

46. Launer, P.J.; Arkles, B. Infrared Analysis of Organosilicon Compounds: Spectra-Structure Relationships. In *Silicon Compounds: Silanes and Silicones*; Arkles, B., Larson, G., Eds.; Gelest Inc.: Morrisville, PA, USA, 2013; pp. 175–178. ISBN 9780578122359.

47. Maurau, R.; Boscher, N.D.; Guillot, J.; Choquet, P. Nitrogen Introduction in pp-HMDSO Thin Films Deposited by Atmospheric Pressure Dielectric Barrier Discharge: An XPS Study. *Plasma Process. Polym.* **2012**, *9*, 316–323. [CrossRef]

48. Jaritz, M.; Hopmann, C.; Wilski, S.; Kleines, L.; Rudolph, M.; Awakowicz, P.; Dahlmann, R. HMDSO-Based Thin Plasma Polymers as Corrosion Barrier Against NaOH Solution. *J. Mater. Eng. Perform.* **2020**, *29*, 2839–2847. [CrossRef]

49. Hegemann, D.; Bülbül, E.; Hanselmann, B.; Schütz, U.; Amberg, M.; Gaiser, S. Plasma polymerization of hexamethyldisiloxane: Revisited. *Plasma Process. Polym.* **2021**, *18*, 2000176. [CrossRef]

50. Cho, S.C.; Hong, Y.C.; Cho, S.G.; Ji, Y.Y.; Han, C.S.; Uhm, H.S. Surface modification of polyimide films, filter papers, and cotton clothes by HMDSO/toluene plasma at low pressure and its wettability. *Curr. Appl. Phys.* **2009**, *9*, 1223–1226. [CrossRef]

51. Balkova, R.; Zemek, J.; Cech, V.; Vanek, J.; Prikryl, R. XPS study of siloxane plasma polymer films. *Surf. Coat. Technol.* **2003**, *174–175*, 1159–1163. [CrossRef]

52. Kan, C.-W.; Kwong, C.-H.; Ng, S.-P. Atmospheric Pressure Plasma Surface Treatment of Rayon Flock Synthetic Leather with Tetramethylsilane. *Appl. Sci.* **2016**, *6*, 59. [CrossRef]

53. Horrocks, A.; Eivazi, S.; Ayesh, M.; Kandola, B. Environmentally Sustainable Flame Retardant Surface Treatments for Textiles: The Potential of a Novel Atmospheric Plasma/UV Laser Technology. *Fibers* **2018**, *6*, 31. [CrossRef]

54. Chaiwong, C.; Rachtanapun, P.; Sarapirom, S.; Boonyawan, D. Plasma polymerisation of hexamethyldisiloxane: Investigation of the effect of carrier gas related to the film properties. *Surf. Coat. Technol.* **2013**, *229*, 12–17. [CrossRef]

55. EN 15987:2015. *Leather-Terminology-Key Definitions for the Leather Trade*; European Committee for Standardization: Brussels, Belgium, 2015.

56. *Directive 94/11/EC of the European Parliament and of the Council of 23 March 1994 on the Approximation of the Laws, Regulations and Administrative Provisions of the Member States Relating to Labelling of the Materials Used in the Main Components of Footwear for Sale to the Consumer*; EUR-Lex: Luxembourg, 1994.

57. Asadollahi, S.; Profili, J.; Farzaneh, M.; Stafford, L. Development of Organosilicon-Based Superhydrophobic Coatings through Atmospheric Pressure Plasma Polymerization of HMDSO in Nitrogen Plasma. *Materials* **2019**, *12*, 219. [CrossRef]

58. Iqbal, M.; Dinh, D.K.; Abbas, Q.; Imran, M.; Sattar, H.; Ul Ahmad, A. Controlled Surface Wettability by Plasma Polymer Surface Modification. *Surfaces* **2019**, *2*, 26. [CrossRef]

59. Kan, C.-W.; Man, W.-S. Parametric Study of Effects of Atmospheric Pressure Plasma Treatment on the Wettability of Cotton Fabric. *Polymers* **2018**, *10*, 233. [CrossRef]

60. *COM/2019/640 Final. Communication from the Commission to the European Parliament, the European Council, the Council, the European Economic and Social Committee and the Committee of the Regions the European Green Deal*; EUR-Lex: Luxembourg, 2019.

Article

Insights on the Atmospheric-Pressure Plasma-Induced Free-Radical Polymerization of Allyl Ether Cyclic Carbonate Liquid Layers

Edyta M. Niemczyk [1,2], **Alvaro Gomez-Lopez** [3], **Jean R. N. Haler** [1], **Gilles Frache** [1], **Haritz Sardon** [3] and **Robert Quintana** [1,*]

1   Department of Materials Research and Technology, Luxembourg Institute of Science and Technology (LIST), 4422 Belvaux, Luxembourg; edyta.niemczyk@list.lu (E.M.N.); jean.haler@list.lu (J.R.N.H.); gilles.frache@list.lu (G.F.)
2   Department of Physics and Materials Science, University of Luxembourg, 4365 Esch-sur-Alzette, Luxembourg
3   POLYMAT and Polymer Science and Technology Department, Faculty of Chemistry, University of the Basque Country UPV/EHU, 20018 Donostia-San Sebastián, Spain; alvaro.gomez@ehu.eus (A.G.-L.); haritz.sardon@ehu.eus (H.S.)
*   Correspondence: roberto.quintana@list.lu; Tel.: +352-275-888-2239

Abstract: Plasma-induced free-radical polymerizations rely on the formation of radical species to initiate polymerization, leading to some extent of monomer fragmentation. In this work, the plasma-induced polymerization of an allyl ether-substituted six-membered cyclic carbonate (A6CC) is demonstrated and emphasizes the retention of the cyclic carbonate moieties. Taking advantage of the low polymerization tendency of allyl monomers, the characterization of the oligomeric species is studied to obtain insights into the effect of plasma exposure on inducing free-radical polymerization. In less than 5 min of plasma exposure, a monomer conversion close to 90% is obtained. The molecular analysis of the oligomers by gel permeation chromatography coupled with high-resolution mass spectrometry (GPC-HRMS) further confirms the high preservation of the cyclic structure and, based on the detected end groups, points to hydrogen abstraction as the main contributor to the initiation and termination of polymer chain growth. These results demonstrate that the elaboration of surfaces functionalized with cyclic carbonates could be readily elaborated by atmospheric-pressure plasmas, for instance, by copolymerization.

Keywords: allyl-substituted cyclic carbonate; free-radical polymerization; atmospheric-pressure plasma

1. Introduction

The synthesis and direct deposition of polymeric thin films by atmospheric-pressure plasma-induced polymerization is an appealing approach for the elaboration of functional surfaces [1]. A major contribution to its success is owed to its fast deposition rates, the good retention of the chemical structure of the monomers in the deposited film and the use of solvent-less, mild reaction conditions, usually at room temperature. Additionally, working at atmospheric pressure eases the scalability of the deposition process [2] and allows the use of precursors in the liquid phase [3]. This extends the application to monomers of very low vapor pressure, which are not suitable for processing in the vapor phase. Vinyl functional monomers are readily polymerized by plasma-induced free-radical polymerization leading to the deposition of thin films with a large variety of functional groups, including cyclic groups, such as epoxide [4,5], lactam [6] and catechol/quinone [7]. These groups are of interest because they can improve adhesion between the thin film and the treated surface. Their reactivity also allows post-polymerization modifications of the surface, for instance, for biomolecule immobilization for practical applications in biomedical [7] and environmental protection fields [4]. Despite the advantages shown by atmospheric-pressure plasma-induced free-radical polymerization in the preservation of the chemical structure of monomers, monomer fragmentation should occur in some extent to initiate

polymerization. This can reduce the amount of cyclic functional groups in the resulting polymer. The retention of epoxide groups, by far the most studied case, has been found to be dependent on the nature of the polymerizable group, i.e., vinyl or allyl. Manakhov et al. reported that the concentration of the epoxide groups in the plasma-polymerized polymer was lower when allyl glycidyl ether (AGE) was used instead of glycidyl methacrylate (GMA) [8]. In addition to the lower retention of the epoxide groups, the polymerization of AGE led to lower deposition rates. This difference could be attributed to the well-known difficulty of allyl monomers to polymerize and the formation of oligomers or medium-molecular-weight polymers [9,10]. Nevertheless, the free-radical polymerization of allyls, either by conventional wet chemistry or by plasma polymerization [11–14], has received less attention than that of their vinyl counterparts.

Cyclic carbonates are gaining attention as sustainable compounds in the context of green and sustainable chemistry. Their synthesis can involve the use of carbon dioxide as a building block, can be applied as green solvents and can substitute toxic reactants currently employed in the chemical industry [15]. Among the different cyclic carbonate sizes, five-membered cyclic carbonates are easily prepared through [3 + 2] CO_2 insertion into their corresponding (bio-based) epoxy precursors [16]. Nonetheless, their low reactivity restricts their use in some applications. Six-membered cyclic carbonates present greater reactivity at room temperature and, additionally, higher stability than seven- and eight-membered cyclic carbonates, which can be crucial to retain their structure under plasma conditions [17]. Moreover, recently, a one-step synthesis procedure has been reported using 1,3-diols and CO_2 at atmospheric pressure and ambient temperature to prepare six-membered cyclic carbonates, increasing the interest for these monomers as green and sustainable reactants [18].

The introduction of pendent groups in cyclic carbonates increases their reactivity and allows the production of functionalized polycarbonates by ring-opening polymerization (ROP). Several functionalized cyclic carbonates have already been explored, such as allyl, alkyne and maleimide. Allyl pendent groups have been considered as the intermediate step for the post-functionalization of polycarbonates by a thiolene coupling reaction [19] and to increase their mechanical stability by free-radical cross-linking [20,21]. Interestingly, recent studies have shown that allyl ether-substituted six-membered cyclic carbonates can be obtained as a value-added byproduct of the upcycling of mixed plastic waste [22], in addition to ring-closing depolymerization [23]. Otherwise, polymers decorated with cyclic carbonates have gained interest in the production of thermoset plastics and coatings [24]. In the latter case, the reaction of the carbonates with amines is exploited to promote the adhesion of the coating on polyurethane-based materials. The reactivity with amines has also been explored for the coupling reaction of biomolecules [25].

The synthesis of polymers with pendent cyclic carbonates by plasma processes has not yet been reported. In comparison with the epoxide group, cyclic carbonates are notably less reactive [24] and might be more stable to plasma exposure. In this work, the plasma-induced polymerization of an allyl ether-substituted six-membered cyclic carbonate (A6CC, 5-((allyloxy)methyl)-5-ethyl-1,3-dioxan-2-one) was studied using a cold, atmospheric-pressure dielectric barrier discharge (DBD) plasma. In particular, the monomer A6CC was exposed to the plasma in the form of a liquid layer due to its very low vapor pressure. After reiterated plasma exposure, both the conversion of the allyl group and the retention of the cyclic carbonate were investigated by FTIR and NMR spectroscopies. High-resolution mass spectrometry (HRMS) analyses of the, as expected, low-molecular-weight products was performed to identify the chemical formula of the products to obtain insights into the plasma-induced polymerization mechanism.

2. Materials and Methods

2.1. Synthesis of 5-((allyloxy)methyl)-5-ethyl-1,3-dioxan-2-one: A6CC

The synthesis of 5-((allyloxy)methyl)-5-ethyl-1,3-dioxan-2-one was carried out as described elsewhere [17]. Ethyl chloroformate (6.81 g, 62.75 mmol, 97%, Sigma-Aldrich,

Madrid, Spain) was added dropwise to a solution of trimethylolpropane allyl ether (TM-PAE) (5.44 g, 31.24 mmol, Sigma-Aldrich, 90%) and triethylamine (6.96 g, 68.73 mmol, Sigma-Aldrich, 99.5%) in 200 mL of dried THF at 0 °C over a period of 40 min. The reaction mixture was then stirred at room temperature for 2 h. The precipitated triethylamine hydrochloride was filtrated off, and the filtrate was concentrated under vacuum. Then, the crude was diluted with ethyl acetate (300 mL) and washed two times with aqueous hydrochloric acid (1 M) and two times with deionized water. The organic phase was dried over anhydrous magnesium sulfate and concentrated under vacuum. The residue was purified by column chromatography (eluent 30/70 ethyl acetate/hexane). The pure product A6CC was obtained as a colorless liquid with 61% yield.

2.2. Atmospheric-Pressure Plasma-Induced Polymerization of A6CC

Thin liquid layers of the monomer were formed over silicon substrates using a spin coater (Laurell Technologies, WS-650-23B, North Wales, PA, United States) operating at 10,000 rpm for 30 s. Any solvent was required in this process. The substrate covered with the thin liquid layer was then transferred to an atmospheric-pressure dielectric barrier discharge (DBD) plasma reactor, described elsewhere [7]. Briefly, A SOFTAL 7010R corona generator provided a 10 kHz sinusoidal electrical excitation, and the plasma power was adjusted to deliver between 0.53 and 1.60 W·cm^{-2}. The active plasma zone of 18.72 cm^2 was created between two parallel and horizontal electrodes. The top electrode was formed by two high voltage (HV) bars, covered with a thick alumina-dielectric barrier material, separated by a third bar used to introduce the plasma gas (Ar 99.999%, 20 slm). The grounded electrode was the moving table where the substrates were placed. The speed of the table was kept constant at 50 mm·s^{-1}, and the number of runs through the plasma zone were 30, 40, 50, 70 or 90 runs. The effective plasma exposure duration for each table run was 3 s. For the series of samples, the following annotation was used: monomer acronym, dash, the number of table runs under plasma; for instance, A6CC-30 refers to a sample that underwent 30 runs through the plasma zone, with 90 s of effective plasma exposure. The samples were washed out with a solvent to recover the polymer from the silicon surface. For characterization, pooled samples of at least 5 replicates were used.

2.3. Characterization

One-dimensional spectra ^{1}H NMR and 2-dimensional spectra heteronuclear single quantum coherence (HSQC), heteronuclear multiple bond correlation (HMBC) and bidimensional ^{1}H-^{1}H correlation spectroscopy (COSY) were acquired on a Bruker Avance-III HD spectrometer (Rheinstetten, Germany) operating at a 1H frequency of 600 MHz. The delay between the scans was 10 s. The following parameters were used: 2048 data points along the f2 dimension, 256 free induction decays in the f1 dimension, a pulse width of 11.05 ms, a spectral width of 3448 Hz (1H) and the number of scans was 16 with a digital resolution of 3.97 Hz per point. Experiments were performed at room temperature. Monomers and plasma-deposited layers were dissolved in deuterated chloroform (CDCl3) at room temperature. Assignments were performed using a combination of COSY, HSQC and HMBC spectra. Chemical shifts are given as d (ppm), and the coupling constants (Hz) were reported as J. Resonances were identified from the literature chemical shift data.

FTIR transmission measurements of the polymer deposited on the silicon wafer were performed on a Bruker Vertex 70 spectrometer (Ettlingen, Germany) equipped with an MCT detector. All FTIR spectra were normalized according to the C=O stretching band at 1755 cm^{-1}. The spectra were acquired between 600 and 4000 cm^{-1} with an accumulation of 128 scans and a resolution of 4 cm^{-1}. Spectra acquisition was controlled by the OPUS 7.2 software package (Bruker Corporation, Billerica, MA, USA).

A 1260 Infinity II gel permeation chromatograph (GPC, Agilent Technologies, Santa Clara, CA, USA) was used to determine the Mn, Mw and PDI of the polymers. The chromatograph was equipped with an integrated RI detector, a PLgel 5 mm MIXED-C, PLgel 5 mm MIXED-D columns and a PLgel guard column (Agilent Technologies, Santa Clara, CA, USA). Chloro-

form was used as an eluent with a flow rate of 1.0 mL min^{-1} at 40 °C. Polystyrene standards (Agilent Technologies, Santa Clara, CA, USA, Mp = 162 − 1500 × 103 g mol^{-1}) were used to perform calibration.

GPC-HRMS analyses were carried out with the HPLC system (Ultimate 3000, Dionex, Thermo Scientific, Waltham, MA, USA) coupled online to an LTQ/Orbitrap Elite mass spectrometer (Thermo Fisher Scientific, San Jose, CA, USA) with an Ion Max source, equipped with a heated electrospray (H-ESI) probe from Thermo Scientific. Samples were dissolved in chloroform and filtered over a 0.45 μm pore size membrane prior to injection. A mesopore column of 3 μm (300 × 7.5 mm) from Agilent Technologies with an exclusion limit of 25 kg·mol^{-1} was used at 30 °C working in THF. The flow rate was set to 1 mL·min^{-1} and split post-column toward the UV detection on one hand and the ESI-HRMS detection on another hand. Ammonium acetate was added post-split to promote ionization. The spray voltage was set to 3.2 kV. The calculations were carried out based on the PolyCalc web-based assignment tool [26].

3. Results

The chemical structure of the A6CC monomer and the experimental set-up used for the polymerization are shown in Figure 1. The monomer is a clear liquid at room conditions and has a very low vapor pressure, both properties facilitated the formation by the spin coating of very thin liquid layers over the silicon substrates. The values of the plasma power used for the plasma-induced polymerization, i.e., 0.53 and 1.60 W·cm^{-2}, were chosen within the most common range of values reported for the plasma polymerization of liquid monomers containing vinyl and allyl groups [7]. The lower value was also the minimal power able to sustain the plasma discharge in the DBD reactor, without modifying the gap between electrodes. After exposition to the plasma, the visual appearance of the initial liquid layer over the silicon surface varied to an oily-like one. When rubbing, the samples showed different degrees of consistency/viscosity, suggesting the formation of products of higher average molecular weights. The samples showing a higher consistency were those obtained using the highest power and longer exposition times. At the lowest power, the liquid-like appearance was always observed. To complement this set of qualitative results and to correlate the effect of the plasma exposure to changes on the chemical structure of the A6CC monomer, Figure S1 shows the FTIR spectra of the monomer and four different samples showing the liquid-like appearance. Considering the bands attributed to allyl groups, i.e., 1648, 993 and 930 cm^{-1} [27,28], after 10 runs, regardless of the plasma power used, a drop in the intensity of these absorption bands was evidenced. Only in the spectrum of the sample polymerized with the highest exposition time and at the highest power were those bands not detectable.

The higher power was then considered in order to carry out a systematic study where the number of runs was increased up to three-fold. Figure 2 shows the recorded FTIR spectra, normalized according to the intensity of the absorption band at 1755 cm^{-1} (C=O stretching carbonate ring), of samples exposed to plasma for 30, 40, 50, 70 and 90 runs. Increasing the exposition time not only led to the decrease in and disappearance of the bands attributed at the allyl groups (Figure 2b), but the formation of alkyl backbone could be detected by the appearance of and increase in the plasma exposition time of the absorption bands in the range of 3050–2800 cm^{-1}, corresponding to C-H stretching, and at 760 cm^{-1}, related to the rocking vibrations of CH$_2$ of the long alkyl chains [8,12,29,30].

The series of samples was also analyzed by NMR spectroscopy (Figure 3). In agreement with the FTIR results, the consumption of the allyl groups was nearly complete as evidenced by the reduction of the signals at 5.85 ppm (a, methine, O-CH$_2$-**CH**=CH$_2$) and 5.23 (b, methylidene, O-CH$_2$-CH=**CH$_2$**) already within 30 runs. Considering the protons of the carbon in the alpha position of the allyl group, **d** (O-**CH$_2$**-CH=CH$_2$), their signal shifted toward a lower chemical shift, from 3.97 to 3.48–3.15 ppm, overlapping with signal **e**, resulting in a broad peak (Figure S2) [31]. Additionally, new peaks (labeled as **1**) at the 1.45–1.70 ppm region appeared. These results evidenced the formation of a polymeric

alkyl backbone. Otherwise, the peaks assigned to the ethyl chain pendent from the cycle, **f** methylene group at 1.52 ppm and **g** methyl group at 0.92 ppm, remained at a similar chemical shift along the polymerization process. The connectivity of **f** (1.56 ppm) with **g** (0.94 ppm) could be stablished by the acquisition of two-dimensional COSY NMR spectra (Figure S3). The conversion of the allyl group was determined by comparison with the integral of the band attributed to the protons of the methyl group (labeled as **g**) with the integrals of protons **a** and **b** of the allyl groups. As shown in Figure 4, the consumption of the carbon–carbon double bond reached 82% for A6CC-30 and remained at 94% for the most prolonged plasma exposed sample, A6CC-90 [32]. This approach to determine the conversion did not consider that methyl groups can also be generated as end groups by the free-radical polymerization of the allyl group; therefore, the reported values can be considered as conservative.
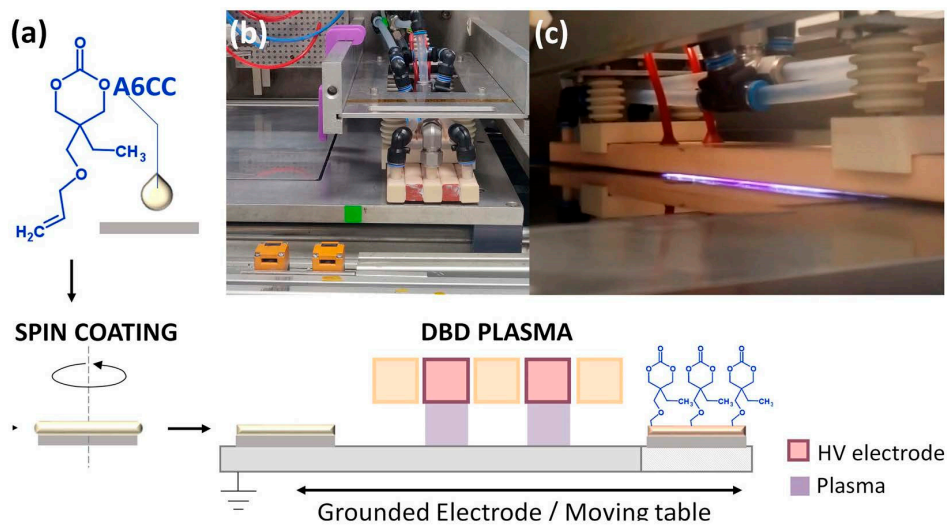
Figure 1. Schematic representation of the process for the atmospheric-pressure plasma-induced polymerization of liquid layers of the allyl ether-substituted cyclic carbonate (A6CC) at room temperature (**a**). Picture of the DBD applicator over the moving table. Plasma gas is supplied in between the two high voltage electrodes (**b**). DBD side view with plasma engaged (**c**).
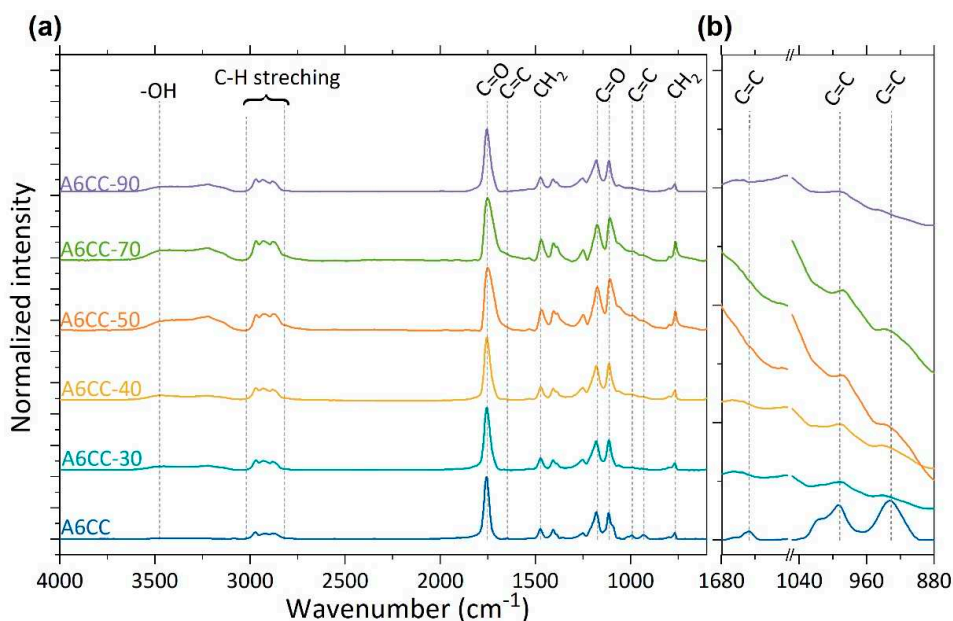
Figure 2. Representative FTIR spectra of the A6CC liquid layers as a function of the number of runs, up to 90, of plasma exposure (power: 1.60 W·cm^{-2}). (**a**,**b**) zoom of the bands attributed to the allyl C-C double bond. The spectra were normalized with respect to the peak of the carbonate carbonyl band.
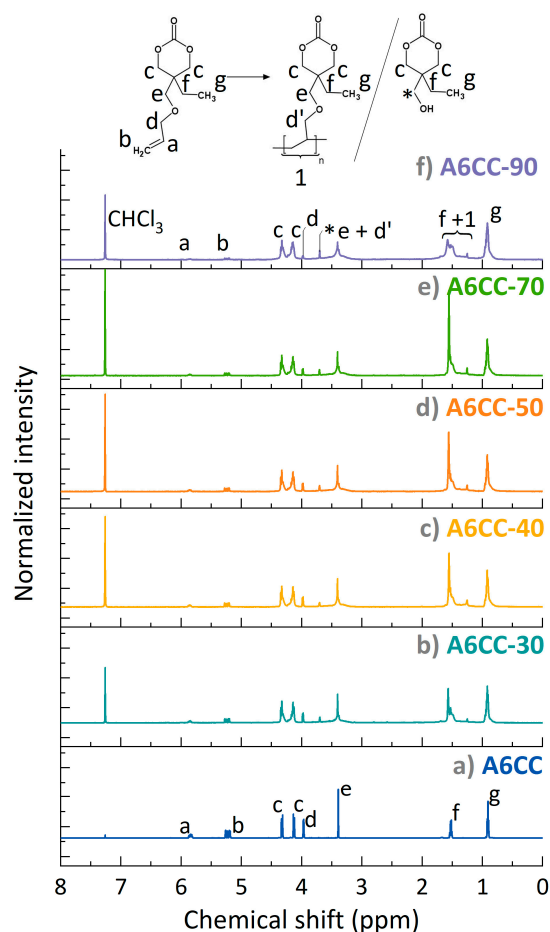
Figure 3. ^{1}H NMR spectra (in CDCl3) normalized according to the methylene group (signal g) of monomer (**a**) A6CC before and after the plasma-induced polymerization. (**b**) A6CC-30, (**c**) A6CC-40, (**d**) A6CC-50, (**e**) A6CC-70 and (**f**) A6CC-90. * assigned to the chemical structure shown in the figure.
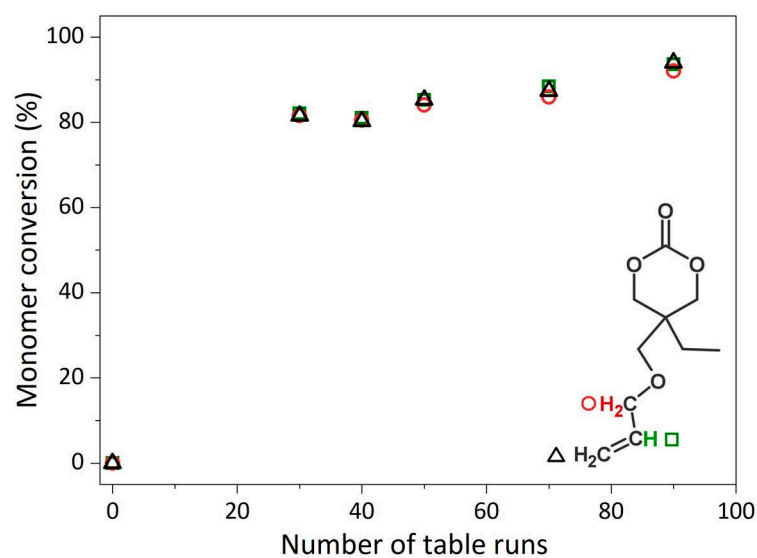
Figure 4. Conversion of the allyl group in function of plasma exposure time (number of table runs) calculated based on the signals from the protons of the allyl group (=CH$_2$, triangle and =CH-, square symbols) and the α-carbon (-CH$_2$-, circle symbol) in the ^{1}H NMR spectra. The integral of the protons of the methyl group were considered as internal reference for the calculation.

While the set of results provided experimental evidence of the step-growth polymerization of the allyl groups, the results were further scrutinized to assess the preservation of the closed structure of the cyclic carbonate. First, in ^{1}H-NMR, the close ring structure is characterized by two distinct doublets (**c**) at resonances 4.13 ppm and 4.33 ppm assigned to the diastereotopic protons H_{eq} and H_{ax}. In all the recorded spectra, the signals were detected, and their integrals remained similar between them. Indeed, the opening of the ring would result in free-rotating protons, which would appear as a single peak at 4.2 ppm (Figure S4) [33].

Further confirmation of the closed ring structure was achieved by the acquisition of two-dimensional NMR spectra. COSY NMR (Figure S3) evidenced the correlation of the diastereotopic protons interlocked in the cycle. HSQC and HMBC mutual proton–carbon correlations (Figures 5 and S5) were carried out to confirm the ring structure is connected, as a pendent group, to the formed polymeric chain. As shown in Figure 5a, the closed ring structure of the monomer implies two cross-peaks between diastereotopic protons forming the cyclic carbonate, labeled as **c** ([1]H 4.13 and 4.33 ppm), and carbonate carbon as revealed by 2D HMBC spectra (**c–h**: [1]H 4.13 and 4.33 ppm/[13]C 148.6 ppm). The quaternary carbon forms 2D HMBC cross-peaks with diastereotopic protons (**c–i**: [1]H 4.13 and 4.33 ppm/[13]C 35.8 ppm), methoxy (**e–i**: [1]H 3.39/[13]C 35.8 ppm) and the ethylene group (methylene **f-i**: [1]H 1.52/[13]C 35.8 ppm and methyl **g–i**: [1]H 0.92/[13]C 35.8 ppm). The same HMBC cross-peaks pattern could be observed for A6CC-30 (Figure 5b) and A6CC-90 (Figure S5). Similarly, their 2D HSQC spectra revealed that the protons with resonance in the range of 3.30–3.45 ppm corresponded to two different carbons with chemical shifts 68.2 and 72.0 ppm. The latter ^{13}C shift, labeled as **d**, resembles the peak signal for the A6CC monomer, confirming that the 2D HSQC cross-peak [1]H 3.32 ppm–[13]C 72.0 ppm is linked to the methoxy group from the former allyl group. For the polymerized A6CCs, the peak was denoted as **d'** [34]. The signal **d'** formed long-distance decoupling with the signal labeled as **f + 1** (2D HSQC, [1]H 1.55 ppm [13]C 72.0 ppm), evidencing the ether link in between the cyclic structure and the polymeric backbone. These results provided clear evidence to confirm the preservation of the pendent cyclic carbonate structure even after long exposures to the plasma. Nevertheless, the presence of new peaks from by-products was also detected. Labeled as (*) ([1]H 3.70 ppm/[13]C 61.00 ppm) could be correlated with protons from methylene groups. COSY-NMR spectra evidenced an interaction between them, and HSQC-HMBC evidenced a correlation of the signal (*) with the closed carbonate cycle. The chemical structure of this compound and its origin are further discussed by mass spectrometry analyses.

The determination of the molecular weights of the deposited products was carried out by GPC. The chromatograms, normalized using the peak with the highest elution time, are shown in Figure 6. They mainly revealed the presence of polydisperse products of low molecular weights, ranging from 200 to 1000 g·mol^{-1}. The presence of traces of higher molecular weight polymers could also be inferred from the chromatograms. Increasing the plasma exposure time shifted the molecular weight distribution curve toward high molecular weights, indicating an increase in the monomer conversion. The range of molecular weights obtained agrees with the low degree of polymerization commonly reported on the free-radical polymerization of allyl monomers by conventional wet chemistry methods [10]. In the gas phase, the plasma-induced free-radical polymerization of allyl alcohol and allylamine has also been reported [10,35]. Then, the same trends were observed with the formation of oligomers not higher than 10–20 repeating units [36]. In all these cases, the main mechanism behind this result has been related to the degradative monomer chain transfer.

The low degree of polymerization of the products made it meaningful to attempt their structural identification by gel permeation chromatography (GPC) coupled with high-resolution mass spectrometry (HRMS). The MW distribution of the samples is shown in Figure S6. As an effect of the exclusion limit of the mesopore column used in the GPC-HRMS setup, in all the samples, a peak at 25 kg·mol^{-1} was observed. This con-

firms the inferred presence of traces of high-molecular-weight polymers. Likewise, the relative intensity of this peak increased with the plasma exposure time. For each sample, the recorded chromatogram with the overlay representation of the HRMS spectra is included in the Supporting Information (Figure S7). As an example, Figure 7 shows the HRMS spectra corresponding to each of the peaks detected in the GPC chromatogram of the sample with the lowest exposition to the plasma, A6CC-30. As a first simple approach, just taking into consideration the m/z value of ionized adducts of $[(A6CC)_n + H^+/NH_4^+]$ oligomers, the number of repeating units reached ca. 7, regardless of the exposure time.
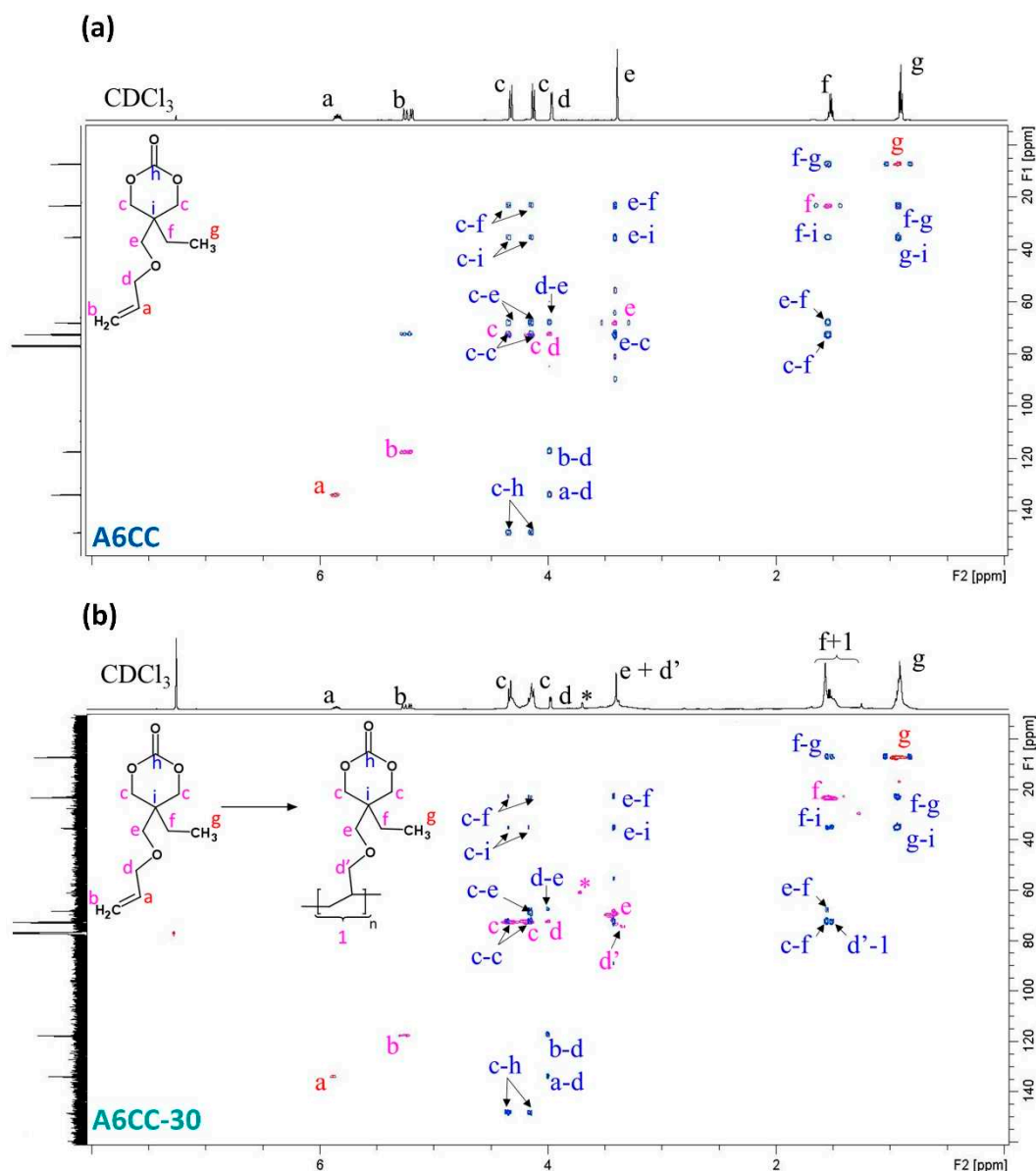
Figure 5. HSQC-HMBC cross-peaks of the (**a**) A6CC and (**b**) A6CC-30 samples, where red (odd) and pink (even) contours represent HSQC, and blue contours correspond to HMBC. HSQC reveals carbon–proton interaction, while HMBC shows the interaction between the proton and neighboring carbons. (*) corresponds to the methylene groups of the detected by-product.
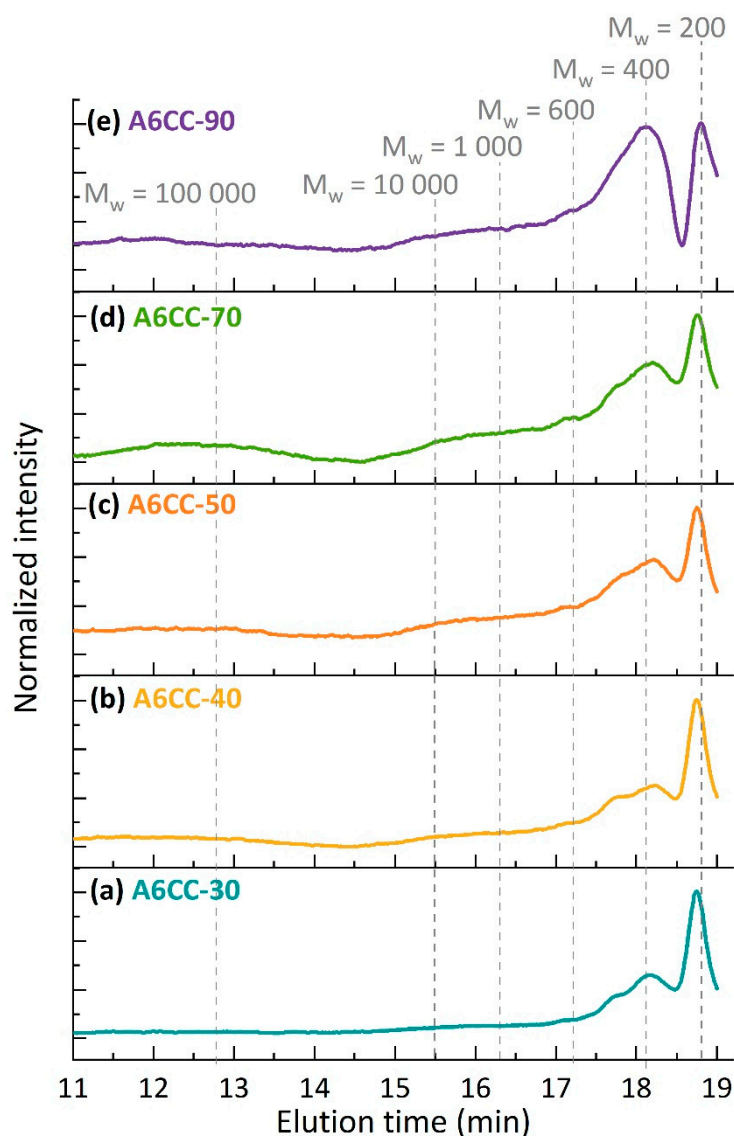
Figure 6. GPC chromatograms of the of the series of A6CC samples in chloroform: (**a**) A6CC-30, (**b**) A6CC-40, (**c**) A6CC-50, (**d**) A6CC-70 and (**e**) A6CC-90. For reference, dashed lines indicate the weight average molecular weights of the polystyrene calibration curve.

As expected for plasma-induced polymerizations, even with a first fractionation by GPC (Figure S8), the high complexity of the HMRS spectra revealed the presence of a mixture of compounds of different chemical structures. Indeed, in absence of a chemical initiator, as it would be the case for conventional radical polymerizations, plasma-induced polymerizations rely on the creation of radical species to initiate the reaction. Since plasmas are composed of a wide variety of reactive species, including highly energetic species, a plurality of non-specific reactions (i.e., fragmentation or dissociation, ionization, recombination or integration) can take place. These radical species can also terminate polymer chain growth. Recent studies by matrix-assisted laser desorption/ionization high-resolution mass spectroscopy (MALDI-HRMS) on plasma-induced polymerized poly (alkyl acrylates) have demonstrated that the simple hypothesis of a single σ-bond breakdown per molecule to initiate the free-radical polymerization was able to resolve most of the recorded spectra. To show that, the authors combined the mass of the repeating unit (and its multiples) with the masses of up to 25 different radical and neutral fragments resulting from a single bond breakdown, considering them either as the initial and/or final end group [37]. For the sake of example, in Figure S8, the structures of potential

radical species are compiled resulting from a single fragmentation of the A6CC monomer by plasma-induced homolytic cleavage.
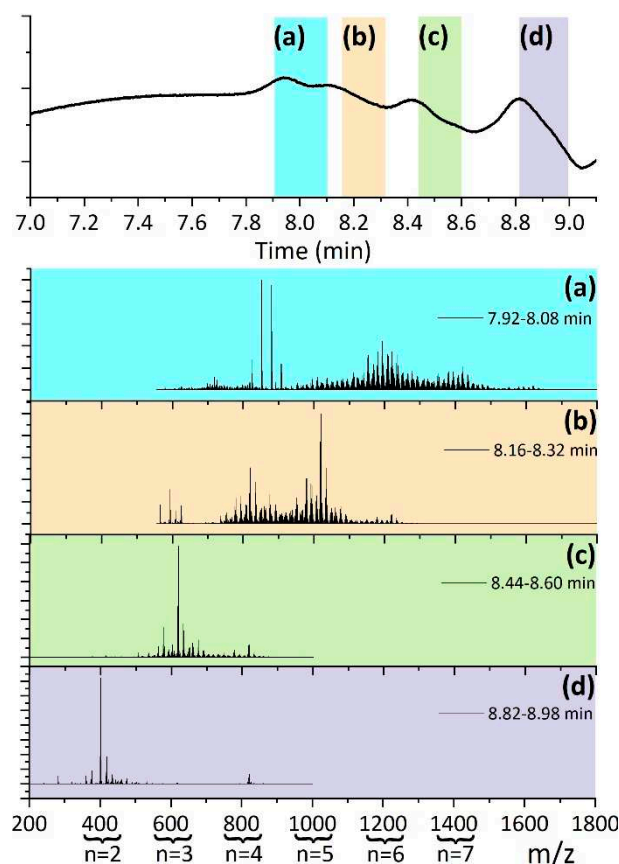
Figure 7. Chromatogram of the A6CC-90 sample obtained by GPC-HRMS. For each elution time range (**a**) 7.92–8.08 min, (**b**) 8.16–8.32 min, (**c**) 8.44–8.60 min and (**d**) 8.82–8.98 min the corresponding HRMS spectrum is displayed. The ranges are indicated by color bands in the GPC chromatogram. For reference, the number of repeating units (n) of the detected oligomers is given.

In this study, only the main peaks and isotopic patterns detected in the HRMS spectra were addressed. For each polymerization time, Figure 8 shows the average mass spectra of all the eluted samples, while the m/z values for the most relevant peaks are summarized in Table S1. In all the spectra, the ionized adducts of the monomer chemical structure (m/z: 201.113 H^+ or 218.139 NH_4^+) were detected, and the signal was used to normalize the spectra. In spite of all the combinations that were assayed considering the potential fragments from a single σ-bond breakdown and the mass of the A6CC repeating unit, most of the masses detected with higher intensity could be correlated with the ionized adducts of oligomers of different degrees of polymerization (n) with structures [H-(A6CC)$_n$-H + H^+/NH_4^+], [H-(A6CC)$_n$-CH$_2$CH=CHOCH$_2$($C_6H_9O_3$) + H^+/NH_4^+] and less abundant [H-(A6CC)$_n$-OH + H^+/NH_4^+] (as shown in Figure 9). While the unexpected high detection of oligomeric species with hydrogen atoms as the initial end group, thus suggesting the chain growth was initiated by a hydrogen radical, will still need to be properly addressed, the combination of the sensibility of allyl monomers to undergo hydrogen abstraction and the ability of plasma to abstract hydrogen atoms, including from allylic carbons by DBD plasma [38], might play a significant role. Otherwise, the detection of oligomers with hydrogen atoms as a terminal end group might reflect the occurrence of chain transfer, characteristic from the well-known allyl polymerization mechanism. Oligomers with the -CH$_2$CH=CHOCH$_2$($C_6H_9O_3$) end group could be related to the structure of the monomeric allyl radical, resulting from the hydrogen abstraction either by chain transfer reaction or by plasma-induced fragmentation. The contribution to the plasma polymerization of

oxygen and water from the atmosphere, because of the open-air configuration of the plasma reactor, could be the origin of the detection of hydroxyl terminated oligomers. The relative concentration of each of these oligomeric structures to the A6CC monomer are plotted in Figure 9 for each polymerization time. As expected, and in agreement with NMR and GPC results, the detection of oligomeric species increases with the increase in plasma exposition time. The distribution of their structures does not seem to be affected by the number of runs under plasma. The abundance of $[H-(A6CC)_n-H + H^+/NH_4^+]$ oligomers is around 2.5 times higher than their $[H-(A6CC)_n-CH_2CH=CHOCH_2(C_6H_9O_3) + H^+/NH_4^+]$ counter parts. Otherwise, the incorporation of hydroxyl groups seems to increase with the plasma exposition time, i.e., longer periods exposed to the atmospheric air.
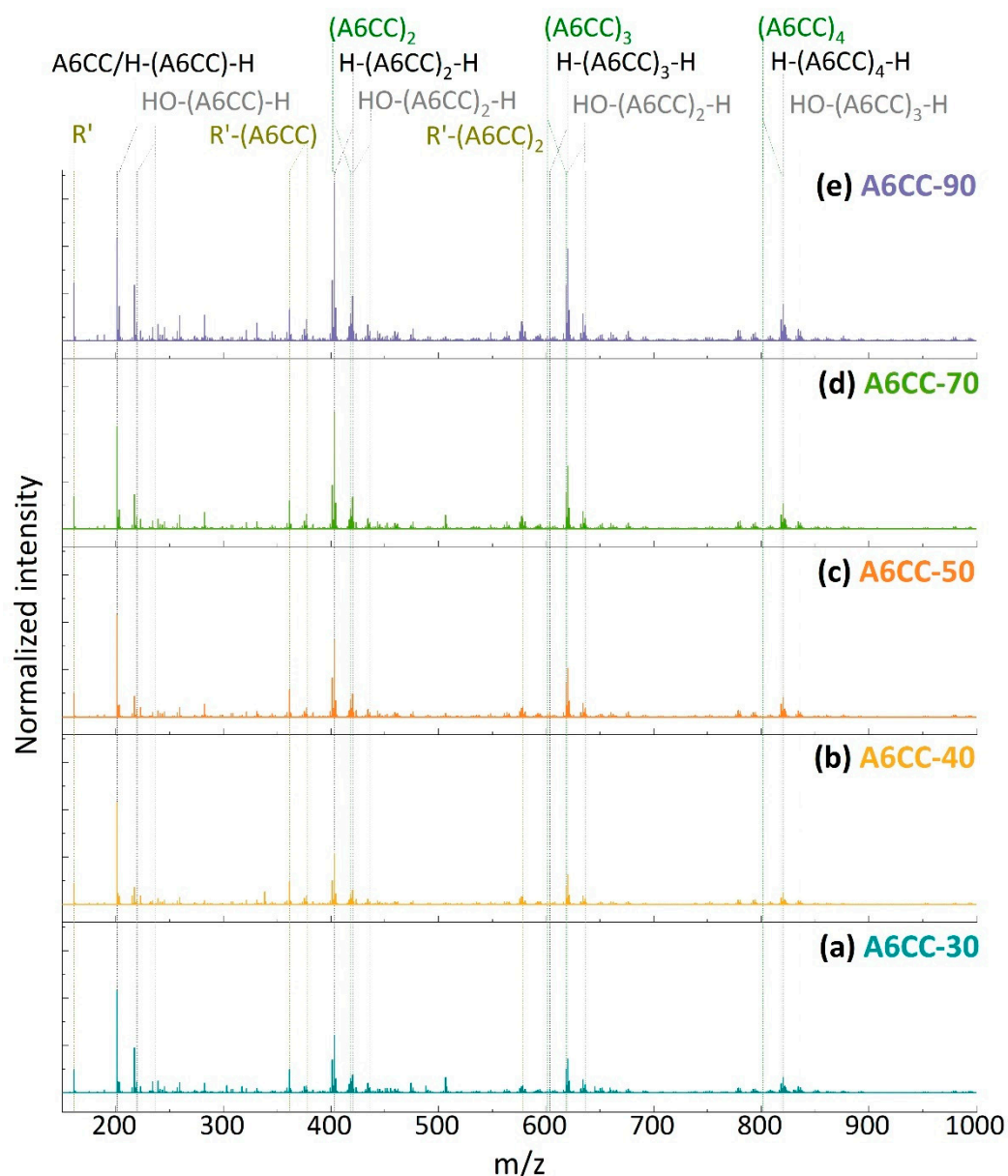
Figure 8. HRMS spectra of plasma-induced polymerization of A6CC in the mass range $m/z = 150–1000$ of (**a**) A6CC-30, (**b**) A6CC-40, (**c**) A6CC-50, (**d**) A6CC-70 and (**e**) A6CC-90. The data plotted are the result of the average spectra between 5.5 and 11 min, and the spectra were normalized to the monomer signal $[A6CC + H^+]$. The mass peaks resulting from the oligomer formation are indicated by dashed lines, where the color corresponds to the structures shown in Figure 9. The exact m/z values assigned to these structures are listed in Table S1.
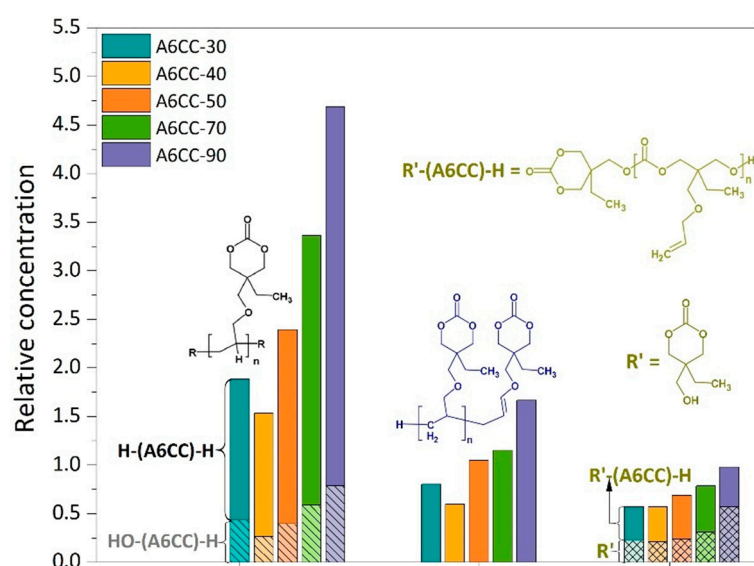
Figure 9. Relative signal intensities to [A6CC + H$^+$] monomer adducts of the products formed by plasma-induced polymerization (data from Table S1).

The HRMS spectra also revealed the presence of a wide variety of signals (especially at low m/z), non-related to those associated with the monomer and oligomers (Figure S9). In particular, the relative high intensity of the peak with the m/z value of 161.081 was addressed. As discussed previously, a byproduct was detected in the NMR analyses. The combination of both HRMS and NMR spectroscopy results allowed us to propose a chemical structure for this byproduct (R' in Figure 9). The simplest mechanism for the formation of this product could be the deallylation of the allyl ether pendent group of the A6CC monomer. While this origin remains speculative, it allowed us to address other peaks of the HRMS spectra where the detected masses supported the presence of an open form of the cyclic carbonate [R-(A6CC)$_n$-H + H$^+$/NH$_4^+$] (where n = 1 or 2 (361.186 and 578.318 m/z H+ or 378.212 m/z NH4+)). The proposed chemical structure, shown in Figure 9, resembles the structure that will be obtained by ring-opening polymerization of the A6CC initiated by the byproduct R'. In such a scheme, the alcohol moiety will act as the initiator by reacting with the carbonate carbon, leading to the production of polycarbonate oligomers [39]. Nevertheless, even if this secondary polymerization mechanism could be further supported with additional work, the HRMS results reported here clearly indicate that the plasma-induced polymerization of the A6CC monomer followed a free-radical polymerization mechanism with a high retention of the pendent cyclic carbonate.

4. Conclusions

For the first time, the feasibility of the plasma-induced free-radical polymerization of an allyl-substituted cyclic carbonate (A6CC) was demonstrated. The reaction products from the exposure of A6CC liquid layers to atmospheric-pressure DBD plasma were extensively investigated regarding the preservation of the pendent cyclic carbonate moieties and the structure of the oligomers formed. FTIR spectra confirmed the reaction of carbon–carbon double bonds and the formation of alkyl chains. Those findings agreed with the NMR results that further demonstrated the preservation of a carbonate cyclic structure, which is characterized by the interlocked diastereotopic protons of the carbonate ring. Increasing the plasma exposure time did not affect the structure of the cyclic carbonate but increased monomer conversion. After 90 s, A6CC conversion already reached 82% and rose by 10% when the exposure time was tripled. GPC analysis revealed the formation of oligomers, which agreed with the well-known low tendency of allyl monomers to homopolymerize. These findings already demonstrate the ability of atmospheric-pressure plasma to induce polymerization of the A6CC monomer. The determination of the chemical structure of the formed oligomers was attempted by coupled GPC-HRMS analyses. For the series

of samples studied, independently of the plasma exposure time, oligomeric species of up to seven repeating units were mainly detected, which agreed with a chain-growth polymerization mechanism and clearly differed from a plasma-state polymerization. While the complexity of the HRMS spectra did not allow us to address all the masses detected, those with the higher intensity could be related to the formation of oligomers with three types of end groups, i.e., hydrogen atoms, hydroxyl and a derived form of the monomeric allyl radical of the A6CC. The role of hydrogen abstraction either by chain transfer or plasma-induced fragmentation was pointed out as a preliminary hypothesis. Additionally, the combination of the NMR and HRMS results allowed us to identify and propose a low-molecular-weight byproduct that was detected in all the studied samples. Tentatively, its origin was attributed to the plasma-induced deallylation of the A6CC monomer and its role as an initiator of a ring-opening polymerization of the cyclic carbonate introduced. Overall, the results presented in this work open the door to the room temperature and atmospheric-pressure copolymerization of allyl- and vinyl-substituted cyclic carbonates for the plasma deposition of functional thin films with pendent cyclic carbonates, for instance, to exploit the high reactivity of six-membered cyclic carbonates toward primary amines for sensing and biotechnological applications.

Supplementary Materials: The following are available online at https://www.mdpi.com/article/10.3390/polym13172856/s1, detailed assignment of the ^{1}H NMR and FTIR spectra from the A6CC monomer. Figure S1: FTIR spectra of the samples after exposure of A6CC to different plasma powers and table runs. Figure S2: ^{1}H NMR spectrum of the samples A6CC-90. Figure S3: COSY spectra of the series of samples. Figure S4: Chemical structures of the A6CC monomer polymerized by the allyl and the cyclic carbonate. Figure S5: HSQC-HMBC spectra of A6CC-40, -50 and -70. Figure S6: MW distribution of the series of samples collected by GPC-HRMS. Figure S7: Overlay representation of the GPC chromatogram and HRMS spectrum of the series of samples. Figure S8: potential structures by single plasma-induced homolytic cleavage of A6CC monomer. Figure S9: zoom of the A6CC-30 sample HRMS spectrum. Table S1: m/z values of the species monitored by high-resolution mass spectrometry.

Author Contributions: Conceptualization, R.Q.; methodology, E.M.N. and G.F.; validation, E.M.N. and A.G.-L.; formal analysis, E.M.N.; investigation, E.M.N., A.G.-L. and J.R.N.H.; resources, H.S. and R.Q.; writing—original draft preparation, E.M.N., A.G.-L. and R.Q.; writing—review and editing, E.M.N., A.G.-L. and R.Q.; visualization, E.M.N.; supervision, R.Q.; project administration, R.Q. and H.S.; funding acquisition, R.Q. All authors have read and agreed to the published version of the manuscript.

Institutional Review Board Statement: Not applicable.

Informed Consent Statement: Not applicable.

Data Availability Statement: The data presented in this study are available on request from the corresponding author.

Conflicts of Interest: The authors declare no conflict of interest.

References

1. Merche, D.; Vandencasteele, N.; Reniers, F. Atmospheric plasmas for thin film deposition: A critical review. *Thin Solid Film.* **2012**, *520*, 4219–4236. [CrossRef]
2. Hopfe, V.; Sheel, D.W. Atmospheric-Pressure Plasmas for Wide-Area Thin-Film Deposition and Etching. *Plasma Process. Polym.* **2007**, *4*, 253–265. [CrossRef]

3. Mariotti, D.; Patel, J.; Švrček, V.; Maguire, P. Plasma-liquid interactions at atmospheric pressure for nanomaterials synthesis and surface engineering. *Plasma Process Polym.* **2012**, *9*, 1074–1085. [CrossRef]

4. Bonot, S.; Mauchauffé, R.; Boscher, N.D.; Moreno-Couranjou, M.; Cauchie, H.-M.; Choquet, P. Self-Defensive Coating for Antibiotics Degradation-Atmospheric Pressure Chemical Vapor Deposition of Functional and Conformal Coatings for the Immobilization of Enzymes. *Adv. Mater. Interfaces* **2015**, *2*, 1500253. [CrossRef]

5. Loyer, F.; Frache, G.; Choquet, P.; Boscher, N.D. Atmospheric Pressure Plasma-Initiated Chemical Vapor Deposition (AP-PiCVD) of Poly(alkyl acrylates): An Experimental Study. *Macromolecules* **2017**, *50*, 4351–4362. [CrossRef]

6. Loyer, F.; Combrisson, A.; Omer, K.; Moreno-Couranjou, M.; Choquet, P.; Boscher, N.D. Thermoresponsive Water-Soluble Polymer Layers and Water-Stable Copolymer Layers Synthesized by Atmospheric Plasma Initiated Chemical Vapor Deposition. *ACS Appl. Mater. Interfaces* **2018**, *11*, 1335–1343. [CrossRef]

7. Czuba, U.; Quintana, R.; De Pauw-Gillet, M.-C.; Bourguignon, M.; Moreno-Couranjou, M.; Alexandre, M.; Detrembleur, C.; Choquet, P. Atmospheric Plasma Deposition of Methacrylate Layers Containing Catechol/Quinone Groups: An Alternative to Polydopamine Bioconjugation for Biomedical Applications. *Adv. Heal. Mater.* **2018**, *7*, e1701059. [CrossRef]

8. Manakhov, A.; Fukova, S.; Necas, D.; Michlicek, M.; Ershov, S.; Elias, M.; Visotin, M.; Popov, Z.; Zajickova, L. Analysis of epoxy functionalized layers synthesized by plasma polymerization of allyl glycidyl ether. *Phys. Chem. Chem. Phys.* **2018**, *20*, 20070–20077. [CrossRef]

9. Zubov, V.P.; Kumar, M.V.; Masterova, M.N.; Kabanov, V.A. Reactivity of Allyl Monomers in Radical Polymerization. *J. Macromol. Sci. Part A-Chem.* **1979**, *13*, 111–131. [CrossRef]

10. Matsumoto, A.; Kumagai, T.; Aota, H.; Kawasaki, H.; Arakawa, R. Reassessment of Free-Radical Polymerization Mechanism of Allyl Acetate Based on End-Group Determination of Resulting Oligomers by MALDI-TOF-MS Spectrometry. *Polym. J.* **2009**, *41*, 26–33. [CrossRef]

11. Hilt, F.; Boscher, N.D.; Duday, D.; Desbenoit, N.; Levalois-Grützmacher, J.; Choquet, P. Atmospheric pressure plasma-initiated chemical vapor deposition (AP-PiCVD) of poly(diethylallylphosphate) coating: A char-forming protective coating for cellulosic textile. *ACS Appl. Mater. Interfaces* **2014**, *6*, 18418–18422. [CrossRef]

12. Kakaroglou, A.; Scheltjens, G.; Nisol, B.; De Graeve, I.; Van Assche, G.; Van Mele, B.; Willem, R.; Biesemans, M.; Reniers, F.; Terryn, H. Deposition and Characterisation of Plasma Polymerised Allyl Methacrylate Based Coatings. *Plasma Process. Polym.* **2012**, *9*, 799–807. [CrossRef]

13. Watkins, L.M.; Lee, A.F.; Moir, J.W.B.; Wilson, K. Plasma-Generated Poly(allyl alcohol) Antifouling Coatings for Cellular Attachment. *ACS Biomater. Sci. Eng.* **2016**, *3*, 88–94. [CrossRef] [PubMed]

14. Hawker, M.J.; Pegalajar-Jurado, A.; Hicks, K.I.; Shearer, J.C.; Fisher, E.R. Allylamine and Allyl Alcohol Plasma Copolymerization: Synthesis of Customizable Biologically-Reactive Three-Dimensional Scaffolds. *Plasma Process. Polym.* **2015**, *12*, 1435–1450. [CrossRef]

15. Pescarmona, P.P. Cyclic carbonates synthesised from CO_2: Applications, challenges and recent research trends. *Curr. Opin. Green Sustain. Chem.* **2021**, *29*, 100457. [CrossRef]

16. Alves, M.; Grignard, B.; Mereau, R.; Jerome, C.; Tassaing, T.; Detrembleur, C. Organocatalyzed coupling of carbon dioxide with epoxides for the synthesis of cyclic carbonates: Catalyst design and mechanistic studies. *Catal. Sci. Technol.* **2017**, *7*, 2651–2684. [CrossRef]

17. Cornille, A.; Blain, M.; Auvergne, R.; Andrioletti, B.; Boutevin, B.; Caillol, S. A study of cyclic carbonate aminolysis at room temperature: Effect of cyclic carbonate structures and solvents on polyhydroxyurethane synthesis. *Polym. Chem.* **2016**, *8*, 592–604. [CrossRef]

18. McGuire, T.M.; López-Vidal, E.M.; Gregory, G.L.; Buchard, A. Synthesis of 5- to 8-membered cyclic carbonates from diols and CO_2: A one-step, atmospheric pressure and ambient temperature procedure. *J. CO$_2$ Util.* **2018**, *27*, 283–288. [CrossRef]

19. Thomas, A.W.; Kuroishi, P.K.; Pérez-Madrigal, M.M.; Whittaker, A.K.; Dove, A.P. Synthesis of aliphatic polycarbonates with a tuneable thermal response. *Polym. Chem.* **2017**, *8*, 5082–5090. [CrossRef]

20. Mindemark, J.; Imholt, L.; Montero, J.; Brandell, D. Allyl ethers as combined plasticizing and crosslinkable side groups in polycarbonate-based polymer electrolytes for solid-state Li batteries. *J. Polym. Sci. Part A Polym. Chem.* **2016**, *54*, 2128–2135. [CrossRef]

21. Kuschmitz, D. Makromolekulare Chemie 1989. *Nachr. Chem. Tech. Lab.* **1990**, *38*, 233–241.

22. Jehanno, C.; Demarteau, J.; Mantione, D.; Arno, M.C.; Ruipérez, F.; Hedrick, J.L.; Dove, A.P.; Sardon, H. Selective Chemical Upcycling of Mixed Plastics Guided by a Thermally Stable Organocatalyst. *Angew. Chem.* **2020**, *133*, 6784–6791. [CrossRef]

23. Olsén, P.; Odelius, K.; Albertsson, A.-C. Ring-Closing Depolymerization: A Powerful Tool for Synthesizing the Allyloxy-Functionalized Six-Membered Aliphatic Carbonate Monomer 2-Allyloxymethyl-2-ethyltrimethylene Carbonate. *Macromolecules* **2014**, *47*, 6189–6195. [CrossRef]

24. Besse, V.; Camara, F.; Voirin, C.; Auvergne, R.; Caillol, S.; Boutevin, B. Synthesis and applications of unsaturated cyclocarbonates. *Polym. Chem.* **2013**, *4*, 4545–4561. [CrossRef]

25. Bayramoglu, G.; Karagoz, B.; Arica, M.Y. Cyclic-carbonate functionalized polymer brushes on polymeric microspheres: Immobilized laccase for degradation of endocrine disturbing compounds. *J. Ind. Eng. Chem.* **2018**, *60*, 407–417. [CrossRef]

26. Desport, J.S.; Frache, G.; Patiny, L. MSPolyCalc: A web-based App for polymer mass spectrometry data interpretation. The case study of a pharmaceutical excipient. *Rapid Commun. Mass Spectrom.* **2020**, *34*, 1–9. [CrossRef] [PubMed]

27. Yuan, H.; Lu, X.; Zeng, Z.; Yang, J.; Chen, Y. Allyl ether-modified unsaturated polyesters for UV/air dual-curable coatings. I: Synthesis and characterization of the oligomers and their cured films. *J. Appl. Polym. Sci.* **2004**, *92*, 2765–2770. [CrossRef]

28. He, F.; Wang, Y.-P.; Liu, G.; Jia, H.-L.; Feng, J.; Zhuo, R.-X. Synthesis, characterization and ring-opening polymerization of a novel six-membered cyclic carbonate bearing pendent allyl ether group. *Polymer* **2008**, *49*, 1185–1190. [CrossRef]

29. Udayakumar, S.; Lee, M.-K.; Shim, H.-L.; Park, S.-W.; Park, D.-W. Imidazolium derivatives functionalized MCM-41 for catalytic conversion of carbon dioxide to cyclic carbonate. *Catal. Commun.* **2009**, *10*, 659–664. [CrossRef]

30. Vijayalakshmi, S.; Mariadoss, A.V.A.; Ramachandran, V.; Shalini, V.; Agilan, B.; Sangeetha, C.C.; Balupillai, A.; Kotakadi, V.S.; Karthikkumar, V.; Ernest, D. Polydatin Encapsulated Poly [Lactic-co-glycolic acid] Nanoformulation Counteract the 7,12-Dimethylbenz[a] Anthracene Mediated Experimental Carcinogenesis through the Inhibition of Cell Proliferation. *Antioxidants* **2019**, *8*, 375. [CrossRef]

31. Mindemark, J.; Tang, S.; Li, H.; Edman, L. Ion Transport beyond the Polyether Paradigm: Introducing Oligocarbonate Ion Transporters for Efficient Light-Emitting Electrochemical Cells. *Adv. Funct. Mater.* **2018**, *28*. [CrossRef]

32. Rokicki, G. Aliphatic cyclic carbonates and spiroorthocarbonates as monomers. *Prog. Polym. Sci.* **2000**, *25*, 259–342. [CrossRef]

33. Höcker, H.; Keul, H.; Kuhllng, S.; Hovestadt, W. Ring-opening polymerization and copolymerization of cyclic carbonates. *Makromol. Chemie. Macromol. Symp.* **1991**, *42–43*, 145–153. [CrossRef]

34. Brar, A.S.; Saini, T. Optimization of atom transfer radical copolymerization of aiiyl butyl ether with acrylonitrile. *Polym. J.* **2007**, *39*, 558–567. [CrossRef]

35. Denis, L.; Cossement, D.; Godfroid, T.; Renaux, F.; Bittencourt, C.; Snyders, R.; Hecq, M. Synthesis of Allylamine Plasma Polymer Films: Correlation between Plasma Diagnostic and Film Characteristics. *Plasma Process. Polym.* **2009**, *6*, 199–208. [CrossRef]

36. Friedrich, J. *The Plasma Chemistry of Polymer Surfaces: Advanced Techniques for Surface Design*; Wiley-VCH Verlag GmbH & Co. KGaA: Weinheim, Germany, 2012. [CrossRef]

37. Loyer, F.; Bengasi, G.; Frache, G.; Choquet, P.; Boscher, N.D. Insights in the initiation and termination of poly(alkyl acrylates) synthesized by atmospheric pressure plasma-initiated chemical vapor deposition (AP-PiCVD). *Plasma Process Polym.* **2018**, *15*, 1–10. [CrossRef]

38. Heyse, P.; Dams, R.; Paulussen, S.; Houthoofd, K.; Janssen, K.P.F.; Jacobs, P.A.; Sels, B.F. Dielectric Barrier Discharge at Atmospheric Pressure as a Tool to Deposit Versatile Organic Coatings at Moderate Power Input. *Plasma Process. Polym.* **2007**, *4*, 145–157. [CrossRef]

39. Dubois, P.; Coulembier, O.; Raques, J.M. *Handbook of Ring-Opening Polymerization*; Wiley: Hoboken, NJ, USA, 2009.

Visualization of Activated Area on Polymers for Evaluation of Atmospheric Pressure Plasma Jets

Dariusz Korzec *[ID], **Thomas Andres, Eva Brandes and Stefan Nettesheim**

Relyon Plasma GmbH, Osterhofener Straße 6, 93055 Regensburg, Germany; t.andres@relyon-plasma.com (T.A.);
e.brandes@relyon-plasma.com (E.B.); s.nettesheim@relyon-plasma.com (S.N.)
* Correspondence: d.korzec@relyon-plasma.com

Abstract: The treatment of a polymer surface using an atmospheric pressure plasma jet (APPJ) causes a local increase of the surface free energy (SFE). The plasma-treated zone can be visualized with the use of a test ink and quantitatively evaluated. However, the inked area is shrinking with time. The shrinkage characteristics are collected using activation image recording (AIR). The recording is conducted by a digital camera. The physical mechanisms of activation area shrinkage are discussed. The error sources are analyzed and methods of error reduction are proposed. The standard deviation of the activation area is less than 3%. Three polymers, acrylonitrile butadiene styrene (ABS), high-density polyethylene (HDPE), and polyoxymethylene (POM), are examined as a test substrate material. Due to a wide variation range of SFE and a small hydrophobic recovery, HDPE is chosen. Since the chemical mixtures tend to temporal changes of the stoichiometry, the pure formamide test ink with 58 mN/m is selected. The method is tested for the characterization of five different types of discharge: (i) pulsed arc APPJ with the power of about 700 W; (ii) piezoelectric direct discharge APPJ; (iii) piezoelectric driven needle corona in ambient air; (iv) piezoelectric driven plasma needle in argon; and (v) piezoelectric driven dielectric barrier discharge (DBD). For piezoelectrically driven discharges, the power was either 4.5 W or 8 W. It is shown how the AIR method can be used to solve different engineering problems.

Keywords: atmospheric pressure plasma jet; dielectric barrier discharge; piezoelectric direct discharge; surface free energy; test ink; surface activation

1. Introduction

The non-equilibrium atmospheric pressure plasma (APP) is broadly used for polymer surface treatment [1–3], especially for the improvement of adhesion [4]. Even though it is a long-known technology, the surface treatment of polymers remains the focus of current research. The application examples are the improvement of adhesion on composites of polymers with natural materials [5] or applications in medical sciences, for example, tailoring of the cell growth [6].

Due to its excellent chemical and mechanical properties, polyethylene (PE) is a widely used engineering material. Its drawback is its low surface free energy (SFE) of 31–37 mJ/m^2 [7,8]. The APP is frequently used to increase the SFE of PE, to allow printing, varnishing, coating, or gluing on its surface. Examples of studies focussing on this subject include the application of dielectric barrier discharge (DBD) for the treatment of high-density polyethylene (HDPE) [9] or ultrahigh-modulus polyethylene (UHMPE) fibers [10].

A very versatile method of APP generation involves using atmospheric pressure plasma jets (APPJ) [11,12]. There exist a large number of gaseous discharge architectures used for such processing tools [13]. The APPJs are also used to increase the SFE of polymers [14,15] and, consequently, to improve the adhesion of glues and molds [5], or printability [16]. There is increasing interest in biomedical applications of cold APPJs [17].

The mechanisms of the surface modification by atmospheric pressure plasma jets (APPJ) are still not completely understood [18]. Different types of APPJ are used for the treatment of PE, for example, the high voltage blown arc [14,19], the capacitive, cold APPJ [20], DBD driven APPJ [21], or piezoelectric direct discharge (PDD) [22]. Several gases are used for APPJ treatment of PE, for example, Argon [23,24] or compressed dried air (CDA) [19]. APPJ improves adhesion to PE in 3D bio-printed structures [25] or modifies the surface properties of shoulder implants made of ultra-high molecular weight polyethylene (UHMWPE) [26]. Compared with traditional polymer surfaces activation methods, such as flaming [27,28] or corona treatment [29–33], the APPJs allow the achievement of locally much higher values of surface free energy.

The diversity of APPJ physics and chemistry makes it difficult to evaluate and compare the efficiency of different APPJs using conventional plasma plume diagnostic techniques, such as electrostatic probe diagnostics [34], dielectric probes [35], optical emission spectroscopy [36,37], absorption spectroscopy between VUV to MIR [38], electron density measurements by millimeter wave interferometry or by IR heterodyne interferometry [39], high-speed photography [40,41], or calorimetric probe [42].

A pragmatic approach for comparative plasma source evaluation is to establish a model process and define a measurable process parameter, for example, deposition rate, etch rate, or activation speed. In this work, the activation area reached after some predefined treatment time on the polymer surface is proposed as such a comparative parameter.

To determine the activation area, a novel activation image recording (AIR) technique is developed. The test inks are investigated in a wide range of the SFE and the optimum ink is selected. Three polymers, acrylonitrile butadiene styrene (ABS), high-density polyethylene (HDPE), and polyoxymethylene (POM) are examined as materials for test substrates. The tests with HDPE show its suitability for AIR.

This study aims to demonstrate that AIR is suitable for the comparison of APPJs belonging to different power classes. On the one hand, the low power (8 W) room temperature PDD type of plasma is used [22]. On the other hand, the powerful (700 W) pulsed atmospheric arc (PAA) type of APPJ is applied [43]. The suitability for different types of APPJ discharges and different gas mixtures should also be evaluated.

2. Materials and Methods

2.1. Atmospheric Pressure Plasma Sources

In this study, the activation area was produced using atmospheric pressure plasma (APP) sources with seven discharge configurations, marked with A to G, illustrated in Figure 1. The typical operation parameters for all configurations are summarized in Table 1.

Table 1. Discharge configurations and default operating parameters. Distance means the distance between the substrate and the orifice of the nozzle for A, the tip of the CeraPlas™ for B and C, the tip of the needle electrode for E, F, and the outer surface of the dielectric barrier for G.

Case	Device	Nozzle	Power [W]	Frequency [kHz]	Distance [mm]	Gas	Gas Flow [SLM]
A	plasmabrush® PB3	A450	700	54	25	CDA	35–80
B	piezobrush® PZ2	CeraPlas™ F	8.0	50	6	air	~20
C	piezobrush® PZ3	CeraPlas™ F	8.0	50	6	air	~10
D	CeraPlas™ package	CeraPlas™ HF	4.5	82	5	CDA	
E	piezobrush® PZ3	needle corona	8.0	50	3–20	air	
F	piezobrush® PZ3	plasma needle	8.0	50	3–25	Ar	3
G	piezobrush® PZ3	DBD	8.0	50	1.0	air	
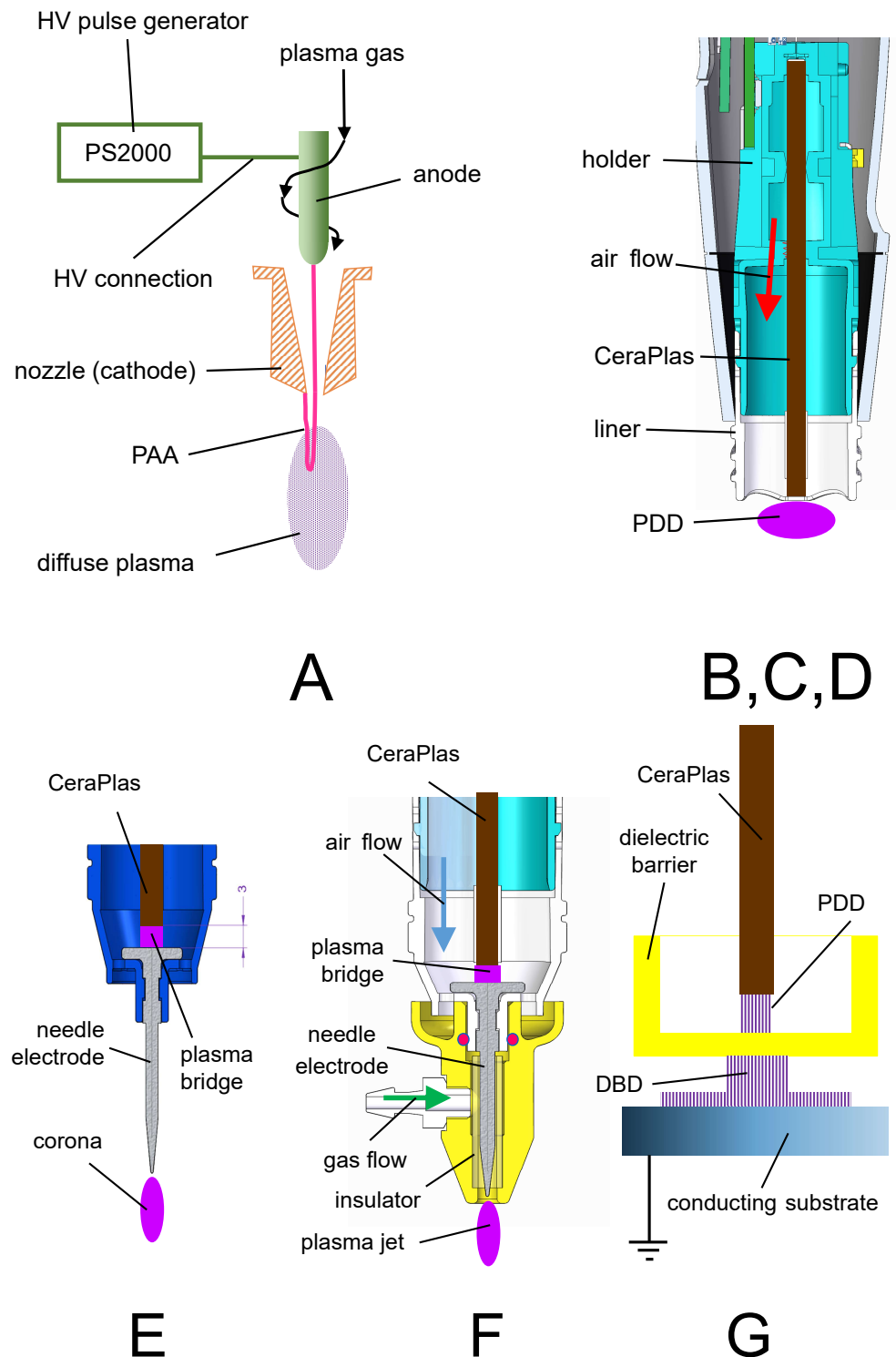
Figure 1. Discharge configurations. A—pulsed atmospheric arc (PAA) based APPJ, (B, C, D— piezoelectric direct discharge (PDD), E—piezoelectrically driven needle corona, F—piezoelectrically driven plasma needle discharge, and G—piezoelectrically driven dielectric barrier discharge (DBD).

In configuration A, the pulsed atmospheric arc (PAA) was used for plasma generation. Its operation principle is explained in detail in [43]. As an example, the plasmabrush® PB3 of Relyon Plasma GmbH with A450 nozzle was used. This APPJ is an industrial device designed for the high-speed treatment and allows control of the plasma ON-time in the ms range.

The configurations B,C, and D are all based on the piezoelectric direct discharge (PDD), described in detail in [22], but representing different technical solutions. The configurations B and C were used in the commercial hand-held devices piezobrush® PZ2 and piezobrush® PZ3 of Relyon Plasma GmbH, respectively. Both applied the piezoelectric transformer CeraPlas™ F [44] for high voltage generation. The main differences between B and C in the physical sense are the different air flows (see Table 1). For some experiments, the PDD was generated using the CeraPlas™ HF (discharge configuration D) [45], which is smaller than CeraPlas™ F. Consequently, its maximum operation power was lower and the operation frequency was higher (compare the operation parameters in Table 1).

In configuration E, a needle corona [46] was supplied with high voltage (HV) from the CeraPlas™ F over a plasma bridge [47]. This HV causes an atmospheric air corona discharge on the tip of the needle electrode.

The configuration F, referred to as a plasma needle [48], consisted of the same needle electrode as in configuration E, but was operated in a gas flow of different gas mixtures [47]. In this study, the results obtained with argon as a plasma gas are presented.

The discharge configuration G produced a dielectric barrier discharge (DBD) with an active electrode being the HV tip of the CeraPlas™ F. Configurations E, F and G are realized technically as replaceable modules for piezobrush® PZ3 [47].

Figure 2a shows a generic setup for substrate surface activation, with the distance d between the treated surface and the plasma source. The meaning of this distance differs depending on the configuration. The plasma source reference position for configuration A is the tip of the copper nozzle A450 of the plasmabrush® PB3. For configurations B, C, and D, this reference is the tip of the piezoelectric transformer CeraPlas™, for configurations E and F, the tip of the needle powered piezoelectrically, and for configuration G, the outer surface of the dielectric barrier.
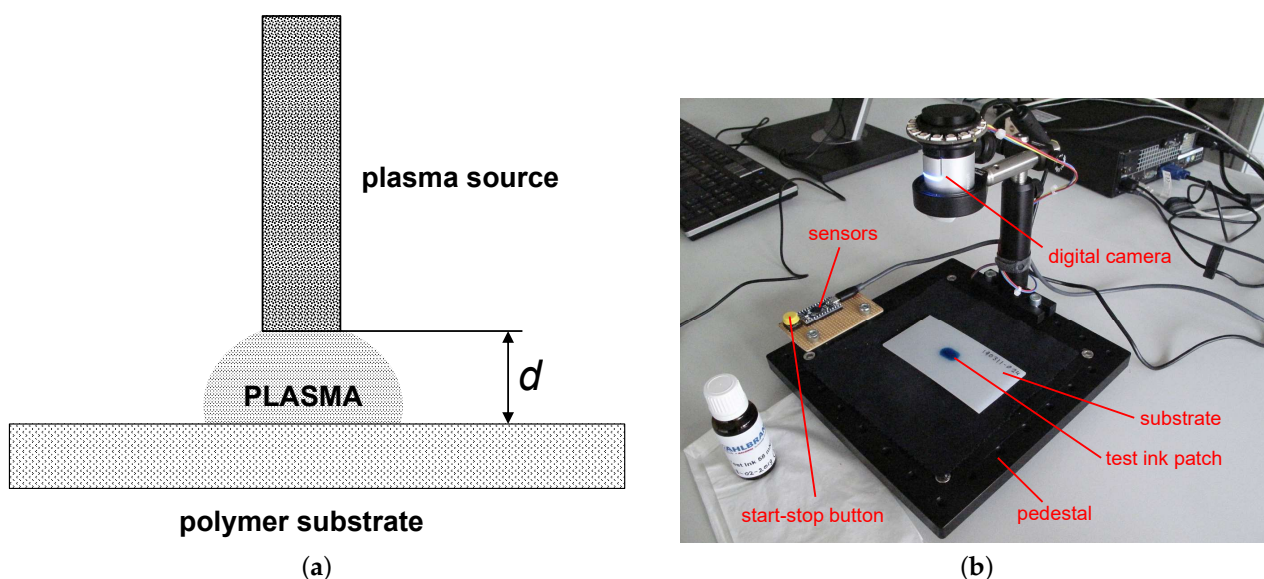
Figure 2. Experimental setup. (**a**) Generic setup for activation of the polymer substrate surface. The meaning of d depends on configuration A–G as defined in Table 1. (**b**) Picture of setup for AIR.

2.2. Visualization of the Activation Area

The activated zone on the surface of the polymer substrate produced using one of the discharge configurations listed in Table 1 can be visualized by spreading a test ink over the substrate surface. The properly chosen value of the test ink (see Section 2.4.3) assures that the ink is wetting only the activated surfaces and rolls off the non-treated surface areas.

The plasma source was positioned at a given distance from the substrate surface and the power was switched on for a short predefined time. Figure 3 shows the shapes of the visualized activation area produced using discharge configuration A, C and G. As can be

expected, the rotationally symmetric configuration A produces a rotationally symmetric activation zone. The difference between pictures A_1 and A_2 is in treatment time, which is 100 ms and 3 s, respectively. In the case of A_2, the treatment time is so long, that the thermal damage in the center of the activation zone occurs, resulting in the reduction of the SFE.

The pictures C_1 and C_2 show the activation zones produced in configuration C. The activation zone visualized in picture C_1 was produced by a 10 s treatment at a distance of 4 mm. The kidney-like shape was caused by the shape of the discharge itself, following the rectangular geometry of the CeraPlas™ F HV tip. The image in C_2 was obtained at the much larger distance of 10 mm and the shorter treatment time of 1 s, resulting in the splitting of the activation zone into two small sub-zones. The activation images produced using configurations B and D are very similar to the image for configuration C because they were also generated by the piezoelectric device of CeraPlas™ type.

The pictures G_1, G_2 and G_3 show the activation areas produced in configuration G. The characteristic four-folded shape in G_2 is caused by the four fixtures used to keep the quartz dielectric barrier cup. The pictures G_1 and G_3 demonstrate how the tilting of the plasma handheld instrument affects the shape of the activation area. The tilting was performed in the direction perpendicular to the narrow and to the wide sides of the CeraPlas™ F, respectively.

The circular activation areas related to the rotationally symmetric needle electrodes of configuration E and F are not shown in Figure 3.
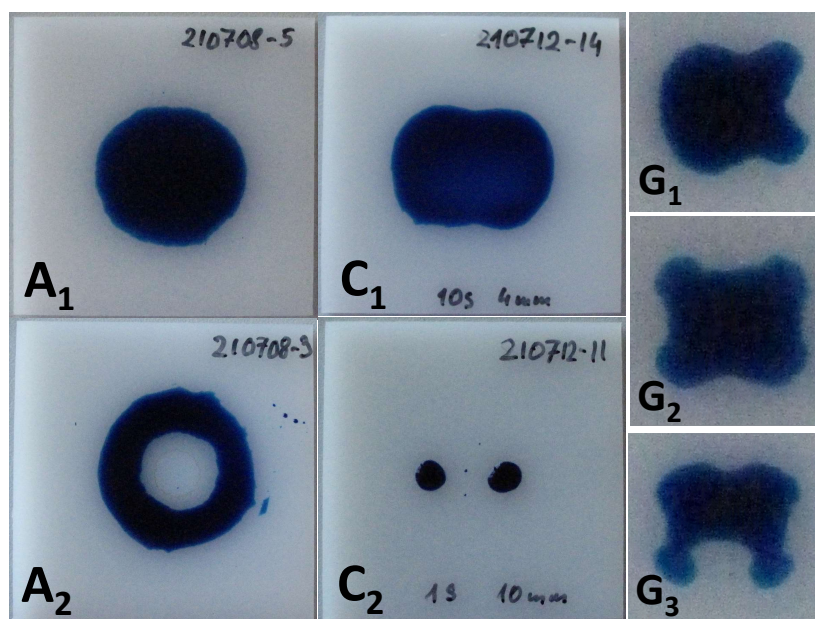
Figure 3. The shapes of the activation area visualized by the 58 mN/m test ink on the HDPE substrate for configurations A, C and G. The sizes of the substrates seen in pictures for A and C are 50 mm × 50 mm. The treatment times are 100 ms, 3 s, 10 s, 1 s and 20 s for A_1, A_2, C_1, C_2, and G_{1-3} respectively.

2.3. Activation Image Recording

The shape of the activation area provides interesting information about the character of the plasma source used for the activation. However, for quantitative evaluation of the plasma source performance, some reference value must be defined. In this study, the area of the activation visualized by the test ink is such a value. To increase the accuracy and repeatability of the evaluation of the test ink patches, the automated method of ink patch area determination was introduced. Since the area of the ink patches changes over time (see Section 3.1.1) the pictures of the ink patch were taken in short intervals with a digital camera (see Figure 2b). The contour of the ink patch was automatically recognized and the number of pixels was counted. By comparison with the number of pixels of the known area

of the entire substrate, the actual area of the test ink patch was calculated. The algorithm applied in the activation image recording (AIR) the method has some limitations. The image recognition was optimized for dark blue ink on a white substrate. If the test ink was of another color or was too pale, errors in recognition of the ink patch boundary could occur. Such errors are also possible if the substrate was dark or if the illumination of the ink patch was weak or not time-stable. In the case of splitting of the activation area into more than one patch, as shown in C_2 in Figure 3, the largest sub-patch was selected for evaluation. The not inked areas within the ink patch, such as the inner circle shown in A_2 in Figure 3, were not subtracted.

2.4. Test Inks

2.4.1. Formamide Based Test Inks

Different liquid mixtures were used for the production of test inks suitable for the determination of the SFE of solid surfaces. The test inks defined in a number of standards [49] and gauging the surface energies from 31 to 58 mN/m were mixed with formamide and 2-ethoxyethanol (alternative names: ethylene glycol monoethyl ether or ethyl Cellosolve—registered trademark of Union Carbide Corp.). The dependence of the gauged SFE on the volume percentage of formamide in the test ink mixture is shown in Figure 4a. For gauging the test inks in the SFE in the range from 58 to 72 mN/m, the mixtures of formamide with DI water were used. The linear approximation of the SFE on the volume percentage of fomamide in a formamid–water mixture is also shown in Figure 4a.
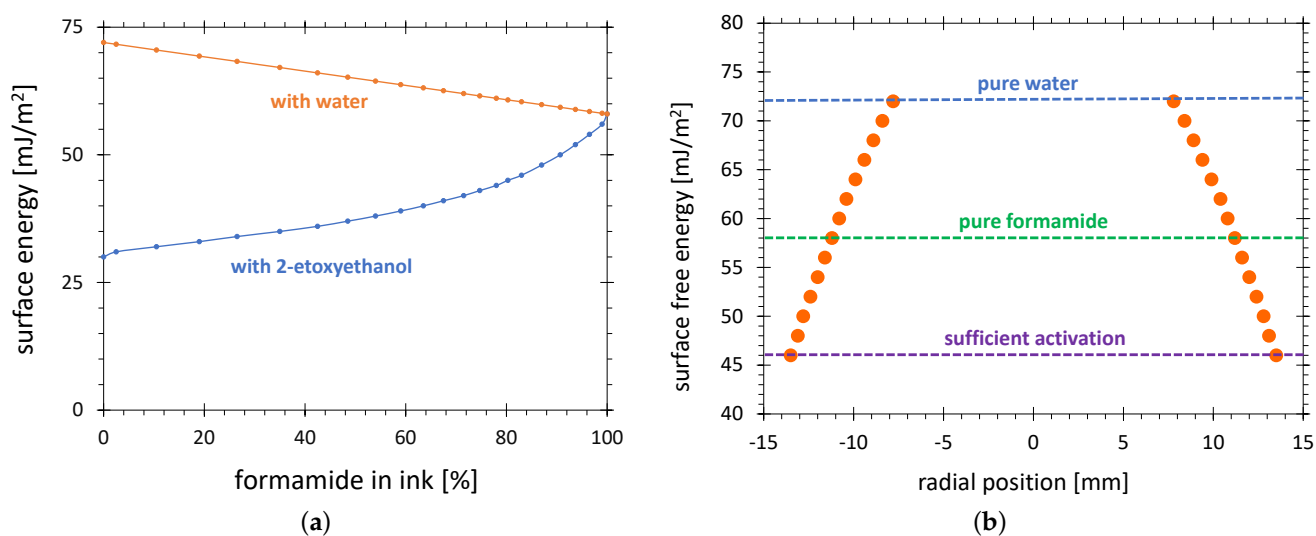
Figure 4. Determination of the SFE by use of the test inks. (**a**) The SFE gauged by the test ink consisting of formamide mixed with 2-ethoxyethanol (blue curve, according to [49]) and formamide mixed with water (red line, linear approximation) as a function of formamide volume percentage; (**b**) The typical radial distribution of the SFE after HDPE treatment in configuration C. The SFE levels for water and formamide test inks, and for the levels sufficient for printing on HDEP, are depicted with dashed lines.

2.4.2. SFE Radial Distribution

Since the chemically active species causing the surface activation were not distributed homogeneously across the plasma plume of an APPJ, the SFE also varies across the activated zone. Consequently, applying the test inks gauged with different SFEs, different sizes of the activation zone were obtained. Figure 4b shows the radial distribution of the SFE on an intensively treated HDPE. The size of the visualized activation zone almost doubled if the test ink 46 mN/m was taken instead of the pure water-based test ink 72 mN/m. On the one hand, the relative accuracy of the AIR method improves with the size of the activation zone. On the other hand, a too low SFE of the test ink results in large visualized areas even for poor activation. The SFE value of 58 mN/m is a good compromise between these two

extremes. The intensive treatment means that a large part of the activation area reaches the saturation value of 72 mN/m. For weak treatment, the SFE distribution curve could be below the 58 mN/m resulting in no visualized activation area. The SFE distributions reaching just over the 58 mN/m line would be not suitable, because the visualized area would be very sensitive to any random influences and the results would be unreproducible. The assumption for the validity of the AIR method is that the treatment time is long enough to assure the intensive treatment.

2.4.3. Aging of Test Ink

Since the 2-ethoxyethanol is more volatile than the formamide, the stoichiometry, and consequently the SFE gauged by test ink mixed from formamide and 2-ethoxyethanol, can increase over time. It corresponds to the movement to the right along the blue line in Figure 4. This test ink will show a smaller activation area than the not aged test ink. No such change of composition is exhibited by the 58 mN/m test ink, because it is made of 100% formamide. The pure formamide has a surface tension of 58.2 mN/m but the commercially available inks are specified with some tolerance, typically ±0.5 mN/m. No sensitivity to stoichiometry was an important reason for the selection of this specific ink as a standard for this study.

Despite using the test ink consisting of a single liquid chemical, strong differences in the visualization result can be observed when older formamide test inks are used. The activated areas visualized with test ink from vials differing in age by more than 2 years differ by more than 25%. On the other hand, the results obtained with fresh ink from different vials are very reproducible with the relative standard deviation of visualized areas of less than 3%.

The other origin of the instability of formamide based test inks is their hygroscopicity [50]. When absorbing moisture from humid air, the test ink dyne number shifts in the direction of higher values causing a decrease of the visualized surface. It corresponds to the movement to the left along the red line in Figure 4.

To avoid the aging of the ink, only fresh ink vials were used and the vial remained open only for a short time of ink application.

2.4.4. Environmental Influences

It is known that environmental conditions, such as air temperature, relative humidity and pressure, have a significant influence on the wetting properties of liquids on polymer surfaces. The liquid temperature has a significant influence on its surface tension. The temperature coefficient of surface tension is −0.1514 and −0.0842 mN/(K·m) for water and formamide, respectively. Consequently, a variation of temperature of more than 10 K would cause the change of the calibration number of the formamide test ink.

It is documented in the literature that the increase of the pressure causes an increase of the contact angle [51], which manifests in a decrease in the activation area.

The humidity influences both the surface tension of the liquid water–air interface [52] and the water contact angle on the solid surface [53].

To evaluate the influence of the environmental factors on the activation area results, these conditions are logged in during the test ink patch evaluation. The temperature, humidity, and pressure sensors are placed at a distance of 10 cm from the optical axis of the digital camera (see Figure 2b).

2.5. Substrates

The substrates used in this study are made of three pristine polymers: acrylonitrile butadiene styrene (ABS), high-density polyethylene (HDPE), and polyoxymethylene (POM) and are delivered by Rocholl GmbH, Germany. It is known that additives, such as stabilizers, have a strong influence on the surface properties of polymers [54]. For test substrates, the "natural" HDPE without additives were used. For plasma treatment and activation area evaluation the substrates with sizes 100 mm × 50 mm × 2 mm or 50 mm × 50 mm ×

2 mm were used. The second one was assumed if no explicit information was included. For plasma treatment, the substrates were fixed on a solid block of HDPE with sizes 100 mm × 100 mm × 10 mm. Only the substrates treated in discharge configuration G were placed on a grounded metal plate.

According to the standard [49], the substrates were preconditioned after delivery at least 40 h under 23 °C and 50% humidity. No cleaning procedure was applied. All substrates were treated with plasma and exposed to the test ink at temperature 23 °C ± 2 K and a relative humidity of 50% ± 5%.

3. Results and Discussion

The results consist of two parts. In the first part, different influences on the visualized activation area are analyzed and the definition of the activation area, as used for the evaluation plasma sources' performance, is proposed. In the second, the proposed definition of the activation area is implemented to evaluate different types of APP sources.

3.1. Activation Area Determination

3.1.1. Shrinkage of the Test Ink Patch

As Section 2.3 stated, the activated area wetted with test ink decreases significantly with time. The strongest change is observed within a few seconds after application of the test ink. The stable value is reached within minutes. The dependence of the visualized activated area on time elapsing after an ink application, as shown in Figure 5a, will be called shrinkage characteristics.
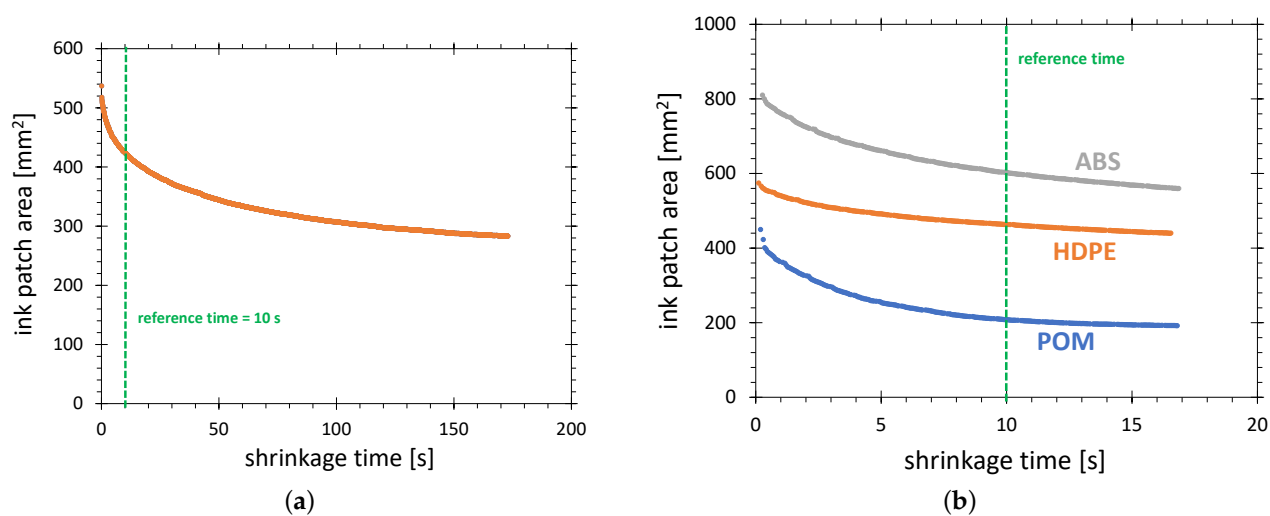
Figure 5. Shrinkage characteristics of the 58 mN/m test ink patch (**a**) taken for 3 min on HDPE, and (**b**) taken 17 s on three substrate materials: ABS, HDPE and POM. The discharge configuration C was used.

In this example, the shrinkage speed of the test ink patch decreases with time. In the first second, the ink patch area decreases by 8%. At 7 s after wetting, the shrinkage speed is about 1.4% per second. At 2 min after wetting, it is only 0.11%/s. As a reference time for the AIR method, the time of 10 s with shrinkage speed of 0.8%/s is set. It is a compromise between a large error in the surface determination for very short times and the influence of material and environmental factors for very long times.

The activation area visualized after 10 s of shrinking corresponds, not exactly, to 58 mN/m. Due to the water absorption in the ink after 10 s, the ink shows the wetting of surfaces with higher surface free energy than 58 mN/m. The value for $t = 0$ s would correspond to exactly 58 mN/m because the test ink has this property immediately after application only. The application recipes for the commercial test inks prescribe that the evaluation of the ink wetting should be conducted within 2 s after application, accepting the disadvantage of the very fast-changing of the ink wetting properties in this time range.

3.1.2. Selection of Substrate Material

The selection of the substrate material has a strong influence on the accuracy and activation area range of the AIR method. On the one hand, it is important that the selected material should have the SFE without plasma treatment far below the value of 58 mN/m. On the other hand, the maximum SFE reachable after the plasma treatment should be significantly higher than 58 mN/m.

The formamide based test inks are "blind" on the polar component of activation on some plastics; an example is a popular polymer PVC (polyvinyl chloride) [55]. Such materials can be excluded as a standard for plasma sources' evaluation. Another group of materials, not suitable for this purpose, is that exhibiting a strong hydrophobic recovery [56,57]. The materials that significantly lose their hydrophilicity obtained by plasma treatment after minutes are, for example, thermoplastic polyurethane (TPU) [58] or polydimethylsiloxane (PDMS) elastomer [59]. A comparatively weak hydrophobic recovery exhibits polyethylene (PE), especially if treated with oxygen-containing plasmas [60]. Its native contact angle with deionized water is about 90° and the SFE of the HDPE substrates used in this study is 36 mN/m. The measurements conducted in our lab with the use of a Krüss droplet test instrument show that the SFE of 66 mN/m and the contact angle of 34° reached after brief plasma treatment remains unchanged after 4 h in ambient air. The contact angle increases in 100 days by 7°, which is much less than for many common polymers. For a change of activation area with storage time after treatment—see Section 3.1.6. Our measurements on ABS substrates plasma-treated in configuration A also show no measurable hydrophobic recovery 4 h after the plasma treatment.

Due to the wide range of SFE after plasma activation and low hydrophobic recovery, the ABS, POM and HDPE are suitable substrate materials for the AIR method. To select the best material among these three, the shrinkage characteristics for these materials were collected. The results are shown in Figure 5b. Two disadvantages of POM can be stated. First, the activation area of POM is much lower than that of ABS and HDPE, causing the reduced resolution of the AIR technique. The second is the speed of variation of the activation area. The ratio of starting area to the area after 10 s of shrinking is 2.07 for POM, compared with 1.35 and 1.25 for ABS and HDPE, respectively.

The possible explanation of the strong variation of the shrinkage characteristics for POM can be its strong water absorption reaching up to 0.5% of water in comparison with HDPE, absorbing only up to 0.01% of water. In the case of POM, the water from the substrate can be absorbed by the hygroscopic formamide, increasing the gauged surface free energy and consequently decreasing the visualized activation area.

The high sensitivity on plasma activation makes ABS advantageous as a reference substrate for the evaluation of weak plasma sources. The well-defined pure water test ink with 72 mN/m can be used in combination with ABS substrate. The red curve in Figure 6a shows the activation area on the ABS surface generated in configuration G as a function of the SFE value of the test ink. The curve shows that, after only a 10 s treatment, a very small variation of the activation area of 7% is observed when changing the SFE of the activation area definition from 46 to 72 mN/m. The consequence is the reduced range of activation area available for the AIR method. A small difference between strongly and weakly activated areas can be expected. In contrast to ABS, the HDPE substrates show a very strong variation of the activation area with SFE value of the test ink, more than doubling, when the SFE value of the test ink decreases from 72 to 46 mN/m. A similar difference is observed for HDPE activated in configuration C (see Figure 6b). This outstanding range of the activation area on HDPE was an important reason for the selection of HDPE as a standard material for the AIR method.
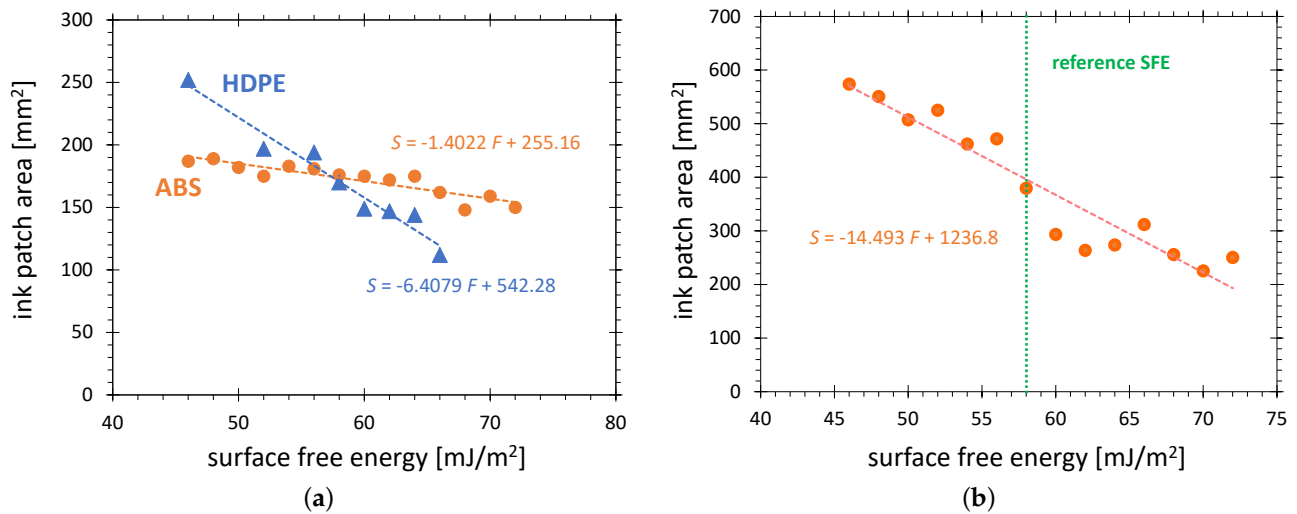
Figure 6. The visualized activation area on a substrate surface as a function of SFE calibration of the test ink. (**a**) Discharge configuration G was used with the treatment time of 20 s on HDPE and 10 s on ABS; (**b**) Discharge configuration C was used for 10 s treatment on HDPE.

3.1.3. Ink Patch Shrinkage Mechanism

In this section, results are presented that support the thesis that the increase in water concentration in the formamide test ink layer is the main reason for the ink patch shrinkage.

During the collection of shrinkage characteristics, the relative humidity in the substrate vicinity was raised intentionally by about 10% for 5 s. During this time, a strong increase in the shrinkage speed can be observed (slope line 2 in Figure 7a). This result confirms the shrinkage mechanism based on the increase of water content in the ink. A significantly smaller shrinkage speed after exposure to higher humidity (slope line 3 in Figure 7a) than before exposure (slope line 1) can be explained by this effect. Since during the exposure of the ink to air with higher humidity, a higher concentration of water in ink is reached, after establishing the previous value of humidity, the shrinkage speed is lower because the concentration gradient of water in the air and the ink is lower.
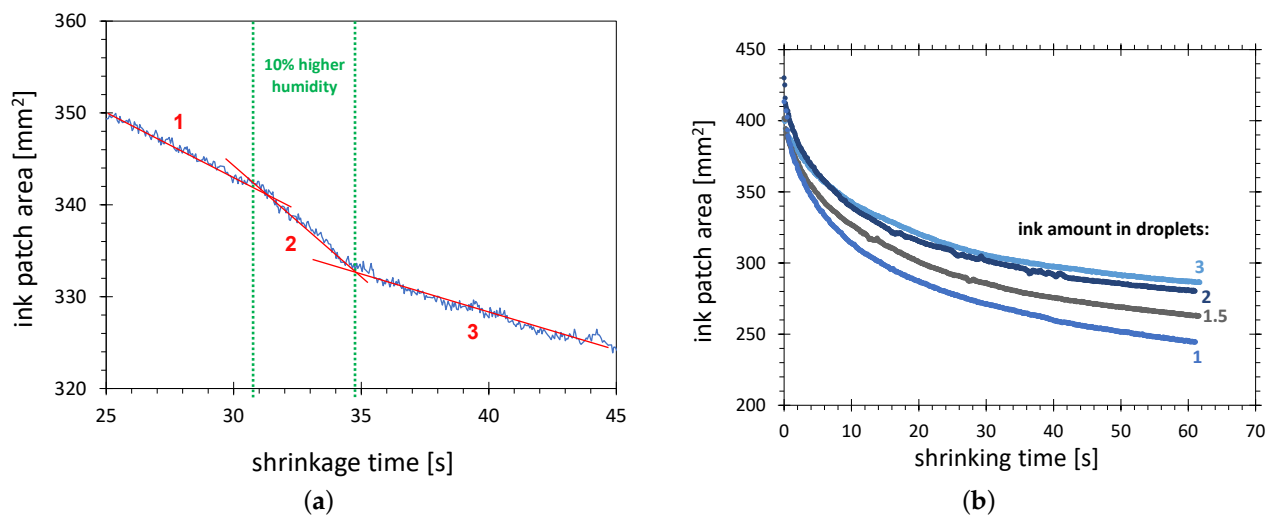
Figure 7. Shrinkage characteristics of the 58 mN/m test ink patch on HDPE plasma-treated in configuration C. (**a**) The segment showing the influence of increased air humidity; (**b**) The influence of the different amounts of applied ink.

The amount of applied test ink has a significant influence on the shrinkage characteristics. In Figure 7b, the curves for the increasing amount of ink, given in droplets (1 droplet ≈ 8 μL), are shown. The strongest variation of the shrinkage characteristics is for the

smallest amount of ink. This correlates with the scenario of humidity penetration from the ambient air into the test ink. The larger the amount of the ink, the lower the water concentration and, consequently, the smaller the SFE change gauged by the test ink. This scenario is also in agreement with the observation that the difference between curves for one and two droplets is much larger than between the curves for two and three droplets.

The differences for the 10 s point are in the range of 10%, which is significant for the AIR method. To minimize the error resulting from this effect, the amount of ink should be proportional to the activation area, to keep the thickness of the ink film constant. The pragmatic rule for the experiments in this study is that the activation areas below 300 mm^2 are visualized with a single ink droplet, and, for activation areas larger than 300 mm^2, with two droplets.

3.1.4. Influence of Ink SFE Value on Shrinkage Characteristics

Figure 8 shows the relative (all values of one curve are divided by its maximum value) shrinkage characteristics for the test inks in the range from 46 to 72 mN/m. They correspond to the activation area points from the plot in Figure 6b. The variation of the shrinkage characteristics from 46 to 58 mN/m, shown in Figure 8a, increases with increasing gauged SFE value, which correlates with an increase in the volume percentage of the formamide in the 2-ethoxyethylene/formamide test ink. In this case, the hygroscopic properties of the the formamide can explain this tendency. The higher volume percentage of the formamide in the test ink, the faster the absorption of the water from humid air in hygroscopic formamide and, consequently, the stronger the change of the gauged SFE. However, a geometrical effect can also play an important role. With the increasing total area of the ink patch, accompanying the test ink SFE value reduction, the same linear shift of the patch boundary during shrinking results in less relative area change.
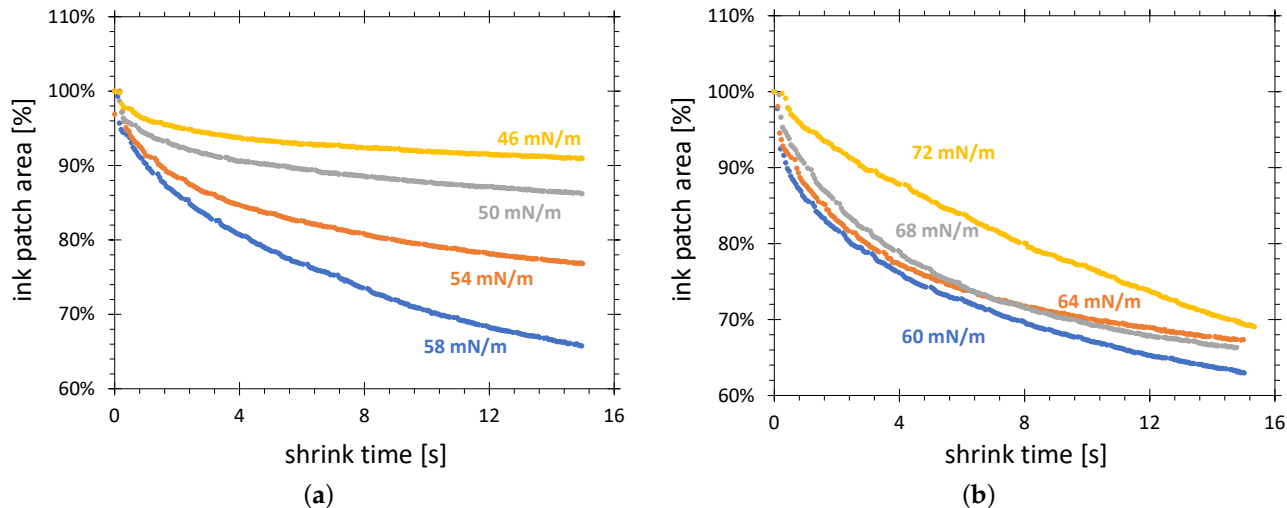
Figure 8. Comparison of relative shrinkage curves for test inks produced as mixtures of formamide with (**a**) 2-ethoxyethylene, and (**b**) water. The HDPE substrate was treated in configuration C.

Figure 8b shows the shrinkage characteristics recorded for the mixture of formamide with water. A shrinkage mechanism different to that described earlier must be considered for an explanation of these curves, because the presence of water in the mixtures excludes a strong change due to water absorption. The faster evaporation of formamide than water could be speculated, but the shrinkage characteristics for test ink gauged with 72 mN/m (100% water) require different explanations most probably based on an interaction between water and the activated HDPE surface.

3.1.5. Renewed Ink Application

For a better understanding of the mechanisms of the ink patch shrinkage, the shrinkage characteristics were collected after renewed test ink application on the same patch. This experiment should show whether the origin of the shrinkage is related to the change of substrate surface properties or ink properties. In Figure 9a, the shrinkage characteristics for the fresh ink patch and the same ink patch refreshed two, four, and six times by the new test ink are shown. It can be observed that the starting points of all four shrinkage characteristics are quite close to each other. This means that the application of fresh ink causes gouging of the starting value of the visualized surface, which allows the conclusion that no substantial change in the activation area between taking two subsequent characteristics occurs. The conclusion of this experiment is that the changes in the test ink properties themselves are responsible for the shrinkage of the test ink patch.
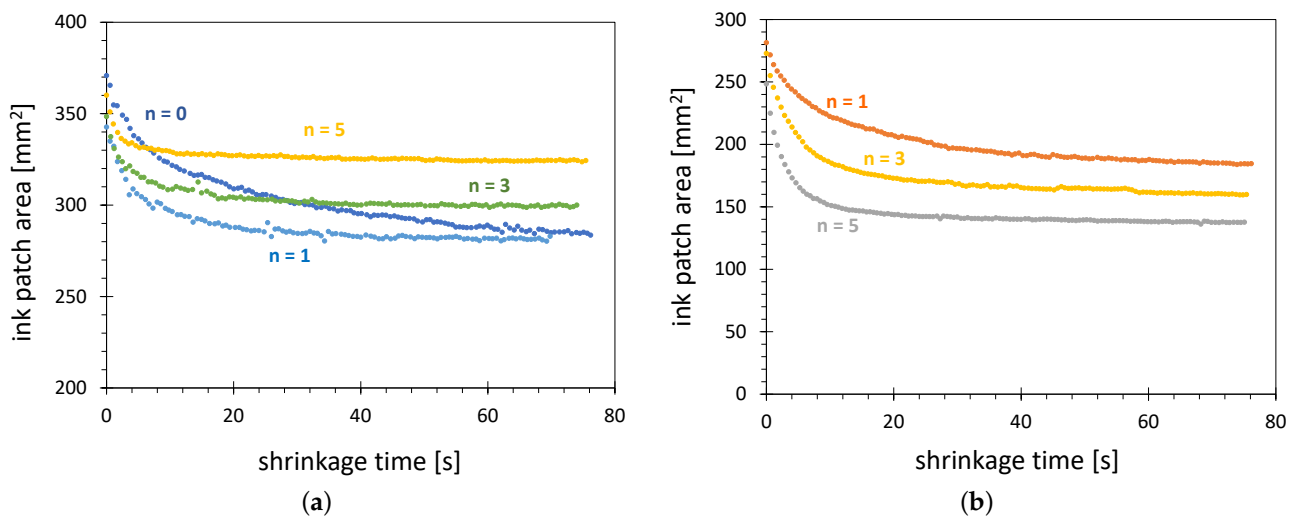
Figure 9. Shrinkage characteristics of the 58 mN/m test ink patches (**a**) directly after first ink application, after 1, 3 and 5 ink re-applications and (**b**) after 1, 3 and 5 ink wiping and renewed application. Treatment conducted in configuration D with the power of 4.5 W at the distance of 5 mm.

To ensure that the shrinkage characteristics start with test ink without water admixture, the series of shrinkage characteristics were collected for fresh ink applied on the activated area after the removal of the previously applied ink. The test ink was removed by dabbing off with cellulose tissue. In Figure 9b, three such characteristics are shown for inking after one, three, and five ink removal/application cycles. It can be observed that the starting point of all characteristics is roughly at the same level, confirming the thesis that no change of the 58 mN/m activation area occurs. The observable change is the shift of the asymptotes to which the characteristics converge. They decrease with the number of whippings and re-applications of the test ink. The possible explanation of such behavior is the decrease of the maximum SFE on the HDPE surface after each wiping of the test ink. It is known that PCT (physical contact treatment), for example by the use of cellulose tissues, causes strong hydrophobic recovery. It was documented for PS, COP and PDMS in [61] that mechanical rubbing the activated surfaces causes the hydrophobic recovery. The ink removal with tissue from the HDPE surface can partially affect the layer of activation and cause the reduction of the SFE values. The flatter surface distribution of SFE results in a larger area decrease by a small change of the SFE gauged by the test ink.

3.1.6. Hydrophobic Recovery

Typically, the hydrophobic recovery refers to the decrease of the SFE during long-term storage. For example, on oxygen-plasma treated polyethylene surfaces, a strong hydrophobic recovery is described [62]. The surface free energy of 46 mJ/m^{-2} reached on

LDPE after corona treatment decreases after 22 days of exposition to air, down to the SFE of 36 mJ/m^{-2} [63], compared with the SFE for non-treated LDPE of 31 mJ/m^{-2}.

In this study, the hydrophobic recovery refers to the reduction of the visualized activation area as a function of storage time. Figure 10 shows such a dependence for HDPE surface treated in configuration D. No hydrophobic recovery is stated in the time scale of the AIR measurement.
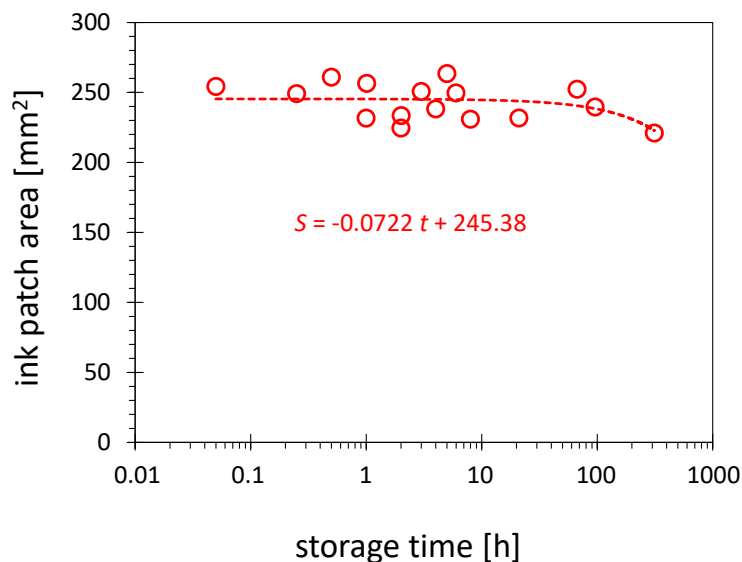
Figure 10. Influence of the storage time on the activation area. The plasma treatment of HDPE substrates was conducted in configuration D and visualized with the 58 mN/m test ink.

Despite the hydrophobic recovery documented for HDPE, no significant reduction of the activation area can be observed after storage of the activated substrates over an extended period. The results in Figure 10 document the changes over 300 h. The trend line shows in this time a decrease of 3 % of the activation area per 100 h. This result is not contradictory to the previously reported hydrophobic recovery results because those are related mainly to the decrease of the maximum value of the SFE reached after plasma treatment. Since the SFE of 58 mN/m used as a threshold for visualization in this work, which is much less than the maximum value of SFE obtained after treatment in configuration D, reaching the SFE of up to 72 mN/m (see Figure 6), the contour with 58 mN/m does not have to be affected much by the decline of the maximum SFE.

3.2. Characterization of Plasma Sources

To demonstrate the plausibility of the results collected with the AIR method, typical examples of operational characteristics of different APPS are presented and discussed. These are the dependence of the activation area (58 mN/m test ink on HDPE) on the treatment time and the distance from the plasma source.

3.2.1. Dependence on Treatment Time

Fricke et al. [64] showed that the width, defined by the use of the profiles of the contact angle, of the activation area produced on the surface of polyethylene with APPJ non-linearly increases with treatment time and shows a tendency to saturate for very long treatment times. A similar behavior is observed for activation areas generated for both the PDD type plasma jets (see Figure 11a) and the PAA based plasma jets (see Figure 11b).
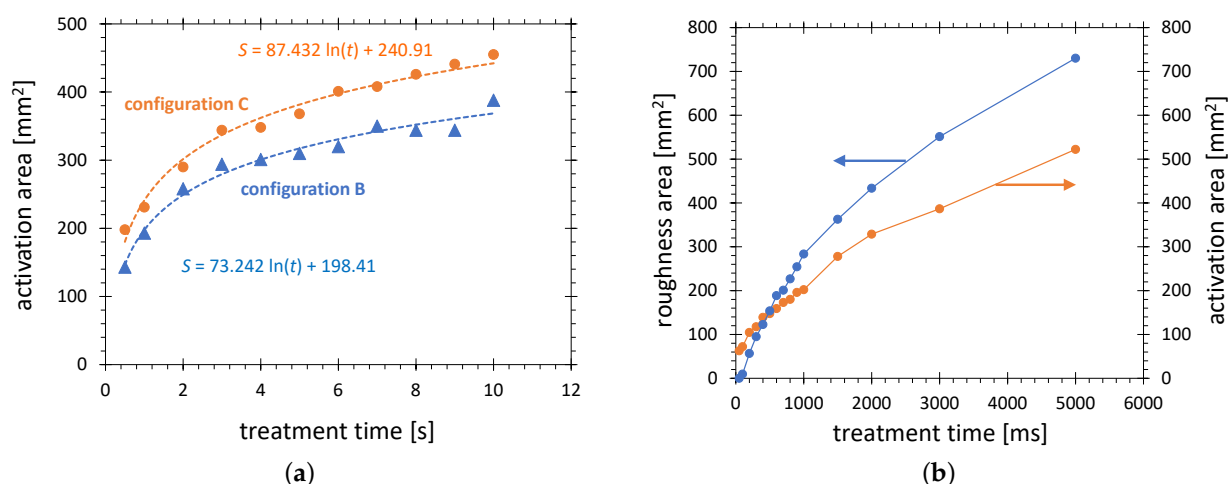
Figure 11. Dependence of activation area (58 mN/m, HDPE) on the treatment time. The plasma treatment is performed in configurations (**a**) B and C, and (**b**) A, operated at conditions from Table 1, respectively. The area of thermally induced loss of glossiness is included for comparison.

The two curves in Figure 11a show the dependences of the activation area on the treatment time for configurations B and C, respectively. The main difference between the operating conditions of these two configurations is different airflow. Configuration B is equipped with a stronger fan. The reduced dilution of the chemically active species in configuration C results in a higher activation efficiency, which is documented by a 17% increase in the activation area.

Configuration A is operated with power two orders of magnitude higher than that of B and C. The consequence is a much higher plasma temperature, which ranges from a few hundred °C in the diffuse plasma zone, to several thousand °C in the arc zone. This thermal difference causes a major difference in plasma chemistry. While the PDD produces ozone and active oxygen as the main chemical species, almost no ozone and high concentrations of nitrogen oxides, such as nitric oxide (NO) and nitrogen dioxide (NO_2), are measured in gaseous products of the PAA plasma jet. Despite this difference, the PAA based plasma tools very efficiently activate the HDPE surface, with maximum SFE reaching 68 mN/m, corresponding to the contact angle of DI water of 35°. With such maximum value of SFE, the formamide gauged for 58 mN/m can be used for the quantitative evaluation of such a plasma jet.

The treatment area for configuration A was determined as a function of the treatment time and is visualized in Figure 11b. Even for the shortest pulse of 50 ms, an activation area of 63 mm^2 is determined. For plasma switched on longer than 50 ms, not only the activation area can be visualized by test ink, but also a glossy HDPE surface becomes visibly mat. Such surface changes can be explained by a preferential material abrasion of low molecular weight materials, which produces changes in surface topography [65]. An interesting point on the time scale is the cross-over of the mat area curve and the activation area curve, occurring at 470 ms. For treatment times longer than 0.5 s a partial melting in the center of the activation area can be observed. The picture of the molten zone in the middle of the mat zone on the HDPE substrate is shown in Figure 12. Such molten areas have much lower SFE compared with a non-molten surface. For treatment times longer than 2 s, the molten zone becomes not wettable with formamide 20–30 s after the ink application. Such a case of partial wetting is shown in Figure 3, picture A_2. After the reference time of 10 s, the molten zones were wettable. Consequently, the points for 3 and 5 s are included in the plot.
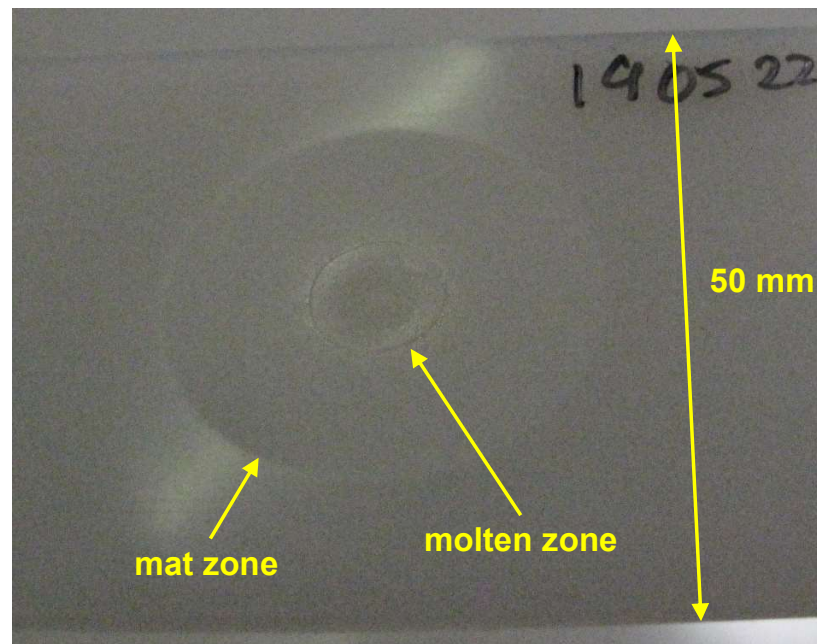
Figure 12. The picture of the HDPE substrate taken after treatment in configuration A operated at conditions from Table 1. The treatment time is 3 s.

3.2.2. Influence of the Substrate Distance

A further physical factor strongly affecting the activation area is the distance between the plasma source and the substrate. For plasma sources in configurations B and D, the activation area decreases with the distance increasing over 5 mm (see Figure 13a). This can be explained by increasing the dilution of the chemically active species and weaker electric fields enhancing the activation. The activation area for configuration B is roughly twice as high as that for configuration D because its operating power is higher by a factor of two. It can be also observed that the treatment with configuration B is possible at a larger distance of about 15 mm than for D, decaying at about 12 mm.
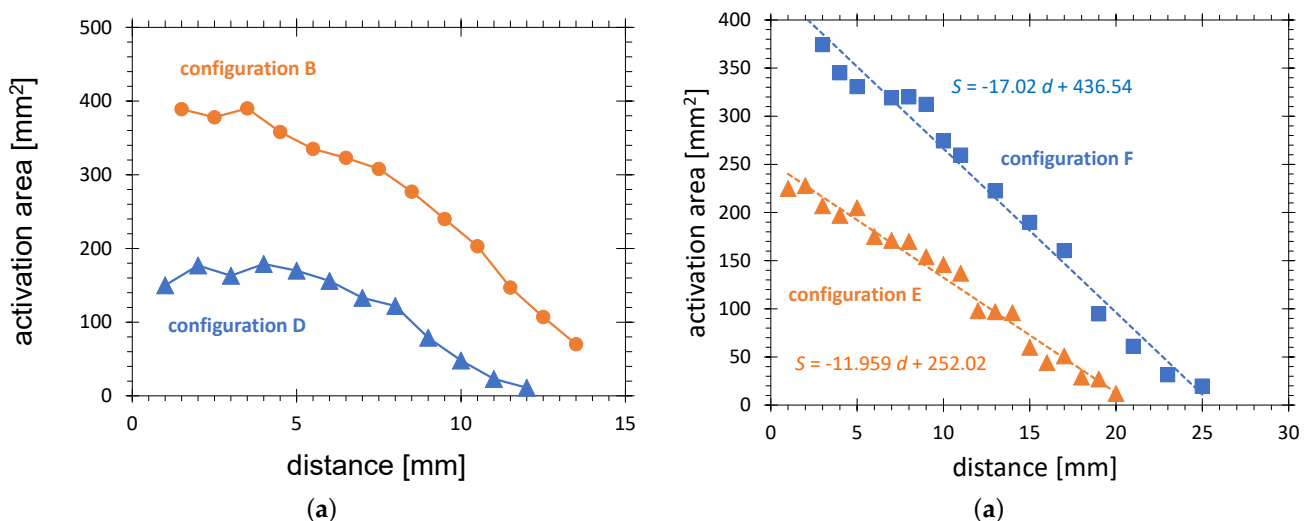
Figure 13. Dependence of the activation area (58 mN/m, HDPE) on distance for (**a**) configuration B and D, and (**b**) configuration E and F.

Much longer activation zones show the plasmas generated in configuration E operated in ambient air and F operated in argon flow. The activation area of both configurations is represented by red and blue lines in Figure 13b, respectively. The points of decay (zero

points of the fitting lines) are 21 and 26 mm, respectively, compared with 15 mm for configuration B. Configuration E is operated without airflow. Consequently, the reason for the elongation of the plasma zone can be the more focussed electric field produced by the needle electrode. The even longer plasma jet in configuration F is caused by the argon flow. It contains long-living activated species, which can be transferred over a longer distance. It also allows us to sustain plasma at much lower electric fields, due to its lower break-down voltage. These tendencies are in agreement with well known results for other types of cold APPJs [66] and confirm the plausibility of the AIR results.

4. Conclusions and Outlook

A novel method for the evaluation of the activation area produced on polymer surfaces by atmospheric pressure plasma jets is proposed. The activation image recording (AIR) with a digital camera is used for the collection of shrinkage characteristics of activation zones wetted by the test ink.

This study demonstrates that AIR can be used as a diagnostic technique for the performance evaluation of atmospheric pressure discharges at different working conditions. It is also shown that it is suitable for the comparison of strongly different types of APPJs.

HDPE is selected as the best suitable material for test substrates thanks to: (i) its wide range of SFE achieved after APPJ treatment; (ii) low hydrophobic recovery; (iii) availability as a polymer without additives; (iv) moderate cost; and (v) high popularity as a reference material for plasma studies.

For activation area visualization, the test ink gauged for 58 mN/m (pure formamide liquid) is selected because: (i) the influence of changes of the proportion of two liquids with different volatility can be avoided; (ii) the SFE value is almost in the middle between the SFE of non-treated HDPE (35 mN/m) and the maximum achievable SFE of (72 mN/m); and (iii) formamide is defined as a component of the test inks in several important international standards.

The reference time on shrinkage characteristics is 10 s after distribution of the test ink on the HDPE surface. It is a compromise between a large absolute error in the area determination for a very short reference time and the influence of material and environmental factors and increasing relative error for a very long reference time.

The optimal treatment time should be selected depending on the kind of discharge and scales inversely proportional with plasma power. For example, to achieve a good resolution of the AIR results for the 700 W plasma device, the plasma treatment time in the ms range is needed. For PDD and other CeraPlas™ driven discharges, the treatment time of 10 or 20 s is optimal.

It is shown that the hydrophobic recovery, defined as change of the activation area with storage time after HDPE treatment with CeraPlas™ based device, is very slow: 3% per 100 h.

The origin of the short-term changes is in the temporal variations of the test ink properties. The most probable reasons for such variations are: (i) the change of stoichiometry of the two-component test ink due to different evaporation speeds of the components; (ii) the absorption of water from air humidity in the pure formamide test ink.

To achieve exact, statistically sound and reproducible results with the AIR method, some assumptions and rules of handling must be fulfilled.

- The AIR results are valid only for intensive discharges, when 72 mN/m saturation on a large part of the activation area on HDPE is reached;
- the treatment time should not exceed the limit for the thermal damage of the HDPE surface;
- only a fresh test ink should be used, and the test ink vial should be opened only for a short time of ink application;
- the amount of the test ink should be adjusted to the size of the activation area; and
- the AIR measurements should be conducted at room temperature and medium humidity.

Even though the physical and chemical mechanisms of the test ink patch shrinkage are not explained in detail, the shrinkage characteristics are successfully used for solving engineering problems during the development and evaluation of the novel plasma tools. Using AIR, the authors approached the following engineering tasks:

- determination of the optimum operating conditions for the maximum surface activation speed;
- investigation of the influence of the constructional changes on the APPJ performance;
- determination of equivalent working point for plasma tool replacing a different one;
- the investigation of the performance changes of the APPJ in course of an endurance test; and
- the analysis of the influence of the type of discharge on the hydrophobic recovery.

The results of this study show that further work on this subject is needed. Among others, the physical–chemical mechanisms of the time-dependent shrinkage of the test ink patches should be investigated in more detail. The experimental development could also further improve the accuracy of the AIR technique. One example is the automation of the test ink application, allowing us to dose an exact amount of the liquid and to determine exactly the starting point for the ink patch shrinkage process.

References

1. Becker, K.H.; Kogelschatz, U.; Schoenbach, K.H.; Barker, R.J. (Eds.) *Non-Equilibrium Air Plasmas at Atmospheric Pressure*; IoP—Institute of Physics Publishing: Bristol, UK; Philadelphia, PA, USA, 2005; Chapter 9, pp. 597–686.
2. Choi, J.H.; Lee, E.S.; Baik, H.K.; Lee, S.J.; Song, K.M.; Lim, Y.S. Analysis of polymer surface treated by dielectric barrier discharge. *Plasma Sources Sci. Technol.* **2005**, *14*, 363–367. [CrossRef]
3. Primc, G. Surface modification of polyamides by gaseous plasma—Review and scientific challenges. *Polymers* **2020**, *12*, 3020. [CrossRef]
4. Wertheimer, M.; Martinu, L.; Klemberg-Sapieha, J.; Czeremuszkin, G. Plasma treatment of polymers to improve adhesion. In *Adhesion Promotion Techniques: Technological Applications*; Mittal, K., Pizzi, A., Eds.; Marcel Dekker, Inc.: New York, NY, USA, 2002; Chapter 5, pp. 139–173.
5. Yáñez-Pacios, A.J.; Martín-Martínez, J.M. Comparative adhesion, ageing resistance, and surface properties of wood plastic composite treated with low pressure plasma and atmospheric pressure plasma jet. *Polymers* **2018**, *10*, 643. [CrossRef] [PubMed]
6. Sasmazel, H.; Alazzawi, M.; Alsahib, N. Atmospheric pressure plasma surface treatment of polymers and influence on cell cultivation. *Molecules* **2021**, *26*, 1665. [CrossRef] [PubMed]
7. Owens, D.K.; Wendt, R.C. Estimation of the surface free energy of polymers. *J. Appl. Polym. Sci.* **1969**, *13*, 1741–1747. [CrossRef]
8. Man, J.U.; Prasad, S.D. Surface treatment of high density polyethylene (HDPE) film by 50 Hz dielectric barrier discharge produced in air and argon/air mixture at atmospheric pressure. *Int. J. Eng. Res. Appl.* **2015**, *5*, 1–9.
9. Neto, J.F.D.M.; Alves de Souza, I.; Feitor, M.C.; Targino, T.G.; Diniz, G.F.; Libório, M.S.; Sousa, R.R.M.; Costa, T.H.D.C. Study of high-density polyethylene (HDPE) kinetics modification treated by dielectric barrier discharge (DBD) plasma. *Polymers* **2020**, *12*, 2422. [CrossRef] [PubMed]

10. Qiu, Y.; Zhang, C.; Hwang, Y.; Bures, B.; McCord, M. The effect of atmospheric pressure helium plasma treatment on the surface and mechanical properties of ultrahigh-modulus polyethylene fibers. *J. Adhes. Sci. Technol.* **2002**, *16*, 99–107. [CrossRef]

11. Laroussi, M.; Akan, T. Arc-free atmospheric pressure cold plasma jets: A review. *Plasma Proces. Polym.* **2007**, *4*, 777–778. [CrossRef]

12. Winter, J.; Brandenburg, R.; Weltmann, K.D. Atmospheric pressure plasma jets: An overview of devices and new directions. *Plasma Sources Sci. Technol.* **2015**, *24*, 064001-19. [CrossRef]

13. Fanelli, F.; Fracassi, F. Atmospheric pressure non-equilibrium plasma jet technology: General features, specificities and applications in surface processing of materials. *Surf. Coat. Technol.* **2017**, *322*, 174–201. [CrossRef]

14. Noeske, M.; Degenhardt, J.; Strudthoff, S.; Lommatzsch, U. Plasma jet treatment of five polymers at atmospheric pressure: surface modifications and the relevance for adhesion. *Int. J. Adhes. Adhes.* **2004**, *24*, 171–177. [CrossRef]

15. Choi, J.; Matsuo, K.; Yoshida, H.; Namihira, T.; Katsuki, S.; Akiyama, H. Double-layered atmospheric pressure plasma jet. *Jpn. J. Appl. Phys.* **2009**, *48*, 086003. [CrossRef]

16. Chen, Q.; Zhang, Y.; Han, E.; Ge, Y. Atmospheric pressure DBD gun and its application in ink printability. *Plasma Sources Sci. Technol.* **2005**, *14*, 670–675. [CrossRef]

17. Laroussi, M. Low temperature plasma jets: Characterization and biomedical applications. *Plasma* **2020**, *3*, 54–58. [CrossRef]

18. Zaplotnik, R.; Vesel, A. Effect of VUV radiation on surface modification of polystyrene exposed to atmospheric pressure plasma jet. *Polymers* **2020**, *12*, 1136. [CrossRef]

19. Sangnal Matt Durandhara Murthy, V.; Vaidya, U. Improving the adhesion of glass/polypropylene (glass-PP) and high-density polyethylene (HDPE) surfaces by open air plasma treatment. *Int. J. Adhes. Adhes.* **2019**, *95*, 102435. [CrossRef]

20. Fei, X.; Kuroda, S.-i.; Mori, T.; Hosoi, K. High-density polyethylene (HDPE) surface treatment using an RF capacitive atmospheric pressure cold Ar plasma jet. *Plasma Sci. Technol.* **2013**, *15*, 577–581. [CrossRef]

21. Van Deynse, A.; Cools, P.; Leys, C.; Morent, R.; De Geyter, N. Surface modification of polyethylene in an argon atmospheric pressure plasma jet. *Surf. Coat. Technol.* **2015**, *276*, 384–390. [CrossRef]

22. Korzec, D.; Hoppenthaler, F.; Burger, D.; Andres, T.; Nettesheim, S. Atmospheric pressure plasma jet powered by piezoelectric direct discharge. *Plasma Process. Polym.* **2020**, *17*, 2000053. [CrossRef]

23. Kostov, K.; Nishime, T.; Castro, A.; Toth, A.; Hein, L. Surface modification of polymeric materials by cold atmospheric plasma jet. *Appl. Surf. Sci.* **2014**, *314*, 367–375. [CrossRef]

24. Van Deynse, A.; Cools, P.; Leys, C.; De Geyter, N.; Morent, R. Surface activation of polyethylene with an argon atmospheric pressure plasma jet: Influence of applied power and flow rate. *Appl. Surf. Sci.* **2015**, *328*, 269–278. [CrossRef]

25. Alavi, S.; Lotz, O.; Akhavan, B.; Yeo, G.; Walia, R.; McKenzie, D.; Bilek, M. Atmospheric pressure plasma jet treatment of polymers enables reagent-free covalent attachment of biomolecules for bioprinting. *ACS Appl. Mater. Interfaces* **2020**, *12*, 38730–38743. [CrossRef] [PubMed]

26. Van Vrekhem, S.; Vloebergh, K.; Asadian, M.; Vercruysse, C.; Declercq, H.; Van Tongel, A.; De Wilde, L.; De Geyter, N.; Morent, R. Improving the surface properties of an UHMWPE shoulder implant with an atmospheric pressure plasma jet. *Sci. Rep.* **2018**, *8*, 4720. [CrossRef]

27. Brewis, D.; Mathieson, I. Flame treatment of polymers to improve adhesion. In *Adhesion Promotion Techniques: Technological Applications*; Mittal, K.; Pizzi, A., Eds.; Marcel Dekker, Inc.: New York, NY, USA, 2002; Chapter 6, pp. 175–190.

28. Farris, S.; Pozzoli, S.; Biagioni, P.; Duó, L.; Mancinelli, S. The fundamentals of flame treatment for the surface activation of polyolefin polymers—A review. *Polymer* **2010**, *51*, 3591–3605. [CrossRef]

29. Goldman, M.; Goldman, A. Corona discharges. In *Gasous Electronics, Vol. I: Electrical Discharges*; Hirsh, M.N., Oskam, H.J., Eds.; Academic Press: New York, NY, USA, 1978; Chapter 4, pp. 219–290.

30. Chang, J.S.; Lawless, P.A.; Yamamoto, T. Corona discharge processes. *IEEE Trans. Plasma Sci.* **1991**, *19*, 1152–1166. [CrossRef]

31. Sutherland, I.; Popat, R.; Brewis, D.; Calder, R. Corona discharge treatment of polyolefins. *J. Adhes.* **1994**, *46*, 79–88. [CrossRef]

32. Pascual, M.; Calvo, O.; Sanchez-Nácher, L.; Bonet, M.; Garcia-Sanoguera, D.; Balart, R. Optimization of adhesive joints of low density polyethylene (LDPE) composite laminates with polyolefin foam using corona discharge plasma. *J. Appl. Polym. Sci.* **2009**, *114*, 2971–2977. [CrossRef]

33. Popelka, A.; Novák, I.; Al-Maadeed, M.A.S.; Ouederni, M.; Krupa, I. Effect of corona treatment on adhesion enhancement of LLDPE. *Surf. Coat. Technol.* **2017**, *335*, 118–125. [CrossRef]

34. Prevosto, L.; Kelly, H.; Mancinelli, B.R. Langmuir probe diagnostics of an atmospheric pressure, vortex–stabilized nitrogen plasma jet. *J. Appl. Phys.* **2012**, *112*, 063302. [CrossRef]

35. Begum, A.; Laroussi, M.; Pervez, M. Dielectric probe: A new electrical diagnostic tool for atmospheric pressure non-thermal plasma jet. *Int. J. Eng. Technol.-Ijet-Ijens* **2011**, *11*, 209–215.

36. Laux, C.O.; Spence, T.G.; Krugr, C.H.; Zare, R.N. Optical diagnostics of atmospheric pressure air plasmas. *Plasma Sources Sci. Technol.* **2003**, *12*, 125 – 138. [CrossRef]

37. Milosavljević, V.; Donegan, M.; Cullen, P.J.; Dowling, D.P. Diagnostics of an O_2–He RF atmospheric plasma discharge by spectral emission. *J. Phys. Soc. Jpn.* **2014**, *83*, 014501. [CrossRef]

38. Reuter, S.; Sousa, J.; Stancu, G.D.; van Helden, J.P.H. Review on VUV to MIR absorption spectroscopy of atmospheric pressure plasma jets. *Plasma Sources Sci. Technol.* **2015**, *24*, 054001. [CrossRef]

39. Lu, X.P.; Laroussi, M. Electron density and temperature measurement of an atmospheric pressure plasma by millimeter wave interferometer. *Appl. Phys. Lett.* **2008**, *92*, 051501. [CrossRef]

40. Lu, X.; Laroussi, M. Dynamics of an atmospheric pressure plasma plume generated by submicrosecond voltage pulses. *J. Appl. Phys.* **2006**, *100*, 063302-1-063302-6. [CrossRef]

41. Lu, X.; Laroussi, M.; Puech, V. On atmospheric-pressure non-equilibrium plasma jets and plasma bullets. *Plasma Sources Sci. Technol.* **2012**, *21*, 034005. [CrossRef]

42. Kewitz, T.; Fröhlich, M.; von Frieling, J.; Kersten, H. Investigation of a commercial atmospheric pressure plasma jet by a newly designed calorimetric probe. *IEEE Trans. Plasma Sci.* **2015**, *43*, 1769–1773. [CrossRef]

43. Korzec, D.; Nettesheim, S. Application of a pulsed atmospheric arc plasma jet for low-density polyethylene coating. *Plasma Process. Polym.* **2020**, *17*, 1900098. [CrossRef]

44. TDK Electronics. Cold Plasma from a Single Component. 2014. Applications & Cases. Available online: https://www.tdk-electronics.tdk.com/en/373562/tech-library/articles/applications---cases/applications---cases/cold-plasma-from-a-single-component/1109546 (accessed on 11 August 2021).

45. EPCOS AG. CeraPlas® HF Series. Piezoelectric Based Plasma Generator. Data Sheet. 2018. Available online: https://www.mouser.de/datasheet/2/400/ceraplas-db-1487530.pdf (accessed on 11 August 2021).

46. Wang, C.; Chen, X.; Ouyang, J.; Li, T.; Fu, J. Pulse current of multi-needle negative corona discharge and its electromagnetic radiation characteristics. *Energies* **2018**, *11*, 3120. [CrossRef]

47. Korzec, D.; Hoppenthaler, F.; Nettesheim, S. Piezoelectric direct discharge: Devices and applications. *Plasma* **2021**, *4*, 1–41. [CrossRef]

48. Stoffels, E.; Flikweert, A.; Stoffels, W.; Kroesen, G. Plasma needle: A non-destructive atmospheric plasma source for fine surface treatment of (bio)materials. *Plasma Sources Sci. Technol.* **2002**, *11*, 383–388. [CrossRef]

49. ASTM International. Standard Test Method for Wetting Tension of Polyethylene and Polypropylene Films. 2004. Available online: https://www.astm.org/DATABASE.CART/HISTORICAL/D2578-04.htm (accessed on 11 August 2021).

50. Open Chemistry Database. CID 713. 2019. Available online: https://pubchem.ncbi.nlm.nih.gov/compound/formamide#section=Computed-Properties (accessed on 11 August 2021).

51. Wu, J.; Farouk, T.; Ward, C. Pressure dependence of the contact angle. *J. Phys. Chem. B* **2007**, *111*, 6189–6197. [CrossRef]

52. Pérez-Díaz, J.L.; Álvarez-Valenzuela, M.A.; García-Prada, J.C. The effect of the partial pressure of water vapor on the surface tension of the liquid water–air interface. *J. Colloid Interface Sci.* **2012**, *381*, 180–182. [CrossRef]

53. Pérez-Díaz, J.L.; Álvarez-Valenzuela, M.A.; Valiente-Blanco, I.; Jimenez-Lopez, S.; Palacios-Cuesta, M.; Garcia, O.; Diez-Jimenez, E.; Sanchez-Garcia-Casarrubios, J.; Cristache, C. On the influence of relative humidity on the contact angle of a water droplet on a silicon wafer. In *Proceedings of the ASME 2013 International Mechanical Engineering Congress and Exposition. Vlume 7A: Fluids Engineering Systems and Technologies, San Diego, CA, USA, 15–21 November 2013*; American Society of Mechanical Engineers: New York, NY, USA, 2013. [CrossRef]

54. Sun, C.; Zhang, D.; Wadsworth, L. Corona treatment of polyolefin films—A review. *Adv. Polym. Technol.* **1999**, *18*, 171–180.

55. Jin, M.; Thomsen, F.; Skrivanek, T.; Willers, T., Why test inks cannot tell the whole truth about surface free energy of solids. In *Advances in Contact Angle, Wettability and Adhesion*; John Wiley & Sons, Ltd.: Hoboken, NJ, USA, 2015; Chapter 17, pp. 419–438.

56. Morra, M.; Occhiello, E.; Marola, R.; Garbassi, F.; Humphrey, P.; Johnson, D. On the aging of oxygen plasma-treated polydimethylsiloxane surfaces. *J. Colloid Interface Sci.* **1990**, *137*, 11–24. [CrossRef]

57. Kim, J.; Chaudhury, M.K.; Owen, M.J. Modeling hydrophobic recovery and electrically discharged polydimethylsiloxane elastomers. *J. Colloid Interface Sci.* **2006**, *293*, 364–375. [CrossRef]

58. Alves, P.; Pinto, S.; de Souse, H.; Gil, M. Surface modification of a thermoplastic polyurethane by low-pressure plasma treatment to improve hydrophilicity. *J. Appl. Polym. Sci.* **2011**, *122*, 2302–2308. [CrossRef]

59. Kim, J.; Chaudhury, M.K.; Owen, M.J.; Orbeck, T. The mechanisms of hydrophobic recovery of polydimethylsiloxane elastomers exposed to partial electrical discharges. *J. Colloid Interface Sci.* **2001**, *244*, 200–207. [CrossRef]

60. Jokinen, V.; Suvanto, P.; Franssila, S. Oxygen and nitrogen plasma hydrophilization and hydrophobic recovery of polymers. *Biomicrofluidics* **2012**, *6*, 016501. [CrossRef]

61. Guckenberger, D.; Berthier, E.; Young, E.; Beebe, D. Induced hydrophobic recovery of oxygen plasma-treated surfaces. *Lab Chip* **2012**, *12*, 2317–2321. [CrossRef] [PubMed]

62. Behnisch, J.; Holländer, A.; Zimmermann, H. Factors influencing the hydrophobic recovery of oxygen-plasma-treated polyethylene. *Surf. Coat. Technol.* **1993**, *59*, 356–358. [CrossRef]

63. Pascual, M.; Balart, R.; Sánchez, L.; Fenollar, O.; Calvo, O. Study of the aging process of corona discharge plasma effects on low density polyethylene film surface. *J. Mater. Sci.* **2008**, *43*, 4901–4909. [CrossRef]

64. Fricke, K.; Tresp, H.; Bussiahn, R.; Schröder, K.; von Woedtke, T.; Weltmann, K.D. On the use of atmospheric pressure plasma for the bio-decontamination of polymers and its impact on their chemical and morphological surface properties. *Plasma Chem. Plasma Process.* **2012**, *32*, 801–816. [CrossRef]

65. Fricke, K.; Steffen, H.; von Woedtke, T.; Schröder, K.; Weltmann, K.D. High rate etching of polymers by means of an atmospheric pressure plasma jet. *Plasma Process. Polym.* **2011**, *8*, 51–58. [CrossRef]

66. Deynse, A.V.; Cools, P.; Leys, C.; Morent, R.; de Geyter, N. Optimising the surface activation of polyethylene using different argon plasmas. In Proceedings of the 22nd International Symposium on Plasma Chemistry, Antwerp, Belgium, 5–10 July 2015.

Local Inflammatory Response after Intramuscularly Implantation of Anti-Adhesive Plasma-Fluorocarbon-Polymer Coated Ti6AI4V Discs in Rats

Charlotte Koppe [1,†], Andreas Hoene [1,†], Uwe Walschus [1], Birgit Finke [2], Holger Testrich [2], Christopher Pohl [1], Nico Brandt [1], Maciej Patrzyk [1], Jürgen Meichsner [3], Barbara Nebe [4] and Michael Schlosser [1,*]

1   Department of General Surgery, Visceral, Thoracic and Vascular Surgery, University Medical Center Greifswald, 17487 Greifswald, Germany; charlotte.koppe@stud.uni-greifswald.de (C.K.); hoene@uni-greifswald.de (A.H.); walschus@web.de (U.W.); christopher.pohl@uni-greifswald.de (C.P.); nico.brandt@protonmail.com (N.B.); patrzyk@uni-greifswald.de (M.P.)
2   Leibniz Institute for Plasma Science and Technology (INP), 17487 Greifswald, Germany; finke-hgw@t-online.de (B.F.); holger.testrich@inp-greifswald.de (H.T.)
3   Institute of Physics, University of Greifswald, 17487 Greifswald, Germany; meichsner@physik.uni-greifswald.de
4   Department of Cell Biology, University Medical Center Rostock, 18057 Rostock, Germany; barbara.nebe@med.uni-rostock.de
*   Correspondence: schlosse@uni-greifswald.de; Tel.: +49-3834-8680422
†   These authors have contributed equally to this work.

Abstract: Orthopaedic implants and temporary osteosynthesis devices are commonly based on Titanium (Ti). For short-term devices, cell-material contact should be restricted for easy removal after bone healing. This could be achieved with anti-adhesive plasma-fluorocarbon-polymer (PFP) films created by low-temperature plasma processes. Two different PFP thin film deposition techniques, microwave (MW) and radiofrequency (RF) discharge plasma, were applied to receive smooth, hydrophobic surfaces with octafluoropropane (C_3F_8) or hexafluorohexane (C_6F_6) as precursors. This study aimed at examining the immunological local tissue reactions after simultaneous intramuscular implantation of four different Ti samples, designated as MW-C_3F_8, MW-C_6F_6, RF-C_3F_8 and Ti-controls, in rats. A differentiated morphometric evaluation of the inflammatory reaction was conducted by immunohistochemical staining of CD68+ macrophages, CD163+ macrophages, MHC class II-positive cells, T lymphocytes, CD25+ regulatory T lymphocytes, NK cells and nestin-positive cells in cryosections of surrounding peri-implant tissue. Tissue samples were obtained on days 7, 14 and 56 for investigating the acute and chronical inflammation (n = 8 rats/group). Implants with a radiofrequency discharge plasma (RF-C_3F_8) coating exhibited a favorable short- and long-term immune/inflammatory response comparable to Ti-controls. This was also demonstrated by the significant decrease in pro-inflammatory CD68+ macrophages, possibly downregulated by significantly increasing regulatory T lymphocytes.

Keywords: titanium (Ti) alloys; low-temperature plasma polymerization; plasma-fluorocarbon-polymer; anti-adhesive surface; inflammatory/immunological response; intramuscularly implantation

1. Introduction

Titanium alloys are still among the most commonly used materials for metallic implants in orthopedic and trauma surgery for long-term use such as joint or hard tissue replacement as well as in temporary fracture fixation devices, including internal and external fixators, intra-medullary nails and screws. This is mainly due to their excellent biocompatibility, high corrosion resistance and low ion-formation tendency [1], which leads to encouraged cell adhesion and the osseointegration process. While this is of great importance for long-term prosthetic applications, the requirements for short-term implants

are quite different. The purpose of temporary implants is to stabilize the fragments of fractured bone in order to allow healing and repair processes to occur but not to integrate into the bone to ensure safe removal [2]. However, to the present day the retrieval of metallic fracture-fixation devices is still associated with a risk of nerve and soft tissue damage, and the possibility of harming the newly formed bone by using a great amount of pullout force, and longer operation times [3,4].

After immediate surface adsorption of blood proteins, the interaction of cells and the implant as well as the characteristics of the metallic surface have a great influence on the initial attachment process. This is mediated by integrin receptors, leading to adhesion as well as a primary immune response of the body [5,6]. It is well established in the literature that the surface microtopography such as roughness or micro-discontinuities, hydrophilicity/-phobicity, chemistry and charge influence molecular adhesion processes [7–9]. Hayes et al. demonstrated that reduced surface roughness through polishing leads to a significant lower osteointegration in vivo [2].

In recent years, low-pressure and low-temperature plasma processes, as a technique for metal surface modification through thin film deposition, have become more important in biomedical engineering. One of the reasons is that the coating can be highly specific, while the characteristics of the coated metal itself remain unchanged resulting in extremely effective implant performance [10].

Considering the initial assumption that the surface structure and charge is a crucial factor for tissue integration, the influence of plasma coating has been demonstrated in previous studies which showed that titanium platelets coated with a thin positively charged plasma polymer from allylamine (PPAAm) had a beneficial effect on osteoblastic adhesion (MG63 cells) in vitro [11] and, dependent on the chosen plasma process conditions, caused an increased or decreased local immune response compared to uncoated controls following implantation in vivo [12].

In contrast, anti-adhesive coatings are beneficial for temporary devices by inhibiting cell attachment, colonisation and growth on the titanium surface. The modification of titanium surfaces by low-temperature plasma thin film deposition is a very promising method for improvement of implant performance. Concerning thin film deposition for anti-adhesive coatings, the use of plasma-fluorocarbon-polymer (PFP) precursors have several advantages including easy thickness control, excellent adhesion to the coated metal and the ability to create a hydrophobic surface [13]. Hydrophobic surfaces tend to have a higher water contact angle than hydrophilic surfaces leading to a reduced wettability, effecting cell attachment and proliferation as described to be higher on hydrophilic than on hydrophobic surfaces [14–16]. The host immune response is determined by the interaction between the implanted material surface and surrounding tissue. Clinically a pro-inflammatory immune response is directly associated with prolonged reconstruction processes and complicated delayed wound healing [17,18].

In general, the immune response after tissue injury due to biomaterial implantation changes in a time-dependent manner. Innate immune cells such as neutrophils recognize danger associated molecular patterns (DAMPs) [19]. Through cytokines like IFN-γ, they coordinate the recruitment of circulating monocytes and initiate the differentiation into different phenotypes of macrophages according to the occurring environment of pro- or anti-inflammatory chemical signals. This is determined by a complex multifactual influence and is also affected by the health condition of the host tissue [20]. Within a few hours following implantation, monocytes/macrophages as early responders, become the dominant cell type in the surrounding tissue [21].

In response to INF-γ, monocytes progress into pro-inflammatory M1-type macrophages. These cells are the key actors in initiating a TH1-response, characterized by INF-γ as the predominant cytokine, which causes a pro-inflammatory response. Although this is important to initiate the natural wound healing process, it can lead to tissue damage in cases of prolonged activation. M1-type macrophages, identified by expression of markers such as CD68 and CD80 [6], can differentiate into M2-type tissue macrophages, known for their

anti-inflammatory modulation. Among other markers, M2 macrophages express CD163. Due to their ability of tissue remodeling and repair, this macrophage switch is essential for the tissue healing and integration processes. However prolonged or overactivation may cause fibrous encapsulation of the implanted devices, impeding a successful implantation. As common in immune responses both phenotypes are crucial for successful tissue healing and remodeling, but balance and sequence of activation are essential [20].

Other important innate immune cells are natural killer cells (NK cells). Apart from their more widely known functions as cytotoxic and cytokine producing cells, NK cells also seem to be engaged in the regulation of other immune cells such as dendritic cells or T lymphocytes. This highlights the possibility of NK cells having the ability to affect the immune response towards a more anti-inflammatory or pro-inflammatory microenvironment [22].

Consistent with the inflammatory reaction described above, professional antigen-presenting cells (MHC class II antigen-presenting cells) are responsible for initiating the adaptive immune answer. Only dendritic cells, macrophages and B cells express MHC class II antigens and are therefore able to present antigens to the T cell-mediated branch of humoral immune response and activate effector T cells [23]. Concerning T cell activation, Interleukin-2 (IL-2) receptor-positive regulatory T cells are of great interest. IL-2 is a cytokine with a pleiotropic biological mechanism reaching from immunostimulatory effects via cytotoxic CD8+ cell activation to immunosuppressive effects by stimulating CD4+ regulatory T cells (T_{reg}) which are important for inducing an anti-inflammatory environment characterized by high levels of IL-10 and TGF-β [24].

While the inflammatory reaction has a great influence on tissue healing, muscle regeneration and vascularization contribute significantly to this process. Myofiber regeneration is a complex process similar to muscle formation during embryogenic development. Intermediate filament (IF) proteins are a necessary component of this pathway. Concerning muscle injury, the IF-protein nestin is of great interest since it has been observed that its upregulation is essential for the induction of myogenic differentiation [25,26].

The aim of the present study was an immunological in vivo evaluation of different anti-adhesive PFP-films on titanium alloy samples, investigating their influence on the local inflammatory tissue response after implantation in Lewis rats. In previous studies Finke et al. examined and characterized titanium alloy platelets (Ti6AI4V) which were coated with different PFP-films precursors and different discharged plasma either applied by means of microwave (MW: higher electron densities and lower electron energies) or radiofrequency (RF: ion bombardments on growing film). This process resulted in very smooth, abrasion resistant, cross-linked PFP-films designated as $MW-C_3F_8$, $MW-C_6F_6$ and $RF-C_3F_8$. All implants exhibited the desired thin film with anti-adhesive properties and a stable hydrophobic character. In vitro studies revealed a decrease in the number and size of MG-63 (Osteoblast) cells cultivated on those PFP-modified titanium samples in comparison to attachment on a non-coated control implant, emphasizing the anti-adhesive character of PFP [27].

The present study postulates that an anti-adhesive coating of titanium implants also evokes a decreased inflammatory local reaction in vivo. To examine this hypothesis, a simultaneous intramuscular implantation of the four different samples (control, $RF-C_3F_8$, $MW-C_3F_8$ and $MW-C_6F_6$) was performed in an established rat animal model for immunohistochemical examination of calcium phosphate-coated titanium implants [28]. For this, a differentiated morphometric evaluation of the inflammatory reaction in the surrounding peri-implant tissue over time (acute phase day 7, intermediate phase day 14 and chronic inflammation day 56) was conducted by immunohistochemical staining of CD68+ monocytes/macrophages (ED1), CD163+ macrophages (ED2), MHC class II positive antigen-presenting cells (OX6), T lymphocytes (R73), CD25+ (IL-2R+) regulatory T lymphocytes (OX39), activated NK cells (ANK61) and nestin-positive cells (Rat 401).

2. Materials and Methods

2.1. Implants and PFP Film Preparation

Titanium alloy plates (Ti6AI4V) with the measurements of $5 \times 5 \times 1$ mm and a defined roughness of Ra = 0.28 μm (Ti6Al4V-P cp, DOT GmbH, Rostock, Germany) were polished and used for low temperature plasma modifications.

The platelets were surface-modified with a plasma-fluorocarbon-polymer (PFP) film using octafluoropropane (C_3F_8) or hexafluorohexane (C_6F_6) as a precursor (Linde Gas AG, Munich, Germany) with a purity of 99.95%, and added H_2 (Messer-Griesheim GmbH, Ludwigshafen, Germany) with a purity of 99.9999%, in the specific manner that the procedure of either microwave- (MW) or capacitively coupled radio frequency (RF)-generated low-temperature plasma discharge demands.

In previous studies optimized parameters for the PFP-film were investigated for minimum cell adhesion and found to be as follows for PFP-MW: 500 W, 10–30 Pa, 1000 s//(2.45 GHz, 500–1200 W, 10–50 Pa, 300–1000 s) and for PFP-RF: 25 W, 20 Pa, 400 s//(13.56 MHz, 20–150 W, 20 60 Pa, 20–1000 s) [27].

The two discs that were treated with a microwave coating process were placed 9 cm downstream of the MW coupling window in an industrial low-plasma reactor (V55G, Plasma finish, Germany). One alloy platelet was steamed with a C_3F_8-precursor and H_2 mixture (C_3F_8/H_2) and the other one with a C_6F_6-precursor and H_2 mixture (C_6F_6/H_2).

The radiofrequency processed samples were placed in a stainless-steel vacuum chamber of 400 mm in diameter and height, on top of a planar electrode which was powered by an RF-generator through a matching network. In order to guarantee low-germ processing environments both reactors used for deposition were combined with a laminar flow box.

Sample series were designated as MW-C_3F_8, MW-C_6F_6 and RF-C_3F_8, respectively. The titanium alloy platelets serving as control plates were without a PFP-film preparation.

2.2. In Vivo Investigations

Twenty-four male Lewis rats (age 100 days) were used in this study. All animal experiments and maintenance were approved by the LALLF Mecklenburg-West Pomerania (reference number 7221.3-1.1-074/11) and performed in accordance with the animal protection law of the Federal Republic of Germany (version of 1 January 1987), which determinates the principles of care for animals in laboratories (proposed by the National Society for Medical Research) and followed the Guideline for Keeping and Using Laboratory Animals (NIH Publication No. 80-23, revised 1985).

Each animal received four implants, one control plate and one sample from each PFP series (RF-C_3F_8, MW-C_3F_8, MW-C_6F_6). As established in previous studies, this approach was chosen to reduce the level of variability among the experimental animals through intra-individual comparison of the inflammatory reactions against samples vs. its own control [12,28]. Accordingly, the samples were simultaneously implanted into small intramuscular pockets (i.m.) clockwise, starting with the control sample in the upper left area of the neck muscle. The intramuscular pockets were separated by at least 2 cm from each other to avoid overlapping local inflammation effects. The implants were fixed with a non-resorbable synthetic polypropylene suture (PROLENE, Ethicon Endo-Surgery, Inc., Hamburg, Germany) to ensure relocation and to track samples on explanation dates. For seven days after the procedure, the rats were screened daily for any untypical behavior, signs of pain and severe weight loss according to a set scoring sheet.

On days 7, 14 and 56 after implantation, eight randomly selected animals were euthanised by carbon dioxide inhalation and the samples with the surrounding peri-implant tissue were carefully explanted. Using the laboratory freezer spray New Envi-Ro-Tech (Thermo Electron Corporation, Pittsburgh, PA, USA), the samples were frozen instantaneously and the Ti6AI4V platelets were carefully removed. The resulting pockets were filled with Shandon Cryomatrix embedding medium (Thermo Electron Corporation, Pittsburgh, PA, USA). For later histological examination, the tissue samples were shock frozen in liquid nitrogen and stored at −80 °C.

2.3. Histological Examination

Cryosections with a thickness of five μm were generated from each tissue sample using a 2800 Frigocut N cryotome (Reichert-Jung, Nussloch, Germany). Seven different antibody-based immunohistochemical staining methods were carried out to detect CD68+ monocytes/macrophages (ED1), CD163+ macrophages (ED2), MHC class II positive antigen-presenting cells (OX6), T lymphocytes (R73), CD25+ (IL-2R+) regulatory T lymphocytes (OX39), activated NK cells (ANK61) and nestin-positive cells (Rat 401). Each staining procedure was conducted according to the manufacturer's protocol (MorphoSys AbD Serotec GmbH, Düsseldorf, Germany). The specific antibody-stained cells were visualized using the APAAP detection system (mouse monoclonal antibody alkaline-phosphatase-anti-alkaline-phosphatase; APAAP, clone AP1B9, Sigma-Aldrich Chemie GmbH, Munich, Germany) and the polyclonal rabbit anti-mouse-immunoglobulin (Z259, Dako DenmarkA/S, Glostrup, Denmark) using New Fuchsin as chromogen. Additionally, mast cells were detected by histochemical toluidine blue staining. Using a digital camera DP20 on a light microscope CX41 (Olympus, Hamburg, Germany), histological images of the different stained sections were obtained.

2.4. Morphometry

The obtained images were morphometrically evaluated by counting of positively stained cells in defined areas using the digital image analysis software ImageJ v1.41 (US National Institutes of Health, Bethesda, Rockville, MD, USA). Five representative squares per histological section of 20,000 pixels along the border zone between surrounding tissue and implant-free pocket were selected for detailed analysis, resulting in a total analyzed area of 100,000 pixels per image. In the chosen microscopic magnification of $100\times$, one pixel equals an area of $0.4796\ \mu m^2$. The results were expressed either as a percentage of positively stained areas (for ED1, ED2, OX6, nestin) or cells per mm^2 for markers with low cell numbers (for R73, OX39, toluidine blue, ANK61).

2.5. Statistics

Data are given as median and interquartile range. All tests were performed two-tailed with *p*-values of less than 0.05 considered as statistically significant. For comparison of measured percentages of positively stained area or positive cells per mm^2 in the peri-implant tissue of implant samples, the non-parametric Kruskal–Wallis test with Gaussian approximation was used. For comparison of implant samples between the different experimental days, the Kruskal–Wallis test with Dunn's multiple comparison post-hoc-test was used for non-paired data sets. For comparison between different implants and different cellular markers on each experimental day, the Mann–Whitney U-test was used. All statistical analysis was performed using the software GraphPad Prism version 4.02 (GraphPad Software, Inc., San Diego, CA, USA).

3. Results

3.1. Overview of Time Course of Different Inflammatory Cell Populations

After simultaneous implantation of different anti-adhesive PFP-coated and uncoated control titanium alloy plates (Ti6AI4V), a distinct time course pattern of inflammatory investigated cells could be observed (Table 1). Whereas the positively stained area of CD68+ monocytes and macrophages (ED1) significantly decreased from day 7 to day 56 for all implants, the positively stained area of CD163+ macrophages (ED2) did not change. Additionally, for MHC class II antigen-presenting cells (OX6), a significant decrease in the positively stained area could be observed for all implants. Except for the RF-C$_3$F$_8$ implants, this was also seen for the nestin-positive cells. Whereas the number of total T lymphocytes (R73) did not change, the number of IL-2R+ regulatory T lymphocytes (OX39) significantly increased from experimental day 7 to 56. The number of mast cells was constant for three implants, whereas for the MW-C$_6$F$_6$ implants a significant change

was observed. Moreover, for NK cells (ANK61), the number of positive cells significantly changed over the examined period.

Table 1. Plasma-fluorocarbon-polymer (PFP) film implants *p*-values; Concerning each marker ED1 (CD68+ monocytes/macrophages), ED2 (CD163+ macrophages), OX6 (MHC class II positive antigen-presenting cells), R73 (T lymphocytes), OX39 (CD25+ (IL-2R+) regulatory T lymphocytes), nestin-positive cells, toluidine blue (mast cells) and ANK61 (NK cells) for comparison of measured percentages of positively stained area or positive cells per mm^2 in the peri-implant tissue of implant samples, the non-parametric Kruskal–Wallis test with Gaussian approximation was carried out.

Marker	Control	RF C_3F_8	MW C_3F_8	MW C_6F_6
	d 7, 14, 56	d 7, 14, 56	d 7, 14, 56	d 7, 14, 56
ED1	0.035	0.0009	0.0399	0.0236
ED2	0.1163	0.1251	0.636	0.3627
OX6	0.0054	0.0193	0.0014	0.0259
R73	0.0912	0.3203	0.6114	0.4744
Nestin	0.0048	0.0854	0.0003	0.0196
OX39	0.011	0.0007	0.001	0.0057
Toluidine blue	0.4838	0.0949	0.2947	0.0029
ANK61	0.0007	0.0013	0.0034	0.0216

3.2. Morphometric Analysis of Different Inflammatory Cell Population

3.2.1. CD68+ Monocytes and Macrophages (ED1)

The time course of pro-inflammatory CD68+ monocytes and macrophages (ED1) is demonstrated in Figure 1A. The positively stained area significantly decreased from day 7 to day 14 for control implants ($p < 0.01$) and more pronouncedly for RF-C_3F_8 implants ($p < 0.001$). Additionally, for both MW implant series, the positively stained area significantly decreased ($p < 0.05$). The median positively stained area varied for all implants between median 3.32–4.66% (interquartile range (IQR) of 2.2–6.23%). On day 14 it fluctuated between median 0.215–1.81% (IQR 0.15–3.07%), and on day 56 between median 1.385% to 2.36% (IQR 0.98–3.44%) for the four different implants. In comparison to control implants, a significantly higher percentage of positively stained area in the surrounding tissue of MW-C_3F_8 discs could be observed on day 14 ($p = 0.0281$) and for MW-C_6F_6 compared to RF-C_3F_8 implants on day 56 ($p = 0.0111$) A similar trend of increase was also seen for MW-C_6F_6 platelets on day 14. In contrast and compared to control implants, the RF-C_3F_8 discs did not induce a significantly different local inflammatory response on any experimental day.

3.2.2. CD163+ Macrophages (ED2)

Figure 1B shows the time course of anti-inflammatory CD163+ macrophages (ED2). Overall, the CD163+ cells did not show any change between the three experimental time points. No switch to an anti-inflammatory macrophage population, which is essential for the tissue healing and integration processes, could be observed. The positively stained area, representing the percentage of tissue macrophages in the peri-implant tissue, remained constant, reflected in similar medians on all observation days. On day 7 the median for all implants varied around the median of 2.38–3.38% (IQR 1.51–4.24%). On day 14 it fluctuated between 1.15% and 3.39% (IQR 0.85–4.44%). On day 56 it ranged from 1.96–2.94% (IQR 1.31–2.38%). In accordance with the CD68+ monocytes and macrophages, the RF-C_3F_8 implants showed a similar attraction of CD163+ tissue macrophages as controls throughout the examined time course. The invasion of tissue macrophages was significantly stronger for MW-C_3F_8 ($p = 0.0379$) and more pronounced for MW-C_6F_6 ($p = 0.0003$) two weeks after implantation compared to controls. No significant difference between the four implants was found on day 7 and day 56.
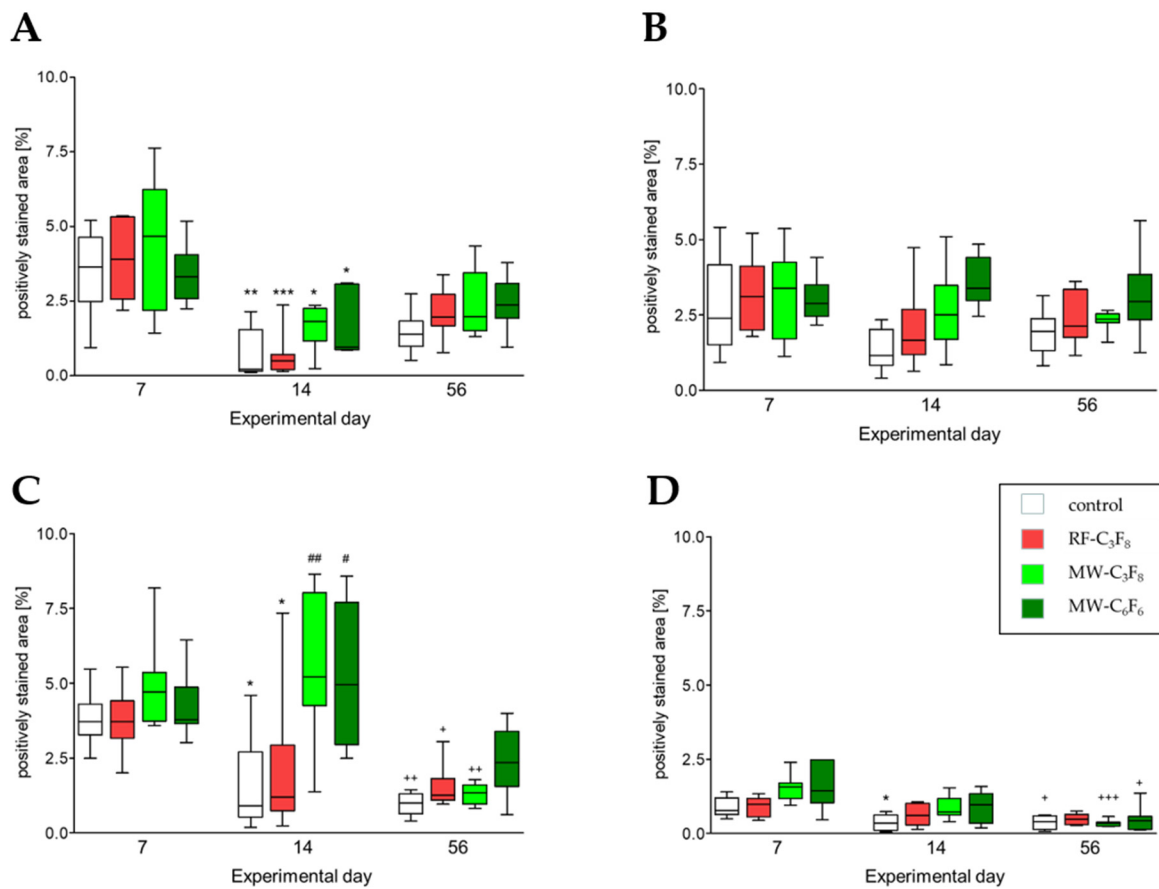
Figure 1. (**A**–**D**). Quantity of positively stained area of (**A**) pro-inflammatory CD68+ (ED1) monocytes/macrophages and (**B**) anti-inflammatory CD163+ (ED2) macrophages, (**C**) MHC class II+ antigen-presenting cells (OX6) and (**D**) nestin-positive cells (Rat 401) in the peri-implant tissue surrounding uncoated Ti6AI4V plates (white bars) and Ti6AI4V plates coated with the anti-adhesive plasma-fluorocarbon-polymers RF-C_3F_8 (red bars), MW-C_3F_8 (light green bars) and MW-C_6F_6 (dark green bars) at days 7, 14 and 56 after simultaneous intramuscular implantation in rats. Boxes represent the median and interquartile range of eight rats per experimental day; *p*-values represent significant differences between experimental days. * $p < 0.05$, ** $p < 0.01$, *** $p < 0.001$ (day 7 vs. day 14), + $p < 0.05$, ++ $p < 0.01$, +++ $p < 0.001$ (day 7 vs. day 56), # $p < 0.05$, ## $p < 0.01$ (day 14 vs. day 56), Kruskal–Wallis test with Dunn's post-hoc test.

3.2.3. MHC Class II Antigen-Presenting Cells (OX6)

Figure 1C shows the time course of positively stained area for MHC class II positive cells, a surface structure that is essential for antigen presentation and is responsible for initiating the adaptive immune response, throughout the examined study period. A significant decrease was seen between days 7 and 14 for control and RF-C_3F_8 plates ($p < 0.05$), between days 7 and 56 for RF-C_3F_8 ($p < 0.05$), control and MW-C_3F_8 plates ($p < 0.01$), and between days 14 and 56 for MW-C_3F_8 and MW-C_6F_6 plates. The positively stained area, resembling the percentage of MHC class II positive cells in the peri-implant tissue, varied on day 7 for all implants, around the medians of 3.71% to 4.71% (IQR 3.17–5.36%). On day 14 it fluctuated between 0.9% and 4.9% (IQR 0.53–7.7%), and on day 56 it drastically reduced compared to day 14 with a smaller range from 1% to 2.34% (IQR 0.64–3.39%). No significant difference among the four implants was observed on day 7. The MHC class II positive stained area differs significantly for MW-C_3F_8 ($p = 0.037$) and for MW-C_6F_6 ($p = 0.02$) from control discs as well as between RF-C_3F_8 and MW-C_3F_8 ($p = 0.014$) and RF-C_3F_8 and MW-C_6F_6 implants ($p = 0.0426$) on day 14. On experimental day 56 the MW-C_6F_6 showed a significantly stronger reaction when compared to both the controls ($p = 0.0047$) and the MW-C_3F_8 implants ($p = 0.0379$).

3.2.4. Nestin-Positive Cells/Area

In general, excluding the RF-C_3F_8 discs, a significant reduction in nestin-positive stained area in the peri-implant tissue was seen for all samples until day 56 (Table 1, Figure 1D). Nestin is essential for the induction of myogenic differentiation and its upregulation can be associated with ongoing tissue healing processes. A significant decrease was seen between days 7 and 14 for control discs ($p < 0.05$) and between days 7 and 56 for control ($p < 0.05$), MW-C_3F_8 ($p < 0.001$) and MW-C_6F_6 plates ($p < 0.05$). The percentage of nestin-positive area varied on day 7 for all implants between medians of 0.77 to 1.56% (IQR 0.56–2.48%). On day 14, it decreased and fluctuated between 0.34 and 0.97% (IQR 0.11–1.33%) and on day 56 the medians ranged from 0.33% to 0.48% (IQR 0.13–0.64%). In contrast to all the other examined markers, nestin showed a significantly stronger reaction for MW-C_3F_8 compared to both controls ($p = 0.014$) and RF-C_3F_8 implants seven days after implantation. Furthermore, on day 14 the positive area significantly increased for MW-C_3F_8 compared to control implants ($p = 0.014$).

3.2.5. T Lymphocytes (R73)

Overall, as demonstrated in Figure 2A, the number of counted T-lymphocytes, cells of the adaptive immune system, did not show any significant change during the observation period. Due to low cell numbers the counted amount was expressed as cells per mm^2. On day 7 the median count varied for all implants around 23–36 cells per mm^2 (IQR 15–55 cells). On day 14 it fluctuated between 22 and 26 cells per mm^2 (IQR 12–51 cells), and on day 56 the median ranged from 20 to 35 cells per mm^2 (IQR 12–43 cells). The highest number of cells compared to controls was counted on day 56 for all three PFP series samples, a significant increase was observed for RF-C_3F_8 ($p = 0.0281$) and MW-C_3F_8 discs ($p = 0.007$). No difference between the four implants was seen on days 7 and 14.

3.2.6. IL-2R+ Regulatory T Lymphocytes (OX39)

In general, and in comparison with T lymphocytes, the number of IL-2R+ regulatory T lymphocytes was low. T_{reg} are important cells in inducing an anti-inflammatory environment. In contrast to the R73+ T-lymphocytes and all other markers investigated, the IL-2R+ regulatory T lymphocytes showed a significant increase in cells per mm^2 over time, reaching their highest numbers for all four implants on day 56 (Table 1, Figure 2B). In particular, a significant increase was seen between days 7 and 56 for all four implants ($p < 0.05$–$p < 0.001$), and between days 14 and 56 for control discs ($p < 0.05$), RF-C_3F_8 ($p < 0.01$) as well as MW-C_6F_6 plates ($p < 0.05$). The increase in cell number per area was accompanied by a constantly increasing median. On day 7, the median count varied for all implants around 1 to 3 cells per mm^2 (IQR 1–9 cells). On day 14 it fluctuated between one and seven cells per mm^2 (IQR 0–8 cells). On day 56 the median increased again, ranging from 7 to 16 cells per mm^2 (IQR 5–21 cells). On day 14 the number of positive cells was significantly increased for MW-C_3F_8 in comparison with both control ($p = 0.0281$) and RF-C_3F_8 implants ($p = 0.0127$), whereas on day 56 the number of positive cells was significantly higher for RF-C_3F_8 implants compared to controls ($p = 0.003$).

3.2.7. Mast Cells

Figure 2C shows the time course of mast cells stained with toluidine blue. Mast cells can ameliorate an anti-inflammatory immune response. Overall, except for MW-C_6F_6 discs, there was no significant change for any of the other coated Ti6AI4V implants in the present study. In comparison to day 7, the number of mast cells was significantly increased on day 14 for the MW-C_6F_6 discs ($p < 0.01$). On day 7 the median count of cells per mm^2 varied for all implants around six to eight cells per mm^2 (IQR 3–13 cells). On day 14 the median for all implants fluctuates between 7 and 17 cells per mm^2 (IQR 5–32 cells). On day 56 the median ranged from 10 to 13 cells per mm^2 (IQR 7–19 cells). Particularly on day 14 for the MW-C_6F_6 implants, the number of mast cells was significantly increased compared to

their respective controls ($p = 0.0037$), RF-C_3F_8 ($p = 0.0003$), MW-C_3F_8 implants ($p = 0.0006$), whereas the number of cells between different implants did not differ on days 7 and 56.
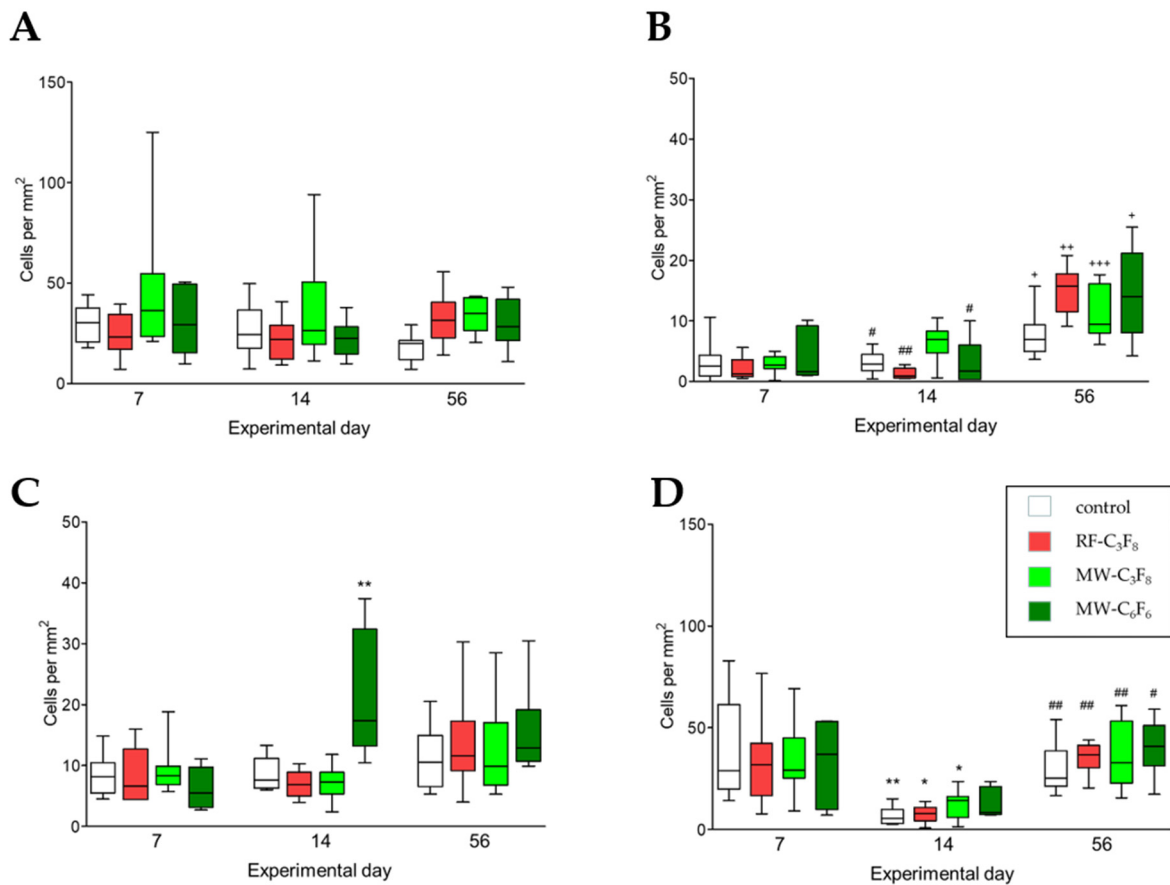
Figure 2. (**A**–**D**). Quantity of positively stained cells per mm^2 for (**A**) total T lymphocytes (R73), (**B**) IL-2R+ regulatory T lymphocytes (OX39), (**C**) mast cells (toluidine blue staining) and (**D**) activated NK cells (ANK61) in the peri-implant tissue surrounding uncoated Ti6AI4V plates (white bars) and Ti6AI4V plates coated with the anti-adhesive plasma-fluorocarbon-polymers RF-C_3F_8 (red bars), MW-C_3F_8 (light green bars) and MW-C_6F_6 (dark green bars) at days 7, 14 and 56 after simultaneous intramuscular implantation in rats. Boxes represent the median and interquartile range of eight rats per experimental day; *p*-values represent significant differences between experimental days. * $p < 0.05$, ** $p < 0.01$ (day 7 vs. day 14), + $p < 0.05$, ++ $p < 0.01$, +++ $p < 0.001$ (day 7 vs. day 56), # $p < 0.05$, ## $p < 0.01$ (day 14 vs. day 56), Kruskal–Wallis test with Dunn's post hoc test.

3.2.8. Activated NK Cells

Figure 2D demonstrates a significant change in the number of natural killer cells (NK) in the peri-implant tissue of all samples throughout the examined study period, with a pronounced decrease at day 14 and a subsequent increase until day 56. The number of positive cells was significantly decreased on day 14 compared to day 7 for the controls ($p < 0.01$), the RF-C_3F_8 and the MW-C_3F_8 implants ($p < 0.05$ for both). In contrast, on day 56 the NK cell count was significant increased for all four implants ($p < 0.05$–$p < 0.01$) compared to day 14. On experimental day 7, the median count for all implants varied around 29 to 37 cells per mm^2 (IQR 10–61 cells). On day 14 the median significantly decreased for all implants and fluctuated around four to five cells per mm^2 (IQR 3–8 cells). On day 56 the median ranged from 25 to 41 cells per mm^2 (IQR 21–53 cells). Compared to the controls a significantly stronger reaction was observed only for MW-C_6F_6 on day 14, whereas the number of cells between different implants did not differ on experimental days 7 and 56.

4. Discussion

Previous studies have shown that the characteristics of metallic surface microtopography such as roughness, micro-discontinuities, hydrophilicity/hydrophobicity, chemistry and charge have a pronounced influence on the initial attachment process to temporary fracture fixation devices [7–9]. In prior studies, it has been demonstrated in vitro [11] and in vivo [12] that plasma technology, precursor chemistry and process parameters influence the cellular response to the modified surface.

The aim of the present study was an in vivo evaluation of different anti-adhesive plasma-fluorocarbon-polymer (PFP) films on titanium alloy samples, investigating their influence on the local inflammatory tissue response after implantation in Lewis rats. For this purpose, Finke et al. developed an anti-adhesive coating for temporary bone fixation devices, using different PFP thin film deposition techniques, microwave (MW: higher electron densities and lower electron energies) or radiofrequency (RF: ion bombardments on growing film) discharge plasma with octafluoropropane (C_3F_8) or hexafluorohexane (C_6F_6) as precursors. Through both applied processes, surfaces with a very smooth, abrasion resistant, and stable hydrophobic character were produced, designated as MW-C_3F_8, MW-C_6F_6 and RF-C_3F_8 [27]. The physico-chemical differences between the two different coating strategies are characterized in detail by Finke et al. [27]. The X-ray photoelectron spectroscopy (XLS) analysis showed that the F/C ratio for the optimized PFP-films was between 1.5 (PFP-MW) and 1.3 (PFP-RF). Fourier transform infrared reflection absorption spectroscopy (FT-IRRAS) revealed similar spectra for PEP-MW and RF surfaces indicating no major differences between the samples, except for a higher CF2 peak for the PFP-RF samples. AFM measurements showed that the arithmetic roughness Ra for PEP-MW was 4.4nm and for PEP-RF only 3.2 nm [27].

The data presented herein suggest that the type of plasma process technology (microwave vs. radiofrequency) significantly influences the inflammatory reactions. In particular, PFP film samples prepared by radiofrequency discharge plasma (RF-C_3F_8) were comparable to controls in vivo and showed a similar low inflammatory response. Additionally, previous in vitro studies conducted by Finke et al. have shown a more efficient inhibition of cellular occupations for hydrophobic RF-C_3F_8 films [27]. This effect of hydrophobicity on cell attachment processes could also be observed by Kuhn et al. for fibroblast adhesion, demonstrating that in vitro plasma modified titanium surfaces with activated organo-silicon monomer hexamethyldisiloxane (ppHMDSO+O_2) led to a diminished colonization and proliferation [16]. The reduced roughness in RF films (3.2 nm) could also contribute to the observed low immune response and would favor this plasma process for short term implantation due to a lower degree of adhesion. Additionally, XPS analyses detected no nitrogen but a trend of increased levels of oxygen in the PFP-RF samples. If significantly increased, imbedded oxygen might possibly lead to oxidative stress further reducing ingrowth.

In accordance with our hypothesis of decreased inflammatory local reactions due to anti-adhesive coatings, the pro-inflammatory M1-like macrophages decreased significantly throughout the study period after an initial increase. This likely represents a switch from acute inflammation to an anti-inflammatory environment around day 7 for all samples, possibly being downregulated by the increasing number of T_{reg} lymphocytes. Surprisingly we did not observe significant changes over time, but rather a relatively constant level of anti-inflammatory M2 macrophages and total T lymphocytes in the peri-implant tissue for the entire study period. Additionally, in accordance with those steady numbers of M2 macrophages, there was, except the temporary increase on day 14 for the MW-C_6F_6 implants, overall, no significant change in the number of mast cells. Though it was observed in other studies [21] that mast cells would have been likely to induce a phenotype switch through IL-4 degranulation we were unable to support their findings.

Interestingly the implants discharged in a microwave manner also followed the common pattern of constant cell reduction but when compared to controls presented a signifi-

cantly higher number of pro-inflammatory CD68+ cells indicating a moderately stronger inflammatory surrounding.

In contrast to those findings, other studies indicate a direct correlation between an activation of the host immune system and the hydrophobicity of metallic alloys [6,29]. Seong and Matzinger hypothesise that exposed hydrophobic structures trigger a DAMP activated immune response [19]. This could be a possible explanation regarding the observed stronger immune reaction evoked by PFP-coated titanium alloys compared to controls. In comparison to the experiments conducted by Moyano et al., the experiments are similar in that both used metals exhibit a hydrophobic surface. However, whereas Moyano et al. injected intravenously hydrophobic nanoparticles, leading to a systemic immune reaction in a mouse model [29], the present study observed a local reaction in peri-implant tissue in a rat model offering significantly fewer contact points for immune cells. In addition, intramuscular implantation resembles the actual clinical situation of long- and short-term implantation devices concerning the inflammatory reaction more closely. While the clinical purpose of fracture-fixation devices lies in bone healing, each bone is typically surrounded by muscles, which are a very well perfused and therefore an especially convenient tissue to survey local inflammatory reactions [12]. With regard to the latter, we recently described an increased amount of NK cells in the peri-implant tissue of hydrophilic positively charged titanium surfaces coated with plasma polymerised ethylendiamine (PPEDA) compared to controls during the acute phase (d7) of inflammation [30]. It is therefore conceivable that the increased adhesion due to hydrophilic surfaces elicits an increased inflammation. Additional data from a previous study supports a surface-dependent expression of cytokines in the serum of Lewis rats with different coated titanium implants [31]. While titanium discs coated with plasma polymerised allyl amine (positive charged, hydrophilic) induced a significant increase in pro-inflammatory cytokines IL-2 and IFN-γ, titanium discs coated with plasma polymerised acrylic acid (negative charged, hydrophobic) expressed steady and lower serum levels of IL-2 and a significant increase in anti-inflammatory IL-4 [31].

M1 macrophages can differentiate into M2 macrophages, known as anti-inflammatory cells, through the release of IL-4 and IL-10 by other modulatory cells [20]. Among those, mast cells are able to recruit and initiate fusion of macrophages into foreign body giant cells (FBGCs) by degranulation of histamine and secretion of IL-4 [21,32]. It should also be taken into consideration that in the present study CD68-positive stained cells were designated as pro-inflammatory M1-like cells and CD163-positive cells were designated as anti-inflammatory M2 macrophages. Until the present day, it is not possible to clearly differentiate histologically between M1 and M2 macrophages in rat tissue using only two markers, since there is no clear marker that is exclusively expressed on only one of the macrophage phenotypes [33–35].

The data herein indicate that titanium alloy implants with a radiofrequency discharge plasma (RF-C_3F_8) coating had a favorable low short- and long-term immune response in vivo in comparison to discs that were coated in a microwave process (MW). The most pronounced of these observed differences between RF- and MW-processed implants were seen for MHC class II antigen-presenting cells. On day 14 both MW-implant series, MW-C_3F_8 and MW-C_6F_6, presented a significant increase in stained cells probably representing a much stronger activation of the adaptive humoral response. In contrast, controls and RF-discs showed a significant reduction in MHC class II antigen-presenting cells throughout the study period associated with less severe or non-activation of the adaptive immune system. This change from acute (d7) to intermediate (d14) to chronic inflammation (d56) and the more severe T cell-mediated response was also observed in our total T lymphocytes staining for MW-implants, although only as a tendency.

Within the microwave coated implants the influence of two distinct precursors, C_3F_8 and C_6F_6, on the inflammatory reaction was biologically examined. Significant differences in the induced local immune reaction could be observed between those two precursors, indicating a more favorable interaction for MW-C_3F_8 compared to MW-C_6F_6 implants. The most pronounced alteration was observed for mast cells on day 14, when the number

of mast cells in the surrounding peri-implant tissue of MW-C_6F_6 discs was significantly elevated compared to controls.

Nestin, essential in the induction of myogenic differentiation and regeneration processes was observed to initially increase its expression number with a subsequent significant reduction in the peri-implant tissue until the end of the study period. This is in agreement with several other studies [25,36] highlighting that the process of myogenic muscle regeneration and healing mainly occurs parallel to the acute inflammation response.

Considering the initial assumption that a change from a pro- to an anti-inflammatory environment happened, IL-2R+ regulatory T lymphocytes (T_{reg}) are important cells inducing anti-inflammatory environments. All four implants showed a significant increase in T_{reg} cells until day 56 indicating a counter-inflammatory regulation happening at the end of the study period. Prabhakara et al. confirmed in in vitro studies that an early domination of T_{reg} cells could prevent a development of chronic inflammation [37]. In the present study CD25+/IL-2-positive stained cells were designated as T_{reg} cells. The IL-2 receptor complex is not only expressed by T_{reg} but also by CD8+ cells. It consists of three subunits IL-2Rα(CD25), IL-2Rß(CD122), and IL-2R.γ(CD132) [38]. However, the expression pattern of these subunits differs between IL-2-regulated cells, making it possible to histologically separate those inversely acting cells. While CD8+ T cells mainly carry the dimeric IL-2Rß(CD122), and IL-2R.γ(CD132) receptors, regulatory T cells express a high level of trimeric IL-2Rα(CD25) receptors [39,40]. This increase in T_{reg} cells could not be observed in the total amount of T lymphocytes since the number of positively stained cells per mm^2 was much lower, with a median ranging from 0.95 to 15.75 cells per mm^2 compared to T lymphocytes with median varying from 23.2 to 34.8 cells per mm^2 for the four implants investigated in this study.

As expected, natural killer cells, since being part of the innate immune system, were observed to be present in the peri-implant tissue in the acute phase of inflammation with a pronounced decrease until day 14. However, in the time that would likely represent a chronic state of inflammation, a subsequent increase for all samples was observed concurrently with a T_{reg} increase. It is therefore conceivable that NK cells could play a so-far-underestimated role in regulation of adaptive immune cells to a more favorable anti-inflammatory environment preventing excessive immune responses. Supporting this hypothesis, Lu et al. found that NK cells are able to influence lymphocyte expansion in particular and promote the development of CD4+ T-cells, while a blocked interaction resulted in lysis of activated autoreactive T cells [41].

Overall, especially the data for T lymphocytes and antigen-presenting cells indicate that humoral immunological reactions against the anti-adhesive films are likely involved in the biological response and should be therefore investigated in further studies. The anti-adhesive effectiveness should be studied in more detail regarding the relationship between physico-chemical properties and biological response.

5. Conclusions

The aim of this study was an in vivo evaluation of different anti-adhesive plasma-fluorocarbon-polymer (PFP) films on titanium alloy samples, investigating their influence on the local inflammatory tissue response after simultaneous implantation in Lewis rats. A differentiated morphometric evaluation of the inflammatory reaction over time was conducted by immunohistochemical staining of cryosections of surrounding peri-implant tissue. Samples were taken on day 7 representing the acute phase of inflammation, on day 14 for an intermediate phase and on day 56 representing chronic inflammation.

In summary, the results of this study support the conclusion that the type of plasma process technology (microwave vs. radiofrequency) significantly influenced the inflammatory reactions. In particular, titanium alloy implants with a radiofrequency discharge plasma coating (RF-C_3F_8) had a more favorable low short- and long-term immune response in vivo as well as a more efficient inhibition of osteoblast occupations in vitro. Within the microwave processed discs, implants coated with the C_3F_8-precursor had a

more favorable elicited cell interaction compared to implants coated with a C_6F_6-precursor. Our data strongly support the thesis of decreased inflammatory local reactions due to anti-adhesive coating. This was observed by the significant decrease in pro-inflammatory M1-like macrophages throughout the study period after an initial expected increase, possibly being downregulated by the significant increasing number of Treg-lymphocytes and activated NK cells. Therefore, the present study further supports the potential of low-temperature radiofrequency discharge plasma for temporary implant devices with PFP-coated anti-adhesive surfaces.

References

1. Elias, C.N.; Lima, J.H.C.; Valiev, R.; Meyers, M.A. Biomedical applications of titanium and its alloys. *J. Miner. Met. Mater. Soc.* **2008**, *60*, 46–49. [CrossRef]
2. Hayes, J.S.; Richards, R.G. Surfaces to control tissue adhesion for osteosynthesis with metal implants: In vitro and in vivo studies to bring solutions to the patient. *Expert Rev. Med. Devices* **2010**, *7*, 131–142. [CrossRef]
3. Busam, M.L.; Esther, R.J.; Obremskey, W.T. Hardware removal: Indications and expectations. *J. Am. Acad. Orthop. Surg.* **2006**, *14*, 113–120. [CrossRef]
4. Togrul, E.; Bayram, H.; Gulsen, M.; Kalaci, A.; Ozbarlas, S. Fractures of the femoral neck in children: Long-term follow-up in 62 hip fractures. *Injury* **2005**, *36*, 123–130. [CrossRef] [PubMed]
5. Lüthen, F.; Lange, R.; Becker, P.; Rychly, J.; Beck, U.; Nebe, J.G.B. The influence of surface roughness of titanium on beta1- and beta3-integrin adhesion and the organization of fibronectin in human osteoblastic cells. *Biomaterials* **2005**, *26*, 2423–2440. [CrossRef]
6. Wei, F.; Liu, S.; Chen, M.; Tian, G.; Zha, K.; Yang, Z.; Jiang, S.; Li, M.; Sui, X.; Chen, Z.; et al. Host Response to Biomaterials for Cartilage Tissue Engineering: Key to Remodeling. *Front. Bioeng. Biotechnol.* **2021**, *9*, 664592. [CrossRef] [PubMed]
7. Hayes, J.S.; Seidenglanz, U.; Pearce, A.I.; Pearce, S.G.; Archer, C.W.; Richards, R.G. Surface polishing positively influences ease of plate and screw removal. *Eur. Cells Mater.* **2010**, *19*, 117–126. [CrossRef]
8. Brunette, D.M. The effects of implant surface topography on the behavior of cells. *Int. J. Oral Maxillofac. Implant.* **1988**, *3*, 231–246.
9. Gittens, R.A.; Olivares-Navarrete, R.; Schwartz, Z.; Boyan, B.D. Implant osseointegration and the role of microroughness and nanostructures: Lessons for spine implants. *Acta Biomater.* **2014**, *10*, 3363–3371. [CrossRef] [PubMed]
10. Förch, R.; Chifen, A.N.; Bousquet, A.; Khor, H.L.; Jungblut, M.; Chu, L.-Q.; Zhang, Z.; Osey-Mensah, I.; Sinner, E.-K.; Knoll, W. Recent and Expected Roles of Plasma-Polymerized Films for Biomedical Applications. *Chem. Vap. Depos.* **2007**, *13*, 280–294. [CrossRef]

11. Finke, B.; Luethen, F.; Schroeder, K.; Mueller, P.D.; Bergemann, C.; Frant, M.; Ohl, A.; Nebe, B.J. The effect of positively charged plasma polymerization on initial osteoblastic focal adhesion on titanium surfaces. *Biomaterials* **2007**, *28*, 4521–4534. [CrossRef]

12. Hoene, A.; Walschus, U.; Patrzyk, M.; Finke, B.; Lucke, S.; Nebe, B.; Schroeder, K.; Ohl, A.; Schlosser, M. In vivo investigation of the inflammatory response against allylamine plasma polymer coated titanium implants in a rat model. *Acta Biomater.* **2010**, *6*, 676–683. [CrossRef]

13. Cho, E.; Kim, M.; Park, J.-S.; Lee, S.-J. Plasma-Polymer-Fluorocarbon Thin Film Coated Nanostructured-Polyethylene Tereph-thalate Surface with Highly Durable Superhydrophobic and Antireflective Properties. *Polymers* **2020**, *12*, 1026. [CrossRef] [PubMed]

14. Altankov, G.; Grinnell, F.; Groth, T. Studies on the biocompatibility of materials: Fibroblast reorganization of substratum-bound fibronectin on surfaces varying in wettability. *J. Biomed. Mater. Res.* **1996**, *30*, 385–391. [CrossRef]

15. Groth, T.; Altankov, G. Studies on cell-biomaterial interaction: Role of tyrosine phosphorylation during fibroblast spreading on surfaces varying in wettability. *Biomaterials* **1996**, *17*, 1227–1234. [CrossRef]

16. Kuhn, S.; Kroth, J.; Ritz, U.; Hofmann, A.; Brendel, C.; Müller, L.P.; Förch, R.; Rommens, P.M. Reduced fibroblast adhesion and proliferation on plasma-modified titanium surfaces. *J. Mater. Sci. Mater. Med.* **2014**, *25*, 2549–2560. [CrossRef]

17. Sirlin, C.B.; Brossmann, J.; Boutin, R.D.; Pathria, M.N.; Convery, F.R.; Bugbee, W.; Deutsch, R.; Lebeck, L.K.; Resnick, D. Shell osteochondral allografts of the knee: Comparison of mr imaging findings and immunologic responses. *Radiology* **2001**, *219*, 35–43. [CrossRef]

18. Fraitzl, C.R.; Egli, R.J.; Wingenfeld, C.; Ganz, R.; Hofstetter, W.; Leunig, M. Time course of biological activity in fresh murine osteochondral allografts paralleled to the recipient's immune response. *J. Investig. Surg.* **2008**, *21*, 109–117. [CrossRef] [PubMed]

19. Seong, S.-Y.; Matzinger, P. Hydrophobicity: An ancient damage-associated molecular pattern that initiates innate immune responses, Nature reviews. *Immunology* **2004**, *4*, 469–478. [CrossRef]

20. Alvarez, M.M.; Liu, J.C.; Trujillo-de Santiago, G.; Cha, B.-H.; Vishwakarma, A.; Ghaemmaghami, A.M.; Khademhosseini, A. Delivery strategies to control inflammatory response: Modulating M1-M2 polarization in tissue engineering applications. *J. Control. Release* **2016**, *240*, 349–363. [CrossRef] [PubMed]

21. Sheikh, Z.; Brooks, P.J.; Barzilay, O.; Fine, N.; Glogauer, M. Macrophages, Foreign Body Giant Cells and Their Response to Implantable Biomaterials. *Materials* **2015**, *8*, 5671–5701. [CrossRef]

22. Vivier, E.; Tomasello, E.; Baratin, M.; Walzer, T.; Ugolini, S. Functions of natural killer cells. *Nat. Immunol.* **2008**, *9*, 503–510. [CrossRef]

23. Schütt, C.; Bröker, B. *Grundwissen Immunologie*, 3rd ed.; Spektrum Akademischer Verlag: Heidelberg, Germany, 2011.

24. Seebach, E.; Kubatzky, K.F. Chronic Implant-Related Bone Infections-Can Immune Modulation be a Therapeutic Strategy? *Front. Immunol.* **2019**, *10*, 1724. [CrossRef]

25. Vaittinen, S.; Lukka, R.; Sahlgren, C.; Hurme, T.; Rantanen, J.; Lendahl, U.; Eriksson, J.E.; Kalimo, H. The expression of intermediate filament protein nestin as related to vimentin and desmin in regenerating skeletal muscle. *J. Neuropathol. Exp. Neurol.* **2001**, *60*, 588–597. [CrossRef]

26. Lindqvist, J.; Torvaldson, E.; Gullmets, J.; Karvonen, H.; Nagy, A.; Taimen, P.; Eriksson, J.E. Nestin contributes to skeletal muscle homeostasis and regeneration. *J. Cell Sci.* **2017**, *130*, 2833–2842. [CrossRef] [PubMed]

27. Finke, B.; Testrich, H.; Rebl, H.; Walschus, U.; Schlosser, M.; Zietz, C.; Staehlke, S.; Nebe, J.B.; Weltmann, K.D.; Meichsner, J.; et al. Plasma-deposited fluorocarbon polymer films on titanium for preventing cell adhesion: A surface finishing for temporarily used orthopaedic implants. *J. Phys. D Appl. Phys.* **2016**, *49*, 234002. [CrossRef]

28. Walschus, U.; Hoene, A.; Neumann, H.-G.; Wilhelm, L.; Lucke, S.; Lüthen, F.; Rychly, J.; Schlosser, M. Morphometric immunohis-tochemical examination of the inflammatory tissue reaction after implantation of calcium phosphate-coated titanium plates in rats. *Acta Biomater.* **2009**, *5*, 776–784. [CrossRef]

29. Moyano, D.F.; Goldsmith, M.; Solfiell, D.J.; Landesman-Milo, D.; Miranda, O.R.; Peer, D.; Rotello, V.M. Nanoparticle hydrophobic-ity dictates immune response. *J. Am. Chem. Soc.* **2012**, *134*, 3965–3967. [CrossRef]

30. Hoene, A.; Patrzyk, M.; Walschus, U.; Straňák, V.; Hippler, R.; Testrich, H.; Meichsner, J.; Finke, B.; Rebl, H.; Nebe, B.; et al. In vivo examination of the local inflammatory response after implantation of Ti6Al4V samples with a combined low-temperature plasma treatment using pulsed magnetron sputtering of copper and plasma-polymerized ethylenediamine. *J. Mater. Sci. Mater. Med.* **2013**, *24*, 761–771. [CrossRef] [PubMed]

31. Walschus, U.; Hoene, A.; Patrzyk, M.; Finke, B.; Polak, M.; Lucke, S.; Nebe, B.; Schroeder, K.; Podbielski, A.; Wilhelm, L.; et al. Serum profile of pro- and anti-inflammatory cytokines in rats following implantation of low-temperature plasma-modified titanium plates. *J. Mater. Sci. Mater. Med.* **2012**, *23*, 1299–1307. [CrossRef]

32. Tang, L.; Jennings, T.A.; Eaton, J.W. Mast cells mediate acute inflammatory responses to implanted biomaterials. *Proc. Natl. Acad. Sci. USA* **1998**, *95*, 8841–8846. [CrossRef] [PubMed]

33. Damoiseaux, J.G.M.C.; Dopp, E.A.; Neefjes, J.J.; Beelen, R.H.J.; Dijkstra, C.D. Heterogeneity of macrophages in the rat evidenced by variability in determinants: Two new antirat macrophage antibodies against a heterodimer of 160 and 95 kd (CD11/CD18). *J. Leukoc. Biol.* **1989**, *46*, 556–564. [CrossRef] [PubMed]

34. Dijkstra, C.D.; Dopp, E.A.; Joling, P.; Kraal, G. The heterogeneity of mononuclear phagocytes in lymphoid organs: Distinct macrophage subpopulations in the rat recognized by monoclonal antibodies ED1, ED2 and ED3. *Immunology* **1985**, *54*, 589–599.

35. Nakagawa, M.; Karim, M.R.; Izawa, T.; Kuwamura, M.; Yamate, J. Immunophenotypical Characterization of M1/M2 Macrophages and Lymphocytes in Cisplatin-Induced Rat Progressive Renal Fibrosis. *Cells* **2021**, *10*, 257. [CrossRef] [PubMed]

36. Lucke, S.; Hoene, A.; Walschus, U.; Kob, A.; Pissarek, J.-W.; Schlosser, M. Acute and chronic local inflammatory reaction after implantation of different extracellular porcine dermis collagen matrices in rats. *BioMed Res. Int.* **2015**, *2015*, 938059. [CrossRef]

37. Prabhakara, R.; Harro, J.M.; Leid, J.G.; Keegan, A.D.; Prior, M.L.; Shirtliff, M.E. Suppression of the inflammatory immune response prevents the development of chronic biofilm infection due to methicillin-resistant Staphylococcus aureus. *Infect. Immun.* **2011**, *79*, 5010–5018. [CrossRef] [PubMed]

38. Minami, Y.; Kono, T.; Miyazaki, T.; Taniguchi, T. The IL-2 receptor complex: Its structure, function, and target genes. *Annu. Rev. Immunol.* **1993**, *11*, 245–268. [CrossRef] [PubMed]

39. Arenas-Ramirez, N.; Woytschak, J.; Boyman, O. Interleukin-2: Biology, Design and Application. *Trends Immunol.* **2015**, *36*, 763–777. [CrossRef]

40. Sakaguchi, S.; Sakaguchi, N.; Asano, M.; Itoh, M.; Toda, M. Immunologic self-tolerance maintained by activated T cells expressing IL-2 receptor alpha-chains (CD25). Breakdown of a single mechanism of self-tolerance causes various autoimmune diseases. *J. Immunol.* **1995**, *155*, 1151–1164.

41. Lu, L.; Ikizawa, K.; Hu, D.; Werneck, M.B.F.; Wucherpfennig, K.W.; Cantor, H. Regulation of activated CD4+ T cells by NK cells via the Qa-1-NKG2A inhibitory pathway. *Immunity* **2007**, *26*, 593–604. [CrossRef]

Tuning the Surface Wettability of Cyclic Olefin Copolymer by Plasma Treatment and Graphene Oxide Deposition and Reduction

Fadi Dawaymeh [1], Yawar Abbas [2] , Maryam Khaleel [3], Anas Alazzam [4],* and Nahla Alamoodi [3],*

[1] Center of Catalysis and Separation (CeCaS), Department of Chemical Engineering, Khalifa University, Abu Dhabi P.O. Box 127788, United Arab Emirates; 100052916@ku.ac.ae

[2] System on Chip Center (SoCC), Department of Physics, Khalifa University, Abu Dhabi P.O. Box 127788, United Arab Emirates; yawar.abbas@ku.ac.ae

[3] Research and Innovation Center in Carbon Dioxide and Hydrogen (RICH), Center of Catalysis and Separation (CeCaS), Department of Chemical Engineering, Khalifa University, Abu Dhabi P.O. Box 127788, United Arab Emirates; maryam.khaleel@ku.ac.ae

[4] System on Chip Center (SoCC), Department of Mechanical Engineering, Khalifa University, Abu Dhabi P.O. Box 127788, United Arab Emirates

* Correspondence: anas.alazzam@ku.ac.ae (A.A.); nahla.alamoodi@ku.ac.ae (N.A.)

Abstract: Selective altering of surface wettability in microfluidic channels provides a suitable platform for a large range of processes, such as the phase separation of multiphase systems, synthesis of reaction controlled, nanoliter sized droplet reactors, and catalyst impregnation. Herein we study the feasibility to tune the wettability of a flexible cyclic olefin copolymer (COC). Two methods were considered for enhancing the surface hydrophilicity. The first is argon/oxygen plasma treatment, where the effect of treatment duration on water contact angle and COC surface morphology and chemistry were investigated, and the second is coating COC with GO dispersions of different concentrations. For enhancing the hydrophobicity of GO-coated COC surfaces, three reduction methods were considered: chemical reduction by Hydroiodic acid (HI), thermal reduction, and photo reduction by exposure of GO-coated COC to UV light. The results show that as the GO concentration and plasma treatment duration increased, a significant decrease in contact angle was observed, which confirmed the ability to enhance the wettability of the COC surface. The increase in hydrophilicity during plasma treatment was associated with the increase in surface roughness on the treated surfaces, while the increase during GO coating was associated with introducing oxygen-containing groups on the GO-coated COC surfaces. The results also show that the different reduction methods considered can increase the contact angle and improve the hydrophobicity of a GO-coated COC surface. It was found that the significant improvement in hydrophobicity was related to the reduction of oxygen-containing groups on the GO-coated COC modified surface.

Keywords: surface wettability; graphene oxide; plasma treatment; cyclic olefin copolymer; GO reduction

1. Introduction

Several materials are used in the fabrication of microfluidic devices. Recently, the fabrication of these devices has relied on polymer based materials such as polydimethylsiloxane (PDMS) and cyclic olefin copolymer (COC) [1–4]. This attention is related to their mechanical and chemical characteristics that make the fabrication of devices faster, easier, and cheaper in comparison to other materials such as silicon and glass [1,2]. Furthermore, PDMS and COC have other desirable features, such as being biologically inert, optically transparent, nonflammable, low cost, and nontoxic [2]. Therefore, it becomes an alternative material for different micromanufacturing models. However, PDMS and COC are hydrophobic in nature, which makes them unsuitable for many bio-applications [5,6]. Several physical and chemical techniques have been developed to modify the surface wettability of

polymer based microchannels for selective applications. These include plasma treatment, chemical vapor deposition (CVD), graft polymer coating, the sol-gel technique, and layer by layer (LBL) deposition [2,7–10]. The oxidation of a PDMS polymer surface by oxygen plasma suffers from being temporary [11]. Storing the oxidized surfaces in water and other high surface-energy media can be used to preserve the hydrophilic surface for some time before the polymer reverts to its original surface properties. However, the exposure of the surface to air or other low surface-energy media results in its hydrophobic recovery [12]. On the other hand, chemical vapor deposition can produce long lasting coatings but only has an effect on chips that are not assembled or connected to other parts or accessories [13]. To achieve a high coating effectiveness, the vapor used for coating should have unrestricted access to the substrate. In a PDMS assembled channel, the use of graft photopolymerization for covalent surface modification faces some challenges, because it does not react on the wall but in the channel cavity. Hu et al. [14] developed a method to solve this challenge by photoinitiator preadsorption before polymerization. However, in addition to multiple washings, this method also requires the manual injection of a photoinitiator and monomer solution into the chip, which makes the process complicated. The sol-gel technique for PDMS modification was used by Abate et al. [15]. This method permanently modifies the PDMS with a glass coating, which has strong resistance to organic solvents and can customize its performance. However, the coating thickness can sometimes be as high as 10 mm, which affects the size of the channel and interferes with the complex geometry of the device. In addition, the critical gelation reaction time lasts for few seconds, making the process delicate and uncontrollable. LBL is simple, clear, and versatile. However, injecting the solution and removing it during washing and the formation of layers is a manual process.

Graphene oxide (GO) and its reduced form are two of the most interesting materials in recent research due to their superior physical and chemical properties. The unique planar structure and the two dimensionality of graphene oxide enable the development of flexible optoelectronics, transparent electrodes, energy harvesting devices, and photodetectors [16–18]. Graphene oxide has a high concentration of oxygen-containing functional groups, which can form hydrogen bonds when in contact with water. Recently, Alazzam and Alamoodi [4,19] have proposed a new surface modification method, taking advantage of the hydrophilicity of GO to pattern water wet surfaces on COC. The COC substrates were patterned with graphene oxide by photolithography. The hydrophilicity of COC and GO-coated COC surfaces was evaluated using water contact angle measurements. The results showed that the contact angle of the COC surface was 120°, indicating strong hydrophobicity, whereas GO-coated COC showed a strong hydrophilic surface with a contact angle of 10°.

While GO is hydrophilic, the oxygen-containing functional groups can be removed by several methods, called reduction methods, to restore graphene like hydrophobicity. These methods include thermal treatment, chemical reducing agents, ultraviolet reduction, electric current, selective laser reduction, or photothermal reduction [16,20–24]. The reduction extent of GO depends on the process conditions of the method used. Although there are numerous studies that investigate the different properties of GO, few have reported on tuning the surface wetting properties of polymers by means of GO coating and reduction process conditions. This is of particular interest in the case of functional coatings for selective patterning of wettability. Such coatings are particularly important for use in biomaterials, self-cleaning surfaces, smart textiles, microelectronics, and microfluidics [25–27]. In this work, we study the feasibility to tune the wettability of flexible COC. Two methods were considered for enhancing the surface hydrophilicity. The first is plasma treatment, where the effect of treatment duration on water contact angle and COC surface morphology and chemistry was investigated, and the second is coating COC with GO dispersions of different concentrations. For enhancing the hydrophobicity of GO-coated COC surfaces, three reduction methods were considered: chemical reduction by Hydroiodic acid (HI), thermal reduction, and photo reduction by exposure of GO film to UV light.

2. Materials and Methods

2.1. Materials

Disc shaped COC polymer substrates (diameter: 6.5 cm, thickness: 175 μm, Tg: 132 °C, MICROFLUIDIC CHIPSHOP, Jena, Germany), aqueous dispersion of GO (4 mg/mL, SIGMA-ALDRICH, Missouri, US), aqueous dispersion of GO (2.5 wt%, GRAPHENEA, San Sebastian, Spain), hydroiodic (HI) acid (≥47.0%, Sigma-Aldrich, MO, USA), ethanol (absolute, >99.8%, Fisher Chemical, Waltham, MA, USA), isopropanol (absolute, >99.8%, Fisher Chemical, Waltham, MA, USA) and deionized water (DI) were used in this study.

2.2. Preparation of GO-Coated COC

Graphene oxide dispersions of water and ethanol at a volume ratio of 1:4 were prepared and used to increase the uniformity of the GO layer coated on the COC substrate. GO (4 mg/mL, SIGMA-ALDRICH, St. Louis, MO, USA) dispersions with different concentrations (0.1, 1, 2, 3 and 4 mg/mL) were prepared to study the effect of GO concentrations on the wettability of the COC surface. Dispersions of 4 mg/mL prepared from GO (2.5 wt%, GRAPHENEA, San Sebastián, Spain) were used for all other experiments. The procedure to coat GO on COC substrates is illustrated schematically in Figure 1. First, the COC substrate was cleaned using isopropanol and DI. Next, the substrate was treated with an argon/oxygen low pressure inductive plasma (HARRICK PLASMA, Model: Expanded plasma cleaner/PDC-002, Ithaca, NY, USA) for a fixed duration (5, 20, 60 and 120 min) to increase the surface energy of the substrate and enhance the bonding between GO and COC substrate [19]. Plasma treatment was performed at a pressure of 626 mtorr, gas flowrates of 1–2 scfh, and a maximum power of 29.6 W with radio frequency (RF) of 12 MHz. As will be discussed in the results section, plasma treatment for more than 5 min did not result in noticeable changes in contact angle for GO-coated COC substrates. Therefore, for the remaining experiments, the time for plasma treatment was fixed at 5 min.
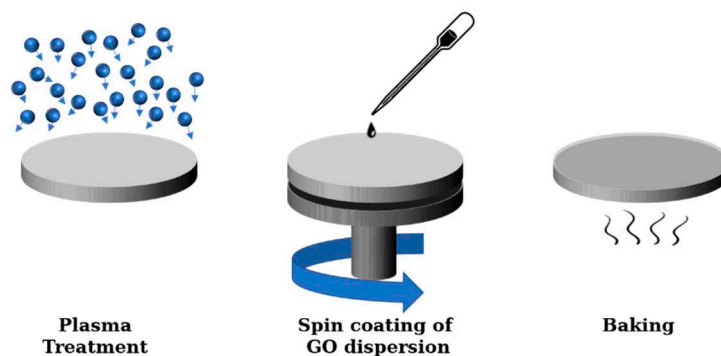
Figure 1. Schematic illustration of the experimental procedure followed to deposit GO films on COC substrates via spin coating.

After plasma treatment, a few drops of graphene oxide dispersion were dispensed on top of the substrate followed by spin coating at 3000 rpm for 1 min. Finally, the coated substrate was baked at 60 °C for 2 min.

2.3. Reduction of GO-Coated COC

2.3.1. UV Reduction

A UV flood exposure system (BACHUR and ASSOCIATES, Model: LS-150-5C2 NUV exposure system, Santa Clara, CA, USA) was used to reduce the GO coating on the COC substrate in a controlled manner. The lamp emits ultraviolet light with wavelengths of 365 nm and 400 nm with an intensity of 10 mW/cm^2. The lamp was warmed for 20 min before it was used in the experiments. Then, GO-coated COC substrates were placed individually under the UV lamp and treated for different durations (10, 30, 60, 120 and 180 min) under atmospheric pressure.

2.3.2. HI Reduction

The GO-coated COC substrates were immersed in (47.0%) HI acid for different durations (10, 30 and 180 min). After that, the partially reduced GO-coated COC substrates were washed with DI water and dried with compressed air.

2.3.3. Thermal Reduction

The GO-coated COC substrates were heated on a hot plate at different temperatures (80, 100 and 120 °C) for 30 min, and then cooled to room temperature.

2.4. Characterization

The topographic images of the plasma treated samples were obtained by using the AC imaging mode of atomic force microscopy (AFM) of ASYLUM MFP-3D. The high frequency silicon tip with apex diameter of 30 nm was used for imaging. The resonance frequency of the tip is about 246 kHz. The images were taken for scan area of 20 μm × 20 μm with an optimized scan frequency of 1 Hz. Field emission scanning electron microscope (FESEM) (JEOL JSM-6710FFEG-SEM) was used to investigate and characterize the coating of graphene oxide sheets on the COC substrates. The FESEM micrographs were taken using the acceleration voltage of 5 kV at the working distance of 5 mm. The GO-coated COC substrates characterized by AFM and SEM were coated with GO dispersion with a concentration of 4 mg/mL. The Bruker Alpha FTIR spectrometer system equipped with diamond attenuated total reflectance (ATR) accessory was used to perform FTIR analysis on all treated samples with a wavenumber ranging from 450–4000 cm^{-1}. Five repetitions with twenty four scans with a resolution of 4 cm^{-1} were performed on each sample. Postprocessing data using smooth tool in Origin Pro software was performed to remove noisy data in hydroxyl and carbonyl FTIR spectrums. The wettability of the surface was characterized by contact angle measurements using a goniometer (Ossila, Model:L2004A1, Sheffield, UK), in which a 5 μL droplet of deionized water was deposited on the treated surface. The images were analyzed using Ossila Contact Angle (v3.1) software, which uses the tangent method for contact angle measurements. For each sample, the contact angle was measured at a minimum of ten droplets of the same volume at different locations and the results were averaged. All surface characterizations were carried out immediately after each treatment method.

3. Results

3.1. Effect of Plasma Exposure Time for COC

Plasma exposure causes photo-oxidation, chain session and crosslinking on the COC surface. The active free radicals, ions and electrons generated during plasma treatment induces C-C and C-H bond scission causing shorter polymer chains, the formation of other molecules through recombination reactions and crosslinking on the surface [28]. Several factors affect the outcome of plasma treatment including the power of the plasma unit, the type of plasma (low pressure plasma or atmospheric plasma), and the treatment duration. The use of a high powered plasma treatment or treating polymer surfaces over a long period of time has also been reported to damage polymer surfaces [29]. In the current work, contact angle measurements on the plasma treated COC surfaces were performed directly after plasma treatment. Figure 2 shows the effect of plasma treatment duration on the water contact angle. Untreated COC has a contact angle of 109° while plasma treatment significantly reduces the contact angle to 11° after a 20-min exposure time. It was also observed that for processing times longer than 20 min, the contact angle increased slightly, reaching a value of 15° at 60 min. To understand the contact angle declination, FTIR analysis and AFM imaging were conducted. FTIR analysis was conducted to analyze changes in the functional groups on the COC surface during plasma treatment. The observed FTIR peaks for plasma treated surfaces are shown in Figure 3. It is seen that, generally, there are no major differences between the FTIR results for the plasma treated COC surfaces at different treatment durations. Compared to untreated COC, aldehydes and carbonyl

groups are generated during the plasma treatment process (the relevant peak appears at $1740 \, cm^{-1}$). These carbonyl-containing groups are formed in the presence of oxygen during plasma treatment [30]. The terminal aldehyde group can be formed by the rearrangement of the peroxy radical intermediate formed by chain scission, or by the decomposition of peroxide and hydroperoxide on the surface of the polymer [28]. AFM images of the surface topography and surface roughness values of untreated and modified COC substrates are shown in Figure 4 and Table 1, respectively. It has been observed that the untreated COC has a smoother surface compared to the plasma modified surface. The surface roughness of the untreated COC substrate was 15.7 nm, while that of the plasma modified COC specimens treated for 5, 20 and 60 min were 33.4 nm, 44 nm and 122.3 nm, respectively. The samples exposed to a long duration of plasma (60 min exposure) showed a very rough surface with occasional holes and cracks observed on the surface (Figure 4d). The increase in the concentration of surface oxygen functional groups and higher surface roughness could contribute to the increase in surface hydrophilicity.
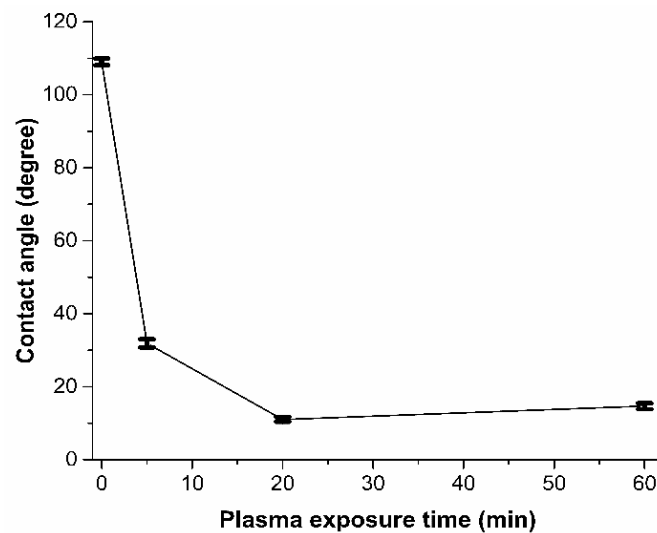
Figure 2. Variation of DI water contact angle with plasma exposure time in plasma treated COC. Each contact angle datapoint shows the average value from ten measurements.
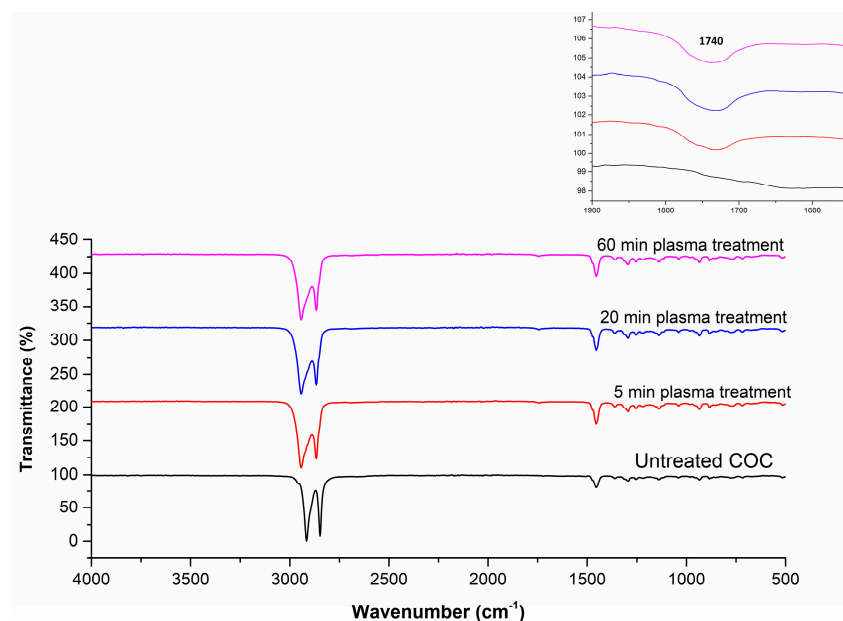
Figure 3. FTIR spectra for plasma−treated COC at different plasma exposure times.
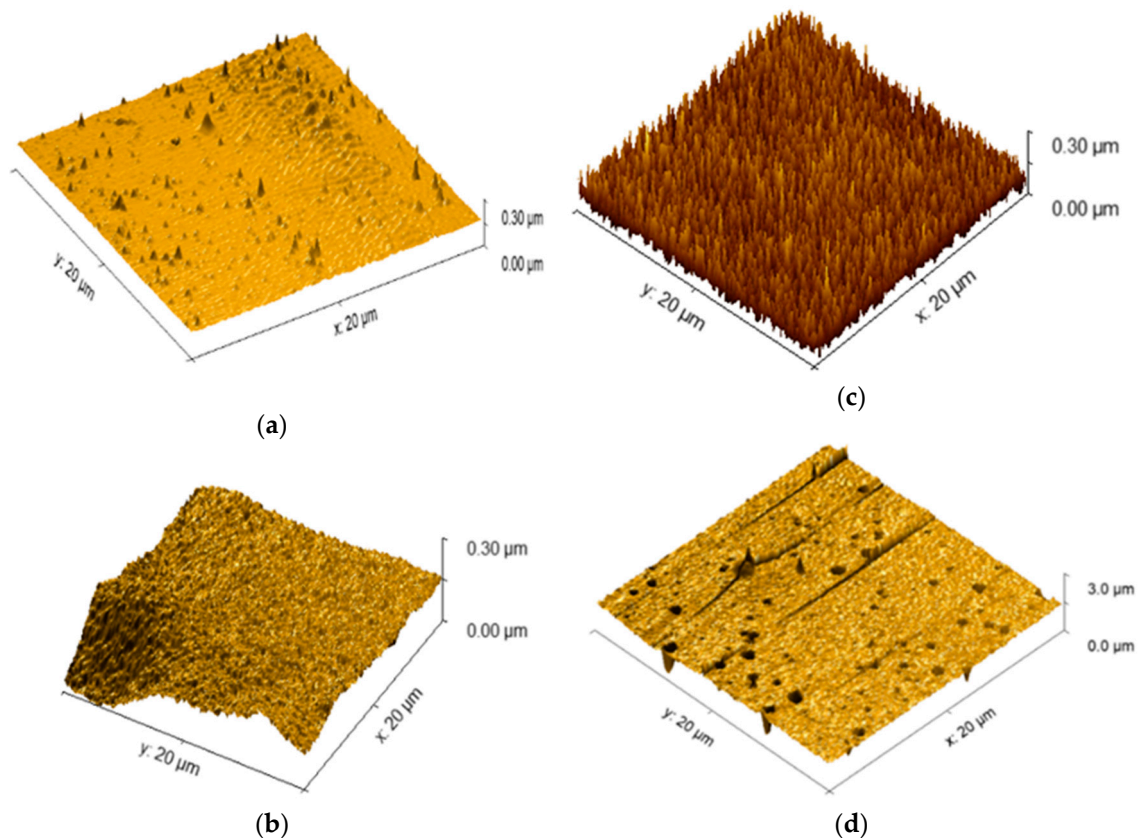
Figure 4. Surface topology of COC substrates using AFM; (**a**) untreated and plasma− treated for (**b**) 5 min, (**c**) 20 min, and (**d**) 120 min.

Table 1. Surface roughness of plasma treated COC at different plasma exposure times.

Plasma Exposure Time (min)	Surface Roughness (nm)
0 (untreated COC)	15.7
5	33.4
20	43
120	122.3

3.2. Structural Characterization of COC Coated with GO

SEM and AFM images of COC substrate coated with 4 mg/mL GO solution, shown in Figure 5, confirm the uniformity of the GO coating and the interconnection of the sheets, with very little delamination and wrinkles. The uniformity of the GO film on the COC substrate could be a consequence of surface roughness and polar species formed during the plasma treatment process. The FTIR spectra of GO, untreated COC, plasma treated COC, and GO-coated COC, shown in Figure 6, were studied to compare the chemical groups on the COC surface. The FTIR spectra for the untreated COC substrate (Figure 6b), shows a peak at 1452 cm^{-1} for the C-H bending mode and peaks in the range of 2913–2847 cm^{-1} for the stretching mode of C-H (aldehydic H and ethynenic H), in agreement with the literature [28,31,32]. Peaks near 1740 and 3313 cm^{-1} for pure GO and GO-coated COC correspond to C=O and –OH groups, respectively. The absorption peak at 1740 cm^{-1} corresponds to the presence of aldehydes and carbonyl groups generated during plasma treatment, however, the intensity of the peak increases with GO modification, confirming the presence of GO on the COC substrate. The absence of a peak at 3313 cm^{-1} in the plasma-treated COC does not necessarily indicate the absence of hydroxyl groups, which may be present in concentrations below the detection limit of FTIR.
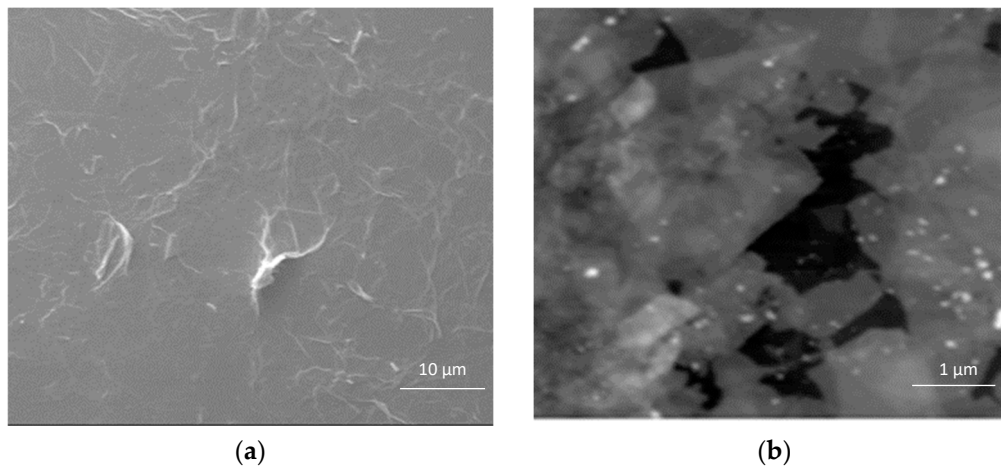
Figure 5. (**a**) SEM and (**b**) AFM images of 4 mg/mL GO−coated COC. The white lines in (**a**) represent the boundaries of the GO flakes.
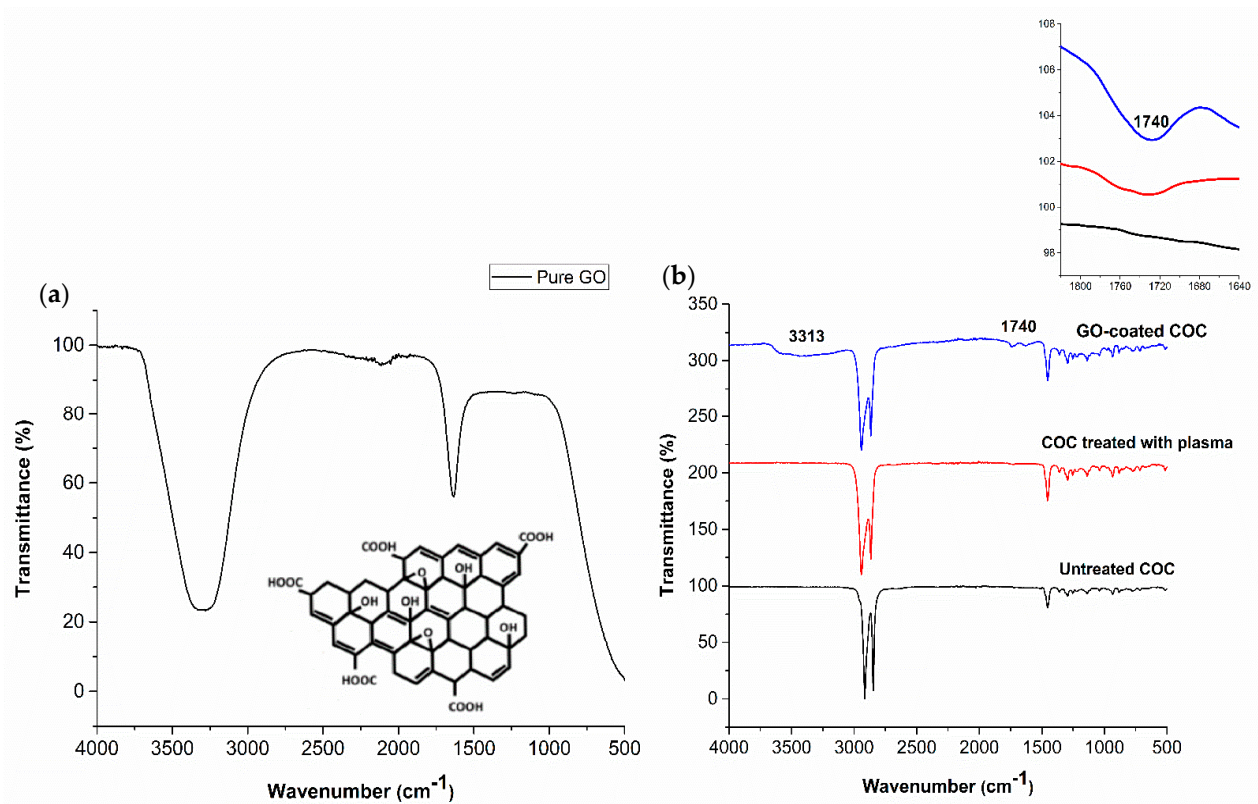
Figure 6. Typical FTIR spectra for (**a**) Graphene oxide and (**b**) untreated COC, COC treated with plasma for 5 min, and 4 mg/mL GO−coated COC.

3.3. Effect of Plasma Treatment on GO Coating

In our recent work [3,4,19] we have shown that treating COC with O_2/Ar plasma followed by spin coating with GO dispersions resulted in stable GO coatings. Here, we investigated whether there is an apparent effect of plasma treatment on the wettability of the COC after the GO deposition. Contact angle measurements were performed on COC substrates treated with plasma for different durations (5, 20, 60 and 120 min), prior to coating them with different concentrations of GO dispersions (Figure 7). It was observed that the contact angle does not change considerably for each GO concentration when exposed to

different plasma treatment durations. Slight changes may result from experimental errors. Therefore, a plasma modification time of 5 min was used in all subsequent experiments.
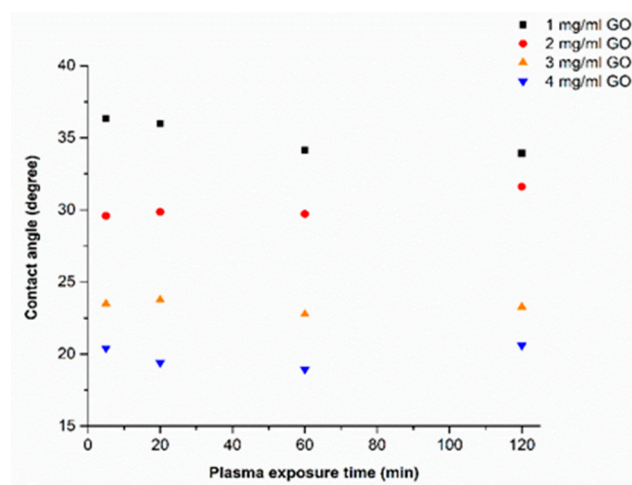
Figure 7. Variation of DI water contact angle with plasma exposure time in plasma pretreated GO−coated COC.

3.4. Effect of GO Concentration

The effect of GO concentration on the wettability of the COC substrate surface was studied using water contact angle measurement. Five GO dispersions were prepared with concentrations of 0.1, 1, 2, 3, and 4 mg/mL, and were deposited on COC substrates pretreated by O_2/Ar plasma for 5 min using a spin coater at a speed of 3000 rpm. Figure 8 shows the effect of the GO concentration on the contact angle. A decrease in water contact angle with an increase in the concentration of GO dispersion was observed. This behavior can be explained by the fact that graphene oxide is rich in oxygen-containing functional groups (see Figure 6a), which can form hydrogen bonds when in contact with water [33]. Higher concentrations of GO result in the deposition of a larger amount of GO flakes and an increase in the surface concentration of oxygen-containing functional groups, thereby increasing the hydrophilicity of the coated COC. Images of the water droplets on the surface of the GO-coated COC substrates are shown in Figure 9 for GO concentrations up to 4 mg/mL, which resulted in minimum contact angle of 20°. The increase in hydrophilicity with GO concentration can be further confirmed from FTIR analysis. Figure 10 illustrates the functional groups appearing on the COC substrates for different GO concentrations and for plasma treatment of 5 min. It is observed that aldehydes and carbonyl groups are generated during plasma treatment, as discussed in the previous section. They also appear after GO deposition with a more pronounced peak as the GO concentration increases (the relevant peak appears at 1740 cm^{-1}). The associated FTIR peak in the range of 3100–3700 cm^{-1} was present in the GO-coated COC samples but not in the plasma treated COC ones. This peak confirms the presence of hydroxyl groups (–OH). The areas and heights of the FTIR peaks are directly proportional to the concentration of each chemical species present on the COC surface [28]. From the changes in peak area and height in Figure 10b,c, it can be seen that the amount of hydroxyl and carbonyl groups increases with the increase of GO concentration, which contributes to the increase in the hydrophilicity of higher concentration GO-coated COC surfaces.
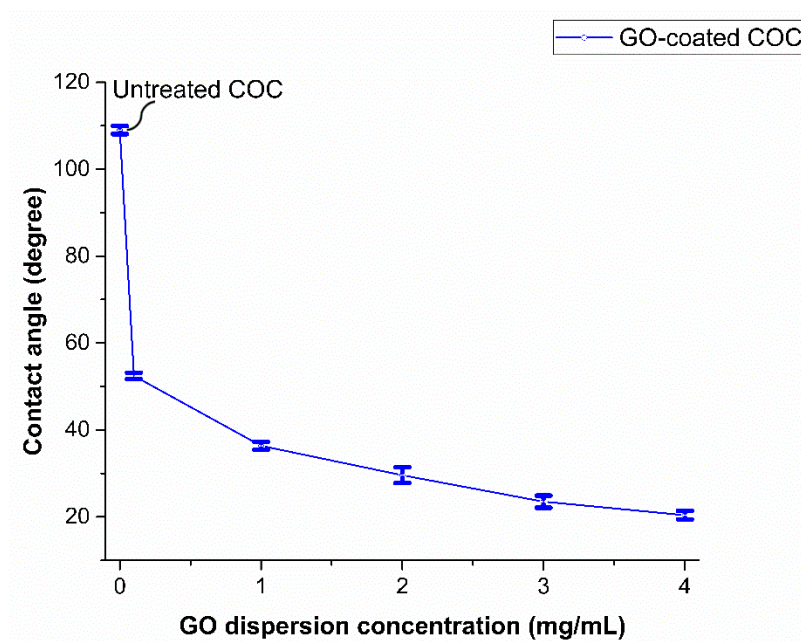
Figure 8. DI water contact angle on GO−coated COC surface as a function of GO dispersion concentration. Contact angle of untreated COC is 109°. All samples were treated for 5 min before the deposition of the GO film.
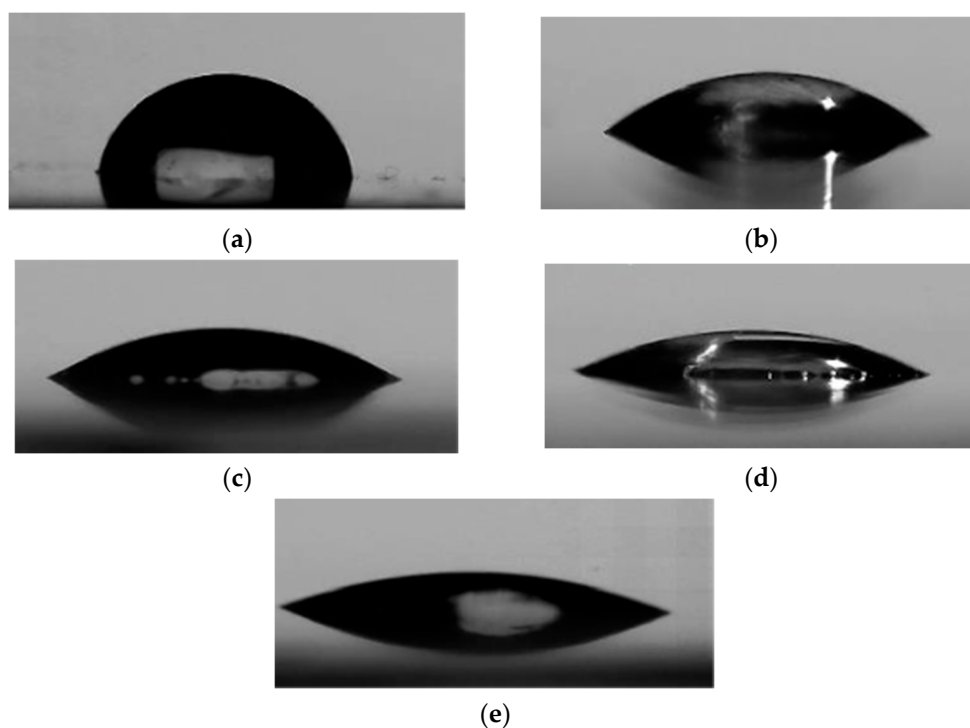
Figure 9. Images of water droplets on the surface of (**a**) COC, and GO−coated COC with GO suspension concentrations of (**b**) 1 mg/mL, (**c**) 2 mg/mL, (**d**) 3 mg/mL, and (**e**) 4 mg/mL at 5 min plasma exposure time. Results were collected immediately after the wafer was fabricated.
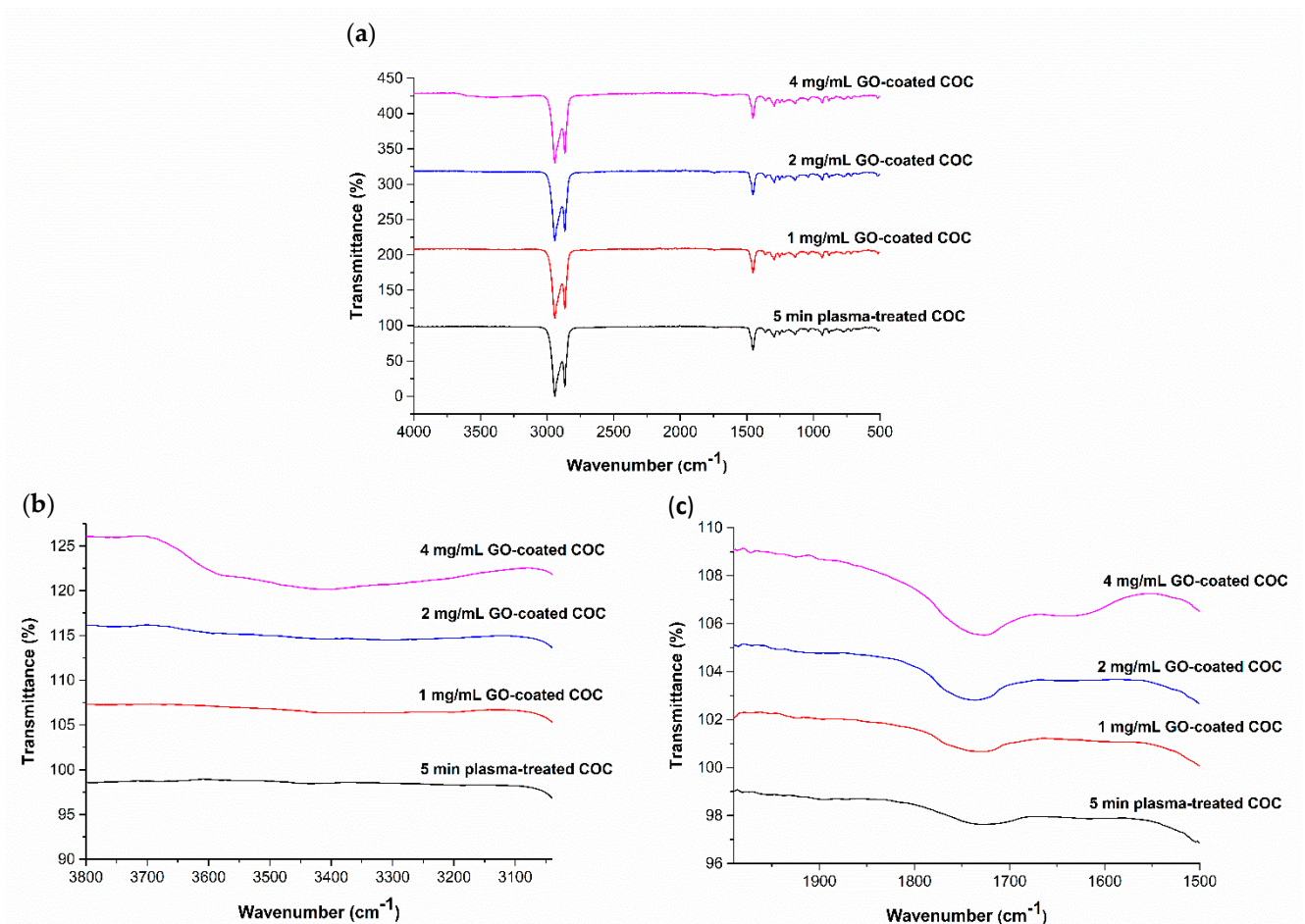
Figure 10. (**a**) FTIR−ATR spectra for five min plasma treated COC and subsequently GO−coated; Expanded regions of FTIR-ATR spectra between (**b**) 3050–3800 cm^{-1} and (**c**) 1500–2000 cm^{-1}.

3.5. Effect of Ultraviolet (UV), Hydroiodic Acid (HI) and Thermal Treatment on the Wettability of GO-Coated COC

As seen from the results presented in the previous section, by coating COC substrates with GO dispersions, the wettability of the surface is greatly enhanced, as reflected by the decrease of the contact angle from 109° (untreated COC) to 20° (4 mg/mL GO-coated COC). The hydrophilicity of the GO-coated COC surface can be further tuned by reducing GO using three different approaches: (a) photo reduction using ultraviolet radiation; (b) chemical reduction using hydroiodic acid and (c) thermal reduction by heating the substrate. The effect of photo reduction, chemical (Figure 11a) and thermal reduction (Figure 11b) on the surface hydrophobicity of GO-coated COC surfaces was evaluated by measuring the water contact angle, as shown in Figure 11. The contact angle of the 4 mg/mL GO-coated COC surface was 33° before treatment. Note that this contact angle is higher than the one mentioned in the previous section as this is due to using GO from a different supplier (Graphenea). It can be seen from Figure 11a that the HI acid treatment significantly increases the contact angle to 82° after a 30-minute immersion time. No further change in contact angle was observed for immersion times beyond 30 min. For UV treatment, the contact angle increases slightly with exposure time reaching a maximum value of 55°, with no further change after 60 min (see Figure 11a). This can be attributed to the UV exposure process, where reduction by UV light occurs at the exposed GO flakes at the surface of the coating, this will be further discussed with FTIR spectra in Figure 12. Finally, the thermal treatment of GO-coated COC significantly increases the contact angle reaching 74° at 100 °C. Further increase in temperature, to 120 °C, results in a slight increase in contact angle, to 79° (Figure 11b). This is unlike the HI acid and UV treatment methods,

where no further changes in the contact angle were observed after 30 min and 60 min, respectively. It is expected that thermal treatment will increase the contact angle further as the temperature rises. However, this was not investigated because of the COC glass transition temperature of 132 °C. It has been reported that as GO is thermally reduced in the range of 25–130 °C, oxygen-containing groups are mildly removed and the lattice of GO gradually contracts, and at temperatures above 130 °C, oxygen-containing groups disappear significantly and GO lattices contract drastically, resulting in a further increase in the contact angle [34].
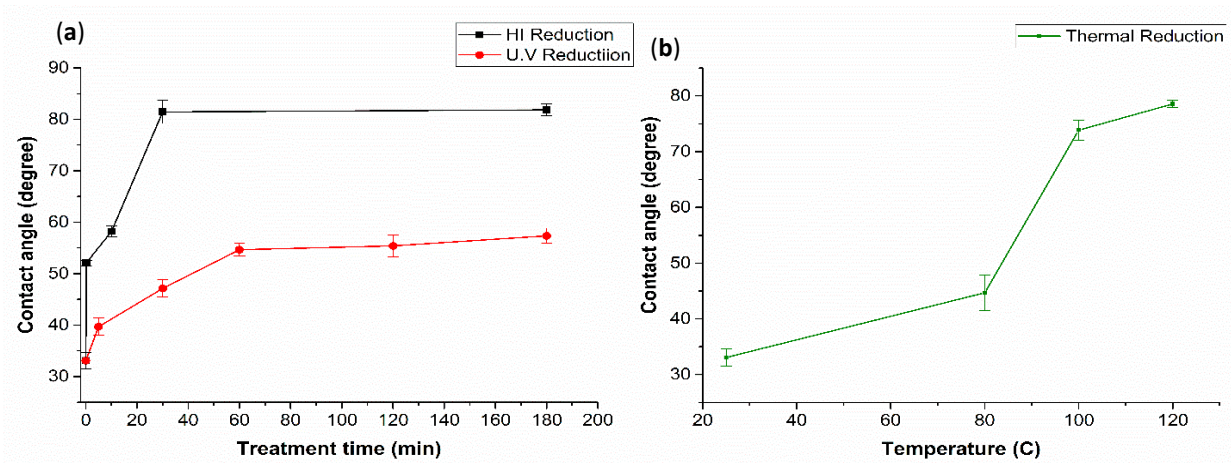
Figure 11. DI water contact angle on the surface of 4 mg/mL GO−coated COC with (**a**) HI and UV reduction time (min) and (**b**) thermal reduction temperature.
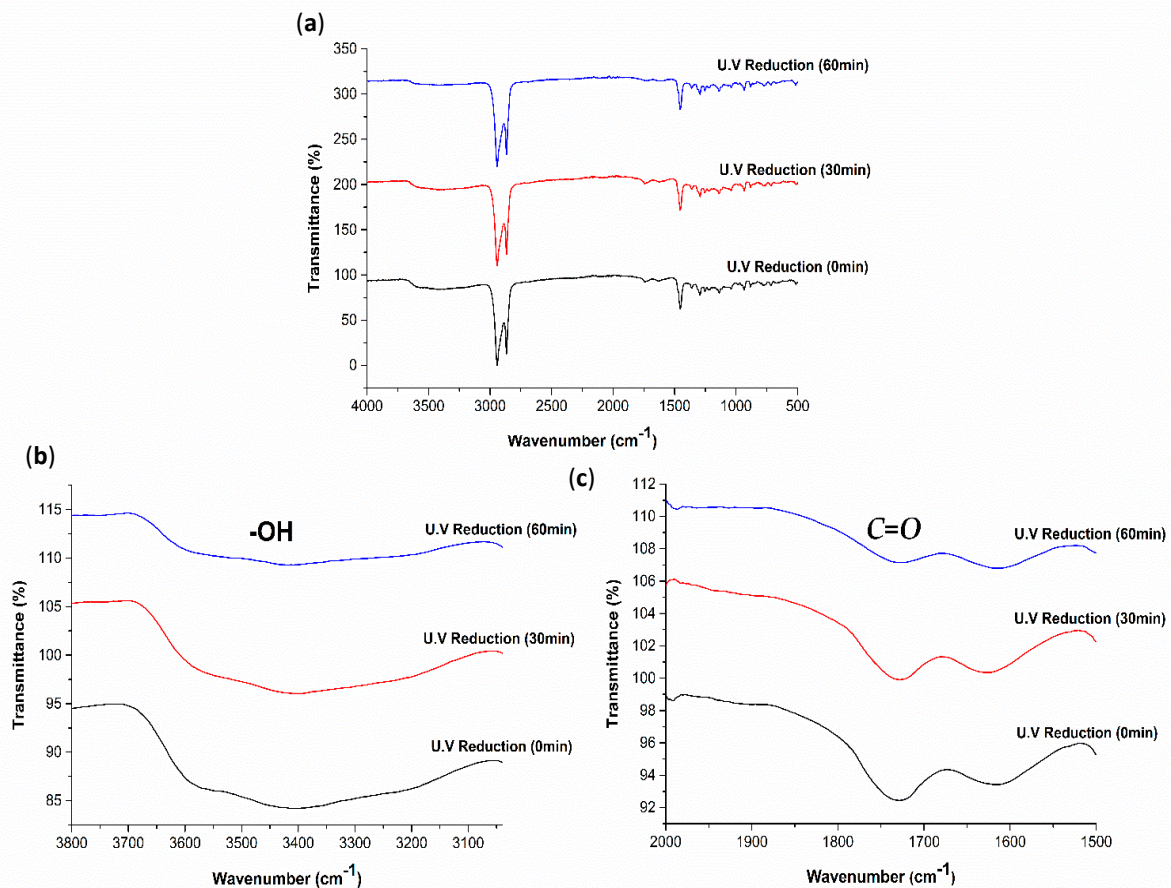
Figure 12. (**a**) FTIR−ATR spectra for 4 mg/mL GO−coated COC treated with UV reduction for different durations and expanded regions of FTIR−ATR spectra between (**b**) 3050–3800 cm^{-1} and (**c**) 1500–2000 cm^{-1}.

To further evaluate the degree of GO-coated COC reduction by the different methods, the FTIR spectra were obtained, as illustrated in Figures 12–14. From the changes in FTIR peak height and area, the amount of hydroxyl and carbonyl groups decrease with the increase in UV exposure time, HI acid immersion time and temperature, which agrees with the reduction of GO and increase of hydrophobicity of GO-coated COC surfaces. The FTIR spectra in Figure 12 shows that after UV exposure of 180 min, hydroxyl groups still exist on the GO coated surface, however, to a lesser extent. The same is observed for the carbonyl groups. In comparison to the FTIR spectra in Figures 13 and 14, the reduction in these groups is minimal with UV exposure. This further confirms that the UV exposure effect is restricted to the exposed GO flakes on the surface of the coating. The expanded FTIR spectra in Figure 13b,c for the HI acid treatments show that the intensity of the oxygen-containing functional groups of the GO-coated COC decreases more than other treatment methods, with the hydroxyl group disappearing completely. This means that the removal of oxygen-containing functional groups in HI acid is greater than other treatment methods for the same duration. At the same time, the absorption peak at 1562 cm^{-1} can be clearly observed during HI reduction, with a higher intensity compared with other methods, which is caused by the stretching vibration of the sp2 carbon–carbon chemical bond in the graphene structure [35,36]. In addition, it has been found that alkyne groups are generated during HI treatment (the relevant peak appears at 2122 cm^{-1}). Figure 14 shows a similar trend for the thermal reduction of the GO-coated COC surface, where the oxygen-containing functional groups decrease as the temperature increases. It is worth mentioning that while the contact angle measurements for 30 min treatments in HI acid and at 120 °C are comparable, the FTIR spectra for both cases are different. This suggests that the reduction using HI acid has a greater effect than just reducing the oxygen-containing functional groups, however, further studies are required to confirm this observation.
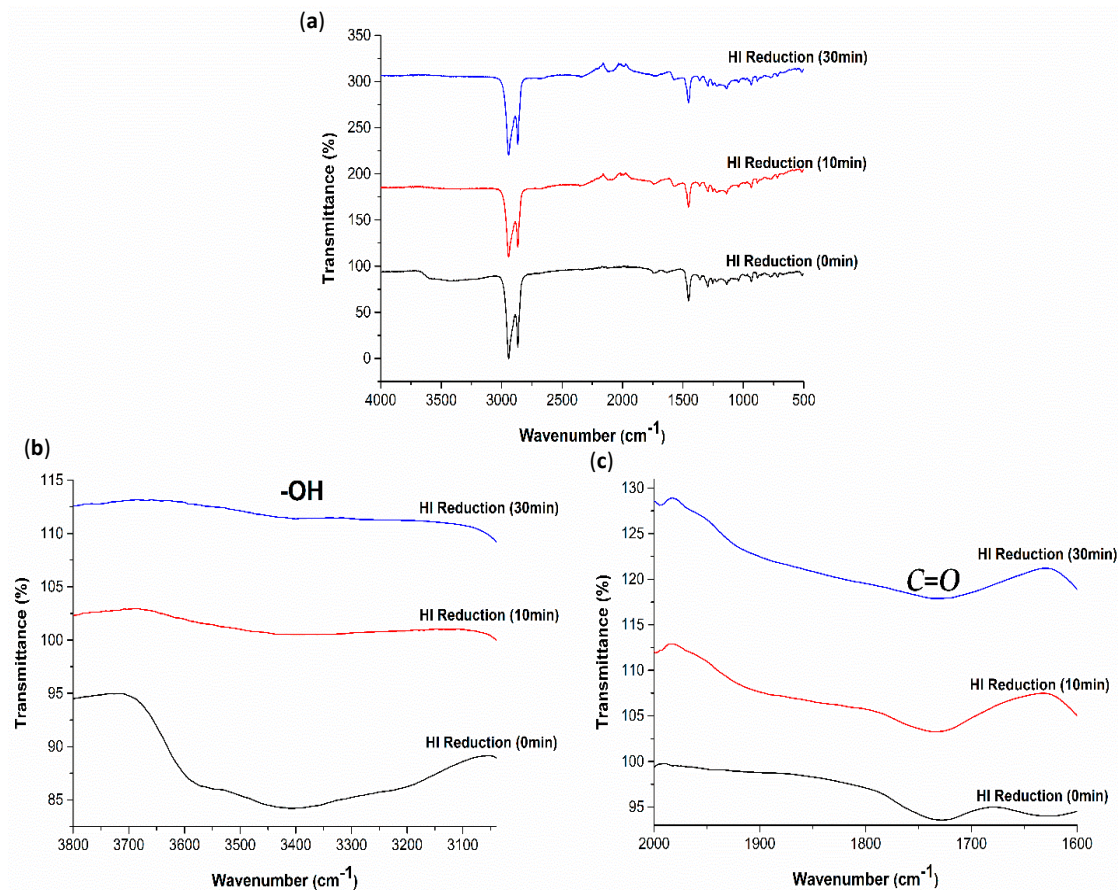
Figure 13. (**a**) FTIR−ATR spectra for 4 mg/mL GO−coated COC treated with HI for different durations and expanded regions of FTIR−ATR spectra between (**b**) 3050–3800 cm^{-1} and (**c**) 1500–2000 cm^{-1}.
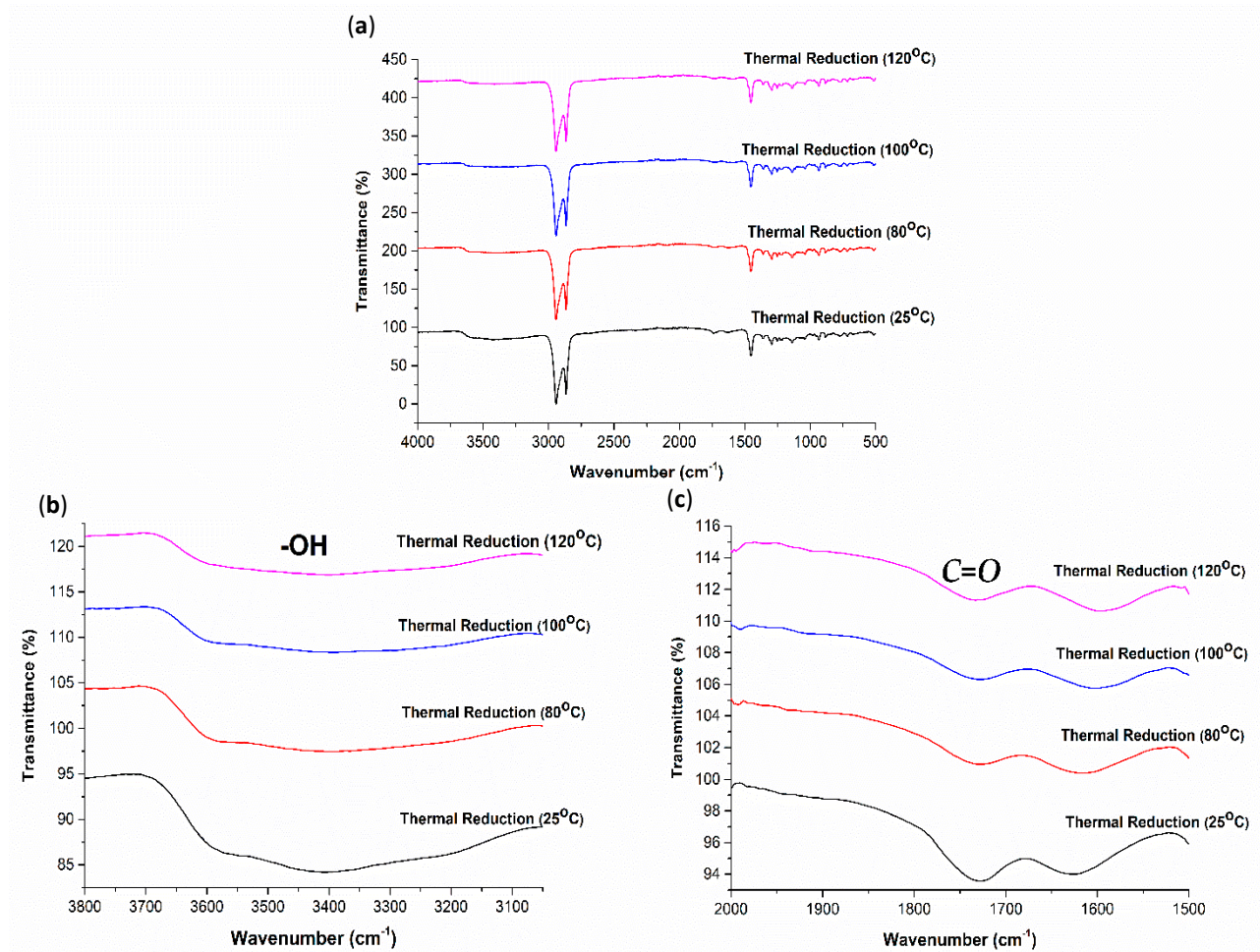
Figure 14. (**a**) FTIR−ATR spectra for 4 mg/mL GO−coated COC treated thermally for different temperatures and expanded regions of FTIR−ATR spectra between (**b**) 3050–3800 cm^{-1} and (**c**) 1500–2000 cm^{-1}.

4. Conclusions

The O_2/Ar plasma treatment and coating of COC with graphene oxide dispersions are effective for enhancing the wettability of natural hydrophobic COC surface. Based on the current work, the hydrophilic characteristic of plasma treated COC is mainly due to its increased surface roughness. Whereas the hydrophilic characteristic of GO-coated COC is mainly due to the increased oxygen-containing groups. Compared with plasma treatment, coating with graphene oxide has better wettability tuning capability because each GO concentration gives a different contact angle measurement as well as selective reduction of GO, specifically chemical and UV exposure reductions, is possible using photolithography techniques, which are difficult to be achieved using plasma treatment. It has been shown that different reduction methods, such as UV exposure, chemical using HI acid, and thermal treatments, can alter the surface wettability from hydrophilic GO-coated COC to hydrophobic reduced GO-coated COC, and can control the behavior of surface wettability as needed. FTIR spectroscopy and contact angle measurements have confirmed the reduction of the GO coatings for each treatment. The results showed that HI acid reduction and thermal reduction increased the hydrophobicity of GO-coated COC more effectively than UV reduction. This can be attributed to the high removal of oxygen-containing groups in chemical and thermal reduction treatments compared to UV reduction. This work provides a basis for the further development of coating materials

on COC substrates, where they can be used to tune the wettability for different industrial applications.

Author Contributions: Conceptualization, A.A. and N.A.; Methodology, A.A. and F.D.; validation, F.D.; formal analysis, F.D., A.A., N.A., and M.K.; data curation, F.D. and Y.A.; writing—original draft preparation, F.D.; writing—review and editing, all authors; supervision, A.A., N.A., and M.K.; project administration, N.A.; funding acquisition, N.A. All authors have read and agreed to the published version of the manuscript.

Data Availability Statement: The data presented in this study are available in article.

Conflicts of Interest: The authors declare no conflict of interest.

References

1. Hsu, S.-Y.; Zhang, Z.-Y.; Tsao, C.-W. Thermoplastic micromodel investigation of two-phase flows in a fractured porous medium. *Micromachines* **2017**, *8*, 38. [CrossRef]
2. Bauer, W.-A.C.; Fischlechner, M.; Abell, C.; Huck, W.T. Hydrophilic PDMS microchannels for high-throughput formation of oil-in-water microdroplets and water-in-oil-in-water double emulsions. *Lab Chip* **2010**, *10*, 1814–1819. [CrossRef]
3. Alazzam, A. Solution-based, flexible, and transparent patterned reduced graphene oxide electrodes for lab-on-chip applications. *Nanotechnology* **2019**, *31*, 075302. [CrossRef]
4. Alazzam, A.; Alamoodi, N. Microfluidic Devices with Patterned Wettability Using Graphene Oxide for Continuous Liquid–Liquid Two-Phase Separation. *ACS Appl. Nano Mater.* **2020**, *3*, 3471–3477. [CrossRef]
5. Carvalho, R.R.; Pujari, S.P.; Vrouwe, E.X.; Zuilhof, H. Mild and Selective C–H Activation of COC Microfluidic Channels Allowing Covalent Multifunctional Coatings. *ACS Appl. Mater. Interfaces* **2017**, *9*, 16644–16650. [CrossRef] [PubMed]
6. Perez-Toralla, K.; Champ, J.; Mohamadi, M.R.; Braun, O.; Malaquin, L.; Viovy, J.-L.; Descroix, S. New non-covalent strategies for stable surface treatment of thermoplastic chips. *Lab Chip* **2013**, *13*, 4409–4418. [CrossRef]
7. Tan, H.M.; Fukuda, H.; Akagi, T.; Ichiki, T. Surface modification of poly (dimethylsiloxane) for controlling biological cells' adhesion using a scanning radical microjet. *Thin Solid Film.* **2007**, *515*, 5172–5178. [CrossRef]
8. Silverio, V.; Canane, P.A.; Cardoso, S. Surface wettability and stability of chemically modified silicon, glass and polymeric surfaces via room temperature chemical vapor deposition. *Colloids Surf. A Physicochem. Eng. Asp.* **2019**, *570*, 210–217. [CrossRef]
9. Wu, D.; Zhao, B.; Dai, Z.; Qin, J.; Lin, B. Grafting epoxy-modified hydrophilic polymers onto poly (dimethylsiloxane) microfluidic chip to resist nonspecific protein adsorption. *Lab Chip* **2006**, *6*, 942–947. [CrossRef]
10. Roman, G.T.; Hlaus, T.; Bass, K.J.; Seelhammer, T.G.; Culbertson, C.T. Sol−gel modified poly (dimethylsiloxane) microfluidic devices with high electroosmotic mobilities and hydrophilic channel wall characteristics. *Anal. Chem.* **2005**, *77*, 1414–1422. [CrossRef]
11. Bodas, D.; Khan-Malek, C. Hydrophilization and hydrophobic recovery of PDMS by oxygen plasma and chemical treatment—An SEM investigation. *Sens. Actuators B Chem.* **2007**, *123*, 368–373. [CrossRef]
12. Bausch, G.G.; Stasser, J.L.; Tonge, J.S.; Owen, M.J. Behavior of plasma-treated elastomeric polydimethylsiloxane coatings in aqueous environment. *Plasmas Polym.* **1998**, *3*, 23–34. [CrossRef]
13. Lahann, J.; Balcells, M.; Lu, H.; Rodon, T.; Jensen, K.F.; Langer, R. Reactive polymer coatings: A first step toward surface engineering of microfluidic devices. *Anal. Chem.* **2003**, *75*, 2117–2122. [CrossRef]
14. Hu, S.; Ren, X.; Bachman, M.; Sims, C.E.; Li, G.; Allbritton, N.L. Surface-directed, graft polymerization within microfluidic channels. *Anal. Chem.* **2004**, *76*, 1865–1870. [CrossRef]
15. Abate, A.R.; Lee, D.; Do, T.; Holtze, C.; Weitz, D.A. Glass coating for PDMS microfluidic channels by sol–gel methods. *Lab Chip* **2008**, *8*, 516–518. [CrossRef]
16. Li, X.; Zhang, G.; Bai, X.; Sun, X.; Wang, X.; Wang, E.; Dai, H. Highly conducting graphene sheets and Langmuir–Blodgett films. *Nat. Nanotechnol.* **2008**, *3*, 538–542. [CrossRef] [PubMed]
17. Dai, B.; Fu, L.; Liao, L.; Liu, N.; Yan, K.; Chen, Y.; Liu, Z. High-quality single-layer graphene via reparative reduction of graphene oxide. *Nano Res.* **2011**, *4*, 434–439. [CrossRef]
18. Li, X.; Cai, W.; An, J.; Kim, S.; Nah, J.; Yang, D.; Piner, R.; Velamakanni, A.; Jung, I.; Tutuc, E.; et al. Large-Area Synthesis of High-Quality and Uniform Graphene Films on Copper Foils. *Science* **2009**, *324*, 1312. [CrossRef]
19. Alamoodi, N.; Alazzam, A. Droplet Coalescence by Selective Wettability Enhancement in Microfluidic Devices. *Nanomaterials* **2020**, *10*, 737. [CrossRef] [PubMed]
20. Si, Y.; Samulski, E.T. Synthesis of Water Soluble Graphene. *Nano Lett.* **2008**, *8*, 1679–1682. [CrossRef] [PubMed]
21. Lomeda, J.R.; Doyle, C.D.; Kosynkin, D.V.; Hwang, W.-F.; Tour, J.M. Diazonium functionalization of surfactant-wrapped chemically converted graphene sheets. *J. Am. Chem. Soc.* **2008**, *130*, 16201–16206. [CrossRef] [PubMed]

22. Williams, G.; Seger, B.; Kamat, P.V. TiO2-Graphene Nanocomposites. UV-Assisted Photocatalytic Reduction of Graphene Oxide. *ACS Nano* **2008**, *2*, 1487–1491. [CrossRef] [PubMed]

23. Teoh, H.; Tao, Y.; Tok, E.; Ho, G.; Sow, C. Electrical current mediated interconversion between graphene oxide to reduced grapene oxide. *Appl. Phys. Lett.* **2011**, *98*, 173105. [CrossRef]

24. Cote, L.J.; Cruz-Silva, R.; Huang, J. Flash reduction and patterning of graphite oxide and its polymer composite. *J. Am. Chem. Soc.* **2009**, *131*, 11027–11032. [CrossRef] [PubMed]

25. Roach, P.; Shirtcliffe, N.J.; Newton, M.I. Progess in superhydrophobic surface development. *Soft Matter* **2008**, *4*, 224–240. [CrossRef]

26. Manoudis, P.N.; Karapanagiotis, I.; Tsakalof, A.; Zuburtikudis, I.; Panayiotou, C. Superhydrophobic composite films produced on various substrates. *Langmuir* **2008**, *24*, 11225–11232. [CrossRef]

27. Wu, Z.; Han, H.; Han, W.; Kim, B.; Ahn, K.H.; Lee, K. Controlling the Hydrophobicity of Submicrometer Silica Spheres via Surface Modification for Nanocomposite Applications. *Langmuir* **2007**, *23*, 7799–7803. [CrossRef]

28. Roy, S.; Yue, C.; Lam, Y.; Wang, Z.; Hu, H. Surface analysis, hydrophilic enhancement, ageing behavior and flow in plasma modified cyclic olefin copolymer (COC)-based microfluidic devices. *Sens. Actuators B Chem.* **2010**, *150*, 537–549. [CrossRef]

29. Ricciardi, M.R.; Papa, I.; Coppola, G.; Lopresto, V.; Sansone, L.; Antonucci, V. Effect of Plasma Treatment on the Impact Behavior of Epoxy/Basalt Fiber-Reinforced Composites: A Preliminary Study. *Polymers* **2021**, *13*, 1293. [CrossRef]

30. Zaharescu, T.; Jipa, S.; Gigante, B. Stabilized polyethylene on the sterilization dose range. *Polym. Bull.* **2006**, *57*, 729–735. [CrossRef]

31. Yang, T.C.-K.; Lin, S.S.-Y.; Chuang, T.-H. Kinetic analysis of the thermal oxidation of metallocene cyclic olefin copolymer (mCOC)/TiO2 composites by FTIR microscopy and thermogravimetry (TG). *Polym. Degrad. Stab.* **2002**, *78*, 525–532. [CrossRef]

32. Forsyth, J.; Perena, J.M.; Benavente, R.; Pérez, E.; Tritto, I.; Boggioni, L.; Brintzinger, H.H. Influence of the polymer microstructure on the thermal properties of cycloolefin copolymers with high norbornene contents. *Macromol. Chem. Phys.* **2001**, *202*, 614–620. [CrossRef]

33. Abunahla, H.; Alamoodi, N.; Alazzam, A.; Mohammad, B. Micro-Pattern of Graphene Oxide Films Using Metal Bonding. *Micromachines* **2020**, *11*, 399. [CrossRef]

34. Huh, S.H. Thermal reduction of graphene oxide. In *Physics and Applications of Graphene—Experiments*; Mikhailov, S., Ed.; InTech: Rijeka, Croatia, 2011; pp. 73–90.

35. Chen, J.; Li, H.; Zhang, L.; Du, C.; Fang, T.; Hu, J. Direct reduction of graphene oxide/nanofibrillated cellulose composite film and its electrical conductivity research. *Sci. Rep.* **2020**, *10*, 3124. [CrossRef] [PubMed]

36. Chua, C.K.; Pumera, M. Renewal of sp 2 bonds in graphene oxides via dehydrobromination. *J. Mater. Chem.* **2012**, *22*, 23227–23231. [CrossRef]

Communication

Electrical Supply Circuit for a Cold Plasma Source at Atmospheric Pressure Based on a Voltage Multiplier

Ovidiu S. Stoican

National Institute for Laser, Plasma and Radiation Physics, 409 Atomistilor Street, P.O. Box MG 36, 077125 Măgurele, Romania; ovidiu.stoican@inflpr.ro

Abstract: A cold plasma source operating at atmospheric pressure powered by a voltage multiplier is reported. In addition to its usual high voltage output, there is an intermediate output of lower voltage and higher current capability. A discharge current is drawn from both outputs. The ratio of the current supplied by each output depends on the operating state, namely, before or after the plasma jet formation. The electrical circuit is equivalent to two dc sources connected in parallel, used to initiate and sustain the electrical discharge. The plasma source is aimed to study the effect of cold plasma on the surface of various liquid or solid materials, including polymers.

Keywords: cold plasma; atmospheric pressure plasma; electrical discharges; voltage multiplier; polymers

1. Introduction

A wide range of applications is based on the effects of interaction between the cold (non-thermal) plasma generated at atmospheric pressure and the surface of various solid or liquid materials. Developments related to this topic are constantly growing, new research approaches are attempted or are already underway [1–7]. There are many solutions to obtain plasma at atmospheric pressure, the differences being mainly given by the electrode geometry and type of electrical supply, namely: dc, low-frequency, rf, microwave or a combination of them. A summary of the output parameters, operating conditions and reported applications for various classes of plasma sources is presented in [1]. Depending on the particular design, the magnitude of the power transferred to the electrical discharge and carrier gas nature, the resulting plasma characteristics can be set in a wide range. Because there are no solid or liquid wastes, plasma technologies are environmentally friendly compared with alternative methods based on chemical treatments. Atmospheric pressure operation simplifies the necessary equipment, because no vacuum system is needed.

Cold plasma technology is already an important tool used to process polymers surface for various scientific and technical purposes [6–9]. By using this technique, the polymer surface characteristics can be modified whereas its bulk properties remain unchanged. The affected layer depth lies in the range 0.005–0.05 μm [8]. There are several areas in which very promising results based on the polymers surface plasma treatment have been reported in the literature, such as: antimicrobial and bioactive coatings [2,10–13]; surface wettability modification [14–18]; changes of the mechanical properties (roughness, bonding and tensile strength) [15,19,20]; cleaning, improvement dyeing and printing properties [16,21].

This work contributes to the realization of a plasma source of type APPJ (atmospheric pressure plasma jet) aimed to study the effect of cold (non-thermal) plasma on the surface of various liquid or solid materials, including polymers.

Its specific use requires that a plasma source to be operated in a non-transferred arc mode. A plasma jet having well-defined, stable and reproducible parameters under various experimental conditions is also a mandatory demand. Some peculiarities of the experimental conditions may lead to plasma jet interruptions. Generally, to initiate an electric discharge, a much larger electric field is required than the one necessary to sustain it [22,23]. As a result, the quick change of the operating mode for the power supply in order

to restart the discharge, followed by a return to the mode corresponding to the discharge sustaining, is necessary. The simplicity of the supply circuit, having in view a possible small-scale plasma source multiplication was also considered. To meet the requirements mentioned above and avoid the difficulties implied by rf or microwave circuits, which need matching networks, a solution based on plasma initiated and sustained by a dc discharge was tested.

2. Materials and Methods

2.1. Mechanical Layout of the Plasma Source

The plasma source mechanical layout used for practical testing and operating parameters measurement of the electrical circuit is shown in Figure 1. It consists of a cylindrical cavity terminated with a conical ejection nozzle, drilled along the longitudinal axis of a cylindrical aluminum block. The narrow head of the nozzle is bored and represents the output hole for the plasma jet. The other head of the cylindrical cavity is closed by an insulating disk made of teflon. A sharpened brass rod enters the cavity, along its longitudinal axis, through an orifice existing in the center of the insulating disk. This rod is held in place by the insulating disk and can slide forward or backward, so that its position is adjusted to attain a stable plasma jet of maximum length under the given experimental conditions. For the plasma source, the aluminum block and the brass rod represent the anode (A), which is connected to ground (GND), and cathode (K), respectively. The carrier gas under pressure is introduced into the cavity through a duct that crosses the aluminum block perpendicular to its longitudinal axis. The geometrical parameters of the plasma source, shown in Figure 1, are: $d = 3$ mm, $d_1 = 8$ mm, $d_2 = 3$ mm, $D = 15$ mm, $L = 22$ mm.
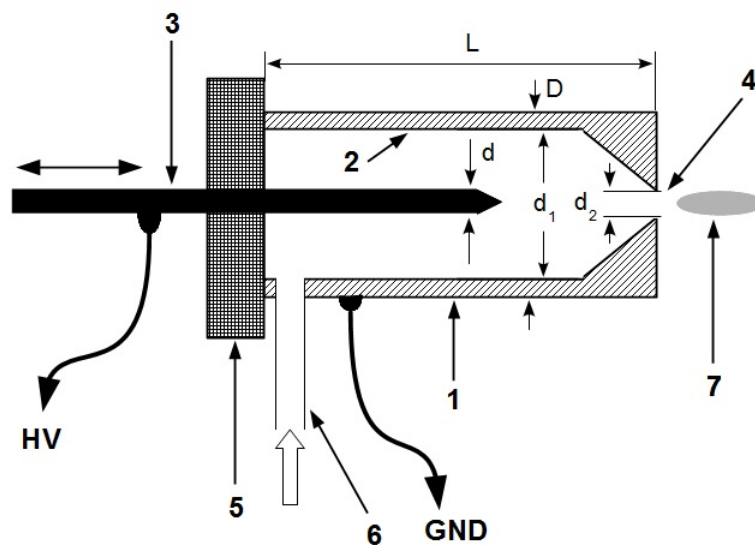
Figure 1. Mechanical layout of the plasma source (not to scale). 1-aluminum block; 2-cylindrical cavity; 3-brass rod; 4-plasma output hole; 5-teflon insulating disk; 6-carrier gas input duct; 7-plasma jet.

2.2. Electrical Supply Circuit

The electrical supply circuit diagram is shown in Figure 2. Its core consists of a voltage multiplier, delimited by the dashed rectangle. Circuit topology follows the classical one, known as Cockcroft–Walton generator (often called Greinacher multiplier, to give credit to the one who described it first) being a network made up of diodes (D_1–D_{10}) and capacitors (C_1–C_{10}) which converts the ac voltage applied between point marked X0, conventionally designed here as multiplier voltage input, and ground (GND), to a dc voltage whose magnitude is several times larger than the peak value of that ac voltage. All capacitors C_1–C_{10} are identical, each of them having a capacitance of 1 μF. In addition, all diodes D_1–D_{10} are identical, BY6-type, rated at 6 kV repetitive peak reverse voltage and 1 A maximum forward current [24]. This network can be considered to be formed by a suite of five identical stages connected in series, numbered from 1 to 5, where the first stage

is the one at the input, terminals X2, X4, X6, X8 and X10 being the output of each stage. Let the time variation of the ac voltage be applied between point X0 and ground expressed by $u_i = \sqrt{2}U_i \sin(2\pi f_0 t)$, characterized by frequency $f_0 = 50$ Hz, peak value $\sqrt{2}U_i$ and consequently the root-mean-squared (*rms*) value U_i. It is preferable to use rms value U_i, to characterize the magnitude of the ac voltage because common ac voltmeters are calibrated to display this parameter. Based on the operating principle of this type of circuit [25–27], theoretically, without any load, taking into account current direction allowed by diodes D_1–D_{10}, the dc voltages between terminals X2, X4, X6, X8, X10 and ground are $-2\sqrt{2}U_i$, $-4\sqrt{2}U_i$, $-6\sqrt{2}U_i$, $-8\sqrt{2}U_i$ and $-10\sqrt{2}U_i$, respectively. Therefore, the maximum negative dc voltage, namely $-10\sqrt{2}U_i$, is obtained at terminal X10. Transformer Tr, having its primary winding connected to the ac power line (230 V_{rms}/50 Hz), is used to ensure galvanic isolation between plasma source electrodes and ac power line. Its secondary winding, providing 400 V_{rms}, is connected across point X0 and ground. The cathode K of the plasma source is simultaneously connected to the terminal X10 through the ballast resistor R_{b1} and to the terminal X2 through the equivalent ballast resistor R_{b2} in series with an additional diode D_{11}, respectively. Element R_{b2} consists of two resistors R_s and R_x connected in series. Resistor R_s has a fixed value of 10 kΩ, limiting the maximum discharge current regardless resistor R_x value, as well being used for discharge current sensing. Resistors R_x can have different values, being used to adjust the discharge current.
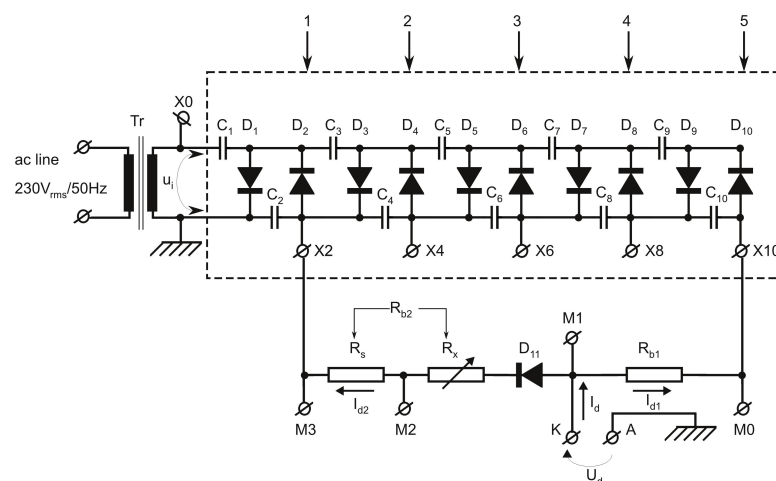
Figure 2. Diagram of the electrical supply circuit. The voltage multiplier, delimited by dashed rectangle, consists of ten identical 1 μF capacitors C_1–C_{10}, and ten diodes D_1–D_{10}. All multiplier diodes D_1–D_{10} and additional diode D_{11} are identical, BY6-type. The nominal values of the resistors are $R_{b1} = 10$ MΩ and $R_s = 10$ kΩ. Resistance $R_{b2} = R_s + R_x$, where R_x may have different values, being used to adjust discharge current. Transformer Tr ensures galvanic isolation between the ac power line and plasma source electrodes. Four voltage dividers are connected to points M0, M1, M2 and M3, to monitor some electrical parameters during plasma source operation.

2.3. Operating Principle

Let the discharge voltage, denoted by U_d, be the dc voltage applied to cathode K. Note that all dc voltages are referenced to ground and their polarity is negative. Let the discharge current, denoted by I_d, be the electric current through the plasma source electrodes, from A to K. The current discharge I_d is the sum of two components: $I_d = I_{d1} + I_{d2}$, where I_{d1} is the current drawn from terminal X10 and I_{d2} is the current drawn from terminal X2, by the electrical discharge. If there is no electrical discharge, then the plasma source electrodes represent electrically an open circuit. Consequently, $I_d = 0$ and the dc voltage applied to cathode is equal to the terminal X10 voltage: $|U_d| \approx 10\sqrt{2}U_i \approx 5.66$ kV, for $U_i = 400$ V_{rms}. To obtain an electrical discharge, implicitly initiate the plasma jet at atmospheric pressure, it is necessary that the X10 terminal voltage to be large enough to generate the breakdown electric field corresponding to the specific mixture air-carrier gas. Therefore, connection

to the terminal X10 is only aimed to apply to the electrodes the high voltage necessary to ignite an electrical discharge between them and to initiate or re-initiate, if necessary, the plasma jet. Due to the large value of the ballast resistor R_{b1}, the current I_{d1} drawn from the terminal X10 is not sufficient to keep the electrical discharge continuous. It is limited to $I_{d1max} < 10\sqrt{2}U_i/R_{b1} \approx 0.57$ mA. The current necessary to sustain the electrical discharge after it is initiated, is drawn from terminal X2. It is limited by the group of resistors denoted R_{b2} ($R_{b2} = R_s + R_x$), so that $I_{d2max} < 2\sqrt{2}U_i/R_s \approx 113$ mA. Due to the diode D$_{11}$ (also BY6-type), the dc current I_{d2} drawn from X2 terminal is null until, in absolute value, the discharge voltage U_d becomes lower than the X2 terminal voltage.

Summarizing, in the absence of plasma (no electrical discharge) or in the case of anomalous operation, when $|U_d| > 2\sqrt{2}U_i$, current drawn from terminal X2, $I_{d2} = 0$. After the electrical discharge is ignited and carrier gas is flowing, the plasma jet begins to form, the discharge current I_d increases whereas the absolute value of the discharge voltage $|U_d|$ decreases until the system reaches a steady state corresponding to the atmospheric plasma glow discharge regime. For the device described here, this state is characterized by a discharge voltage satisfying condition $|U_d| < 2\sqrt{2}U_i$, at a discharge current I_d of the order of ten mA, having as a result a stable plasma jet. To achieve this regime, by varying the resistance R_x, different values of the ballast resistance R_{b2} were tested experimentally before a suitable range of values was found. The component I_{d1} is not null after the plasma jet is formed and becomes stable, but it can be neglected as compared to the component I_{d2}, and practically, $I_d \approx I_{d2}$. If, for various reasons, the plasma jet is accidentally interrupted during operation, the diode D$_{11}$ blocks the current through the terminal X2 and the voltage applied to the electrodes is switched automatically to $-10\sqrt{2}U_i$, allowing the re-ignition of the electrical discharge. No supplementary electronic circuit is necessary for that.

3. Results

3.1. Measurement Setup

For testing purposes, in order to record voltages values during the plasma source operation, under various experimental conditions, the measurement setup shown in Figure 3 has been used. Four voltage dividers R_0–R_{d0}, R_1–R_{d1}, R_2–R_{d2} and R_3–R_{d3} have been connected to points M0, M1, M2 and M3, respectively. To smooth the dividers output voltage ripple, shunt capacitors C$_{d0}$, C$_{d1}$, C$_{d2}$ and C$_{d3}$ have been added. The voltage divider elements nominal values are: $R_0 = R_1 = R_2 = R_3 = 40$ MΩ, $R_{d0} = R_{d1} = R_{d2} = R_{d3} = 11$ kΩ, $C_{d0} = C_{d1} = C_{d2} = C_{d3} = 20$ µF. A Meilhaus Electronic RedLab 1608FS USB-based Analog and Digital I/O module has been used as a data acquisition system (DAQ). This device performs A/D conversion and transfer data to a personal computer via the USB port. The dividers output voltages are applied to the analog input channels CH0, CH1, CH2 and CH3 of the DAQ system.

Let U_{M0}, U_{M1}, U_{M2} and U_{M3} be voltages at points M0, M1, M2 and M3, respectively. These are calculated by measuring the output voltage of the dividers R_0–R_{d0}, R_1–R_{d1}, R_2–R_{d2} and R_3–R_{d3}, and considering the corresponding voltage ratio. All voltage dividers have been previously calibrated in order to calculate the actual voltage ratio. To preclude the effect of ac line voltage fluctuations during measurements, the primary winding of the transformer Tr has been connected to the ac line through an automatic ac voltage regulator. The experimental values against theoretical ones, of dc voltages at terminals X2 and X10, for $U_i = 400$ V$_{rms}$ (≈ 566 V peak value), in the absence of plasma, are given in Table 1.
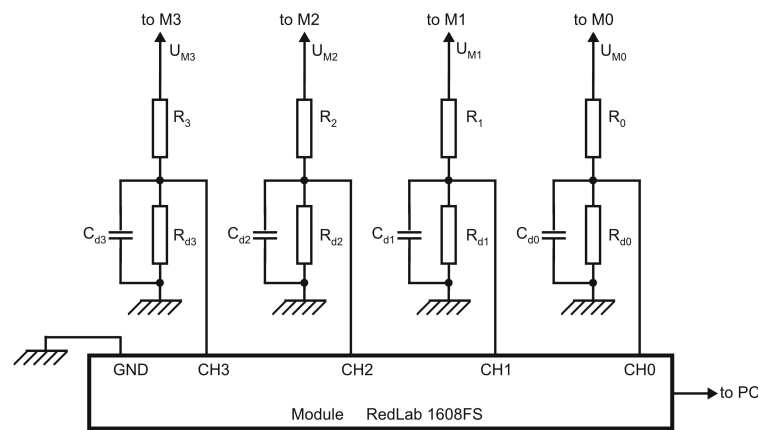
Figure 3. Schematic diagram of the measurement setup. The voltage divider elements nominal values are: $R_0 = R_1 = R_2 = R_3 = 40$ MΩ, $R_{d0} = R_{d1} = R_{d2} = R_{d3} = 11$ kΩ, $C_{d0} = C_{d1} = C_{d2} = C_{d3} = 20$ μF.

Table 1. Comparison between calculated and measured magnitude of the dc voltage at terminals X2 and X10 of the circuit shown in Figure 2, having as load only voltage dividers, for the ac voltage applied to the input X0, $U_i = 400$ V$_{rms}$.

Terminal	X2	X10
Multiple of ac input peak voltage [kV]	−1.13	−5.66
Measured voltage [kV] Voltage dividers connected to M0 and M4. Diode D_{11} and resistor R_{b1} are disconnected.	−1.13	−5.36

The electrical supply circuit main parameters during plasma source operation result as:

- Discharge voltage representing the dc voltage applied to the cathode $U_d = U_{M1}$;
- Voltage multiplier X10 terminal voltage equal to U_{M0};
- Voltage multiplier X2 terminal voltage equal to U_{M3};
- Current drawn from terminal X10 by the electrical discharge calculated as:

$$I_{d1} \approx \frac{|U_{M0} - U_{M1}|}{R_{b1}} \tag{1}$$

- Current drawn from terminal X2 by the electrical discharge, calculated as:

$$I_{d2} \approx \frac{|U_{M3} - U_{M2}|}{R_s} \tag{2}$$

by neglecting the current through the voltage divider R_2–R_{d2} (<0.03 mA).

As can be seen in the next subsection, during normal operation, the discharge voltage U_d is about 200 V, so that the current through the voltage divider R_1–R_{d1} is about 5 μA and may be neglected in comparison with the current drawn by the electrical discharge either from terminal X2 or from terminal X10. Due to the additional load consisting of the voltage divider R_0–R_{d0}, the total current supplied to the outside from terminal X10, denoted I_{X10}, is higher than I_{d1}. Taking into account that $R_{d0} \ll R_0$, it is given by:

$$I_{X10} \approx I_{d1} + \frac{|U_{M0}|}{R_0} \tag{3}$$

The second term in Equation (3) is comparable to I_{d1}, and the existence of this additional load contributes to the discrepancy between the calculated and measured value of the voltage at terminal X10, shown in Table 1 [27]. However, this leakage current has no significant effect on the plasma source operation and will not be discussed further.

3.2. Measurement Results during a Normal Operation Regime

The operating regime for various values of the ballast resistance R_{b2} has been tested. Firstly, the electrodes K and A are connected to the supply circuit as shown in Figures 1 and 2. The corresponding electric field is not enough to initiate an electric discharge in the air, at atmospheric pressure. Afterwards, the carrier gas, consisting of Ar, is introduced into the cylindrical cavity of the plasma source by means of a gas flow controller (Alicat Scientific MC-20SLPM). A plasma jet is formed and becomes stable a few seconds after the carrier gas flow is switched on and stabilized at a settled value. By using Ar as carrier gas, at a constant flow rate of 3 LPM, a stable plasma plume of about 5 mm in length was formed. Figure 4 shows a stable plasma jet during normal operation.

Figure 4. Plasma jet during normal operation. Experimental conditions: $U_i = 400$ V$_{rms}$, $R_{b2} = 20$ kΩ, Ar as carrier gas at flow rate of 3 LPM.

The time variation of the voltages U_{M0}, U_{M1}, U_{M2} and U_{M3} has been recorded for a certain amount of time, by using the measurement setup described above. Data acquisition started after the plasma jet was formed and became stable. Four datasets have been acquired corresponding to $R_{b2} = 10, 20, 30$ and 40 kΩ. The acquisition time was 300 s, at a scan rate of 1 Hz. In all cases, $U_i = 400$ V$_{rms}$ whereas carrier gas was Ar at a constant flow rate of 3 LPM. The averaged electrical parameters of the electric supply circuit during the normal operation regime, corresponding to the four datasets, are listed in Table 2. The normal operation regime is considered to be the state in which the plasma jet was formed whereas the voltage and current discharge became relative stable. The average voltage values considered here are calculated as the arithmetic mean of the corresponding data acquired by DAQ:

$$\overline{U}_{Mi} = \frac{\sum\limits_{k=1}^{N} U_{Mi}(t_k)}{N} \tag{4}$$

where $i = 0, 1, 2, 3$ represents the DAQ channel index, N is the total sample number and $U_{Mi}(tk)$ represents the voltage corresponding to the channel i and sample number k, acquired at t_k seconds from the beginning of the measurement operation, sample number 1 being considered the origin of the time ($t_1 = 0$). Therefore, for an acquisition time of 300 s, at a scan rate 1 Hz, $N = 300$ samples and $t_k = k - 1$ seconds. The averaged currents drawn by electrical discharge $\overline{I}_{d1}$ from terminal X10, and $\overline{I}_{d2}$ from terminal X2, listed in Table 2, are calculated according to Equations (1) and (2), respectively, where voltages values are replaced by averaged voltages values, calculated according Equation (4).

Table 2. Averaged electrical parameters of the electric supply circuit during the normal operation regime for $U_i = 400$ V$_{rms}$ and different ballast resistance R_{b2}.

Parameter Description	Symbol	Units	R_{b2}			
			40 kΩ	30 kΩ	20 kΩ	10 kΩ
Voltage at cathode (discharge voltage)	$\overline{U}_d = \overline{U}_{M1}$	kV	−0.212	−0.208	−0.206	−0.210
Voltage at terminal X10	$\overline{U}_{M0}$	kV	−3.01	−2.76	−2.40	−1.84
Current drawn by electrical discharge from terminal X10	$\overline{I}_{d1}$	mA	0.28	0.26	0.22	0.16
Voltage at terminal X2	$\overline{U}_{M3}$	kV	−0.71	−0.65	−0.57	−0.44
Current drawn by electrical discharge from terminal X2 (discharge current)	$\overline{I}_d \approx \overline{I}_{d2}$	mA	12.77	14.95	18.03	22.97

Figure 5 presents the time variation of the discharge voltage U_d (**a**) and discharge current I_d (**b**), respectively, for different ballast resistance R_{b2}. The graphs shown are based on the datasets used to fill Table 2.

(**a**)   (**b**)
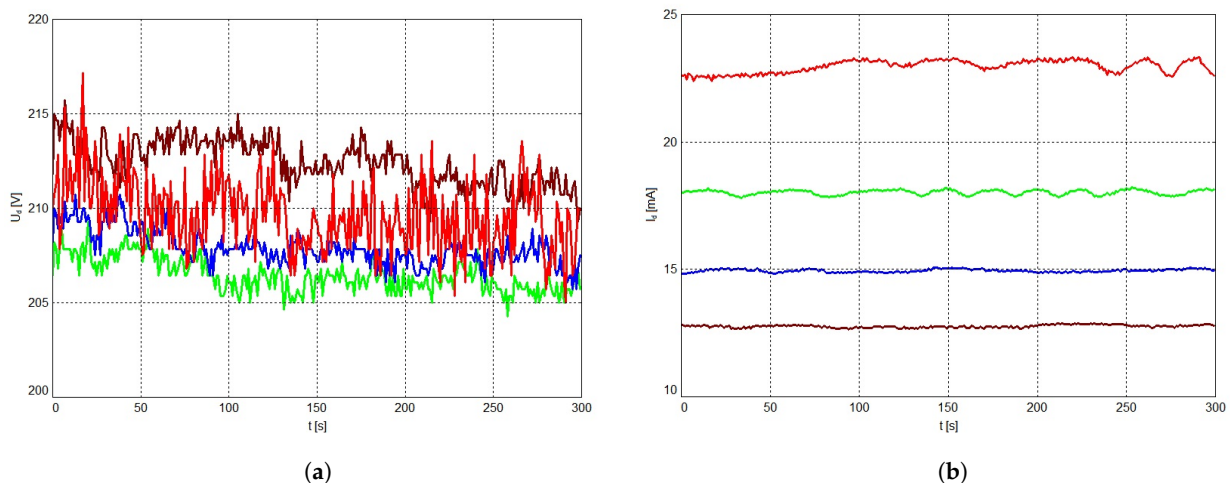
Figure 5. Time variation of the discharge voltage U_d (**a**) and discharge current I_d (**b**) for ballast resistance R_{b2} equal to 10 kΩ (red), 20 kΩ (green), 30 kΩ (blue) and 40 kΩ (brown).

The gas temperature, measured by means of a K-type thermocouple, placed at 2 mm from the output hole of the plasma jet, and the power dissipated by the electrical discharge calculated as: $P_d = \overline{U}_d \times \overline{I}_d$, for different ballast resistance R_{b2}, are given in Table 3.

Table 3. Gas temperature T_g and power dissipated by the electrical discharge P_d, for different ballast resistance R_{b2}.

R_{b2} [kΩ]	T_g [°C]	P_d [W]
10	96	4.8
20	78	3.7
30	68	3.1
40	58	2.7

4. Discussion and Conclusions

The operation of a cold plasma source powered by a simple electrical circuit based on a voltage multiplier was experimentally demonstrated. Basically, the electrical supply circuit is equivalent to two dc sources connected in parallel, consisting of the two outputs X2 and X10, respectively, of the voltage multiplier. One of them (corresponding to the

output X10) provides the very high voltage necessary to initiate the electrical discharge, whereas the other one (corresponding to the output X2) is aimed to sustain the discharge. After a plasma jet was formed, the contribution of the very high voltage source to the discharge current can be neglected as it can be seen in Table 2. A similar approach has already been described in [28]. Unlike the solution described in [28], the circuit presented in this paper has the following distinct features:

- The plasma generation is based on a pure dc electrical discharge. This characteristic combined with a stable regime mode allows to minimize the rf perturbations emission. Technical issues related to the matching circuits required by rf or microwave generators do not exist.
- A very simple electrical supply circuit. The two dc voltage sources switch "naturally", running simultaneously or separately, as a function of plasma electrical parameters.

No specialized electronic circuit is required for switching between the two dc sources, for example, based on monitoring the discharge current and comparing it with a threshold value.

As shown by the experimental results, the gas temperature can be adjusted in a wide range by modifying the ballast resistor in series with the dc source which sustains electrical discharge, without affecting ignition and stability of the resulting plasma jet. This is an important feature necessary for biological and medical applications [29,30]. In principle, for polymers, the gas temperature must not exceed the maximum service temperature, above which the material subjected to the plasma treatment loses its mechanical properties. For common polymers existing on the market (e.g., Acrylonitrile Butadiene Styrene-ABS, Polyethylene Terephthalate-PET, Polypropylene-PP, etc), this specific temperature is provided by the manufacturer and can be found in various databases usually available online (e.g., [31]). In the case of the experimental samples, containing new materials, biopolymers or living cells, the plasma gas temperature must be maintained as low as possible and, if necessary, progressively increased after a few preliminary tests. As an example, chitosan is one of the polymers intensively studied due to its multiple potential uses [32–35]. According to [33], during thermal processing, chitosan goes through two or three degradation stages, the first of them occurring at 30–110 °C. For bacterial inactivation, gas temperatures are reported to be about 50 °C [1,6]. Therefore, the gas temperature must be previously observed under various operation conditions, taking into account in particular its variation with carrier gas flow rate and the discharge current, for the given electrodes geometry. Furthermore, the operation conditions will be adapted to set the gas temperature within the acceptable range.

Table 4 presents the maximum relative deviation of the discharge voltage (ΔU_{dmax}) and current (ΔI_{dmax}) from their averaged values for different ballast resistance R_{b2} obtained by picking up the maximum value of the expressions:

$$\Delta U_d = \frac{|U_{M1} - \overline{U}_{M1}|}{|\overline{U}_{M1}|} \times 100 \tag{5}$$

and

$$\Delta I_d = \frac{|I_d - \overline{I}_d|}{|\overline{I}_d|} \times 100 \tag{6}$$

Table 4. Maximum relative deviation of the discharge voltage (ΔU_{dmax}) and current (ΔI_{dmax}) from average values for different ballast resistance R_{b2}.

Relative Deviation	R_{b2}			
	40 kΩ	30 kΩ	20 kΩ	10 kΩ
ΔU_{dmax} [%]	1.6	1.4	1.4	3.6
ΔI_{dmax} [%]	1.0	0.9	1.3	2.5

The results indicate that, after the plasma jet is formed, under the investigated experimental conditions (10 kΩ ≤ ballast resistance ≤ 40 kΩ), the discharge voltage and current remain approximately constant, exhibiting small variations around their average values, proving a stable operation regime, whereas the gas temperature can be maintained in an appropriate range. However, for lower ballast resistance, the discharge current and voltage deviation from their average values increases. In a first approach, the dc discharge stability depends on the fulfillment of the Kaufmann criterion [36,37]:

$$R_{b2} + dU_d/dI_d > 0 \tag{7}$$

We consider that for lower ballast resistance, the fluctuation in the differential resistance dU_d/dI_d cannot be fully compensated to satisfy Equation (7), so that the discharge tends to become unstable, as it can be seen in Figure 5.

The plasma jet generated by the device (design shown in Figure 1) has a small section which allows to be applied on a precise material area. On the other hand, in other applications, this could be a disadvantage. As a further development, the possibility to adapt this topology to supply simultaneously multiple plasma jet sources (several, such as the one in Figure 1) will be considered.

Finally, it can be concluded that the electrical circuit described above is a suitable solution for the requirements that were the reason for initiating this work.

Institutional Review Board Statement: Not applicable.

Informed Consent Statement: Not applicable.

Data Availability Statement: Not applicable.

Conflicts of Interest: The author declares no conflict of interest. The funders had no role in the design of the study; in the collection, analyses, or interpretation of data; in the writing of the manuscript, or in the decision to publish the results.

References

1. Winter, J.; Brandenburg, R.; Weltmann, K.-D. Atmospheric pressure plasma jets: An overview of devices and new directions. *Plasma Sources Sci. Technol.* **2015**, *24*, 064001. [CrossRef]
2. Tabares, F. L.; Junkar, I. Cold Plasma Systems and their Application in Surface Treatments for Medicine. *Molecules* **2021**, *26*, 1903. [CrossRef] [PubMed]
3. Bruggeman, P.J.; Kushner, M.J.; Locke, B.R.; Gardeniers, J.G.E.; Graham, W.G.; Graves, D.B.; Hofman-Caris, R.C.H.M.; Maric, D.; Reid, J.P.; Ceriani, E.; et al. Plasma–liquid interactions: A review and roadmap. *Plasma Sources Sci. Technol.* **2016**, *25*, 053002. [CrossRef]
4. Bruggeman, P.J.; Iza, F.; Brandenburg, R. Foundations of atmospheric pressure non-equilibrium plasmas. *Plasma Sources Sci. Technol.* **2017**, *26*, 123002. [CrossRef]
5. Rezaei, F.; Vanraes, P.; Nikiforov, A.; Morent, R.; De Geyter, N. Applications of Plasma-Liquid Systems: A Review. *Materials* **2019**, *12*, 2751. [CrossRef] [PubMed]
6. Penkov, O.V.; Khadem, M.; Lim, W.-S.; Kim, D.-E. A review of recent applications of atmospheric pressure plasma jets for materials processing. *J. Coat. Technol. Res.* **2015**, *12*, 225–235. [CrossRef]
7. Weltmann, K.-D.; Kolb, J.F.; Holub, M.; Uhrlandt, D.; Šimek, M.; Ostrikov, K.; Hamaguchi, S.; Cvelbar, U.; Černák, M.; Locke, B.; et al. The future for plasma science and technology. *Plasma Process Polym.* **2019**, *16*, e1800118. [CrossRef]
8. Yanling, C.; Yingkuan, W.; Chen, P.; Deng, S.; Ruan, R. Non-thermal plasma assisted polymer surface modification and synthesis: A review. *Int. J. Agric. Biol. Eng.* **2014**, *7*, 1–9. [CrossRef]
9. Kuettner, L.A. Use of Atmospheric-Pressure Plasma Jet for Polymer Surface Modification: An Overview. In *Los Alamos National Laboratory Report LA-UR-17-22230*; 2017. Available online: https://permalink.lanl.gov/object/tr?what=info:lanl-repo/lareport/LA-UR-17-22230 (accessed on 20 June 2021).
10. Popelka, A.; Novák, I.; Lehocký, M.; Chodák, I.; Sedliačik, J.; Gajtanska, M.; Sedliačiková, M.; Vesel, A.; Junkar, I.; Kleinová, A.; et al. Anti-bacterial Treatment of Polyethylene by Cold Plasma for Medical Purposes. *Molecules* **2012** , *17* 762–785. [CrossRef]
11. Fricke, K.; Tresp, H.; Bussiahn, R.; Schröder, K.; von Woedtke, T.; Weltmann, K.-D. On the Use of Atmospheric Pressure Plasma for the Bio-Decontamination of Polymers and Its Impact on Their Chemical and Morphological Surface Properties. *Plasma Chem. Plasma Process.* **2012** , *32*, 801–816. [CrossRef]

12. Pankaj, S.K.; Bueno-Ferrer, C.; Misra, N.N.; Milosavljević, V.; O'Donnell, C.P.; Bourke, P.; Keener, K.M.; Cullen, P.J. Applications of cold plasma technology in food packaging. *Trends Food Sci. Technol.* **2014**, *35*, 5–17. [CrossRef]
13. Honarvar, Z.; Farhoodi, M.; Khani, M.R.; Mohammadi, A.; Shokri, B.; Ferdowsi, R.; Shojaee-Aliabad, S. Application of cold plasma to develop carboxymethyl cellulose-coated polypropylene films containing essential oil. *Carbohydr. Polym.* **2017** , *176*, 1–10. [CrossRef]
14. Cheng, C.; Liye, Z.; Zhan, R.-J. Surface modification of polymer fibre by the new atmospheric pressure cold plasma jet. *Surf. Coat. Technol.* **2006**, *200*, 6659–6665. [CrossRef]
15. Vishnuvarthanan, M.; Rajeswari, N. Effect of mechanical, barrier and adhesion properties on oxygen plasma surface modified PP. *Innov. Food Sci. Emerg. Technol.* **2015**, *30*, 119–126. [CrossRef]
16. Zille, A.; Oliveira, F.R.; Souto, A.P. Plasma Treatment in Textile Industry. *Plasma Process. Polym.* **2015**, *12*, 98–131. [CrossRef]
17. Wiącek, A.E.; Terpiłowski, K.; Jurak, M.; Worzakowska, M. Low-temperature air plasma modification of chitosan-coated PEEK biomaterials. *Polym. Test.* **2016**, *50*, 325–334. [CrossRef]
18. Ma, C.; Wang, L.; Nikiforov, A.; Onyshchenko, Y.; Cools, P.; Ostrikov, K.; De Geyter, N.; Morent, R. Atmospheric-pressure plasma assisted engineering of polymer surfaces: From high hydrophobicity to superhydrophilicity. *Appl. Surf. Sci.* **2021**, *535*, 147032. [CrossRef]
19. Dowling, D.P.; O'Neill, F.T. ; Langlais, S.J.; Law, V.J. Influence of dc Pulsed Atmospheric Pressure Plasma Jet Processing Conditions on Polymer Activation. *Plasma Process. Polym.* **2011**, *8*, 718–727. [CrossRef]
20. Abourayana, H.; Dobbyn, P.; Dowling, D. Enhancing the mechanical performance of additive manufactured polymer components using atmospheric plasma pre-treatments. *Plasma Process Polym.* **2018**, *15*, e1700141. [CrossRef]
21. Morent, R.; De Geyter, N.; Verschuren, J.; De Clerck, K.; Kiekens, P.; Leys, C. Non-thermal plasma treatment of textiles. *Surf. Coatings Technol.* **2008**, *202*, 3427–3449. [CrossRef]
22. Schütze, A.; Jeong, J.Y.; Babayan, S.E.; Park, J; Selwyn, G.S.; Hicks, R.F. The Atmospheric-Pressure Plasma Jet: A Review and Comparison to Other Plasma Sources. *IEEE Plasma Sci.* **1998**, *26*, 1685–1694. [CrossRef]
23. Bárdos, L.; Baránková, H. Plasma processes at atmospheric and low pressures. *Vacuum* **2009**, *83*, 522–527. [CrossRef]
24. BY4...BY16 Datasheet. Available online: https://diotec.com/tl_files/diotec/files/pdf/datasheets/by4.pdf (accessed on 23 May 2021).
25. Kuffel, E.; Zaengl, W.S.; Kuffel, J. *High Voltage Engineering. Fundamentals*, 2nd ed.; Butterworth-Heinemann: Woburn, MA, USA, 2000; pp. 13–21. ISBN 0 7506 3634 3
26. Iqbal, S.; Besar, R. A Bipolar Cockcroft-Walton Voltage Multiplier for Gas Lasers. *Am. J. Appl. Sci.* **2007**, *4*, 795–801. [CrossRef]
27. Ruzbehani, M. A Comparative Study of Symmetrical Cockcroft-Walton Voltage Multipliers. *J. Electr. Comput. Eng.* **2017**, *2017*, 4805268. [CrossRef]
28. Stoican, O.S. High voltage pulses circuit for generating a plasma plume at atmospheric pressure. *Rom. Rep. Phys.* **2019**, *71*, 406.
29. Weltmann, K.D.; Kindel, E.; von Woedtke, T.; Hähnel, M.; Stieber, M.; Brandenburg, R. Atmospheric-pressure plasma sources: Prospective tools for plasma medicine. *Pure Appl. Chem.* **2010**, *82*, 1223–1237. [CrossRef]
30. Tanaka, H.; Ishikawa, K.; Mizuno, M.; Toyokuni, S.; Kajiyama, H.; Kikkawa, F.; Metelmann, H.-R.; Hori, M. State of the art in medical applications using non-thermal atmospheric pressure plasma. *Rev. Mod. Plasma Phys.* **2017**, *1*. [CrossRef]
31. Maximum Continuous Service Temperature—Plastic Properties. Available online: https://omnexus.specialchem.com/polymer-properties/properties/max-continuous-service-temperature (accessed on 20 June 2021).
32. Vartiainen, J.; Rättö, M.; Tapper, U.; Paulussen, S.; Hurme, E. Surface modification of atmospheric plasma activated BOPP by immobilizing chitosan. *Polym. Bull.* **2005**, *54*, 343–352. [CrossRef]
33. Szymańska, E.; Winnicka, K. Stability of Chitosan—A Challenge for Pharmaceutical and Biomedical Applications. *Mar. Drugs* **2015**, *13*, 1819–1846. [CrossRef] [PubMed]
34. Dreghici, D.B.; Butoi, B.; Predoi, D.; Iconaru, S.L.; Stoican, O.; Groza, A. Chitosan–Hydroxyapatite Composite Layers Generated in Radio Frequency Magnetron Sputtering Discharge: From Plasma to Structural and Morphological Analysis of Layers. *Polymers* **2020**, *12*, 3065. [CrossRef] [PubMed]
35. Nikitin, D.; Lipatova, I.; Naumova, I.; Sirotkin, N.; Pleskunov, P.; Krakovský, I.; Khalakhan, I.; Choukourov, A.; Titov, V.; Agafonov, A. Immobilization of Chitosan Onto Polypropylene Foil via Air/ Solution Atmospheric Pressure Plasma Afterglow Treatment. *Plasma Chem. Plasma Process.* **2020**, *40*, 207–220. [CrossRef]
36. Nedelchev, I. Y. Stability of the Indirect Plasmatron in the Plasma Spray Coating Process. *TEM J.* **2016**, *5*,15–20. [CrossRef]
37. Schoenbach, K.H.; Becker, K. 20 years of microplasma research: A status report. *Eur. Phys. J. D* **2016**, *70*, 29. [CrossRef]

The Oleofobization of Paper via Plasma Treatment

Matic Resnik [1,*] , Eva Levičnik [1], Žiga Gosar [2] , Rok Zaplotnik [1] , Janez Kovač [1], Jernej Ekar [1] , Miran Mozetič [1] and Ita Junkar [1]

[1] Department of Surface Engineering, Jožef Stefan Institute, Jamova 39, 1000 Ljubljana, Slovenia; eva.levicnik@ijs.si (E.L.); rok.zaplotnik@ijs.si (R.Z.); janez.kovac@ijs.si (J.K.); jernej.ekar@ijs.si (J.E.); miran.mozetic@ijs.si (M.M.); ita.junkar@ijs.si (I.J.)
[2] Elvez d.o.o., Ulica Antona Tomšiča 35, 1294 Višnja Gora, Slovenia; ziga.gosar@elvez.si
* Correspondence: matic.resnik@ijs.si

Abstract: Cellulose is a promising biomass material suitable for high volume applications. Its potential lies in sustainability, which is becoming one of the leading trends in industry. However, there are certain drawbacks of cellulose materials which limit their use, especially their high wettability and low barrier properties, which can be overcome by applying thin coatings. Plasma technologies present a high potential for deposition of thin environmentally friendly and recyclable coatings. In this paper, two different plasma reactors were used for coating two types of cellulose-based substrates with hexamethyldisiloxane (HMDSO). The changes in surface characteristics were measured by atomic force microscopy (AFM), scanning electron microscopy (SEM), surface free energy and contact angles measurements, X-ray photoelectron spectroscopy (XPS), and secondary ion mass spectrometry (SIMS). Successful oleofobization was observed for an industrial scale reactor where pure HMDSO was used in the absence of oxygen.

Keywords: oleofobization; paper; cellulose; plasma; HMDSO

1. Introduction

High-volume industries are seeking new alternative materials to become sustainable and decrease pollution. One of the most promising materials being implemented is cellulose, a biomass derived raw material which is abundant, renewable, inexpensive, and biodegradable. Thus, the use of cellulose is expected to increase [1], as it has high potential of application in various industries. Major industries implementing materials made from cellulose nanofibrils (CNF) and microfibrillated cellulose (MFC) are the wood, paper, and textile industries. However, only cellulose with appropriately tailored surface properties can be used for separating oil from water [2], food packaging [3], self-cleaning surfaces [4,5], microchips [6], antibacterial agents [7], etc. Various surface finishing procedures were proposed and studied to achieve hydrophobic or oleophobic surface properties for cellulose-based products. They can be divided into wet chemical methods (like liquid spray-coating [8,9], dip-coating [10], sol-gel [11], etc.), where usually organic solvents are required [12]; or dry methods, that are more environmentally friendly, such as liquid flame spray [13] or plasma-based techniques [14,15].

PECVD (plasma enhanced chemical vapor deposition) is a commonly used technique for depositing thin layers [16] on surfaces. Various precursors can be used to apply Si-containing thin films, with hexamethyldisiloxane (HMDSO) being among the most popular ones. HMDSO is a non-toxic liquid [17] and an easy-to-handle monomer; however, deposition of HMDSO films by plasma polymerization is hard to control, mainly due to the diversity of functional groups produced by the multitude of possible chemical reactions [18]. The structure and composition of plasma polymerized HMDSO films have been widely studied for its application in biocompatible coatings [19–21], barrier and protective coatings [20,22], as well as for water repellence [23,24]. It is used to deposit thin

films ranging from HMDSO-like polymer films to almost pure SiOx films. The HMDSO plasma polymerization of cellulose-based products, such as paper for food packaging, has considerable benefits compared to other coating methods. The quantity of deposited material by PECVD is orders of magnitude smaller, making the process more cost-efficient and the product recyclable [3]. With the recent advantages in plasma techniques, both low-pressure [4,7] and atmospheric pressure [2,3,25] plasma can be successfully employed. The initial investment in PECVD systems in case of low-pressure plasma might be high, while the operating costs are low, and any high-volume industry should on the long run profit using these systems.

HMDSO is a liquid at atmospheric pressure. It has a high vapor pressure (about 50 mbar at room temperature) and can, therefore, be introduced into the processing chamber via a leak valve or gas flow regulator. In the processing chamber, a non-equilibrium gas plasma is created by discharge, where free electrons (with temperature of approximately 10,000 K) cause radicalization and ionization of the precursor. Plasma is often excited by high-frequency discharges [26]. The reactive particles disperse inside the chamber and eventually reach a surface where they adhere with a certain probability. Substrates are often activated before application to improve adhesion. Different coatings can be applied depending on the plasma parameters.

One extreme is a coating of polydimethylsiloxane like films. Such a coating is obtained at a very low power density (in order to preserve the original composition of HMDSO) and in the absence of other gases. The other extreme is a thin layer of silicon dioxide that grows when oxygen-containing gas is present in the chamber, like water vapor, which is usually present in vacuum chambers, or sometimes oxygen is added intentionally to form purer SiOx [27,28]. Between these extremes, all types of coatings can be achieved, depending on the processing parameters. The flow of radicals to the surface (and thus the rate of deposition) obviously increases with increasing pressure and power density. At elevated pressure (more than 10 Pa), however, the radicals begin to agglomerate already in the gas phase, so that the coating becomes granular, which is often considered harmful in industrial systems. If the power density is increased, the dissociation of the precursor is intense, so that carbon atoms or even dimers can be incorporated into the SiOx film, making it less transparent. Another obstacle is the uniformity of the plasma; dissociation and ionization events are more intense closer to the electrodes, so the SiOx film is applied mainly to the electrodes instead of the substrates [29].

The work presented herein aims to apply Si-coatings using HMDSO deposited by plasma to prepare surfaces suitable for food-packaging applications. Two different low-pressure plasma systems were used, the small-scale laboratory reactor and large-scale industrial reactor, to study the effects of plasma treatment on two different types of papers. The influence on surface chemistry, morphology, and hydrophilic and oleophobic properties were studied and assessed for its industrial applicability. The main goal was to improve the oleophobicity of the paper substrates by Si-based coatings. Such modification might be of great interest to high-volume industries, such as the food packaging industry. Cellulose has all of the benefits sought by such an industry, except for the oleophobicity and desired barrier properties.

2. Materials and Methods

2.1. Paper Samples

Two different types of pre-coated papers were used for surface modification with HMDSO. The first paper was made from a combination of softwood (eucalyptus) and hardwood with production rests, and pre-coated with $CaCO_3$, kaolin fillers, and a latex binder. For the purpose of this text, this type of paper will be referred to paper 1. The other paper, referred as paper 2, was made from deinked pulp, mechanical pulp, and consisted of 18–24% inorganic parts, and pre-coated with starch. This type of paper had a much higher organic part in the coating compared to paper 1. Both papers were used for the deposition of HMDSO coating on the surface to study the coating morphology, chemical composition,

and wettability, as well as oleophobic properties of the coating. The papers were treated in A4 format and analyzed with different surface analyzing techniques, as described in the following sections.

2.2. Plasma Enhanced Chemical Vapor Deposition (PECVD)

Two different types of plasma reactors were used for modification of papers: the laboratory reactor operating at microwave (MW) discharge, and the industrial reactor operating at radiofrequency (RF) discharge. Due to the specifics of the two plasma systems, different treatment conditions were used for surface modification and presented in more detail below.

2.2.1. Laboratory Reactor

A low-pressure microwave (MW) plasma was generated in the LA400 plasma system (SurfaceTreat, Turnov, Czech Republic) [30]. A double stage rotary vacuum pump with 65 m^3/h nominal pumping speed was used to evacuate the 64 L processing chamber to a base pressure of 1 Pa. The processing chamber made of aluminum had a magnetron mounted on top, with microwaves entering the chamber through a quartz glass. The heated HMDSO container was mounted close to the chamber and leaked into it. The flow of HMDSO and oxygen, the MW generator's power, the distance between the magnetron and the sample, and the exposure time were varied to reach the optimal parameters.

The samples of paper 1 and 2 were prepared by 10 min plasma deposition with MW plasma, where the feeding gas was a mixture of HMDSO and O_2 (ratio 7:1, respectively) at 50 Pa of combined pressure and MW power of 200 W. The distance between the magnetron and the sample was approximately 0.2 m.

2.2.2. Industrial Reactor

An industrial scale reactor for PECVD was used for depositing HMDSO on paper samples. The reactor was cylindrically shaped with a 0.95 m radius and a height of 1.8 m. Multiple vacuum pumps were used for sustaining low pressures inside the reactor. Diffusion pumps were supported by roots and rotary pumps and a cold trap, together reaching a base pressure in the range of 0.01 Pa. A perforated tube was used to evenly distribute the gas fed into the reactor via flow controllers. Plasma at low pressure was sustained by an asymmetric capacitively coupled RF discharge. Two powered electrodes (0.5 m^2 each) were located close to the grounded reactor housing (approximately 17 m^2). Powered electrodes were connected to a RF generator with adjustable power output (up to 8 kW) operating at the frequency of 40 kHz. More about this reactor, including its schematic, can be found in an earlier paper by Gosar et al. [22,31].

The samples of paper 1 and 2 were mounted onto planetary stands with two rotational movements, one around its own axis and another one around the center of reactor. This kind of movement should ensure equal treatment for all samples. Afterwards, the reactor was pumped to a base pressure, and a 20-min cycle of PECVD of HMDSO began.

2.3. Surface Morphology Analysis

2.3.1. Scanning Electron Microscopy

Morphological properties of the samples were analyzed using scanning electron microscopy (SEM). Approximately 5 × 5 mm^2 pieces of treated and untreated paper were cut from the material. They were attached onto aluminum stubs using conductive carbon tape, and their edges connected to the stub surface using carbon paste and coated with a thin gold layer (10–12 nm thick) using a Balzers SCD 050 sputter coater (BAL-TEC GmbH, Schalksmühle, Germany). The SEM images were obtained using a Jeol JSM-7600F Schottky Field Emission scanning electron microscope (Jeol Ltd., Tokyo, Japan).

2.3.2. Atomic Force Microscopy

Changes in surface morphology of paper samples were analyzed by Atomic force microscope (AFM) Solver PRO (NT-MDT, Moscow, Russia) in non-contact mode in air. Samples were cut into small pieces, and the surface was scanned by a standard Si cantilever with a force constant of 22 Nm^{-1} and at a resonance frequency of 325 kHz. The cantilever's tip radius was 10 nm, the tip length was 95 μm, and the scan rate was set at 1.2 Hz. Every measurement was repeated at least five times. Average surface roughness (Sa) was measured from representative images on 5×5, 2×2, and 1×1 μm² areas with the Nova AFM software (NT-MDT, Moscow, Russia). Paper 2 in untreated state was too rough to be analyzed with our AFM device.

2.4. Surface Free Energy and Contact Angle

The surface wettability was performed with the Drop Shape Analyser DSA-100 (Krüss GmbH, Hannover, Germany) by a sessile drop method to measure a static contact angle. Surface wettability was analyzed immediately after plasma treatment. The relative humidity was around 45% and the operating temperature was 21 °C, which did not vary significantly during continuous measurements.

The Krüss GmbH device for measuring surface wettability had a platform, which automatically moved by the X and Y axes (Figure 1). After setting X and Y positions for the simultaneous deposition of a drop, a contact angle was recorded. Surface energy was determined from contact angle measurements. According to the Tappi T 5580m 97 standard, the OWRK (Owens, Wendt, Rabel and Kaelble) fitting method with water (2.5 μL drop of deionized water) and diiodomethane (1.5 μL drop of diiodomethane) was used by the Drop Shape Analyser. Additionally, pumpkin oil (1.5 μL drop manually added by a syringe) was used to determine oleophobic properties of the coating.
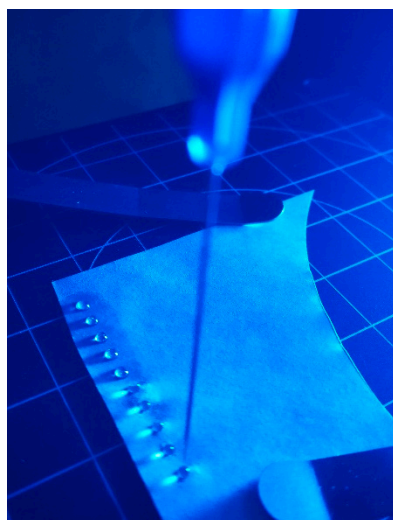
Figure 1. An array of distilled water and diiodomethane drops with a volume of 1.5 μL applied to the paper surface with a distance of 3 mm between individual drops.

2.5. Surface Chemistry Analysis

2.5.1. X-ray Photoelectron Spectroscopy

The X-ray photoelectron spectroscopy (XPS or ESCA) analyses of papers were carried out by a PHI-TFA XPS spectrometer produced by Physical Electronics Inc. (Physical Electronics Inc., Chanhassen, MN, USA). Samples were placed on metallic support and introduced in ultra-high vacuum spectrometer. The analyzed area was 0.4 mm in diameter, and the analyzed depth was about 3–5 nm. This high surface sensitivity is a general characteristic of the XPS method. Sample surfaces were excited by X-ray radiation from monochromatic Al source at a photon energy of 1486.6 eV. The high-energy resolution spectra were acquired with an energy analyzer operating at a resolution of about 0.6 eV

and pass energy of 29 eV. During data processing, the spectra from the surface were aligned by setting the C 1s peak at 285.0 eV, characteristic for C–C bonds. The accuracy of binding energies was about ± 0.3 eV. Quantification of surface composition was performed from XPS peak intensities considering relative sensitivity factors provided by the instrument manufacturer [32]. Three different XPS measurements were performed on each sample and average composition was calculated.

In order to analyze thickness and in-depth distribution of elements in the SiO_2 films, the XPS depth profiling was performed in combination with ion sputtering. Ar ions of 4 keV energy were used. The velocity of the ion sputtering was estimated to be 2.0 nm/min, calibrated on the SiO_2 structure of the known thickness.

2.5.2. Secondary Ion Mass Spectrometry

TOF-SIMS (Time-of-flight secondary ion mass spectrometry) analyses were made on the TOF.SIMS 5 instrument produced by the IONTOF company (IONTOF GmbH, Münster, Germany). As the analytical beam, we used Bi^{3+} primary ions with energy of 30 keV. Analytical depth with the settings used was around 2 nm and detection limits were around 1 ppm of species of interest in the sample. As the paper samples were nonconductive, the low energy electron beam had to be applied to neutralize excessive positive charge.

Positive and negative surface spectra were recorded in the areas of 250×250 μm^2 while measuring secondary ions in the *m/z* range from 0 to 875. Mass resolution (m/Δm) was between 3500 and 7000, depending on the peak of interest. Micrographs of positive secondary ions of interest were also recorded in the areas of 500×500 μm^2. The lateral resolution of micrographs was 180 nm and quality was 512×512 pixels. Depth profiles of positive secondary ions were recorded on the 100×100 μm^2 areas while rastering the 1 keV O^{2+} primary ion sputter beam over the area of 400×400 μm^2.

3. Results

3.1. Surface Morphology

Untreated paper 1 and paper 2 have different surface morphologies, as presented in Figure 2. On paper 1, a grain like structure is observed, with visible kaolin particles; while on paper 2, the surface exhibits grain like structure together with smoother parts that can be ascribed to the organic parts of the coating. Figure 2a represents a sample of paper 1 before plasma treatment. Microparticles with relatively wide size distribution were observed. Larger kaolin particles were also clearly visible, with their distinctive edges and flat surfaces. There were many empty spaces between the grains in the case of paper 1, which makes it porous. In case of paper 2 (Figure 2b), microparticles were not so well observed, as it seemed they were covered with the organic parts of the coating. However, in this case, the microroughness, according to AFM, was much higher as it was not possible to obtain useful AFM data on these surfaces.

Interestingly, after plasma treatment, similarities can be observed for both paper samples. After the deposition of HMDSO in a laboratory plasma system, the entire surface was covered in what appeared to be fine nano grains (Figure 2c,d). Many of the former grain boundaries between macroparticles and empty spaces seemed to be covered with a HMDSO coating. In the case of plasma treatment of paper 1 in the laboratory reactor (Figure 2c), the coating was not completely flat and dark pores were still present, probably due to a relatively thin layer of HMDSO coating (a few nanometers). Paper 2 treated in the laboratory reactor is shown in Figure 2d, where a unified fine-grained surface was clearly visible. The HMDSO coating seemed to fill even the small gaps between the pores.

Further on, the SEM images of both samples of paper treated in the industrial reactor reveal what appeared to be a thicker and more dense coating compared to the one from the laboratory reactor. The surface of paper 1 treated in the industrial reactor exhibited a densely packed grain-like structure, which seemed to have fewer gaps in the structure (Figure 2e) compared to surfaces treated in laboratory plasma reactor. Similarly, a dense coating with less pronounced grain-like structure was observed on paper 2 treated in the

industrial reactor (Figure 2f). The sample of paper 2 treated in the industrial reactor for 20 min appears to be fully covered with a HMDSO like coating, and only random clusters of grains can be observed under the HMDSO coating.

(**a**) Paper 1 untreated

(**b**) Paper 2 untreated

(**c**) Paper 1 treated in laboratory reactor

(**d**) Paper 2 treated in laboratory reactor

(**e**) Paper 1 treated in industrial reactor

(**f**) Paper 2 treated in industrial reactor
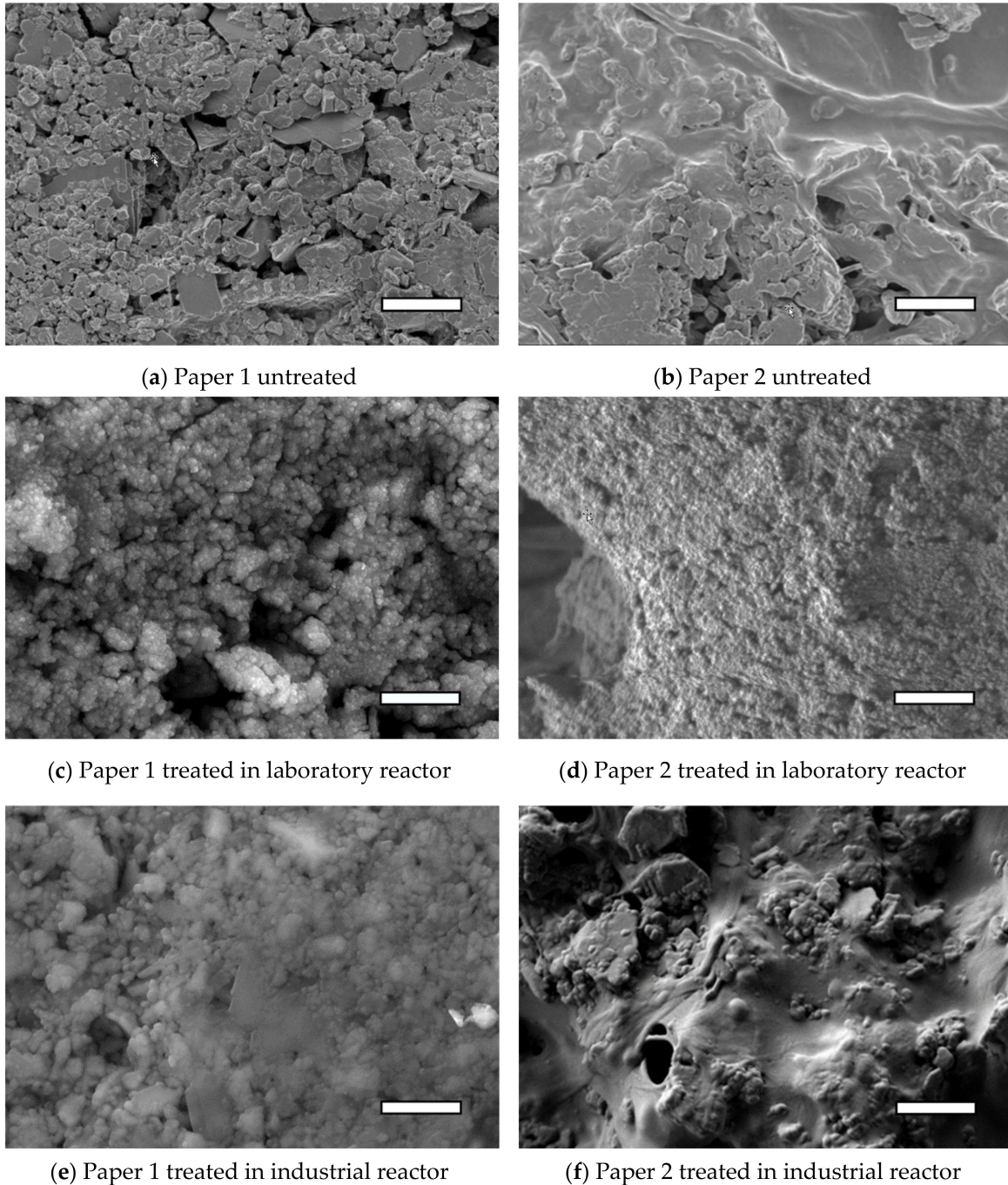
Figure 2. Comparison of SEM, higher magnification coatings on paper 1 and 2 with two different plasma systems. On the left there is paper 1, (**a**) untreated, (**c**) treated in laboratory reactor, (**e**) treated in industrial reactor. On the right there is paper 2, (**b**) untreated, (**d**) treated in laboratory reactor, (**f**) treated in industrial reactor. White bar represents 1 μm scale.

Similar results were reported by Babaei et al. [3], where the samples of Kraft paper were exposed to atmospheric pressure plasma polymerization of HMDSO under helium (He). Their sample had microfibril structures visible at higher magnifications, which also remained visible after being uniformly covered with HMDSO grains in the process of PECVD. According to the results of this study, the coating was comprised of SiOCH, which

was not uniformly distributed. The amount of organosilicon coating gradually decreased in the direction away from the HMDSO gas inlet. Hydrophobic surfaces were obtained, with a water contact angle of about 140°.

The AFM images conducted on paper 1 provided more detailed analysis of surface morphology. After plasma treatment in both plasma systems, fine grain structures were observed on the paper surface, which seemed to cover the initial paper micro topography uniformly. Untreated paper 1 had a relatively wide distribution of micro and nano particles, with gaps between the grain boundaries (Figure 3a). In contrast, paper 1 treated in laboratory reactor was covered with smaller and more defined grains, with uniform grain size distribution ranging from 100 to 200 nm. The grain borders were visible and seemed to also cover the spaces between the micro particles. The grain-like structure that was observed in the case of paper 1 treated in industrial reactor was denser, with bigger grains ranging from 200 to 600 nm. The average roughness was also analyzed. However, due to high nonuniformity of the surface, especially due to its microstructure, it was hard to compare changes in roughness between the samples. In a study by Nättinen et al., where HMDSO was deposited onto LDPE (low density polyethylene) and cotton fabric for its hydrophobic effect [33], the shape and size of grains reported were similar to the ones presented herein after laboratory-plasma treatment.

(**b**) Paper 1 treated in laboratory reactor

(**a**) Paper 1 untreated

(**c**) Paper 1 treated in industrial reactor
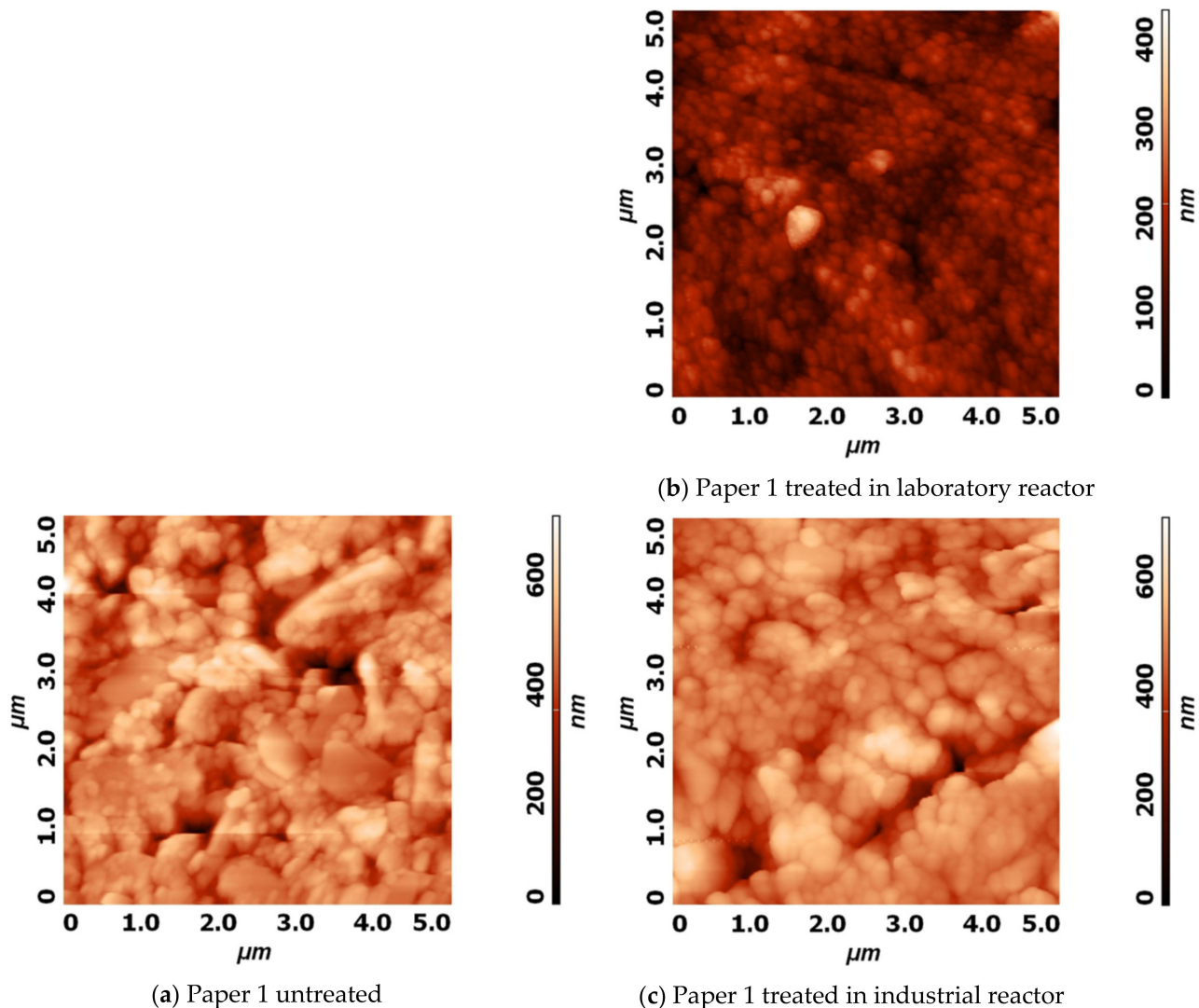
Figure 3. AFM images of height profiles on paper 1 before (**a**) and after plasma treatment in laboratory (**b**) and industrial (**c**) reactor.

3.2. Surface Free Energy and Hydrophilic/Oleophobic Properties

According to the wettability analysis, two different trends were observed after deposition of the HMDSO coating. According to the wettability data, presented in Table 1, the untreated paper 1 and 2 are hydrophobic. After plasma treatment in the laboratory reactor, where oxygen was also present, both papers became hydrophilic and the surface free energy rose. However, this was not the case with the industrial scale reactor, where only HMDSO was present during plasma treatment (no addition of oxygen). After industrial plasma treatment, paper 1 became significantly more hydrophobic, while paper 2 kept its hydrophobicity. It should be emphasized that nanotopographic features (according to SEM) on both papers were similar, while the initial microtopography was different, which could partially influence the wettability. Wettability changes were also observed for Si–O–Si, Al–O, and Zr–O ceramic-based sol-gel treated CNF films by Vartiainen et al., who reported an increase in water contact angle from 54 to 102 degrees after the coating [34]. In this study, decreased water vapor transmission was also reported. Compared to the untreated sample, the surface free energy dropped close to 5 and 2-fold for industrially treated paper 1 and paper 2, respectively. Similar behavior was also observed by Vartiainen et al., where roll-to-roll atmospheric plasma deposition of HMDSO onto cellulose films was studied. Vartiainen et al. reported water contact angles of 23° and 103° for untreated cellulose nanofibrils and coated cellulose nanofibrils, respectively [1].

Table 1. The results of water contact angles and surface energy measurements of paper 1 and 2 in untreated state and immediately after plasma coating treatment in laboratory and industrial reactor.

	Paper 1			**Paper 2**		
	WCA (°)	**SE (mN/m)**	**CA of Oil (°)**	**WCA (°)**	**SE (mN/m)**	**CA of Oil (°)**
Untreated	71.4 ($\pm$6.7)	48.8 ($\pm$3.9)	<5	115.0 ($\pm$4.0)	31.2 ($\pm$1.3)	<5
Laboratory plasma	21.4 ($\pm$0.9)	69.8 ($\pm$2.5)	<5	41.0 ($\pm$2.8)	57.4 ($\pm$2.3)	<5
Industrial plasma	124.9 ($\pm$2.5)	11.6 ($\pm$2.6)	59.2 ($\pm$1.8)	109.8 ($\pm$7.9)	14.4 ($\pm$2.5)	68.5 ($\pm$3.4)

The increase in oleophobic properties was not observed for untreated and laboratory-plasma treated samples, as the oil was fully spread on the paper. In the case of industrial-plasma treatment, the HMDSO coating on both papers seemed to prevent the oil from penetrating into the paper, as shown in Figure 4. This kind of effect is highly desired in food industry applications. Oil drop time-lapse can be observed in Figures 4 and 5 for paper 1 and 2 before and after treatment in industrial plasma reactor, respectively. The oil drop did not spread much after 24 h; however, slight differences between paper 1 and 2 were observed. It seemed that oil drop on paper 1 tended to spread slower compared to the one on paper 2. This could be partially ascribed to the difference in initial microtopography of both papers, as paper 2 seemed to have deeper pores that were probably not fully covered with the HMDSO-like coating. The difference in surface properties of papers coated by two plasma reactors can also be partially ascribed to differences in surface nanotopography and density of grains and pores, however, it will become evident in the second section that surface chemistry was significantly altered due to the use of two different plasma systems at different plasma treatment conditions.
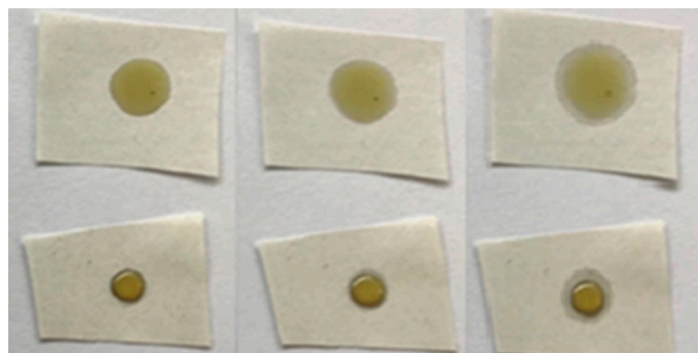
Figure 4. Time lapse of untreated (**above**) and industrial-plasma treated (**below**) paper 1, from left to right, immediately after plasma treatment, 10 min after plasma treatment, and 24 h after plasma treatment.
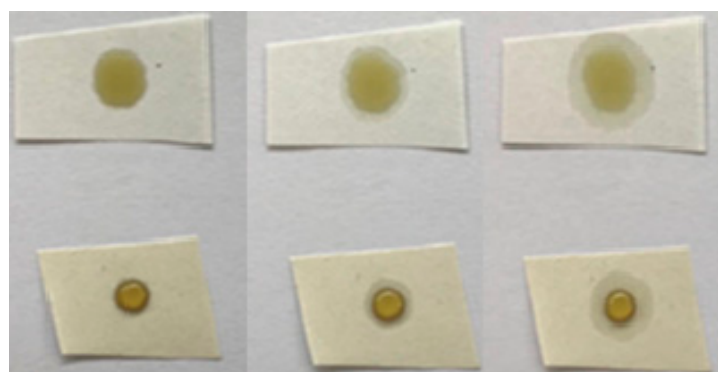
Figure 5. Time lapse of untreated (**above**) and industrial-plasma treated (**below**) paper 2, from left to right, immediately after plasma treatment, 10 min after plasma treatment, and 24 h after plasma treatment.

3.3. Surface Chemistry

3.3.1. XPS Analyses

XPS analyses were performed to get insight into surface chemistry. Figure 6 and Table 2 show surface composition in at.%, obtained by XPS method, for paper 1. Figure 7a–c show a stack of high energy resolution XPS spectra C 1s and O 1s from untreated paper, a laboratory-plasma treated paper, and an industrial-plasma treated paper. The C 1s spectrum from untreated paper consisted of peak at 284.8 eV assigned to C–C/C–H bonds and a peak at 286.0 eV assigned to the C–OH bonds. In addition, there was a notable peak at 289.5 eV, which originated from CO_3 bonds ($CaCO_3$ particles). The O 1s spectrum of the untreated sample was at 531.5 eV, which may be assigned to OH/C–O bonds present in the coating of the untreated paper. Similar atomic concentration of C, O, and Si were detected for paper 2, while in this case a much lower amount of Ca was detected (about 2 at%). The laboratory-plasma treated sample showed XPS spectra characteristic for SiO_2-like coating; the surface composition (Figure 6) mainly reassembled the pure SiO_2 coating, the O 1s peak was at 533.2 eV, and Si 2p peak was at 103.5 eV, and both were assigned to SiO_2 bonds. The SiO_2-like coating seemed to completely cover the paper surface since no signal of Ca was detected on the plasma treated paper. The industrial-plasma treated paper had a different surface layer than the laboratory-plasma treated one, which can be recognized from surface composition in Figure 6 as well as from the different shape of the XPS spectra. The concentrations of C (45 at.%), O (30 at.%), and Si (25 at.%) indicated the presence of a HMDSO-like coating on the surface. The C 1s XPS spectrum positioned at 285.0 eV, O 1s spectrum at 532.6 eV, and Si 2p spectrum at 102.5 eV were related to the formation of the C–Si–O bonds, which confirms the HMDSO-like coating on the industrial-plasma treated

paper. Similar effects after treatment in laboratory plasma and industrial plasma reactor were observed also in the case of paper 2, but results are not shown.
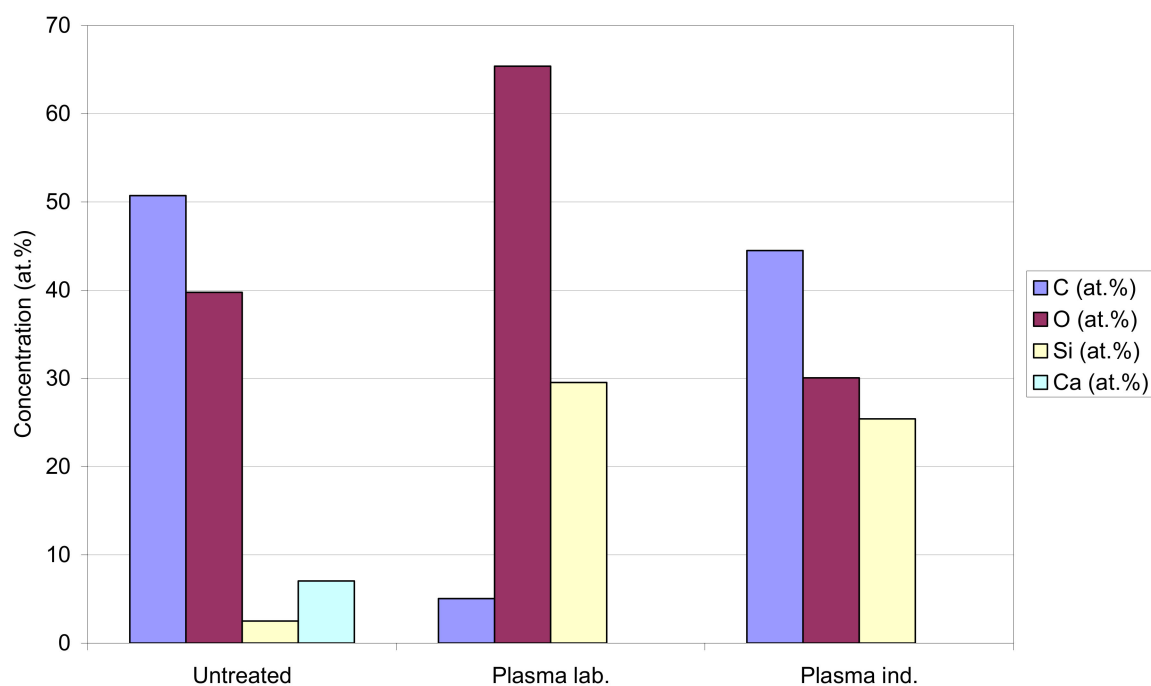
Figure 6. Surface composition in at.% of untreated, laboratory plasma, and industrial plasma treated samples analyzed by XPS method.

Table 2. Surface composition in at.% obtained by XPS analyses.

Sample	C (at. %)	O (at. %)	Si (at. %)	Ca (at. %)
Untreated	50.7	39.8	2.5	7.0
Laboratory plasma	5.1	65.4	29.6	0.0
Industrial plasma	44.5	30.1	25.4	0.0
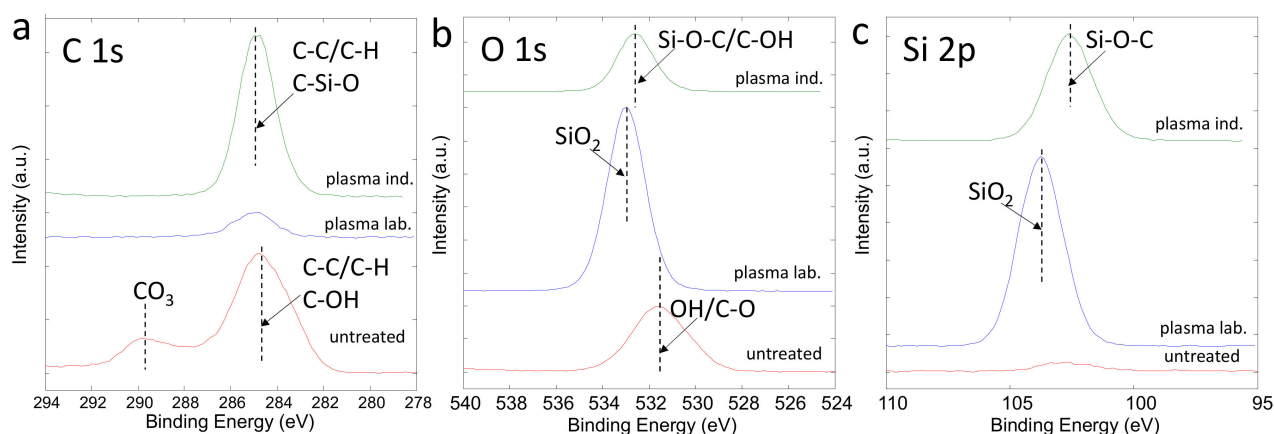
Figure 7. High energy resolution XPS spectra C 1s (**a**), O 1s (**b**), and Si 2p (**c**) from untreated (read line), laboratory plasma (blue line), and industrial plasma (green line) treated samples.

3.3.2. SIMS Analysis

Further analysis of the coating was conducted by SIMS on both papers before and after treatment in two types of plasma reactors. Positive secondary ion spectra show the difference between different types of papers. Paper 1 was enriched with calcium salts; while on paper 2, different C, O, and H based fragments were detected, originating from the cellulose. The positive spectra of both papers are presented in Figure 8. The negative secondary ion spectra, on the other hand, showed no significant difference, with mainly cellulose fragments and some sulfonate detergents for both paper types (data not shown).
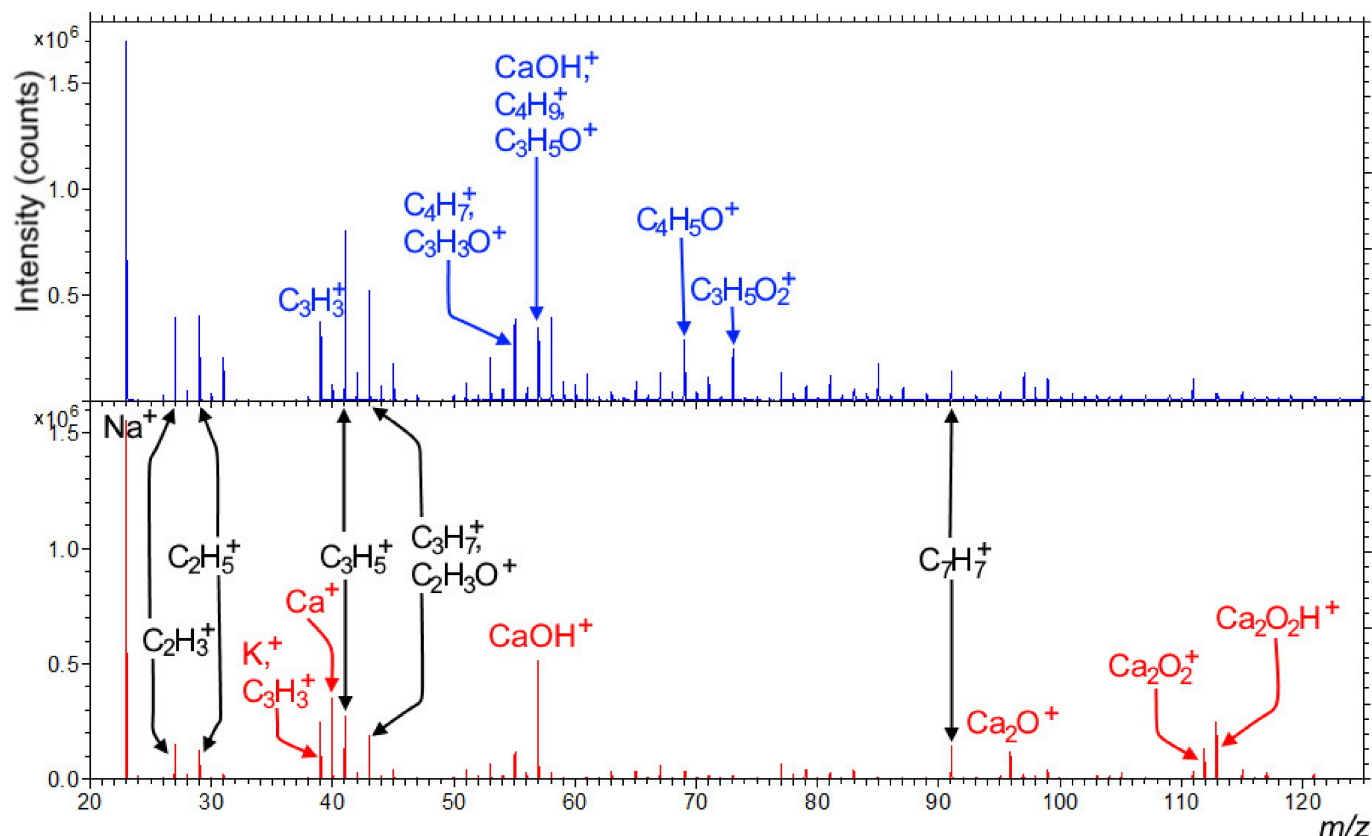
Figure 8. Positive secondary ion spectra of paper 2 (**upper**, blue spectrum) and paper 1 (**bottom**, red spectrum) in the *m/z* range from 20 to 125. The most important peaks were assigned with the blue color representing only paper 2, red only paper 1, and black signals equivalently found in both of the papers.

SIMS analysis on paper 1 and 2 coated with HMDSO by laboratory plasma reactor show that the surface was covered by a SiO_2 layer. HMDSO seemed to convert into a SiO_2 layer, an intense signal for the $SiOH^+$ fragment was observed, which was also confirmed by XPS analysis. In Figure 9, spectra of the positive secondary ions emitted from the surface of the laboratory plasma treated paper 1 was presented, and similar results were obtained also for paper 2 (data not shown).

In contrast, papers coated with HMDSO in the industrial plasma reactor exhibit very different surface composition compared to papers treated in laboratory plasma reactor. The spectrum of positive secondary ions emitted from paper 1 coated in industrial plasma reactor is shown in Figure 10. In this case, mainly $SiCH_5^+$ fragments were detected at the same nominal mass as the $SiOH^+$ fragment before. The intensity of the $SiOH^+$ is very low, indicating the absence of SiO_2. Furthermore, many positive secondary ions originating from organosilicon compounds were seen in the spectrum (Figure 10). Some organosilicon fragments we also found in the spectrum in Figure 9. However, they were less prominent compared to the ones detected in Figure 10.
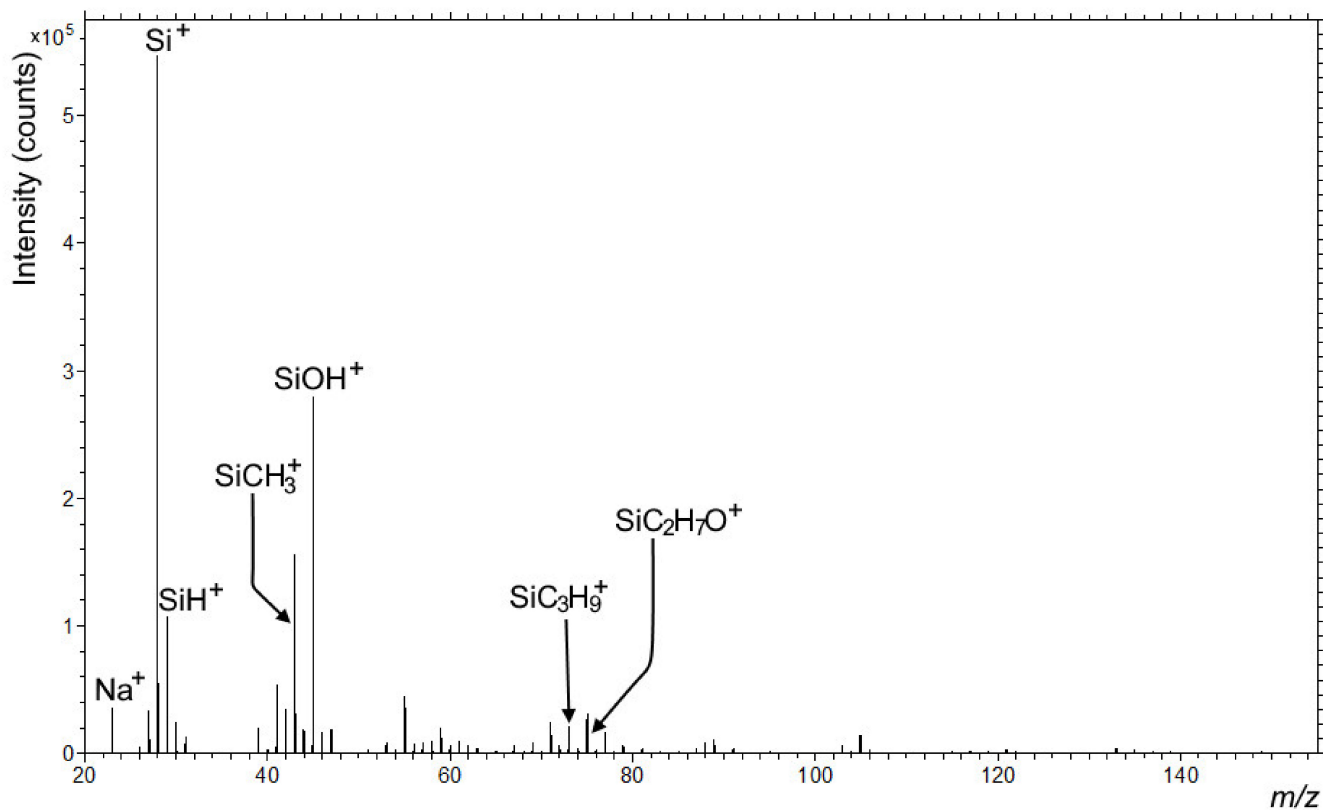
Figure 9. Positive secondary ion spectrum of the paper 1 coated with HMDSO in laboratory plasma reactor in the *m/z* range from 20 to 155.
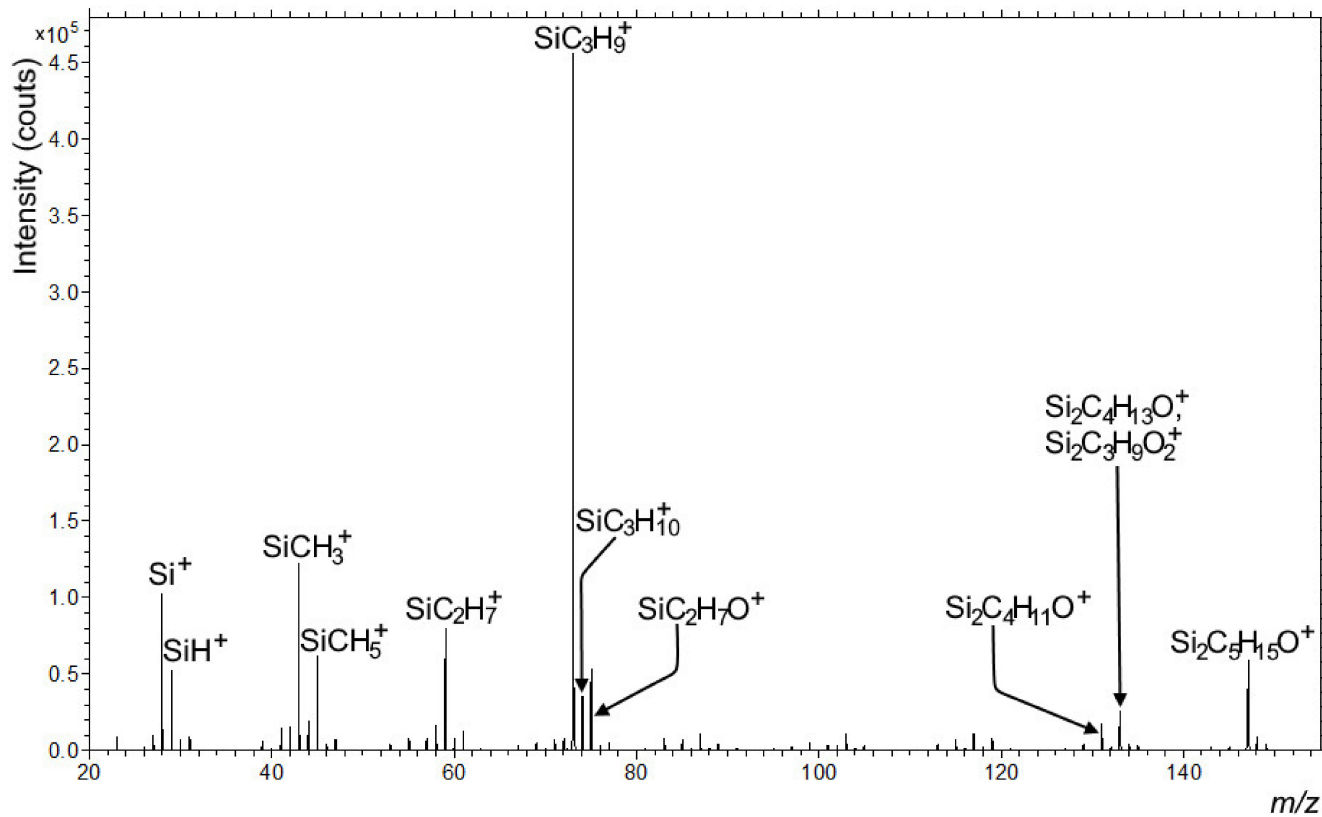
Figure 10. Positive secondary ion spectrum of the paper 2 coated with HMDSO in industrial plasma reactor in the *m/z* range from 20 to 155.

Even more pronounced differences between papers coated with HMDSO using the laboratory plasma and the industrial plasma reactor can be observed at the negative SIMS spectra. As it can be seen in Figure 11 (upper, green spectrum), only $Si_xO_y^-$ and $Si_xO_yH^-$ fragments, originating from the SiO_2 layer (besides C_2H^-, Si^- and O_2^-), can be found when analyzing laboratory plasma treated paper. On the other hand, when the industrial plasma reactor was used (Figure 11, bottom, orange spectrum), only SiO_2^-, SiO_2H^-, and SiO_3H^- fragments were present, but with much lower intensity than in the case of laboratory plasma reactor. Most of the other signals belong to the organosilicon fragments originating from the HMDSO. It must also be emphasized that comparing two different types of HMDSO coated papers was not problematic, as SIMS was a surface-sensitive technique where only a few topmost atomic/molecular monolayers with a thickness of approximately 2 nm were analyzed. Thus, no information about the underlying paper was gathered during the surface spectra analysis.
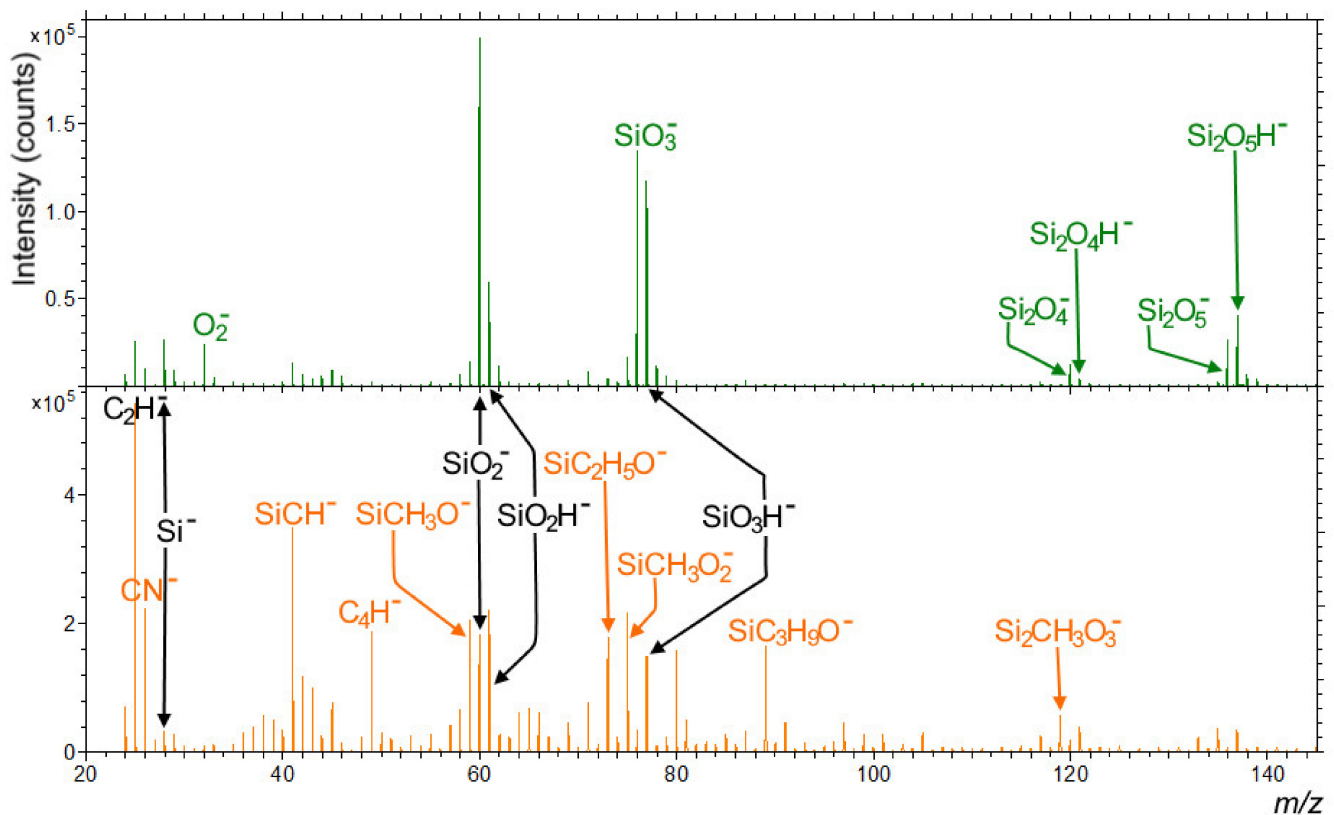
Figure 11. Negative secondary ion spectra of the HMDSO covered paper 1 by laboratory plasma reactor (**upper**, green spectrum) and the one treated in an industrial plasma reactor (**bottom**, orange spectrum) in the *m/z* range from 20 to 145. The most important peaks are assigned, with the green color representing only paper 1 treated in laboratory plasma reactor, orange representing only paper 1 treated in the industrial plasma reactor, and black representing signals equivalently found in both cases of the plasma treatment.

To present the uniformity of the coating, micrographs were taken as well and are shown in Figure 12. It was evident from these micrographs that there was a more or less uniform HMDSO layer spread over the whole surface of the paper, as it can be seen in the left micrograph (paper 1 treated in industrial plasma reactor) in Figure 12. There were still some areas with increased concentration of Na, K, and Ca (right micrograph in Figure 12), but they were not significantly prominent. Coating with HMDSO in industrial plasma as well as in laboratory plasma (data not shown) seemed to provide uniform coverage for the relatively rough surface of the paper.

(a)

(b)
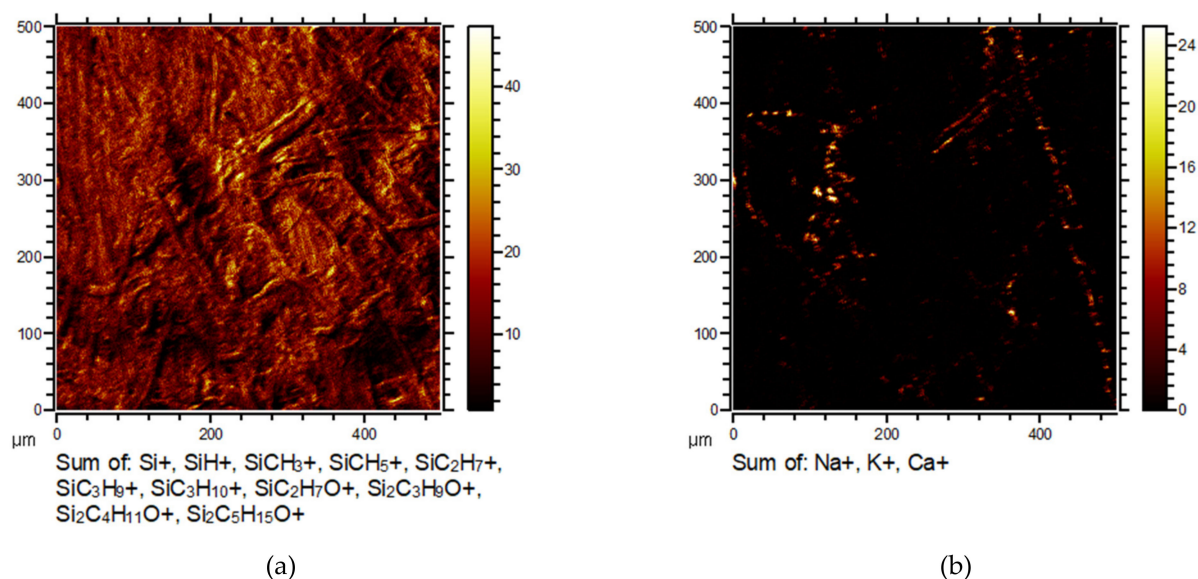
Figure 12. Micrographs of positive secondary ions emitted from paper 1 covered with HMDSO like layer by industrial plasma reactor. On the micrograph (**a**) are ions representing the HMDSO layer and on the micrograph (**b**), Na, K, and Ca ions.

4. Conclusions

Two different types of papers and two different types of plasma reactors were used for coating paper with HMDSO. Results of our study show that regardless of the papers' initial differences in morphology and chemical composition, both plasma treatments enabled uniform coverage of the paper surface. However, significant differences between the two plasma systems were observed. In the case of laboratory plasma, practically pure SiO_2 coating was obtained on both types of papers, as determined from XPS and SIMS analysis. Surfaces were fully hydrophilic and no changes in oleophobic properties were observed. The oil drop was fully absorbed and spread on these papers, which could be partially explained by the fragile SiO_2 coating formed on the surface. In the case of industrial plasma, surfaces were coated by a HMDSO-like coating, which increased its hydrophobic and oleophobic properties. The oil drop was not absorbed into the paper; even after 24 h of contact, only slight absorption on the edges was observed. Slight differences in absorption of oil were, however, observed between two different types of paper. Overall, HMDSO-like coating of papers could present an interesting approach to alter surface properties of paper for specific applications, like for the food packaging industry. Increasing coating thickness could further improve the oleophobicity as well as barrier properties. However, treatment times should be significantly reduced to reach the demand for rapid treatment conditions used in paper industry.

References

1. Vartiainen, J.; Malm, T. Surface hydrophobization of CNF films by roll-to-roll HMDSO plasma deposition. *J. Coat. Technol. Res.* **2016**, *13*, 1145–1149. [CrossRef]
2. Meunier, L.F.; Profili, J.; Babaei, S.; Asadollahi, S.; Sarkissian, A.; Dorris, A.; Beck, S.; Naudé, N.; Stafford, L. Modification of microfibrillated cellulosic foams in a dielectric barrier discharge at atmospheric pressure. *Plasma Process. Polym.* **2020**, e2000158. [CrossRef]
3. Babaei, S.; Profili, J.; Asadollahi, S.; Sarkassian, A.; Dorris, A.; Beck, S.; Stafford, L. Analysis of transport phenomena during plasma deposition of hydrophobic coatings on porous cellulosic substrates in plane-to-plane dielectric barrier discharges at atmospheric pressure. *Plasma Process. Polym.* **2020**, *17*, 2000091. [CrossRef]
4. Rani, K.V.; Chandwani, N.; Kikani, P.; Nema, S.; Sarma, A.K.; Sarma, B. Hydrophobic surface modification of silk fabric using plasma-polymerized HMDSO. *Surf. Rev. Lett.* **2018**, *25*, 1850060. [CrossRef]
5. Teisala, H.; Tuominen, M.; Kuusipalo, J. Superhydrophobic Coatings on Cellulose-Based Materials: Fabrication, Properties, and Applications. *Adv. Mater. Interfaces* **2014**, *1*, 1300026. [CrossRef]
6. Gao, B.; Liu, H.; Gu, Z. Bottom-up fabrication of paper-based microchips by blade coating of cellulose microfibers on a patterned surface. *Langmuir* **2014**, *30*, 15041–15046. [CrossRef]
7. Ražić, S.E.; Peran, J.; Kosalec, I. Functionalization of cellulose-based material by surface modifications using plasma and organosilicone/Ag compounds. In Proceedings of the ICNF 2015 from Nature to Market, 2nd International Conference on Natural Fibers, Azores, Portugal, 27–29 April 2015.
8. Wang, Z.; Ma, H.; Chu, B.; Hsiao, B.S. Fabrication of cellulose nanofiber-based ultrafiltration membranes by spray coating approach. *J. Appl. Polym. Sci.* **2017**, *134*. [CrossRef]
9. Huang, J.; Wang, S.; Lyu, S.; Fu, F. Preparation of a robust cellulose nanocrystal superhydrophobic coating for self-cleaning and oil-water separation only by spraying. *Ind. Crop. Prod.* **2018**, *122*, 438–447. [CrossRef]
10. Arbatan, T.; Zhang, L.; Fang, X.-Y.; Shen, W. Cellulose nanofibers as binder for fabrication of superhydrophobic paper. *Chem. Eng. J.* **2012**, *210*, 74–79. [CrossRef]
11. Tomšič, B.; Simončič, B.; Orel, B.; Černe, L.; Tavčer, P.F.; Zorko, M.; Jerman, I.; Vilčnik, A.; Kovač, J. Sol-gel coating of cellulose fibres with antimicrobial and repellent properties. *J. Sol-Gel Sci. Technol.* **2008**, *47*, 44–57. [CrossRef]
12. Rabnawaz, M.; Liu, G.; Hu, H. Fluorine-free anti-smudge polyurethane coatings. *Angew. Chem.* **2015**, *127*, 12913–12918. [CrossRef]
13. Teisala, H.; Tuominen, M.; Aromaa, M.; Stepien, M.; Mäkelä, J.M.; Saarinen, J.J.; Toivakka, M.; Kuusipalo, J. High-and low-adhesive superhydrophobicity on the liquid flame spray-coated board and paper: Structural effects on surface wetting and transition between the low-and high-adhesive states. *Colloid Polym. Sci.* **2013**, *291*, 447–455. [CrossRef]
14. Marchand, D.J.; Dilworth, Z.R.; Stauffer, R.J.; Hsiao, E.; Kim, J.-H.; Kang, J.-G.; Kim, S.H. Atmospheric rf plasma deposition of superhydrophobic coatings using tetramethylsilane precursor. *Surf. Coat. Technol.* **2013**, *234*, 14–20. [CrossRef]
15. Pawlat, J.; Terebun, P.; Kwiatkowski, M.; Diatczyk, J. RF atmospheric plasma jet surface treatment of paper. *J. Phys. D Appl. Phys.* **2016**, *49*, 374001. [CrossRef]
16. Martinu, L.; Poitras, D. Plasma deposition of optical films and coatings: A review. *J. Vac. Sci. Technol. A Vac. Surf. Film.* **2000**, *18*, 2619–2645. [CrossRef]
17. Do Prado, M.; Da Silva, E.M.; das Neves Marques, J.; Gonzalez, C.B.; Simão, R.A. The effects of non-thermal plasma and conventional treatments on the bond strength of fiber posts to resin cement. *Restor. Dent. Endod.* **2017**, *42*, 125. [CrossRef] [PubMed]
18. Dai, X.J.; Church, J.S.; Huson, M.G. Pulsed plasma polymerization of hexamethyldisiloxane onto wool: Control of moisture vapor transmission rate and surface adhesion. *Plasma Process. Polym.* **2009**, *6*, 139–147. [CrossRef]
19. Teske, M.; Wulf, K.; Fink, J.; Brietzke, A.; Arbeiter, D.; Eickner, T.; Senz, V.; Grabow, N.; Illner, S. Controlled biodegradation of metallic biomaterials by plasma polymer coatings using hexamethyldisiloxane and allylamine monomers. *Curr. Dir. Biomed. Eng.* **2019**, *5*, 315–317. [CrossRef]
20. Lommatzsch, U.; Ihde, J. Plasma polymerization of HMDSO with an atmospheric pressure plasma jet for corrosion protection of aluminum and low-adhesion surfaces. *Plasma Process. Polym.* **2009**, *6*, 642–648. [CrossRef]
21. Hsiao, C.-R.; Lin, C.-W.; Chou, C.-M.; Chung, C.-J.; He, J.-L. Surface modification of blood-contacting biomaterials by plasma-polymerized superhydrophobic films using hexamethyldisiloxane and tetrafluoromethane as precursors. *Appl. Surf. Sci.* **2015**, *346*, 50–56. [CrossRef]
22. Gosar, Ž.; Kovač, J.; Mozetič, M.; Primc, G.; Vesel, A.; Zaplotnik, R. Deposition of SiOxCyHz protective coatings on polymer substrates in an industrial-scale PECVD reactor. *Coatings* **2019**, *9*, 234. [CrossRef]

23. Choudhury, A.; Barve, S.; Chutia, J.; Pal, A.; Kishore, R.; Pande, M.; Patil, D. RF-PACVD of water repellent and protective HMDSO coatings on bell metal surfaces: Correlation between discharge parameters and film properties. *Appl. Surf. Sci.* **2011**, *257*, 8469–8477. [CrossRef]

24. Ji, Y.-Y.; Hong, Y.-C.; Lee, S.-H.; Kim, S.-D.; Kim, S.-S. Formation of super-hydrophobic and water-repellency surface with hexamethyldisiloxane (HMDSO) coating on polyethyleneteraphtalate fiber by atmosperic pressure plasma polymerization. *Surf. Coat. Technol.* **2008**, *202*, 5663–5667. [CrossRef]

25. Odrásková, M.; Szalay, Z.; Ráhel, J.; Zahoranová, A.; Cernák, M. Diffuse coplanar surface barrier discharge assisted deposition of water repellent films from N2/HMDSO mixtures on wood surface. In Proceedings of the 28th International Conference on Phenomena in Ionized Gases, Prague, Czech Republic, 15–20 July 2007; pp. 15–20.

26. Alexander, M.; Jones, F.; Short, R. Radio-frequency hexamethyldisiloxane plasma deposition: A comparison of plasma-and deposit-chemistry. *Plasmas Polym.* **1997**, *2*, 277–300. [CrossRef]

27. Goujon, M.; Belmonte, T.; Henrion, G. OES and FTIR diagnostics of HMDSO/O2 gas mixtures for SiOx deposition assisted by RF plasma. *Surf. Coat. Technol.* **2004**, *188*, 756–761. [CrossRef]

28. Hegemann, D.; Vohrer, U.; Oehr, C.; Riedel, R. Deposition of SiOx films from O2/HMDSO plasmas. *Surf. Coat. Technol.* **1999**, *116*, 1033–1036. [CrossRef]

29. Hegemann, D.; Brunner, H.; Oehr, C. Deposition rate and three-dimensional uniformity of RF plasma deposited SiOx films. *Surf. Coat. Technol.* **2001**, *142*, 849–855. [CrossRef]

30. Šourková, H.; Primc, G.; Špatenka, P.J.M. Surface functionalization of polyethylene granules by treatment with low-pressure air plasma. *Materials* **2018**, *11*, 885. [CrossRef]

31. Gosar, Ž.; Kovač, J.; Mozetič, M.; Primc, G.; Vesel, A. Characterization of Gaseous Plasma Sustained in Mixtures of HMDSO and O$_2$ in an Industrial-Scale Reactor. *Plasma Chem. Plasma Process.* **2020**, *40*, 25–42. [CrossRef]

32. Moulder, J.F.; Chastain, J.; King, R.C. *Handbook of X-ray Photoelectron Spectroscopy: A Reference Book of Standard Spectra for Identification and Interpretation of XPS Data*; Physical Electronics: Eden Prairie, MN, USA, 1995.

33. Nättinen, K.; Nikkola, J.; Minkkinen, H.; Heikkilä, P.; Lavonen, J.; Tuominen, M. Reel-to-reel inline atmospheric plasma deposition of hydrophobic coatings. *J. Coat. Technol. Res.* **2011**, *8*, 237–245. [CrossRef]

34. Vartiainen, J.; Rose, K.; Kusano, Y.; Mannila, J.; Wikström, L. Hydrophobization, smoothing, and barrier improvements of cellulose nanofibril films by sol-gel coatings. *J. Coat. Technol. Res.* **2020**, *17*, 305–314. [CrossRef]

Digital Sublimation Printing on Knitted Polyamide 6.6 Fabric Treated with Non-Thermal Plasma

Marcia Cristina Silva [1,*], Gilberto Petraconi [2], Ricardo Rodrigues Ramos Cecci [3], Adriano Alves Passos [3], Wanderson Ferraz do Valle [3], Bruno Braite [1], Sérgio Ricardo Lourenço [1] and Fernando Gasi [1]

1   Center for Engineering, Modeling and Applied Social Sciences, Federal University of ABC (UFABC), Santo André, São Paulo 09210-580, Brazil; bruno.braite@ufabc.edu.br (B.B.); sergio.lourenco@ufabc.edu.br (S.R.L.); fernando.gasi@ufabc.edu.br (F.G.)
2   Technological Institute of Aeronautics, ITA, São Jose dos Campos, São Paulo 12228-900, Brazil; petra@ita.br
3   SENAI Innovation Institute for Biosynthetic and Fibres, SENAI CETIQT, Rio de Janeiro 20961-020, Brazil; rrcecci@cetiqt.senai.br (R.R.C.); apassos@cetiqt.senai.br (A.A.P.); wfvalle@cetiqt.senai.br (W.F.d.V.)
*   Correspondence: marcia.s@ufabc.edu.br; Tel.: +55-11-98132-3807

Abstract: The garment industry demands stamping processes that are increasingly more agile and less damaging to the environment. In this scenario, digital printing, with the sublimation transfer printing technique, presents itself as a viable option for synthetic textile substrates. Among the synthetic fibres, polyamide (P.A.) fibres stand out, as they are light, soft, durable, and boast moderate sweat absorption; however, before sublimation, superficial treatment is necessary in order to present good results such as withstanding washing and maintaining colour intensity. This study addresses the surface modification of the PA6.6 textile substrate by activating non-thermal plasma at atmospheric pressure to receive dye through the sublimation method with dispersed dye. The knitted PA6.6 fabric surface treatment was performed with plasma application at atmospheric pressure using air in the Plasmatreater AS400 equipment. The sublimation transfer effects were evaluated by wash fastness and colourimetric tests. To assess the wettability effect of the control and treated samples, a contact angle test was carried out on PA6.6 samples. Fourier transform infrared spectroscopy (FTIR) proved the changes in chemical functional groups in the fibres. The results showed a decrease in the contact angle of the textile surface, 4–5 grayscale results for colour change and transfer for washing, and an increase in colour strength. In the FTIR tests, there is an increase in the transmittance value of aromatic, carboxylic groups (C=O, 580 cm^{-1}), amides (N=H, 1630 cm^{-1}), and methyl groups (CH 1369 to 1463 cm^{-1}) as well as the presence of new functional groups in the 3064 cm^{-1} and 2860 cm^{-1} bands. These conditions allowed sublimation in the knitted PA6.6 fabric and showed increased colour strength and good wash fastness.

Keywords: plasma; sublimation; PA6.6

1. Introduction

The clothing industry demands faster printing processes and on minor scales to meet and keep up with fashion designs. Another major challenge for the textile industry is the search for a less environmentally damaging process—for example, the conventional dyeing process uses a lot of energy and a large volume of water and also has the need for effluent treatment [1,2]. Digital printing offers solutions for various textile materials. Among other factors, the choice of the process and the type of dye depend on the textile material fibres, the end use, and the possibility of pre-treating the textile substrate [3].

The process begins with the creation of the image and its printing on special paper with sublimated ink. The transfer of the image to the textile substrate is done using a table press or calendaring rolls, applying pressure and heat for a determined time. Direct printing on the fabric can also be done, but the dye is fixed using steam [4].

Dispersed dye is used in sublimation inks, this dye does not require a fixing agent; with the increase in temperature, it sublimates; that means that it changes from the solid to the gaseous state without going through the liquid form [4]. As the temperature rises, the textile fibres open spaces where the sublimated dye enters. As the temperature decreases, the fibres close and hold the dye in its solid state, providing the textile substrate with good wash and light fastness [5].

The number of synthetic fibres produced in the world exceeds the production of natural origin fibres. The polyamide fibre 6.6 (PA6.6) stands out, as it is a light, soft, durable fibre with moderate sweat absorption. Such conditions allow the structure of the knitted fabric to produce lingerie, sportswear, and socks. PA6.6 is a synthetic chemical polymeric fibre known as nylon, with excellent mechanical properties, including high tensile strength, high flexibility, and good chemical resistance, among others. The flexibility of the aliphatic segments in the amorphous regions of the polyamide is also responsible for its high tenacity [6,7]. They have excellent durability due to the low friction coefficient (self-lubricating), high melting temperature, and glass transition temperature, resulting in good mechanical properties at elevated temperatures [8,9].

PA6.6 is the polymer in which the structural units are linked by amide groupings (-CONH-). PA6.6 is obtained in linear polycondensation hexamethylenediamine (H2N (CH2) 6NH2). In polyamide 6.6, the first 6 represents the number of carbons in the diacid, and the second 6 represents the number of carbons in the diamine. It is important to define the concept of polymerisation per step, which occurs through the reaction between two different functional groups, for example, –O.H. and –COOH or –NH2; R-NCO and –O.H. or –NH2; where O.H. = hydroxyl; COOH = carboxyl; NH2 = amine. Then, each stage of the polymerisation of polyamide 6.6 is verified: nH2N (CH2) 6NH2 + nHO2C (CH2); H [NH—(CH2) 6—NHCO—(CH2) 4—CO] n OH + (2n − 1) H2O. Polymerisation proceeds with approximately 80% to 90% conversion [10,11].

The dyeing of P.A. fibres is done mainly with acid dyes. It connects the amino-terminal content groups of the fibres and the content of sulfonic groups of the dye in a reaction that occurs in an organic acid medium, with pH between 4.5 and 5.5. As the chemical bonds do not present the necessary conditions for dyeing, the dye sublimation technique dispersed in knitted PA6.6 fabrics has low washing strength [12].

Reactive dyes are also used in dyeing polyamide, as they have an electrophilic group capable of forming covalent bonds with amine groups in polyamides. The main groups of reactive dyes contain the azo and anthraquinone function; chromophoric groups, chlorotriazine, and sulfatoethylsulfonyl groups. Lightfastness results are similar to those obtained with acid dye; however, the colour depth is limited [13].

The process of dyeing PA6.6 fibres with dispersed dye obtains low wash fastness. Due to the interaction of the amine groups with the chromophores, many of the PA6.6 substrate's shades are changed, and the colours are generally vivid, except for red shades [13].

The practical application of a textile material depends, among others, on technical characteristics, surface properties such as adhesion, gloss, permeability, dyeing, printing capacity, and surface cleaning, without changing the fibres' bulk properties. Similar to dyeing, many treatments to modify the surface of the textile material are carried out in a humid environment and with chemicals that, after use, become industrial effluents, using large amounts of water and energy and placing workers in unhealthy environments [14].

With the modernisation of textile processes and a focus on sustainability, plasma technology has been used in various applications for textile surfaces treatment, and different surface modifications can be obtained with the selection of gas and the plasma's process conditions [15], such as the use of plasma for mechanical changes and tactile performance in mixed wool/cashmere fabrics [16], the modification of the surface to improve the hydrophobicity of the textile substrate and make it more attractive for self-cleaning and waterproof product development [17], and the inhibition of the growth of microorganisms and the biodeterioration of natural fibre fabrics [18].

The process of modifying polymers' characteristics and properties, and changing the chemistry on the surface is called plasma functionalisation. It presents itself as an advantageous alternative to wet chemical treatments when environmental and safety aspects are considered [19].

The physical principle of plasma technology is the change of state. A matter fed with energy passes from the solid state to the liquid and from the liquid to the gaseous. When the gaseous matter is provided with energy, ionisation occurs, entering the plasma state, where electrons are released from atoms or molecules [20]. The electrons in the plasma acquire energy in the range of 0.1–10 eV. The ions and molecules reach energy in the range of 0.025 eV, without presenting a condition of thermodynamic equilibrium, without which neutral ions and molecules disintegrate [21,22].

Most textile materials are heat-sensitive polymers, so the type of plasma used in textile processes is non-thermal plasma or cold plasma and can be applied at atmospheric pressure or low pressure. High-energy electrons and low-energy molecular species can initiate reactions in the plasma volume without excess heat that causes degradation of the textile substrate [23,24].

The types of plasma that can be used on textile substrates and atmospheric pressure are plasma jet (PJ), glow discharge (GD), corona discharge (CD), and dielectric barrier discharge [8]. The PJ operated at atmospheric pressure is a recent technique for modifying the surface of textile substrates that enables smooth and highly effective application at room temperature. The advantage of DBD is that it can be applied to any geometric surface [12].

Active species and energetic electrons present in plasma can break chain bonds, generating free radicals on the surface. As a result of this, there is the possibility of cross-linking on the surface or creation of functional groups such as carboxylic acid groups, hydroxyl groups, and amine groups, due to the interaction of free radicals with plasma species, such as ozone or when it comes into contact with ambient air [19,21].

Many researchers have researched the application of non-thermal plasma and atmospheric pressure, for example, surface modification of polyester textile substrates to receive silicone nano emulsion [23] and surface modification of polyamide nets to receive antifouling treatment for use in fish farming [24].

This work addresses the surface modification of the PA6.6 substrate with the non-thermal plasma treatment under atmospheric pressure in receiving dye through the sublimation method using dispersed dye and presents values of high durability to washing and colour strength. For the textile industry, this study is critical because it breaks the paradigm that it is impossible to make sublimation print transfer on PA6.6 substrate, obtaining vivid colours and with a solid wash.

2. Materials and Methods

2.1. Materials

2.1.1. Knitted Fabric

Plasma treatment was applied on a knitted fabric made with 1x 80/68 PA6.6 yarn with 20 denier elastane, made on a circular loom with 38 needles per inch with a weight of 180 g/m^2. The same fabric, without plasma treatment, was used as a reference to evaluate the results.

2.1.2. Sublimation Transfer Printing

The preparation of sublimation transfer printing was done on the Printer: Epson SureColor F9200, loaded with Epson UltraChrome® DS Sublimation ink on Epson Sublimation 90 g/m^2 paper.

2.2. Methods

2.2.1. Preparation of Samples and Plasma Treatment

The knitted PA6.6 fabric was cut into 25 × 60 cm specimens and sent to the plasma application.

Plasma treatment was performed using the Model AS400 Atmospheric Pressure Plasma System manufactured by Plasma Treat GmbH (Steinhagen, Germany), which was installed at the Beneficiation Laboratory of SENAI CETIQT (Figure 1).
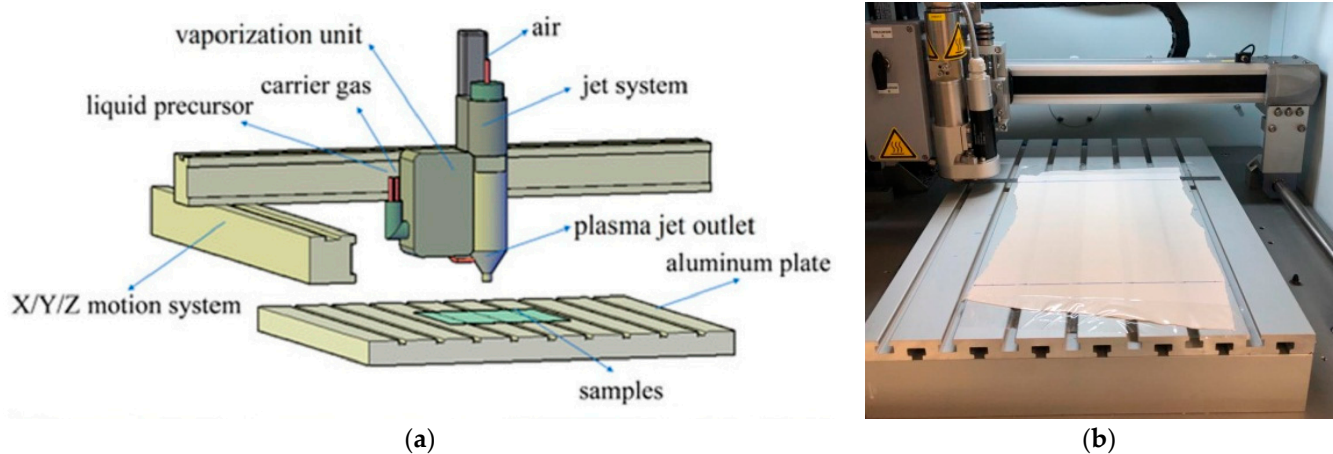
Figure 1. (**a**) Schematic drawing of the experimental apparatus [25] and (**b**) Sample of PA 6.6 textile substrate submitted to plasma treatment.

The workspace for the discharge of luminescent plasma has the dimensions of 33 cm by 12.5 cm, and the plasma system is powered by an R.F. energy source (19 kHz).

Atmospheric air was used to generate the plasma. The substrates were fixed on an aluminium plate, and the plasma jet was controlled by an X/Y/Z movement system. The plasma voltage was adjusted to 300 V, the current was adjusted to 0.3 A, and the power was adjusted to 480 W. The distance between the sample and the nozzle was kept constant at 12.5 mm. The jet travel speed and the number of passages for each sample are described in Table 1. All experiments were carried out under controlled conditions.

Table 1. Experiment's parameters.

Sample	Speed	Passages
1 (Control)	-	-
2	15 m/min	3
3	15 m/min	4
4	20 m/min	3
5	20 m/min	4

2.2.2. Sublimation

The material was subjected to sublimation in a 38 cm × 38 cm flat press with a LIVE brand drawer, with an alligator opening, at a temperature of 180° and a time of 15 s. The colours applied were red, yellow, and blue.

2.2.3. Contact Angle

The sessile drop method, which measures the contact angle (θ) of a drop of water on the material surface, was used to characterise the wettability properties of the knitted 6.6 polyamides fabrics before and after plasma treatment. A surface analyser (Drop shape analyser) DSA-100, Kruëss Co, Hamburg, Germany was used for the measurement. The samples were placed on the base of the analyser, and a drop of water was introduced on the surface using a micro-syringe. The contact angles at steady state were measured using a 1 μL drop of deionised water. At least three different measurements were performed at room temperature and evaluated with the aid of the Advance software. All samples were analysed with the same light settings and adjustment algorithms. The value of the contact

angle, θ, indicates whether the surface is hydrophilic or hydrophobic: θ < 90° corresponds to a hydrophilic surface, while θ > 90° implies a hydrophobic surface [26].

2.2.4. Wash Fastness

According to the technical standard ABNT NBR ISO 105-C 06: 2006, the sublimated material was subjected to a wash fastness assessment to determine the degree of fastness of a given colour and the gaining of the dye from the processed fabrics.

The greyscale was used to assess durability, according to technical standards ABNT NBR ISO 105-A02: 2006: grayscale to determine colour change, ABNT NBR ISO 105-A03: 2006: Greyscale to assess colour transfer, which varies from 1 to 5 with 5 being the maximum score, that is, when there is no colour change [27–29].

2.2.5. Colour Measurement and Colour Strength

For the colourimetry tests, eight simple measurements were made in the included specular geometry (SCI). The average of the eight sets of reflectance values was used. The equipment used for measuring was a spectrophotometer of the brand Minolta, model CM-3720d. The reflectance values were used to construct the colour representation space in the Ciel standard (L* a* b). The comparison between the samples is obtained by the Euclidean Distance (ΔE) in that colour space. Colouristic strength was calculated using the Kubelka–Munk theory [30].

2.2.6. FTIR (Fourier Transform Infrared Spectroscopy)

The samples were analysed using the spectroscopy technique in the mid-infrared region (700 to 4000 cm^{-1}) to obtain quantitative and qualitative information on the material under analysis. This study will be applied to evaluate the number of chemical components that contribute to the molecular formation in the fibres under investigation. A BRIRKER VERTEX 80 FTIR device was used, with a resolution of 4 cm^{-1}, 16 scans, a sample scan time of 16 s, a background scan time of 16 s, a measurement time of 1 s, a range of 4500 cm^{-1}–370 cm^{-1}. Resulting spectrum: transmittance, Accessories: 4225/Q Platinum ATR, Multiple Crystals CRY: Diamond, Beamsplitter: KBrO.

2.2.7. Scanning Electron Microscopy (SEM)

SEM analyses performed using a Thermo Scientific microscope (Waltham, MA, USA) model Prisma E, from the SENAI CETIQT Characterization Laboratory, equipped with an energy-dispersive X-ray spectrometer (EDS). The equipment was operated with an electron acceleration voltage of 20 kV in backscattering and secondary electrons. Preparation samples by gold deposition (sputtering) using an SC7620 Mini Sputter Coater/Glow Discharge System by Quorum. A vacuum with an ultra-pure argon atmosphere was used, applying a current of 15 mA for 60 s and a gold target.

3. Results

3.1. Contact Angle—θ

One of the methods for confirming the outer chemical structure is surface wettability verification. It is possible to identify hydrophobic and hydrophilic functional groups in the surface layer of the polymer [31]. The measurement of the static contact angle of the water drop (SWCA) assesses the effect of the jet plasma application speed on the surface wettability.

PA6.6 surface wettability substrate after plasma treatment was carried out with the SWCA measurement in samples treated with plasma varying the number of passages from three to four in the control sample. All analyses were performed immediately after treatment at three dry points in the samples.

Figure 2 shows the SWCA data collected during the first seconds of the water drop contact with the PA6.6 surface at the plasma speed conditions of 15 and 20 m/min.
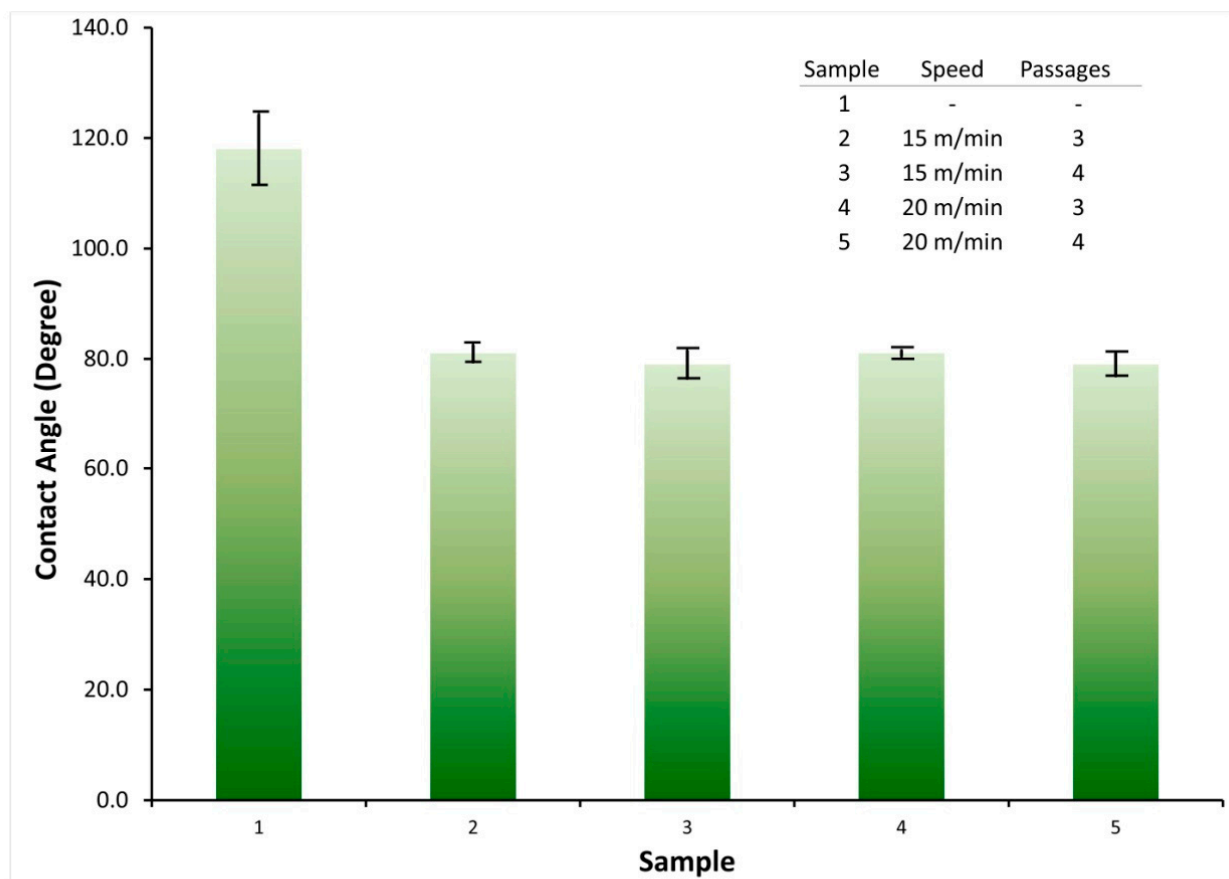
Figure 2. Measurement of the contact angle for PA6.6 textile substrate samples submitted to surface treatment with atmospheric plasma and control sample. Application speed 15 m/min and speed 20 m/min. Contact angle at steady state was measured after placing the drop of deionised water on the fabric surface (t = 0) and immediately after plasma application.

The initial value of the contact angle of the control sample was $(118.0 \pm 7.0)°$, which demonstrates the hydrophobic nature of the substrate tissue of PA6.6. These results show that the surface before the treatment was classified as not wettable (θ is greater than 90°), and the contact angle θ starts to reduce with each passage of the atmospheric plasma, becoming wettable (θ less than 90°) [26].

For the substrates treated with a speed of 15 m/min, they presented values of $(81.0 \pm 1.5)°$ and $(81.0 \pm 0.6)°$ for three and four passes, respectively. When the speed is increasing to 20 m/min, the results for SWCA were $(78.0 \pm 3.0)°$ and $(78.0 \pm 2.5)°$ for three and four passes, respectively. These results indicate the change in the surface of the samples from hydrophobic to hydrophilic. This can be explained by the concentration of polar functional groups such as hydroxyl (OH), carboxyl (COOH), and amino (NH_2), as these groups become soluble in a polar solvent, water, which is a situation that allows water to spread on the surface [19]. The verification of the functional groups' presence will be in the FTIR analysis.

3.2. Test for Colourfastness

The colour change and the transfer in the washing of the sublimated fabric were classified as good or very good (4–5; 5). The colour change was between 4 and 4–5. It is possible to observe in Table 2 that there was no significant difference in the transfer of samples between cotton treated with plasma and cotton without treatment, highlighting the improvement in the transfer of the colour red.

Table 2. Colour fastness to wash.

Colour	Sample	Plasma Application		Colour Change	Colour Staining					
		Speed (m/min)	N		WO	PAC	PES	PA	CO	CA
Red	1	Control			5	5	4–5	4	4–5	3–4
	2	15	3	4–5	5	5	4–5	4	4–5	3–4
	3	15	4	4	4–5	5	4–5	4	4–5	3–4
	4	20	3	4	4–5	5	4–5	4	5	3
	5	20	4	4	4–5	5	4–5	4	5	3
Blue	1	Control			5	5	5	4–5	5	4–5
	2	15	3	4–5	5	5	5	4	5	4–5
	3	15	4	4–5	5	5	5	4	5	4
	4	20	3	4–5	5	5	5	4	5	4–5
	5	20	4	4–5	5	5	4–5	4	5	4–5
Yellow	1	Control			5	5	5	4–5	5	4–5
	2	15	3	4–5	5	5	5	4–5	5	4–5
	3	15	4	4–5	5	5	5	4–5	5	4–5
	4	20	3	4–5	5	5	5	4–5	5	4–5
	5	20	4	4–5	5	5	5	4–5	5	4–5

N—Passage quantity; CA—Acetate; CO—Cotton; PA—Polyamide; PES—Polyester; PAC—Acrylic; WO—Wool.

3.3. Colourimetry and Colouristic Strength

It was possible to observe that the colours of the fabrics submitted to the plasma treatment are more intense than the untreated fabric (Table 3). The luminosity values (L*) are lower in the materials treated for all colours, except for sample 4, blue (with plasma application at 20 m/min and three passages).

Table 3. Colour reading in CIELAB space for polyamide fabrics dyed by sublimation transfer printing, illuminant D65/10°.

Colour	Sample	D65/10°				
		L*	a*	b*	ΔE	Colour Strength (%)
Red	1 (Control)	58.89	44.93	15.85		
	2	57.58	48.44	18.05	1.81	119.5
	3	54.85	51.21	20.01	3.58	154.99
	4	57.44	47.9	17.6	1.54	121.96
	5	54.08	50.98	19.01	3.43	159.9
Blue	1 (Control)	72.29	−18.19	−26.15		
	2	70.02	−18.24	−28.57	1.59	124.26
	3	69.00	−18.09	−29.38	2.2	134.6
	4	74.24	−17.74	−23.26	1.72	80.95
	5	69.62	−17.97	−29.17	2	127.89
Yellow	1 (Control)	89.11	−8.14	55.00		
	2	88.98	−7.89	54.69	0.18	99.14
	3	88.50	−7.6	56.89	0.85	117.83
	4	88.48	−7.67	57.7	1.11	119.96
	5	88.76	−7.81	55.73	0.37	106.32

It is possible to observe that the coordinates a* and b* increase in the colour red in the treated samples. In the colours blue and yellow, the coordinates oscillate higher or lower than the coordinates of the untreated sample.

It is possible to observe in Figure 3 that almost all the samples with plasma applied increased the colouristic strength, except for sample 4 of the colour blue and sample 2

of the colour yellow. The control sample before and after washing was considered the standard sample. The colour red achieved good results (159.9%) of colouristic strength, reaching 60% more power than the control sample. The blue colour achieved 134.5% of colouristic strength, showing the efficacy of the plasma treatment in the sublimation of the PA6.6 textile substrate.
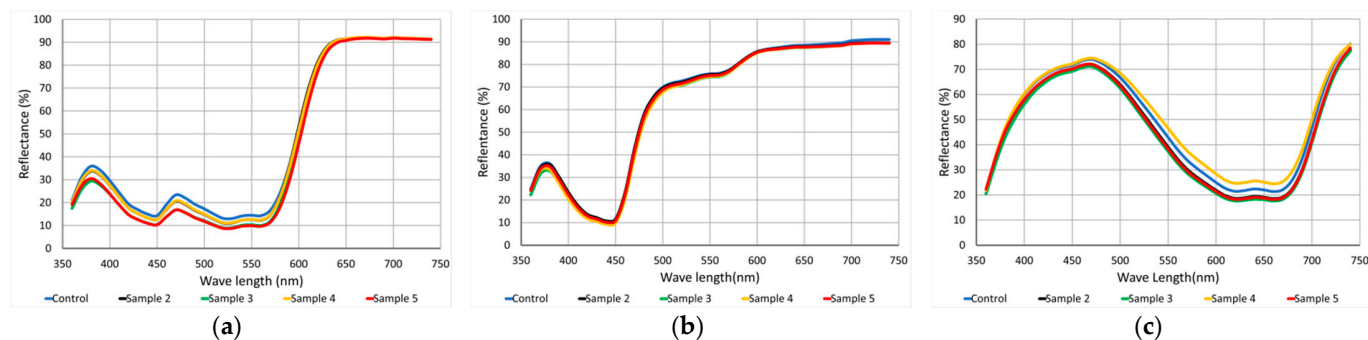
Figure 3. Reflectance × wavelength of colour (**a**) red; (**b**) yellow; (**c**) blue.

However, after the samples were washed, the colour strength dropped dramatically. The strength reached 35% more than the control sample for the colour blue, and even after washing, the samples still showed considerable colour strength. The colour yellow showed the lowest values of colouristic power, being 20% stronger than the sample without treatment, and there was no significant change after washing. This variation may be associated with the instability of atmospheric plasma and corrected with the variation of the applied energy.

3.4. FTIR Analysis

To assess changes in the functional polyamide 6.6 groups before and after surface treatment with atmospheric plasma, Fourier transforms infrared spectrometry (FTIR) performed assays in the medium infrared. The resulting spectrum is shown in Figure 4.

When a molecule is illuminated by infrared light, the absorbed light became a molecular vibration. The infrared spectrum represents the transmittance value, the energy ratio that strikes the sample, and the energy transmitted at each frequency value or number of waves. The vibrations can be of the type of axial deformation and angular deformation.

Sample 1—PA6.6 control sample has the bands inherent to the material observed at 3290 cm^{-1} (free NH asymmetric axial stretch), 2927 cm^{-1} and 2850 cm^{-1} (CH stretch in CH2), 1633 cm^{-1} (amide I), 1538 cm^{-1} (δ NH + υ group of CN—amide II), 1371 cm^{-1} (CN stretch with NH deformation), 1262 cm^{-1} (axial deformation group CN), 1199 cm^{-1} (carbonyl vibration mode in crystalline phase), and the bands that can be used to characterise the amide group in polyamides are 690 cm^{-1} group (NH), 580 cm^{-1} (group C=O) [32].

In Figure 4, it is possible to verify that plasma-treated samples (2, 3, 4, and 5) demonstrate an increase in the transmittance values of the groups corresponding to C=O (580 cm^{-1}) and NH (690 cm^{-1}) in the region of amide IV, CH (1396 to 1463 cm^{-1}), (1532 cm^{-1}) in the region of amine II, and NH (1630 cm^{-1}) in the region of amide I [33]. These changes may be associated with changes in the microenvironment and oxygen to the treated surface and contribute to the fabric dyeing affinity [22,32]. The increase in the transmittance values was also verified for the NH groups. There is symmetric and asymmetric CH stretching in the bands of 3290 and 2860 cm^{-1}, which can be related to the formation of low molecular weight etched materials resulting from the treatment of the textile substrate and corroborate the established method to produce hydrophilic surfaces in polymers by introducing new polar groups [19].
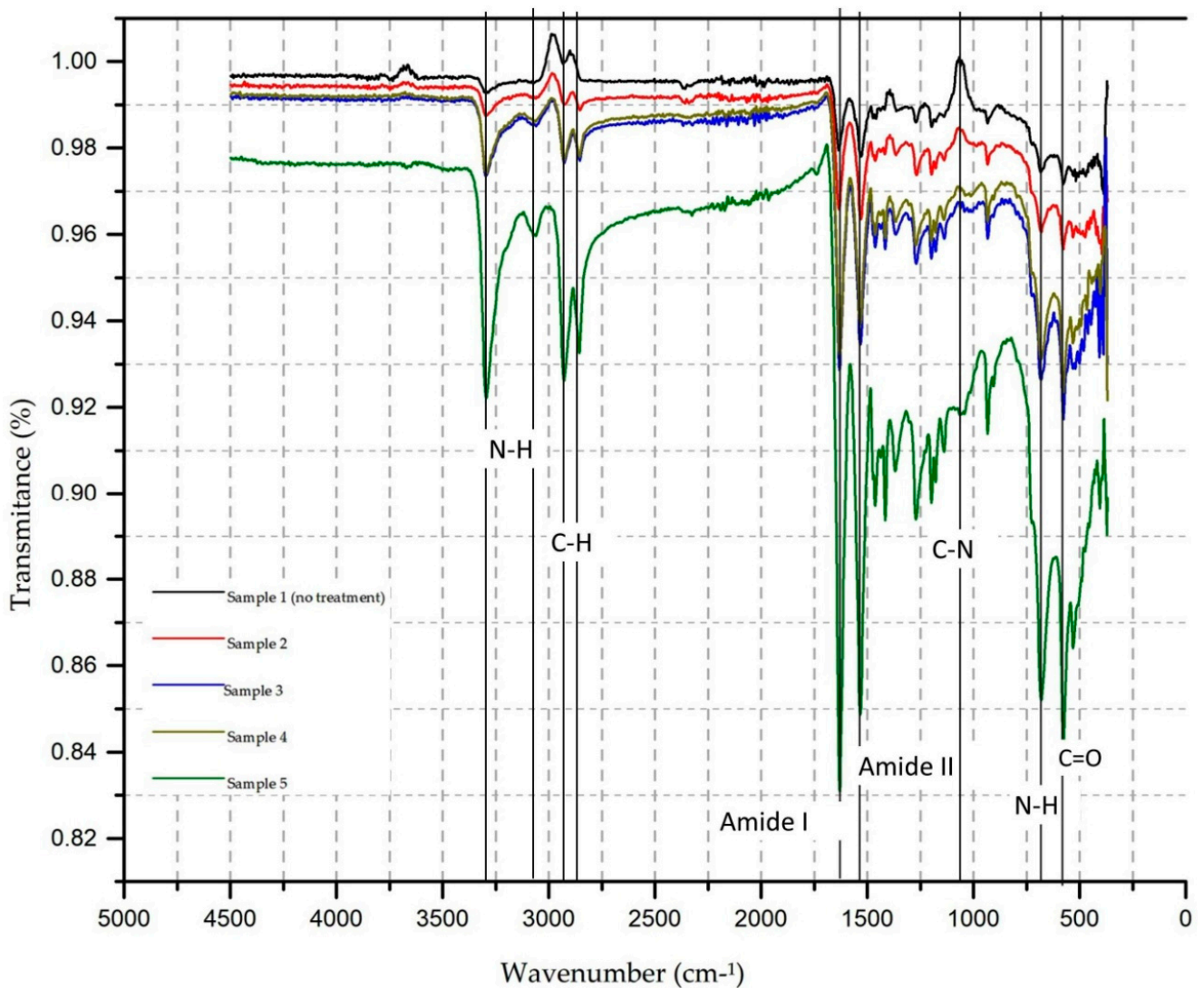
Figure 4. FTIR spectra of PA6.6 textile substrate: 1—control sample (black line); samples with plasma treatment 15 m/min three passages (2—red line), four passages (3—blue line); samples with plasma treatment 20 m/min three passages (4—brown line) and four passages (5—green line).

In Figure 5b–d, it is possible to observe that new functional groups appear, which are associated with the vibration of symmetrical stretching in the CH region in the 2860 cm^{-1} band and the NH region in the 3064 cm^{-1} bands. To illustrate more clearly the position of the new functional groups, the comparison between sample 1 and sample 5 is shown in Figure 6.

In Figure 6, it is possible to observe the location of the new functional groups in a magnified way. For each adjustment in the test parameters and after plasma treatment, it is possible to observe the appearance of new functional groups and increase transmittance until reaching sample 5 (20 m/min, four passages), with the most striking difference between the control sample and the treated sample.
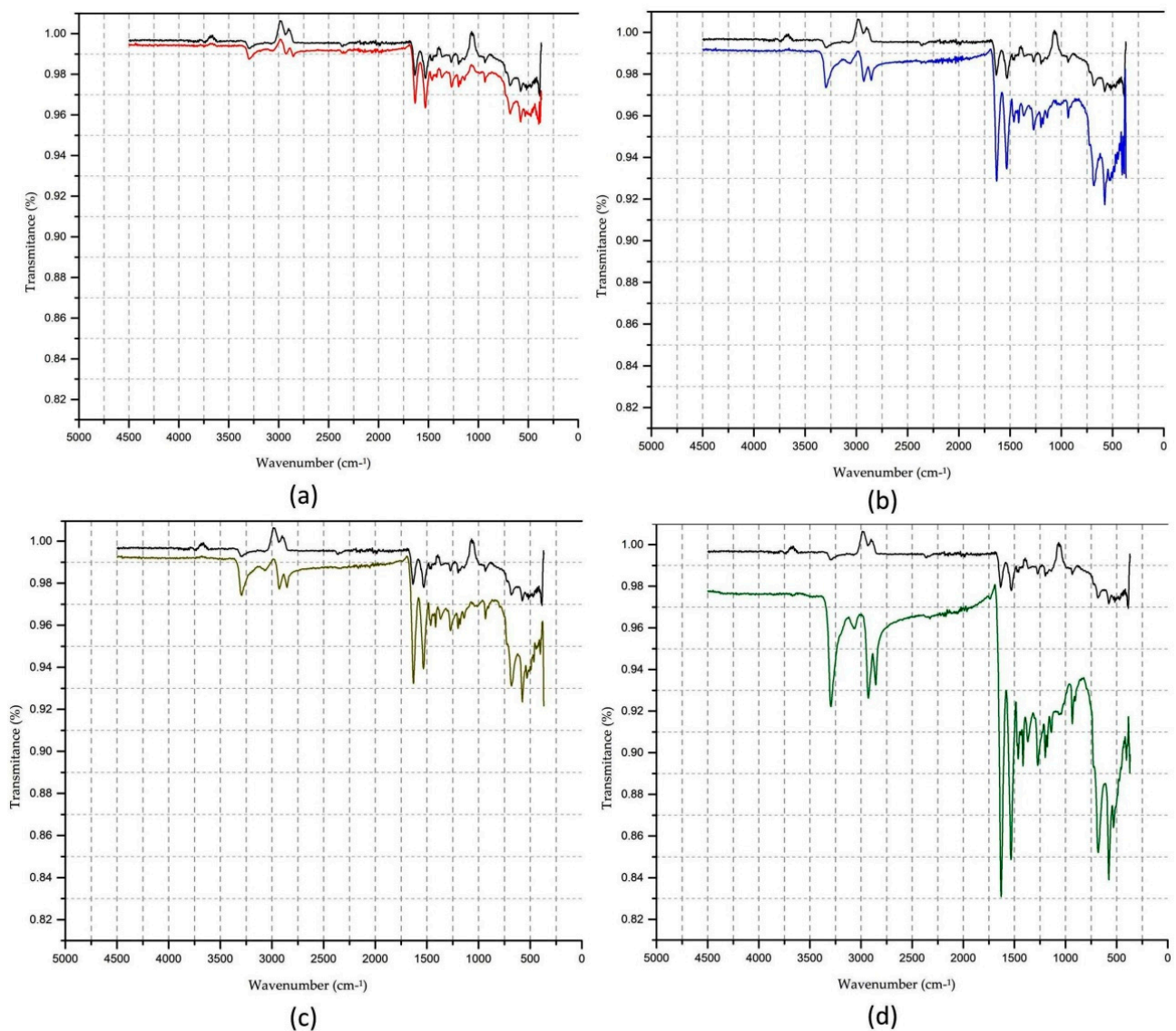
Figure 5. Comparison of FTIR spectra of PA6.6 textile substrate: (**a**) Sample 1—control, no plasma treatment × sample 2—plasma-treated 15 m/min, three passages; (**b**) Sample 1—control, no plasma treatment × sample 3—plasma-treated 15 m/min, four passages; (**c**) Sample 1—control, no plasma treatment × sample 4—plasma-treated 20 m/min, three passages; (**d**) Sample 1—control, no plasma treatment × sample 5—Plasma-treated 20 m/min, four passages.

Therefore, the electron energy induced by applying atmospheric plasma on the knitted PA6.6 fabric's surface causes the polymer bonds to break with energy less than 10 eV of the C-N bond, precisely because it is the weakest chain. After being broken and in contact with the reactive species created by the plasma, it can generate a low molecular weight molecule containing carboxylic and amino groups.

The changes in the properties of the textile surface produced by plasma treatment are strongly related to the differences in the transmittance values, which correspond to the CH, NH, and CN groups.
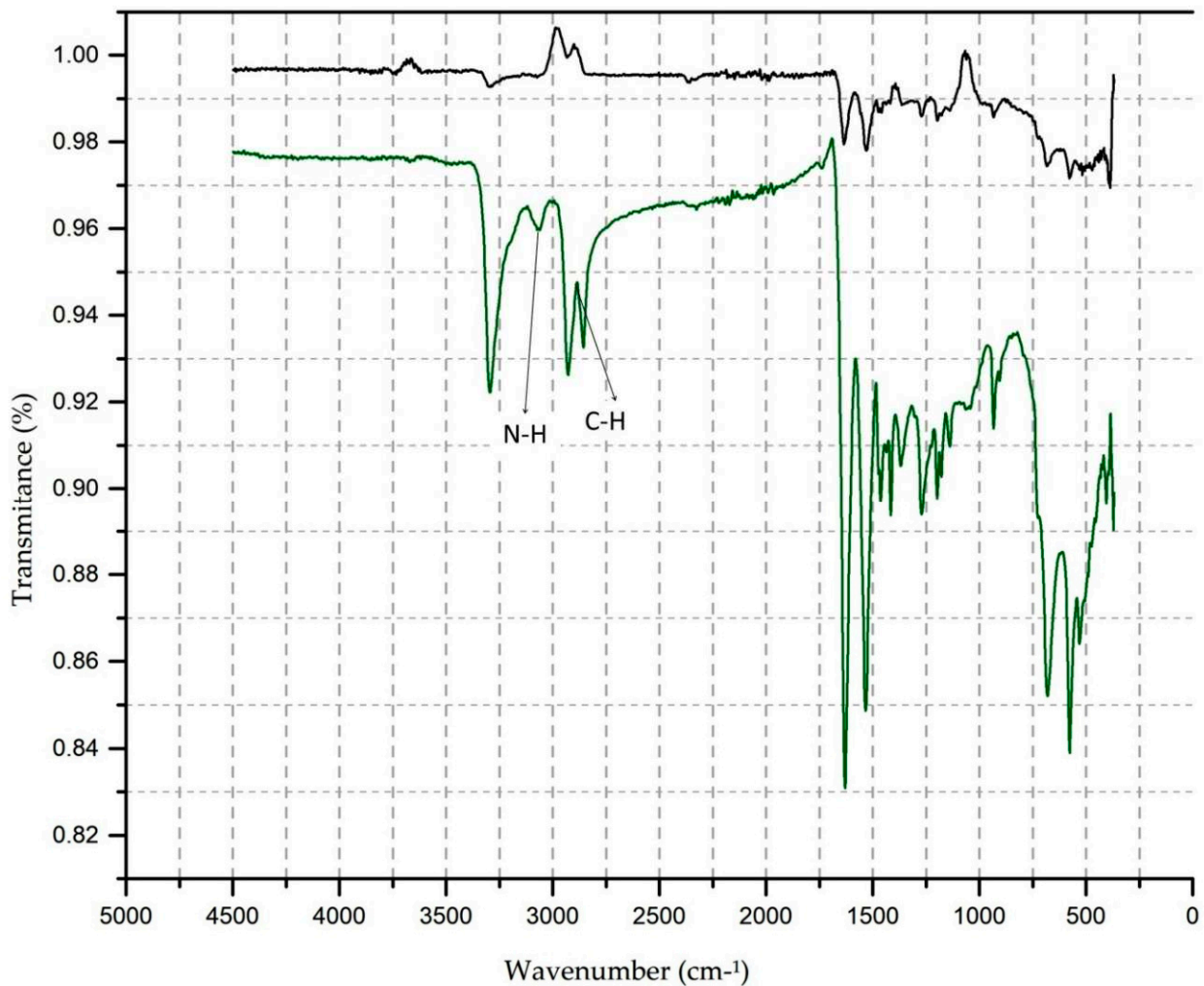
Figure 6. Comparison of FTIR spectra of PA6.6 textile substrate: Sample 1—control, no plasma treatment × sample 5—Plasma-treated 20 m/min, four passages.

This condition provides a greater affinity for dyeing, allowing for the realisation of sublimation transfer printing with excellent fastness characteristics to washing and colour intensity, including increasing the three colours' colour strength.

3.5. Scanning Electron Microscopy (SEM)

Scanning electron microscopy (SEM) images were obtained. In Figure 5, it is possible to observe the PA6.6 control sample's surface and compare it with the samples submitted to plasma treatment.

As previously demonstrated (in Section 3.1), the plasma modified the wettability of the polyamide fabric. For this reason, in this section, the SEM was used to verify the surface modifications in the samples. A comparison of the results shown in Figure 7 did not observe significant changes in surface roughness on amplification used.
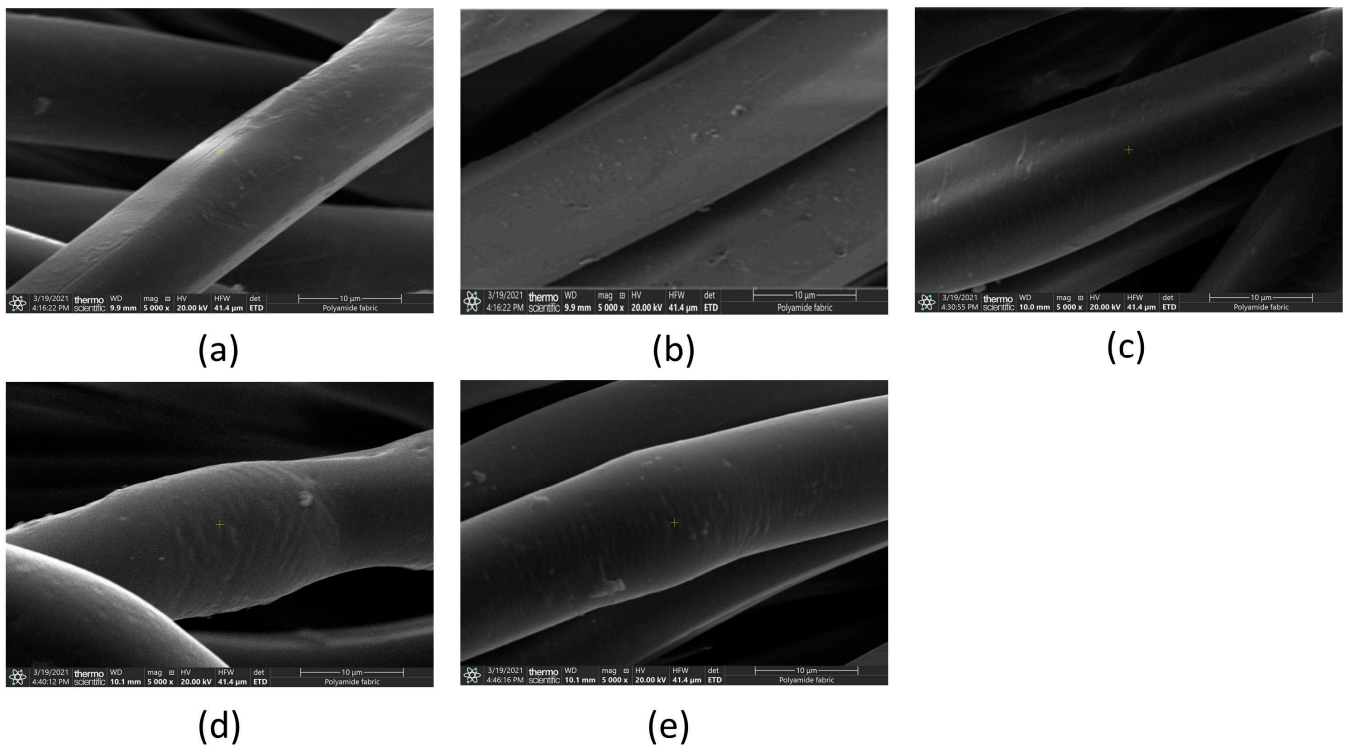
Figure 7. SEM for PA6.6 textile substrate. Amplification 5000×. (**a**) 1—Control samples subjected to atmospheric plasma surface treatment; (**b**) 2—speed 15 m/min, three passages; (**c**) 3—speed 15 m/min, four passages; (**d**) 4—speed 20 m/min, three passages; (**e**) 5—speed of 20 m/min, four passages.

4. Conclusions

The sublimation process consists of transferring the print paper to the textile substrate. It provides agility in the production and development of new products.

The contact between the paper and the substrate is intense, fast, and occurs at an average temperature of 180 °C. The textile fibre most used in this process is polyester (PES), as the results are characterised by high colour intensity and excellent wash fastness.

Polyamide 6.6 (PA6.6) fibre, on the other hand, has different characteristics from that of PES, as it provides greater thermal comfort and moisture absorption than PES (0.4% for PES and 4% for PA6.6).

This difference explains the interest in validating the sublimation process in PA6.6, which is an objective that had not been achieved until then.

Until today, the results obtained with this technique in PA6.6 did not reach the colour intensity demanded by the designs and high levels of fastness to washing. The results found in this study present an innovative solution, which is already in the process of obtaining a patent for textile dyeing processes in Brazil and in the world for sublimation transfer printing on the PA6.6 substrate with the use of dispersed dye in the sublimation ink.

The developed phases of the project will be described below, as well as the conclusions obtained.

1. Decrease in the contact angle of the static drop on the material surface. The increase in hydrophilicity on the surface of the textile substrate is essential so that there is a more significant dye absorption at the time of sublimation

From the results presented, it was possible to notice that the plasma treatment decreased the contact angle formed by the drop on the surface, which shows the increased hydrophilicity of the textile substrate with water.

The plasma treatment was able to modify the surface of the textile substrate, making it hydrophilic (greater absorption power). The initial value of the contact angle of the control

sample was $(118.0 \pm 7.0)°$. After treatment of the substrate with plasma, the results were as follows: for the substrates treated with a speed of 15 m/min, they presented values of $(81.0 \pm 1.5)°$ and $(81.0 \pm 0.6)°$ (speed 15 m/min, three and four passes, respectively). When the speed is increased to 20 m/min, the results for SWCA were $(78.0 \pm 3.0)°$ and $(78.0 \pm 2.5)°$ for three and four passes, respectively.

2.   Colourimetry and colouristic strength

From the colourimetry analyses, it is noted that there was an apparent increase in the colour strength of the colours red, blue, and yellow, in the samples that were subjected to plasma treatment. The most significant gains were in the colour red applied in sample 5 with a colouristic force of 159.9% and the colour blue applied in sample 3 with a colouristic force of 134.6%. After washing, the colour strength of the colour red was considerably reduced, while those of the colours blue and yellow did not show any significant change.

3.   Test for colourfastness

Concerning the washing strength, there were no significant differences between the control sample and the treated samples. This result validates the sublimation process on the PA6.6 substrate due to the high values of fastness to washing presented.

4.   FTIR analysis

In the FTIR tests, there is an increase in the transmittance value of aromatic, carboxylic groups (C=O, 580 cm^{-1}), amides (N=H, 1630 cm^{-1}), and methyl groups (CH 1369 to 1463 cm^{-1}), for the NH groups and symmetrical and asymmetric CH stretching in the bands of 3290, 3068, and 2860 cm^{-1}.

The new functional groups are essential, and they are associated with the vibration of symmetrical stretching in the CH region in the 2860 cm^{-1} band and the NH region in the 3064 cm^{-1} bands.

As shown in Figure 6, the property changes of the textile surface produced by plasma treatment are strongly related to the differences in the transmittance values, which correspond to the CH, NH, amide, C=O, and CN groups and the presence of new functional groups associated with symmetrical stretching vibration in the CH region in the 2860 cm^{-1} band and the NH region in the 3064 cm^{-1} bands.

These changes (increased transmittance and new functional groups presence) allowed sublimation in the PA6.6 textile substrate and may explain the increase in colour strength and good wash fastness.

5.   Scanning electron microscopy (SEM)

The images of the control sample and the samples treated with plasma, despite the change in the surface of the textile substrate, did not show significant changes in the roughness of the material.

Institutional Review Board Statement: Not applicable.

Informed Consent Statement: Not applicable.

Data Availability Statement: The data presented in this study are available on request from the corresponding author.

References

1. Choi, S.; Cho, K.H.; Namgoong, J.W.; Kim, J.Y.; Yoo, E.S.; Lee, W.; Jung, J.W.; Choi, J. The synthesis and characterisation of the perylene acid dye inks for digital textile printing. *Dye. Pigment.* **2019**, *163*, 381–392. [CrossRef]
2. Wang, L.; Yan, K.; Hu, C.; Ji, B. Preparation and investigation of a stable hybrid inkjet printing ink of reactive dye and CHPTAC. *Dye. Pigment.* **2020**, *181*, 108584. [CrossRef]
3. Cie, C. Fixing Inkjet Printed Textiles. In *Ink Jet Textile Printing*; Elsevier: Amsterdam, The Netherlands, 2015; pp. 99–110.
4. Ujiie, H. Chapter 20—Fabric Finishing: Printing Textiles. In *Textiles and Fashion*; Sinclair, R., Ed.; Woodhead Publishing Series in Textiles; Woodhead Publishing: Cambridge, UK, 2015; pp. 507–529. ISBN 978-1-84569-931-4.
5. Cie, C. Inks for digital printing. In *Ink Jet Textile Printing*; Elsevier: Amsterdam, The Netherlands, 2015; pp. 85–97.
6. Associação Brasileira da Industria Têxtil e de Confecção Perfil do Setor. Available online: https://www.abit.org.br/cont/perfil-do-setor (accessed on 15 June 2020).
7. Louzi, V.C.; de Carvalho Campos, J.S. Corona treatment applied to synthetic polymeric monofilaments (P.P., PET, and PA-6). *Surf. Interfaces* **2019**, *14*, 98–107. [CrossRef]
8. Nascimento, L.; Gasi, F.; Landers, R.; da Silva Sobrinho, A.; Aragão, E.; Fraga, M.; Petraconi, G.; Chiappim, W.; Pessoa, R. Physicochemical Studies on the Surface of Polyamide 6.6 Fabrics Functionalised by DBD Plasmas Operated at Atmospheric and Sub-Atmospheric Pressures. *Polymers* **2020**, *12*, 2128. [CrossRef] [PubMed]
9. Xiang, C.; Etrick, N.R.; Frey, M.W.; Norris, E.J.; Coats, J.R. Structure and Properties of Polyamide Fabrics with Insect-Repellent Functionality Electrospinning and Oxygen Plasma-Treated Surface Coating. *Polymers* **2020**, *12*, 2196. [CrossRef]
10. Starczak, R.; Wąs-Gubała, J. UV–Vis microspectrophotometric study of wool and polyamide fibres dyed with analogous gryfalan dyes. *Dye. Pigment.* **2016**, *132*, 58–63. [CrossRef]
11. Gasi, F. *Comparativo das Propriedades de Permeabilidade ao Vapor, Capilaridade e Proteção Ultravioleta em Tecidos de Poliamida 6.6 e Poliéster em Tecido de Malha para Atividade Física*; Universidade Estadual de Campinas: Campinas, Brazil, 2010; Available online: http://repositorio.unicamp.br/jspui/handle/REPOSIP/267089 (accessed on 7 May 2021).
12. Saleem, M.A.; Pei, L.; Saleem, M.F.; Shahid, S.; Wang, J. Sustainable dyeing of nylon fabric with acid dyes in decamethylcyclopentasiloxane (D5) solvent for improving dye uptake and reducing raw material consumption. *J. Clean. Prod.* **2021**, *279*, 123480. [CrossRef]
13. Hunger, K.; Bauer, W.; Berneth, H.; Clausen, T.; Engel, A.; Filosa, M.; Gregory, P. *Industrial Dyes Chemistry, Properties, Applications*; WILEY-VCH Verlag GmbH & Co.: Weinheim, Germany, 2003; ISBN 3-527-30426-6.
14. Nadi, A.; Boukhriss, A.; Bentis, A.; Jabrane, E.; Gmouh, S. Evolution in the surface modification of textiles: A review. *Text. Prog.* **2018**, *50*, 67–108. [CrossRef]
15. Haji, A.; Naebe, M. Cleaner dyeing of textiles using plasma treatment and natural dyes: A review. *J. Clean. Prod.* **2020**, *265*, 121866. [CrossRef]
16. Zanini, S.; Citterio, A.; Leonardi, G.; Riccardi, C. Characterization of atmospheric pressure plasma treated wool/cashmere textiles: Treatment in nitrogen. *Appl. Surf. Sci.* **2018**, *427*, 90–96. [CrossRef]
17. Sohbatzadeh, F.; Shakerinasab, E.; Eshghabadi, M.; Ghasemi, M. Characterization and performance of coupled atmospheric pressure argon plasma jet with n-hexane electrospray for hydrophobic layer coatings on cotton textile. *Diam. Relat. Mater.* **2019**, *91*, 34–45. [CrossRef]
18. Szulc, J.; Urbaniak-Domagała, W.; Machnowski, W.; Wrzosek, H.; Łącka, K.; Gutarowska, B. Low temperature plasma for textiles disinfection. *Int. Biodeterior. Biodegrad.* **2018**, *131*, 97–106. [CrossRef]
19. Muzammil, I.; Dinh, D.K.; Abbas, Q.; Imran, M.; Sattar, H.; Ul Ahmad, A. Controlled Surface Wettability by Plasma Polymer Surface Modification. *Surfaces* **2019**, *2*, 349–371. [CrossRef]
20. Zille, A. Plasma Technology in Fashion and Textiles. In *Sustainable Technologies for Fashion and Textiles*; Elsevier: Amsterdam, The Netherlands, 2020; pp. 117–142.
21. Dave, H.; Ledwani, L.; Nema, S.K. Non-Thermal Plasma: A Promising Green Technology to Improve the Environmental Performance of Textile Industries. In *The Impact and Prospects of Green Chemistry for Textile Technology*; Elsevier: Amsterdam, The Netherlands, 2019; pp. 199–249.
22. Gasi, F.; Petraconi, G.; Bittencourt, E.; Lourenço, S.R.; Castro, A.H.R.; Miranda, F.D.S.; Essiptchouk, A.M.; Nascimento, L.; Petraconi, A.; Fraga, M.A.; et al. Plasma Treatment of Polyamide Fabric Surface by Hybrid Corona-Dielectric Barrier Discharge: Material Characterisation and Dyeing/Washing Processes. *Mater. Res.* **2020**, *23*. [CrossRef]
23. Parvinzadeh, M.; Ebrahimi, I. Atmospheric air-plasma treatment of polyester fibre to improve the performance of nanoemulsion silicone. *Appl. Surf. Sci.* **2011**, *257*, 4062–4068. [CrossRef]
24. Amara, I.; Miled, W.; Ben Slama, R.; Chevallier, P.; Mantovani, D.; Ladhari, N. Surface modifications by plasma treatment, chemical grafting and over dyeing of polyamide nets to improve the antifouling performance in the aquaculture field. *Dye. Pigment.* **2019**, *166*, 107–113. [CrossRef]

25. Yan, X.; Liu, G.-S.; Yang, J.; Pu, Y.; Chen, S.; He, H.-W.; Wang, C.; Long, Y.-Z.; Jiang, S. In Situ Surface Modification of Paper-Based Relics with Atmospheric Pressure Plasma Treatment for Preservation Purposes. *Polymers* **2019**, *11*, 786. [CrossRef]

26. López-García, J.; Praveen, K.M. Chapter 10—Wettability Analysis and Water Absorption Studies of Plasma Activated Polymeric Materials. In *Non-Thermal Plasma Technology for Polymeric Materials*; Thomas, S., Mozetič, M., Cvelbar, U., Špatenka, P., Eds.; Elsevier: Amsterdam, The Netherlands, 2019; pp. 261–285; ISBN 978-0-12-813152-7.

27. ABNT. ABNT-NBR-ISO 105-A03—Textile—Test for Colour Fastness. Part A03: Grey Scale for Assessing Staining 2006. Available online: https://www.abntcatalogo.com.br/norma.aspx?ID=1462 (accessed on 7 May 2021).

28. ABNT. ABNT-NBR-ISO 105-A02—Textile—Test for Colour Fastness. Part A02: Grey Scale for Assessing Change in Colour 2006. Available online: https://www.abntcatalogo.com.br/norma.aspx?ID=1469 (accessed on 7 May 2021).

29. ABNT. ABNT-NBR-ISO 105-C06—Textile—Test for Colour Fastness. Part C06: Colourfastness to Domestic and Commercial Laundering 2010. Available online: https://www.abntcatalogo.com.br/norma.aspx?ID=63626 (accessed on 7 May 2021).

30. Zhou, Q.; Rather, L.J.; Ali, A.; Wang, W.; Zhang, Y.; Rizwanul Haque, Q.M.; Li, Q. Environmental friendly bioactive finishing of wool textiles using the tannin-rich extracts of Chinese tallow (*Sapium sebiferum* L.) waste/fallen leaves. *Dye. Pigment.* **2020**, *176*, 108230. [CrossRef]

31. Vandenabeele, C.R.; Lucas, S. Technological challenges and progress in nanomaterials plasma surface modification—A review. *Mater. Sci. Eng. R Rep.* **2020**, *139*, 100521. [CrossRef]

32. Oliveira, F.R.; Zille, A.; Souto, A.P. Dyeing mechanism and optimisation of polyamide 6,6 functionalised with double barrier discharge (DBD) plasma in air. *Appl. Surf. Sci.* **2014**, *293*, 177–186. [CrossRef]

33. Charles, J.; Ramkumaar, G.R.; Azhagiri, S.S. Gunasekaran FTIR and thermal studies on nylon-66 and 30% glass fibre reinforced nylon-66. *E-J. Chem.* **2009**, *6*, 23–33. [CrossRef]

Preliminary Validation of a Continuum Model for Dimple Patterns on Polyethylene Naphthalate via Ar Ion Beam Sputtering

Jun-Yeong Yang [1,2,3,†] , **Sunghoon Jung** [1,4,†], **Eun-Yeon Byeon** [1], **Hyun Hwi Lee** [5], **Do-Geun Kim** [1],
Hyo Jung Kim [2,3], **Ho Won Jang** [6] and **Seunghun Lee** [1,*]

1 Department of Nano-Bio Convergence, Korea Institute of Materials Science, 797 Changwondae-ro, Changwon 51508, Korea; yjy8184@kims.re.kr (J.-Y.Y.); hypess@kims.re.kr (S.J.); whereks@kims.re.kr (E.-Y.B.); dogeunkim@kims.re.kr (D.-G.K.)
2 Department of Organic Material Science and Engineering, Pusan National University, Busan 46241, Korea; hyojkim@pusan.ac.kr
3 School of Chemical Engineering, Pusan National University, Busan 46241, Korea
4 Department of Materials Science and Engineering, Seoul National University, Seoul 08826, Korea
5 Pohang Accelerator Laboratory, POSTECH, Pohang 790-784, Korea; hhleec@postech.ac.kr
6 Department of Materials Science and Engineering, Research Institute of Advanced Materials, Seoul National University, Seoul 08826, Korea; hwjang@snu.ac.kr
* Correspondence: seunghun@kims.re.kr
† These authors are contributed equally.

Abstract: This work reports the self-organization of dimple nanostructures on a polyethylene naphthalate (PEN) surface where an Ar ion beam was irradiated at an ion energy of 600 eV. The peak-to-peak roughness and diameter of dimple nanostructures were 29.1~53.4 nm and 63.4~77.6 nm, respectively. The electron energy loss spectrum at the peaks and troughs of dimples showed similar C=C, C=O, and O=CH bonding statuses. In addition, wide-angle X-ray scattering showed that Ar ion beam irradiation did not induce crystallization of the PEN surface. That meant that the self-organization on the PEN surface could be due to the ion-induced surface instability of the amorphous layer and not due to the partial crystallinity differences of the peaks and valleys. A nonlinear continuum model described surface instability due to Ar ion-induced sputtering. The Kuramoto–Sivashinsky model reproduced the dimple morphologies numerically, which was similar to the experimentally observed dimple patterns. This preliminary validation showed the possibility that the continuum equation used for metal and semiconductor surfaces could be applied to polymer surfaces where ion beam sputtering occurred.

Keywords: ion beam sputtering; polymer; continuum equation

1. Introduction

Since the self-organization of nano-dots by ion beam sputtering was introduced by Facsko, diverse nano-structures have been fabricated by ion beam sputtering on semiconductor surfaces [1–3]. Regular ripples and dots have been created on the surfaces of Si, InP, and GaSb by noble gas ion beam irradiation [1,4–7]. Ion-induced surface instability results in self-organization, which has been successfully described by a continuum model including terms of roughening and smoothing [8]. The continuum model accounts for different sputtering yields at peaks and troughs, dependency on the ion's incident angle, ion-induced effective surface diffusion, thermal diffusion, and surface viscous flow [9]. The similarity between experimentally observed surface morphology and theoretical calculation showed the possibility of exact prediction for self-organization by ion beam sputtering. Nano-dots, ripples, and dimples on polymer substrates also have been observed in surface treatments using ion beam irradiations. M. Goyal reported that a 40 keV oblique argon

ion beam resulted in ripple or dot nanostructures on polypropylene (PP) surfaces [10]. We reported that dimple nanostructures were obtained by 1 keV oxygen ion beam treatments on polyethylene terephthalate (PET) surfaces [11]. Polyethylene naphthalate (PEN) surfaces irradiated by an Ar ion beam showed dimple patterns, which resembled the patterns calculated by the continuum equation, especially the Kuramoto–Sivashinsky (KS) model [9]. This similarity implied the possibility of applying the continuum equation to describe the self-organization of polymer surfaces by noble gas ion beam sputtering. In this work, we fabricated dimple patterns on PEN surfaces via 600 eV Ar ion beam irradiation. Surface analysis was performed to find a clue regarding whether ion beam sputtering was the main reaction making the dimple patterns. A nonlinear continuum equation was solved by MATLAB^{TM} software and compared to the dimple patterns obtained by Ar ion beam irradiation.

2. Materials and Methods

2.1. Materials

A dimple pattern was fabricated on a commercially available PEN film surface by Ar ion beam bombardment. 125 μm PEN film (Dupont Teijin Films, Chester, VA, USA) was prepared by cutting it to a size of 100×100 mm^2. After removing the protective film on the surface, the PEN film was attached to the linear moving stage located in the vacuum chamber.

2.2. Ion Beam Treatment

The vacuum chamber was evacuated with a base pressure of 5.0×10^{-5} Torr, and then Ar gas was injected into the linear ion source. A gridless ion source was used to generate linear Ar ion beams with a width of 300 mm [11,12]. The PEN samples were treated at a linear moving speed of 10 mm/s. The ion dose per scan was 1.2×10^{14} cm^{-2}, according to measurement by a Faraday cup. The ion energy distribution function was measured by an ion energy analyzer (Figure S1) [13]. Ar ion beams were irradiated under normal incidence conditions.

2.3. Field-Emission Scanning Electron Microscopy

The PEN surface was observed using field-emission scanning electron microscopy (FE-SEM; JSM 6700F, JEOL, Tokyo, Japan) in secondary electron (SE) mode. The accelerating voltage was maintained at 5 kV.

2.4. Atomic Force Microscopy

The morphology of the dimple nanostructures was measured by atomic force microscopy (AFM, NX10, Park Systems, Suwon, Korea) in non-contact mode.

2.5. Field-Emission Transmission Electron Microscopy and the Electron Energy Loss Spectrum

A localized cross-linking on the dimple nanostructures was verified via cross-sectional field-emission transmission electron microscopy (FE-TEM, JEM-ARM, JEOL, Tokyo, Japan) with electron energy loss spectroscopy (EELS, JEOL, Tokyo, Japan). The FE-TEM measurements were performed at an accelerating voltage of 200 kV. The cross-sectional specimens of FE-TEM were prepared using a liquid metal ion source (Ga$^+$) equipped with a focused ion beam with a coarse milling current (4 nA) and a fine milling current (20 pA) at 30 kV. The 90 nm–thick PEN sample was prepared with a focused ion beam.

3. Results and Discussion

Figure 1 shows surface morphologies and profiles. Figure 1a,b show AFM images of PEN surfaces treated by 600 eV Ar ion beam bombardment with ion doses of 2.4×10^{15} cm^{-2} and 4.8×10^{15} cm^{-2}, respectively. As the ion dose was increased, the irregular dimple patterns were formed clearly. In Figure 1c,d, the peak-to-peak roughness (R_z) was increased from 29.1 ± 4.7 nm and 53.4 ± 8.4 nm as the ion dose was increased. In

Figure 1e, a scanning probe image processor (SPIP^{TM}, Image Metrology, Diplomvej, Denmark) showed that dimple diameter was increased from 63.4 ± 18.6 nm to 77.6 ± 23.1 nm as the ion dose was increased (Figure S2). In addition, the aspect ratio (R_z/diameter) of dimples were increased from 0.45 to 0.68.
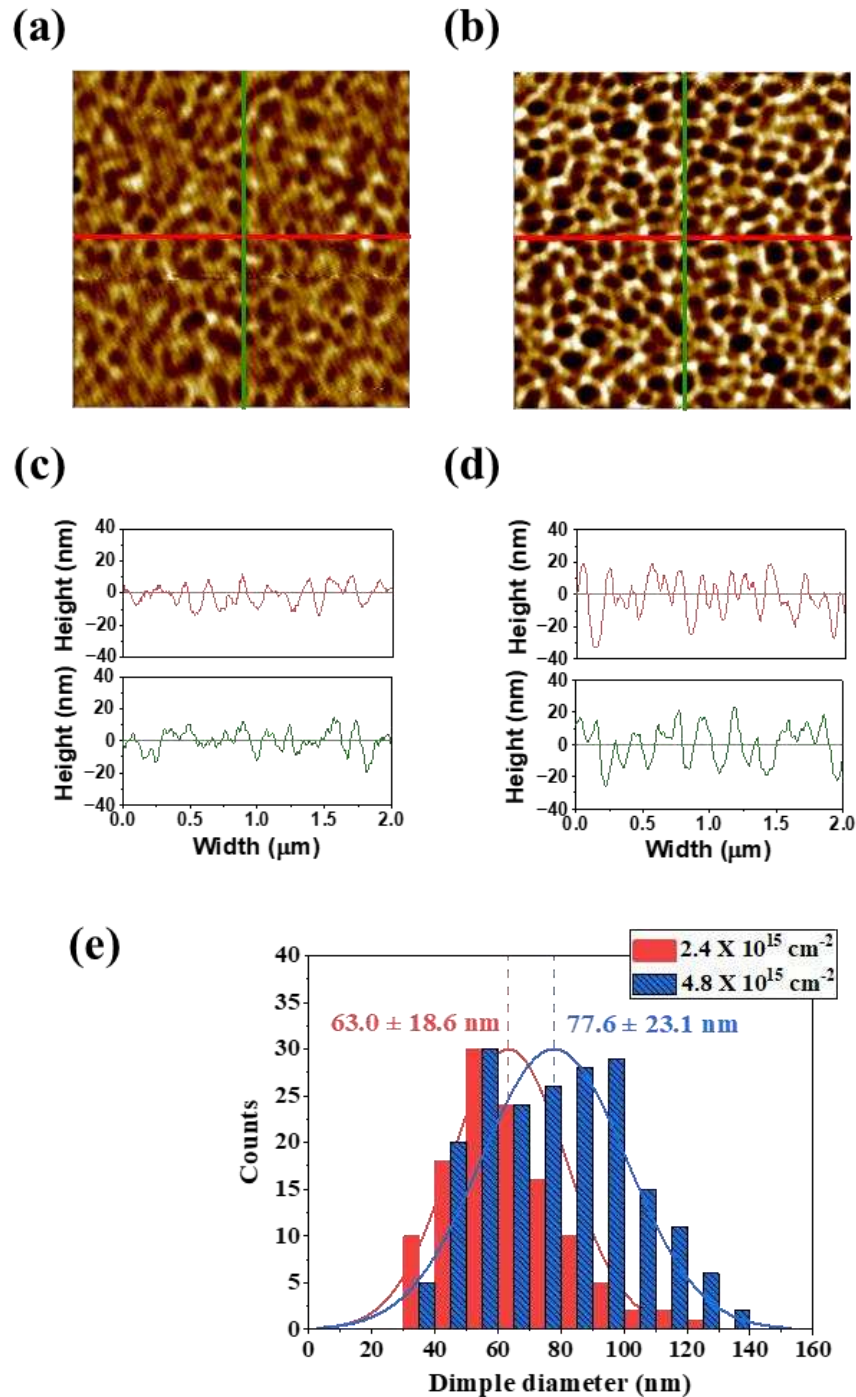
Figure 1. AFM images (area: 2 μm × 2 μm) of dimple patterns on a PEN surface by 600 eV Ar ion beam bombardment with ion doses of (**a**) 2.4×10^{15} cm^{-2} and (**b**) 4.8×10^{15} cm^{-2}. *X*-axis and *Y*-axis line profiles: (**c**) 2.4×10^{15} cm^{-2}, (**d**) 4.8×10^{15} cm^{-2}. (**e**) Distribution of dimple diameter in the 2 μm × 2 μm area.

Self-organization by ion beam irradiation has been explained by two mechanisms. One is the semi-crystallinity of cross-linked polymers. The sputtering yield of a semi-

crystalline polymer is lower than that of the amorphous phase [14]. For instance, He ion bombardment on polytetrafluoroethylene surfaces left the backbones of the crystallized polymer chains, which formed worm-like structures [15]. Another possibility is surface instability induced by ion bombardments. Ion-induced surface instability results in roughening and smoothing of the amorphous layer [2]. The self-organization of ordered morphologies by ion beam sputtering is independent from the orientation of surface materials because self-organization by surface instability occurs in the amorphous layer formed by ion beam irradiation [2]. If the polymer surface is in the amorphous phase during ion beam sputtering, ion-induced surface instability could explain the pattern formation.

In Figure 2, FE-TEM and EELS show the cross-sectional images and the chemical bond statuses at the valleys and hills of the dimple structures. The EELS was measured at the peak (point A in Figure 2a) and trough (point B in Figure 2b). The EELS signal showed aromatic C=C (285 eV), ketone C=O (286.3–286.8 eV), and aldehyde O=CH (286.3–286.8 eV) functional groups, which existed similarly at the peak and trough [16]. If the partially distributed crystalline chains induced the dimple patterns, the binding status at the peak position would differ from that at the trough region. This revealed that the patterning mechanism was not partial semi-crystallization. Wide angle X-ray scattering (WAXS) showed that semi-crystallization was not induced by Ar ion beam irradiation (Figure S3). The EELS and WAXS results mean that the self-organization on the PEN samples could be due to the ion-induced surface instability of the amorphous layer.
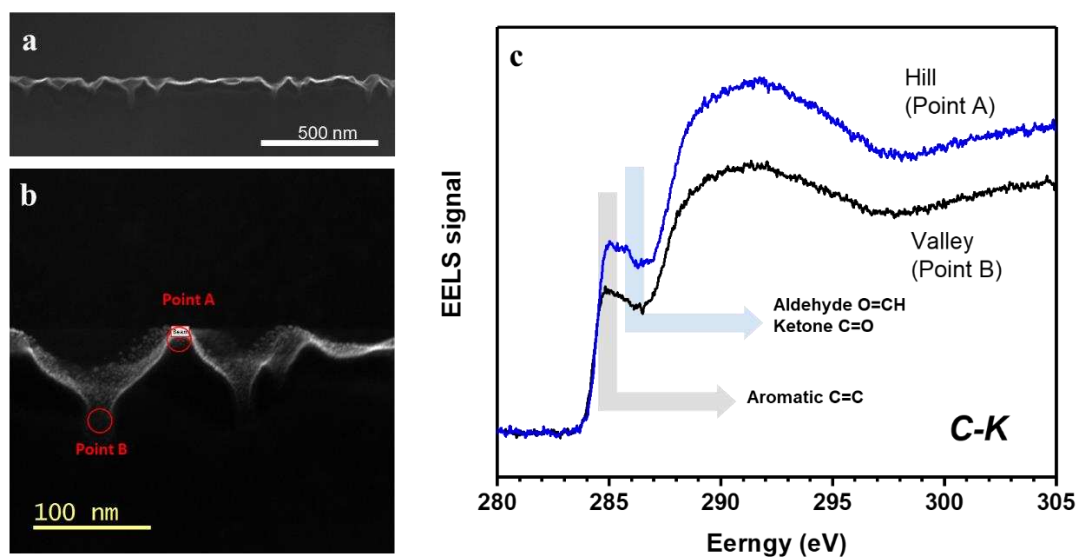
Figure 2. (**a**) Cross-sectional SEM image of dimple pattern, (**b**) the points of EELS measurement at a peak and trough. (**c**) EELS at the selected peak and trough.

The KS model could explain the self-organization of dimple structures on the PEN surface by ion-induced surface instability. The mechanism of pattern formation by ion bombardment has been extensively investigated using a continuum equation [8,9]. The KS equation describes the morphology evolution during an ion bombardment. The KS equation is given by

$$\frac{\partial h}{\partial t} = \nu \nabla^2 h - D \nabla^4 h - K \nabla^4 h - \lambda (\nabla h)^2 + \eta \tag{1}$$

where h is the height of the ion-bombarded surface as a function of time t, ν is the effective surface tension generated by the erosion process or viscous flow due to surface stress, D is the diffusion coefficient from ion-induced diffusion, K is a thermal diffusion coefficient, λ describes the tilt-dependent sputtering yield, and η is Gaussian white noise resulting from the stochastic nature of the erosion process. We tried to reproduce the dimple structures on

PEN surfaces by Ar ion beam irradiations using the KS model. Numerical simulation was executed on an equally spaced, 2-dimensional 200×200 mesh by integration of Equation (1) using a standard discretization method with periodic boundary conditions. The integration began from a random surface with a height randomly distributed from 0 to 0.1 with spatial step $dx = 0.5$ nm, time step $dt = 0.002$ s, $\nu = -0.0553$ nm^2/s, $\lambda = -0.177$ nm/s, $D = 0.0138$ nm^4/s, and $K = 0$. The coefficients were calculated by ion species (Ar), polymer density (1.36 g/cm^{-3}), ion energy (600 eV), and a definition of coefficients from previous work [8,17]. The sputtering yield was calculated by SRIM code [17]. The sign of the nonlinear term λ determined dot or dimple structures. A positive λ induced dot formation and a negative λ described dimple formation [2,8]. In this normal incident condition, Equation (1) yielded an isotropic, partial differential equation with a negative nonlinear λ term, which implied dimple formation. Figure 3 compares simulation results using Equation (1) with FE-SEM images of experimentally fabricated samples. The images reveal a similarity of surface morphology between the simulation and the experiment. In the simulation, the disconnected patterns developed after 50 s, which corresponded to 20 scans (Figure 3a). After 100 s (40 scans), dimple patterns formed (Figure 3b). As experimental bombardment proceeded (Figure 3c), a partially disconnected network structure was observed after 20 scans. For longer irradiation times, the pattern formed after 40 scans (Figure 3d). The spatiotemporal pattern predicted by Equation (1) showed good correlation with experimental observations.
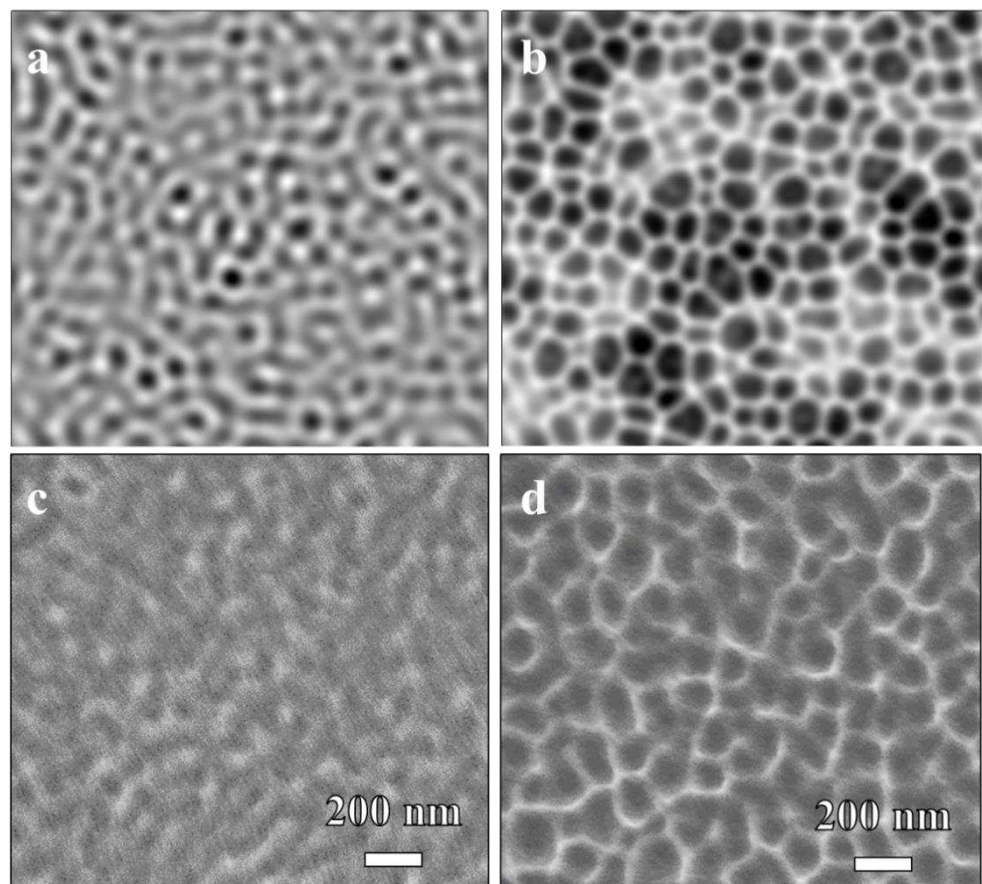
Figure 3. Simulation results by iterating the DKS equation: (**a**) ion flux = 4.83×10^{13} cm^{-2}s^{-1}, time = 50 s for 20 scans (**b**) ion flux = 4.83×10^{13} cm^{-2}s^{-1}, time = 100 s for 40 scans. Experimentally obtained dimple patterns on the PEN surface: (**c**) 20 scans, (**d**) 40 scans.

The successful prediction of self-organization means that ion beam irradiation on the PEN surface mainly results in surface sputtering. The continuum equation is based on

the sputtering reaction on the ion beam irradiated surface. Ion irradiation on the polymer surface simultaneously induces cross-linking and sputtering. Ion energy transfer by nuclear collision affects the ratio of cross-linking to sputtering. If surface atoms receive sufficient energy to break surface binding with energetic recoils and ions, surface displacement induces sputtering. Energy transfer by recoils and ions depends on the atomic number density of the target polymer. The concept of displacement per atom (DPA), which is proportional to the energy transfer by the nuclear stopping reaction, could be a quantitative value for evaluating the degree of displacement [18]. PEN density (1.36 g/cm^3) was sufficient to induce multiple atomic displacements of polymer atoms at the surface. The 600 eV Ar collision on the PEN surface showed a DPA of 4 to 8, a value sufficient for inducing frequent sputtering by ion bombardments. Thus, the continuum model based on sputtering reactions showed similar surface morphology to an Ar ion beam-irradiated PEN surface.

4. Conclusions

The comparison of the KS model and the dimple pattern showed the validity of applying the continuum model to the self-organization of a polymer surface using ion beam irradiation. The continuum model based on sputtering reactions could be applied to the limited polymer material, which has a density that induces sufficient surface displacement and sputtering by ion beam irradiation.

The discrepancy between the simulation and the experiment is due to a limitation in explaining the exact ion-induced sputtering yield of the polymer substrate that consists of several atoms such as carbon, hydrogen, and oxygen. The SRIM code supplied a statistically averaged sputtering yield for the polymer substrate.

This approach could be useful to fabricate nanostructures applied to sensors such as surface-enhanced Raman spectroscopy, which uses the enhancement of local electric fields wherein the surface morphology has a several nm gap [19,20]. The dimple patterns could be applied to form hot spots on polymer surfaces using a simple, top-down process.

Institutional Review Board Statement: Not applicable.

Informed Consent Statement: Not applicable.

Data Availability Statement: Not applicable.

References

1. Facsko, S.; Dekorsy, T.; Koerdt, C.; Trappe, C.; Kurz, H.; Vogt, A.; Hartnagel, H.L. Formation of ordered nanoscale semiconductor dots by ion sputtering. *Science* **1999**, *285*, 1551–1553. [CrossRef] [PubMed]
2. Wei, Q.; Zhou, X.; Joshi, B.; Chen, Y.; Li, K.; Wei, Q.; Sun, K.; Wang, L. Self-Assembly of Ordered Semiconductor Nanoholes by Ion Beam Sputtering. *Adv. Mater.* **2009**, *21*, 2865–2869. [CrossRef]

3. Castro, M.; Cuerno, R.; Vázquez, L.; Gago, R. Self-organized ordering of nanostructures produced by ion-beam sputtering. *Phys. Rev. Lett.* **2005**, *94*, 16102. [CrossRef] [PubMed]

4. Bobek, T.; Facsko, S.; Kurz, H.; Dekorsy, T.; Xu, M.; Teichert, C. Temporal evolution of dot patterns during ion sputtering. *Phys. Rev. B* **2003**, *68*, 85324. [CrossRef]

5. Facsko, S.; Kurz, H.; Dekorsy, T. Energy dependence of quantum dot formation by ion sputtering. *Phys. Rev. B* **2001**, *63*, 165329. [CrossRef]

6. Cuerno, R.; Makse, H.A.; Tomassone, S.; Harrington, S.T.; Stanley, H.E. Stochastic model for surface erosion via ion sputtering: Dynamical evolution from ripple morphology to rough morphology. *Phys. Rev. Lett.* **1995**, *75*, 4464. [CrossRef]

7. Frost, F.; Schindler, A.; Bigl, F. Roughness evolution of ion sputtered rotating InP surfaces: Pattern formation and scaling laws. *Phys. Rev. Lett.* **2000**, *85*, 4116. [CrossRef] [PubMed]

8. Keller, A.; Facsko, S. Ion-induced nanoscale ripple patterns on Si surfaces: Theory and experiment. *Materials* **2010**, *3*, 4811–4841. [CrossRef]

9. Facsko, S.; Bobek, T.; Stahl, A.; Kurz, H.; Dekorsy, T. Dissipative continuum model for self-organized pattern formation during ion-beam erosion. *Phys. Rev. B* **2004**, *69*, 153412. [CrossRef]

10. Goyal, M.; Aggarwal, S.; Sharma, A.; Ojha, S. Surface structuring in polypropylene using Ar + beam sputtering: Pattern transition from ripples to dot nanostructures. *Appl. Surf. Sci.* **2018**, *439*, 380–385. [CrossRef]

11. Lee, S.; Byun, E.Y.; Kim, J.K.; Kim, D.G. Ar and O2 linear ion beam PET treatments using an anode layer ion source. *Curr. Appl. Phys.* **2014**, *14*, S180–S182. [CrossRef]

12. Jung, S.; Byeon, E.-Y.; Kim, D.-G.; Lee, D.-G.; Ryoo, S.; Lee, S.; Shin, C.-W.; Jang, H.W.; Yang, J.-Y.; Kim, H.J. Copper-Coated Polypropylene Filter Face Mask with SARS-CoV-2 Antiviral Ability. *Polymers* **2021**, *13*, 1367. [CrossRef] [PubMed]

13. Böhm, C.; Perrin, J. Retarding-field analyzer for measurements of ion energy distributions and secondary electron emission coefficients in low-pressure radio frequency discharges. *Rev. Sci. Instrum.* **1993**, *64*, 31–44. [CrossRef]

14. Junkar, I.; Cvelbar, U.; Vesel, A.; Hauptman, N.; Mozetič, M. The role of crystallinity on polymer interaction with oxygen plasma. *Plasma Process. Polym.* **2009**, *6*, 667–675. [CrossRef]

15. Coen, M.C.; Lehmann, R.; Groening, P.; Schlapbach, L. Modification of the micro-and nanotopography of several polymers by plasma treatments. *Appl. Surf. Sci.* **2003**, *207*, 276–286. [CrossRef]

16. Vollmer, C.; Kepaptsoglou, D.; Leitner, J.; Busemann, H.; Spring, N.H.; Ramasse, Q.M.; Hoppe, P.; Nittler, L.R. Fluid-induced organic synthesis in the solar nebula recorded in extraterrestrial dust from meteorites. *Proc. Natl. Acad. Sci. USA* **2014**, *111*, 15338–15343. [CrossRef] [PubMed]

17. Ziegler, J.F.; Ziegler, M.D.; Biersack, J.P. SRIM–The stopping and range of ions in matter (2010). *Nucl. Instrum. Methods Phys. Res. Sect. B* **2010**, *268*, 1818–1823. [CrossRef]

18. Lee, S.; Byeon, E.; Jung, S.; Kim, D.-G. Heterogeneity of hard skin layer in wrinkled PDMS surface fabricated by Ar ion-beam irradiation. *Sci. Rep.* **2018**, *8*. [CrossRef] [PubMed]

19. Jeon, T.Y.; Park, S.; Kim, D.; Kim, S. Standing-Wave-Assisted Creation of Nanopillar Arrays with Vertically Integrated Nanogaps for SERS-Active Substrates. *Adv. Funct. Mater.* **2015**, *25*, 4681–4688. [CrossRef]

20. Wang, X.; Park, S.; Ko, J.; Xiao, X.; Giannini, V.; Maier, S.A.; Kim, D.; Choo, J. Sensitive and Reproducible Immunoassay of Multiple Mycotoxins Using Surface-Enhanced Raman Scattering Mapping on 3D Plasmonic Nanopillar Arrays. *Small* **2018**, *14*, 1801623. [CrossRef] [PubMed]

Microwave Discharges in Liquid Hydrocarbons: Physical and Chemical Characterization

Yuri A. Lebedev ![ORCID]

Abstract: Microwave discharges in dielectric liquids are a relatively new area of plasma physics and plasma application. This review cumulates results on microwave discharges in wide classes of liquid hydrocarbons (alkanes, cyclic and aromatic hydrocarbons). Methods of microwave plasma generation, composition of gas products and characteristics of solid carbonaceous products are described. Physical and chemical characteristics of discharge are analyzed on the basis of plasma diagnostics and 0D, 1D and 2D simulation.

Keywords: microwave discharge; discharges in liquids; microwave discharge in liquid hydrocarbons; methods of generation; plasma properties; gas products; solid products; plasma diagnostics; plasma modeling

1. Introduction

Recently, electrical discharges in liquids [1–10] and, in particular, microwave discharges [11–13] have been intensively studied. Microwave discharges in liquids are less studied. These discharges exhibit properties that distinguish them from widely used DC, HF and high-voltage discharges. They can be used to produce hydrogen, coatings, nanoparticles and nanotubes, for water purification, etc. [13]. Several papers on modeling of electrodynamics and plasma processes in such discharges have been published [14–26]. Microwave plasma in liquids is an extremely interesting object for investigation, since it is often non-equilibrium, heterogeneous, with large spatial gradients of parameters. Plasma as a rule is unsteady and existing under conditions of permanent exchange by energy and particles with the surrounding liquid medium.

One of the key problems of discharges in liquids is answering the question of what is first: discharge produces the gas bubble or discharge is generated in the existing gas bubble. There are several theories of bubble generation by discharges, which are reviewed in [6,10]. Considering the known results on microwave discharges, it can be stated that, although they talk about microwave discharges in a liquid, in fact microwave plasma is created in a gas bubble (a few millimeters in diameter) inside the liquid. The bubbles can be created in different ways: (a) by evaporation of the liquid in the vicinity of the antenna tip heated by the microwave field; (b) by creation of artificial bubbling by introduce of additional gases (argon is most often used); and (c) by action of ultrasonic waves. The surface of the bubbles is located near the high-temperature plasma zone, which ensures a high-rate input of evaporated molecules of fluids in the bubble. This bubble can be considered as a mini plasma chemical reactor. As a result of the intense flow of molecules into the bubble, high concentrations of active particles (atoms, radicals and charged particles) are created in the plasma. Therefore, the efficiency of physical and chemical processes in this reactor is high. Accordingly, the rate of formation of products is also high. Moreover, the small dimension of plasma region produces high gradients of parameters and high rate of stabilization of products. These features are the major differences from conventional gas phase microwave plasma processing.

This article summarizes the results obtained in the study of microwave discharges in liquid hydrocarbons. Almost the entire spectrum of liquid hydrocarbons has been used in studies of microwave discharges in liquids including alkanes (C_nH_{2n+2}), cyclic (C_nH_{2n}) and aromatic hydrocarbons, industrial and engine oils and their wastes, oil and heavy oil products.

Since gas and solid products are formed in such discharges, as well as the liquid itself is exposed to the discharge, all these results are consistently considered in the article. In addition, the results obtained in the diagnosis and modeling of such discharges are described.

It should be noted that the dielectric constant is approximately the same for non-polar liquid hydrocarbons ($\varepsilon \sim 2.0$) and the tangent of losses for non-polar hydrocarbons is of the order of 10^{-4}, thus the loss of microwave energy for heating the liquid is small. Unfortunately, in the process of burning a discharge in liquid hydrocarbons, one of the products is a solid carbon-containing phase, which naturally increases the loss tangent. For polar liquids, the loss tangent is greater, and the dielectric parameters depend on temperature.

Note that non-polar hydrocarbons are transparent in the visible wavelength range; this is important for carrying out spectral-optical measurements, which are practically the only method for diagnosing such discharges. In the process of burning a discharge in hydrocarbons, solid particles appearing in a liquid reduce its transparency.

2. Experimental Setups and Methods of Diagnostics

The general scheme of microwave discharges setup in liquids does not differ from that used to generate microwave discharges in the gas phase (Figure 1). It is considered in detail in [27] and includes a microwave generator (as a rule, magnetrons with a frequency of 2.45 GHz and a power of up to several kilowatts in continuous or pulsed modes), a circulator to protect the generator from reflected power, an incident and reflected power meters, matching device, discharge chamber, gas supply system, exhaust gas sampling and exhaust pump system. Discharges in liquids are created at pressures from units of kPa to atmospheric pressure. The pressure in the plasma region is determined by the pressure provided by the pumping system above the liquid surface and differs from it by the pressure of the liquid column above the plasma region.
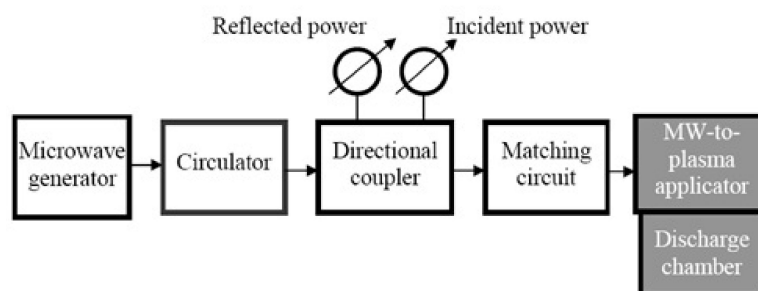
Figure 1. The general scheme of microwave discharges setup.

Various microwave-to-plasma applicators are used for generation of microwave discharges in different liquid dielectrics. Their task is to create the microwave field, having the strength sufficient to create and sustain a discharge in the gas bubble. There are four main types of discharge devices (Figure 2). Plasma is generated near microwave antennas of different types.
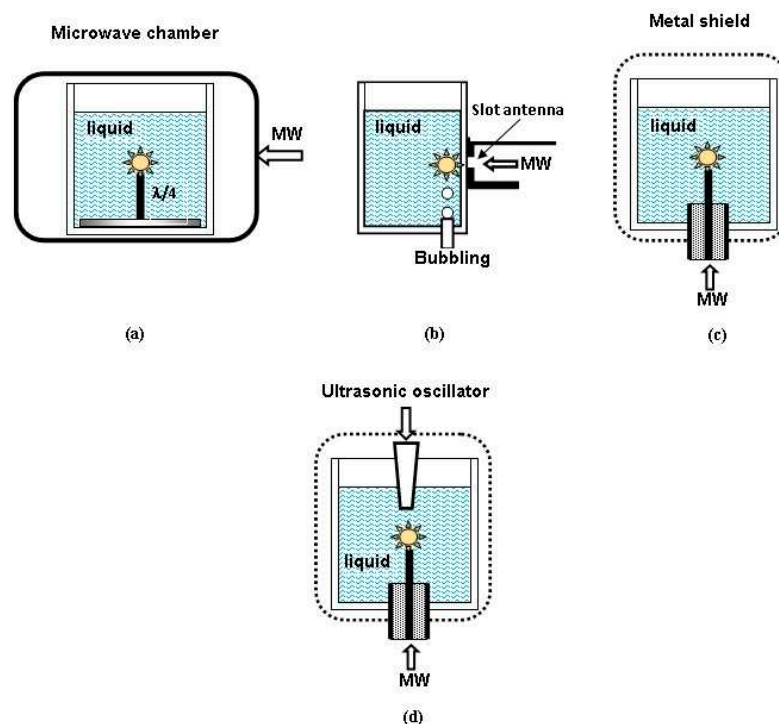
Figure 2. Schematics of different types of microwave discharges in liquids: (**a**) discharge on the base of quarter-wavelength antenna; (**b**) discharge on the base of slot antenna; (**c**) discharge with energy input through the coaxial line; and (**d**) microwave discharge in combination with ultrasonic radiation.

The first and simplest one is the use of quarter-wavelength metal antennas mounted on the metal basement (Figure 2a), at the end of which a discharge is ignited in the gas bubble. The antenna length should be equal to a quarter of the wavelength of the liquid radiation ($\lambda = c/f\sqrt{\varepsilon}$, where c is the speed of light in vacuum, f is the frequency and ε is the dielectric constant of the liquid). For non-polar liquid hydrocarbons, the antenna length is about 2 cm. This means that the antenna length is practically the same for all such hydrocarbons. The antenna is placed in a heat-resistant glass with low loss in the microwave frequency range, filled with liquid hydrocarbon. The glass is located in the microwave chamber. Therefore, energy can be supplied to the antenna through the liquid layer. Since the strength of the microwave field at the antenna increases with a decrease in its diameter, the power required to initiate a discharge decreases. Additional gas can be supplied via a channel in the antenna.

This method is implemented, for example, in [28–31]. A conventional microwave oven was used as a microwave chamber [28], and the discharge was ignited in a glass placed in the oven chamber. To increase the efficiency of plasma processes, not one antenna can be used, but a system of whip antennas [28]. A special metal chamber into which the microwave energy was supplied from three magnetrons is described in [29–31].

One of the disadvantages of this system is the destruction of the end of the antenna in the plasma or the growth of deposits on it. This leads to a change in its length and violation of the condition of its equality to a quarter of the wavelength and to unstable operation of the device. To reduce the role of antenna erosion, various methods are proposed, in particular the use of refractory metals (such as molybdenum or tungsten), coating of antennas with heat-resistant dielectrics (see, e.g., [14]) or the use of pulse regime of microwave generator [32]. Antennas of various shapes are used to excite the discharge. For example, the authors of [33] described the use of a broken ring antenna.

The second type of antenna used is the slotted antenna (Figure 2b). Gas bubbles are created near it surface due to heating of liquid by microwaves (it should be noted that many bubbles can appear simultaneously along the slot) or by the introduction of additional gas (the so-called "multibubble system") [34–36]. Bubble formation at the antenna leads

to unstable operation of the device and a decrease in the efficiency of energy transfer to the discharge. Simulations and experiments have shown that this can be eliminated by introducing a bubble control element, which is a quartz plate with holes placed close to the antenna [35]. Multiple slot antennas can be used to increase the efficiency of the device. By artificially creating bubbles, plasma can be created at pressures up to atmospheric pressure.

Another method of microwave plasma generation in liquids is the coaxial input of microwave energy into the liquid, in which the discharge is ignited at the end of the central conductor of coaxial line (Figure 2c). It is the most widespread method of microwave plasma generation in liquids (see, e.g., [14,15,28,37–45]). Modeling of electrodynamics of quarter wavelength [30] and coaxial [44] antenna systems has shown that in the latter system the microwave field strength at the tip of antenna is much less sensitive to the antenna length. As plasma is generated at the tip of antenna, this provides more stable operation of plasma generator.

All problems with antenna erosion considered above exist also in this case. The methods of suppressing this effect are also the same.

A more complex method can be used, in which both the microwave and ultrasonic radiation simultaneously act on the liquid (Figure 2d) [46–48]. In this case, acoustic oscillations (with a frequency of 24.5 kHz, 10–30 W) are a source of bubbles in a liquid, in which a plasma is created when exposed to microwave radiation (2.45 GHz, 50–200 W). The authors of [46] called it "sonoplasma", and, in contrast to "sonoluminescence," it gives a constant radiation in time, which is caused by the absorption of microwave energy and not by the energy released during bubble collapse. After ignition of the discharge, ultrasonic radiation can be switched off and discharge maintained only by microwave radiation.

Discharges in liquids are generated at both reduced pressures and atmospheric pressure. Generally, microwave generators with a frequency of 2.45 GHz are used to create the plasma.

Note that, if one does not take special measures, microwave discharges in carbon-containing liquids are nonstationary [43]. This is due to the formation of solid carbon-containing particles, which are distributed in the volume of the liquid due to convective flows. This leads to the absorption of microwave radiation, decreased liquid transparency for plasma radiation and discharge failure. To eliminate this phenomenon, it is necessary to organize the circulation of the liquid with its purification from solid particles. This must be done when creating technological processes.

The appearance of carbon-containing solid particles in the liquid is also manifested in another effect [43]. It leads to the fact that the composition of the liquid wall evaporating into the bubble contains more carbon than at the beginning of the experiment in pure hydrocarbon and the discharge is maintained in a medium with a time-varying composition of the evaporating boundary. Thus, the nonstationarity of the discharge in liquid hydrocarbons is associated not only with the formation of a gas bubble with plasma and its dynamics, but also with a change in the composition of the evaporating liquid wall of the gas bubble during the course of the discharge burning and the associated change in the composition of the gas phase in the bubble.

Microwave discharges in liquids are extremely difficult for experimental study. Using contact diagnostic methods is difficult because the plasma is in a microwave field and the insertion of foreign objects in plasma distorts both the structure of the microwave field and plasma. In addition, the microwave field can lead to the damage of diagnostic devices. Therefore, the only method for studying the plasma parameters is the optical methods. Most papers contain results of optical emission spectroscopy (these results are mainly related with measurements of excitation temperatures of plasma particles and gas temperatures).

As discharges in hydrocarbons produces the gas and solid particles, to study these components, various special methods of diagnostics are used: gas chromatography, mass-spectrometry, Raman spectroscopy, field emission scanning electron microscope, etc.

Additional possibilities in study of discharge parameters are provided by modeling, which is rather complicated, since the discharge is non-stationary and constantly exchanges in energy and matter with the liquid wall. The results of zero-, one- and two-dimensional modeling of processes in plasma are described in [14–26].

3. Gas Products of Microwave Discharges in Liquid Hydrocarbons

As noted above, almost the entire spectrum of liquid hydrocarbons has been used for studying microwave discharges in liquids. For example, Figure 3 shows two successive frames of microwave discharge in the engine oil obtained in the installation with quarter wavelength antenna described in [29–31]. The figure shows that discharge exists at the tip of antenna. Two successive frames of microwave discharge in the engine oil obtained in installation with coaxial input of microwave energy described in [41,43–45] are shown in Figure 4. Figure 5 shows the frames of discharge in *n*-heptane in the same installation. The presented photographs reflect the non-stationary nature of microwave discharges in liquids.

(**a**)   (**b**)
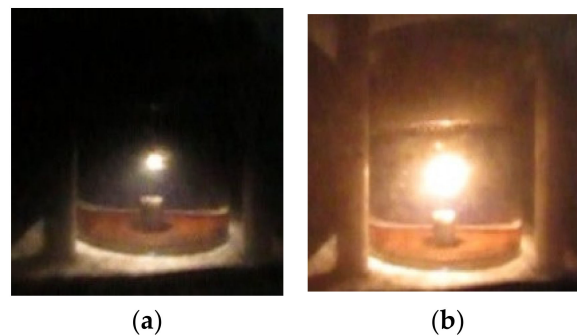
Figure 3. Two successive frames of microwave discharge in engine oil obtained in the installation with quarter wavelength antenna described in [29–31] (shooting speed is 240 frames per second, time interval between figures (**a**) and (**b**) is of 4 ms).

(**a**)   (**b**)
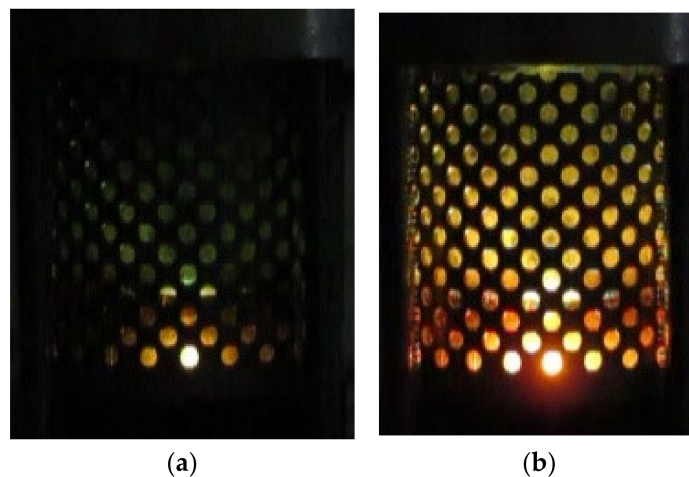
Figure 4. Two successive frames of microwave discharge in engine oil in installation with coaxial input of microwave energy described in [41,43–45] (shooting speed is 240 frames per second, time interval between figures (**a**) and (**b**) is of 4 ms).
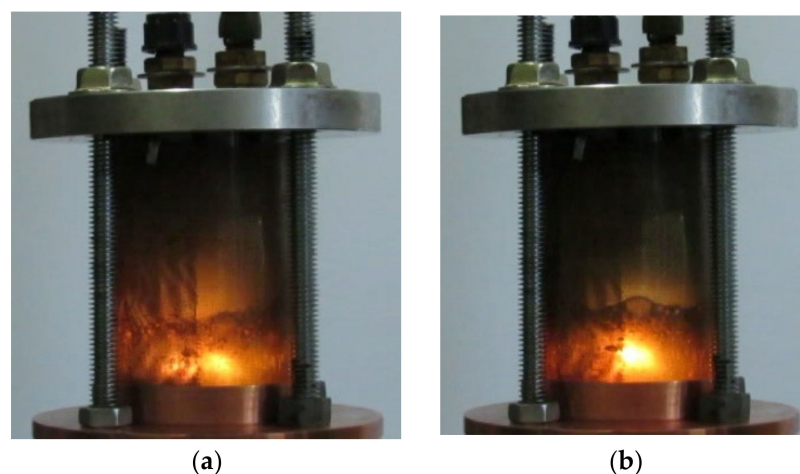
Figure 5. Two successive frames of microwave discharge in *n*-heptane in installation with coaxial input of microwave energy described in [41,43–45] (shooting speed is 25 frames per second, time interval between figures (**a**) and (**b**) is 40 ms).

Gas products of microwave discharge in *n*-heptane are studied much better than in other hydrocarbons [43], and it is possible to compare these results with the results obtained in other conditions.

Since *n*-heptane is the main component of reference and surrogate fuels for internal combustion engines, and is a convenient object for studying thermal transformations of higher *n*-alkanes, much attention is paid to the study of its combustion and oxidation processes [49–52], as well as pyrolysis [53–55]. Data on the composition of the products and the kinetics of pyrolysis of *n*-heptane were used to establish the mechanism of its oxidation and combustion and to build the kinetic schemes of processes [56].

It is of interest to compare the results on the gas-phase products of a microwave discharge in liquid *n*-heptane with known data on the decomposition of *n*-heptane under various conditions.

The results of experimental study of pyrolysis of *n*-heptane are partly summarized in the reviews [53–55]. Processes were studied in a flow reactor when the reagent was diluted with nitrogen [57,58], argon [59,60], water vapor [61,62] and without dilution with a carrier gas [63], as well as processes in the shock tube [64,65]. It was found that decomposition of *n*-heptane under the action of temperature is a radical-chain process and is described by the Kosyakov–Rice mechanism with additions [53–55,57]. The main products of pyrolysis of *n*-heptane are hydrogen, methane, ethylene, ethane and propylene [57–63]. α-olefins C_4–C_6 (butene-1, pentene-1 and hexene-1) are also always present in the product mixture; the first of them at moderate temperatures and small degrees of conversion belongs to the main products. Among the products, the following are also identified: butenes-2, butadiene-1,3 and pentenes. In minor and trace amounts at pressures of the order of 0.1 MPa and below, there are propane, *n*-butane and *n*-pentane. As the pressure increases, the rate constant of *n*-heptane decomposition increases and the selectivity of products changes due to the faster growth of the rates of bimolecular processes, such as the detachment of the H atom leading to the formation of alkanes, as compared to monomolecular reactions such as the breakdown of radicals, leading to the formation of ethylene [53]. As a result, the selectivity of the formation of hydrogen and ethylene decreases, while the formation of *n*-alkanes, starting from ethane and α-olefins increases [59,63]. Increase in the temperature leads to increase in the selectivity of the formation of light products, especially methane, ethylene and hydrogen [53,63]. With a further increase in temperature to 1300 K or more, new products appear, such as acetylene, methyl acetylene, allene, vinyl acetylene, pentadiene-1,3 isomers, hexadiene-1,5 and benzene [60,64,65].

Decomposition of *n*-heptane was also investigated in a barrier discharge [66–68]. It is established in [66] that monotonous growth of the methane, ethylene, ethane and propane

yields is observed with increase in the electric field strength. In [67], the influence of the alkane structure and the type of diluent gas on the yields of hydrogen and other products is investigated. Gas phase products were determined for *n*-heptane: hydrogen, methane, hydrocarbons C_2 (ethylene + acetylene, ethane), C_3 (propylene, etc.) and C_4. In [68], a kinetic study of the conversion of *n*-alkanes C_6–C_9 is carried out. It is established in [67,68] that, as the number of C atoms in the alkane molecule increases, its degree of conversion and energy efficiency increase, in contrast to the results obtained in [66].

Comparison of distributions of gas-phase products in pyrolysis of *n*-heptane in different conditions is given in Table 1.

Table 1. Comparison of distributions of gas-phase products in pyrolysis of *n*-heptane [57,58,61,62] and microwave discharge in liquid *n*-heptane [43]. All values are given in wt. % (all data were recalculated on the basis of data from the original articles).

Reference	[61]	[57]	[59]	[58]	[62]	[43]
Diluent	Steam		Argon	Nitrogen	Steam	
Temperature and pressure	760 °C, 101 kPa	700 °C, 9.2 kPa	640 °C, 101 kPa	810 °C, 400 kPa	760 °C, 101 kPa	~1700 °C, 101 kPa
Conversion, %	52.51	12	15	87.8	64.3	
Component						
hydrogen	2.08	0.11	0.059	1.6	0.34	7.13
methane	5.39	0.91	1.11	7.1	5.41	4.02
ethane	1.24	0.62	1.69	2.1	1.52	0.489
ethylene	23.1	4.25	4.02	47.8	32.0	12.45
acetylene				0.6		28.39
propane	0.39	0.053	0.13	0.5	0.38	0.052
propylene	7.47	2.24	2.98	17.3	13.3	0.779
methylacetylene				0.3	0.00	0.247
allene				0.1	0.00	0.067
n-butane	0.070		0.12	tr.	0.08	0.0031
isobutane				0.2	0.00	0.000
1-butene	4.84	1.83	2.26	4.6	6.28	0.105
trans-2-butene	0.11			0.5	0.26	0.0024
cis-2-butene	0.10					0.0019
isobutene				0.1	0.00	0.0010
1,3-butadiene	1.17		0.13	4.3	2.02	0.106
vinylacetylene						0.207
1-butyne (ethylacetylene)						0.0068
2-butyne (dimethylacetylene)						0.0007
diacetylene						0.354
n-pentane						0.0074
isopentane	0.042				0.05	0.0038
neopentane						0.000
cyclopentane						0.0018
1-pentene	1.91	1.27	1.69		1.72	0.0193
trans-2-pentene	0.070				0.09	0.0006
cis-2-pentene	0.10					0.0004
2-methyl-1-butene						0.0002
2-methyl-2-butene						0.0012
3-methyl-1-butene						0.0007
cyclopentene						0.000
isoprene						0.000
cyclopentadiene				0.3		0.012
n-hexane						0.0017

Table 1. *Cont.*

Reference	[61]	[57]	[59]	[58]	[62]	[43]
cyclohexane						
methylcyclopentane						
cyclohexene						0.0003
1-methylcyclopentene						0.00
1-hexene	0.82	0.71	0.81		0.55	0.00
trans-2-hexene						0.0001
cis-2-hexene						
benzene				0.4		0.020
other NA C_5–C_6				3.7		
n-heptane	47.5	88.0	85.0	12.2	35.7	45.1
toluene				0.1		0.0005
ethylbenzene				traces		
xylenes				traces		
styrene				traces		
naphthalene				traces		
other C_7–C_{12}				traces		0.390
C_{12+}				traces		
CO	3.57				0.24	
CO_2					0.06	
SUMMA	100.0	100.0	100.0	100.0	100.0	100.0

In microwave discharge [43], among the products, acetylene and its homologs, as well as allene, absent in low-temperature experiments [57,59,61,62], were determined. The same products were fixed at temperatures of more than 800 °C in flow reactors [58,60] and in the shock tube [41,42]. High yields of acetylene and hydrogen are obtained in [43], which indicates high temperatures in the discharge. This is confirmed by estimated temperatures based on the emission Swan bands.

Comparison of the results of chemical analysis of products obtained in a microwave discharge [43] in liquid *n*-heptane and barrier discharge [66–68] showed that the composition of products obtained in microwave discharge is much richer.

The main gas products and their related concentrations in microwave discharge in *n*-heptane are in agreement with the results of modeling [22,25,26]. Composition of main gas products of microwave discharge in different hydrocarbons is shown in Table 2.

The results shown in Table 2 can be summarized as follows:

- Increase of the molecular weight of alkanes is accompanied by increase in the yield of acetylene and decrease in the yield of hydrogen (in the series C_7–C_{16}, including cycloalkanes).
- Hydrogen and acetylene are predominantly formed in aromatic compounds.
- Gas products of microwave discharge in the investigated liquid cycloalkanes and aromatic compounds without radical groups practically do not contain methane or ethylene. As the number of radical groups increases, the composition approaches the composition of the discharge products in alkanes.

Estimations based on results of experiments with microwave discharge in liquid dodecane showed that the amount of energy needed to generate 1 mol of hydrogen is 640 kJ/mol [28].

Table 2. Relative volume concentrations (relative to hydrogen concentration) of the main gas products of microwave discharges in liquid hydrocarbons at atmospheric pressure (numbers in brackets show the volume concentration of hydrogen).

Hydrocarbon, Boiling Temperature and Structure of Molecule	H_2	CH_4	C_2H_4	C_2H_2	Ref.
n-Heptane C_7H_{16} (T_{boil} = 98.2 °C)	(71.2) 1	0.042	0.11	0.25	[44]
n-Heptane + Ar 0 6.8 L/h 17.3 36.8	1 1 1 1	0.059 0.049 0.037 0.040	0.18 0.23 0.26 0.18	0.27 0.31 0.34 0.28	[43]
n-Octane C_8H_{18} (T_{boil} = 125.52 °C)	(72) 1	0.03	0.104	0.25	[44]
Decane $C_{10}H_{22}$ ((T_{boil} = 174.1 °C)	(71.7) 1	0.024	0.088	0.28	[44]
Dodecane $C_{12}H_{26}$ (T_{boil} = 216.2 °C)	(74) 1	0.027	0.027	0.27	[28]
Pentadecane $C_{15}H_{32}$ (T_{boil} = 270.6 °C)	(67.6) 1	0.019	0.09	0.37	[44]
Hexadecane $C_{16}H_{34}$ (T_{boil} = 286.79 °C)	(65.6) 1	0.015	0.083	0.43	[44]
Isooctane C_8H_{18} (T_{boil} = 99.3 °C)	(71) 1	0.087	0.057	0.26	[44]
Cyclohexane C_6H_{12} (T_{boil} = 80.74 °C)	(73.4) 1	0	0.12	0.24	[44]
Benzene C_6H_6 (T_{boil} = 80.1 °C)	(88.80) 1	0	0	0.13	[44]
Toluene C_6H_5-CH_3 (T_{boil} = 110.6 °C)	(86.1) 1	0.021	0	0.14	[44]
Ortho-xylole C_6H_5-$(CH_3)_2$ (T_{boil} = 144 °C)	(74.6) 1	0.048	0.075	0.19	[44]
Petroleum solvent "Nefras S2 80/120" (mixture of light hydrocarbons with boiling temperature range of 33–205 °C)	(66.5) 1	0.09	0.13	0.3	[44]

Hydrogen is the main component of exhaust gases of microwave discharge in any liquid hydrocarbons independently of the method of plasma generation. This is illustrated by the results in [48], where microwave discharge is generated in the presence of ultrasonic oscillation (Figure 2d) at pressure 250 hPa. Measured volume concentration of hydrogen in different liquids were: 81/79 in *n*-dodecane, 67/76 in benzene, 66/73 in cooking oil, 71/65 in waste cooking oil, 74/65 in engine oil and 73/65 in waste engine oil (here, the numerator corresponds to the results obtained in case of combine action of microwave and ultrasonic radiation and the denominator corresponds to the results obtained in the case of switching off the ultrasonic radiation just after the ignition of discharge).

Several comments should be done on the role of electron impact in the process of hydrocarbon decomposition in microwave discharge in liquid hydrocarbons. This problem was considered in detail for the case of plasma in liquid *n*-heptane [19,20,69]. 2D modeling shows that:

(i)   Electron-impact dissociation occurs only in a narrow region adjacent to the electrode because the microwave field is concentrated near the end of central electrode and falls rapidly with increasing distance from it.

(ii)   Electron impact affects the dissociation of *n*-heptane only during a short time period from discharge ignition ($\leq 10^{-3}$ s), when the gas temperature is low (<1300 K).

(i)   At times greater than 10^{-3} s, the dissociation of *n*-heptane occurs thermally. The role of plasma electrons in the decomposition of *n*-heptane is reduced to heating the gas inside the plasma bubble (Figure 6).
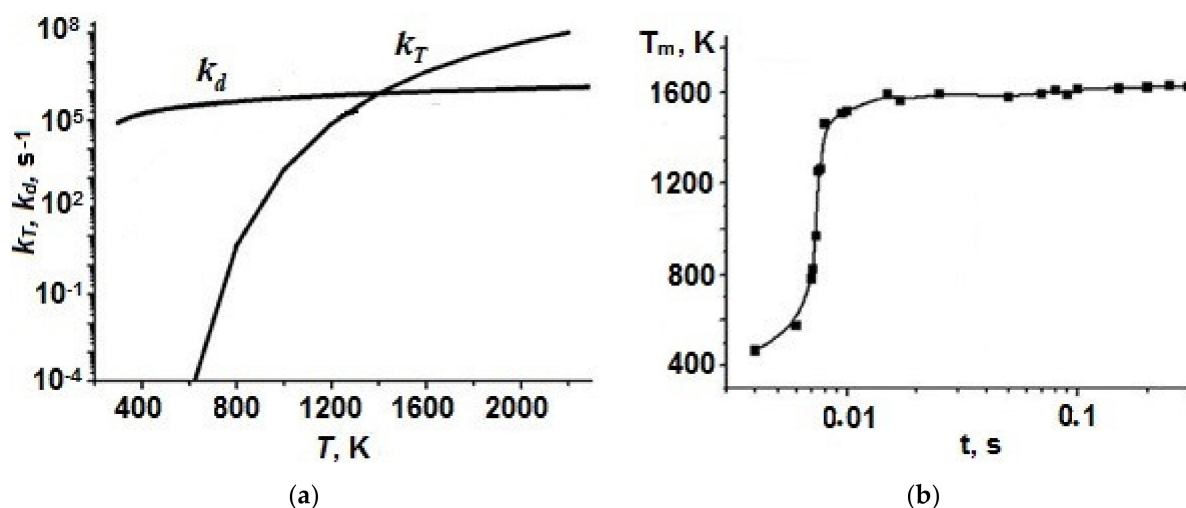
Figure 6. (**a**) Rate constants of thermal dissociation (k_T) and electron impact dissociation (k_d) at microwave field 1.5×10^4 V/cm and electron density $n_e = 10^{14}$ cm^{-3}; and (**b**) change of maximum gas temperature in time.

4. Solid Products of Microwave Discharges in Liquid Hydrocarbons

It is known that MW discharges in liquid hydrocarbons are accompanied by formation of nanosize carbon-containing particles (see, e.g., [28,31]) and the liquid becomes saturated with black particles and loses its transparency both for microwaves and light.

The first question is where the solid phase is formed by the discharge in liquid hydrocarbons, namely in the liquid phase or in the region of gas-phase microwave discharge. On the one side, numerous investigations of various gas discharges in carbon-containing media at atmospheric pressure point to efficient formation of sooty particles. On the other side, in the case of in-liquid microwave discharge, the question is caused by the fact that insignificant amounts (<1%) of polycyclic aromatic hydrocarbons are detected in liquid hydrocarbon after centrifugation and isolation of dispersed phase 29 (this result is analyzed in Section 4). These polyaromatic compounds can be precursors of creation of carbon-containing particles directly in liquid hydrocarbons.

To answer the question, we took snapshots of discharge chamber immediately after processing of heavy hydrocarbon (engine oil) in discharge when hydrocarbon has not yet been heated (Figure 7). Engine oil with high viscosity is chosen for visualization of traces of solid particles in order to suppress the turbulence of the liquid and the spreading process of particles. The snapshot (Figure 6a) exhibits a column of soot particles spreading up from the tip of the antenna into the liquid. Thus, we can conclude that carbon-containing particles are produced in the region of gas bubble with microwave discharge at the tip of the antenna. Then, the particles are transferred into the liquid. Vortex flows (Figure 6b) emerging during heating the liquid hydrocarbon spread the solid particles over the entire volume of the liquid.

(**a**) (**b**)
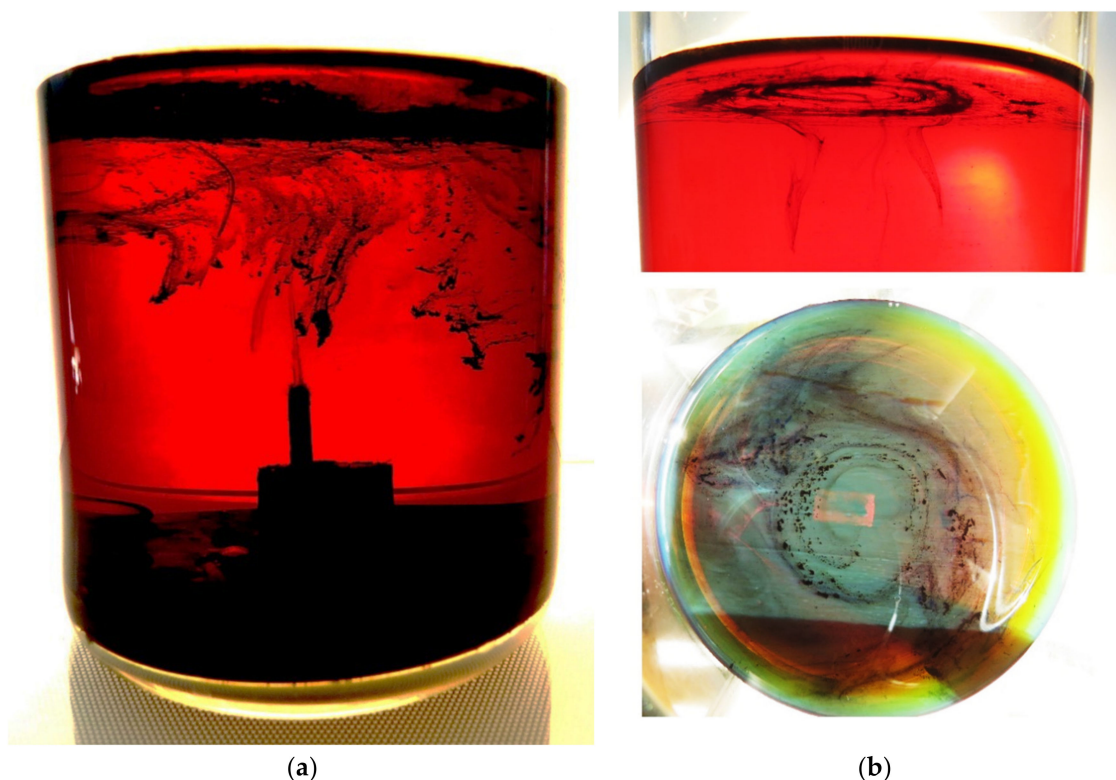
Figure 7. Snapshot of traces of carbonaceous particles in the engine oil just after switching-off the microwave discharge (**a**); and view of vortex structure creating by solid particles (**b**).

Solid particles produced by in-liquid MW plasma at atmospheric pressure in a series of alkanes (C_nH_{2n+2}, n = 7, 8, 10, 15, 16) are studied in [31]. These hydrocarbons differ in their molecular mass and boiling points (*n*-heptane: 98.42 °C; isooctane: 99.24 °C; decane: 174.1 °C; hexadecane: 286.79 °C). The alkanes were chosen for several reasons. Firstly, as with all nonpolar hydrocarbons, alkanes possess low loss tangent in the microwave range ($\sim10^{-4}$). This made it possible to neglect their direct heating by microwave field. They all have nearly the same dielectric constant (~2) in the microwave frequency range. The study [31] was run in the discharge produced by a resonance antenna (Figure 2a), which was the same in all experiments with all hydrocarbons. Secondly, all alkanes are transparent in the visible range of electromagnetic spectrum, which is important for carrying out optical and spectral measurements of in-liquid plasma.

Figure 8 shows SEM micrographs of the solid products obtained after centrifugation of various liquid hydrocarbons processed with microwave plasma. The size of the grains lays in the range of 100–200 nm, the size increasing with an increase in the number of carbon atoms per hydrocarbon molecule.

EDS analysis of the solid samples for partial contents of carbon, oxygen and copper atoms has shown that the samples consist of carbon (80–90%), oxygen (2–15%) and copper (below 2%). Oxygen content lowers and the concentrations of other elements grow with raising the number of carbon atoms in the hydrocarbon chain.

Occurrence of oxygen in the analyzed samples cannot be attributed to the action of plasma because plasma was produced in oxygen-free atmosphere. It should be noted that the carbonaceous products, after isolation from the plasma reactor, were kept in air atmosphere before subjected to further analysis by, e.g., FTIR and Raman methods. It is known that adsorption of nitrogen and oxygen on carbon materials is nearly the same, while the rate of nitrogen absorption is ten times lower than the rate of oxygen absorption. Carbon nanostructures effectively adsorb the oxygen from the ambient atmosphere [70]. Oxygen is frequently observed in the carbonaceous materials produced in plasma after exposing to the air. Insignificant amount of copper in the samples is explained by the fact

that the quarter-wave antenna employed in our case to excite the discharge was made from copper. Plasma erosion of this antenna could be a source of copper contamination.
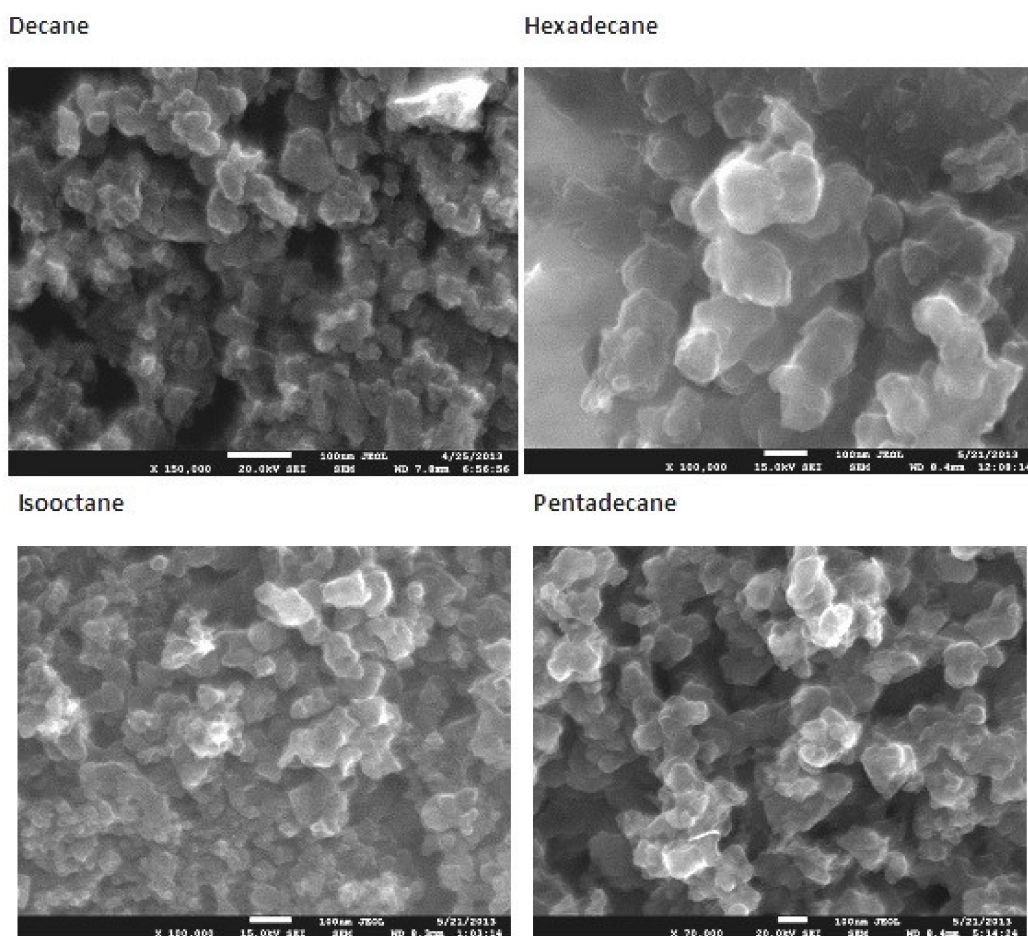
Figure 8. SEM micrographs of the solid products of microwave plasma in different liquid hydrocarbons.

For all solid studied products, Raman spectra have exhibited a set of necessary bands permitting to categorize these solids as a "damaged graphene", and mainly not single-layered one. NMR spectra of solid products obtained from *n*-heptane, isooctane and pentadecane reveal that generation of MW plasma in liquid alkanes leads to strong aromatization and formation of various unsaturated molecular fragments in solid products.

The results in [28], obtained in microwave discharge in liquid dodecane, show that hydrogen at a rate of 26 mL/s was simultaneously produced with carbon-contained solids at a maximum rate of 4 mg/s in this process.

Additional information should be obtained for the solid product deposited on the tip of antenna when discharge was generated in liquid hydrocarbons having high viscosity. Microwave discharge in such hydrocarbons (e.g., engine oils, crude oil and liquid residues of heavy petroleum feedstock) produces growth of tree-like structure on antenna (see Figure 9).

(**a**)   (**b**)

Figure 9. Photographs of tree-like structures formed: in microwave discharge in liquid engine oil (**a**); and in liquid residues of heavy petroleum feedstock (**b**).

These solid products have special interest for the processing of crude oil and liquid residues of heavy petroleum feedstock. The results in [71–73] demonstrate a possible new field in application of microwave discharges in liquid hydrocarbons related with extracting a concentrate of valuable metals contained in heavy petroleum and liquid residues of heavy petroleum feedstock.

Heavy crude oil and heavy products of its processing are characterized by an increased content of compounds of some valuable metals (V, Ni, Mo, Co, etc.) [74]. These metals are usually present in combination with naphthenic acid as soaps and in the form of complex organometallic compounds such as metalloporphyrins. Existing methods for extracting metals from heavy petroleum feedstocks (deasphalting and demetallization) either do not give the required degree of purification of raw materials from metal compounds or their use on an industrial scale is not economically feasible (multi-stage, energy-consuming and capital-intensive processes). Therefore, an important task is to search for new methods for isolation of metals. The results in [71–73] show that microwave discharge in these liquid compounds give a promising path to solve this problem. The results are summarized in Table 3. One can see that the material deposited on the antenna contains 10–20 times higher concentrations of metals than those in the source heavy hydrocarbons.

Table 3. Illustration of enrichment of products of microwave discharge in crude oil and liquid residues of heavy petroleum feedstock in valuable metals.

Metals	Content of Metals (Weight %)			
	Source Crude Oil [72]	**Tree-Like Structure on Antenna [72]**	**Source Heavy Petroleum Feedstock [71]**	**Tree-Like Structure on Antenna [71]**
Al	0.00028	0.0028	0.0019	0.0068
Co	0.000053	0.00012	0.000047	0.0006
Cu	0.0002	0.0014	0.00065	0.0025
Fe	0.00064	0.0032	0.0019	0.034
Mo	0.00032	0.00067	0.067	0.98
Ni	0.008	0.013	0.0049	0.018
V	0.057	0.089	0.019	0.071
Zn	$\leq$0.000002	0.00028	<0.000002	0.002

The reason for this phenomenon is not entirely clear. It can be expected that the formation of a tree-like structure and its enrichment by metals are coupled phenomena and due to the transfer of charged particles to the antenna. It is well known that any object immersed in plasma gains negative charge relative to plasma. This causes transportation of positively charged particles from plasma to this object. Microwave antenna is such an object. The tip of the antenna is surrounded with plasma, which provides the charged particles flux to its surface. Positively charged particles are the "bricks" to build the tree-like structure. Heavy charged particles, among other things, contain cations of metal-containing oil complexes [75].

5. Liquid Hydrocarbons after Treatment by Microwave Discharge

After removal of the carbon-containing solid particles formed in the discharge from liquid hydrocarbons (centrifuged at 3000 rpm for 10 min), the initially transparent colorless liquids acquired color (Figure 10).
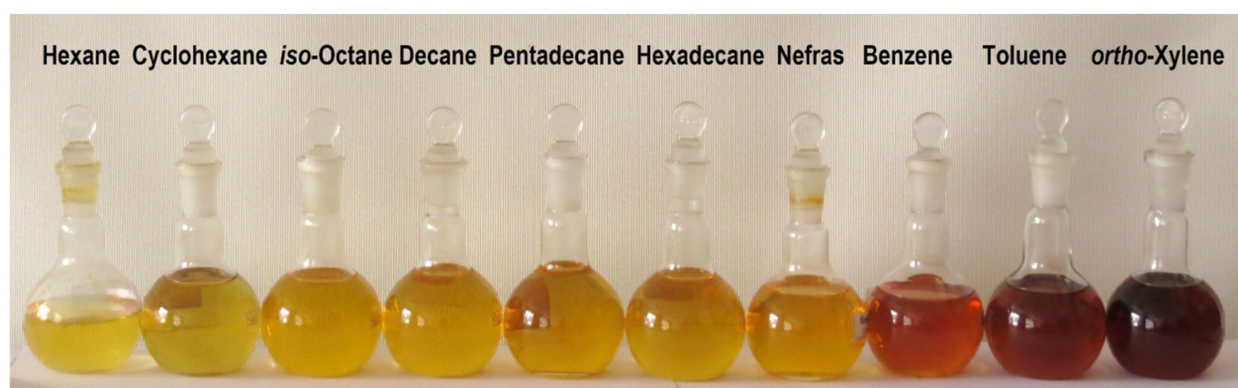
Figure 10. Photos of colored liquid hydrocarbons after treatment by microwave discharge and disposal of solid particles.

Hydrocarbons thus purified were analyzed by GC/MS [76]. The composition of the liquid was determined by GC/MS on a Thermo Focus DSQII gas chromatography/mass spectrometer. It was shown that the composition of the liquid hydrocarbon determined by this method does not differ from the initial one (some examples are given in Figure 11).

To measure the minor impurities that were not detected in the measurements described above, the sample was concentrated by evaporation and residue was analyzed on the same device as above. In addition, a Bruker Tensor II FT-IR spectrometer was used for the analysis.

Residues contain a wide spectrum of hydrocarbons up to C40. Detected substances such as naphthalene, acenaphthylene and dicotylphthalate have a color from light yellow to brown. They can give color to hydrocarbons after microwave plasma treatment.

FT-IR spectra of the evaporated precipitate detect the presence in the sample of unsubstituted polyaromatic compounds such as naphthalene and phenanthrene, as well as nitrogen-containing aromatic compounds such as pyroll.

In [77], a study is presented of the evaporated sediment of liquid hydrocarbons after the ignition of a microwave discharge in them with bubbling air. The authors showed that, despite the fact that plasma is created in the presence of air, oxygen- and nitrogen-containing products are practically not observed in liquid hydrocarbons. It means that the composition of the plasma has practically no effect on the surrounding hydrocarbon.
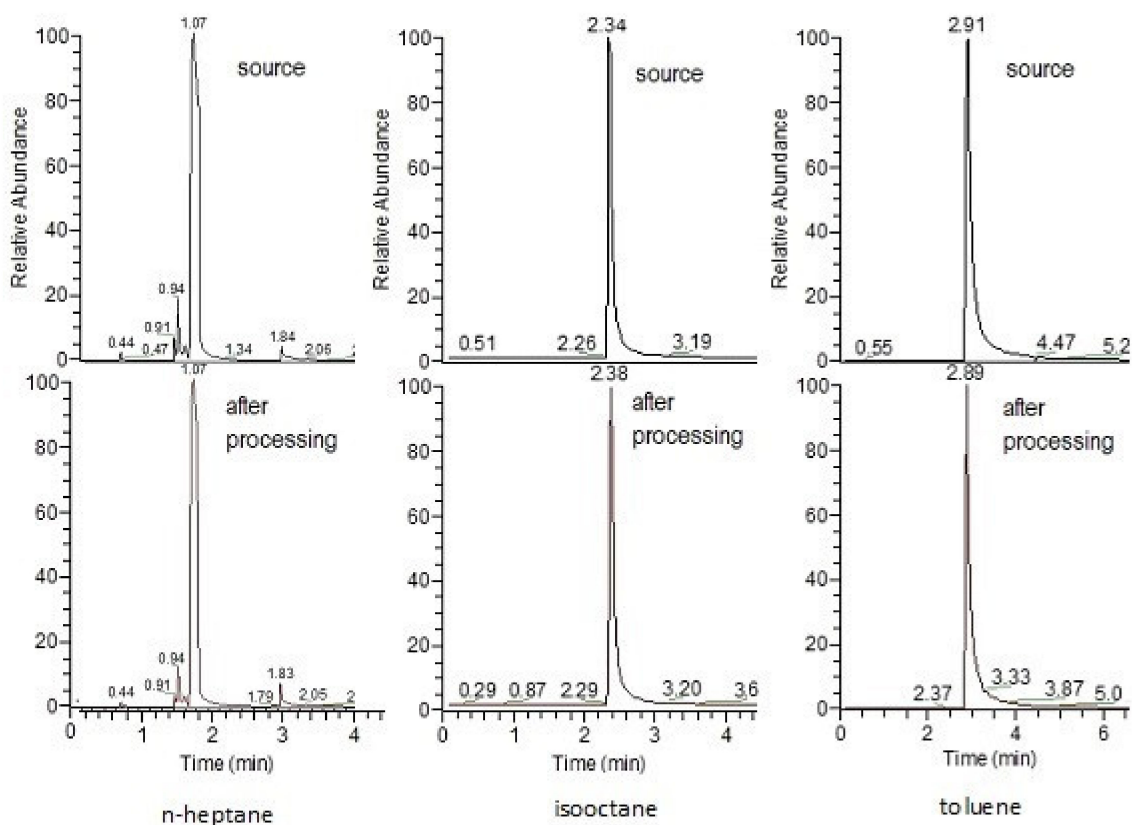
Figure 11. Examples of main components detected in: the source hydrocarbons (**top**); and processed hydrocarbons (**bottom**).

It should be noted that all these substances are contained in hydrocarbons in trace quantities.

Changes in the liquid *n*-hexane and *n*-heptane after treatment in microwave discharge are also studied in [78]. Discharge was ignited in liquids mixed with carbon fiber. Products C_8–C_{12} were identified. In *n*-hexane, these substances are (in mg/L): phenylethyne C_8H_6 (0.85), styrene; 1,3,5,7-cyclooctatetraene C_8H_8 (0.45), ethylbenzene C_8H_{10} (0.41), naphthalene $C_{10}H_8$ (0.31) and 4-propylheptane $C_{10}H_{22}$ (0.91). In *n*-htptane, they are: phenylethyne (4.9), styrene; 1,3,5,7-cyclooctatetraene (10.7), naphthalene (8.4) and biphenylene $C_{12}H_8$ (2.8).

It is known that the color of a liquid can be imparted by nanoparticles contained in it, which are not removed by centrifugation and do not precipitate. An example is solutions containnig fullerenes [79] or metal nanoparticles due to surface plasmon resonance [80]. To indicate the nanoparticles and determine their sizes, the method of dynamic light scattering was used with the analysis of the spectral power density of Doppler shifts (light beat spectroscopy). The measurements were carried out on a Zetatrac laser (λ = 750 nm) analyzer (NanotracWave) using the reflection method (the scattered signal recording angle was 180° with respect to the direction of the primary beam). The range of sizes of scattering particles registered by the device (their hydrodynamic diameters) was 0.001–6.500 μm. Signal processing and calculations were performed in the approximation of optically opaque spherical particles.

It was shown that the hydrocarbon contains nanoparticles with sizes of 1–3 nm. Some of results are shown in Figure 12.

The naphthalene and acenaphthylene found in the liquid at room temperature are crystals (melting temperature ≥80 °C), and thus it can be assumed that these crystals are the detected nanoparticles in the solution.
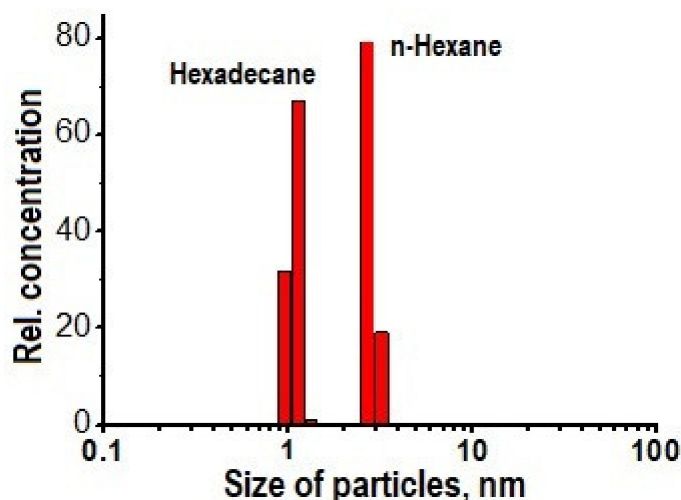
Figure 12. Examples of nanoparticles detected in processed hydrocarbons.

6. Basic Information about Plasma Properties (Diagnostics and Modeling)

6.1. Diagnostics

The main, if not the only, method for determining plasma parameters in liquids, including liquid hydrocarbons, is optical emission spectroscopy. The results of using this method for diagnosing a microwave discharge at atmospheric pressure in liquid hydrocarbons are given in [30,45,81].

Optical emission spectra of microwave discharge in liquid *n*-heptane with and without bubbling of argon and air are shown in Figure 13. The spectrum of the microwave discharge without bubbling gases is represented by Swan bands (transition $C_2\left(d^3\Pi_g - a^3\Pi_u\right)$) sequences $\Delta v = 0$ (maximum at 516.5 nm), $\Delta v = 1$ (maximum at 563.5 nm), $\Delta v = -1$ (maximum at 473.75 nm) and $\Delta v = -2$, and the band at 436.5 nm ($\Delta v = -2$) is overlaid with the 0-0 emission band of CH at 431.2 nm (CH transition $CH\left(A^2\Delta - X^2\Pi\right)$). No hydrogen emission lines and bands are observed. In addition, a broadband emission spectrum of solid carbon-containing particles is observed (see the curve for C_7H_{16} in Figure 13). This continuum gives the temperature of solid particles in the range 3500–4000 K.
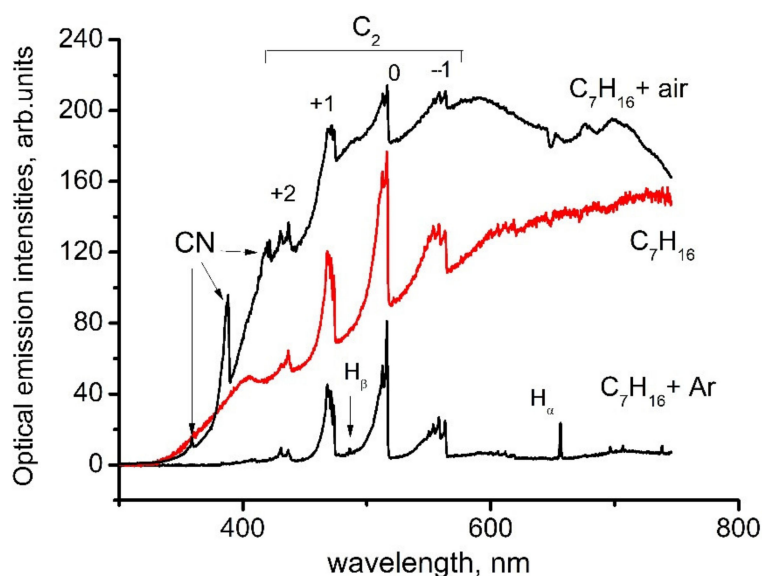
Figure 13. Examples of optical emission spectra of microwave discharge in liquid pure *n*-heptane and with bubbling of Ar and air. Spectra are given in arbitrary units for clear illustration the role of bubbling gases.

A similar structure of the spectrum is also observed at low argon consumption.

At high argon consumption, the structure of the spectrum changes qualitatively [43]. The H_α line appears in it (the threshold is 12.09 eV), and, as the argon consumption increases, the H_β line (the threshold is 12.75 eV) and the argon emission lines with thresholds of the order of 13.3 eV also appears. Since the excitation of the emitting states of atoms occurs in collisions with electrons, the appearance of atomic lines in the emission spectrum indicates an increase in the role of electron impact with the addition of argon. This effect is discussed in detail in [43]. In addition, the radiation intensity of the continuum decreases (see the lower curve in Figure 13), which is associated with a decrease in the rate of formation of carbon-containing particles due to dilution of hydrocarbon vapors with argon.

The appearance of hydrogen lines upon the addition of argon made it possible to determine the range of microwave field strengths in plasma. The calculations were carried out under the assumption that the excitation of the emission of hydrogen lines occurs by electron impact. The electric field strength is in the range of 2000–4000 V/cm [43].

Air bubbling leads to the appearance of CN bands (358.4, 388.3 and 421.6 nm) in the emission spectrum. The emission of hydrogen lines and bands, as in the discharge without bubbling, is not observed (Figure 13).

The unexpected results were obtained during the study of plasma emission spectra in aromatic hydrocarbons [45]. The sequence of Swan band with $\Delta v = 0$ in spectra measured in toluene and *ortho*-xylene was overlapped with the molecular emission band with maximum at 511 nm. Attempts to measure spectra of discharge in benzene were unsuccessful as spectra were presented by continuum emission of solid particles. The most pronounced additional band was observed in experiments with toluene. With an increase in the number of CH_3 groups in a molecule (one group is in toluene and two groups are in *ortho*-xylene), the intensity of additional band decreases and it almost disappeared in other hydrocarbons. It seems that trace of this band presents in spectra of plasma in other liquid hydrocarbons.

Analysis of literature data [45] bring to conclusion that this emission can be caused by emission of linear carbon cluster C_5 (transition $C_5\left({}^1\Pi_u \rightarrow X^1\Sigma_u^+\right)$). This cluster was previously observed only in absorption. This means that microwave discharge in liquid aromatic hydrocarbons produced particular conditions for C_5 generation and its emission.

Several reasons can lead to a high concentration of C_5 in a microwave discharge in liquid aromatic hydrocarbons. First, and this fact is noted in many publications on microwave discharges in liquids, the rates of product formation in microwave discharges are higher in comparison with other discharges. This is caused by high rates of formation of active particles. Another reason of high concentration of the emitting state of the C_5 linear cluster can be effective stabilization of hydrocarbon decomposition products, which is caused by a large temperature gradient (at the center of discharge the temperature is of 2000 K, and at the boundary the temperature is equal to the boiling point of the hydrocarbon). The observation of a new emission band only in aromatic hydrocarbons may be because the rate of formation of the solid phase in them is much higher than in other hydrocarbons. It was shown in our experiments. Therefore, it can be expected that the rate of formation of active particles is also high.

Sequences of Swan bands are often used for calculation of rotational temperature T_r in plasma. This procedure can be realized in two methods. One is the use of spectral devices with high wavelength resolution. It makes possible building the Boltzmann plot of rotational population to calculate the rotational temperature. Use of low-resolution optical devices give nonresolved rotational structure of spectrum and T_r as usual can be obtained from comparison of measured and modeled spectra of Swan sequences. The last method was used for processing of Swan sequences in [30,45,81].

Analysis of the obtained spectra of Swan bends showed that the sequence $\Delta v = -1$ is the least noisy. Moreover, this sequence is free of overlapping with other bands. Thus, this sequence fives more reliable information on the rotational temperature. In the microwave

discharge in all studied hydrocarbons, the rotational temperature T_r turned out to be the same and equal to 2000 ± 300 K.

In the experimental conditions described above T_r is equal to the gas temperature T_g. The problem of equality of rotational and gas temperatures for these conditions was analyzed in detail in [80]. To satisfy the equality $T_r = T_g$, it is necessary to fulfill several conditions [82]: (I) the characteristic time of energy exchange between translational and rotational degrees of freedom (τ_{exch}) is much less than the time of their radiative decay (τ_{rad}) and less the times of the processes leading to a change in the population of radiating levels of molecules; (II) τ_{exch} is much less than the residence time of molecules in the discharge zone; and (III) there is no radiation distortion due to reabsorption, refraction and reflections from elements of the optical system, among others. The results in [81] show that in our case these requirements are satisfied.

Thus, it was shown that the gas temperature in microwave plasma in a wide class of liquid hydrocarbons (alkanes, cyclic and aromatic hydrocarbons) at atmospheric pressure does not depend on the type of hydrocarbon and is equal to 2000 ± 300 K [45].

With decreasing pressure together with Swan bands, emission lines of atomic hydrogen appear in the emission spectrum of a microwave discharge in liquid hydrocarbons. Plasma excitation temperature determined from the relative intensities of the H_α and H_β lines was approximately 5000 K [48].

A large amount of information about plasma parameters and processes in it can be obtained by modeling a discharge.

6.2. Modeling

In its simplest form, modeling consists of solving electrodynamic problems that allow choosing the optimal geometry of a microwave reactor, taking into account the electrical properties of a liquid hydrocarbon, but without taking into account plasma. It gives the dimensions of the antenna and the strength of the microwave field at its end where the plasma will be generated [14–17,30,44]. For example, as noted above, this made it possible to carry out a comparative analysis of the reactor with a quarter-wavelength antenna and with coaxial energy input into the discharge and show the lower sensitivity of the latter to the antenna length (and its possible change due to the deposition of carbon-containing particles) [44].

A microwave discharge in liquid *n*-heptane at atmospheric pressure has been studied in most detail by the method of mathematical modeling. 2D, 1D and 0D models of the discharge have been developed, including those in *n*-heptane with argon bubbling.

6.2.1. 2D Model: Problem Formulation and Main Results

The model describes the system with coaxial input of microwave energy in reactor filled with liquid *n*-heptane. In 2D model [19,20] the following assumptions was made:

- Gas bubbles are created by evaporation of liquid into the bubble.
- In plasma formed inside the bubble, the main ion is $C_7H_{16}^+$.
- Heating of the bubble is due to Joule heating of plasma electrons.
- Cooling of the bubble is due to energy transfer to ambient liquid for evaporation and endothermic pyrolysis of *n*-heptane.
- The size and shape of the bubbles is determined by the surface tension and the sum of the pressure forces.
- Lifting of the bubble is determined by the Archimedean force and viscosity.
- The initial temperature of the liquid and gas phase is equal to the boiling point.
- A small bubble of evaporated gas of atmospheric pressure is set inside the near-electrode cavity.

Here, we note that the model contains only a simplified brutto mechanism for the dissociation of *n*-heptane, and detailed kinetics of gas products and solid carbonaceous particles is absent.

The code is based on joint solution of the Maxwell equations, Navier–Stokes equation, heat conduction equation, continuity equations for electrons (written in the ambipolar diffusion approximation) and the *n*-heptane concentration (including its thermal decomposition and dissociation by electron impact), the Cann–Hillard equation described the gas–liquid transition layer and the Boltzmann equation for free plasma electrons.

The main results of the simulations can be formulated as follows:

- Boiling process depends on the input power. There is a certain range of input power, when there is a regime of periodic formation of bubbles and their further rise.
- The plasma burns only inside the bubble, in close proximity to the central electrode. When a bubble floats up, plasma disappears inside it. This is due to the fact that the microwave field is concentrated near the end of the central electrode and falls very sharply outside it. At a power >500 W, the microwave field at the electrode end reaches 10 kV/cm. The temperature in this area is about 1500–1700 K, which is in good agreement with our experimental data. The maximum electron density is about 10^{14} cm^{-3}.
- As the bubble rises, it cools very quickly due to energy transfer to ambient boiling liquid needed for its evaporation. Thus, temperature of the rising bubble very soon becomes approximately equal to the boiling point.
- For times less than 10^{-3}, the dissociation of *n*-heptane occurs under the action of electron impact, and then is dominated by thermal dissociation. The role of the plasma is reduced to the formation of gas bubbles and initiation of thermal reactions.

6.2.2. Modeling of Carbonaceous Particle Growth

Carbonaceous particles are one of the main products of microwave discharge in liquid hydrocarbons. According to modern views, the soot formation includes the following stages: decomposition of the starting hydrocarbon into a variety of radicals and stable molecules, the formation of molecular precursors of the soot from these fragments, surface growth and coagulation of solid particles. The growth of carbonaceous particles in microwave discharge in liquid *n*-heptane was considered in the frame of 0D [21] and 1D [22] models.

The models contain the detail mechanism for *n*-heptane pyrolysis, as published in [49,83]. Acetylene is the most important agent in the formation of soot particles. The mechanism published by Wang and Frenklach [84] for the description of pyrolysis of acetylene was used.

It is currently believed that the formation of precursors of carbonaceous particles (nuclei) comes from polyaromatic hydrocarbons (PAH) in reactions with acetylene and other hydrocarbons. According to the well-known HACA mechanism ("H-abstraction-C_2H_2-addition"), the growth of molecules occurs when the sequence of two stages is repeated: detachment of the H-atom from the molecule of PAH due to collision with other H-atom and addition of the molecule C_2H_2 from the gas phase to the vacant site.

The linear and planar mechanisms of the molecular precursor size growth were considered, but the best results in comparison with results of experiments ware obtained for planar mechanism. This mechanism is presented below.

At the first stage of the formation of solid particles, polyaromatic hydrocarbons grow from pyrene to a nucleus molecule consisting of eight benzene rings. The mechanism of formation of the nucleus of a solid particle consists of a repeating sequence of addition of new aromatic rings in reactions with acetylene and hydrogen. Figure 14 shows the transition from pyrene to 1,12-Benzoperylene. Subsequently, these reactions are repeated until the formation of a nucleus consisting of eight benzene rings, and then the growth of a solid particle begins. Its superficial growth is carried out using the same chain of reactions. The surface of the soot particle is considered as the edge of a large PAH molecule covered with C–H bonds. This assumption determines the nature of the active centers, which interact with acetylene molecules from the gas phase, and makes it possible to calculate the growth rate of the particle surface.
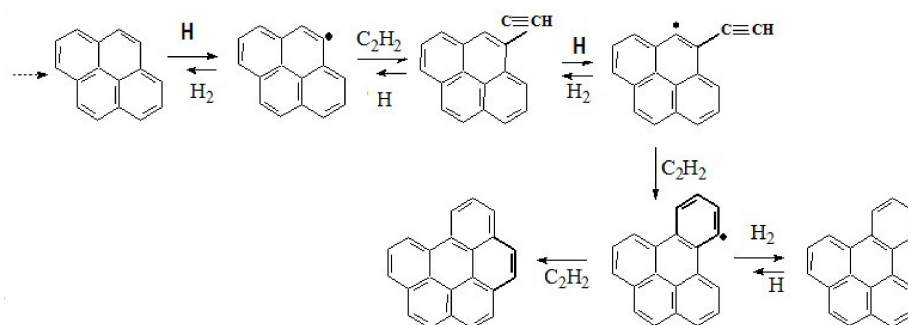
Figure 14. The mechanism of formation of the precursor molecule.

For the coagulation of solid particles, an equation of the type of the Smoluchowski equation was used.

Solids are classified into 17 groups based on their size. The maximum size of the particles considered in the model is about 20 nm.

A full set of balance equations for each component of the gas phase and solid products has been solved numerically. The kinetic simulations have been implemented using COMSOL Multiphysics—Reaction Engineering Laboratory. The processes take place inside a spherical bubble, which is regarded as a continuous stirred tank reactor (CSTR) of constant pressure and volume with continuous input of gaseous *n*-heptane, which evaporates into the bubble from the external liquid.

Some simulation results are shown in Figures 15 and 16.
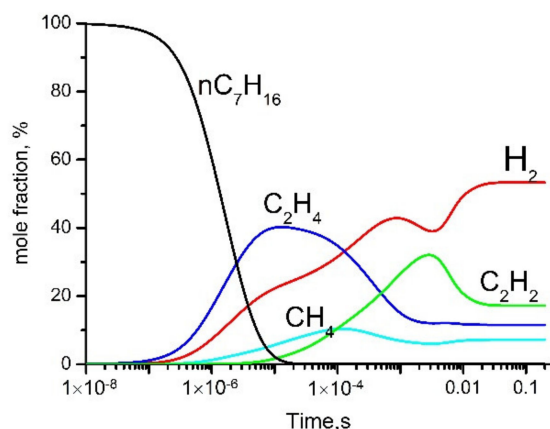
Figure 15. Evolution of gas phase products. Simulation at T = 1500 K, p = 1 atm.
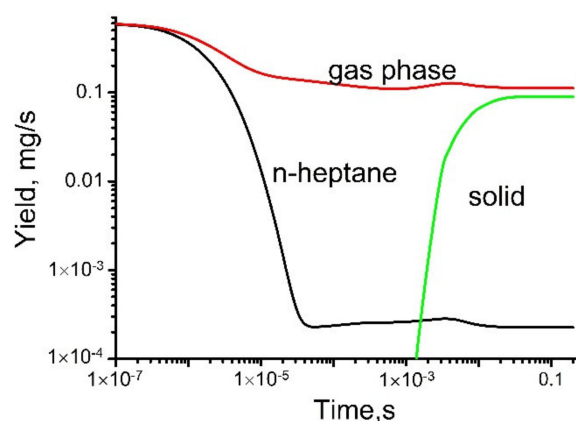
Figure 16. Evolution of the total yields of the gas-phase and solid products and rate of *n*-heptane loss.

The modeling approach used in [21] was applied by the authors of [22] within a one-dimensional model to study plasma processes in a gas bubble surrounded by liquid *n*-heptane. A shortened kinetic scheme of chemical processes was designed and used which gives a good match with the full scheme. The problem was solved in the approximation of spherical symmetry at atmospheric pressure. It was believed that the central electrode is located in the center of a gas bubble of a given diameter, surrounded by a liquid. The size of the bubble was taken from experiments. The model takes into account the influx of vaporized *n*-heptane molecules from the liquid phase surrounding the gas bubble.

It was shown that microwave field drops sharply near the electrode, and then is almost constant along the radius. When the gas temperature reaches about 1000 K, a sharp decomposition front of *n*-heptane appears which moves to the boundary of the gas bubble with speeds of the order of several tens of centimeters per second. The temporal distributions of the gas temperature, electron concentrations, main gas-phase products, solid particles and microwave field were obtained. Table 4 shows the comparison of calculated and obtained in experiment concentrations of main gas products. The data of modeling were obtained by averaging stationary profiles of gas products over the volume of the bubble. The calculation results are consistent with the results of experiment.

Table 4. Contents of stationary concentration of main gas products of microwave discharge in liquid *n*-heptane obtained in experiment [42] and modeling [22].

Products	H_2 (vol. %)	C_2H_2 (vol. %)	C_2H_4 (vol. %)	CH_4 (vol. %)
Exper. [42]/Model. [22]	71/63.5	18/23.8	8/7.5	3/5.2

6.2.3. The Role of Argon Bubbling and Charging of Carbonaceous Particle (0D Models)

Argon is often used to produce the gas bubble what simplify ignition of discharge in liquids. Thus, the discharge exists in the mixture of argon and vapor of hydrocarbon. The influence of argon on the properties of microwave plasma in bubble inside the liquid *n*-heptane is analyzed in [25] on the basis of non-stationary 0D model.

It is known that bodies immersed in plasma acquire a negative charge and are at a floating potential [85,86]. This phenomenon has been studied in detail when studying processes in the so-called "dusty plasma" [87,88]. Particle charging leads to a change in the coagulation conditions of particles and affects the process of their growth in plasma. The carbonaceous particles formed in microwave discharge in liquid *n*-heptane should be charged, and this process can influence both on plasma parameters and on particle growth. This complex problem was solved on the basis of the zero-dimensional non-stationary mathematical model described in detail in [25]. The model described in [25] was extended to take into account the charging process of particles and give possibility to analyze both effect of argon addition (with volume concentration $\theta = 0$–90%) and particle charging on the plasma processes. Thus, the model [26] is the most complete for microwave discharge in plasma bubble in *n*-heptane with admixture argon as it includes equations for the kinetics of neutral and charged plasma components, equations describing the formation and growth of solid particles from *n*-heptane decomposition products, an equation for the plasma microwave field and an equation of solid particle charging.

Herem we give the main results only.

Particle charging and the addition of argon do not affect the composition of the main gas-phase products, which are hydrogen and acetylene. It does not affect the composition of positive ions. The main ion is the $C_2H_2^+$ ion.

Charging the produced solid particles leads to the fact that the quasi-neutral plasma is mainly provided by a negative charge of solid particles, and the electron concentration is 1–2 orders of magnitude lower than the total concentration of positive ions. However, it should be noted that, with the introduction of a large portion of argon (80–90%), the difference between the total concentration of ions and electrons decreases (Figure 17). This

is due to the fact that the total concentration of solid particles decreases in the mixture of hydrocarbon vapor diluted with argon, which reduces the effect of an additional channel for charged particles loss on their surface.
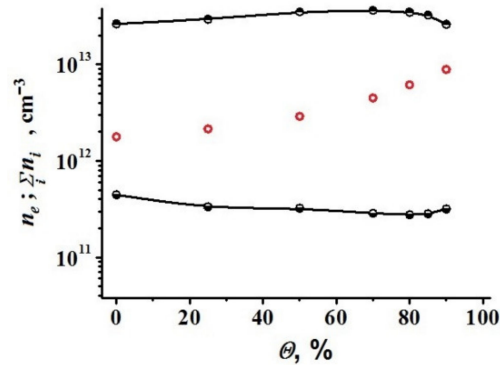
Figure 17. Dependences of the stationary values of the total concentration of ions (upper curve) and electrons (lower curve) on the volume fraction of argon introduced into the discharge. The curves are calculated taking into account the charge of solid particles. Hollow circles denote the equilibrium concentrations $n_e = \sum n_i$ obtained in calculations for the same power without taking into account the charge of solid particles. The power absorbed in the discharge is 50 W.

Particle charging suppresses the coagulation process for large solid particles and, accordingly, changes the size distribution of the formed solid particles and leads to the formation of maximum of the particle size distribution function in the medium-sized particle region (Figure 18).
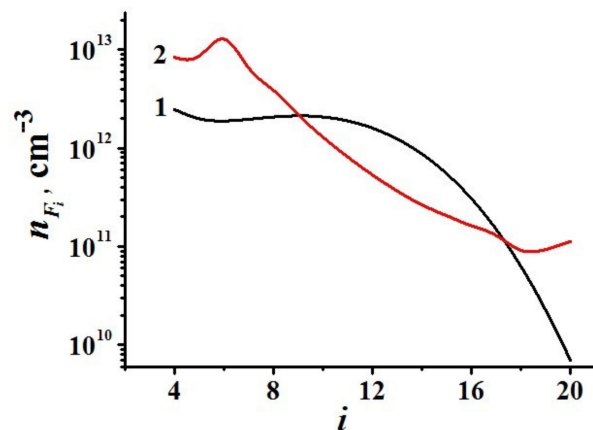
Figure 18. Concentrations of solid particles of groups F_i depending on their size. Index i characterizes a solid particle containing 2^i aromatic rings. Curve 1 is obtained taking into account the charging of solid particles, while Curve 2 is obtained without taking into account charging. The volume fraction of argon is $\theta = 80\%$. The absorbed microwave power is 100 W.

The results obtained make it possible to determine ways to control the plasma parameters and the size of the formed solid particles.

General results presented above were obtained by simulating a microwave discharge in *n*-heptane. However, it is very likely that the general conclusions of the work on the nature of the effect of the charging of solid particles and the addition of argon will be valid for other liquid hydrocarbons.

7. Conclusions

Microwave discharges in liquid hydrocarbons are a relatively new and promising area in plasma physics and plasma application. Various methods have been developed

for producing microwave discharges in liquids. The study of this type of discharge is still far from complete, but at present a fairly large amount of knowledge about it has been accumulated. With the help of experimental research methods and 0D, 1D and 2D modeling, a lot of information has been obtained about plasma parameters and products obtained as a result of plasma chemical reactions. Thus, the main gas products are hydrogen, acetylene, methane and ethylene, and up to 80 vol. % of them is hydrogen. Carbon-containing nanoparticles are formed as a result of plasma chemical reactions, and graphene structures are found in them. The possibility of using such discharges for the extraction of various metals from heavy oils and products of their processing is shown. It is shown that the charge of solid particles formed in the discharge has a great influence on the plasma parameters and processes in it. The unique properties of the discharge made it possible to observe in the emission spectra of the discharge in aromatic hydrocarbons a molecular band with maxima at about 511 nm, which can be attributed to the emission of the carbon complex C_5. This molecule has not been previously observed in radiation. The liquid hydrocarbon itself remains practically unchanged after the discharge is created in it.

Many problems of microwave discharges remain unexplored. These are questions of the development of the discharge, its temporal characteristics, detailed study of physical parameters of discharges and thermodynamic state of plasma, as well as discharges with bubbling of chemically active gases. The latter systems may be of interest for the development of plasma-chemical processes, in particular, to obtain hydrogen.

8. Patents

Lebedev, Y.A.; Khadzhiev, S.N.; Kadiev, K.M.; Averin, K.A.; Visaliev, M.Y.; Mokochunina, T.V. Method of allocating concentrate of valuable metals contained in heavy oils and products of their processing. 2017, RU Patent 2631427.

References

1. Bruggeman, P.; Leys, C. Non-thermal plasmas in and in contact with liquids. *J. Phys. D Appl. Phys.* **2009**, *42*, 053001. [CrossRef]
2. Samukawa, S.; Hori, M.; Rauf, S.; Tachibana, K.; Bruggeman, P.; Kroesen, G.; Whitehead, J.C.; Murphy, A.B.; Gutsol, A.F.; Starikovskaia, S.; et al. The 2012 Plasma Roadmap. *J. Phys. D Appl. Phys.* **2012**, *45*, 253001. [CrossRef]
3. Bruggeman, P.J.; Kushner, M.J.; Locke, B.R.; Gardeniers, J.G.; Graham, W.G.; Graves, D.B.; Hofman-Caris, R.C.; Maric, D.; Reid, J.P.; Ceriani, E.; et al. Plasma–liquid interactions: A review and roadmap. *Plasma Sources Sci. Technol.* **2016**, *25*, 053002. [CrossRef]
4. Adamovich, I.; Baalrud, S.D.; Bogaerts, A.; Bruggeman, P.J.; Cappelli, M.; Colombo, V.; Czarnetzki, U.; Ebert, U.; Eden, J.G.; Favia, P.; et al. The 2017 Plasma Roadmap: Low temperature plasma science and technology. *J. Phys. D Appl. Phys.* **2017**, *50*, 323001. [CrossRef]
5. Malik, M.A.; Ghaffar, A.; Malik, S.A. Water purification by electrical discharges. *Plasma Sources Sci. Technol.* **2001**, *10*, 82–91. [CrossRef]
6. Foster, J. Plasma-based water purification: Challenges and prospects for the future. *Phys. Plasmas* **2017**, *24*, 055501. [CrossRef]
7. Rezaei, F.; Vanraes, P.; Nikiforov, A.; Morent, R.; De Geyter, N. Applications of Plasma-Liquid Systems: A Review. *Materials* **2019**, *12*, 2751. [CrossRef] [PubMed]
8. Locke, B.R. Environmental Applications of Electrical Discharge Plasma with Liquid Water—A Mini Review. *Int. J. Plasma Environ. Sci. Technol.* **2012**, *6*, 194–203.
9. Rybkin, V.V.; Shutov, D.A. Atmospheric-Pressure Electric Discharge as an Instrument of Chemical Activation of Water Solutions. *Plasma Phys. Rep.* **2017**, *43*, 1089–1113. [CrossRef]

10. Vanraes, P.; Bogaerts, A. Plasma physics of liquids—A focused review. *Appl. Phys. Rev.* **2018**, *5*, 031103. [CrossRef]

11. Lebedev, Y.A. Microwave Discharges in Liquid Dielectrics. *Plasma Phys. Rep.* **2017**, *43*, 685–695. [CrossRef]

12. Horikoshi, S.; Serpone, N. In-liquid plasma: A novel tool in the fabrication of nanomaterials and in the treatment of wastewaters. *RSC Adv.* **2017**, *7*, 47196–47218. [CrossRef]

13. Lebedev, Y.A. Microwave Discharges in Liquids: Fields of Applications. *High Temp.* **2018**, *56*, 811–820. [CrossRef]

14. Hattori, Y.; Mukasa, S.; Nomura, S.; Toyota, H. Optimization and analysis of shape of coaxial electrode for microwave plasma in water. *J. Appl. Phys.* **2010**, *107*, 063305. [CrossRef]

15. Hattori, Y.; Mukasa, S.; Toyota, H.; Yamashita, H.; Nomura, S. Improvement in preventing metal contamination from an electrode used for generating microwave plasma in liquid. *Surf. Coat. Technol.* **2012**, *206*, 2140–2445. [CrossRef]

16. Mukasa, S.; Nomura, S.; Toyota, H. Observation of Microwave In-Liquid Plasma using High-Speed Camera. *Jan. J. Appl. Phys.* **2007**, *46*, 6015–6021. [CrossRef]

17. Hattori, Y.; Mukasa, S.; Toyota, H.; Nomura, S. Electrical breakdown of microwave plasma in water. *Curr. Appl. Phys.* **2013**, *13*, 1050–1054. [CrossRef]

18. Gidalevich, E.; Boxman, R.L. Microwave excitation of submerged plasma bubbles. *J. Phys. D Appl. Phys.* **2012**, *45*, 245204. [CrossRef]

19. Tatarinov, A.V.; Lebedev, Y.A.; Epstein, I.L. Simulation of Microwave-induced Formation of Gas Bubbles in Liquid n-Heptane. *High Energy Chem.* **2016**, *50*, 144–149. [CrossRef]

20. Lebedev, Y.A.; Tatarinov, A.V.; Epstein, I.L.; Averin, K.A. The Formation of Gas Bubbles by Processing of Liquid n-Heptane in the Microwave Discharge. *Plasma Chem. Plasma Proc.* **2016**, *36*, 535–552. [CrossRef]

21. Lebedev, Y.A.; Tatarinov, A.V.; Epstein, I.L.; Bilera, I.V. A 0D kinetic model for the microwave discharge in liquid *n*-heptane including carbonaceous particles production. *J. Phys. D Appl. Phys.* **2018**, *51*, 214007.

22. Lebedev, Y.A.; Tatarinov, A.V.; Epstein, I.L. 1D Modeling of the Microwave Discharge in Liquid *n*-Heptane Including Production of Carbonaceous Particles. *Plasma Chem. Plasma Proc.* **2019**, *39*, 787–808. [CrossRef]

23. Levko, D.; Sharma, A.; Raja, L.L. Plasmas generated in bubbles immersed in liquids: Direct current streamers versus microwave plasma. *J. Phys. D Appl. Phys.* **2016**, *49*, 285205. [CrossRef]

24. Levko, D.; Sharma, A.; Raja, L.L. Microwave plasmas generated in bubbles immersed in liquids for hydrocarbons reforming. *J. Phys. D Appl. Phys.* **2016**, *49*, 22LT01. [CrossRef]

25. Lebedev, Y.A.; Tatarinov, A.V.; Epstein, I.L. Simulation of Microwave Discharge in Liquid n-Heptane in the Presence of Argon in the Discharge Region. *High Energy Chem.* **2020**, *54*, 217–226. [CrossRef]

26. Lebedev, Y.A.; Tatarinov, A.V.; Epstein, I.L. Effect of charging solid particles on their growth process and parameters of microwave discharge in liquid n-heptane. *Plasma Sources Sci. Technol.* **2020**, *29*, 065013. [CrossRef]

27. Lebedev, Y.A. Microwave discharges at low pressures and peculiarities of the processes in strongly non-uniform plasma. *Plasma Sources Sci. Technol.* **2015**, *24*, 053001. [CrossRef]

28. Nomura, S.; Toyota, H.; Mukasa, S.; Yamashita, H.; Maehara, T.; Kawashima, A. Production of hydrogen in a conventional microwave oven. *J. Appl. Phys.* **2009**, *106*, 073306. [CrossRef]

29. Lebedev, Y.A.; Konstantinov, V.S.; Yablokov, M.Y.; Shchegolikhin, A.N.; Surin, N.M. Microwave Plasma in Liquid *n*-Heptane: A Study of Plasma Chemical Reaction Products. *High Energy Chem.* **2014**, *48*, 385–388. [CrossRef]

30. Lebedev, Y.A.; Epstein, I.L.; Shakhatov, V.A.; Yusupova, E.V.; Konstantinov, V.S. Spectroscopy of Microwave Discharge in Liquid C_7–C_{16} Hydrocarbons. *High Temp.* **2014**, *52*, 319–327. [CrossRef]

31. Averin, K.A.; Lebedev, Y.A.; Shchegolikhin, A.N.; Yablokov, M.Y. Nanosize Carbon Products Formed in Microwave Discharge in Liquid Alkanes. *Plasma Proc. Polym.* **2017**, *14*, e201600227. [CrossRef]

32. Horikoshi, S.; Sawada, S.; Sato, S.; Serpone, N. Microwave-Driven In-liquid Plasma in Chemical and Environmental Applications. III. Examination of Optimum Microwave Pulse Conditions for Prolongation of Electrode Lifetime, and Application to Dye Contaminated Wastewater. *Plasma Chem. Plasma Proc.* **2019**, *39*, 51–62. [CrossRef]

33. Toyota, H.; Nomura, S.; Mukasa, S. A practical electrode for microwave plasma processes. *Int. J. Mater. Sci. Appl.* **2013**, *2*, 83–88. [CrossRef]

34. Ishijima, T.; Hotta, H.; Sugai, H. Multibubble plasma production and solvent decomposition in water by slot-excited microwave discharge. *Appl. Phys. Lett.* **2007**, *91*, 121501. [CrossRef]

35. Ishijima, T.; Sugiura, H.; Satio, R.; Toyada, H.; Sugai, H. Efficient production of microwave bubble plasma in water for plasma processing in liquid. *Plasma Sources Sci. Technol.* **2010**, *19*, 015010. [CrossRef]

36. Ishijima, T.; Nosaka, K.; Tanaka, Y.; Uesugi, Y.; Goto, Y.; Horibe, H. A high-speed photoresist removal process using multibubble microwave plasma under a mixture of multiphase plasma environment. *Appl. Phys. Lett.* **2013**, *103*, 142101. [CrossRef]

37. Wang, B.; Sun, B.; Zhu, X.; Yan, Z.; Liu, Y.; Liu, H. Effect of reactor parameters on matching properties of microwave discharge in liquid. *J. Phys. Conf. Ser.* **2013**, *418*, 012099. [CrossRef]

38. Wang, B.; Sun, B.; Zhu, X.; Yan, Z.; Liu, Y.; Liu, H. Degradation of Methylene Blue by Microwave Discharge Plasma in Liquid. *Contrib. Plasma Phys.* **2013**, *53*, 697–702. [CrossRef]

39. Shu, T.; Sun, B.; Zhu, X.; Wang, L.; Xin, Y.; Liu, J. Mechanism analysis of hydrogen production by microwave discharge in ethanol liquid. *J. Anal. And Appl. Pyrolysis* **2021**, *156*, 105111.

40. Wang, B.; Sun, B.; Zhu, X.; Yan, Z.; Liu, Y.; Liu, H.; Lui, Q. Hydrogen production from alcohol solution by microwave discharge in liquid. *Int. J. Hydrogen Energy* **2016**, *4*, 7280–7291. [CrossRef]

41. Averin, K.A.; Lebedev, Y.A.; Shakhatov, V.A. Some results of study of a microwave discharge in heavy liquid hydrocarbons. *Plasma Phys. Rep.* **2018**, *44*, 110–113. [CrossRef]

42. Hattory, Y.; Mukasa, S.; Toyota, H.; Inoue, T.; Nomura, S. Synthesis of zinc and zinc oxide nanoparticles from zinc electrode using plasma in liquid. *Mater. Lett.* **2011**, *65*, 188–190. [CrossRef]

43. Averin, K.A.; Bilera, I.V.; Lebedev, Y.A.; Shakhatov, V.A.; Epstein, I.L. Microwave discharge in liquid *n*-heptane with and without bubble flow of argon. *Plasma Process Polym.* **2019**, *16*, e1800198. [CrossRef]

44. Lebedev, Y.A.; Averin, K.A.; Tatarinov, A.V. Main Gaseous Products of Microwave Discharge in Various Liquid Hydrocarbons. *High Energy Chem.* **2019**, *54*, 331–335.

45. Lebedev, Y.A.; Shakhatov, V.A. Optical emission spectra of microwave discharge in different liquid hydrocarbons. *Plasma Process Polym.* **2020**, *17*, e2000003. [CrossRef]

46. Nomura, S.; Toyota, H. Sonoplasma generated by a combination of ultrasonic waves and microwave irradiation. *Appl. Phys. Lett.* **2003**, *83*, 4503–4505. [CrossRef]

47. Mukasa, S.; Nomura, S.; Toyota, H. Measurement of Temperature in Sonoplasma. *Jpn. J. Appl. Phys.* **2004**, *43*, 2833–2837. [CrossRef]

48. Nomura, S.; Toyota, H.; Tawara, M.; Yamashota, H. Fuel gas production by microwave plasma in liquid. *Appl. Phys. Lett.* **2006**, *88*, 231502. [CrossRef]

49. Curran, H.J.; Gaffuri, P.; Pitz, W.J.; Westbrook, C.K. A comprehensive modeling study of n-heptane oxidation. *Combust. Flame* **1998**, *114*, 149–177. [CrossRef]

50. Simmie, J.M. Detailed chemical kinetic models for the combustion of hydrocarbon fuels. *Prog. Energy Combust. Sci.* **2003**, *29*, 599–634. [CrossRef]

51. Ahmed, S.S.; Mauss, F.; Moreac, G.; Zeuch, T. A comprehensive and compact n-heptane oxidation model derived using chemical lumping. *Phys. Chem. Chem. Phys.* **2007**, *9*, 1107–1126. [CrossRef]

52. Seidel, L.; Moshammer, K.; Wang, X.; Zeuch, T.; Kohse-Höinghaus, K.; Mauss, F. Comprehensive kinetic modeling and experimental study of a fuel-rich, premixed n-heptane flame. *Combust. Flame* **2015**, *162*, 2045–2058. [CrossRef]

53. Rebick, C. Pyrolysis of Heavy Hydrocarbons in Pyrolysis. In *Theory and Industrial Practice*; Albright, L.F., Crynes, B.L., Corcoran, W.H., Eds.; Academic Press: Cambridge, MA, USA, 1983; pp. 69–87.

54. Ranzi, E.; Dente, M.; Pierucci, S.; Biardi, G. Initial product distributions from pyrolysis of normal and branched paraffins. *Ind. Eng. Chem. Fundam.* **1983**, *22*, 132–139. [CrossRef]

55. Safarik, I.; Strausz, O.P. The thermal decomposition of hydro-carbons. Part 1. *n*-alkanes (C ≥ 5). *Res. Chem. Intermed.* **1996**, *22*, 275–314. [CrossRef]

56. Held, T.J.; Marchese, A.J.; Dryer, F.L. A semi-empirical reaction mechanism for n-heptane oxidation and pyrolysis. *Combust. Sci. Technol.* **1997**, *123*, 107–146. [CrossRef]

57. Murata, M.; Saito, S. Prediction of initial product distribution from n-paraffin pyrolysis at higher temperatures by considering ethyl radical decomposition. *J. Chem. Eng. Jpn.* **1974**, *7*, 389–391. [CrossRef]

58. Zamostny, P.; Belohlav, Z.; Starkbaumova, L.; Patera, J. Experimental study of hydrocarbon structure effects on the composition of its pyrolysis products. *J. Anal. Appl. Pyrolysis* **2010**, *87*, 207–216. [CrossRef]

59. Chakraborty, J.P.; Kunzru, D. High pressure pyrolysis of n-heptane. *J. Anal. Appl. Pyrolysis* **2009**, *86*, 44–52. [CrossRef]

60. Yuan, T.; Zhang, L.; Zhou, Z.; Xie, M.; Ye, L.; Qi, F. Pyrolysis of n-Heptane: Experimental and Theoretical Study. *J. Phys. Chem. A* **2011**, *115*, 1593–1601. [CrossRef]

61. Bajus, M.; Veselý, V.; Leclercq, P.A.; Rijks, J.A. Steam Cracking of Hydrocarbons. 1. Pyrolysis of Heptane. *Ind. Eng. Chem. Prod. Res. Dev.* **1979**, *18*, 30–37. [CrossRef]

62. Olahová, N.; Bajus, M.; Hájeková, E.; Šugár, L.; Markoš, J. Kinetics and modelling of heptane steam–cracking. *Chem. Pap.* **2014**, *68*, 1678–1689. [CrossRef]

63. Wu, Y.; Wang, X.; Song, Q.; Zhao, L.; Su, H.; Li, H.; Zeng, X.; Zhao, D.; Xu, J. The effect of temperature and pressure on n-heptane thermal cracking in regenerative cooling channel. *Combust. Flame* **2018**, *194*, 233–244. [CrossRef]

64. Garner, S.; Sivaramakrishnan, R.; Brezinsky, K. The high-pressure pyrolysis of saturated and unsaturated C7 hydrocarbons. *Proc. Combust. Inst.* **2009**, *32*, 461–467. [CrossRef]

65. Yasunaga, K.; Yamada, H.; Oshita, H.; Hattori, K.; Hidaka, Y.; Curran, H. Pyrolysis of *n*-pentane, *n*-hexane and *n*-heptane in a single pulse shock tube. *Combust. Flame* **2017**, *185*, 335–345. [CrossRef]

66. Dey, G.R.; Singh, B.N.; Kumar, S.D.; Das, T.N. Dielectric Barrier Discharge Initiated Gas-Phase Decomposition of CO_2 to CO and C_6–C_9 Alkanes to C_1–C_3 Hydrocarbons on Glass, Molecular Sieve $_{10}$X and TiO_2/ZnO Surfaces. *Plasma Chem. Plasma Process.* **2007**, *27*, 669–679. [CrossRef]

67. Taghvaei, H.; Jahanmiri, A.; Rahimpour, M.R.; Shirazi, M.M.; Hooshmand, N. Hydrogen production through plasma cracking of hydrocarbons: Effect of carrier gas and hydrocarbon type. *Chem. Eng. J.* **2013**, *226*, 384–392. [CrossRef]

68. Yao, S.; Weng, S.; Jin, Q.; Wu, Z.; Jiang, B.; Tang, X.; Lu, H.; Han, J.; Cao, Y.; Zhang, X. Comparison of Gasoline-Ranged n-Alkanes Conversions Using Dielectric Barrier Discharge: A Kinetic Study. *Plasma Chem. Plasma Process.* **2017**, *37*, 137–148. [CrossRef]

69. Lebedev, Y.A.; Tatarinov, A.V.; Epstein, I.L. On the role of electron impact in an atmospheric pressure microwave discharge in liquid n-heptane. *Plasma Phys. Rep.* **2017**, *43*, 510–513. [CrossRef]

70. Belousov, V.P.; Belousova, I.M.; Ermakov, A.V.; Kiselev, V.M.; Sosnov, E.N. Oxygen adsorption by fullerenes and carbon nanostructures. *Russ. J. Phys. Chem. A* **2007**, *81*, 1650–1657. [CrossRef]

71. Averin, K.A.; Lebedev, Y. A Redistribution of Metal Concentrations in the Products of Microwave Discharge in Liquid Residues of Heavy Petroleum Feedstock. *High Energy Chem.* **2018**, *52*, 263–265. [CrossRef]

72. Lebedev, Y.A.; Averin, K.A. Extraction of valuable metals by microwave discharge in crude oil. *J. Phys. D Appl. Phys.* **2018**, *51*, 214005. [CrossRef]

73. Lebedev, Y.A.; Khadzhiev, S.N.; Kadiev, K.M.; Averin, K.A.; Visaliev, M.Y.; Mokochunina, T.V. Method of Allocating Concentrate of Valuable Metals Contained in Heavy Oils and Products of Their Processing. RU Patent 2,631,427, 22 September 2017.

74. Khadzhiev, S.N.; Shpirt, M.Y. *Trace Elements in Crude Oils and Their Refining Products*; Nauka: Moscow, Russia, 2012. (In Russian)

75. Khuhawar, M.Y.; Aslam Mirza, M.; Jahangir, T.M. Determination of Metal Ions in Crude Oils. In *Crude Oil Emulsions-Composition Stability and Characterization*; InTech: Rijeka, Croatia, 2012.

76. Lebedev, Y.A.; Averin, K.A.; Borisov, R.S.; Garifullin, A.R.; Bobkova, E.S.; Kurkin, T.S. Microwave Discharge in Liquid Hydrocarbons: Study of a Liquid Hydrocarbon after Exciting the Discharge. *High Energy Chem.* **2018**, *52*, 324–329. [CrossRef]

77. Averin, K.A.; Borisov, R.S.; Lebedev, Y.A. Microwave Discharge in Liquid Hydrocarbons: Study of a Liquid Hydrocarbon after Its Discharge Treatment Including Air Bubbling. *High Energy Chem.* **2020**, *54*, 210–216. [CrossRef]

78. Skorobogatov, G.A.; Krylov, A.A.; Moskvin, A.L.; Povarov, V.G.; Tret'yachenko, S.A.; Khripun, V.K. Chemical Transformations of Liquid Chloroform, Hexane, and Heptane in Microwave Plasmoid Field. *High Energy Chem.* **2016**, *50*, 406–410. [CrossRef]

79. Scrivens, W.A.; Tour, J.M. Synthesis of gram quantities of C60 by plasma discharge in a modified round-bottomed flask. Key parameters for yield optimization and purification. *J. Org. Chem.* **1992**, *57*, 6932–6936. [CrossRef]

80. Garcia, M.A. Surface plasmons in metallic nanoparticles: Fundamentals and applications. *J. Phys. D Appl. Phys.* **2011**, *44*, 283001. [CrossRef]

81. Lebedev, Y.A.; Shakhatov, V.A. Gas temperature in the microwave discharge in liquid n-heptane with argon bubbling. *Eur. Phys. J. D* **2019**, *73*, 167–173. [CrossRef]

82. Ochkin, V.N. *Spectroscopy of Low Temperature Plasma*; Wiley-VCH: Weinheim, Germany, 2009.

83. Mehl, M.; Pitz, W.J.; Westbrook, C.K.; Curran, H. Kinetic modeling of gasoline surrogate components and mixtures under engine conditions. *J. Proc. Combust. Inst.* **2011**, *33*, 193–200. [CrossRef]

84. Wang, H.; Frenklach, M. A detailed kinetic modeling study of aromatics formation in laminar premixed acetylene and ethylene flames. *Combust. Flame* **1997**, *110*, 173–221. [CrossRef]

85. Smirnov, B.M. Cluster plasma. *Phys. Uspekhi* **2000**, *43*, 453–491. [CrossRef]

86. Khrapak, S.A.; Ratynskaia, S.V.; Zobnin, A.V.; Usachev, A.D.; Yaroshenko, V.V.; Thoma, M.H.; Kretschmer, M.; Höfner, H.; Morfill, G.E.; Petrov, O.F.; et al. Particle charge in the bulk of gas discharges. *Phys. Rev. E* **2005**, *72*, 016406. [CrossRef] [PubMed]

87. Bouchoule, A. *Dusty Plasmas: Physics, Chemistry and Technological Impacts in Plasma Processing*; John Wiley & Sons Inc.: Hoboken, NJ, USA, 1999.

88. Fortov, V.; Ivlev, S.; Khrapak, S.; Khrapak, A.; Morfill, G. Complex (dusty) plasmas: Current status, open issues, perspectives. *Phys. Rep.* **2005**, *421*, 1–103. [CrossRef]

On the Effectiveness of Oxygen Plasma and Alkali Surface Treatments to Modify the Properties of Polylactic Acid Scaffolds

Ricardo Donate *[iD], María Elena Alemán-Domínguez [iD] and Mario Monzón [iD]

Grupo de Investigación en Fabricación Integrada y Avanzada, Departamento de Ingeniería Mecánica, Universidad de Las Palmas de Gran Canaria, Campus Universitario de Tafira s/n, 35017 Las Palmas, Spain; mariaelena.aleman@ulpgc.es (M.E.A.-D.); mario.monzon@ulpgc.es (M.M.)
* Correspondence: ricardo.donate@ulpgc.es

Abstract: Surface modification of 3D-printed PLA structures is a major issue in terms of increasing the biofunctionality and expanding the tissue engineering applications of these parts. In this paper, different exposure times were used for low-pressure oxygen plasma applied to PLA 3D-printed scaffolds. Alkali surface treatments were also evaluated, aiming to compare the modifications introduced on the surface properties by each strategy. Surface-treated samples were characterized through the quantification of carboxyl groups, energy-dispersive X-ray spectroscopy, water contact angle measurements, and differential scanning calorimetry analysis. The change in the surface properties was studied over a two-week period. In addition, an enzymatic degradation analysis was carried out to evaluate the effect of the surface treatments on the degradation profile of the 3D structures. The physicochemical characterization results suggest different mechanism pathways for each type of treatment. Alkali-treated scaffolds showed a higher concentration of carboxyl groups on their surface, which enhanced the enzymatic degradation rate, but were also proven to be more aggressive towards 3D-printed structures. In contrast, the application of the plasma treatments led to an increased hydrophilicity of the PLA surface without affecting the bulk properties. However, the changes on the properties were less steady over time.

Keywords: polymer; low-pressure plasma; plasma treatment; surface modification; biomedical applications; additive manufacturing; toluidine blue method; enzymatic degradation

1. Introduction

The use of 3D scaffolds constitutes one of the most promising approaches in the biomedical field to regenerate damaged tissue. As scaffolds act as artificial structures that support and direct new tissue formation, various requirements must be fulfilled, including biocompatibility, suitable mechanical properties, interconnected porosity, promotion of cell's attachment and growth, supported vascularization, and ease of sterilization [1]. Unlike other commonly used biomaterials in the tissue engineering (TE) field, such as titanium [2] and bioceramic materials [3], polymeric scaffolds also possess a distinctive feature: their biodegradability. As the byproducts of the polymer's degradation process are excreted through the usual metabolic pathways, a complete integration of the scaffold can be achieved, avoiding the need for an explant surgical procedure [4]. Conversely, the degradation profile of polymeric scaffolds needs to be carefully adjusted to ensure sufficient mechanical support during new tissue formation and that no immune or inflammatory response happens in the implantation site due to the release of acidic byproducts [5].

Polylactic acid (PLA) is a biodegradable thermoplastic aliphatic polyester that is used extensively for scaffold manufacturing. Apart from its biocompatibility, adjustable biodegradability, and suitable mechanical properties, PLA has good processability by Additive Manufacturing (AM) techniques (ISO/ASTM 52900:2015), allowing for the development of patient-specific constructs [6]. The use of AM technologies for biopolymer manufacturing and biological and medical applications gained interest over the last decades [7]

mainly due to the great control that they offer in terms of pore size, pore shape, and porosity of the structures [8,9]. On the other hand, the main drawbacks for the biomedical application of PLA scaffolds include (a) release of acidic degradation byproducts; (b) poor toughness; (c) lack of reactive side chain groups, which limits the treatments available for improving its surface properties, and (d) low hydrophilicity, which hinders cell attachment and scaffold–tissue interaction.

To overcome the limitations of PLA, different surface treatments can be applied to the scaffold to modify its topography or surface chemistry, including plasma deposition, plasma sputtering and etching, physical entrapment of small functional molecules, aminolysis, and hydrolysis [10,11]. Among them, one simple and effective strategy is the alkali treatment, based on the immersion of the PLA scaffolds in sodium hydroxide (NaOH) solutions. The hydrolysis of the ester bonds of PLA occurs due to the nucleophilic attack of hydroxide ions on the carbonyl carbon [12,13], leading to the incorporation of hydroxyl (-OH) groups and the increase of surface roughness; thus, increasing the hydrophilicity of the base material [14,15]. Generally, after alkali hydrolysis, the samples are washed with inorganic acids to remove the excess of NaOH. However, if organic acids are used instead, the carboxyl groups (–COOH) of these compounds can hydrolyze the PLA's ester bonds [14] while also removing the excess of NaOH. Carboxyl groups incorporated into the PLA surface lead to an enhancement of roughness and wettability [14,16], serving as anchoring points for biological substances [17,18] and promoting the cell adhesion and proliferation processes [19,20]. The modifications generated by alkali treatment methods depend strongly on the concentration of the solution used, and the treatment time could affect the surface morphology and mechanical properties of the scaffolds [21].

In contrast, plasma treatments allow for the modification of the polymeric surface without affecting the bulk properties. The effects generated on the surface depend on the working conditions (power/voltage and time of exposure) and the carrier gas used. In the case of oxygen plasma treatments, hydroxyl and carboxyl groups can be incorporated into the surface of PLA scaffolds [22,23], achieving a reduction of the water contact angle while affecting the roughness of the samples at a nanometric scale [23,24]. Overall, the plasma treatment of PLA samples can lead to an enhanced cell adhesion, morphology, and proliferation [23,25,26]. The change on the chemical structure of the surface material may also have an impact on the bulk crystallinity of 3D-printed structures, as the width of the struts is low enough to be affected by the changes on the surface. While in some cases the modifications introduced by these surface treatments are enough to fulfill the requirements for the tissue-engineered PLA scaffolds [25], these treatments are usually combined with a later coating step based on the immobilization of bioactive substances within the polymeric matrix [18,27]. A subsequent coating procedure or the direct application of the surface-treated scaffolds should not be delayed too long, as the modifications generated by these treatments are not permanent, showing a progressive decay of the modifications generated on the polymer´s surface [28–30].

In this work, a comparison between alkali and plasma treatments of PLA scaffolds obtained by AM was carried out. These methods are broadly considered simple and cost-effective strategies to improve the biofunctionality of polymeric surfaces [10,31]. Furthermore, oxygen plasma treatment is a safe and environmentally friendly process (minimal consumption of gas, no reagents, no toxic gases, etc.) which can generate uniform changes throughout the treated samples [31]. Different treatment times were selected to assess the modifications introduced by oxygen plasma treatments, while for alkali treatments, the NaOH solution concentration was varied. In addition, the use of organic and inorganic acids as a final washing step after alkali treatment was evaluated. Few examples can be cited from the literature comprising an experimental assessment of different treatment methods with varying conditions applied to PLA surfaces, including films [32] and composite samples [33], but no references were found regarding 3D structures. In addition, there is a lack of information in the literature about the comparison of how the surface modifications on PLA surfaces evolve over time. These data would be essential if the

induced modifications are intended to be used for coating the structures or if storage before utilization is needed (as it is for commercially availability).

The characterization of the surface-treated PLA scaffolds included the assessment on the incorporation of carboxyl groups, the evaluation of the hydrophilicity by measuring the water contact angle, and the analysis of the surface's chemical composition by energy-dispersive X-ray spectroscopy. Also, the effect of the treatments on the degree of crystallinity and calorimetric properties of the PLA samples was studied by differential scanning calorimetry analysis. Two weeks after applying the treatments, the samples were tested again to evaluate the aforementioned loss of modifications over time. Finally, an enzymatic degradation test using proteinase K enzymes was carried out to assess the degradation rate of the structures, the pH, and the conductivity profile of the media during the five-day test and the morphological and mechanical properties of the surface-treated scaffolds after degradation.

2. Materials and Methods

2.1. Materials

PLA L105 was purchased from Corbion Purac (Diemen, The Netherlands). This material, supplied in powder form, has a melt flow index of 65 g/10 min and a molecular weight of approximately 105,000 g/mol. The reagents used in this study include sodium hydroxide (NaOH; 30620, Honeywell Fluka™, Mt Laurel, NJ, USA), hydrochloric acid (HCl; 131020, Panreac AppliChem, Darmstadt, Germany), citric acid (20282, VWR Chemicals, Fontenay-sous-Bois, France), and acetic acid (ACAC-GIA-2K5, Labkem, Barcelona, Spain).

2.2. Manufacturing of Scaffolds

PLA scaffolds were manufactured using a material extrusion process (ISO/ASTM 52900:2015), commonly known as fused deposition modelling (FDM). Specifically, a BQ Hephestos 2 3D printer (Madrid, Spain) was used to manufacture scaffolds with 9.8 mm diameter, 7 mm height, rectangular 0/90 pattern, square-shaped pores, and a 50% theoretical porosity. Other printing settings included a nozzle diameter of 0.4 mm, a layer height of 0.3 mm, a speed of extrusion of 40 mm/s, and a printing temperature of 215 °C.

The continuous PLA filaments fed to the 3D-printed (mean diameter of around 1.75 mm) were obtained using a lab prototype extruder consisting of an 8 mm screw, a cylinder with an L/D ratio of 10, and a 1.6 mm diameter nozzle tip. The extrusion of PLA L105 powder was carried out at a rotating speed of 7 rpm, a temperature of 180 °C, and with a final air- and water-cooling stage.

Apart from the PLA scaffolds, flat-surface samples were manufactured by compression molding to better characterize the PLA surface after applying the different treatments. A Collin P 200 P/M press and the following cycle were used: heating up to 190 °C at a heating rate of 20 °C/min; maintaining the temperature at that constant value for 90 s at 10 bars of pressure, and finally cooling at a rate of 20 °C/min while maintaining the pressure applied in the second step.

As the first step of every experiment included in this work, the samples were measured and weighted to ensure that there were no significant differences regarding these parameters between the different groups tested.

2.3. Surface Treatment

2.3.1. Oxygen Plasma Treatments

The plasma treatment of the samples was carried out in a low-pressure device (Zepto Diener electronic GmbH, Ebhause, Germany) comprising a high-frequency generator of 40 kHz. At high frequencies, a more uniform, efficient, and almost continuous discharge can be sustained to maintain the plasma state at lower pressures and energy levels in comparison to direct current (DC) discharges [34]. Oxygen was used as carrier gas (Carburos Metálicos SA, Madrid, Spain), containing less than 500 ppb of H_2O and less than 400 ppb of N_2. Oxygen plasma is the most common option for the formation of oxygen functionalities

by ion implantation onto the polymeric surface, being proved as a useful and effective surface modification method [11]. The oxygen pressure inside the chamber was fixed at 1.8 mbar, and the surface treatment was applied at a power of 30 W for 1 or 10 min. Both sides of the samples were treated. Depending on the treatment time, the plasma-treated group of samples are referred in this text as PLASMA 1 min or PLASMA 10 min.

2.3.2. Alkali Treatments

PLA samples were placed in a 24-well plate (144530, Thermo Scientific™ Nunc™, Waltham, MA, USA) and immersed during 1 h at room temperature in 2 mL of 0.2 N or 1 N NaOH solutions. Then, the samples were rinsed with distillate water, washed with a 0.1 N HCl solution, and rinsed again with distillate water. PLA samples treated with these methods are referred in the text as 0.2 N NaOH and 1 N NaOH.

In a third alkali surface treatment evaluated, the samples were immersed in 2 mL of 0.2 N NaOH solution, rinsed with distillate water, washed with a 0.05 g/L citric acid solution, and finally rinsed again with distillate water. Samples treated with this method are referred in the text as 0.2 N NaOH + citric acid.

2.4. Physicochemical Characterization

2.4.1. Evaluation of Carboxyl Groups on the Treated Surface

The relative surface concentration of carboxyl groups was evaluated by using the Toluidine Blue O (TBO) method [35]. This cationic dye binds to carboxyl groups in a 1:1 molar ratio in a basic medium and can later be desorbed with an acid solution [35,36]. Four replicas of each of the treated scaffold's groups were tested right after applying the different surface treatments. PLA scaffolds were used as control. The samples were placed individually in centrifuge tubes (CFT011150, 15 mL sterile tubes, Jet Biofil, Guangzhou, China) and immersed in 2 mL of a 0.5 mm Toluidine Blue O (T3260, Sigma Aldrich, St. Louis, MO, USA) solution in 0.1 mm NaOH (pH 10). After 20 h, the samples were transferred to a 24-well plate and rinsed thrice with 1 mL of 0.1 mm NaOH solution. Then, the bounded toluidine was desorbed by adding 2 mL of 50% (v/v) acetic acid solution for 10 min in each well. Finally, the samples were discarded, and the solutions' absorbance was measured using a BioTek ELx800 reader (Bio Tek Instruments Inc., Winooski, VT, USA) at an excitation wavelength of 595 nm. The 50% (v/v) acetic acid solution was used as blank of the measurements.

This procedure was also applied to PLA scaffolds that were surface-treated and then stored in a desiccator for two weeks to evaluate whether the modifications introduced are maintained during that period.

2.4.2. Energy-Dispersive X-ray (EDX) Spectroscopy Analysis

The assessment of the chemical composition of the nontreated, plasma-treated, and alkali-treated PLA samples was carried out by a scanning electron microscope (SEM; Hitachi TM 3030 at an acceleration voltage of 15 kV, Hitachi Ltd., Tokyo, Japan) coupled with an EDX detector. Flat-surface samples obtained by compression molding (as detailed in Section 2.2) were used for this test. The main result of the EDX analysis is the oxygen/carbon ratio (O/C), which is an important indicator of the effectiveness of the proposed treatments to incorporate oxygen groups into the PLA surface. Four measurements were obtained per group on the treatment day. The analysis was repeated two weeks later using the same samples and procedure.

2.4.3. Water Contact Angle (WCA) Measurements

The sessile drop method was used to analyze the WCA of the surface-treated samples, and therefore, the effect of the treatments on the hydrophilicity of the base material. As it is recommended to use flat-surface samples for this test, the samples obtained by compression molding described in Section 2.2 were used. The WCA measurements ($n = 4$) were carried out at room temperature using an Ossila WCA measuring device (Ossila Ltd., Sheffield,

UK) and the opensource software ImageJ was used to measure the static contact angle of 2 μL distilled water. The WCA was measured every 24 h during 2 weeks after applying the different surface treatments.

2.4.4. Differential Scanning Calorimetry (DSC) Analysis

Samples extracted from nontreated and treated scaffolds were subjected to DSC analysis in a differential scanning calorimeter DSC 4000 (Perkin Elmer, Waltham, MA, USA). The scaffolds were surface-treated on the same day or two weeks before the analysis. The samples ($n = 4$) were placed in aluminum crucibles and subjected to a heating/cooling/heating cycle from 30–230 °C, with a nitrogen flow of 20 mL/min and heating and cooling rates of 10 °C/min. The calorimetric data obtained include the glass transition temperature, the onset temperature (at which melting process start), the peak melting temperature and the melting enthalpy. Then, the melting enthalpy values were used to calculate the crystallinity of each group of samples according to the following equation:

$$\%X_C = 100 \cdot \frac{\Delta H_f}{\Delta H_f^\circ} \tag{1}$$

where Xc is the degree of crystallinity, ΔH_f is the melting enthalpy of the sample and ΔH_f° the melting enthalpy of 100% crystalline PLA. The value for ΔH_f° was 93.7 J/g [37].

2.5. Enzymatic Degradation Study

An enzymatic degradation test was carried out to evaluate the effect of the oxygen plasma and alkali surface treatments on the degradation rate of the PLA scaffolds. proteinase *K* enzymes from Tritirachium album (30 units per mg of protein, Merck, Darmstadt, Germany) were used to accelerate the degradation study of the PLA samples [38]. The enzymes were diluted in Tris-HCl buffer (pH 8.6, BioReagent, Merck) at a concentration of 0.2 mg/mL. Sodium azide (ReagentPlus®, ≥99.5%, Merck) was added at the same concentration to avoid possible bacterial contamination.

Four replicas per group were placed in a nontreated 24-well plate and 2 mL of degradation media were added per well. PLA scaffolds were used as control. The well plate was maintained in an incubator at 37 °C for 5 days. To avoid the denaturation of the enzymes (due to the lactic acid released during the scaffolds degradation) and therefore maintain a high enzymatic activity, the buffer-enzyme solution was replaced daily. The pH (sensIONTM+PH1, ±0.01, HACH) and conductivity (COND7+, ±0.01, Labbox) of the media were measured every day to follow up the evolution of these parameters during the enzymatic degradation process.

The weight loss of the structures after five days was assessed by using an analytical balance (±0.1 mg, A&D Scales Gemini Series, GR-200, Braunschweig, Germany), while the porosity change of the structures was determined with the following equation [39]:

$$\%porosity = 100 \cdot \left(1 - \frac{\rho_{ap}}{\rho_{bulk}}\right) \tag{2}$$

where ρ_{ap} is the apparent density of the structure and ρ_{bulk} is the density of the bulk material. The latter parameter was estimated by measuring the mass and the dimensions of short filaments of material ($n = 8$), giving a result of 1.22 ± 0.03 g/cm^3. The apparent density was calculated following a similar protocol for the 3D-printed scaffolds.

Finally, the degraded scaffolds were mechanically characterized under compression test in a LIYI (LI-1065, Dongguan Liyi Environmental Technology Co., Ltd., Dongguan, China) testing machine in displacement control mode. Crosshead speed was set at 1 mm/min. The compressive modulus, offset compressive yield strength (2% deviation from linearity), compression strength, and strain at maximum strength were calculated according to ASTM D695-15. Nondegraded PLA scaffolds were used as reference control (RC).

2.6. Statistical Analysis

Statistical analysis was performed using MATLAB software (MATLAB and Statistics Toolbox Release 2021a, The MathWorks, Inc., Natick, MA, USA). The data obtained during this study were analyzed by the Kruskal–Wallis test except for those cases where only two groups were compared. In the latter case, the Wilcoxon two-sided rank sum test was used. The significance level was set to * $p < 0.05$, ** $p < 0.01$ and, *** $p < 0.001$, for statistically significant, highly statistically significant, and very highly statistically significant differences, respectively. All figures and tables show the mean values obtained for each group tested. Standard deviations are represented with error bars in the case of figures.

3. Results

3.1. Physicochemical Characterization

3.1.1. Weight Loss Due to the Application of the Surface Treatments

To assess the effect of the evaluated surface treatments on the PLA scaffold structure, the weight of each group of samples ($n = 4$) was measured before and after treatment. The scaffolds tested had an initial weight of 0.258 ± 0.01 g, with statistically insignificant differences between groups. After the application of the surface treatments, as shown in Table 1, a statistically significant weight loss was obtained for the 1 N NaOH and 0.2 N NaOH + citric acid groups. The weight loss in the case of alkali treatments was related to NaOH concentration, as the weight decreased more for the most concentrated solution. These data evidenced that these treatments are the most aggressive among the ones tested, so it is expected that they affected the bulk properties of the material (as described below for crystallinity). For plasma-treated samples, the effect of the treatment depends on the time of exposure; scaffolds treated for 10 min showed a statistically significant weight loss ($p < 0.05$) compared with that of the ones treated for 1 min, although in both cases the values remain below 1%.

Table 1. Weight loss (%) due to the application of the different surface treatments evaluated.

Group of Samples	%Weight Loss
PLASMA 1 min	0.01 ± 0.02
PLASMA 10 min	0.21 ± 0.02
0.2 N NaOH	1.93 ± 0.11
1 N NaOH	5.85 ± 0.25 [1]
0.2 N NaOH + citric acid	2.08 ± 0.12 [2]

[1] $p < 0.05$ compared with PLASMA 10 min and $p < 0.01$ compared with PLASMA 1 min. [2] $p < 0.05$ compared with PLASMA 1 min.

3.1.2. Evaluation of Carboxyl Groups on the Treated Surface

The incorporation of carboxyl groups into the PLA surface was achieved with the three alkali treatments proposed, as demonstrated by the results obtained at day 0 (day of treatment) with the TBO method (as illustrated in Figure 1).

As expected, the highest mean value of absorbance was obtained for the group of samples treated with 0.2 N NaOH + citric acid (0.17 ± 0.06 a.u.), which showed a significantly higher value of this parameter compared with the samples treated with plasma for 1 min and the nontreated PLA scaffolds used as control. On the other hand, the results suggest that there is no concentration of carboxyl groups on the surface when applying the PLASMA 1 min treatment method, as this is the only group that showed an insignificant difference with the control group at day 0 (absorbance value equal to 0.01 ± 0.01 a.u. in both cases). At day 14, this statement becomes true for all the groups tested.
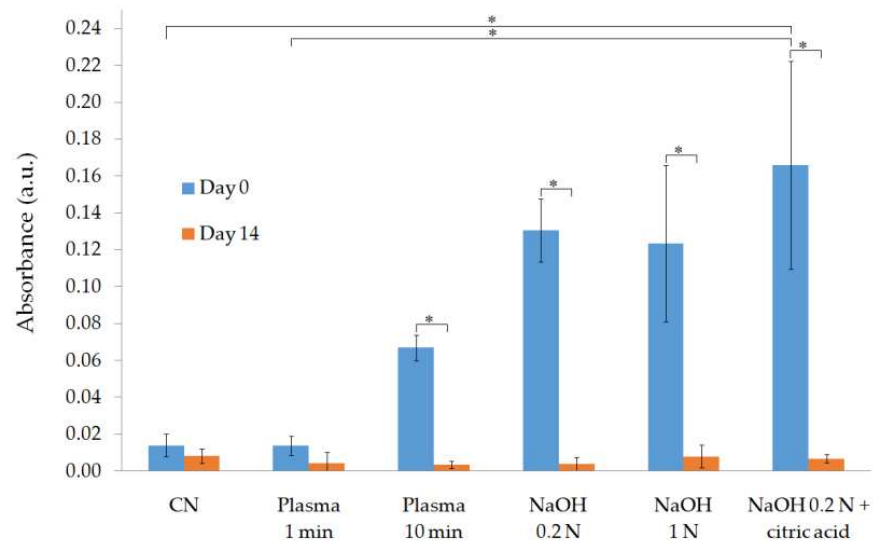
Figure 1. Physicochemical characterization of surface-treated samples by the Toluidine Blue O (TBO) test. * $p < 0.05$.

3.1.3. EDX Analysis

The O/C ratio of each group of samples is represented in Figure 2. In comparison to the PLA control group (O/C ratio equal to 0.693 ± 0.004), statistically significant and highly statistically significant differences were obtained for the 0.2 N NaOH (0.718 ± 0.001) and 1 N NaOH groups (0.737 ± 0.015), respectively. The incorporation of oxygen groups to the PLA surface is especially relevant for 1 N NaOH group, since it showed the highest value at day 0 and is the only group that maintained a significantly higher O/C ratio (0.702 ± 0.008) after 14 days.
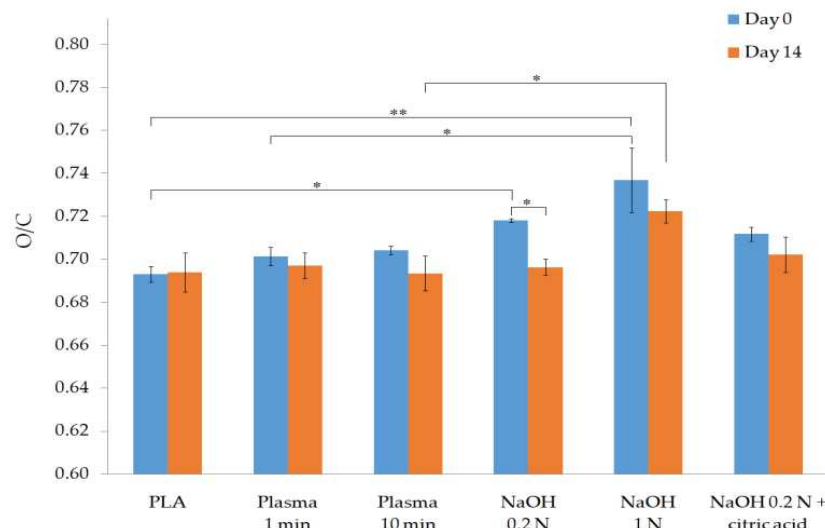
Figure 2. Physicochemical characterization of surface-treated samples by EDX analysis. * $p < 0.05$ and ** $p < 0.01$.

3.1.4. WCA Measurements

The evolution of the samples' WCA across two weeks is shown in Figure 3. The mean WCA value of the PLA samples right after treatment (day 0) decreased from the value of $77.2 \pm 0.9°$ (nontreated PLA) to $48.5 \pm 3.0°$ and $45.1 \pm 5.2°$ for the PLASMA 1 min and PLASMA 10 min groups, respectively. The 1 N NaOH group showed a similar result ($50.7 \pm 3.0°$), while the lowest WCA values were obtained for the 0.2 N NaOH ($67.4 \pm 1.8°$) and 0.2 N NaOH + citric acid ($66.8 \pm 2.7°$) treatments. The surface-treated samples tend to

recover their initial state but follow a different profile: the effects induced by the oxygen plasma were lost at a higher rate, with the samples treated for 1 min showing a WCA similar to that of the base material in only 4 days (6 days for 10-min plasma); alkali-treated samples, however, reached the WCA value of the base material 13 days after treatment.
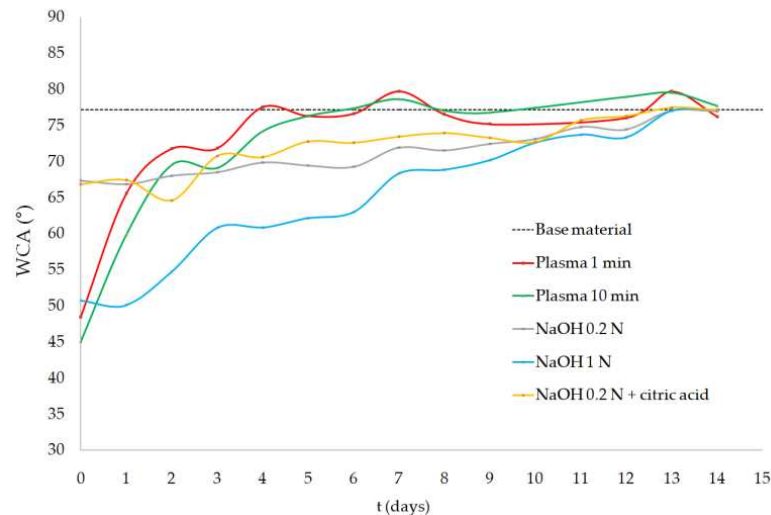
Figure 3. Water contact angle (WCA) measurements of surface-treated samples.

3.1.5. Differential Scanning Calorimetry Analysis (DSC)

As shown in Table 2, the proposed surface treatments affect the calorimetric properties of the bulk material. Thus, at day 0, a statistically significant reduction was obtained for the samples treated with 1 N NaOH in terms of glass transition temperature in comparison to the plasma-treated samples. The onset and melting temperatures also tend to be reduced for surface-treated samples. Finally, a significant increase in the melting enthalpy and the crystallinity values were obtained for the 0.2 N NaOH group. This increase in crystallinity, despite being statistically insignificant, was also observed for the PLASMA 10 min and the rest of the alkali treatments.

Table 2. DSC results of all groups of samples on day of treatment (a) and two weeks later (b).

(a)					
Group of Samples	**T_g (°C)**	**T_{onset} (°C)**	**T_{peak} (°C)**	**ΔH (J/g)**	**%X_c**
PLA	63.5 ± 1.2	167.0 ± 3.2	176.0 ± 0.1	47.0 ± 1.5	50.1 ± 1.6
PLASMA 1 min	64.2 ± 0.6	169.0 ± 0.1	175.6 ± 0.2	46.8 ± 1.5	50.0 ± 1.6
PLASMA 10 min	64.4 ± 0.5	169.3 ± 0.2	175.6 ± 0.1 [2]	49.5 ± 1.1	52.9 ± 1.2
0.2 N NaOH	61.5 ± 0.6	169.7 ± 1.2	175.9 ± 0.1	50.5 ± 1.4 [3]	53.9 ± 2.4 [4]
1 N NaOH	60.3 ± 0.6 [1]	169.5 ± 1.2	175.7 ± 0.1	50.3 ± 1.4	53.6 ± 2.7
0.2 NaOH + citric acid	63.4 ± 0.6	164.8 ± 1.2	175.7 ± 0.1	48.8 ± 1.4	52.1 ± 2.1
(b)					
Group of Samples	**T_g (°C)**	**T_{onset} (°C)**	**T_{peak} (°C)**	**ΔH (J/g)**	**%X_c**
PLA	63.5 ± 1.2	167.0 ± 3.2	176.0 ± 0.1	47.0 ± 1.5	50.1 ± 1.6
PLASMA 1 min	63.9 ± 0.2	169.2 ± 0.2	176.3 ± 0.1 *	47.1 ± 3.0	49.6 ± 2.1
PLASMA 10 min	63.8 ± 0.4	169.3 ± 0.3	176.0 ± 0.1 *	47.8 ± 2.9	51.0 ± 3.1
0.2 N NaOH	63.4 ± 0.4 *	167.8 ± 2.3	176.1 ± 0.1 *	50.9 ± 0.9	54.3 ± 0.9
1 N NaOH	63.2 ± 0.9 *	168.0 ± 2.4	176.0 ± 0.1 *	46.4 ± 2.0 *	49.6 ± 2.1
0.2 NaOH + citric acid	63.5 ± 0.2	166.0 ± 2.3	175.8 ± 0.1 [1]	49.2 ± 2.8	52.5 ± 3.0

(**a**) [1] $p < 0.01$ compared with PLASMA 10 min and $p < 0.05$ compared with PLASMA 1 min. [2] $p < 0.05$ compared with PLA. [3] $p < 0.05$ compared with PLASMA 1 min. [4] $p < 0.05$ compared with PLA and PLASMA 1 min. (**b**) * $p < 0.05$ compared with result at day 0. [1] $p < 0.01$ compared with PLASMA 1 min.

On the other hand, the differences mentioned at day 0 were not found in the samples treated and analyzed two weeks later. As shown in Table 2b, statistically significant differences were obtained for the value of most of the groups and parameters analyzed compared with day 0, leading to the loss of the modifications introduced by the proposed treatments.

3.2. Enzymatic Degradation Study

The weight loss of each group of scaffolds after the five-day enzymatic degradation test is shown in Figure 4. Alkali-treated scaffolds showed a higher level of degradation, with a mean weight loss of around 9% and a statistically significant difference obtained for the 1 N NaOH group compared to that of the nontreated PLA samples.
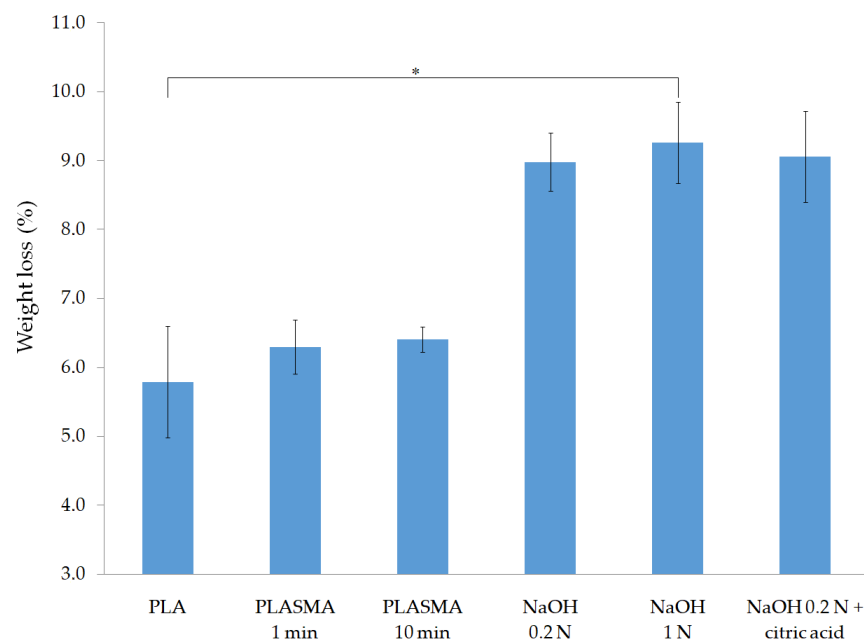
Figure 4. Enzymatic degradation test results of surface-treated samples: % weight loss after five days. * $p < 0.05$.

Regarding the pH variation of the degradation media (as illustrated in Figure 5), PLASMA 1min samples maintained the initial pH (7.94) almost until day 2, and then rapidly decreased to a value of 4.36 ± 0.01 at day 3. In the case of PLASMA 10 min samples, the pH decreased from day 1, resulting in a less pronounced slope of the curve of pH variation. Alkali-treated groups showed a pH around 4.5 across all 5 days of testing. From day 3, similar results were obtained for all the groups of samples tested.

An increase in the porosity of the scaffolds was also obtained as a consequence of the enzymatic degradation of the structure (as illustrated in Table 3). This increment is statistically significant for the 0.2 N NaOH and 1 N NaOH groups.

Despite being statistically insignificant, the compression test results (as illustrated in Table 3) of the degraded scaffolds showed a reduction in the elastic modulus, compressive yield strength, and compressive strength of the surface-treated scaffolds. The decrease in mechanical properties is more pronounced in the alkali-treated samples, especially for the NaOH 0.2 N + citric acid group, which showed the lowest values for all the parameters evaluated. Notably, the break point of the nondegraded PLA scaffolds, used as reference control (RC), was not reached during the test.
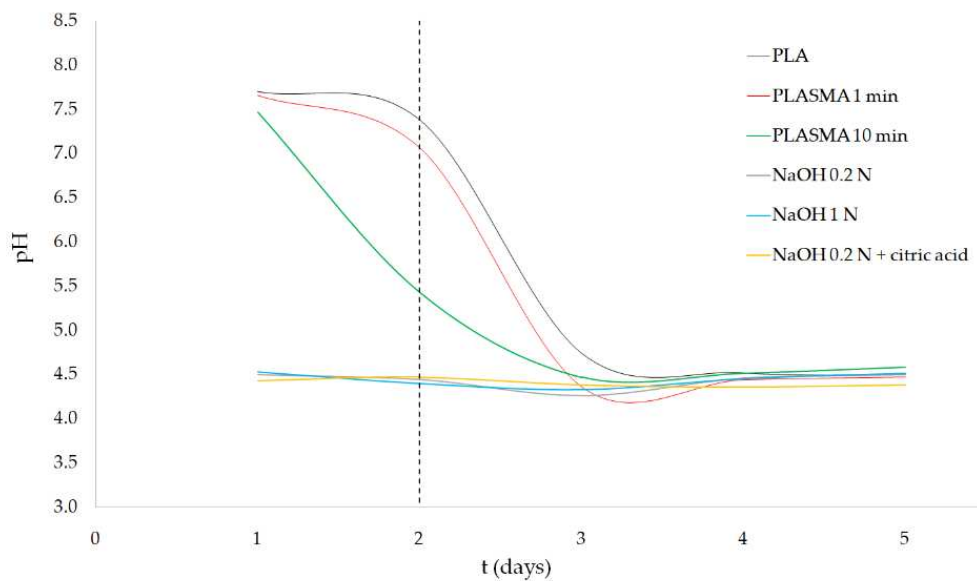
Figure 5. Enzymatic degradation test results of surface-treated samples: pH variation.

Table 3. Porosity values (before and after the degradation test) and compression test results.

Group of Samples	Initial Porosity (%)	Final Porosity (%)	Elastic Modulus (MPa)	Compressive Yield Strength (MPa)	Compression Strength (MPa)	Strain at Maximum Strength
RC (compression test)			83.6 ± 7.9	7.2 ± 1.0	-	-
PLA	55.5 ± 2.9	58.0 ± 3.0	81.0 ± 10.7	7.0 ± 1.5	9.7 ± 2.0	0.24 ± 0.07
PLASMA 1 min	56.0 ± 2.5	59.0 ± 2.1	72.7 ± 4.9	6.5 ± 1.7	9.9 ± 2.9	0.27 ± 0.04
PLASMA 10 min	56.1 ± 1.6	58.8 ± 1.5	73.7 ± 13.3	6.6 ± 1.4	9.2 ± 1.9	0.24 ± 0.03
NaOH 0.2 N	55.9 ± 1.8	60.1 ± 1.7 *	69.2 ± 13.5	6.9 ± 1.5	8.9 ± 0.9	0.23 ± 0.04
NaOH 1 N	58.8 ± 0.9	61.7 ± 1.6 *	67.7 ± 8.4	6.0 ± 0.8	8.4 ± 1.1	0.25 ± 0.01
NaOH 0.2 N + citric acid	56.4 ± 2.4	60.8 ± 2.3	63.2 ± 7.5	5.2 ± 0.8	8.2 ± 1.8	0.26 ± 0.02

* $p < 0.05$ compared with initial porosity of this group.

4. Discussion

The use of material extrusion techniques offers the possibility of obtaining PLA scaffolds with controlled pore size and porosity so that the characteristics of the 3D construct can be tailored to the patient and target tissue. The precision in the design and manufacturing of the scaffolds is severely compromised when applying an alkali surface treatment, as the weight loss of the samples will surely be accompanied by changes in the struts' dimensions, microporosity, and mechanical properties of the structure [21]. The percentage of weight loss for scaffolds treated with NaOH depends on the concentration of the solution, being in this study around 2% for 0.2 N NaOH solutions and more than 5% for 1 N NaOH treatment (as illustrated in Table 1). On the other hand, scaffolds treated with plasma showed an insignificant difference of weight before and after treatment for 1 min. When the time of exposure to the oxygen plasma was increased to 10 min, the value of weight loss significantly increased ($p < 0.05$) to 0.21 ± 0.02% compared to that of the group of PLASMA 1 min. Thus, the weight loss depends in this case on the time of treatment, which can be adjusted to maximize the incorporation of oxygen groups while reducing the effects on the structure.

Regarding the physicochemical characterization of the treated samples, the results of the EDX analysis at day 0 revealed that all treatments effectively introduce new oxygen groups on the PLA surface, as the mean O/C ratio increased in comparison to that of the control group in all cases (as illustrated in Figure 2). Alkali treatments showed the highest values of O/C ratio, with significant differences for the 0.2 N NaOH and 1 N NaOH groups

compared with the nontreated PLA group. A n insignificant increase of the O/C ratio was obtained when comparing PLA and PLASMA 1 min groups of samples. Similar results were obtained in previous studies that carried out a comparison between oxygen plasma and alkali treatments [32]. Reactive species contained in the oxygen plasma (which include neutral oxygen molecules and atoms, radicals, free electrons, and positively and negatively charged ions [22,40]) are less prone to react with the carbonyl groups of the polymer chain than hydroxide ions, giving the strong nucleophilic nature of the latter [41]. Thus, a greater amount of oxygen groups incorporated into the polymeric surface is expected for alkali treatments.

Results of the TBO test (as illustrated in Figure 1) showed that the 0.2 N NaOH + citric acid group had the highest concentration of carboxyl groups on their surface. This was an expected result, since carboxyl groups are predominantly incorporated when applying an alkali treatment method [32] and the subsequent washing step with an organic acid adds more of these hydrophilic groups onto the PLA surface by ester bond´s hydrolysis [14,18]. Carboxyl groups were also generated, albeit to a lesser extent, by applying the alkali treatments coupled with a washing step using an inorganic acid (HCl) or in the scaffolds treated with the PLASMA 10 min method.

Despite being the only group that showed a nonsignificant difference compared with the control group in the TBO test, the PLASMA 1 min samples showed a reduction of the WCA from $77.2 \pm 0.9°$ to $48.5 \pm 3.0°$ (as illustrated in Figure 3). This highly statistically significant difference ($p < 0.01$) was also observed for the group of PLASMA 10 min, for which the lowest mean WCA value was obtained ($45.1 \pm 5.2°$). These results, coupled with the ones obtained by EDX analysis (as illustrated in Figure 2), suggest that the oxygen groups incorporated to the plasma-treated PLA surface were mainly hydroxyl groups [22,23]. In the case of the alkali treatments, a statistically significant ($p < 0.05$) reduction of the WCA was only obtained for the 1 N NaOH group. The difference in WCA observed between this group and the ones treated with 0.2 N NaOH could be related to the distinct surface roughness generated depending on the solution concentration [15]. Overall, the incorporation of hydroxyl groups and the changes in the surface roughness seem to have a more important effect on the hydrophilicity improvement of the PLA surface than the incorporation of carboxyl groups.

The modifications introduced on the PLA surface were lost after two weeks, as confirmed by the results showed in Figures 1–3. Since the WCA was evaluated for 14 days, it was possible to determine the time at which the properties recovered their initial values. The decay on the modifications introduced can be explained by the reorientation and diffusion of the polar groups introduced [30], the rearrangement of hydrophilic and hydrophobic macromolecules fragments within the polymer [28], and the adsorption of ambient humidity [29]; however, samples were kept on a desiccator to limit the latter cause. The rearrangement of the polymer's chains, which caused the migration of hydrophobic macromolecules fragments to the surface, was evidenced by the recovery of the initial crystallinity value after two weeks (as illustrated in Table 2). In addition, the results suggest that the diffusion or reorientation of the hydroxyl groups introduced is faster than that of the carboxyl groups; samples treated with plasma recovered their initial WCA value in 4–6 days, while for the alkali-treated samples (with a higher formation of carboxyl groups), it took almost two weeks.

The same loss of the modifications introduced by the treatments was observed for the calorimetric properties of the scaffolds (as illustrated in Table 2). At day 0, however, a reduction in glass transition, onset, and peak temperatures was obtained for the treated groups compared with that of the nontreated PLA scaffolds. An increase in the crystallinity of the bulk material was also observed, which could be explained by the increased mobility of the polymer´s chains due to the absorption of water molecules (for alkali treatments) and the incorporation of new oxygen groups into the polymer surface. Both factors affect the movement of the chains in the amorphous region, allowing a rearrangement in part of them to a crystalline structure, according to the principle of thermodynamic equilibrium [29,30].

Another option is the scission of chains in the amorphous regions as a consequence of the surface treatments applied [42]. As previously mentioned, the crystallinity of the base material was recovered within two weeks possibly because hydrophobic macromolecule fragments migrated to the PLA surface [28]. These results give relevant information for the design of procedures regarding scaffold treatment, application of subsequent modifications (such as coating procedures), and storage conditions, thereby having important implications for industrial practice.

Results concerning the enzymatic degradation study showed a significantly higher degradation of the alkali-treated scaffolds after five days (as illustrated in Figure 4), which can be explained by two factors: a) increased surface roughness, expected from the significant weight loss of the scaffolds after treatment (as illustrated in Table 1), and b) higher concentration of carboxyl groups on the scaffold´s surface, which promotes the enzyme–material interaction [43]. Despite the relatively low hydrophilicity of the samples treated with 0.2 N NaOH, according to the WCA measurements (as illustrated in Figure 3), the degradation rate of these groups was as high as that of the 1 N NaOH group. From these results, it can be concluded that the incorporation of carboxyl groups, which are present in the three alkali-treated groups, has a more significant effect on the degradation of the 3D structures than the wettability of the surface.

In Appendix A, the results of a one-day enzymatic degradation test carried out using PLA and 0.2 N NaOH + citric acid groups are presented. While for the alkali-treated group the weight of the scaffolds was reduced by around only 1%, the pH decreased significantly to a value of 4.57 ± 0.01. Similar Ph values were measured every day of the 5-day test (as illustrated in Figure 5) for all three alkali-treated groups, as well as for the plasma-treated groups after day 3. These results suggest that the degradation of the alkali-treated PLA scaffolds progressed to a point where the concentration of dissolved lactic acid was high enough to cause denaturation of the enzymes, stopping the degradation process [44]. This limiting concentration of lactic acid is related to the minimum pH measured during the test.

In contrast to alkali-treated samples, the groups treated with oxygen plasma maintained a higher level of pH during the first two days of the experiment, which could be related to the limited presence of carboxyl groups on their surface. The TBO test (as illustrated in Figure 1) showed that the application of the plasma treatment for 10 min allowed for the incorporation of carboxyl groups, while an insignificant difference was obtained for the PLASMA 1 min group compared with that of the control. Carboxyl groups incorporated into the PLASMA 10 min group enhanced the interaction of the enzymes with the polymer [43] from the beginning of the test, which led to a less drastic decrease in the pH between days 2 and 3 compared with that of the profile observed for the PLASMA 1 min group. In the case of PLA and PLASMA 1 min groups, the enzymatic degradation progressed by a surface-erosion mechanism [45] that enhances the surface roughness with a minimal weight reduction during the first days of the test (similar to the results shown for nontreated PLA scaffolds in Appendix A). From this point, the degradation of the structure is accelerated as new regions of the polymer are exposed to the enzymes due to the increased surface roughness and chains' cleavage reactions [45]. According to these assumptions, the differences observed in terms of weight loss for the different groups of samples tested (as illustrated in Figure 4) can be related to the first two days of the experiment. The increase of conductivity (for plasma-treated samples) followed by the maintenance of a value around 2.55 mS for all groups tested after day 3 (as illustrated in Figure 6) supported the latter conclusions.
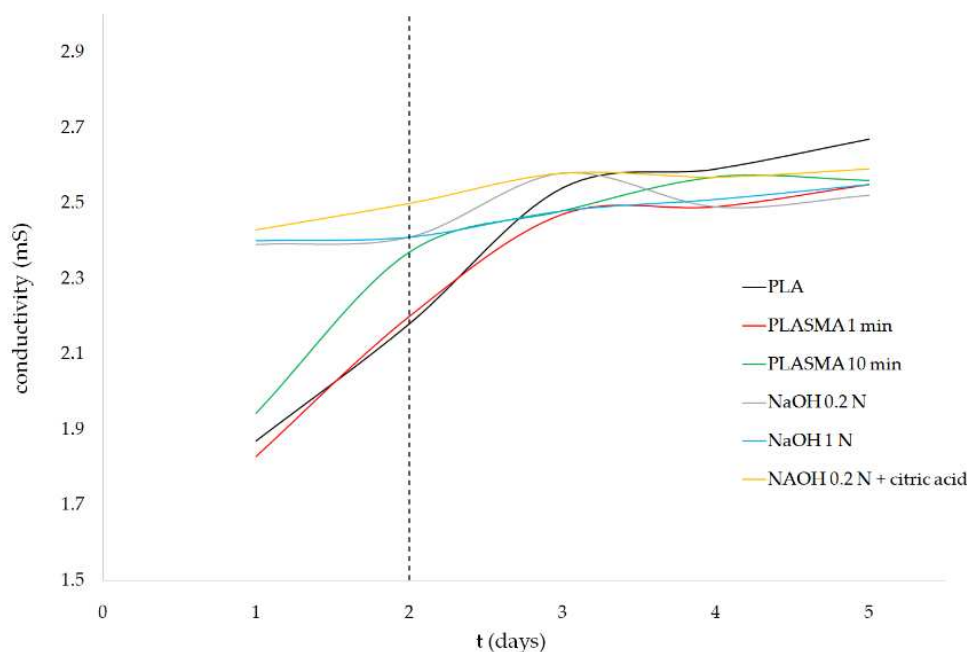
Figure 6. Enzymatic degradation test results of surface-treated samples: conductivity variation.

The abrupt release of acidic degradation byproducts could generate a strong inflammatory response, hindering cell growth and affecting the surrounding tissues [46]. Therefore, the degradation profile of PLA scaffolds must be precisely adjusted by optimizing the surface treatment conditions and/or combining the polymeric matrix with ceramic additives that can act as buffers [47,48]. The later strategy could be applied to develop biodegradable 3D structures that gradually release different ceramic particles to counteract the pH decrease of the surrounding environment over time, based on the concept of 4D printing of scaffolds [49,50]. The objective in the addition of ceramic or natural biomaterials to the PLA structure can also be related to the need to ensure enough mechanical support during new tissue formation. As shown in Table 3, a reduction of mechanical properties takes place as the degradation of the PLA scaffolds progresses. Finally, the treated surface of the PLA scaffolds must promote cell adhesion and growth to allow for tissue regeneration. This requirement can be fulfilled by the methods proposed in this study, mainly with the incorporation of carboxylic groups in the case of alkali treatments [19] and the decrease in the inherent hydrophobicity of the base material to values suitable for cell attachment [51] by applying a plasma treatment.

5. Conclusions

The present study involves a comparative experimental study between alkali and plasma treatments applied to PLA scaffolds manufactured by AM. The results obtained suggest an important contribution by the carboxyl groups incorporated to the base material surface on the degradation profile of the 3D structures, but not on the hydrophilicity improvement, which was concluded to be more related to the incorporation of hydroxyl groups. The evaluation of these properties over time showed a recovery of the initial state of the surface within two weeks. These findings are of the utmost importance when defining the treatment procedure of the PLA scaffold for biomedical applications, especially if the proposed methods are transferred to the clinic. According to the results, the scaffolds tested possess suitable properties to be further evaluated for biomedical applications.

administration, M.M.; funding acquisition, M.M. All authors have read and agreed to the published version of the manuscript.

Institutional Review Board Statement: Not applicable.

Informed Consent Statement: Not applicable.

Data Availability Statement: The data presented in this study are available on request from the corresponding author.

Appendix A

An enzymatic degradation test was carried out using PLA scaffolds treated with 0.2 N NaOH and washed with citric acid for one day, following the procedure described in Section 2.5. PLA scaffolds were used as control. The results of this test are shown in Table 1, including weight loss of the samples, pH and conductivity of the media, and porosity change after degradation.

Table 1. Results of the one-day enzymatic degradation test.

Group of Samples	Weight Loss (%)	pH	Conductivity (mS)	Initial Porosity (%)	Final Porosity (%)
PLA	0.01 ± 0.01	7.56 ± 0.01	2.00 ± 0.01	44.1 ± 3.8	43.1 ± 2.2
NaOH 0.2 N + citric acid	1.37 ± 0.11 [1]	4.57 ± 0.01 [1]	2.41 ± 0.01 [1]	41.0 ± 1.3	44.2 ± 2.8

[1] $p < 0.05$ compared with PLA.

References

1. Puppi, D.; Chiellini, F.; Piras, A.M.; Chiellini, E. Polymeric materials for bone and cartilage repair. *Prog. Polym. Sci.* **2010**, *35*, 403–440. [CrossRef]
2. Wang, X.; Xu, S.; Zhou, S.; Xu, W.; Leary, M.; Choong, P.; Qian, M.; Brandt, M.; Xie, Y.M. Topological design and additive manufacturing of porous metals for bone scaffolds and orthopaedic implants: A review. *Biomaterials* **2016**, *83*, 127–141. [CrossRef] [PubMed]
3. Vallet-Regí, M.; Ruiz-Hernández, E. Bioceramics: From bone regeneration to cancer nanomedicine. *Adv. Mater.* **2011**, *23*, 5177–5218. [CrossRef] [PubMed]
4. Ulery, B.D.; Nair, L.S.; Laurencin, C.T. Biomedical applications of biodegradable polymers. *J. Polym. Sci. Part B Polym. Phys.* **2011**, *49*, 832–864. [CrossRef] [PubMed]
5. Liu, X.; Ma, P.X. Polymeric scaffolds for bone tissue engineering. *Ann. Biomed. Eng.* **2004**, *32*, 477–486. [CrossRef]
6. Foresti, R.; MacAluso, C.; Rossi, S.; Selleri, S.; Perini, P.; Freyrie, A.; Raposio, E.; Fenaroli, P.; Concari, G.; De Filippo, M.; et al. 3D reconstruction cutting and smart devices for personalized medicine. In Proceedings of the 2020 Italian Conference on Optics and Photonics, Parma, Italy, 9–11 September 2020.
7. Foresti, R.; Ghezzi, B.; Vettori, M.; Bergonzi, L.; Attolino, S.; Rossi, S.; Tarabella, G.; Vurro, D.; von Zeppelin, D.; Iannotta, S.; et al. 3D printed masks for powders and viruses safety protection using food grade polymers: Empirical tests. *Polymers* **2021**, *13*, 617. [CrossRef] [PubMed]
8. Germain, L.; Fuentes, C.A.; van Vuure, A.W.; des Rieux, A.; Dupont-Gillain, C. 3D-printed biodegradable gyroid scaffolds for tissue engineering applications. *Mater. Des.* **2018**, *151*, 113–122. [CrossRef]

9. Zhao, H.; Li, L.; Ding, S.; Liu, C.; Ai, J. Effect of porous structure and pore size on mechanical strength of 3D-printed comby scaffolds. *Mater. Lett.* **2018**, *223*, 21–24. [CrossRef]

10. Richbourg, N.R.; Peppas, N.A.; Sikavitsas, V.I. Tuning the biomimetic behavior of scaffolds for regenerative medicine through surface modifications. *J. Tissue Eng. Regen. Med.* **2019**, *13*, 1275–1293. [CrossRef]

11. Chu, P.K.; Chen, J.Y.; Wang, L.P.; Huang, N. Plasma-surface modification of biomaterials. *Mater. Sci. Eng. R Rep.* **2002**, *36*, 143–206. [CrossRef]

12. Croll, T.I.; O'Connor, A.J.; Stevens, G.W.; Cooper-White, J.J. Controllable surface modification of poly(lactic-co-glycolic acid) (PLGA) by hydrolysis or aminolysis I: Physical, chemical, and theoretical aspects. *Biomacromolecules* **2004**, *5*, 463–473. [CrossRef]

13. De Jong, S.J.; Arias, E.R.; Rijkers, D.T.S.; Van Nostrum, C.F.; Kettenes-Van Den Bosch, J.J.; Hennink, W.E. New insights into the hydrolytic degradation of poly(lactic acid): Participation of the alcohol terminus. *Polymers* **2001**, *42*, 2795–2802. [CrossRef]

14. Guo, C.; Xiang, M.; Dong, Y. Surface modification of poly (lactic acid) with an improved alkali-acid hydrolysis method. *Mater. Lett.* **2015**, *140*, 144–147. [CrossRef]

15. Nam, Y.S.; Yoon, J.J.; Lee, J.G.; Park, T.G. Adhesion behaviours of hepatocytes cultured onto biodegradable polymer surface modified by alkali hydrolysis process. *J. Biomater. Sci. Polym. Ed.* **1999**, *10*, 1145–1158. [PubMed]

16. Shao, J.; Chen, S.; Du, C. Citric acid modification of PLLA nano-fibrous scaffolds to enhance cellular adhesion, proliferation and osteogenic differentiation. *J. Mater. Chem. B* **2015**, *3*, 5291. [CrossRef]

17. Lao, L.; Tan, H.; Wang, Y.; Gao, C. Chitosan modified poly(l-lactide) microspheres as cell microcarriers for cartilage tissue engineering. *Colloids Surf. B Biointerfaces* **2008**, *66*, 218–225. [CrossRef]

18. Martin, V.; Ribeiro, I.A.; Alves, M.M.; Gonçalves, L.; Claudio, R.A.; Grenho, L.; Fernandes, M.H.; Gomes, P.; Santos, C.F.; Bettencourt, A.F. Engineering a multifunctional 3D-printed PLA-collagen-minocycline-nanoHydroxyapatite scaffold with combined antimicrobial and osteogenic effects for bone regeneration. *Mater. Sci. Eng. C* **2019**, *101*, 15–26. [CrossRef]

19. Arima, Y.; Iwata, H. Preferential adsorption of cell adhesive proteins from complex media on self-assembled monolayers and its effect on subsequent cell adhesion. *Acta Biomater.* **2015**, *26*, 72–81. [CrossRef]

20. Li, B.; Ma, Y.; Wang, S.; Moran, P.M. Influence of carboxyl group density on neuron cell attachment and differentiation behavior: Gradient-guided neurite outgrowth. *Biomaterials* **2005**, *26*, 4956–4963. [CrossRef]

21. Chen, W.; Nichols, L.; Brinkley, F.; Bohna, K.; Tian, W.; Priddy, M.W.; Priddy, L.B. Alkali treatment facilitates functional nano-hydroxyapatite coating of 3D printed polylactic acid scaffolds. *Mater. Sci. Eng. C* **2021**, *120*, 111686. [CrossRef]

22. Scaffaro, R.; Lopresti, F.; Sutera, A.; Botta, L.; Fontana, R.M.; Gallo, G. Plasma modified PLA electrospun membranes for actinorhodin production intensification in *Streptomyces coelicolor* immobilized-cell cultivations. *Colloids Surf. B Biointerfaces* **2017**, *157*, 233–241. [CrossRef]

23. Nakagawa, M.; Teraoka, F.; Fujimoto, S.; Hamada, Y.; Kibayashi, H.; Takahashi, J. Improvement of cell adhesion on poly(L-lactide) by atmospheric plasma treatment. *J. Biomed. Mater. Res. Part A* **2006**, *77*, 112–118. [CrossRef] [PubMed]

24. Jordá-Vilaplana, A.; Fombuena, V.; García-García, D.; Samper, M.D.; Sánchez-Nácher, L. Surface modification of polylactic acid (PLA) by air atmospheric plasma treatment. *Eur. Polym. J.* **2014**, *58*, 23–33. [CrossRef]

25. Wang, M.; Favi, P.; Cheng, X.; Golshan, N.H.; Ziemer, K.S.; Keidar, M.; Webster, T.J. Cold atmospheric plasma (CAP) surface nanomodified 3D printed polylactic acid (PLA) scaffolds for bone regeneration. *Acta Biomaterialia* **2016**, *46*, 256–265. [CrossRef] [PubMed]

26. Yamaguchi, M.; Shinbo, T.; Kanamori, T.; Wang, P.C.; Niwa, M.; Kawakami, H.; Nagaoka, S.; Hirakawa, K.; Kamiya, M. Surface modification of poly(L-lactic acid) affects initial cell attachment, cell morphology, and cell growth. *J. Artif. Organs* **2004**, *7*, 187–193. [CrossRef]

27. Teixeira, B.N.; Aprile, P.; Mendonça, R.H.; Kelly, D.J.; da Silva Moreira Thiré, R.M. Evaluation of bone marrow stem cell response to PLA scaffolds manufactured by 3D printing and coated with polydopamine and type I collagen. *J. Biomed. Mater. Res. Part B Appl. Biomater.* **2019**, *107*, 37–49. [CrossRef]

28. Moraczewski, K.; Stepczyńska, M.; Malinowski, R.; Rytlewski, P.; Jagodziński, B.; Zenkiewicz, M. Stability studies of plasma modification effects of polylactide and polycaprolactone surface layers. *Appl. Surf. Sci.* **2016**, *377*, 228–237. [CrossRef]

29. Li, J.; Oh, K.; Yu, H. Surface rearrangements of oxygen plasma treated polystyrene: Surface dynamics and humidity effect. *Chin. J. Polym. Sci.* **2005**, *23*, 187–196. [CrossRef]

30. Canal, C.; Molina, R.; Bertran, E.; Erra, P. Wettability, ageing and recovery process of plasma-treated polyamide 6. *J. Adhes. Sci. Technol.* **2004**, *18*, 1077–1089. [CrossRef]

31. Cheng, Y.L.; Wang, Y.K.; Chen, P.; Deng, S.B.; Ruan, R. Non-thermal plasma assisted polymer surface modification and synthesis: A review. *Int. J. Agric. Biol. Eng.* **2014**, *7*, 1–9.

32. Durán, I.R.; Vanslambrouck, S.; Chevallier, P.; Hoesli, C.A.; Laroche, G. Atmospheric pressure cold plasma versus wet-chemical surface treatments for carboxyl functionalization of polylactic acid: A first step toward covalent immobilization of bioactive molecules. *Colloids Surf. B Biointerfaces* **2020**, *189*, 110847. [CrossRef] [PubMed]

33. Gibeop, N.; Lee, D.W.; Prasad, C.V.; Toru, F.; Kim, B.S.; Song, J. Il Effect of plasma treatment on mechanical properties of jute fiber/poly (lactic acid) biodegradable composites. *Adv. Compos. Mater.* **2013**, *22*, 389–399. [CrossRef]

34. Denes, F.S.; Manolache, S. Macromolecular plasma-chemistry: An emerging field of polymer science. *Prog. Polym. Sci.* **2004**, *29*, 815–885. [CrossRef]

35. Uchida, E.; Uyama, Y.; Ikada, Y. Sorption of low-molecular-weight anions into thin polycation layers grafted onto a film. *Langmuir* **1993**, *9*, 1121–1124. [CrossRef]

36. Liu, Y.; He, T.; Gao, C. Surface modification of poly(ethylene terephthalate) via hydrolysis and layer-by-layer assembly of chitosan and chondroitin sulfate to construct cytocompatible layer for human endothelial cells. *Colloids Surf. B Biointerfaces* **2005**, *46*, 117–126. [CrossRef] [PubMed]

37. Garlotta, D. A literature review of poly(lactic acid). *J. Polym. Environ.* **2001**, *9*, 63–84. [CrossRef]

38. Tsuji, H.; Muramatsu, H. Blends of aliphatic polyesters: V. Non-enzymatic and enzymatic hydrolysis of blends from hydrophobic poly(L-lactide) and hydrophilic poly(vinyl alcohol). *Polym. Degrad. Stab.* **2001**, *71*, 403–413. [CrossRef]

39. Yang, G.H.; Kim, M.; Kim, G. Additive-manufactured polycaprolactone scaffold consisting of innovatively designed microsized spiral struts for hard tissue regeneration. *Biofabrication* **2017**, *9*, 015005. [CrossRef]

40. Vesel, A.; Mozetic, M. New developments in surface functionalization of polymers using controlled plasma treatments. *J. Phys. D Appl. Phys.* **2017**, *50*, 293001. [CrossRef]

41. Ouellette, R.J.; Rawn, J.D. Nucleophilic Substitution and Elimination Reactions. In *Organic Chemistry Study Guide*; Elsevier: Amsterdam, The Netherlands, 2015; pp. 169–182.

42. Yip, J.; Chan, K.; Sin, K.M.; Lau, K.S. Comprehensive study of polymer fiber surface modifications Part 2: Low-temperature oxygen-plasma treatment. *Polym. Int.* **2004**, *53*, 634–639. [CrossRef]

43. Ye, P.; Wan, R.B.; Wang, X.P. Quantitative enzyme immobilization: Control of the carboxyl group density on support surface. *J. Mol. Catal. B Enzym.* **2009**, *61*, 296–302. [CrossRef]

44. Hegyesi, N.; Zhang, Y.; Kohári, A.; Polyák, P.; Sui, X.; Pukánszky, B. Enzymatic degradation of PLA/cellulose nanocrystal composites. *Ind. Crop. Prod.* **2019**, *141*, 111799. [CrossRef]

45. Tsuji, H.; Ishida, T. Poly(l-lactide). X. Enhanced surface hydrophilicity and chain-scission mechanisms of poly(l-lactide) film in enzymatic, alkaline, and phosphate-buffered solutions. *J. Appl. Polym. Sci.* **2002**, *87*, 1628–1633. [CrossRef]

46. Araque-Monrós, M.C.; Vidaurre, A.; Gil-Santos, L.; Gironés Bernabé, S.; Monleón-Pradas, M.; Más-Estellés, J. Study of the degradation of a new PLA braided biomaterial in buffer phosphate saline, basic and acid media, intended for the regeneration of tendons and ligaments. *Polym. Degrad. Stab.* **2013**, *98*, 1563–1570. [CrossRef]

47. Schiller, C.; Epple, M. Carbonated calcium phosphates are suitable pH-stabilising fillers for biodegradable polyesters. *Biomaterials* **2003**, *24*, 2037–2043. [CrossRef]

48. Niaza, K.V.; Senatov, F.S.; Kaloshkin, S.D.; Maksimkin, A.V.; Chukov, D.I. 3D-printed scaffolds based on PLA/HA nanocomposites for trabecular bone reconstruction. *J. Phys. Conf. Ser.* **2016**, *741*, 012068. [CrossRef]

49. Rafiee, M.; Farahani, R.D.; Therriault, D. Multi-Material 3D and 4D Printing: A Survey. *Adv. Sci.* **2020**, *7*. [CrossRef]

50. Foresti, R.; Rossi, S.; Selleri, S. Bio composite materials: Nano functionalization of 4D bio engineered scaffold. In Proceedings of the 2019 IEEE International Conference on BioPhotonics, Taipei, Taiwan, 15–18 September 2019.

51. Chen, S.; Guo, Y.; Liu, R.; Wu, S.; Fang, J.; Huang, B.; Li, Z.; Chen, Z.; Chen, Z. Tuning surface properties of bone biomaterials to manipulate osteoblastic cell adhesion and the signaling pathways for the enhancement of early osseointegration. *Colloids Surf. B Biointerfaces* **2018**, *164*, 58–69. [CrossRef] [PubMed]

Enhancement of Adhesion Characteristics of Low-Density Polyethylene Using Atmospheric Plasma Initiated-Grafting of Polyethylene Glycol

Taghreed Abdulhameed Al-Gunaid [1,2], Igor Krupa [1], Mabrouk Ouederni [3], Senthil Kumar Krishnamoorthy [3] and Anton Popelka [1,*]

[1] Center for Advanced Materials, Qatar University, P.O. Box 2713 Doha, Qatar; ta090196@qu.edu.qa (T.A.A.-G.); Igor.Krupa@qu.edu.qa (I.K.)

[2] Materials Science and Technology Program, College of Arts and Science, Qatar University, P.O. Box 2713 Doha, Qatar

[3] Product Development & Innovation, Qatar Petrochemical Company (QAPCO), P.O. Box 756 Doha, Qatar; m.ouederni@qapco.com.qa (M.O.); s.krishnamoorthy@qapco.com.qa (S.K.K.)

* Correspondence: anton.popelka@qu.edu.qa; Tel.: +974-4403-5676

Abstract: The low-density polyethylene/aluminum (LDPE/Al) joint in Tetra Pak provides stability and strength to food packaging, ensures protection against outside moisture, and maintains the nutritional values and flavors of food without the need for additives in the food products. However, a poor adhesion of LDPE to Al, due to its non-polar surface, is a limiting factor and extra polymeric interlayers or surface treatment is required. Plasma-assisted grafting of the LDPE surface with different molecular weight compounds of polyethylene glycol (PEG) was used to improve LDPE/Al adhesion. It was found that this surface modification contributed to significantly improve the wettability of the LDPE surface, as was confirmed by contact angle measurements. The chemical composition changes after plasma treatment and modification process were observed by X-ray photoelectron spectroscopy (XPS) and Fourier transform infrared spectroscopy (FTIR). A surface morphology was analyzed by scanning electron microscopy (SEM) and atomic force microscopy (AFM). Adhesion characteristics of LDPE/Al adhesive joints were analyzed by the peel tests. The most significant adhesion improvement of the PEG modified LDPE surface was achieved using 10.0 wt.% aqueous (6000 M) PEG solution, while the peel resistance increased by approximately 54 times in comparison with untreated LDPE.

Keywords: polyethylene; surface modification; corona discharge; polyethylene glycol; adhesion

1. Introduction

Polyolefins are the largest class of synthetic thermoplastic polymers that are employed in a wide variety of applications nowadays, particularly food packaging, industrial applications, consumable products, structural plastics, and medical applications [1,2]. This is because these polymers are distinguished by light weight, excellent chemical and physical properties, cost effectiveness, as well as ease of processing [3,4]. Polyolefins are manufactured by cracking the petrochemical sources such as crude oil and natural gas [5,6]. Polyethylene (PE) polymers including low-density polyethylene (LDPE) and high-density polyethylene (HDPE) are the most famous polyolefins commonly employed in the food packaging industry, since they are easily heat sealable, can be fabricated into rigid films, with a good barrier against moisture and water vapor [7,8]. In spite of such features, their poor surface properties, including adhesion, wettability, and cytocompatibility, impede their integration with other materials to form multi-layered laminates. In fact, PE materials have low surface reactivity and hydrophobic nature due to the lack of functional groups and low proportion of polar regions on their surfaces, and therefore incomplete adhesion with other materials [9,10]. Therefore, several surface modification methods have been

developed in recent decades. All these methods increase the surface energy of the polymer films, resulting in better wettability and thus higher bond strength [11]. The surface modification methods are basically classified into three sections: physical modification based on plasma technologies and flame treatment, chemical modification via surface functionalization, and mechanical abrasion [12–14]. However, previous studies found that mechanical abrasion could lead to significant damage of the treated surfaces [15]. The flame treatment is difficult to control, and bonding must be carried out shortly after exposure to flame [3]. Therefore, the use of plasma techniques and chemical methods are preferable in the surface treatment of polyolefins.

In the industrial scale, corona plasma discharge is a preferred cold plasma technique in surface modification of PE. It promotes surface activation, which leads to enhanced wetting and adhesion characteristics for applications related to adhesive bonding and printing [16,17]. Corona discharge is characterized by fast operation and completion (few seconds for treatment), cost effectiveness, easily adaptable to in-line operations, and environmentally friendly without the need to use aggressive chemicals during operation [3,18]. Corona discharge occurs when ambient air molecules are ionized at atmospheric pressure into charged particles such as electrons and ions. A high electric potential difference is formed between two asymmetric conductive electrodes (high-potential electrode and a grounded electrode) separated by a gap containing air. This creates a large electric field that accelerates the charged particles toward the polymer surface, which leads to the incorporation of reactive functional groups on the surface such as carbonyl, hydroxyl, hydroperoxides, aldehydes, ethers, esters, etc. The formed functional groups increase the polar part of surface energy and thus also the overall surface energy. Consequently, the surface is oxidized, its roughness and wettability increase, and finally its adhesion with other materials remarkably improves [11,17,19,20].

Chemical modification of the polymeric surfaces using graft polymerization plays a vital role in biomedical, environmental, and industrial applications [21,22], since it contributes to positive changes in the physical and chemical properties, morphology, and biocompatibility of the polymer [23–25]. Polyethylene glycol (PEG) is a versatile hydrophilic polyether that is immobilized onto the polymer surfaces using various techniques as physical adsorption, graft polymerization, covalent grafting, blending, etc. [26–29]. It is synthesized via chain-growth ring-opening polymerization of ethylene oxide in the presence of methanol or water as an initiator [30]. PEG is available as linear or branched chain polymers with an oxyethylene (-O-CH2-CH2-) repeating units that bonded with hydroxyl groups on either side of its chain [26,31,32]. The molecular weight of PEG plays a considerable role in specifying its properties. PEG is known as polyethylene oxide (PEO) when it is present in the form of a solid crystalline powder with molecular weight (M) greater than 20,000 g/mol, while PEG exists as viscous liquid (M < 1000 g/mol) or wax-like solid form (M: 1000–20000 g/mol) [26,33]. PEG and PEO compounds are soluble in both aqueous and organic solvents [34,35]. Recently, many studies focused on the development of the surface modification of hydrophobic polymers via graft polymerization with PEGs. Liu et al. worked on surface modification of polyester urethane (SPEU) films with different molecular weights of PEG compounds, Mn = 1200, 2400, and 4000 g/mol, for biomedical purposes. The SPEU surface was modified by grafting PEG on its surface, since PEG can effectively prevent protein adsorption and platelet adhesion due to its low interfacial free energy with water, unique solution properties, hydrophilicity, high chain mobility, and steric stabilization effect. The results showed that with increasing the molecular weight of PEG, there was a significant decrease in the water contact angle on PEG-g-SPEU, which indicated an increase in the surface energy and polarity, and thus strongly hydrophilic SPEU surface. Also, this can be attributed to high grafting density of PEG on the SPEU-PEG surface [36]. Adib and Raisi studied the surface modification of polyether sulfone membrane by grafting with hyperbranched PEG in combination with corona air plasma with the aim of enhancing anti-fouling properties. This led to improvement of the anti-fouling

property and oil–water permeability of all modified membranes without any significant changes in oil rejection [37].

In this work, the plasma imitated grafting of PEG/PEO on the LDPE surfaces were employed to improve adhesion characteristics without changing bulk properties. In fact, this research shed light on studying the effect of the difference in the molecular weights of PEG/PEO as well as the concentration of the PEG/PEO-based prepared aqueous solutions in the enhancement of the surface properties of LDPE in order to achieve higher interfacial adhesion of modified LDPE with Al to form LDPE/Al adhesive laminates that are commonly used for food packaging and processing applications (e.g., Tetra Pak containers). However, evident changes in surface characteristics of LDPE specimens after PEG/PEO grafting were demonstrated using several analysis techniques. These include surface hydrophilicity or wettability, chemical compositions of the surface, as well as surface roughness and morphology. Last but not least, the adhesion strength between modified LDPE and Al was improved. The adhesion characteristics were analyzed using two different methods, namely peel test at constant 90° angle, and work of adhesion calculations based on contact angle measurements.

2. Materials and Methods

2.1. Materials

Low-density polyethylene (LDPE) from Qatar Petrochemical Company (QAPCO, Mesaieed, Qatar) with code number: EC01-049 was used in this research. The used LDPE in granular form were hot-pressed into a thin transparent sheet using a hydraulic press machine (Carver, Wabash, IN, USA). Some characteristics of the LDPE are summarized in Table 1. LDPE sheets were bonded with aluminum (Al) foil (GLAD®, Qingdao, Shandong, China) to produce a coherent adhesive joint (LDPE/Al laminates), achieving the main purpose of this work.

Table 1. The properties/technical information of low-density polyethylene (LDPE) (EC01-049, QAPCO).

LDPE Properties	Description
Density at temperature 23 °C	0.918 g/cm^3 (ASTM D-1505)
Melt flow index	8.0 g/10 min, 190 °C/2.16 kg (ASTM D-1238)
Crystalline melting point	105 °C
Recommended uses	Extrusion coating at high speed

In addition, acetone (min.99.8% assay by G.C. method, Scharlab S.L., Barcelona, Spain) was used to remove any impurities or contaminants from the LDPE and Al surfaces prior to applying the surface treatment. For the wettability investigation of LDPE surfaces, ultra-pure water (Purity ≥ 99%, water purification system Direct-Q®, Millipore Corporation, Molsheim, France), formamide (Purity > 98%, FLUKA™, Merelbeke, Belgium), ethylene glycol (Purity ≥ 98%, FLUKA™, Morris Plains, NJ, Belgium) were used as testing liquids with different surface tension to determine the changes in surface total surface free energy and its components of the LDPE samples based on contact angle measurements. For surface modification of LDPE surfaces via grafting, PEG compounds with different molecular weights (M): 1000 g/mol (Fluka Chemika, Buchs, Switzerland), and 6000 g/mol (Merck KGaA, Darmstadt, Germany), as well as PEO with M = 300,000 g/mol (Sigma-Aldrich corporation, MO, St. Louis, USA) were used to increase the adhesion characteristics of LDPE surfaces. These compounds were dissolved into distilled water to prepare aqueous solutions at specific concentrations.

2.2. Preparation of LDPE Thin Sheets and LDPE-Al Laminate

The LDPE granulates were converted into coherent thin sheets using a hydraulic mounting press machine (Carver, Wabash, IN, USA). Ten grams of LDPE granules were placed between two transparent polyester sheets inside two highly polished stainless-steel plates, with a concern that granules were positioned adjacent to each other and on one level.

After that, all the previously prepared were entered between the upper and lower molding plates of the hydraulic press machine. LDPE granules were heated up into a temperature slightly higher than the melting temperature (160 °C). Once the desired temperature was reached, a one-ton load was applied into the LDPE granules for two minutes, to convert these granules into a thin sheet under the influence of applied temperature and force. Finally, the prepared LDPE sheet was cooled down gradually until room temperature. The thickness of the LDPE sheets was found to be approximately 290 μm and LDPE samples were cleaned by acetone in order to remove all undesirable contaminants from the surface prior to every post treatment/modification process. Furthermore, the LDPE/Al adhesive joints were fabricated by lamination process using mounting hot press machine with almost the same steps as LDPE sheet preparation (two tons compression molding for 2 min at 160 °C, then cooling to room temperature).

2.3. Surface Modification of LDPE Surface Using Corona Discharge

The LDPE surface was treated using corona plasma discharge in order to introduction of polar functional groups. A laboratory scale corona plasma system (CVE-L, Softal, Hamburg, Germany) (Figure 1) was employed for surface treatment of LDPE foils under atmospheric pressure using 300 W of nominal power and 17.20 kHz of frequency. The plasma treatment process of LDPE was optimized by varying treatment time from 1 to 7 s, while the optimal treatment time was achieved using 5 s, which was associated with the best achieved wettability. This system contains a catalytic ozone removal system ensuring a safe working environment. Applied high potential between the biased and grounded electrode (1.5 mm gap distance) using ambient air was responsible for homogeneous surfaces treatment of LDPE. The LDPE samples were treated from both sides.
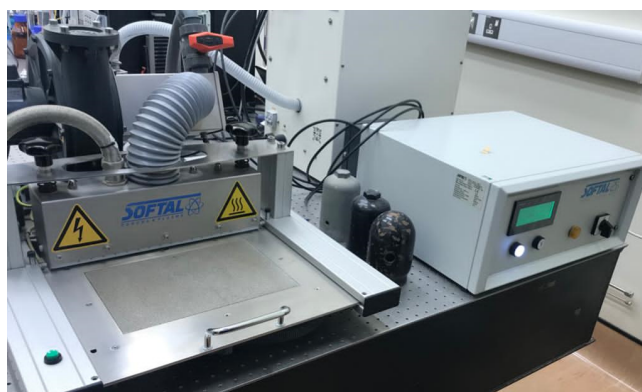
Figure 1. Corona plasma discharge system (Softal, Hamburg, Germany).

2.4. Grafting PEG/PEO onto LDPE

The corona-treated LDPE specimens were completely immersed into specific concentrations of PEG- or PEO-based aqueous solutions at room temperature for 24 h (Figure 2). After the modification process, the LDPE specimen was thoroughly rinsed with distilled water immediately after extraction from the solution, to remove unreacted species from the LDPE surface. Thereafter, it was left to totally dry at room temperature prior to other characterizations and lamination with Al. Six different aqueous solutions were used in this work, regarding two different concentrations per each PEG/PEO molecular weight, to investigate the influence of changing the molecular weight of PEG/PEO chains, and concentration of prepared PEG/PEO aqueous solutions on the surface characteristics of LDPE. These concentrations were as follows: 1.5 wt.%, and 10.0 wt.% for 1000 M PEG, 1.5 wt.% and 10.0 wt.% for 6000 M PEG, and 1.5 wt.% and 5.0 wt.% (maximal solubility in water) for 300,000 M PEO.
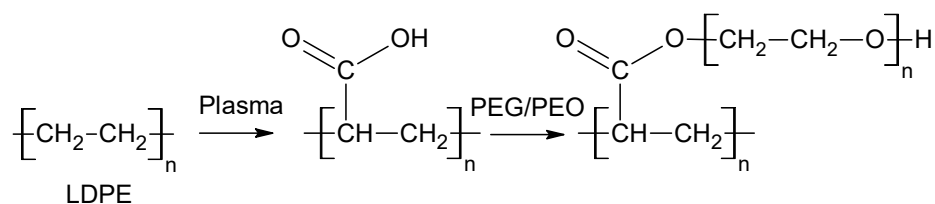
Figure 2. Scheme of proposed grafting mechanism of polyethylene glycol or polyethylene oxide (PEG/PEO) onto corona-treated LDPE.

2.5. Grafting Efficiency (GE) Evaluation

Grafting efficiency (GE) in the grafting process was defined as the percentage of the amount of the grafted monomer, which is linked into the polymer backbone to the total amount of the free polymer. GE values of the PEG/PEO grafted on LDPE (PEG/PEO-g-LDPE) specimens were calculated gravimetrically using Equation (1)

$$\text{GE } [\%] = \left(\frac{m_1 - m_0}{m_0} \right) \times 100\% \tag{1}$$

where m_0 is the mass of the LDPE sample before grafting, m_1 is the mass of the LDPE sample after grafting with PEG/PEO.

2.6. Determination of Surface Wettability

The changes in surface wettability after plasma treatment and modification of the LDPE samples were investigated by measuring the contact angle of selected testing liquids. Three testing liquids with different surface tensions and polarities were employed in sessile drop contact angle measurements, such as water, formamide, and ethylene glycol (see Table 2). Contact angle measuring system OCA 35 (Dataphysics, Filderstadt, Germany) was used for this purpose. This system was connected to an optical video-base imaging system linked to high-resolution USB camera (up to 2200 images/s). According to the sessile drop method, 3 μL volume droplet of each testing liquid was deposed softly with constant dosing rate of 2 μL/s on the LDPE samples with the dimensions of 8 cm length × 2 cm width. Then, the contact angle was measured after 3 s to ensure that the liquid droplet spreads evenly and completely over the surface, while thermodynamic equilibrium was achieved. At least five separate readings for each testing liquid were taken to obtain one representative average contact angle value that was subsequently used in the calculation of solid/liquid interfacial tension based on the Owens-Wendt-Rabel-Kaelble method (OWRK-model). OWRK-model expresses the interfacial interactions along the solid and liquid molecules (γ_{sl}) in term of three components, the total surface free energy (γ) and its components: polar (γ^p) and dispersive (γ^d) components, by Equation (2).

$$\gamma_{sl} = \gamma_s + \gamma_l - 2\left(\sqrt{\left(\gamma_s^d . \gamma_l^d\right)} + \sqrt{\left(\gamma_s^p . \gamma_l^p\right)} \right) \tag{2}$$

2.7. Determination of the Adhesion Strength of LDPE/Al Laminate

The 90° peel test measurements were employed for the evaluation of the adhesion characteristics between LDPE and Al components that form together a coherent laminate. Peel tester LF-Plus (Lloyd Instruments, West Sussex, UK) based on ASTM D6862 standard test method was employed in the adhesion strength measurements. This system was connected to NEXYGENPlus testing software, which allows entering the basic data and experimental conditions that fit the test type, as well as the results displayed as numerical values and representative graphs. Laminated LDPE/Al strips with dimensions approximately of 8 cm height and 2 cm width were attached tightly on an acrylic two sided tape (3 M 4910 k, VHBTM) prior to starting the test. The peel strength (the force per unit width of the laminate) was measured under dynamic conditions: 1-kN load cell was applied at

90° angle peeling on the specimen, operated at slow speed rate (v = 10 mm/min) to ensure the applied peeling force is evenly distributed over the surface, and the test time was set at 360 s to ensure that LDPE ultra-thin layer was completely separated from the Al foil. The peel resistance (peel force per width) was evaluated from a 10–50 mm distance of the LDPE/Al laminate. Following the Standard Test Method for 90 Degree Peel Resistance of Adhesives (ASTM D6862); 4–5 separate readings of LDPE-Al adhesives were taken to acquire one average value of the peel resistance, and subsequently compared with the work of adhesion computed from contact angle measurements.

Table 2. Surface free energy and its components: dispersion and polarity of testing liquids at 23 °C.

Testing Liquid	Surface Energy, γ_l (mN/m)	Dispersion, γ_l^d (mN/m)	Polarity, γ_l^p (mN/m)
Water	72.1	19.9	52.2
Formamide	56.9	23.5	33.4
Ethylene glycol	48.0	29.0	19.0

2.8. Calculation of the Work of Adhesion

The work of adhesion (W_{12}) for a solid–solid combination is defined as the reversible thermodynamic work (energy change per unit area) that is required to separate two adherent materials to form a laminate from the equilibrium state into a separation distance of infinity (Figure 3) [38]. In this work, quantities W_{12} of untreated, plasma treated and modified LDPE in the LDPE/Al laminate were calculated from contact angle measurements depending on the polarity and dispersion values of the surface energy by the Young–Dupré equation (Equation (3)), as follows [39]:

$$W_{12} = \gamma_1 + \gamma_2 - \gamma_{12} \tag{3}$$

where γ_1 is the surface energy of LDPE, γ_2 is the surface energy of Al, γ_{12} is the interfacial energy between LDPE and Al (solid–solid interface) and can be determined by the following equation.

$$\gamma_{12} = \gamma_1 + \gamma_2 - 2\left(\gamma_1^P \times \gamma_2^P\right)^{\frac{1}{2}} - 2\left(\gamma_1^d \times \gamma_2^d\right)^{\frac{1}{2}} \tag{4}$$

by substituting Equation (4) into Equation (3); the work of adhesion (W_{12}) is obtained as follows:

$$W_{12} = 2[\left(\gamma_1^P \times \gamma_2^P\right)^{\frac{1}{2}} + \left(\gamma_1^d \times \gamma_2^d\right)^{\frac{1}{2}}] \tag{5}$$

where subscripts '1' and '2' refer to LDPE and Al respectively; the superscript 'd' represents to the non-polar/dispersive contribution; and the superscript 'p' refers to the polar contribution to the surface free energy.
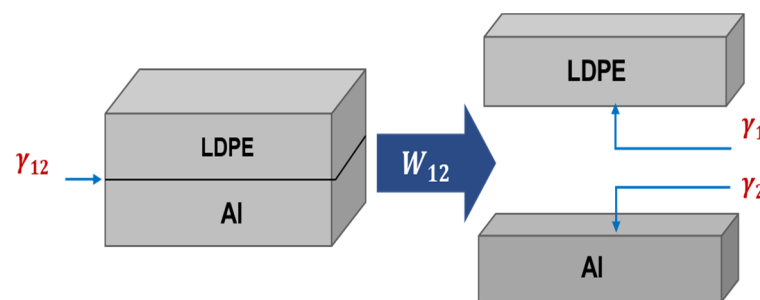

Figure 3. Illustrative scheme of work of adhesion between LDPE substrate and Al film.

2.9. Surface Morphology Analysis

The changes in two-dimensional surface morphology and roughness of the LDPE samples before and after surface modification were investigated by scanning electron microscopy (SEM) (Nova NanoSEM 450, Hillsboro, OR, USA). The LDPE specimens were observed at a high magnification (20,000×) and at high spatial resolution in order to achieve a high quality of the observed images. The working distance (WD) between the source of electrons and the exposed surface of the sample was set within the range of 4.6–5.1 mm. Furthermore, the SEM system was operated with moderate acceleration voltage equal to 5.0 kV. LDPE surfaces were coated by a thin layer (few angstroms thickness) of a gold (Au) to ensure higher resolution of captured SEM images, as well as to prevent charging of the surface and to promote the emission of secondary electrons [40].

The three-dimensional changes in the surface topography and roughness of the LDPE after plasma treatment and modification by PEG/PEO were determined using atomic force microscopy (AFM). The AFM images were obtained by an MFP-3D AFM device (Oxford Instruments Asylum Research, Abingdon, Oxford, UK) using AC160TS probe (Veeco model, OLTESPA, Olympus, Tokyo, Japan), which is covered with a thin reflex aluminum coating in order to prevent the light directed from the microscope lens towards the sample surface being scattered or lost. Furthermore, AFM measurements were conducted under ambient conditions in the dynamic mode in air (AC mode) known also as tapping mode. This mode is preferred due to it overcoming technical problems related with friction, adhesion, electrostatic forces that may appear after a plasma treatment and cause image data to be distorted [41]. Moreover, AFM is an ideal tool to quantitatively measure the dimensional surface roughness in nano-scale and to visualize the surface nano-texture of the deposited film, via commonly parameter that describe the vertical dimensions of the surface, namely average surface roughness line (Ra). Ra is defined as an arithmetical mean height of a line of the irregularities in the direction perpendicular to the sample surface [42,43].

2.10. Surface Composition Evaluation

Fourier-transform infrared spectroscopy (FTIR) was employed to identify the changes in chemical composition of the LDPE samples after plasma treatment and modification process. FTIR spectra were recorded using (Spectrum 400, PerkinElmer, Waltham, MA, USA) equipped with a ZnSe crystal allowing the analysis of data from 1.66 μm of the penetration depth. This FTIR spectra were captured within a wavenumber range of 500–4000 cm^{-1} at spectral resolution of 4 cm^{-1} in the absorbance mode to collect 8 scans with the aim to obtain accurate FTIR spectra.

The elemental and chemical compositions of the untreated, plasma-treated, and modified LDPE samples were evaluated using X-ray photoelectron spectroscopy (XPS) (Axis Ultra DLD, Kratos Analytical, Manchester, UK). XPS spectra were collected by irradiating a monoenergetic X-rays to the surface of a material, causing the emission of photoelectrons that are located within 10 nm from the underneath surface. Thus, the kinetic energy of the electrons emitted from each element present on the surface is analyzed, and the spectrum is obtained as a plot of the number of detected electrons per energy interval versus their kinetic energy. Furthermore, quantitative data were calculated based on the peaks formed by the individual elements according to the peak heights, areas, positions, and certain spectral features [44].

3. Results

3.1. Grafting Efficiency (GE)

The changes in the grafting efficiency (GE) of corona-treated LDPE surfaces modified by PEG/PEO are shown in Figure 4. The corona surface treatment had a significant effect on PEG/PEO grafting onto LDPE surfaces due to formation of radicals or reactive sites, which can react with PEG/PEO chains that are introduced into the surface. However, most probably, the grafting mechanism can be caused by an esterification process [45] as the result of interactions between the incorporated carboxylic groups in LDPE and

hydroxyl groups of PEG/PEO [31] as was confirmed by FTIR measurements. This leads to an increase in the mass of the modified specimen, thus increasing GE [9]. It was noted that GE increased with increasing the PEG/PEO monomer concentration in the aqueous solution, due to incorporation of PEG/PEO chains onto LDPE surfaces. This was confirmed by the presence of the band at 1100 cm^{-1} (C-O-C) in the FTIR spectra [46]. Moreover, the highest GE was achieved for 5.0 wt.% PEO (300,000 M)-g-LDPE films preceded by 5 s of plasma surface treatment, while GE was approximately 0.6%. This can be explained by PEO (300,000 M) having ultrahigh molecular weights that can create a thicker layer on the LDPE surface in comparison to another PEG being used.
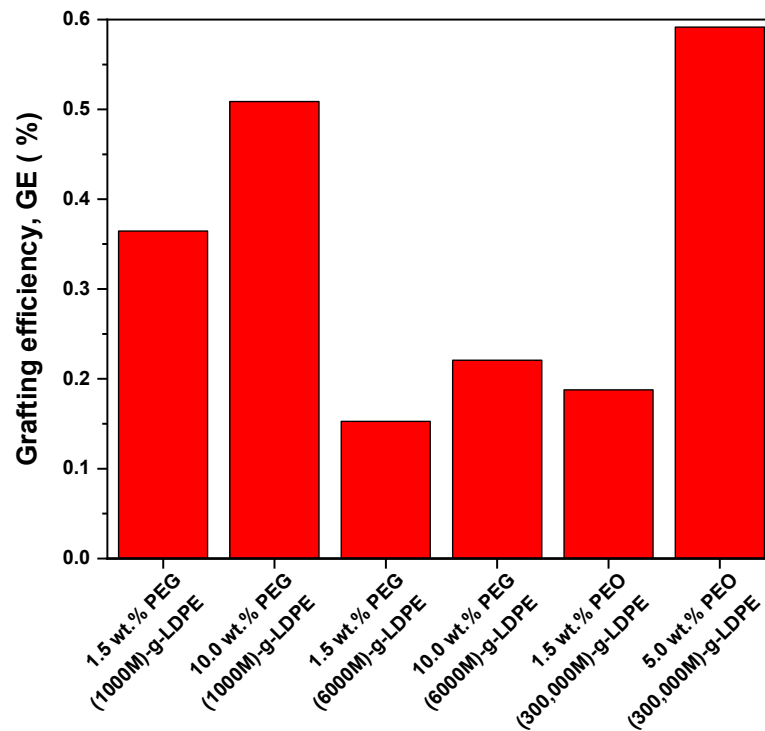
Figure 4. Effect of plasma treatment on grafting efficiency (GE) of PEG/PEO-g-LDPE.

3.2. Surface Wettability Analysis

The wettability property refers to the ability of a liquid to maintain in contact with a solid surface and it is characterized by the contact angle when a droplet of liquid is placed on a flat, horizontal solid surface. In this work, three testing liquids with various surface tension and polarity, namely water, formamide, and ethylene glycol, were used to study the changes in the wettability after plasma treatment and surface modification of LDPE. As can be seen from Figure 5a, a dramatic decrease in the contact angle values was observed with increasing the surface treatment time via corona discharge. The maximum decrease in the contact angle values was recorded after 5 s of surface treatment, so it can be considered as the optimum treatment time for LDPE surfaces. The contact angle values were decreased from 72.3° to 57.5° for water, from 64.5° to 41.7° for formamide, and from 57.8° to 29.1° for ethylene glycol corresponding to untreated and 5 s corona-treated LDPE surfaces. However, the relatively low values of contact angles of testing liquids for untreated LDPE were probably affected by the processing additives as was confirmed by pre-sent oxygen-containing groups observed by XPS. Plasma treatment leads to surface oxidation and introduction of new polar functional groups such as C=O, –OH, COOH, C–O–C, into the LDPE surfaces responsible for a wettability increase [47]. In addition, the effect of PEG/PEO grafting on the wettability of LDPE was studied (Figure 5b). A noticeable reduction in the contact angles of the PEG/PEO-g-LDPE surfaces were recorded compared to untreated LDPE surfaces. This can be explained by changes in

surface roughness as a result of PEG/PEO grafting [48]. However, a slight increase was observed in the contact angle values for all the PEG/PEO-g-LDPE in comparison with only corona-treated LDPE, as a result of chemical nature of PEG/PEO. Furthermore, it was revealed that as the concentration of PEG/PEO aqueous solutions increased, the contact angle became slightly lower for the same molecular weight, due to enriching the modified surface with PEG/PEO grafted on the LDPE surface, as well as hydrophilic properties of the PEG/PEO molecules themselves [49].

Figure 6 shows the change in the surface free energy and the corresponding polar and dispersive contributions of the untreated and modified LDPE samples. It became clear that the surface free energies were significantly increased after surface treatment with corona discharge from 30.3 mN/m for untreated LDPE to 42.6 mN/m for corona-treated LDPE due to introduction of characteristic polar functional groups, such as C=O, –OH, COOH, COO–, C–O–C, to the substrate surface [47]. It was confirmed that surface modification of LDPE via plasma-initiated grafting of PEG/PEO contributed to an improvement of the wettability properties of LDPE surfaces, as an increase in both the surface energies and polarities were observed for all PEG/PEO used with estimated percentages of 31.3% and 63.0%, respectively at the minimum. This indicated that the chemical character of grafted PEG/PEO affected on the surface hydrophilicity of LDPE substrate [50].

(**a**)

Figure 5. *Cont.*

(**b**)
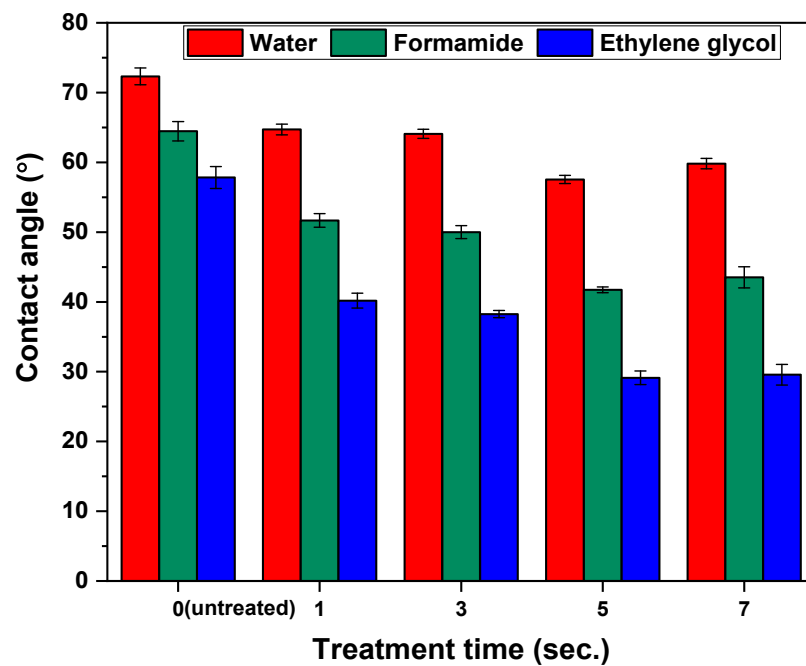
Figure 5. Contact angle of (**a**) LDPE samples vs. corona-treatment time, (**b**) PEG/PEO-g-LDPE.
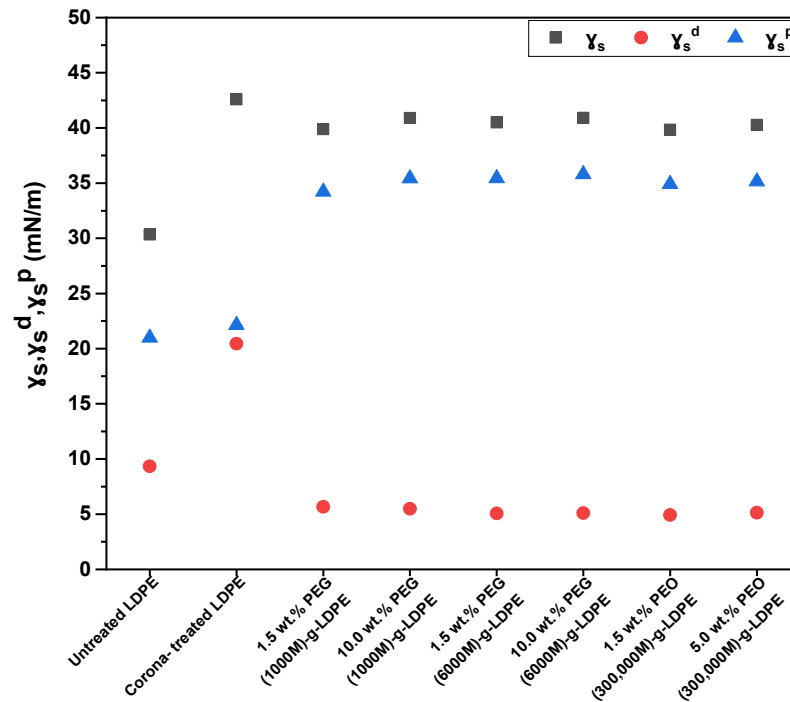
Figure 6. Surface energy (γ_s) and its components: polarity (γ_s^p), and dispersion (γ_s^d) of LDPE surfaces.

3.3. Surface Morphology Analysis
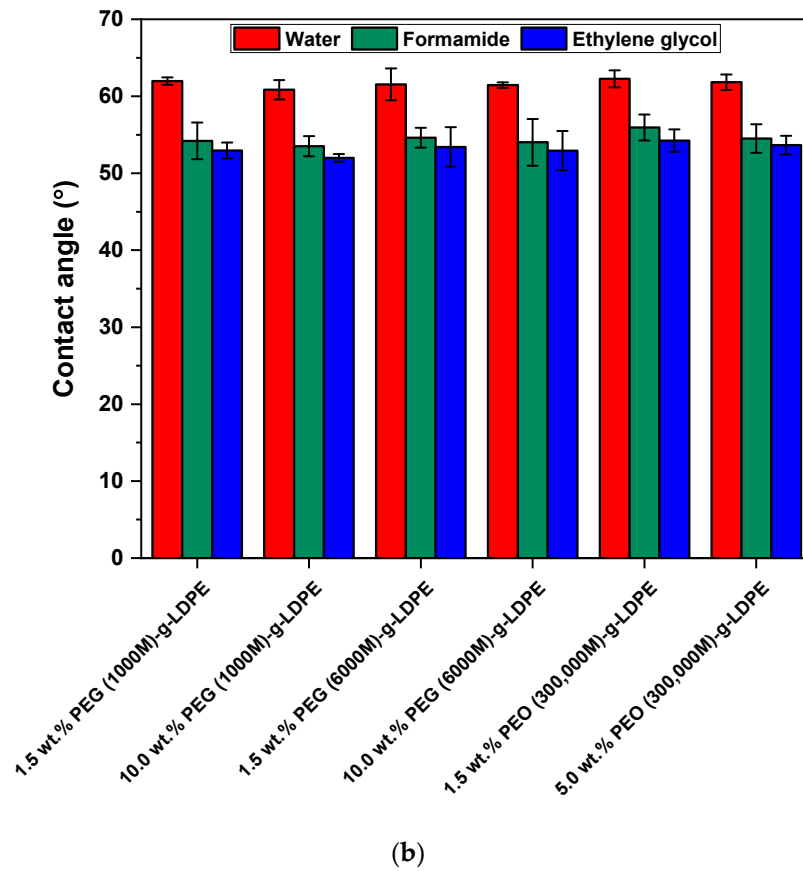
The changes in the morphological characteristics of the corona-treated (5 s) and PEG/PEO grafted LDPE samples were investigated by SEM analysis, as shown in Figure 7. The SEM image of untreated LDPE surface (Figure 7a) showed it excelled at low levels of surface roughness, while a noticeable increase in surface roughness was observed to the corona-treated LDPE samples as a consequence of surface ablation and etching processes (Figure 7b). In contrast, a slight increase was observed in surface roughness predominantly in the amorphous phase of PEG/PEO-g-LDPE surfaces affected by 5 s of continuous treatment by corona discharge (Figure 7c–h). However, it can be seen that the surface roughness of the PEG/PEO-g-LDPE samples is lower compared to the only corona-treated LDPE surface due to the formation of a compact PEG/PEO layer.

The AFM measurements were performed in order to analyze detailed surface morphology/topography changes in the LDPE surface after plasma treatment and modification processes (Figure 8). The changes in the surface roughness were quantified by the surface roughness parameter (Ra). AFM images showed that the surface of the untreated LDPE is relatively smooth with low value of average roughness (Ra = 3.4 nm), as demonstrated in Figure 8a. Correspondingly, the surface treatment of the LDPE surface with 5 s of corona treatment led to an increase in the surface roughness, while Ra increased to 4.5 nm as a result of etching and ablation processes (Figure 8b). The morphologies/topographies of the corona-treated grafted PEG/PEO LDPE specimens were detected by AFM analysis, as evidenced in Figure 8c–h. It was observed that surface roughness of the PEG/PEO-g-LDPE specimens were greater than the untreated LDPE, due to the PEG/PEO graft on the modified surfaces. These results are consistent with contact angle measurements, because rougher surfaces reduce hydrophobicity and thus improve the wettability characteristics [48]. It was noticed that surface roughness decreased after PEG/PEO grafting onto the LDPE surfaces compared to corona-treated surfaces, due to a formation of PEG layer onto the LDPE surface. Moreover, it was found that increasing the concentration of the PEG/PEO-based aqueous solution resulted in less rough LDPE surface, due to high grafting density of PEG/PEO that leads to the creation of a thin layer. Moreover, it was observed that all LDPE films grafted by high concentrations of PEG/PEO had the same surface roughness (Ra = 3.6 nm)

3.4. Chemical Composition Investigation

The FTIR analysis was used to identify the changes in the chemical composition of the LDPE surface after plasma treatment and surface modification by PEG/PEO (Figure 9). Generally, FTIR spectrum of untreated LDPE is characterized by characteristic absorption peaks, which coincide well with the relevant published literature, such as: out of phase and in-phase rock of the $-CH_2-$ at 720 cm^{-1} and 731 cm^{-1}, weak asymmetric bending vibration of carbon-hydrogen bond (C–H) along the vertical axis (b-axis) of the LDPE chain at 1478 cm^{-1}, asymmetric bending vibration of the CH3 groups along the horizontal axis (a-axis bend) at 1463 cm^{-1}, as well as symmetric and asymmetric stretching vibrational bands that represent methylene group (C–H2) at 2848 cm^{-1} and 2916 cm^{-1}, respectively [51]. The surface treatment by corona discharge led to significant appearance of new absorption bands at 1750 cm^{-1} and 1110 cm^{-1} associated with stretching vibrations of C=O (COOH) and –O– respectively. In addition, the hydroxyl functional group (–OH) was represented by a less intense and broad absorption peak between 3500 cm^{-1} and 3180 cm^{-1}. The emergence of these oxygen-containing functional groups in the LDPE surfaces was caused by an oxidation process. In addition, the FTIR spectra of PEG/PEO-g-LDPE surfaces exhibited a noticeable increase in the peak intensity corresponding to –O– compared with only corona-treated LDPE samples, while the peak intensity of C–H decreased. Moreover, the FTIR spectra clearly indicated the disappearance of the COOH-associated absorption bands in the PEG/PEO-g-LDPE samples, which were utilized in the grafting process.
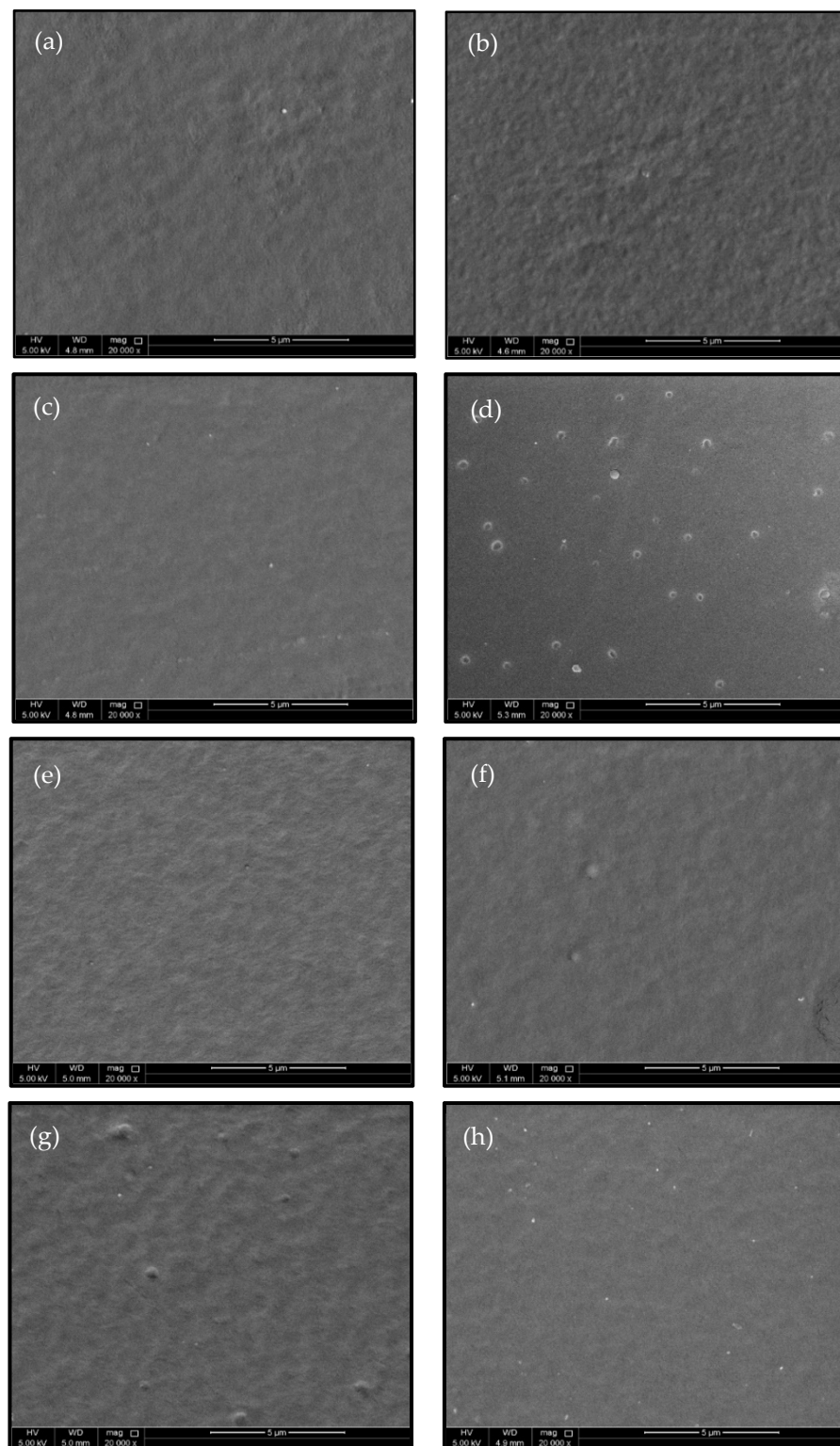
Figure 7. SEM micrographs of LDPE surface: (**a**) untreated, (**b**) corona treated, (**c**) 1.5 wt.% PEG (1000 M)-g-LDPE, (**d**) 10.0 wt.% PEG (1000 M)-g-LDPE, (**e**) 1.5 wt.% PEG (6000 M)-g-LDPE, (**f**) 10.0 wt.% PEG (6000 M)-g-LDPE, (**g**) 1.5 wt.%PEO (300,000 M)-g-LDPE, (**h**) 5.0 wt.% PEO (300,000 M)-g-LDPE.
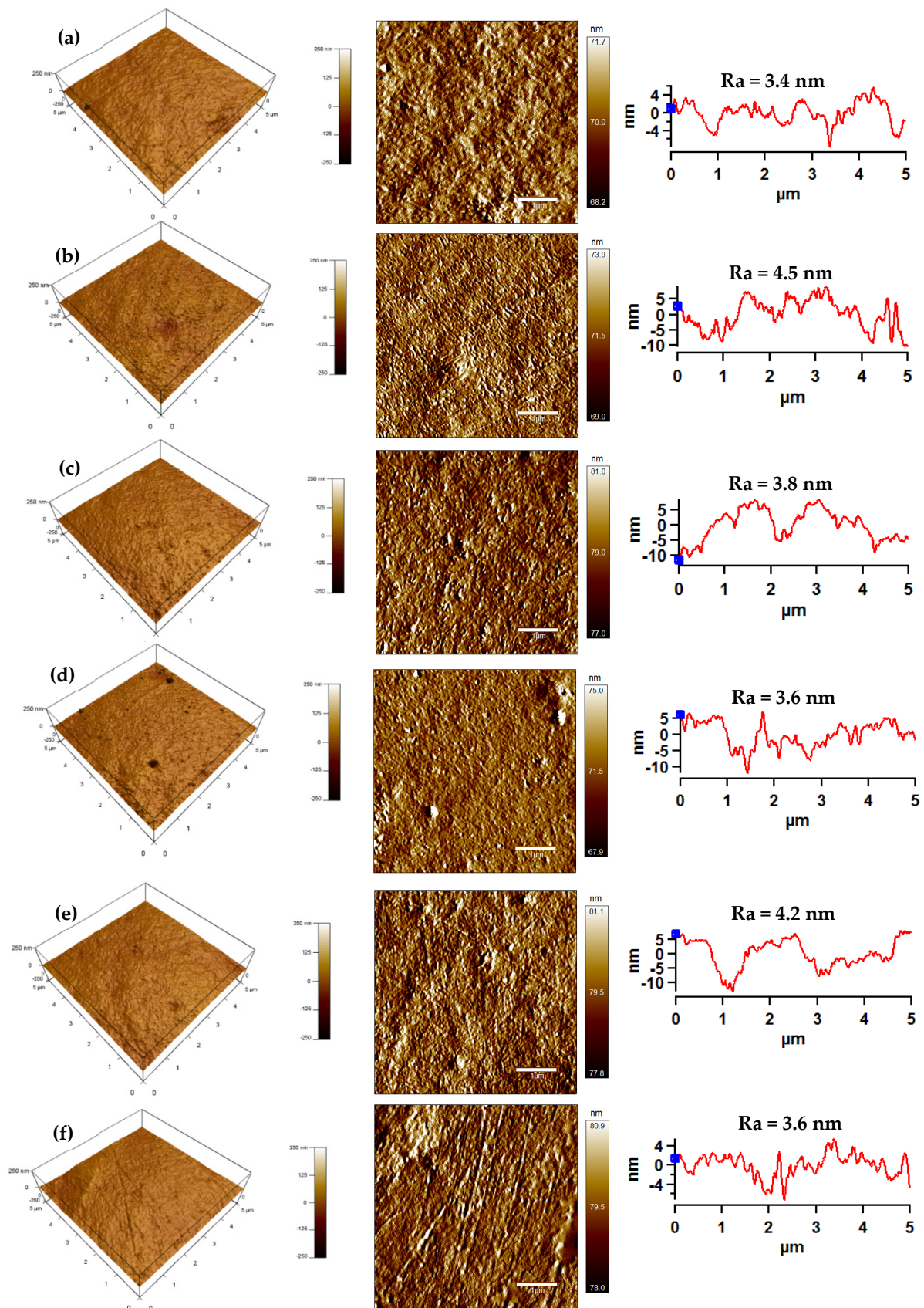
Figure 8. *Cont.*
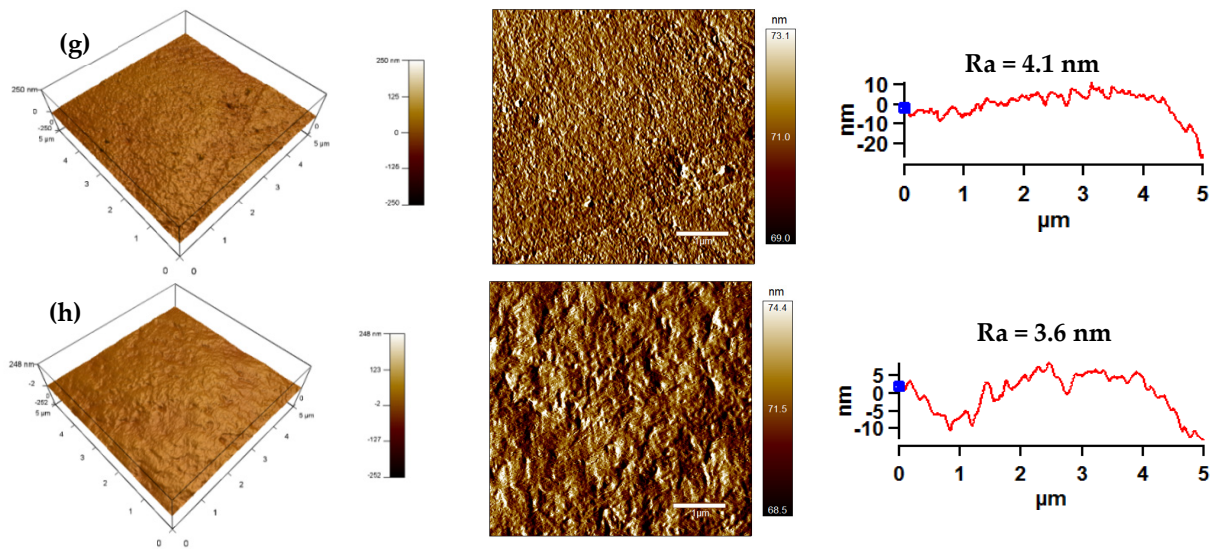
Figure 8. Atomic force microscopy (AFM) images (3D Height, Amplitude, line profile) with Ra roughness parameter of LDPE surface: (**a**) untreated, (**b**) corona-treated, (**c**) 1.5 wt.% PEG (1000 M)-g-LDPE, (**d**) 10.0 wt.% PEG (1000 M)-g-LDPE, (**e**) 1.5 wt.% PEG (6000 M)-g-LDPE, (**f**) 10.0 wt.% PEG (6000 M)-g-LDPE, (**g**) 1.5 wt.%PEO (300,000 M)-g-LDPE, (**h**) 5.0 wt.% PEO (300,000 M)-g-LDPE.
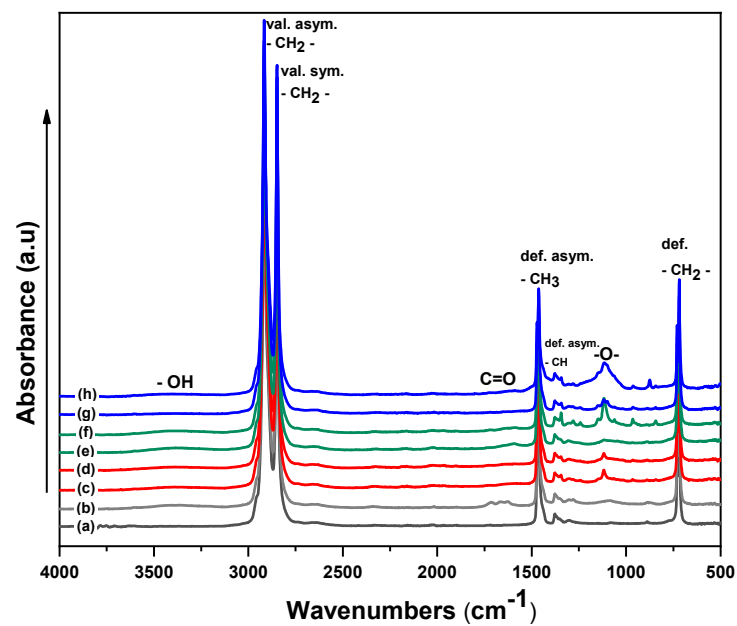
Figure 9. FTIR spectra of LDPE surfaces: (**a**) untreated, (**b**) corona-treated, (**c**) 1.5 wt.%PEG (1000 M)-g-LDPE, (**d**) 10.0 wt.%PEG (1000 M)-g-LDPE, (**e**) 1.5 wt.%PEG (6000 M)-g-LDPE, (**f**) 10.0 wt.%PEG (6000 M)-g-LDPE, (**g**) 1.5 wt.%PEO (300,000 M)-g-LDPE, (**h**) 5.0 wt.%PEO (300,000 M)-g-LDPE.

The XPS technique provides quantitative information about the elemental compositions of the untreated, corona-treated, and modified LDPE surfaces as seen in Figure 10 and Table 3. As can be seen, there are two characteristic XPS peaks corresponding to the C1s and O1s at binding energy values of 284.8 and 532.8 eV, respectively. A slightly increase in the oxygen content was observed after corona treatment, while at.% of O1s increased from 8.6 to 11.3% for untreated and corona-treated LDPE, respectively, due to the enriching of the surface with oxygen-containing functional species. However, the presence of oxygen species in the untreated LDPE structure may be related to the processing additives. After PEG/PEO grafting onto LDPE surfaces via plasma treatment, it was found that the at.%

of carbon element increased compared to untreated LDPE as results of higher carbon to oxygen ratio in PEG/PEO. Furthermore, a slight increase in the oxygen content was observed as the concentration of the PEG/PEO solutions increased and therefore at.% of carbon decreased, indicating higher density of PEG/PEO grafted on the LDPE surface. Furthermore, a decrease in the nitrogen content was observed on the LDPE surfaces with increasing the molecular weight of grafted PEG chains (>1000) due to a formation of a thin coating layer on the LDPE surface, which hinders the detection of the internal nitrogen element [36].
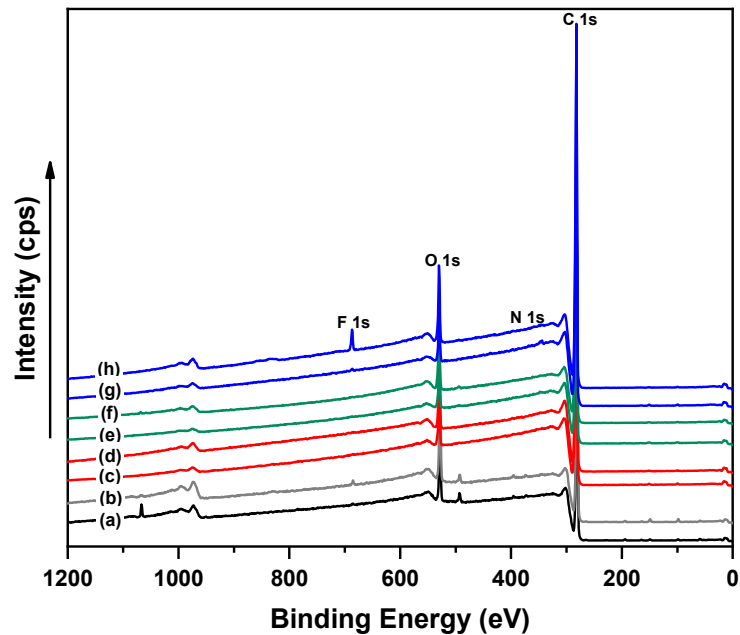
Figure 10. XPS spectra of LDPE surfaces.

Table 3. Elemental composition of LDPE surfaces by XPS analysis.

Samples	Element, Atomic Conc. (at. %)		
	C 1s	O 1s	N 1s
(a) Untreated-LDPE	91.2	8.6	0.2
(b) Corona-treated LDPE	88.5	11.3	0.2
(c) 1.5 wt.% PEG (1000M)-g-LDPE	95.2	4.6	0.2
(d) 10.0 wt.% PEG (1000M)-g-LDPE	93.6	6.1	0.3
(e) 1.5 wt.% PEG (6000M)-g-LDPE	95.3	4.5	0.00
(f) 10.0 wt.% PEG (6000M)-g-LDPE	92.3	7.5	0.04
(g) 1.5 wt.% PEO (300,000M)-g-LDPE	95.1	5.2	0.03
(h) 5.0 wt.% PEO (300,000M)-g-LDPE	90.6	9.2	0.0

3.5. Adhesive Strength Measurements

The adhesive strength of the untreated, plasma treated and PEG/PEO-g-LDPE laminates with Al were analyzed using peeling resistance measurements, as shown in Figure 11. It can be seen that the peel resistance of the untreated LDPE/Al joints were nearly 3 N/m due to poor adhesion between the LDPE and Al laminate components. This can be interpreted to hydrophobic nature and low wettability of pristine LDPE surfaces. The peel resistance of LDPE/Al laminates remarkably increased (≈62.5 N/m) after plasma treatment using corona discharge as a result of improved wettability and roughness. In addition, it was observed that LDPE/Al adhesion joints prepared using the PEG/PEO-g-LDPE samples had a notable increase in peel resistance compared to untreated LDPE. This increase in peel resistance was mainly due to increase in the wettability and surface roughness

caused by the incorporation of oxygen-rich functional. In addition, the highest peeling resistance values were recorded at high concentrations of PEG/PEO aqueous solutions, which was consistent with the surface wettability results obtained from the contact angle measurements of PEG/PEO-g-LDPE surfaces. The maximum peel resistance (163.0 N/m) of LDPE/Al adhesive joint was observed for LDPE/10.0% PEG (6000 M), which suggested as the optimum value. In contrast, the corona-treated LDPE grafted by PEO (300,000 M) surfaces exhibited the lowest adhesion values compared to other PEG used. This might be because as the molecular weight of PEG increased, the mole fraction of the reactive -OH groups decreased, to the point where the active bonding sites available on the LDPE surface are saturated and no more extend. Thus affecting on their surface hydrophilicity and thus led to reduced adherence to Al [52]. Moreover, work of adhesion (W_{12}) for the LDPE/Al adhesive joints were calculated using surface free energy and its components. It was found that W_{12} values showed similar behavior as the peel resistance for all conditions used. The reason for the lower values of W_{12} than peeling resistance of LDPE/Al adhesion joint was the fact that W_{12} counts with infinite slow peeling rate, while crosshead speed during the peel resistance measurement was 10 mm/min. However, it was found that all modified PEG/PEO-g- LDPE surfaces had higher values of W_{12} compared to untreated and corona-treated LDPE surfaces because of higher values of the polar component of the surface energy resulted from the improved wettability.
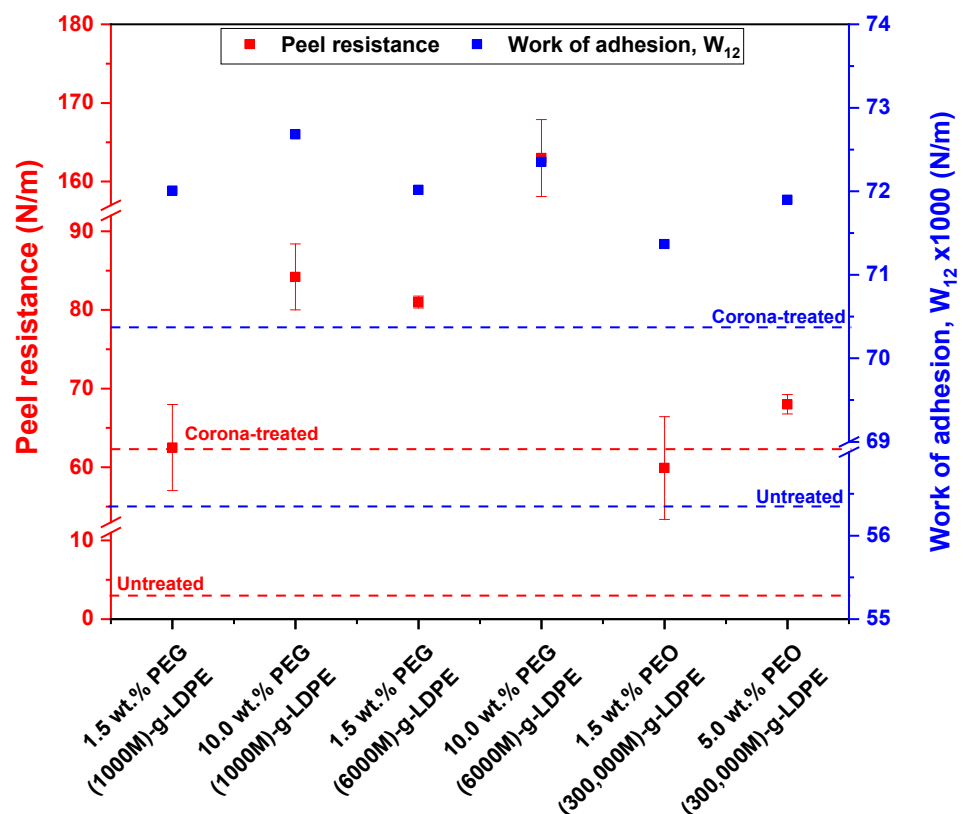
Figure 11. Effect of corona treatment on the peel resistance and work of adhesion of PEG/PEO-g-LDPE adhesive joint with Al.

4. Conclusions

In this work, the surface characteristics of low-density polyethylene (LDPE) were enhanced using plasma-initiated grafting of different molecular weight polyethylene glycol or polyethylene oxide (PEG/PEO) onto LDPE surfaces in order to improve the adhesion to aluminum (Al) for industrial purposes. This surface modification improved the surface wettability as was confirmed by a decrease in the contact angles, and thus increased both the surface free energy and its polar component as a consequence of the change in the

chemical composition of the modified LDPE surfaces. Moreover, the chemical composition analyses confirmed the presence of PEG/PEO on the corona-treated LDPE surface through esterification process. This led to considerable enhancement in the interfacial adhesion between LDPE and Al compared to the untreated and corona-treated surfaces. It was found that the adhesion strength between LDPE and Al surfaces were achieved at high concentrations of aqueous solutions containing PEG/PEO compounds. This could be due to improved wettability of the treated surfaces as confirmed by contact angle measurements as well as results obtained from typical surface analyzes. However, the highest adhesion in the LDPE/Al laminate was achieved by grafting with a 10% PEG (6000 M) aqueous solution onto 5 s corona-treated LDPE surface, where the peel resistance increased by approximately 54 times and 2.6 times compared to the peel resistance of untreated and corona-treated LDPE surfaces, respectively.

Author Contributions: Conceptualization, A.P., I.K., M.O., and S.K.K.; methodology, A.P. and I.K.; validation, A.P.; formal analysis, T.A.A.-G. and A.P.; investigation, T.A.A.-G. and A.P.; resources, I.K., M.O. and S.K.K.; data curation, A.P.; writing—original draft preparation, T.A.A.-G.; writing—review and editing, A.P.; visualization, T.A.A.-G.; supervision, A.P.; project administration, I.K.; funding acquisition, I.K. All authors have read and agreed to the published version of the manuscript.

Conflicts of Interest: The authors declare no conflict of interest.

References

1. Manjula, B.; Reddy, A.B.; Sadiku, E.R.; Sivanjineyulu, V.; Molelekwa, G.F.; Jayaramudu, J.; Kumar, K.R. Use of polyolefins in hygienic applications. In *Polyolefin Fibres*; Elsevier: Amsterdam, The Netherlands, 2017; pp. 539–560.
2. Olabisi, O. Polyolefins. In *Handbook of Thermoplastics*; Olabisi, O., Adewale, K., Eds.; CRC Pres: Boca Raton, FL, USA, 2015; pp. 1–2.
3. Petrie, E.M. Adhesive Bonding of Polyolefin. *Polyurethane* **2013**, *38*, 85.
4. Lohse, D.J. POLYOLEFINS. In *Applied Polymer Science: 21st Century*; Craver, C.D., Carraher, C.E., Eds.; Pergamon: Oxford, UK, 2000; pp. 73–91.
5. AlMa'adeed, M.A.-A.; Krupa, I. Polyolefin compounds and materials. In *Springer Series on Polymer and Composite Materials*; Springer: Cham, Switzerland, 2016; pp. 271–284.
6. Posch, W. 3-Polyolefins. In *Applied Plastics Engineering Handbook*; Kutz, M., Ed.; William Andrew Publishing: Oxford, UK, 2011; pp. 23–48.
7. Yang, F.; Wang, X.; Ma, Z.; Wang, B.; Pan, L.; Li, Y. Copolymerization of propylene with higher α-olefins by a Pyridylamidohafnium catalyst: An effective approach to polypropylene-based elastomer. *Polymers* **2020**, *12*, 89. [CrossRef]
8. Cruz, R.M.S.; Rico, B.P.M.; Vieira, M.C. 9-Food packaging and migration. In *Food Quality and Shelf Life*; Galanakis, C.M., Ed.; Academic Press: Cambridge, MA, USA, 2019; pp. 281–301.
9. Kasalkova, N.S.; Slepicka, P.; Kolska, Z.; Svorcik, V. Wettability and other surface properties of modified polymers. *Wetting Wettability* **2015**, *12*, 323–356.
10. Drnovska, H.; Lapčík, L.; Buršíková, V.; Zemek, J.; Barros-Timmons, A.M. Surface properties of polyethylene after low-temperature plasma treatment. *Colloid Polym. Sci.* **2003**, *281*, 1025–1033. [CrossRef]
11. Lindner, M.; Rodler, N.; Jesdinszki, M.; Schmid, M.; Sängerlaub, S. Surface energy of corona treated PP, PE and PET films, its alteration as function of storage time and the effect of various corona dosages on their bond strength after lamination. *J. Appl. Polym. Sci.* **2018**, *135*, 45842. [CrossRef]
12. Gilliam, M. Polymer Surface Treatment and Coating Technologies. In *Handbook of Manufacturing Engineering and Technology*; Nee, A., Ed.; Springer: London, UK, 2013; pp. 1–23.
13. Sharpe, P. Making Plastics: From Monomer to Polymer. *Chem. Eng. Prog.* **2015**, *111*, 24–29.
14. Ozdemir, M.; Yurteri, C.U.; Sadikoglu, H. Physical polymer surface modification methods and applications in food packaging polymers. *Crit. Rev. Food Sci. Nutr.* **1999**, *39*, 457–477. [CrossRef]

15. Pinto, A.G.; Magalhaes, A.; da Silva, F.G.; Baptista, A.M. Shear strength of adhesively bonded polyolefins with minimal surface preparation. *Int. J. Adhes. Adhes.* **2008**, *28*, 452–456. [CrossRef]
16. Pascual, M.; Sanchis, R.; Sánchez, L.; García, D.; Balart, R. Surface modification of low density polyethylene (LDPE) film using corona discharge plasma for technological applications. *J. Adhes. Sci. Technol.* **2008**, *22*, 1425–1442. [CrossRef]
17. Santos, L.P.; Bernardes, J.S.; Galembeck, F. Corona-treated polyethylene films are macroscopic charge bilayers. *Langmuir* **2013**, *29*, 892–901. [CrossRef] [PubMed]
18. Amirou, S.; Zerizer, A.; Haddadou, I.; Merlin, A. Effects of corona discharge treatment on the mechanical properties of biocomposites from polylactic acid and Algerian date palm fibres. *Sci. Res. Essays* **2013**, *8*, 946–952.
19. Chapter 17-Adhesive Bonding. In *Handbook of Plastics Joining*, 2nd ed.; Troughton, M.J. (Ed.) William Andrew Publishing: Boston, MA, USA, 2009; pp. 145–173.
20. Chapter 3-Material Surface Preparation Techniques. In *Adhesives Technology Handbook*, 2nd ed.; Ebnesajjad, S. (Ed.) William Andrew Publishing: Norwich, NY, USA, 2009; pp. 37–46.
21. Nikolic, V.; Velickovic, S.; Popovic, A. Biodegradation of polystyrene-graft-starch copolymers in three different types of soil. *Environ. Sci. Pollut. Res.* **2014**, *21*, 9877–9886. [CrossRef] [PubMed]
22. Sánchez, L.D.; Brack, N.; Postma, A.; Pigram, P.J.; Meagher, L. Surface modification of electrospun fibres for biomedical applications: A focus on radical polymerization methods. *Biomaterials* **2016**, *106*, 24–45. [CrossRef] [PubMed]
23. Kim, P.-H.; Kim, S.W. Polymer-based delivery of glucagon-like peptide-1 for the treatment of diabetes. *Int. Sch. Res. Not.* **2012**, *2012*, 340632. [CrossRef]
24. Mohammadi Sejoubsari, R.; Martinez, A.P.; Kutes, Y.; Wang, Z.; Dobrynin, A.V.; Adamson, D.H. "Grafting-through": Growing polymer brushes by supplying monomers through the surface. *Macromolecules* **2016**, *49*, 2477–2483. [CrossRef]
25. Pergal, M.V.; Antic, V.V.; Tovilovic, G.; Nestorov, J.; Vasiljevic-Radovic, D.; Djonlagic, J. In vitro biocompatibility evaluation of novel urethane–siloxane co-polymers based on poly (ε-caprolactone)-block-poly (dimethylsiloxane)-block-poly (ε-caprolactone). *Biomater. Sci. Polym. Ed.* **2012**, *23*, 1629–1657. [CrossRef]
26. Zarrintaj, P.; Saeb, M.R.; Jafari, S.H.; Mozafari, M. Chapter 18-Application of compatibilized polymer blends in biomedical fields. In *Compatibilization of Polymer Blends*; Ajitha, A.R., Thomas, S., Eds.; Elsevier: Amsterdam, The Netherlands, 2020; pp. 511–537.
27. McPherson, T.B.; Shim, H.S.; Park, K. Grafting of PEO to glass, nitinol, and pyrolytic carbon surfaces by gamma irradiation. *J. Biomed. Mater. Res.* **1997**, *38*, 289–302. [CrossRef]
28. Lakshmi, S.; Jayakrishnan, A. Migration resistant, blood-compatible plasticized polyvinyl chloride for medical and related applications. *Artif. Organs* **1998**, *22*, 222–229. [CrossRef]
29. Cheng, G.; Cai, Z.; Wang, L. Biocompatibility and biodegradation of poly(hydroxybutyrate)/poly(ethylene glycol) blend films. *J. Mater. Sci. Mater. Med.* **2003**, *14*, 1073–1078. [CrossRef]
30. Zacchigna, M.; Cateni, F.; Drioli, S.; Bonora, G.M. Multimeric, multifunctional derivatives of poly (ethylene glycol). *Polymers* **2011**, *3*, 1076–1090. [CrossRef]
31. Sun, D.; Iqbal, K.; Siddiqui, M.O.R. 20-Thermal analysis of temperature responsive fibrous materials. In *Thermal Analysis of Textiles and Fibers*; Jaffe, M., Menczel, J.D., Eds.; Woodhead Publishing: Cambridge, UK, 2020; pp. 335–353.
32. Hutanu, D.; Frishberg, M.D.; Guo, L.; Darie, C.C. Recent applications of polyethylene glycols (PEGs) and PEG derivatives. *Mod. Chem. Appl.* **2014**, *2*, 1–6. [CrossRef]
33. Du, H.; Bandara, S.; Carson, L.E.; Kommalapati, R.R. Association of Polyethylene Glycol Solubility with Emerging Membrane Technologies, Wastewater Treatment, and Desalination. In *Water Quality-Science, Assessments and Policy*; IntechOpen: London, UK, 2019.
34. Zia, F.; Anjum, M.N.; Saif, M.J.; Jamil, T.; Malik, K.; Anjum, S.; BiBi, I.; Zia, M.A. Chapter 16-Alginate-Poly(Ethylene) Glycol and Poly(Ethylene) Oxide Blend Materials. In *Algae Based Polymers, Blends, and Composites*; Zia, K.M., Zuber, M., Ali, M., Eds.; Elsevier: Amsterdam, The Netherlands, 2017; pp. 581–601.
35. Gelardi, G.; Mantellato, S.; Marchon, D.; Palacios, M.; Eberhardt, A.B.; Flatt, R.J. 9-Chemistry of chemical admixtures. In *Science and Technology of Concrete Admixtures*; Aïtcin, P.-C., Flatt, R.J., Eds.; Woodhead Publishing: Cambridge, UK, 2016; pp. 149–218.
36. Liu, L.; Gao, Y.; Zhao, J.; Yuan, L.; Li, C.; Liu, Z.; Hou, Z. A mild method for surface-grafting PEG onto segmented poly (ester-urethane) film with high grafting density for biomedical purpose. *Polymers* **2018**, *10*, 1125. [CrossRef] [PubMed]
37. Adib, H.; Raisi, A. Surface modification of a PES membrane by corona air plasma-assisted grafting of HB-PEG for separation of oil-in-water emulsions. *RSC Adv.* **2020**, *10*, 17143–17153. [CrossRef]
38. Ebnesajjad, S.; Landrock, A.H. Chapter 2-Surface Tension and Its Measurement. In *Adhesives Technology Handbook*, 3rd ed.; Ebnesajjad, S., Landrock, A.H., Eds.; William Andrew Publishing: Boston, MA, USA, 2015; pp. 19–34.
39. Wu, S. Adhesion: Basic Concept and Locus of Failure. In *Polymer Interface and Adhesion, 1*; CRC Press: Boca Raton, FL, USA; Taylor & Francis: London, UK, 1982; pp. 337–354.
40. Leslie, S.A.; Mitchell, J.C. Removing gold coating from SEM samples. *Palaeontology* **2007**, *50*, 1459–1461. [CrossRef]
41. Takke, V.; Behary, N.; Perwuelz, A.; Campagne, C. Surface and adhesion properties of poly (ethylene glycol) on polyester (polyethylene terephthalate) fabric surface: Effect of air-atmospheric plasma treatment. *Appl. Polym. Sci.* **2011**, *122*, 2621–2629. [CrossRef]
42. Kumar, B.R.; Rao, T.S. AFM studies on surface morphology, topography and texture of nanostructured zinc aluminum oxide thin films. *Digest J. Nanomater. Biostructures* **2012**, *7*, 1881–1889.

43. Gaff, M.; Gašparík, M.; Kvietková, M. Evaluation of wood surface quality depending on the embossing parameters. *Wood Res.* **2017**, *62*, 751–762.
44. Chastain, J.; King Jr, R.C. Handbook of X-ray photoelectron spectroscopy. *Perkin-Elmer Corp.* **1992**, *40*, 221.
45. Chen, G.; Zhang, Y.; Zhu, Y.; Xu, J. Grafting of PEG400 onto the surface of LLDPE/SMA film. *Front. Chem. Eng. China* **2007**, *1*, 128–131. [CrossRef]
46. Zanini, S.; Müller, M.; Riccardi, C.; Orlandi, M. Polyethylene glycol grafting on polypropylene membranes for anti-fouling properties. *Plasma Chem. Plasma Process.* **2007**, *27*, 446–457. [CrossRef]
47. Popelka, A.; Krupa, I.; Novák, I.; Al-Maadeed, M.A.S.; Ouederni, M. Improvement of aluminum/polyethylene adhesion through corona discharge. *Phys. D Appl. Phys.* **2016**, *50*, 035204. [CrossRef]
48. Barish, J.; Goddard, J. Polyethylene Glycol Grafted Polyethylene: A Versatile Platform for Nonmigratory Active Packaging Applications. *Food Sci.* **2011**, *76*, E586–E591. [CrossRef] [PubMed]
49. Ganji, M.; Docter, M.; Le Grice, S.F.; Abbondanzieri, E.A. DNA binding proteins explore multiple local configurations during docking via rapid rebinding. *Nucleic Acids Res.* **2016**, *44*, 8376–8384. [CrossRef] [PubMed]
50. Kumar, S.; Fujioka, M.; Asano, K.; Shoji, A.; Athipettah, J.; Yoshida, Y. Surface modification of poly(ethylene terephthalate) by plasma polymerization of poly(ethylene glycol). *Mater. Sci. Mater. Med.* **2007**, *18*, 1831–1835. [CrossRef] [PubMed]
51. Jung, M.; Horgen, D.; Orski, S.; Rodriguez, C.V.; Beers, K.; Balazs, G.; Jones, T.; Work, T.; Brignac, K.; Royer, S.-J.; et al. Validation of ATR FT-IR to identify polymers of plastic marine debris, including those ingested by marine organisms. *Mar. Pollut. Bull.* **2017**, *127*. [CrossRef] [PubMed]
52. Elbadawi, M. Rheological and mechanical investigation into the effect of different molecular weight poly (ethylene glycol) s on polycaprolactone-ciprofloxacin filaments. *ACS Omega* **2019**, *4*, 5412–5423. [CrossRef]

Plasma-Assisted Synthesis of Multicomponent Nanoparticles Containing Carbon, Tungsten Carbide and Silver as Multifunctional Filler for Polylactic Acid Composite Films

Nichapat Boonyeun [1,2], Ratana Rujiravanit [1,2,*] and Nagahiro Saito [3]

1   The Petroleum and Petrochemical College, Chulalongkorn University, Bangkok 10330, Thailand; Nichapat.B@student.chula.ac.th
2   Center of Excellence on Petrochemical and Materials Technology, Chulalongkorn University, Bangkok 10330, Thailand
3   Department of Chemical Systems Engineering, Graduate School of Engineering, Nagoya University, Nagoya 464-8603, Japan; Hiro@sp.material.nagoya-u.ac.jp
*   Correspondence: Ratana.r@chula.ac.th; Tel.: +662-218-4132

Abstract: Multicomponent nanoparticles containing carbon, tungsten carbide and silver (carbon-WC-Ag nanoparticles) were simply synthesized via in-liquid electrical discharge plasma, the so-called solution plasma process, by using tungsten electrodes immersed in palm oil containing droplets of $AgNO_3$ solution as carbon and silver precursors, respectively. The atomic ratio of carbon:W:Ag in carbon-WC-Ag nanoparticles was 20:1:3. FE-SEM images revealed that the synthesized carbon-WC-Ag nanoparticles with particle sizes in the range of 20–400 nm had a spherical shape with a bumpy surface. TEM images of carbon-WC-Ag nanoparticles showed that tungsten carbide nanoparticles (WCNPs) and silver nanoparticles (AgNPs) with average particle sizes of 3.46 nm and 72.74 nm, respectively, were dispersed in amorphous carbon. The carbon-WC-Ag nanoparticles were used as multifunctional fillers for the preparation of polylactic acid (PLA) composite films, i.e., PLA/carbon-WC-Ag, by solution casting. Interestingly, the coexistence of WCNPs and AgNPs in carbon-WC-Ag nanoparticles provided a benefit for the co-nucleation ability of WCNPs and AgNPs, resulting in enhanced crystallization of PLA, as evidenced by the reduction in the cold crystallization temperature of PLA. At the low content of 1.23 wt% carbon-WC-Ag nanoparticles, the Young's modulus and tensile strength of PLA/carbon-WC-Ag composite films were increased to 25.12% and 46.08%, respectively. Moreover, the PLA/carbon-WC-Ag composite films possessed antibacterial activities.

Keywords: atmospheric pressure plasma; filler; polylactic acid; polymer composite

1. Introduction

Nowadays, due to increasing environmental concerns and climate change worldwide, bio-derived and biodegradable polymers such as polylactic acid (PLA), polyhydroxybutyrate (PHB) and poly(3-hydroxybutyrate-co-3-hydroxyvalerate) (PHBV) have received much attention as alternatives to petroleum-based polymers [1–3]. Among bio-derived and biodegradable polymers, PLA is one of the most studied polymers and has been investigated for many applications, such as packaging materials [4], membranes for separation processes [5] and biomaterials for biomedical applications [6]. Nevertheless, the major drawbacks of PLA that limit its utilization as a replacement for petroleum-based polymers are low thermal stability, inferior mechanical properties and low crystallization rate when compared with petroleum-based polymers. Therefore, the incorporation of fillers into PLA to obtain PLA composites has been considered as an effective method to overcome these limitations. To date, PLA composites have been developed by the incorporation of a wide variety of fillers, such as clay [7], silver nanoparticles [8], zinc oxide (ZnO) [9], tungsten disulfide (WS_2) nanotubes [10] and various types of carbon materials [11–13].

Among the investigated fillers, carbon materials have been considered as efficient candidates for the development of PLA composites because of their outstanding properties, such as high surface area, high thermal and chemical stability, high absorption ability and low cost [14,15]. However, the incorporation of monocomponent fillers could improve only specific properties of polymers [16,17]. Hence, the incorporation of multicomponent fillers into polymers has been employed in order to accomplish simultaneous improvement of the multifunctional properties of polymers, such as mechanical properties, thermal properties, crystallization behavior and antibacterial activities [18,19]. According to previous reports, the aggregation and non-homogeneous dispersion of each component in polymer matrices could occur, resulting in the deterioration of the properties of polymers [20,21]. To overcome these problems, nanohybrid fillers such as cellulose/silver nanoparticles and multiwall carbon nanotubes (MWCNTs)/silver nanoparticles were fabricated and incorporated into polymers [8,22,23]. However, the preparation methods of the nanohybrid fillers commonly involved time-consuming processes and the utilization of chemical agents.

The solution plasma process (SPP), an electrical discharge of plasma occurring in a liquid phase, has been considered as an emerging technology that has been investigated in carbon synthesis [24–26], surface modification of carbon materials [27], synthesis of metal nanoparticles [28,29] and synthesis of carbon-supported metal nanoparticles [30,31]. SPP is operated by applying electric potential between a pair of metal electrodes that are immersed in a liquid phase. Energetic electrons that are released from the electrodes collide with molecules near the electrodes, resulting in the formation of a variety of highly active species, such as excited molecules, free electrons, free radicals and positively and negatively charged species. Moreover, as a result of electron bombardment at the surfaces of electrodes, the erosion of the electrodes may occur, leading to the formation of metal nanoparticles released from the electrodes [30,32]. For example, when tungsten electrodes were used in carbon synthesis by SPP, to some extent, tungsten carbide nanoparticles were generated together with the formation of carbon as a result of the sputtering of tungsten electrodes [33]. Under this circumstance, SPP can provide several benefits, such as accelerating reaction rate, lowering reaction temperature and reduction of chemicals used in various reactions, e.g., synthesis of metal nanoparticles [34,35]. Recently, different types of organic solvents, including benzene, cyclohexane and hexane, have been investigated as carbon precursors to synthesize carbon by using SPP [24,33,36]. However, the organic solvents are high-cost raw materials and their wastes from the reactions may cause environmental problems. As an alternative to organic solvents, palm oil, a carbon-rich renewable raw material consisting of triglycerides and fatty acids [37,38], is a potential carbon precursor for synthesis of carbon by SPP. It was postulated that long-chain hydrocarbon moieties in fatty acids that are present in palm oil can be converted to carbon by SPP. The mechanism for the conversion of carbon precursors to carbon materials by SPP was proposed by Morishita T et al., 2016 [36].

In the last decade, inorganic fillers with intrinsic antimicrobial properties, such as titanium dioxide [39,40], zinc oxide [41], graphene oxide (GO) [42], metal-organic frameworks (MOFs) [43] and silver nanoparticles (AgNPs) [44], have been applied to polymer composites in order to introduce antimicrobial functions to the composites. It is known that AgNPs are one of the most powerful antimicrobial agents. Nowadays, AgNPs are extensively utilized in a broad range of applications, such as conductive materials [45], catalysts [46], anticancer [47] and biomaterials [48]. However, the stability of AgNPs is an important issue hindering their application. As their particle sizes are in the nano-scale, the surface energy of AgNPs is high, resulting in a tendency to undergo aggregation [49]. The aggregation of AgNPs results in a reduction in their performance, such as their catalytic efficiency and antimicrobial activities [50,51]. In order to prevent the aggregation of AgNPs, the deposition of AgNPs on various supporting materials, such as silica, zeolite and carbon, has been explored [52,53]. Among the most widely used supporting materials, carbon materials have many advantages, including high surface area, stability in acid and base media and low cost. Therefore, carbon materials are considered as potential candidates for use as supporting materials for AgNPs to obtain carbon-supported AgNPs [54,55]. Nowa-

days, carbon-supported AgNPs are extensively used as reinforcing fillers for polymer composites [22,56,57]. According to the literature, carbon-supported AgNPs can be synthesized by several methods, such as hydrothermal reduction [58], thermal annealing [56] and sputtering deposition [59]. However, the preparation of carbon-supported AgNPs is generally based on multi-step processes together with the use of reducing agents and long reaction times.

In this study, multicomponent nanoparticles containing carbon, tungsten carbide and silver, i.e., carbon-WC-Ag nanoparticles, were synthesized in one step via SPP by using palm oil containing droplets of silver nitrate ($AgNO_3$) solution as carbon and silver precursors, respectively. By applying SPP, carbon and AgNPs were synthesized from palm oil and $AgNO_3$, respectively, whereas tungsten carbide nanoparticles (WCNPs) were generated by the sputtering of tungsten electrodes together with the simultaneous formation of carbon during plasma discharge. The morphology and elemental composition of carbon-WC-Ag nanoparticles were characterized. Carbon-WC-Ag nanoparticles were then used as multifunctional fillers for the preparation of polylactic acid (PLA) composite films, i.e., PLA/carbon-WC-Ag, by solution casting. The effect of carbon-WC-Ag nanoparticles on the non-isothermal crystallization behavior and mechanical and thermal properties of the obtained PLA composite films was investigated. The antibacterial activities of PLA/carbon-WC-Ag composite films against *Escherichia coli*, a Gram-negative bacterium, and *Staphylococcus aureus*, a Gram-positive bacterium, were also examined.

2. Materials and Methods

2.1. Materials

Polylactic acid (PLA) (Ingeo^{TM} 4043D) with 94% L-lactide and 6% D-lactide was provided by Natureworks LLC (Minnetonka, MN, USA) (molecular weight (M_w) of 1.5×10^5 g/mol and polydispersity index (PDI) of 1.81). The melt flow index and density of PLA are 6.0 g/10 min and 1.24 g/cm^3, respectively. Activated charcoal was purchased from Sigma-Aldrich Inc. (Lyon, France). Silver nitrate ($AgNO_3$) was supplied by Fisher Scientific Co., Ltd. (Loughboroug, UK). Tungsten (W) and silver (Ag) electrodes (diameter of 1 mm, 99.95% purity) were obtained from The Nilaco Corporation, Japan. Chloroform ($CHCl_3$) and hexane (C_6H_8) were analytical-grade and bought from RCI Labscan Co., Ltd. (Bangkok, Thailand). Palm oil was provided by Oleen Co., Ltd. (Samutsakhon, Thailand). *Escherichia coli* strain TISTR 527 and *Stapphylococcus aureus* strain TISTR 2329 were supplied by the Microbiological Resource Center, Thailand Institute of Scientific and Technological Research (TISTR). Bacteriological-grade beef extract, peptone and agar powder were purchased from HiMedia Laboratory Co., Ltd. (Maharashtra, India).

2.2. Preparation of Carbon-WC, Carbon-Ag and Carbon-WC-Ag Nanoparticles via SPP

The experimental setup of SPP is shown in Figure 1a. The plasma discharge was carried out at room temperature and atmospheric pressure by using a bipolar pulsed power supply (model Pekuris MPS-06K01C-WP1 from Kurita Seisakusho Co., Ltd., Kyoto, Japan). The plasma discharge was generated between a pair of metal electrodes equipped in a glass reactor that was filled with palm oil (40 mL). Two types of metal electrodes, i.e., tungsten (W) and silver (Ag) electrodes, were used to synthesize carbon-WC and carbon-Ag nanoparticles, respectively. The metal electrodes were insulated by ceramic tubes. The gap between the electrodes, voltage, pulse frequency, pulse width and plasma discharge time were 0.5 mm, 1.64 kV, 15 kHz, 2 μs and 90 min, respectively. Palm oil was used as a carbon precursor to synthesize carbon via SPP, whereas tungsten carbide nanoparticles (WCNPs) were generated by sputtering of tungsten electrodes and subsequently combining tungsten and carbon. For the synthesis of carbon-WC-Ag nanoparticles, $AgNO_3$ solution (10 mL) at a concentration of 0.02 M was added into palm oil (40 mL) under strong agitation to form small droplets of $AgNO_3$ solution that dispersed in palm oil while plasma discharge was taking place. The operating conditions for plasma discharge were the same as those for the synthesis of carbon-WC and carbon-Ag nanoparticles.
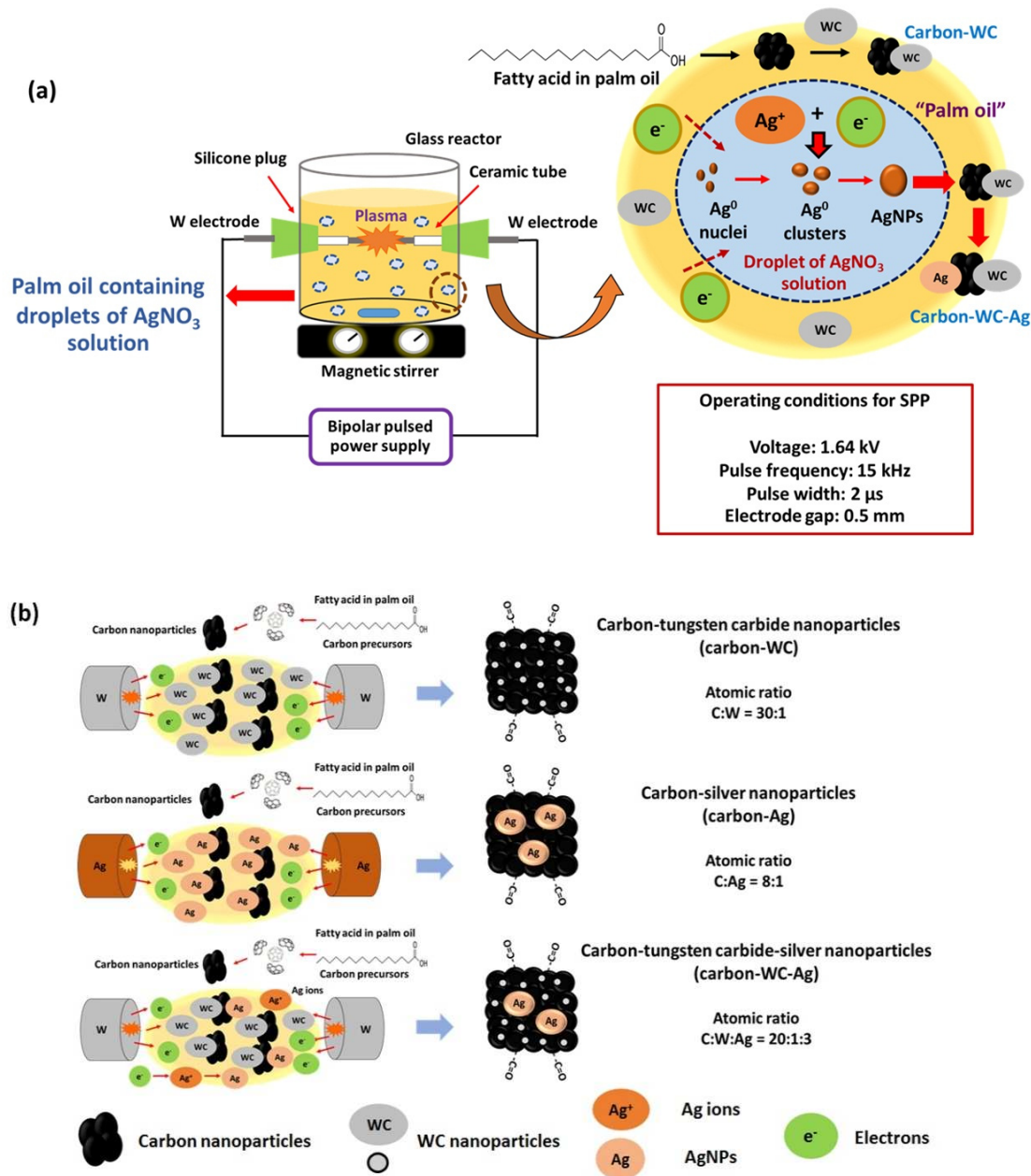
Figure 1. (**a**) Schematic diagrams of SPP and formation of AgNPs in a droplet of AgNO$_3$ solution dispersed in palm oil, and (**b**) formation of carbon-based nanoparticles, i.e., carbon-WC, carbon-Ag and carbon-WC-Ag nanoparticles, synthesized by SPP using tungsten (W) and silver (Ag) electrodes.

By applying SPP and using tungsten electrodes, palm oil and AgNO$_3$ solution acted as carbon and Ag precursors to synthesize carbon-WC-Ag nanoparticles in one step. Based on the types of electrodes, i.e., tungsten and silver electrodes, there were three types of synthesized carbon-based nanoparticles, i.e., carbon-tungsten carbide (carbon-WC), carbon-silver (carbon-Ag) and carbon-tungsten carbide-silver (carbon-WC-Ag) nanoparticles, as illustrated in Figure 1b. After the plasma discharge, the synthesized carbon-based nanoparticles were collected and separated from palm oil by centrifugation at a rotational speed of 12,000 rpm for 15 min. Then, the synthesized carbon-based nanoparticles were rinsed with an excess amount of hexane to remove the residual oil, followed by centrifugation at a rotational speed of 12,000 rpm for 15 min. The washing process was repeated 3 times. The synthesized carbon-based nanoparticles were dried in an oven at 60 °C for 3 h.

2.3. Preparation of Neat PLA and PLA Composite Films

For preparation of neat PLA films, a PLA solution at a concentration of 4% (*w*/*v*) was prepared by dissolving PLA pellets of 4 g in chloroform 100 mL, followed by stirring at 60 °C for 2 h until PLA pellets were completely dissolved [60]. Then, the PLA solution was cast on Petri dishes and left at room temperature for 48 h to obtain neat PLA films. For preparation of PLA composite films, the fillers, i.e., activated charcoal, carbon-WC, carbon-Ag and carbon-WC-Ag nanoparticles, were dispersed in the PLA solutions, followed by sonication for 10 min. The filler contents in the PLA composite films were varied to be 0.25, 0.75, 1.23, 1.72 and 2.20 wt%, as shown in Table 1. After this, the PLA solutions containing each type of filler were cast on Petri dishes and left at room temperature for 48 h to evaporate the solvent, and PLA composite films having a thickness of 95.5 μm were obtained.

Table 1. The amounts of fillers, PLA and chloroform for the preparation of PLA composite films.

Fillers (g)	PLA (g)	Chloroform (mL)	Filler Content in PLA Composite Films (wt%)
0.01	4.00	100.00	0.25
0.03	4.00	100.00	0.75
0.05	4.00	100.00	1.23
0.07	4.00	100.00	1.72
0.09	4.00	100.00	2.20

2.4. Characterization

The synthesized carbon-based nanoparticles were characterized in comparison with the commercial activated charcoal. Wide angle X-ray diffraction (WAXD) measurements were done by using SmartLab (Rigaku Corporation, Tokyo, Japan) with CuKα radiation (λ = 0.154 nm) operating at 40 kV and 30 mA. The values of degree of crystallinity (χ_c) of neat PLA and the PLA composite films were determined according to Equation (1):

$$\chi_c\ (\%) = [(A_c/(A_c + A_a)] \times 100\% \tag{1}$$

A_c represents the area under the total crystalline region and A_a represents the area under the total amorphous region [61].

Chemical compositions of activated charcoal and the synthesized carbon-based nanoparticles were analyzed by XPS (model Kratos Axis Ultra DLD from Kratos Analytical Co., Ltd., Manchester, UK) with an Al Kα X-ray source at 15 kV. Raman spectra of the synthesized carbon-based nanoparticles were detected by Spectra GX (Perkin Elmer Inc., Waltham, MA, USA). TEM and FE-SEM images of the synthesized carbon-based nanoparticles were taken using a JEOL (model JEM-2100 from JEOL Co., Ltd., Tokyo, Japan) and Hitachi (model s-4800 from Hitachi Co., Ltd., Tokyo, Japan), respectively. The elemental compositions of activated charcoal and the synthesized carbon-based nanoparticles were determined by scanning electron microscopy with energy dispersive X-ray (SEM-EDX) (Hitach Co., Ltd., Tokyo, Japan).

Surface and cross-sectional morphology of neat PLA and PLA composite films was observed by FE-SEM (Hitachi s-4800, Japan). All samples were coated with platinum before measurements. The thermal properties of neat PLA and PLA composite films were investigated using TGA (model Netzsch 209F3 from Netzsch Co., Ltd., Selb, Germany) under a nitrogen atmosphere. All samples were heated from 35 °C to 900 °C at a heating rate of 10 °C/min. The crystallization behavior of neat PLA and PLA composite films was investigated by differential scanning calorimetry (DSC) (model Netzsch 204F1 Phoenix from Netzsch Co., Ltd., Selb, Germany) under a nitrogen atmosphere. For all samples, the first heating scan was performed by heating the samples to 200 °C at a heating rate of 10 °C/min to eliminate thermal histories. After this, the samples were cooled down to 25 °C at a cooling rate of 10 °C/min. The second heating scan was performed by heating the samples to 200 °C at a heating rate of 10 °C/min. The glass transition temperature (T$_g$), the

cold crystallization temperature (T_{cc}) and the melting temperature (T_m) were determined from the second heating scan. Alumina crucible pans (Netzsch Co., Ltd., Selb, Germany) were used for TGA and DSC measurements. Young's modulus and tensile strength of neat PLA and PLA composite films were measured by using a universal testing machine (model Lloyd LRX from Lloyd Instruments Co., Ltd., West Sussex, UK) according to the ASTM D882 with a 500-N load cell. Each datum was the average of 5 specimens. Antibacterial activities of neat PLA, PLA/activated charcoal, PLA/carbon-WC and PLA/carbon-WC-Ag composite films against *Escherichia coli* (*E. coli*) and *Staphylococcus aureus* (*S. aureus*) were investigated by using the colony-forming unit assay according to the modified procedure of Janpetch et al. 2016 [62]. The bacterial reduction rate (BRR) was calculated according to Equation (2):

$$\text{Bacterial reduction rate} = [(N_1 - N_2)/N_1] \times 100\% \tag{2}$$

where N_1 represents the number of colonies from the blank cell suspension and N_2 represents the number of colonies from the cell suspension containing PLA samples.

2.5. Statistical Analysis

The significant differences in the selected parameters were evaluated via analysis of variance (ANOVA) according to Turkey's HSD (honestly significant difference) test at *p*-value < 0.05 using IBM SPSS Statistics 26 software (SPSS Inc., Chicago, IL, USA).

3. Results and Discussion

3.1. Characterization of Carbon-WC and Carbon-WC-Ag Nanoparticles

According to the previous studies on SPP, active species such as H, C_2 and W radicals were generated during plasma discharge in organic solvents by using tungsten electrodes due to the dissociation of the molecules of organic solvents and the sputtering of tungsten electrodes [26,33]. The formation of carbon mainly depended on the interactions of the generated C_2 radicals with each other, resulting in the formation of polycyclic structures. In this study, the pathways of carbon formation from palm oil by SPP were postulated to involve the transformation of hydrocarbon moieties of fatty acids existing in palm oil to cyclic compounds. Subsequently, the cyclic compounds underwent recombination to form polycyclic structures and eventually converted to a network structure of carbon, as described in previous studies [33,36].

In addition, tungsten carbide (WC) could be formed during plasma discharge by the reaction between W and C_2 radicals and subsequently embedded in the simultaneously generated carbon, resulting in the formation of carbon containing tungsten carbide (carbon-WC). Figure 2a displays the XRD pattern of carbon-WC in comparison with that of activated charcoal. The characteristic peaks of activated charcoal at $2\theta = 23°$ and $43°$ corresponding to the reflections of the (002) and (100) planes, respectively, indicated an amorphous state of activated charcoal. From the XRD pattern of carbon-WC, a very broad peak at $2\theta = 25°$ suggested the amorphous state of carbon-WC. However, the peaks at $2\theta = 36.7°$, $42.6°$, $61.8°$, $74.1°$ and $78.0°$, corresponding to the (111), (200), (220), (311) and (222) planes of metastable tungsten carbide (WC_{1-x}), were also observed in the XRD pattern of carbon-WC [33,63]. Furthermore, a peak at $2\theta = 38.5°$ corresponding to the (110) plane of tungsten metal appeared at a very low intensity. This might be explained by the fact that tungsten metal originated from the erosion of tungsten electrodes during plasma discharge [33,64]. The amount of tungsten metal incorporated into carbon-WC was relatively low due to the very low intensity of the peak of tungsten metal. Accordingly, carbon-WC synthesized by SPP in this study was referred to as the synthesized carbon that contained metastable tungsten carbide and a negligible amount of tungsten metal.
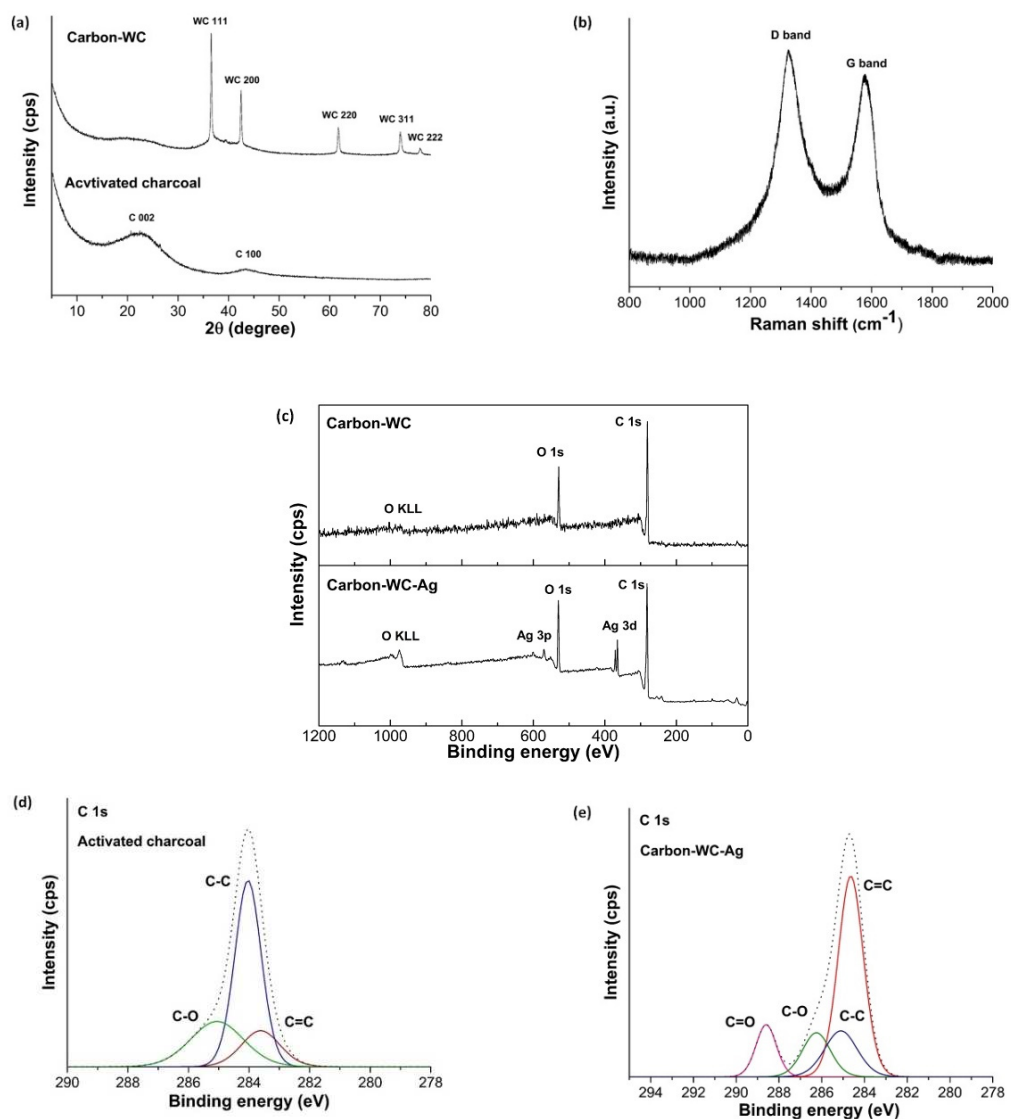
Figure 2. (**a**) XRD patterns of carbon-WC and activated charcoal, (**b**) Raman spectrum of carbon-WC, (**c**) wide-scan XPS spectra of carbon-WC and carbon-WC-Ag nanoparticles, and (**d**) narrow-scan XPS spectra of C 1s of activated charcoal and (**e**) carbon-WC-Ag nanoparticles.

In Figure 2b, the Raman spectrum of carbon-WC consists of two peaks at 1350 cm^{-1} and 1580 cm^{-1} which correspond to the D band and G band, respectively. The D band is attributed to the occurrence of defects and disorder in the graphitic structure, whereas the G band is attributed to the formation of a well-organized graphitic structure. According to the obtained Raman spectrum, the intensity of the D band was slightly higher than the intensity of the G band, indicating an amorphous state of carbon-WC.

The wide-scan XPS spectra of carbon-WC and carbon-WC-Ag nanoparticles are shown in Figure 2c. The peaks of carbon C 1s and oxygen O 1s were detected for carbon-WC and carbon-WC-Ag nanoparticles, whereas the wide-scan XPS spectrum of carbon-WC-Ag nanoparticles shows the characteristic peaks of Ag 3d at 368.05 eV and 374.1 eV and the characteristic peaks of Ag 3p at 572.98 eV and 604.3 eV [20]. The narrow-scan XPS spectra of activated charcoal and carbon-WC-Ag nanoparticles are shown in Figure 2d,e, respectively. For activated charcoal, the C 1s spectra consisted of three peaks located at 283.70 eV, 284.00 eV and 285.3 eV, which corresponded to C=C, C-C and C-O, respectively. For carbon-WC-Ag nanoparticles, the C 1s spectra consisted of four peaks located at 284.64 eV, 285.09 eV, 286.26 eV and 288.59 eV, which corresponded to C=C, C-C, C-O and

C=O, respectively. The C=O was present in carbon-WC-Ag nanoparticles but was absent in activated charcoal. It was suggested that carbonyl groups could be incorporated into the structure of carbon prepared by SPP [27,65].

FE-SEM images of carbon-WC and carbon-WC-Ag nanoparticles are shown in Figure 3a,b, respectively. It was found that the particle sizes of carbon-WC and carbon-WC-Ag nanoparticles were in the ranges of 10–50 nm and 20–400 nm, respectively. Additionally, the average particle sizes of carbon-WC and carbon-WC-Ag nanoparticles were 22.60 nm and 129.06 nm, respectively. The particle size distribution of carbon-WC and carbon-WC-Ag nanoparticles is shown in Figure S1a,b. Interestingly, the FE-SEM image of carbon-WC-Ag nanoparticles (Figure 3b) shows spherical nanoparticles with bumpy surfaces. The presence of WC nanoparticles (WCNPs) in carbon-WC and carbon-WC-Ag nanoparticles was evidenced by TEM images, as shown in Figure 4b–d. It can be seen that WCNPs with particle sizes in the range of 2–5 nm were dispersed in amorphous carbon, whereas the TEM image of activated charcoal (Figure 4a) confirmed the amorphous state of activated charcoal. In Figure 4c,d, TEM images of carbon-WC-Ag nanoparticles show that AgNPs having particle sizes in the range of 10–400 nm and an average particle size of 72.74 nm were embedded in amorphous carbon, where WCNPs also dispersed. The particle size distribution of AgNPs existing in carbon-WC-Ag nanoparticles is shown in Figure S1c. The results of TEM are in good agreement with the results of XRD and Raman spectroscopy.

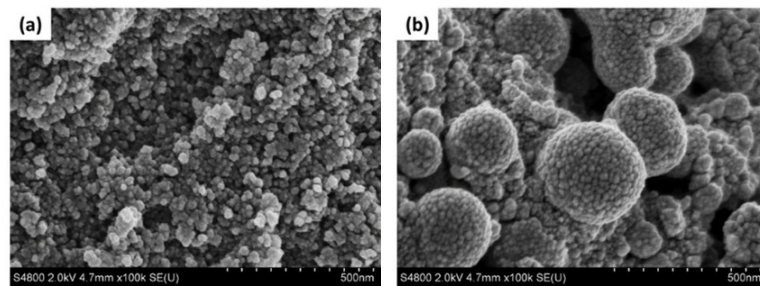**Figure 3.** FE-SEM images of (**a**) carbon-WC and (**b**) carbon-WC-Ag nanoparticles at magnification of 100,000×.
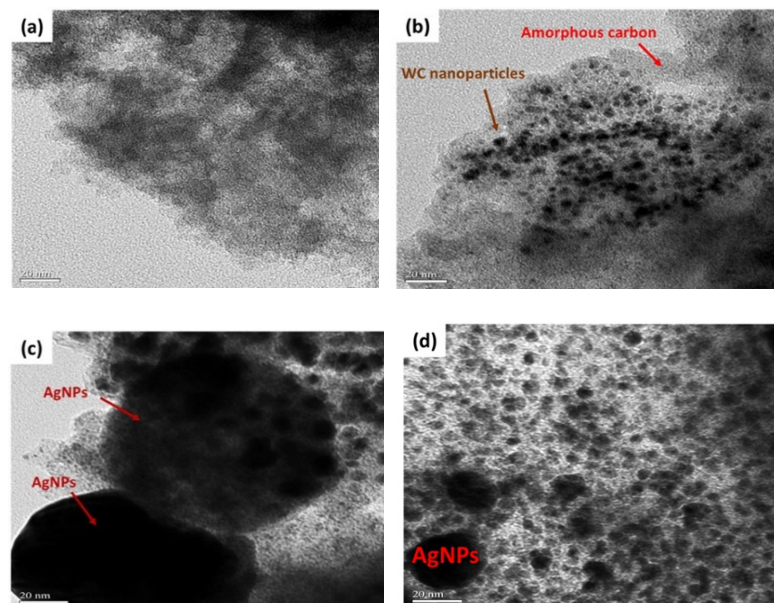

Figure 4. TEM images of (**a**) activated charcoal, (**b**) carbon-WC, (**c,d**) carbon-WC-Ag nanoparticles at magnification of 200,000×.

Furthermore, atomic percentages of each element in activated charcoal, carbon-WC, carbon-Ag and carbon-WC-Ag nanoparticles were investigated by scanning electron microscopy with energy dispersive X-ray (SEM-EDX) analysis and the results are shown in Table 2. The tungsten contents in carbon-WC and carbon-WC-Ag nanoparticles were 3.59% and 3.81%, respectively, whereas the silver contents in carbon-Ag and carbon-WC-Ag nanoparticles were 10.81% and 11.20%, respectively.

Table 2. Elemental compositions of activated charcoal, carbon-WC, carbon-Ag and carbon-WC-Ag nanoparticles (*n* = 3).

Type of Elements	Atomic Percentage (%) $\pm$ SD			
	Activated Charcoal	Carbon-WC	Carbon-Ag	Carbon-WC-Ag
Carbon (C)	94.42 $\pm$ 0.16	91.15 $\pm$ 0.46	82.10 $\pm$ 1.44	75.35 $\pm$ 2.04
Oxygen (O)	5.58 $\pm$ 0.16	5.35 $\pm$ 0.72	7.08 $\pm$ 0.85	9.64 $\pm$ 1.60
Tungsten (W)	-	3.59 $\pm$ 1.07	-	3.81 $\pm$ 0.83
Silver (Ag)	-	-	10.81 $\pm$ 1.06	11.20 $\pm$ 1.18

3.2. Morphology of Neat PLA and PLA Composite Films

The SEM images of the surface morphology of neat PLA and PLA/carbon-WC-Ag composite films with different filler contents of 0.25, 0.75, 1.23, 1.72 and 2.20 wt% were taken (Figure S2). While the neat PLA film (Figure S2a) had a smooth surface, the PLA/carbon-WC-Ag composite films (Figure S2b–f) had rugged surfaces due to the presence of carbon-WC-Ag nanoparticles in the composite films. The SEM images of the composite films indicated that, at the filler contents of 0.25, 0.75 and 1.23 wt% (Figure S2b–d), carbon-WC-Ag nanoparticles had low aggregation and could maintain random dispersion in the PLA matrix. However, at the higher filler contents of 1.72 and 2.20 wt% (Figure S2e–f), the aggregation of carbon-WC-Ag nanoparticles in the PLA matrix was obviously observed. Accordingly, the PLA/carbon-WC-Ag composite films with the filler content of 1.23 wt% were used for further studies. In addition, an SEM image of the cross-sectional morphology of the PLA/carbon-WC-Ag composite film at the filler content of 1.23 wt% was taken (Figure S3). It is clearly shown that carbon-WC-Ag nanoparticles were embedded in the PLA matrix and the average film thickness was measured to be 95.5 $\pm$ 0.52 μm (*n* = 3).

3.3. Thermogravimetric Analysis

TGA of neat PLA and PLA composite films, i.e., PLA/activated charcoal, PLA/carbon-WC, PLA/carbon-Ag and PLA/carbon-WC-Ag, at the filler content of 1.23 wt%, was performed and the values of the initial degradation temperature (T_{int}), the 50% weight loss temperature (T_{50}) and the degradation temperature (T_{max}) are listed in Table 3. According to the TGA results, the T_{int} of PLA/carbon-WC-Ag composite film was significantly higher than that of the neat PLA film, indicating the increment of thermal stability of the PLA/carbon-WC-Ag composite film at the initial state of thermal degradation. This might be due to the heat capacity of WCNPs and AgNPs, which could absorb heat during the initial state of thermal degradation. It is known that various types of transition metals and alkali earth metal oxides favor the thermal decomposition of PLA, leading to a reduction in the thermal stability of PLA [7,66–68]. Compared with the neat PLA film, a reduction in T_{50} and T_{max} of PLA/carbon-WC composite films was observed. This result suggested that the presence of carbon-WC in the composite films could accelerate the thermal degradation of PLA. On the contrary, only a slight reduction in thermal stability of PLA/carbon-Ag composite film was observed when compared with the neat PLA film. Similarly, it has been reported that the presence of silver in the PLA matrix slightly affected the thermal stability of PLA composites [69,70].

Table 3. Initial degradation temperature (T_{int}), 50% weight loss temperature (T_{50}) and degradation temperature (T_{max}) of neat PLA and PLA composite films at a filler content of 1.23 wt%.

Composite Films	T_{int} (°C)	T_{50} (°C)	T_{max} (°C)
Neat PLA	102.4 [a]	360.7 [a]	366.5 [a]
PLA/activated charcoal	104.9 [a]	358.9 [a,b]	364.8 [a,b]
PLA/carbon-WC	107.1 [a]	355.8 [a]	363.3 [a]
PLA/carbon-Ag	111.0 [a]	359.5 [a,b]	365.7 [a]
PLA/carbon-WC-Ag	112.1 [a]	357.8 [a]	364.6 [a,b]

The superscript letter "a" refers to significant differences among T_{int}, T_{50} and T_{max} of the PLA composite films at p-value < 0.05. The superscript letter "b" refers to non-significant difference between T_{50} of PLA/activated charcoal and PLA/carbon-Ag and non-significant difference between T_{max} of PLA/activated charcoal and PLA/carbon-WC-Ag at p-value < 0.05.

Considering the T_{50} and T_{max} of PLA/carbon-WC-Ag composite films, the reduction in the thermal stability of PLA/carbon-WC-Ag composite films was less than that of PLA/carbon-WC composite films but higher than that of PLA/carbon-Ag composite films. As mentioned previously, carbon-WC could accelerate the thermal degradation of PLA, whereas AgNPs slightly affected the thermal stability of the composite films. It might be implied that the coexistence of AgNPs in carbon-WC-Ag could hinder the effect of WCNPs on the degradation of PLA upon heating. Nevertheless, the PLA/carbon-WC-Ag composite films had intrinsic thermal degradation properties. Therefore, the PLA/carbon-WC-Ag composite film is a potential candidate for use as an environmentally friendly material.

3.4. Differential Scanning Calorimetry

The effect of the incorporation of the fillers, i.e., activated carbon, carbon-WC, carbon-Ag and carbon-WC-Ag nanoparticles, into PLA on the non-isothermal crystallization behavior of PLA was investigated by DSC via heating–cooling–heating scans and the results are shown in Figure 5. The glass transition temperature (T_g), the cold crystallization temperature (T_{cc}) and the melting temperature (T_m) of neat PLA and the PLA composite films are detailed in Table 4. No significant change in the T_g of all the PLA composite films was observed when compared with the neat PLA film, indicating that the presence of the synthesized carbon-based nanoparticles, i.e., carbon-WC, carbon-Ag and carbon-WC-Ag, in PLA matrix did not affect the mobility of PLA chains in amorphous regions [39,71].
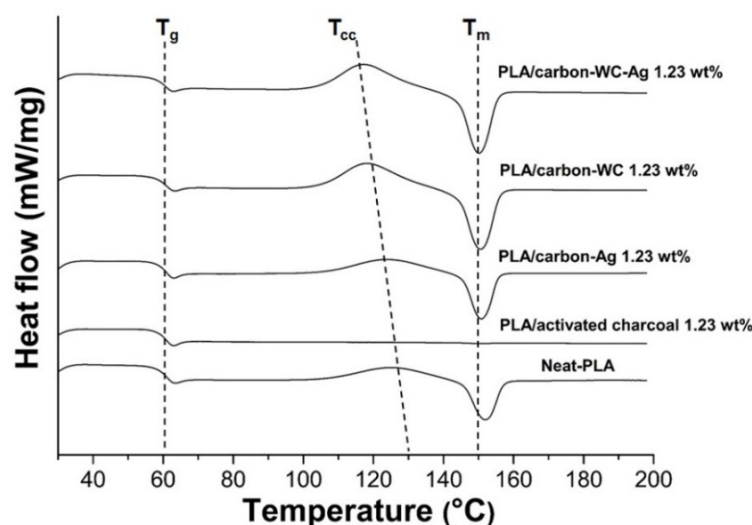

Figure 5. DSC thermograms of neat PLA and the PLA composite films at a filler content of 1.23 wt%.

Table 4. Glass transition temperature (T_g), cold crystallization temperature (T_{cc}) and melting temperature (T_m) at the second heating scan of neat PLA and the PLA composite films at a filler content of 1.23 wt%.

Composite Films	T_g (°C)	T_{cc} (°C)	T_m (°C)
Neat PLA	60.1 [b]	124.8 [a]	152.0 [a]
PLA/activated charcoal	59.6 [b]	-	150.7 [b]
PLA/carbon-WC	59.9 [b]	118.1 [a]	150.6 [b]
PLA/carbon-Ag	59.8 [b]	123.9 [a]	150.7 [b]
PLA/carbon-WC-Ag	59.3 [b]	117.1 [a]	150.1 [b]

The superscript letter "a" refers to significant differences among T_{cc} of the PLA composite films at *p*-value < 0.05. The superscript letter "b" refers to non-significant differences among T_g and T_m of the PLA composite films at *p*-value < 0.05.

On the other hand, it was found that the incorporation of carbon-WC, carbon-Ag and carbon-WC-Ag nanoparticles as fillers in the PLA composite films resulted in shifts in the T_{cc} of the PLA composite films to lower temperatures compared with that of the neat PLA film, indicating the nucleating effect of the fillers. Due to the presence of polar functional groups such as carbonyl groups and high surface area, the synthesized carbon-based nanoparticles could interact with PLA and create nucleating sites to initiate the crystallization of PLA, resulting in an increase in the crystallization of PLA.

The presence of WCNPs and AgNPs in the synthesized carbon-based nanoparticles affected the nucleation ability of the synthesized carbon-based nanoparticles on the crystallization of PLA. It was found that the cold crystallization peak of PLA/carbon-WC was sharper and shifted to a lower temperature when compared to that of PLA/carbon-Ag (Figure 5). The lower T_{cc} in the second heating scan indicated the faster crystallization of PLA, which was induced by the added carbon-WC [10]. It might be implied that the presence of WCNPs in the synthesized carbon-based nanoparticles could promote the interaction between the synthesized carbon-based nanoparticles and PLA chains and subsequently enhance the nucleation ability of the synthesized carbon-based nanoparticles to accelerate the crystallization process of PLA.

Moreover, the T_{cc} of PLA/carbon-WC-Ag was lower than those of PLA/carbon-WC and PLA/carbon-Ag, suggesting the synergetic effect of the nucleation ability of WCNPs and AgNPs, accelerating the crystallization process of PLA. The T_m of all the PLA composite films shifted to lower temperatures when compared with that of the neat PLA film. This might be due to the transformation of the crystalline structure of PLA to the imperfect crystal forms during cold crystallization and the imperfect crystal forms could re-melt at a lower temperature [9,72].

3.5. X-ray Diffraction

Figure 6 shows XRD patterns of neat PLA and the PLA composite films, i.e., PLA/activated charcoal, PLA/carbon-Ag, PLA/carbon-WC and PLA/carbon-WC-Ag, at the filler content of 1.23%wt. The XRD pattern of the neat PLA film exhibited a diffraction peak at $2\theta = 16.64°$, which corresponds to the (110)/(200) planes of crystalline PLA [73]. It was found that the intensity of the diffraction peak at $2\theta = 16.64°$ in the XRD pattern of PLA/carbon-WC-Ag was much higher than those of neat PLA, PLA/activated charcoal, PLA/carbon-Ag and PLA/carbon-WC. From XRD analysis, it was found that the values of the degree of crystallinity (χ_c) of neat PLA, PLA/activated charcoal, PLA/carbon-Ag, PLA/carbon-WC and PLA/carbon-WC-AgNPs were 1.43%, 1.52%, 2.20%, 5.94% and 14.23%, respectively. This evidence confirmed that carbon-WC-Ag nanoparticles could lead to an improved crystalline structure of PLA by the co-nucleation ability of WCNPs and AgNPs coexisting in carbon-WC-Ag nanoparticles.
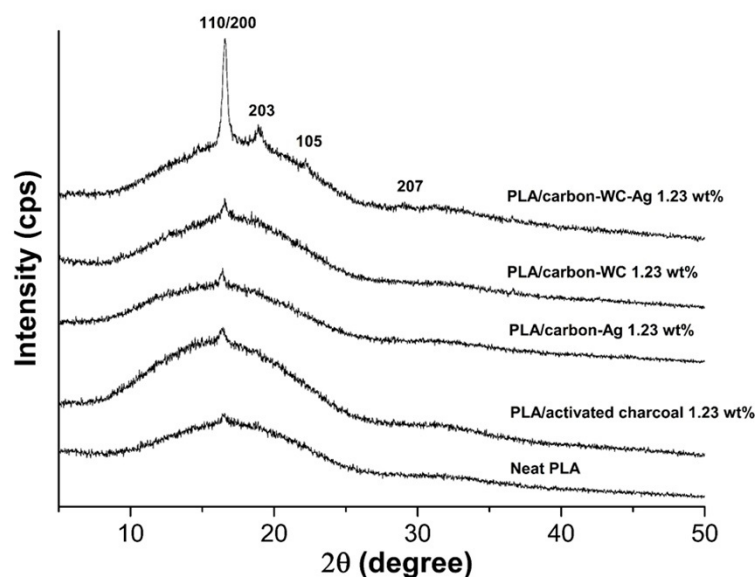
Figure 6. XRD patterns of neat PLA and the PLA composite films at a filler content of 1.23 wt%.

3.6. Mechanical Test

In general, there are two possible factors that can influence the mechanical properties of PLA. The first is the dispersion of fillers in the PLA matrix and the second is the crystallinity of PLA, which depends largely on the crystallization behavior of PLA [39,74]. In this study, the Young's modulus of the neat PLA film was 6.45 GPA. At the filler content of 1.23 wt%, the values of the Young's modulus of PLA/activated charcoal, PLA/carbon-WC, PLA/carbon-Ag and PLA/carbon-WC-Ag composite films were 7.24, 7.74, 7.97 and 8.07 GPa, respectively. These results indicated that the presence of activated charcoal, carbon-WC, carbon-Ag and carbon-WC-Ag in the PLA matrix led to an increase in the Young's modulus of PLA. The increased Young's modulus was related to the DSC results showing that the co-nucleation of WCNPs and AgNPs coexisting in carbon-WC-Ag nanoparticles could accelerate the crystallization process of PLA, resulting in a better crystalline structure and higher Young's modulus of PLA/carbon-WC-Ag composite films.

The values of tensile strength of the neat PLA, PLA/activated charcoal, PLA/carbon-WC, PLA/carbon-Ag and PLA/carbon-WC-Ag composite films were 19.92, 26.75, 21.16, 31.02 and 29.10 MPa, respectively. Due to the presence of some degree of aggregation of carbon-WC in the PLA matrix, the tensile strength of the PLA/carbon-WC composite film was not much higher than that of the neat PLA film. However, the incorporation of 1.23 wt% carbon-WC-Ag nanoparticles into the PLA matrix resulted in an increase in the tensile strength of PLA/carbon-WC-Ag composite films by 46.08% when compared with that of the neat PLA film. Since carbon-WC-Ag nanoparticles had bumpy surfaces, as evidenced by the SEM images, the surface roughness of carbon-WC-Ag nanoparticles might help to reduce the aggregation of carbon-WC-Ag nanoparticles in the PLA matrix, leading to a decrease in the stress concentrated point and consequently an increase in tensile strength [75]. Accordingly, it might be concluded that the incorporation of carbon-WC-Ag nanoparticles as fillers in the PLA matrix, even at a low filler content of 1.23 wt%, could significantly improve the Young's modulus and tensile strength of the resulting PLA/carbon-WC-Ag composite films.

3.7. Antibacterial Test

Antibacterial activities against *E. coli* and *S. aureus* of the neat PLA and the PLA composite films were evaluated by colony-forming unit assay. The cell suspensions without the addition of tested samples were used as controls. It was found that the neat PLA film had no antibacterial activity against *E. coli* and *S. Aureus*, whereas the presence of activated charcoal and carbon-WC in the PLA composite films resulted in negligible

inhibitory effects on *E. coli* and *S. Aureus*. The bacterial reduction rate (BRR) of the PLA composite film containing 1.23 wt% of carbon-WC-Ag nanoparticles against *E. coli* and *S. aureus* was 61.22% and 52.17%, respectively. It is well-known that AgNPs are used as a powerful antimicrobial agent. However, the deposition of AgNPs on a supporting material such as carbon may hinder the diffusion of AgNPs, resulting in lower antimicrobial activity than the corresponding unbound AgNPs. On the other hand, this may lead to better biocompatibility [22,76,77] when AgNPs deposited on a supporting material are incorporated into biomaterials for use in contact with living cells, such as in medical implants. Accordingly, the PLA/carbon-WC-Ag composites may be further developed for not only packaging materials but also biomedical applications.

4. Conclusions

Carbon-WC-Ag nanoparticles were simply synthesized in one step with the aid of SPP by using palm oil containing droplets of $AgNO_3$ solution as carbon and silver precursors, respectively. Instead of using chemical agents, highly active species generated during plasma discharge induced the formation of carbon-WC-Ag nanoparticles. The synthesized carbon-WC-Ag nanoparticles were subsequently examined as multifunctional fillers for the preparation of PLA composite films fabricated by solution casting. The optimum content of carbon-WC-Ag nanoparticles in the PLA/carbon-WC-Ag composite film was 1.23 wt%. Interestingly, WCNPs and AgNPs coexisting in carbon-WC-Ag nanoparticles exhibited a co-nucleation ability to accelerate the crystallization process of PLA, resulting in an enhanced crystalline structure of the PLA/carbon-WC-Ag composite films. It was found that the degree of crystallinity of PLA/carbon-WC-Ag composite films was roughly ten times higher than that of neat PLA film. Consequently, the Young's modulus and tensile strength of the PLA/carbon-WC-Ag composite films could be significantly improved. Moreover, WCNPs in the PLA composite films might be involved in the enhancement of the thermal degradation of PLA, leading to an advantage in their degradation. Due to the presence of AgNPs, the PLA/carbon-WC-Ag composite films exhibited antibacterial activities against *E. coli* and *S. aureus*. The evidence in this study indicates that SPP is a powerful tool for the synthesis of multicomponent nanoparticles. Moreover, multicomponent nanoparticles such as carbon-WC-Ag nanoparticles are useful as multifunctional fillers for the development of PLA composites aimed at packaging and biomaterial applications.

Conflicts of Interest: The authors declare no conflict of interest.

References

1. Fazita, M.R.N.; Jayaraman, K.; Bhattacharyya, D.; Hossain, M.S.; Haafiz, M.K.M.; Khalil, A. Disposal options of bamboo fabric-reinforced poly(Lactic) acid composites for sustainable packaging: Biodegradability and recyclability. *Polymers* **2015**, *7*, 1476–1496. [CrossRef]
2. Guo, Y.; Wang, L.; Chen, Y.; Luo, P.; Chen, T. properties of luffa fiber reinforced PHBV biodegradable composites. *Polymers* **2019**, *11*, 1765. [CrossRef] [PubMed]
3. Huh, M.; Jung, M.; Park, Y.; Kim, B.-J.; Kang, M.; Holden, P.; Yun, S. Effect of carbon nanotube functionalization on the structure and properties of poly(3-hydroxybutyrate)/MWCNTs biocomposites. *Macromol. Res.* **2014**, *22*, 765. [CrossRef]
4. Li, T.; Sun, H.; Wu, B.; Han, H.; Li, D.; Wang, J.-K.; Zhang, J.; Huang, J.; Sun, D. High-performance polylactic acid composites reinforced by artificially cultured diatom frustules. *Mater. Des.* **2020**, *195*, 109003. [CrossRef]
5. Le Phuong, H.A.; Izzati Ayob, N.A.; Blanford, C.F.; Mohammad Rawi, N.F.; Szekely, G. Nonwoven membrane supports from renewable resources: Bamboo fiber reinforced poly(Lactic Acid) composites. *ACS Sustain. Chem. Eng.* **2019**, *7*, 11885–11893. [CrossRef]
6. Xu, A.; Wang, Y.; Gao, J.; Wang, J. Facile fabrication of a homogeneous cellulose/polylactic acid composite film with improved biocompatibility, biodegradability and mechanical properties. *Green Chem.* **2019**, *21*, 4449–4456. [CrossRef]
7. Gorrasi, G.; Milone, C.; Piperopoulos, E.; Lanza, M.; Sorrentino, A. Hybrid clay mineral-carbon nanotube-PLA nanocomposite films. Preparation and photodegradation effect on their mechanical, thermal and electrical properties. *Appl. Clay Sci.* **2013**, *71*, 49–54. [CrossRef]
8. Khan, B.A.; Chevali, V.S.; Na, H.; Zhu, J.; Warner, P.; Wang, H. Processing and properties of antibacterial silver nanoparticle-loaded hemp hurd/poly(lactic acid) biocomposites. *Compos. B Eng.* **2016**, *100*, 10–18. [CrossRef]
9. Chen, P.; Zhou, H.; Liu, W.; Zhang, M.; Du, Z.; Wang, X. The synergistic effect of zinc oxide and phenylphosphonic acid zinc salt on the crystallization behavior of poly (lactic acid). *Polym. Degrad. Stab.* **2015**, *122*, 25–35. [CrossRef]
10. Naffakh, M.; Marco, C.; Ellis, G. Non-isothermal cold-crystallization behavior and kinetics of poly(l-lactic Acid)/WS$_2$ inorganic nanotube nanocomposites. *Polymers* **2015**, *7*, 2175–2189. [CrossRef]
11. Wang, N.; Zhang, X.; Ma, X.; Fang, J. Influence of carbon black on the properties of plasticized poly(lactic acid) composites. *Polym. Degrad. Stab.* **2008**, *93*, 1044–1052. [CrossRef]
12. Zhou, Y.; Lei, L.; Yang, B.; Li, J.; Ren, J. Preparation and characterization of polylactic acid (PLA) carbon nanotube nanocomposites. *Polym. Test* **2018**, *68*, 34–38. [CrossRef]
13. Pan, W.; Xiao, X.; Li, J.; Deng, S.; Shan, Q.; Yue, Y.; Tian, Y.; Nabar, N.R.; Wang, M.; Hao, L. The comparison of biocompatibility and osteoinductivity between multi-walled and single-walled carbon nanotube/PHBV composites. *J. Mater. Sci. Mater. Med.* **2018**, *29*, 189. [CrossRef]
14. Yang, S.; Wang, S.; Liu, X.; Li, L. Biomass derived interconnected hierarchical micro-meso-macro- porous carbon with ultrahigh capacitance for supercapacitors. *Carbon* **2019**, *147*, 540–549. [CrossRef]
15. Pontiroli, D.; Scaravonati, S.; Magnani, G.; Fornasini, L.; Bersani, D.; Bertoni, G.; Milanese, C.; Girella, A.; Ridi, F.; Verucchi, R.; et al. Super-activated biochar from poultry litter for high-performance supercapacitors. *Microporous Mesoporous Mater.* **2019**, *285*, 161–169. [CrossRef]
16. Aup-Ngoen, K.; Noipitak, M. Effect of carbon-rich biochar on mechanical properties of PLA-biochar composites. *Sustain. Chem. Pharm.* **2020**, *15*, 100204. [CrossRef]
17. Takagi, H.; Kako, S.; Kusano, K.; Ousaka, A. Thermal conductivity of PLA-bamboo fiber composites. *Adv. Compos. Mater.* **2007**, *16*, 377–384. [CrossRef]
18. Yu, H.; Sun, B.; Zhang, D.; Chen, G.; Yang, X.; Yao, J. Reinforcement of biodegradable poly(3-hydroxybutyrate-co-3-hydroxyvalerate) with cellulose nanocrystal/silver nanohybrids as bifunctional nanofillers. *J. Mater. Chem. B* **2014**, *2*, 8479–8489. [CrossRef]
19. Bai, T.; Zhu, B.; Liu, H.; Wang, Y.; Song, G.; Liu, C.; Shen, C. Biodegradable poly(lactic acid) nanocomposites reinforced and toughened by carbon nanotubes/clay hybrids. *Int. J. Biol. Macromol.* **2020**, *151*, 628–634. [CrossRef]
20. Fortunati, E.; Armentano, I.; Zhou, Q.; Iannoni, A.; Saino, E.; Visai, L.; Berglund, L.A.; Kenny, J.M. Multifunctional bionanocomposite films of poly(lactic acid), cellulose nanocrystals and silver nanoparticles. *Carbohydr. Polym.* **2012**, *87*, 1596–1605. [CrossRef]
21. Yu, H.-Y.; Yang, X.-Y.; Lu, F.-F.; Chen, G.-Y.; Yao, J.-M. Fabrication of multifunctional cellulose nanocrystals/poly(lactic acid) nanocomposites with silver nanoparticles by spraying method. *Carbohydr. Polym.* **2016**, *140*, 209–219. [CrossRef]
22. Tsou, C.H.; Yao, W.H.; Lu, Y.C.; Tsou, C.Y.; Wu, C.S.; Chen, J.; Wang, R.Y.; Su, C.; Hung, W.S.; De Guzman, M.; et al. Antibacterial property and cytotoxicity of a poly(lactic acid)/nanosilver-doped multiwall carbon nanotube nanocomposite. *Polymers* **2017**, *9*, 100. [CrossRef] [PubMed]
23. Zhang, H.; Yu, H.-Y.; Wang, C.; Yao, J. Effect of silver contents in cellulose nanocrystal/silver nanohybrids on PHBV crystallization and property improvements. *Carbohydr. Polym.* **2017**, *173*, 7–16. [CrossRef]

24. Kang, J.; Li, O.L.; Saito, N. Synthesis of structure-controlled carbon nano spheres by solution plasma process. *Carbon* **2013**, *60*, 292–298. [CrossRef]

25. Matsuda, N.; Nakashima, T.; Kato, T.; Shiroishi, H. Synthesis of multiwall carbon nanotube-supported platinum catalysts by solution plasma processing for oxygen reduction in polymer electrolyte fuel cells. *Electrochim. Acta* **2014**, *146*, 73–78. [CrossRef]

26. Panomsuwan, G.; Saito, N.; Ishizaki, T. Nitrogen-doped carbon nanoparticles derived from acrylonitrile plasma for electrochemical oxygen reduction. *Phys. Chem. Chem. Phys.* **2015**, *17*, 6227–6232. [CrossRef]

27. Nemoto, S.; Ueno, T.; Hieda, J.; Bratescu, M.A.; Saito, N.; Watthanaphanit, A. Simple introduction of carboxyl head group with alkyl spacer onto multiwalled carbon nanotubes by solution plasma process. *Jpn. J. Appl. Phys.* **2017**, *56*, 096202. [CrossRef]

28. Saito, N.; Hieda, J.; Takai, O. Synthesis process of gold nanoparticles in solution plasma. *Thin Solid Films* **2009**, *518*, 912–917. [CrossRef]

29. Tong, D.G.; Wu, P.; Su, P.K.; Wang, D.Q.; Tian, H.Y. Preparation of zinc oxide nanospheres by solution plasma process and their optical property, photocatalytic and antibacterial activities. *Mater. Lett.* **2012**, *70*, 94–97. [CrossRef]

30. Kang, J.; Li, O.L.; Saito, N. A simple synthesis method for nano-metal catalyst supported on mesoporous carbon: The solution plasma process. *Nanoscale* **2013**, *5*, 6874–6882. [CrossRef]

31. Panomsuwan, G.; Chantaramethakul, J.; Chokradjaroen, C.; Ishizaki, T. In situ solution plasma synthesis of silver nanoparticles supported on nitrogen-doped carbons with enhanced oxygen reduction activity. *Mater. Lett.* **2019**, *251*, 135–139. [CrossRef]

32. Panomsuwan, G.; Saito, N.; Ishizaki, T. Fe–N-doped carbon-based composite as an efficient and durable electrocatalyst for the oxygen reduction reaction. *RSC Adv.* **2016**, *6*, 114553–114559. [CrossRef]

33. Kim, D.-w.; Li, O.L.; Pootawang, P.; Saito, N. Solution plasma synthesis process of tungsten carbide on N-doped carbon nanocomposite with enhanced catalytic ORR activity and durability. *RSC Adv.* **2014**, *4*, 16813–16819. [CrossRef]

34. Takai, O. Solution plasma processing (SPP). *Pure Appl. Chem.* **2008**, *80*, 2003–2011. [CrossRef]

35. Prasertsung, I.; Damrongsakkul, S.; Saito, N. Degradation of β-chitosan by solution plasma process (SPP). *Polym. Degrad. Stab.* **2013**, *98*, 2089–2093. [CrossRef]

36. Morishita, T.; Ueno, T.; Panomsuwan, G.; Hieda, J.; Yoshida, A.; Bratescu, M.A.; Saito, N. Fastest formation routes of nanocarbons in solution plasma processes. *Sci. Rep.* **2016**, *6*, 36880. [CrossRef]

37. Salifairus, M.J.; Abd Hamid, S.B.; Soga, T.; Alrokayan, S.A.; Khan, H.A.; Rusop, M. Structural and optical properties of graphene from green carbon source via thermal chemical vapor deposition. *J. Mater. Res.* **2016**, *31*, 1947–1956. [CrossRef]

38. Ishak, A.; Dayana, K.; Mamat, M.H.; Malek, M.F.; Rusop, M. Nano-structured amorphous carbon films using novel palm oil precursor for solar cell applications. *Optik* **2015**, *126*, 1610–1612. [CrossRef]

39. Fonseca, C.; Ochoa, A.; Ulloa, M.T.; Alvarez, E.; Canales, D.; Zapata, P.A. Poly(lactic acid)/TiO$_2$ nanocomposites as alternative biocidal and antifungal materials. *Mater. Sci. Eng. C* **2015**, *57*, 314–320. [CrossRef]

40. Villani, M.; Consonni, R.; Canetti, M.; Bertoglio, F.; Iervese, S.; Bruni, G.; Visai, L.; Iannace, S.; Bertini, F. Polyurethane-Based Composites: Effects of Antibacterial Fillers on the Physical-Mechanical Behavior of Thermoplastic Polyurethanes. *Polymers* **2020**, *12*, 362. [CrossRef]

41. Marra, A.; Silvestre, C.; Duraccio, D.; Cimmino, S. Polylactic acid/zinc oxide biocomposite films for food packaging application. *Int. J. Biol. Macromol.* **2016**, *88*, 254–262. [CrossRef]

42. Alammar, A.; Park, S.-H.; Williams, C.J.; Derby, B.; Szekely, G. Oil-in-water separation with graphene-based nanocomposite membranes for produced water treatment. *J. Membr. Sci.* **2020**, *603*, 118007. [CrossRef]

43. Rubin, H.N.; Neufeld, B.H.; Reynolds, M.M. Surface-Anchored Metal–Organic Framework–Cotton Material for Tunable Antibacterial Copper Delivery. *ACS Appl. Mater. Interfaces* **2018**, *10*, 15189–15199. [CrossRef]

44. Al Aani, S.; Gomez, V.; Wright, C.J.; Hilal, N. Fabrication of antibacterial mixed matrix nanocomposite membranes using hybrid nanostructure of silver coated multi-walled carbon nanotubes. *Chem. Eng. J.* **2017**, *326*, 721–736. [CrossRef]

45. Chen, D.; Qiao, X.; Qiu, X.; Chen, J. Synthesis and electrical properties of uniform silver nanoparticles for electronic applications. *J. Mater. Sci.* **2009**, *44*, 1076–1081. [CrossRef]

46. Zakaria, M.A.; Menazea, A.A.; Mostafa, A.M.; Al-Ashkar, E.A. Ultra-thin silver nanoparticles film prepared via pulsed laser deposition: Synthesis, characterization, and its catalytic activity on reduction of 4-nitrophenol. *Surf. Interfaces* **2020**, *19*, 100438. [CrossRef]

47. Boca, S.C.; Potara, M.; Gabudean, A.M.; Juhem, A.; Baldeck, P.L.; Astilean, S. Chitosan-coated triangular silver nanoparticles as a novel class of biocompatible, highly effective photothermal transducers for in vitro cancer cell therapy. *Cancer Lett.* **2011**, *311*, 131–140. [CrossRef]

48. Abdel-Halim, E.S.; Al-Deyab, S.S. Antimicrobial activity of silver/starch/polyacrylamide nanocomposite. *Int. J. Biol. Macromol.* **2014**, *68*, 33–38. [CrossRef] [PubMed]

49. Cañamares, M.V.; Garcia-Ramos, J.V.; Gómez-Varga, J.D.; Domingo, C.; Sanchez-Cortes, S. Comparative study of the morphology, aggregation, adherence to glass, and surface-enhanced Raman scattering activity of silver nanoparticles prepared by chemical reduction of Ag+ using citrate and hydroxylamine. *Langmuir* **2005**, *21*, 8546–8553. [CrossRef] [PubMed]

50. Li, Z.; Fan, L.; Zhang, T.; Li, K. Facile synthesis of Ag nanoparticles supported on MWCNTs with favorable stability and their bactericidal properties. *J. Hazard. Mater.* **2011**, *187*, 466–472. [CrossRef] [PubMed]

51. Kumar, R.; Munstedt, H. Silver ion release from antimicrobial polyamide/silver composites. *Biomaterials* **2005**, *26*, 2081–2088. [CrossRef] [PubMed]

52. Lin, Y.; Qiao, Y.; Wang, Y.; Yan, Y.; Huang, J. Self-assembled laminated nanoribbon-directed synthesis of noble metallic nanoparticle-decorated silica nanotubes and their catalytic applications. *J. Mater. Chem.* **2012**, *22*, 18314–18320. [CrossRef]

53. Bhaduri, B.; Polubesova, T. Facile synthesis of carbon-supported silver nanoparticles as an efficient reduction catalyst for aqueous 2-methyl-p-nitrophenol. *Mater. Lett.* **2020**, *267*, 127546. [CrossRef]

54. Vijayakumar, P.S.; Prasad, B.L. Intracellular biogenic silver nanoparticles for the generation of carbon supported antiviral and sustained bactericidal agents. *Langmuir* **2009**, *25*, 11741–11747. [CrossRef] [PubMed]

55. Sudhakar, P.; Soni, H. Catalytic reduction of nitrophenols using silver nanoparticles-supported activated carbon derived from agro-waste. *J. Environ. Chem. Eng.* **2018**, *6*, 28–36. [CrossRef]

56. Surudžić, R.; Janković, A.; Bibić, N.; Vukašinović-Sekulić, M.; Perić-Grujić, A.; Mišković-Stanković, V.; Park, S.J.; Rhee, K.Y. Physico–chemical and mechanical properties and antibacterial activity of silver/poly(vinyl alcohol)/graphene nanocomposites obtained by electrochemical method. *Compos. B Eng.* **2016**, *85*, 102–112. [CrossRef]

57. Gan, L.; Geng, A.; Wu, Y.; Wang, L.; Fang, X.; Xu, L.; Mei, C. Antibacterial, flexible, and conductive membrane based on MWCNTs/Ag coated electro-Spun PLA nanofibrous scaffolds as wearable fabric for body motion sensing. *Polymers* **2020**, *12*, 120. [CrossRef]

58. Cheng, Y.; Li, H.; Fang, C.; Ai, L.; Chen, J.; Su, J.; Zhang, Q.; Fu, Q. Facile synthesis of reduced graphene oxide/silver nanoparticles composites and their application for detecting heavy metal ions. *J. Alloy. Compd.* **2019**, *787*, 683–693. [CrossRef]

59. Tammeveski, L.; Erikson, H.; Sarapuu, A.; Kozlova, J.; Ritslaid, P.; Sammelselg, V.; Tammeveski, K. Electrocatalytic oxygen reduction on silver nanoparticle/multi-walled carbon nanotube modified glassy carbon electrodes in alkaline solution. *Electrochem. Commun.* **2012**, *20*, 15–18. [CrossRef]

60. Ahmed, J.; Arfat, Y.A.; Castro-Aguirre, E.; Auras, R. Thermal properties of ZnO and bimetallic Ag–Cu alloy reinforced poly(lactic acid) nanocomposite films. *J. Therm. Anal. Calorim.* **2016**, *125*, 205–214. [CrossRef]

61. Abdul Rahaman, M.H.; Khandaker, M.U.; Khan, Z.R.; Kufian, M.Z.; Noor, I.S.M.; Arof, A.K. Effect of gamma irradiation on poly(vinyledene difluoride)–lithium bis(oxalato)borate electrolyte. *Phys. Chem. Chem. Phys.* **2014**, *16*, 11527–11537. [CrossRef] [PubMed]

62. Janpetch, N.; Saito, N.; Rujiravanit, R. Fabrication of bacterial cellulose-ZnO composite via solution plasma process for antibacterial applications. *Carbohydr. Polym.* **2016**, *148*, 335–344. [CrossRef] [PubMed]

63. Tanaka, S.; Bataev, I.; Oda, H.; Hokamoto, K. Synthesis of metastable cubic tungsten carbides by electrical explosion of tungsten wire in liquid paraffin. *Adv. Powder Technol.* **2018**, *29*, 2447–2455. [CrossRef]

64. Liu, C.; Zhou, D.; Zhou, J.; Xie, Z.; Xia, Y. Synthesis and characterization of tungsten carbide and application to electrocatalytic hydrogen evolution. *RSC Adv.* **2016**, *6*, 76307–76311. [CrossRef]

65. Kim, H.; Saito, N. One-pot synthesis of purple benzene-derived MnO_2-carbon hybrids and synergistic enhancement for the removal of cationic dyes. *Sci. Rep.* **2018**, *8*, 4342. [CrossRef]

66. Cam, D.; Marucci, M. Influence of residual monomers and metals on poly (l-lactide) thermal stability. *Polymer* **1997**, *38*, 1879–1884. [CrossRef]

67. Fan, Y.; Nishida, H.; Mori, T.; Shirai, Y.; Endo, T. Thermal degradation of poly(l-lactide): Effect of alkali earth metal oxides for selective l,l-lactide formation. *Polymer* **2004**, *45*, 1197–1205. [CrossRef]

68. Vijayalakshmi, S.P.; Madras, G. Thermal degradation of water soluble polymers and their binary blends. *J. Appl. Polym. Sci.* **2006**, *101*, 233–240. [CrossRef]

69. Doganay, D.; Coskun, S.; Kaynak, C.; Unalan, H.E. Electrical, mechanical and thermal properties of aligned silver nanowire/polylactide nanocomposite films. *Compos. B Eng.* **2016**, *99*, 288–296. [CrossRef]

70. Ramos, M.; Fortunati, E.; Peltzer, M.; Dominici, F.; Jiménez, A.; del Carmen Garrigós, M.; Kenny, J.M. Influence of thymol and silver nanoparticles on the degradation of poly(lactic acid) based nanocomposites: Thermal and morphological properties. *Polym. Degrad. Stab.* **2014**, *108*, 158–165. [CrossRef]

71. Piekarska, K.; Sowinski, P.; Piorkowska, E.; Haque, M.M.U.; Pracella, M. Structure and properties of hybrid PLA nanocomposites with inorganic nanofillers and cellulose fibers. *Compos. Part A Appl. Sci. Manuf.* **2016**, *82*, 34–41. [CrossRef]

72. Wang, L.; Wang, Y.-n.; Huang, Z.-g.; Weng, Y.-x. Heat resistance, crystallization behavior, and mechanical properties of polylactide/nucleating agent composites. *Mater. Des. (1980–2015)* **2015**, *66*, 7–15. [CrossRef]

73. Dai, X.; Cao, Y.; Shi, X.; Wang, X. Non-isothermal crystallization kinetics, thermal degradation behavior and mechanical properties of poly(lactic acid)/MOF composites prepared by melt-blending methods. *RSC Adv.* **2016**, *6*, 71461–71471. [CrossRef]

74. Liu, S.-Q.; Wu, G.-H.; Xiao, Y.-C.; Guo, H.-X.; Shao, F.-J. Crystallization behavior and mechanical properties of poly(lactic acid) complex fiber toughened by carbon nanotube nanocapsules. *Text. Res. J.* **2017**, *88*, 1616–1627. [CrossRef]

75. Mat Desa, M.S.Z.; Hassan, A.; Arsad, A.; Mohammad, N.N.B. Mechanical properties of poly(lactic acid)/multiwalled carbon nanotubes nanocomposites. *Mater. Res. Innov.* **2014**, *18* (Suppl. 6), S6-14–S6-17. [CrossRef]

76. Castle, A.B.; Gracia-Espino, E.; Nieto-Delgado, C.; Terrones, H.; Terrones, M.; Hussain, S. Hydroxyl-functionalized and N-Doped multiwalled carbon nanotubes decorated with silver nanoparticles preserve cellular function. *ACS Nano* **2011**, *5*, 2458–2466. [CrossRef] [PubMed]

77. Seo, Y.; Hwang, J.; Kim, J.; Jeong, Y.; Hwang, M.P.; Choi, J. Antibacterial activity and cytotoxicity of multi-walled carbon nanotubes decorated with silver nanoparticles. *Int. J. Nanomed.* **2014**, *9*, 4621–4629.

Article

In-Situ Iodine Doping Characteristics of Conductive Polyaniline Film Polymerized by Low-Voltage-Driven Atmospheric Pressure Plasma

Jae Yong Kim [1,†] , **Shahzad Iqbal** [1,†] , **Hyo Jun Jang** [1] , **Eun Young Jung** [1] , **Gyu Tae Bae** [1] , **Choon-Sang Park** [2] **and Heung-Sik Tae** [1,3,*]

1   School of Electronic and Electrical Engineering, College of IT Engineering, Kyungpook National University, Daegu 41566, Korea; jyk@knu.ac.kr (J.Y.K.); shahzadiqbal@knu.ac.kr (S.I.); bs00201@knu.ac.kr (H.J.J.); eyjung@knu.ac.kr (E.Y.J.); doctor047@knu.ac.kr (G.T.B.)
2   Department of Electrical and Computer Engineering, College of Engineering, Kansas State University, Manhattan, KS 66506, USA; purplepcs@ksu.edu
3   School of Electronics Engineering, College of IT Engineering, Kyungpook National University, Daegu 41566, Korea
*   Correspondence: hstae@ee.knu.ac.kr; Tel.: +82-53-950-6563
†   These authors contributed equally to this work.

Abstract: In-situ iodine (I_2)-doped atmospheric pressure (AP) plasma polymerization is proposed, based on a newly designed AP plasma reactor with a single wire electrode that enables low-voltage-driven plasma polymerization. The proposed AP plasma reactor can proceed plasma polymerization at low voltage levels, thereby enabling an effective in-situ I_2 doping process by maintaining a stable glow discharge state even if the applied voltage increases due to the use of a discharge gas containing a large amount of monomer vapors and doping materials. The results of field-emission scanning electron microscopy (FE-SEM) and Fourier transformation infrared spectroscopy (FT-IR) show that the polyaniline (PANI) films are successfully deposited on the silicon (Si) substrates, and that the crosslinking pattern of the synthesized nanoparticles is predominantly vertically aligned. In addition, the in-situ I_2-doped PANI film fabricated by the proposed AP plasma reactor exhibits excellent electrical resistance without electrical aging behavior. The developed AP plasma reactor proposed in this study is more advantageous for the polymerization and in-situ I_2 doping of conductive polymer films than the existing AP plasma reactor with a dielectric barrier.

Keywords: polyaniline (PANI); conductive polymer; plasma polymerization; aniline; atmospheric pressure plasma reactor (AP plasma reactor); in-situ iodine (I_2) doping

1. Introduction

Plasma polymerization is a methodology for synthesizing polymeric composites with high crosslinking density from reactive monomer vapors generated via gaseous or solution plasma processes [1–7]. In particular, atmospheric pressure (AP) plasma polymerization primarily uses a non-thermal glow discharge to synthesize highly crosslinked polymer films from the various radicals and reactive species generated from the discharge gas, monomer vapor, or atmosphere [8–14]. In synthesizing conjugated polymers, the AP plasma polymerization method has several important advantages, such as a simple one-step synthesis process, an eco-friendly polymerization process that does not produce chemical waste, a dry process that uses a small amount of monomer, and a room temperature process with low-power consumption. In recent years, the present research group has reported effective AP plasma polymerization methods using a proposed atmospheric pressure plasma jet (APPJ) array structure with a guide tube and bluff body [15–21]. Using this APPJ array reactor, various conjugated polymer films of polyaniline (PANI), polythiophene (PTh), and polypyrrole (PPy), as well as a co-polymer composite film of PANI and PPy, were

successfully synthesized [15–17,21]. Among various conjugated polymers, polyaniline (PANI) is attracting great attention due to its good electrical conductivity and environmental stability [22–24]. In particular, the electrical properties of PANI can be reversibly controlled by altering the oxidation state of the main chain through protonating the amine nitrogen chain [25,26]. Several studies are being conducted on attempts to use these properties as electrodes and electrochromic materials for displays or electronic devices [27–29], and as an active layer for gas/bio-sensors [30–32].

In the development of an electrically conductive polymer film, it is important not only to synthesize the conjugated polymer film, but also to impart the film with electrical properties. A widely-used approach to making the conjugated polymer film conductive is that of doping with iodine (I_2) as an electron acceptor (proton donor) [33–36]. When I_2 is used as a dopant, the electrons in the double bonds of the conjugated polymer backbone are transferred to the iodine, leaving the units of the polymer chain positively charged, thus resulting in an imbalanced electron arrangement that makes the polymer film conductive [37]. In particular, due to the advantages of low cost and process simplicity, many studies have described the ex-situ I_2 doping process in which the doping step is performed after the synthesis of the polymer film [38–41]. However, this approach still has the major drawback that the corresponding electrical resistance is initially quite high and continues to increase with time. By contrast, in-situ I_2 doping is an in-line processing method that is highly suitable for plasma polymerization in which nucleation reaction and crosslinking occur in the gas phase. Nevertheless, in sharp contrast to the many studies on the use of in-situ doping in the vacuum plasma process [42–44], there are only a few studies related to the use of in-situ doping in atmospheric pressure plasma polymerization. This is because the discharge becomes unstable due to dopant injection, which adversely affects plasma polymerization steps such as the fragmentation, recombination, and nucleation of monomers.

Recently, the present research group introduced an in-situ I_2 doping method in which a flow of monomer vapor was supplied and I_2 was sublimated simultaneously during AP plasma polymerization in order to fabricate polymer films with good conducting properties [17]. Moreover, the in-situ I_2-doped conjugated polymer films exhibit much better electrical conductivity than those produced by ex-situ I_2 doping, making them very promising materials for both research and industry, with potential applications as the conductive layer in emerging display technologies, gas sensors, molecular electronics, and optoelectronics. Detailed studies of the in-situ doping process involving a systematic experimental approach were therefore required in order to further improve the electrical conductivity of the resulting conjugated polymer films by maximizing the in-situ I_2 doping effect. In the previous study, however, the inevitable increase in discharge voltage and plasma instability due to an increase in the sublimated I_2 content of the Ar gas meant that the injection of sublimated I_2 could only be determined at flow rates of less than 30 sccm [17]. Nevertheless, an increase in the concentration of sublimated I_2 is necessary in order to enhance the conductivity of the polymer films via functionalization. Therefore, it is necessary to develop a low-voltage-driven AP plasma reactor capable of maintaining a stable glow discharge even when the applied voltage increases due to the use of a large amount of sublimated I_2.

Hence, the present paper describes the use of a newly developed AP plasma reactor driven at a low applied voltage via a bare wire electrode exposed to the plasma generating space. Aniline vapor is injected into the Ar glow plasma and sublimated I_2 is co-injected to synthesize the in-situ I_2-doped PANI film. The discharge characteristics of the newly developed AP plasma reactor are investigated via digital photography, intensified charge coupled device (ICCD) imaging, voltage/current/light-emission waveform analysis, and optical emission spectroscopy. The characteristics of the resulting PANI thin film are also investigated via field-emission scanning electron microscopy (FE-SEM) and Fourier transform infrared spectroscopy (FT-IR). Finally, the PANI film is deposited onto an inter-digitated electrode (IDE) substrate via the in-situ doping technique, and then the electrical

resistance is measured using a two-probe method in order to determine the suitability of the obtained film for use as the detecting layer in a gas sensor.

2. Materials and Methods

2.1. Preparation of the AP Plasma Reactor Device

For the efficient fabrication of plasma polymerized films, a new AP plasma reactor was developed that spatially separates the gas emission and the voltage application regions. As shown in Figure 1a, the reactor consists of the following four components: (i) a narrow glass tube, (ii) a wide glass tube, (iii) a polytetrafluoroethylene (PTFE) stand, and (iv) a tungsten wire electrode. The tungsten wire electrode is covered with a glass capillary, with just the 2 mm tip of the wire remaining completely exposed for plasma generation [45]. The wire tip is positioned away from the edge of the wide tube and points towards the center at an angle of approximately 50°. Thus, the exposed tip is aligned with the center of both the narrow tube and the PFTE stand, as shown in Figure 1b. It is well known that the exposed sharp tip of a wire electrode will locally enhance the electric field to significantly reduce the breakdown voltage [46]. In the newly designed AP plasma reactor, the discharge breakdown voltage provided a peak voltage of 2.8 kV, and the driving voltage was adjusted to a peak value of 5 kV for stable glow plasma during plasma polymerization. Thus, the new AP plasma reactor design makes it possible to simultaneously increase the amounts of monomer vapor and sublimated I_2 while maintaining a stable plasma state.

(**a**)	(**b**)
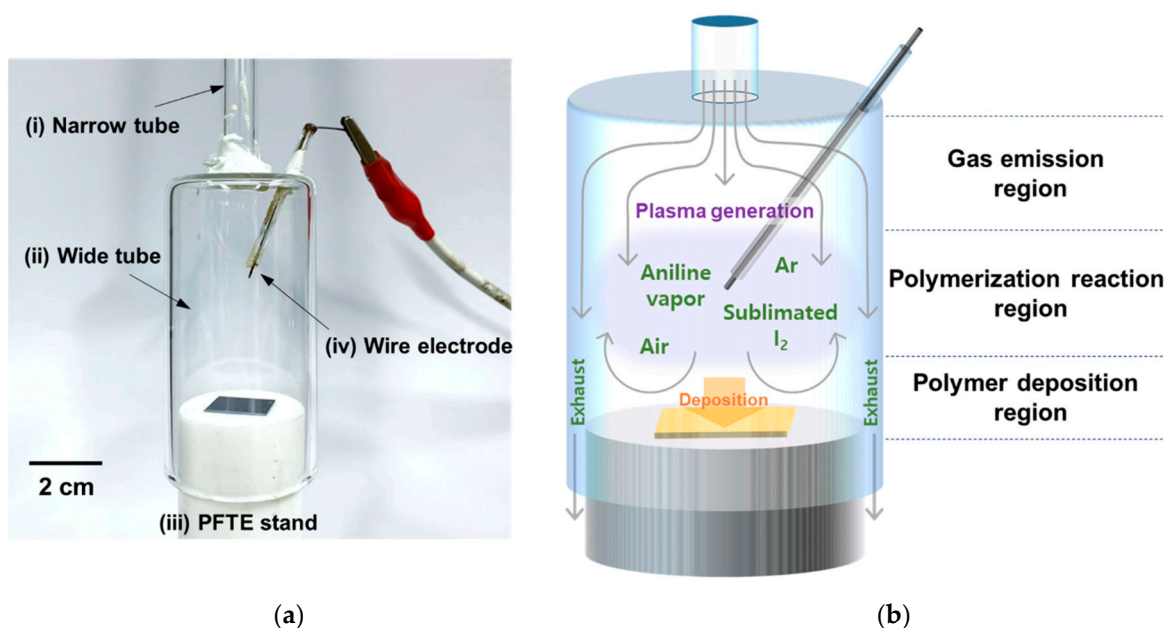
Figure 1. The new atmospheric pressure (AP) plasma reactor design: (**a**) photographic image with the main components labeled, and (**b**) a schematic diagram of the in-situ iodine (I_2)-doped plasma polymerization procedure. Abbreviations: PFTE: polytetrafluoroethylene.

The linear gas velocity in a cylindrical tube is inversely proportional to the square of the radius (half the inner diameter) of the cross-sectional area [47]. Thus, when the discharge gas flows from the narrow tube (ID = 6.8 mm) to the wide tube (ID = 34 mm), the 5-fold increase in diameter leads to a 25-fold decrease in the linear gas velocity. This allows the discharge gas to remain inside the gas emission region of the wide tube for a longer time (Figure 1b). Meanwhile, the PTFE stand functions both as a support for the substrate and as a barrier against which the gas flow emerging from the narrow tube collides [15–18]. Thus, the gas flow becomes evenly distributed in the center of the wide tube and is retained in the polymerization reaction region for a longer time.

2.2. Entire Assembled System for AP Plasma Polymerization

A schematic diagram of the fully-assembled system used in the present study for in-situ I_2 doping AP plasma polymerization is presented in Figure 2. The system consisted of the gas supply part, the plasma polymerization part, and the power supply part. Argon (Ar) gas (HP grade with purity of 99.999%) was employed for the in-situ I_2-doped AP plasma polymerization, and the gas feed line was divided into two for independent control of the Ar gas flow rates for the aniline vapor and sublimated I_2 supplies. Liquid aniline monomer (MW = 93 g·mol^{-1}, Sigma–Aldrich Co., St. Louis, MO, USA) was connected to one of the gas feed lines using a glass bubbler, and was vaporized by Ar gas at a flow rate of 500 standard cubic centimeters per minute (sccm). For the in-situ I_2 doping, a 50 mL glass bottle containing 3 g of iodine pellets (Daejung Chemical & Materials Corp., Siheung, South Korea) was connected to the other gas feed line, and Ar gas was supplied at a flow rate of 500 sccm. Thus, the aniline vapor and sublimated I_2 molecules were simultaneously introduced into the AP plasma reactor via the Ar gas flow. For AP polymerization in the absence of in-situ I_2 doping, the iodine bottle was simply removed from the system (red dashed area in Figure 2). An inverter type driving circuit was used to amplify the low primary voltage to a high secondary voltage. In the present study, a sinusoidal voltage with a peak value of 5 kV and a frequency of 30 kHz was applied to the AP plasma reactor. The experimental conditions for the AP plasma polymerization, including the in-situ I_2 doping process, are summarized in Table 1.
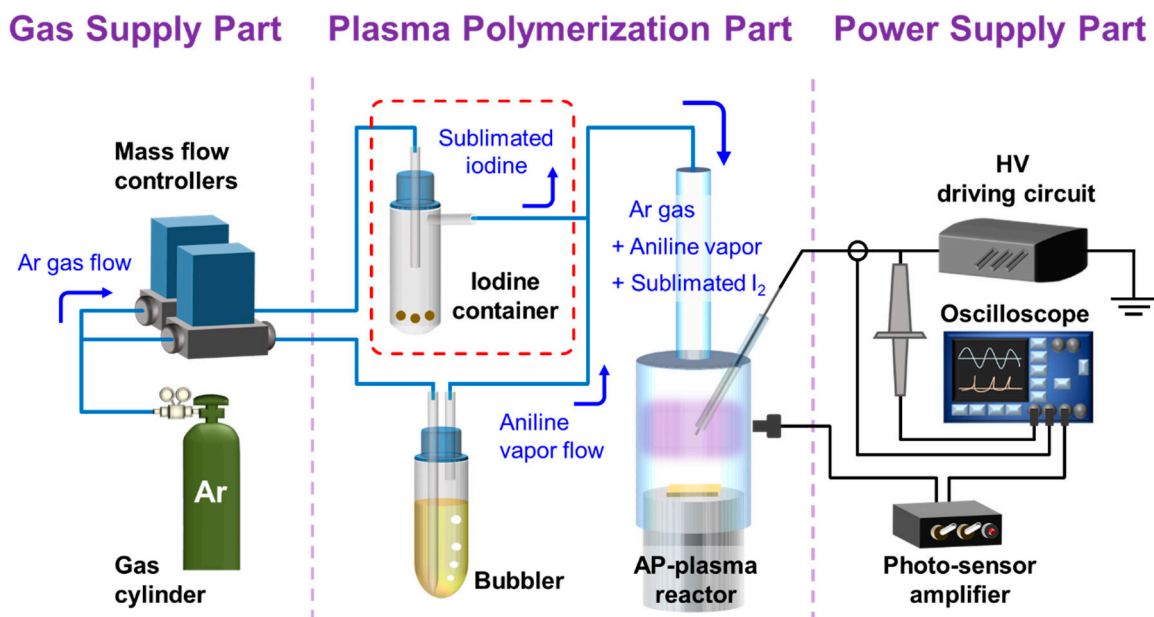
Figure 2. Schematic diagram of the fully-assembled system for the in-situ I_2-doped AP plasma polymerization procedure.

2.3. Characterization of the AP Plasma during Plasma Polymerization

During AP plasma polymerization, the electrical characteristics of the generated plasma were monitored by displaying the voltage and current waveforms on a digital oscilloscope (WaveRunner 64Xi, Teledyne LeCroy Inc., Chestnut Ridge, NY, USA) using a high voltage (HV) probe (P6015A, Tektronix Inc., Beaverton, OR, USA) and a current monitor (4100, Pearson Electronics Inc., Palo Alto, CA, USA), respectively. The discharge current was obtained by subtracting the current waveform obtained when the plasma was turned off by stopping the Ar gas supply from the current waveform that was measured when the plasma was turned on.

Table 1. Experimental conditions for AP plasma polymerization with in-situ I_2 doping.

	Experimental Conditions	AP Plasma Reactor
Device Configuration	Electrode type	Single electrode
	Electrode material	Tungsten wire
	Inner diameter of narrow glass tube	6.8 mm
	Inner diameter of wide glass tube	34 mm
	Substrate stand material	Polytetrafluoroethylene (PTFE)
	Diameter of substrate stand	30 mm
Driving Conditions	Driving type	AC
	Voltage waveform	Sinusoidal
	Plasma initiation voltage	2.8 kV
	Plasma driving voltage	5 kV
	Driving frequency	30 kHz
Gas Conditions	Gas type	Ar
	Gas purity	HP grade (99.999%)
	Flow rate for aniline monomer vapor	500 sccm
	Flow rate for sublimated iodine	500 sccm

The wavelength-unresolved optical emission of the generated plasma was observed with a photo-sensor amplifier (C6386-01, Hamamatsu Corp., Hamamatsu, Japan). An infrared (IR) filter with a 1 mm slit was placed in the front of the optical fiber of the photo-sensor amplifier to detect optical emission from the Ar discharge and avoid any unwanted light signals from the environment. Thus, the optical emission waveform covering a wavelength range of 720–1100 nm was plotted on the digital oscilloscope.

The diagnostic use of optical emission spectroscopy (OES) for light-emitting regions allows a better understanding of highly complex phenomena such as high-pressure plasma, dusty plasma, and solution plasma [48–50]. A fiber optic spectrometer (USB-2000+, Ocean Optics Inc., Dunedin, FL, USA) was employed to identify a variety of reactive species generated by the glow plasma during the AP plasma polymerization process.

Photographs of the AP plasma reactor and the IDE substrates were acquired using a digital single lens reflex (DSLR) camera (D5300, Nikon Corp., Tokyo, Japan) with a Macro 1:1 lens (Tamron SP AF 90 mm F2.8 Di, Tamron Co., Ltd., Saitama, Japan) and an ICCD camera (PI-MAX II, Princeton Instruments Inc., Trenton, NJ, USA) was used in the shutter mode to identify the spatial behavior of the glow plasma.

2.4. Characterization of the PANI Films

The surface and cross-sectional morphology of the PANI films was monitored via field-emission scanning electron microscopy (FE-SEM; SU8220, Hitachi High-Technologies, Tokyo, Japan) with accelerated electrons at a voltage of 3 kV and a current of 10 mA. Prior to measurement, the PANI films were coated with conductive platinum to avoid any surface charging problems.

The chemical molecular structures of the PANI films were detected by Fourier transformation infrared spectroscopy (FT-IR; Vertex 70, Bruker Corp., Ettlingen, Germany) at the Korea Basic Science Institute (KBSI; Daegu). The FT-IR spectra were measured by averaging 128 scans at a wavenumber resolution of 0.6 cm^{-1} in the range of 650–4000 cm^{-1} using the attenuated total reflection (ATR) mode.

The electrical resistances of the in-situ I_2-doped PANI films deposited on Si substrates with interdigitated electrodes (IDEs) were measured at room temperature by a two-probe method using an electrometer (Fluke 179, Fluke Corp., Everett, WA, USA).

3. Results and Discussion

3.1. Optical and Electrical Properties of Plasmas Generated by the AP Plasma Reactor

In the typical APPJ configuration, the discharge gas flows through a tube and a high voltage is applied to an electrode connected to the tube for electrical breakdown [51–55]. The newly developed AP plasma reactor is based on this configuration and consists of the four components described in Section 2.1. Photographic and ICCD images of the plasma generated inside the AP plasma reactor during the AP polymerization process are presented in Figure 3a. Here, the glow discharge initiated around the exposed tip of the wire electrode is seen to be evenly dispersed in the absence of a counter electrode, thus enabling the synthesis of a homogeneous polymer film. Moreover, the complete separation of the gas emission and polymerization reaction regions allowed the plasma polymerization to proceed close to the substrate (Figure 1b), thus enabling the effective synthesis of the I_2-doped polymer film.
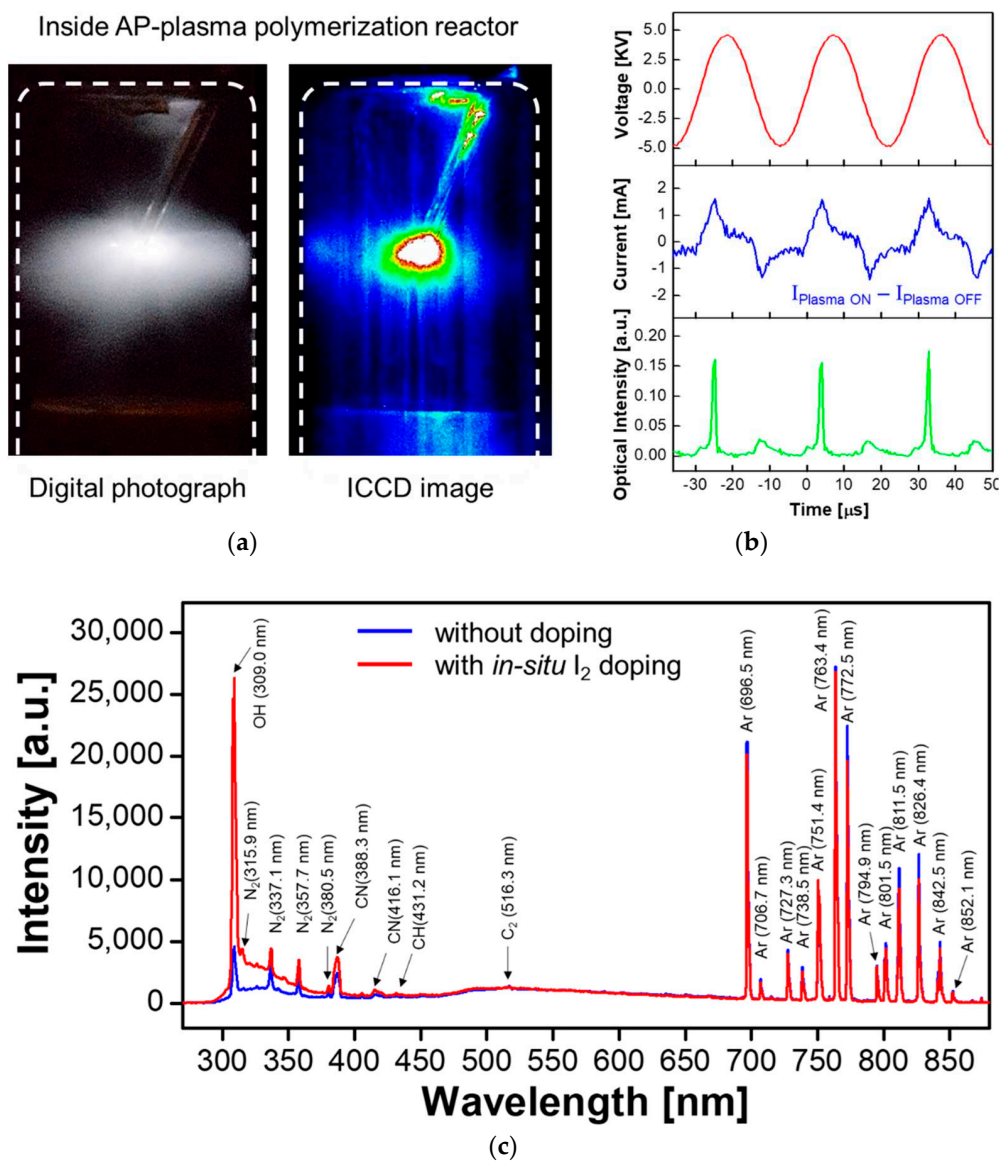
Figure 3. Optical and electrical properties of glow plasmas during in-situ I_2-doped AP plasma polymerization: (**a**) photograph and intensified charge coupled device (ICCD) image inside the AP plasma reactor, (**b**) temporal behaviors of applied voltage, discharge current, and optical emission of generated glow plasma, and (**c**) emission spectra measured in the polymerization reaction region with and without the in-situ I_2 doping technique.

The temporal behaviors of the applied voltage, discharge current, and optical emission of the generated plasma are shown in Figure 3b. Because the sinusoidal voltage waveform is not distorted by electrical discharge, the voltage waveform before and after the glow discharge does not change at all. The current waveform consists of two components: the displacement current and the discharge current. Since the amplitude of the displacement current in the sinusoidal form is large and predominant, even if the discharge current component is added during the glow discharge, the current waveform changes only slightly. Therefore, the discharge current waveform is extracted and plotted as shown in the middle graph of Figure 3b to examine the current characteristics during electrical discharge. The discharge current waveform is seen to be sustained for a period of time, with the discharges occurring continuously during both the rising and falling periods of the voltage waveform, due to the exposed wire electrode tip. In addition, the intensity of the optical emissions in the plasma polymerizing area is seen to be higher when the slope of the voltage waveform is rising than when the latter is falling, and the same behavior is observed during the three voltage cycles shown in Figure 3b, thus indicating a stable discharge. This is the typical discharge behavior for a plasma generated using a single powered electrode device.

The reactive species generated by the newly designed AP plasma reactor are revealed by the OES spectra obtained during plasma polymerization with or without in-situ I_2 doping (Figure 3c). Thus, when the plasma polymerization and I_2 doping process proceeded simultaneously, the reactive iodine species are seen to have absorbed several positive ions (e.g., H_2O^+, H_3O^+, O_2^+, and $O^+(H_2O)$) from the atmosphere [56], leading to a remarkable increase in the peak intensity for the OH radical at 308 nm compared to that observed in the absence of in-situ I_2 doping. This clearly demonstrates that the in-situ I_2 doping influences the plasma state which, in turn, is responsible for the nucleation of the aniline monomer during the AP plasma polymerization. Moreover, this observation is in agreement with our previous report, which first introduced the in-situ I_2 doping method in AP plasma polymerization [17].

3.2. The AP Plasma Polymerized Aniline Film

Using this AP plasma polymerization system, the in-situ I_2-doped PANI films are deposited on the silicon (Si) substrate for 60 min. The surface and cross-sectional morphologies of the in-situ I_2-doped PANI films are indicated at various magnifications by the FE-SEM images in Figure 4. Thus, the low-magnification surface view image in Figure 4a reveals the uniform distribution of the irregular crosslinking pattern over the surface of the PANI film. In addition, the high-magnification images in Figure 4b,c indicate that this growth pattern consists of irregularly crosslinked nanoparticles with a porous network. Meanwhile, the cross-sectional FE-SEM images provide information on the film growth, indicating that the crosslinked nanoparticles are predominantly aligned in the vertical direction rather than the horizontal direction (Figure 4d,e). This vertically aligned crosslinking pattern indicates that when the AP plasma polymerization process proceeds at a low voltage, the reactive monomer species have insufficient energy to make very many irregular crosslinks with each other. Consequently, the reactive monomer species are crosslinked in the order in which they reach the substrate from the plasma polymerization space, thus forming the vertical crosslinking pattern. The low magnification cross-sectional image indicates that the crosslinked PANI film is porous and rough, but the thickness is highly consistent, thus revealing the homogenous film growth (Figure 4d). This image also reveals the good adhesion of the synthesized polymer film to the Si substrate. The high-magnification cross-sectional images also reveal the coral reef-like bumpy shapes of the crosslinked nanoparticles, with several protruding branches (Figure 4e,f). After 60 min of AP plasma polymerization, the thickness of the PANI film deposited on the Si substrate was approximately 12 μm (Figure 4e).
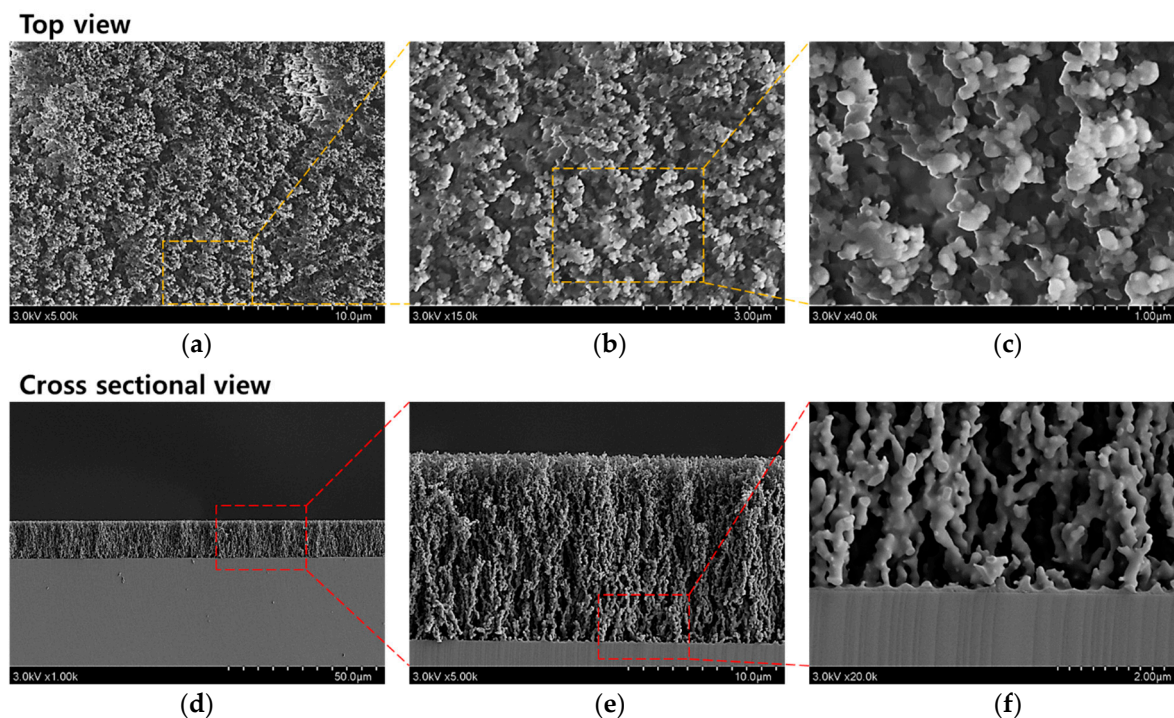
Figure 4. Field-emission scanning electron microscopy (FE-SEM) characterization of the polyaniline (PANI) films deposited on silicon (Si) substrates via the newly designed AP plasma polymerization process: (**a**–**c**) surface views, and (**d**–**f**) cross-sectional views.

The FT-IR characteristics of the PANI films deposited on Si substrates using the proposed AP plasma reactor system with and without in-situ I_2 doping are presented in Figure 5. Here, both spectra exhibit the characteristic peaks of the PANI polymer structures at 3365, 2959, 2844, 1601, 1501, 1313, 1250, and 763 cm^{-1}. The FT-IR peak assignments of the PANI film, deposited using the proposed AP plasma reactor system, are given in Table 2. Thus, the peaks at 1501 and 1601 cm^{-1} are attributed to the benzenoid and quinoid ring stretching vibrations, respectively. The peak at 763 cm^{-1} is ascribed to the C-H out-of-plane deformation from the aromatic ring, and the bands at 1250 and 1313 cm^{-1} are ascribed to the C-N stretching vibration [57]. Moreover, the peaks at 2888 cm^{-1} and 2959 cm^{-1} are attributed to the aliphatic of C-H stretching within the polymer chains, and the peak at 3365 cm^{-1} is ascribed to the N-H stretching vibration [41,58,59]. Notably, the peaks corresponding to the conjugated bonds (1250, 2844, 2959, and 3365 cm^{-1}) exhibit higher intensities in the spectrum of the in-situ doped PANI film than those of the film that was deposited without doping, thus indicating that the degree of polymerization was improved by doping. In particular, a remarkable increase in the intensity of the C-N bond absorption peak (1250 cm^{-1}) is observed for the in-situ I_2-doped PANI film, thus reflecting the relationship between the C-N bonds and the electrical conductivity of the PANI polymer film. Specifically, the C-N bond is closely related to the electrical conductivity for the proton acid, which is preferred to the N of the quinone ring [60,61].

3.3. The In-Situ Iodine Doped PANI Film

The in-situ I_2 doping process allows iodine (I_2), iodide (I^-), and polyiodides (I_3^- and I_5^-) to directly participate in the formation of charge carriers during plasma polymerization and become evenly distributed throughout the PANI film layer. These reactive iodine species can easily absorb various positively charged species such as N_2^+, N_2H^+, H_2O^+, H_3O^+, O_2^+, $O^+(H_2O)$ [56], thus enhancing the electrical properties of the PANI film by injecting proton donors that serve as charge carriers. To examine the suitability of the active layer for applications in future display and gas sensor technologies, the electrical resistance

of the in-situ I_2-doped PANI film was examined for long term changes under normal storage conditions and the ambient atmosphere. First, the PANI film on a Si substrate was supplied with IDEs, as shown in Figure 6. The IDEs were made of gold and had an interdigitated comb-like two-electrode structure with 20 pairs of microelectrodes. The width of each microelectrode was 10.8 μm and the spacing between microelectrodes was 2.54 μm (Figure 6a). The porous crosslinking pattern that was observed in the above FE-SEM analysis resulted in diffuse reflection of visible light, giving the in-situ I_2-doped PANI film a non-glossy, beige colored appearance (Figure 6b).
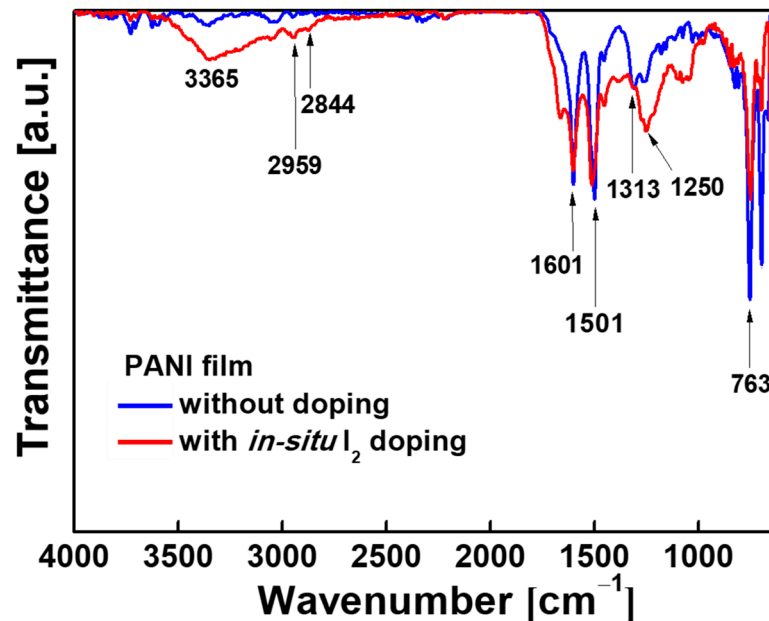
Figure 5. The Fourier transformation infrared spectroscopy (FT-IR) spectra of the PANI films deposited on Si substrates using the newly designed AP plasma reactor with and without in-situ I_2 doping.

Table 2. The FT-IR absorption peaks and corresponding molecular structures for the in-situ I_2-doped PANI films deposited using the newly designed AP-plasma reactor system.

Wavenumber/cm^{-1}	Vibration Mode
763	C-H out of plane bending
1250	C-N bending
1313	C-N stretching
1501	C=C stretching vibrations of the benzenoid
1601	C=C stretching vibrations of quinoid rings
2844	C-H asymmetric stretching
2959	C-H asymmetric stretching
3365	N-H stretching

The resistance of the in-situ I_2-doped PANI film during 2 weeks of continuous measurement is shown in Figure 7. Here, the initial resistance is seen to be 3.2 kΩ, and the subsequent changes fall into three phases. In Phase I, the resistance rapidly increases to 9 kΩ over a period of 12 h. This is followed by a gradual increase to 12.5 kΩ over a period of 60 h (Phase II). From day 3 onwards (Phase III), the resistance of the PANI film has become saturated at 12.5 kΩ ± 7% and no further changes are observed during storage under ambient conditions for a total of 2 weeks.
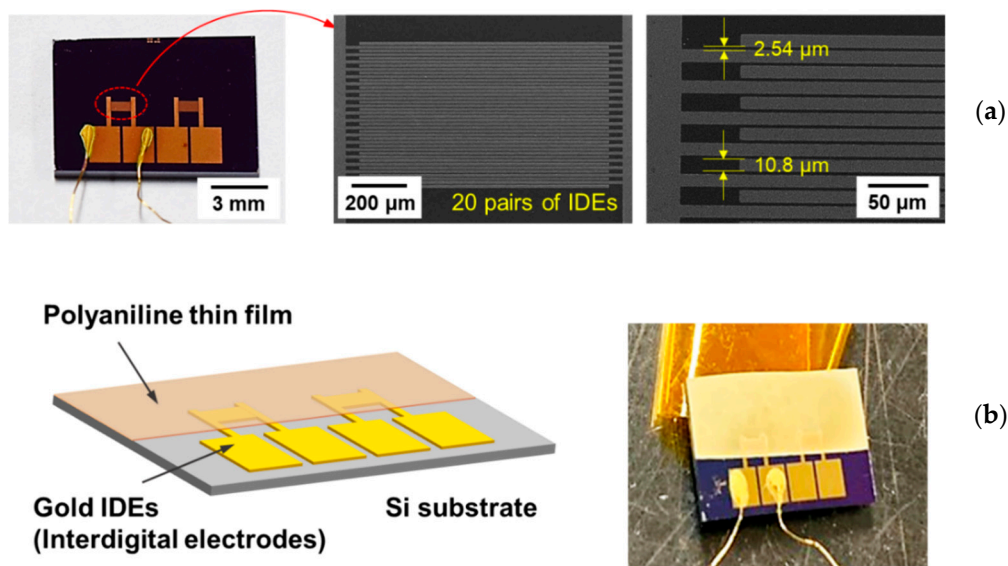
Figure 6. (**a**) Gold interdigitated electrode (IDE) patterns on Si substrate (**b**) PANI film on IDE substrate for electrical resistance measurement.
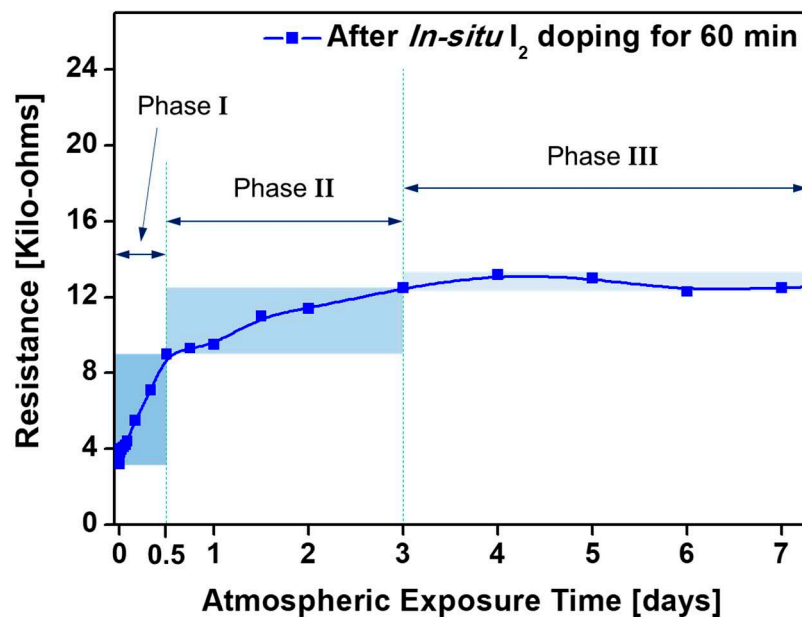
Figure 7. Changes in electrical resistance of in-situ I_2-doped PANI film on IDE substrate.

Because the doping and polymerization processes occur simultaneously, the in-situ doping method effectively reduces the possibility of oxidation upon subsequent exposure to the atmosphere by forming charge transfer complexes inside the polymer film. Nevertheless, polymer oxidation cannot be completely avoided under the ambient atmosphere, as residual reactive species that formed C-I bonds in the polymer networks may react with atmospheric oxygen [17]. Hence, oxidation of the fabricated PANI film inevitably occurred during exposure to the atmosphere after AP plasma polymerization, thus leading to the resistance changes shown in Figure 7. The experimental results confirmed that it took 3 days for the resistance to stabilize. Nevertheless, the electrical resistance stabilized at a low value of 12.5 kΩ and remained unchanged thereafter.

Consequently, the newly proposed AP plasma polymerization method, capable of synthesizing the PANI thin film with excellent electrical conductivity, is expected to help overcome the limitations of the conventional plasma polymerization system. The conduc-

tive polymer film obtained by generating glow discharge using a single electrode structure without a counter electrode indicates that the polymer films can be stably deposited onto not only Si substrates, but also glass and flexible plastic substrates. The polymer layers deposited through this one-step synthesis technique can provide a unique advantage as a conductive layer based on a variety of nanomaterials/structures for future gas/bio-sensor, display technology, plasma thrusters, molecular electronics, optoelectronics and bio-nanotechnology applications.

4. Conclusions

In this study, a newly designed AP plasma reactor was described, in which a bare wire electrode exposed to the discharge area enabled the AP plasma polymerization process to occur at a low voltage. Thus, during the fabrication of an in-situ I_2-doped PANI film, both the aniline monomer and iodine molecules could be vaporized at a much higher Ar gas flowrate than previously reported, while maintaining a stable glow discharge and successfully performing the plasma polymerization and in-situ doping process. The chemical composition and structure of the resulting PANI were confirmed by FT-IR spectroscopy and FE-SEM imaging, while electrical resistance measurements confirmed that the film had excellent electrical conductivity without electrical aging behavior. The detailed examination of the newly fabricated PANI film is expected to provide key clues to overcome the performance limitations of the PANI films polymerized by the conventional APPJ array with dielectric barriers. It is also anticipated that the new PANI films grown at room temperature using the proposed AP plasma reactor can offer versatile advantages as electrodes and active layers for future displays and polymer gas sensors. Moreover, PANI films without electrical aging behavior will become increasingly promising for detecting layers for specific molecular species, including various gaseous molecules, ethanol, acetone, and bio-molecules such as glucose, DNA and viruses.

Author Contributions: J.Y.K., S.I., H.J.J., C.-S.P. and H.-S.T. conceived and designed the study; J.Y.K., S.I., H.J.J., and G.T.B. performed the experiments; H.J.J., E.Y.J. and G.T.B. contributed the analytical tools; J.Y.K., S.I., H.J.J. and E.Y.J. and H.-S.T. analyzed the data; J.Y.K., S.I., E.Y.J. and H.-S.T. wrote the majority of the paper. All authors have read and agreed to the published version of the manuscript.

Conflicts of Interest: The authors declare no conflict of interest.

References

1. Thiry, D.; Konstantinidis, S.; Cornil, J.; Snyders, R. Plasma diagnostics for the low-pressure plasma polymerization process: A critical review. *Thin Solid Films* **2016**, *606*, 19–44. [CrossRef]
2. Teslaru, T.; Topala, I.; Dobromir, M.; Pohoata, V.; Curecheriu, L.; Dumitrascu, N. Polythiophene films obtained by polymerization under atmospheric pressure plasma conditions. *Mater. Chem. Phys.* **2016**, *169*, 120–127. [CrossRef]
3. Cho, S.-H.; Park, Z.-T.; Kim, J.-G.; Boo, J.-H. Physical and optical properties of plasma polymerized thin films deposited by PECVD method. *Surf. Coat. Technol.* **2003**, *174*, 1111–1115. [CrossRef]
4. Friedrich, J. Mechanisms of Plasma Polymerization—Reviewed from a Chemical Point of View. *Plasma Process. Polym.* **2011**, *8*, 783–802. [CrossRef]
5. Vasquez-Ortega, M.; Ortega, M.; Morales, J.; Olayo, M.G.; Cruz, G.J.; Olayo, R. Core–shell polypyrrole nanoparticles ob-tained by atmospheric pressure plasma polymerization. *Polym. Int.* **2014**, *63*, 2021–2029. [CrossRef]
6. Shin, J.-G.; Shin, B.J.; Jung, E.Y.; Park, C.-S.; Kim, J.Y.; Tae, H.-S. Effects of a dielectric barrier discharge (DBD) on characteris-tics of polyaniline nanoparticles synthesized by a solution plasma process with an Ar gas bubble channel. *Polymers* **2020**, *12*, 1939. [CrossRef] [PubMed]

7. Shin, J.-G.; Park, C.-S.; Jung, E.-Y.; Shin, B.J.; Tae, H.-S. Synthesis of a polyaniline nanoparticle using a solution plasma pro-cess with an Ar gas bubble channel. *Polymers* **2019**, *11*, 105. [CrossRef] [PubMed]

8. Van Deynse, A.; Cools, P.; Leys, C.; De Geyter, N.; Morent, R. Surface activation of polyethylene with an argon atmospheric pressure plasma jet: Influence of applied power and flow rate. *Appl. Surf. Sci.* **2015**, *328*, 269–278. [CrossRef]

9. Petersen, J.; Becker, C.M.; Fouquet, T.; Addiego, F.; Toniazzo, V.; Dinia, A.; Ruch, D. Nano-ordered thin films achieved by soft atmospheric plasma polymerization. *RSC Adv.* **2013**, *3*, 4416–4424. [CrossRef]

10. Kasih, T.P.; Kuroda, S.-I.; Kubota, H. Poly(methyl methacrylate) Films Deposited via Non-Equilibrium Atmospheric Pressure Plasma Polymerization Using Argon as Working Gas. *Plasma Process. Polym.* **2007**, *4*, 648–653. [CrossRef]

11. Lee, J.-H.; Kim, Y.-H.; Choi, E.-H.; Kim, K.-M.; Kim, K.-N. Development of hydrophilic dental wax without surfactant using a non-thermal air atmospheric pressure plasma jet. *J. Phys. D Appl. Phys.* **2014**, *47*, 235402. [CrossRef]

12. De Geyter, N.; Morent, R.; Van Vlierberghe, S.; Dubruel, P.; Leys, C.; Gengembre, L.; Schacht, E.; Payen, E. Deposition of polymethyl methacrylate on polypropylene substrates using an atmospheric pressure dielectric barrier discharge. *Prog. Org. Coat.* **2009**, *64*, 230–237. [CrossRef]

13. Van Vrekhem, S.; Morent, R.; De Geyter, N. Deposition of a PMMA coating with an atmospheric pressure plasma jet. *J. Coat. Technol. Res.* **2018**, *15*, 679–690. [CrossRef]

14. Cools, P.; Sainz-Garcı, E.; Geyter, N.D.; Nikiforov, A.; Blajan, M.; Shimizu, K.; Alba-Elıas, F.; Leys, C.; Morent, R. Influence of DBD inlet geometry on the homogeneity of plasma-polymerized acrylic acid films: The use of a microplasma–electrode in-let configuration. *Plasma Process. Polym.* **2015**, *12*, 1153–1163. [CrossRef]

15. Park, C.-S.; Kim, D.H.; Shin, B.J.; Tae, H.-S. Synthesis and Characterization of Nanofibrous Polyaniline Thin Film Prepared by Novel Atmospheric Pressure Plasma Polymerization Technique. *Materials* **2016**, *9*, 39. [CrossRef] [PubMed]

16. Park, C.-S.; Jung, E.Y.; Kim, D.H.; Cho, B.-G.; Shin, B.J.; Tae, H.-S. TOF-SIMS study on nano size conducting polymer pre-pared by simple atmospheric pressure plasma polymerization technique for display applications. *Mol. Cryst. Liq. Cryst.* **2017**, *651*, 16–25. [CrossRef]

17. Park, C.-S.; Kim, D.Y.; Kim, D.H.; Lee, H.-K.; Shin, B.J.; Tae, H.-S. Humidity-independent conducting polyaniline films syn-thesized using advanced atmospheric pressure plasma polymerization with in-situ iodine doping. *Appl. Phys. Lett.* **2017**, *110*, 033502. [CrossRef]

18. Park, C.-S.; Jung, E.Y.; Kim, D.H.; Kim, D.Y.; Lee, H.-K.; Shin, B.J.; Lee, D.H.; Tae, H.-S. Atmospheric Pressure Plasma Polymeriza-tion Synthesis and Characterization of Polyaniline Films Doped with and without Iodine. *Materials* **2017**, *10*, 1272. [CrossRef]

19. Kim, D.H.; Park, C.-S.; Jung, E.Y.; Shin, B.J.; Kim, J.Y.; Bae, G.T.; Jang, H.J.; Cho, B.-G.; Tae, H.-S. Effects of iodine dopant on atmospheric pressure plasma polymerized pyrrole in remote and coupling methods. *Mol. Cryst. Liq. Cryst.* **2018**, *677*, 135–142. [CrossRef]

20. Kim, D.H.; Park, C.-S.; Jung, E.Y.; Kum, D.S.; Kim, J.Y.; Kim, D.; Bae, G.T.; Cho, B.-G.; Shin, B.J.; Lee, N.H.; et al. Experimental study on atmospheric pressure plasma polymerized conducting polymer under coupling and remote conditions. *Mol. Cryst. Liq. Cryst.* **2018**, *663*, 108–114. [CrossRef]

21. Jang, H.J.; Park, C.-S.; Jung, E.Y.; Bae, G.T.; Shin, B.J.; Tae, H.-S. Synthesis and Properties of Thiophene and Aniline Copolymer Using Atmospheric Pressure Plasma Jets Copolymerization Technique. *Polymer* **2020**, *12*, 2225. [CrossRef] [PubMed]

22. Wang, G.; Vivek, R.; Wang, J.-Y. Polyaniline Nanoparticles: Synthesis, Dispersion and Biomedical Applications. *Mini-Rev. Org. Chem.* **2017**, *14*, 56–64. [CrossRef]

23. Goktas, H.; Demircioglu, Z.; Sel, K.; Gunes, T.; Kaya, I. The optical properties of plasma polymerized polyaniline thin films. *Thin Solid Films* **2013**, *548*, 81–85. [CrossRef]

24. Qin, Q.; Tao, J.; Yang, Y. Preparation and characterization of polyaniline film on stainless steel by elecrochemical polymer-ization as a counter electrode of DSSC. *Synth. Met.* **2010**, *160*, 1167–1172. [CrossRef]

25. Trchová, M.; Stejskal, J. Polyaniline: The infrared spectroscopy of conducting polymer nanotubes (IUPAC Technical Report). *Pure Appl. Chem.* **2011**, *83*, 1803–1817. [CrossRef]

26. Morales, J.; Olayo, M.G.; Cruz, G.J.; Olayo, R. Synthesis by plasma and characterization of bilayer aniline-pyrrole thin films doped with iodine. *J. Polym. Sci. Part B Polym. Phys.* **2002**, *40*, 1850–1856. [CrossRef]

27. Popov, A.; Brasiunas, B.; Damaskaite, A.; Plikusiene, I.; Ramanavicius, A.; Ramanaviciene, A. Electrodeposited Gold Nanostruc-tures for the Enhancement of Electrochromic Properties of PANI–PEDOT Film Deposited on Transparent Electrode. *Polymer* **2020**, *12*, 2778. [CrossRef]

28. Gosselin, D.; Gougis, M.; Baque, M.; Navarro, F.P.; Belgacem, M.N.; Chaussy, D.; Bourdat, A.-G.; Mailley, P.; Berthier, J. Screen-Printed Polyaniline-Based Electrodes for the Real-Time Monitoring of Loop-Mediated Isothermal Amplification Reactions. *Anal. Chem.* **2017**, *89*, 10124–10128. [CrossRef]

29. Wang, X.; Deng, J.; Duan, X.; Liu, D.; Guo, J.; Liu, P. Crosslinked polyaniline nanorods with improved electrochemical per-formance as electrode material for supercapacitors. *J. Mater. Chem. A* **2014**, *2*, 12323–12329. [CrossRef]

30. German, N.; Ramanaviciene, A.; Ramanavicius, A. Formation and electrochemical evaluation of polyaniline and polypyr-role nanocomposites based on glucose oxidase and gold nanostructures. *Polymers* **2020**, *12*, 3026. [CrossRef]

31. Fratoddi, I.; Venditti, I.; Cametti, C.; Russo, M.V. Chemiresistive polyaniline-based gas sensors: A mini review. *Sens. Actuators B Chem.* **2015**, *220*, 534–548. [CrossRef]

32. Virji, S.; Huang, J.; Kaner, R.B.; Weiller, B.H. Polyaniline Nanofiber Gas Sensors: Examination of Response Mechanisms. *Nano Lett.* **2004**, *4*, 491–496. [CrossRef]

33. Pron, A.; Rannou, P. Processible conjugated polymers: From organic semiconductors to organic metals and superconductors. *Prog. Polym. Sci.* **2002**, *27*, 135–190. [CrossRef]

34. Elmas, S.; Beelders, W.; Nash, J.; Macdonald, T.J.; Jasieniak, M.; Griesser, H.J.; Nann, T. Photo-doping of plasma-deposited polyaniline (PAni). *RSC Adv.* **2016**, *6*, 70691–70699. [CrossRef]

35. Fan, L.; Xu, X. A simple strategy to enhance electrical conductivity of nanotube-conjugate polymer composites via io-dine-doping. *RSC Adv.* **2015**, *5*, 78104–78108. [CrossRef]

36. Takechi, K.; Shiga, T.; Motohiro, T.; Akiyama, T.; Yamada, S.; Nakayama, H.; Kohama, K. Solar cells using iodine-doped polythiophene–porphyrin polymer films. *Sol. Energy Mater. Sol. Cells* **2006**, *90*, 1322–1330. [CrossRef]

37. Le, T.-H.; Kim, Y.; Yoon, H. Electrical and Electrochemical Properties of Conducting Polymers. *Polymer* **2017**, *9*, 150. [CrossRef]

38. Mansuroglu, D.; Uzun-Kaymak, I.U. Investigation into Ex-Situ and In-Situ Iodine Doped Plasma Polymerized Fluo-rene-type Thin Film. In *Materials Today: Proceedings*; Elsevier: Amsterdam, The Netherlands, 2019; Volume 18, pp. 1955–1963.

39. Wang, J.; Neoh, K.G.; Kang, E.T. Comparative study of chemically synthesized and plasma polymerized pyrrole and thio-phene thin films. *Thin Solid Films* **2004**, *446*, 205–217. [CrossRef]

40. Silverstein, M.; Visoly-Fisher, I. Plasma polymerized thiophene: Molecular structure and electrical properties. *Polymer* **2002**, *43*, 11–20. [CrossRef]

41. Mathai, C.J.; Saravanan, S.; Anantharaman, M.; Venkitachalam, S.; Jayalekshmi, S. Effect of iodine doping on the bandgap of plasma polymerized aniline thin films. *J. Phys. D Appl. Phys.* **2002**, *35*, 2206–2210. [CrossRef]

42. Kim, T.-W.; Lee, J.-H.; Back, J.-W.; Jung, W.-G.; Kim, J.-Y. Deposition and in-situ plasma doping of plasma-polymerized thi-ophene films using PECVD. *Macromol. Res.* **2009**, *17*, 31–36. [CrossRef]

43. Bazaka, K.; Jacob, M.V. Effects of Iodine Doping on Optoelectronic and Chemical Properties of Polyterpenol Thin Films. *Nanomaterials* **2017**, *7*, 11. [CrossRef] [PubMed]

44. Sajeev, U.S.; Mathai, C.J.; Saravanan, S.; Ashokan, R.R.; Venkatachalam, S.; Anantharaman, M.R. On the optical and electrical properties of rf and a.c. plasma polymerized aniline thin films. *Bull. Mater. Sci.* **2006**, *29*, 159–163. [CrossRef]

45. Kim, D.B.; Rhee, J.K.; Gweon, B.; Moon, S.Y.; Choe, W. Comparative study of atmospheric pressure low and radio frequency microjet plasmas produced in a single electrode configuration. *Appl. Phys. Lett.* **2007**, *91*, 151502. [CrossRef]

46. Park, H.S.; Kim, S.J.; Joh, H.M.; Chung, T.H.; Bae, S.H.; Leem, S.H. Optical and electrical characterization of an atmospheric pressure microplasma jet with a capillary electrode. *Phys. Plasmas* **2010**, *17*, 33502. [CrossRef]

47. Kim, J.Y.; Ballato, J.; Kim, S.-O. Intense and Energetic Atmospheric Pressure Plasma Jet Arrays. *Plasma Process. Polym.* **2012**, *9*, 253–260. [CrossRef]

48. Djurovic, S.; Roberts, J.R.; Sobolewski, M.A.; Olthoff, J.K. Absolute Spatially- and Temporally-Resolved Optical Emission Measurements of rf Glow Discharges in Argon. *J. Res. Natl. Inst. Stand. Technol.* **1993**, *98*, 159–180. [CrossRef]

49. Popescu, S.; Jerby, E.; Meir, Y.; Barkay, Z.; Ashkenazi, D.; Mitchell, J.B.A.; Le Garrec, J.-L.; Narayanan, T. Plasma column and nano-powder generation from solid titanium by localized microwaves in air. *J. Appl. Phys.* **2015**, *118*, 023302. [CrossRef]

50. Kim, H.-J.; Shin, J.-G.; Park, C.-S.; Kum, D.S.; Shin, B.J.; Kim, J.Y.; Park, H.-D.; Choi, M.; Tae, H.-S. In-Liquid Plasma Process for Size- and Shape-Controlled Synthesis of Silver Nanoparticles by Controlling Gas Bubbles in Water. *Materials* **2018**, *11*, 891. [CrossRef]

51. Lu, X.; Jiang, Z.; Xiong, Q.; Tang, Z.; Hu, X.; Pan, Y. An 11cm long atmospheric pressure cold plasma plume for applications of plasma medicine. *Appl. Phys. Lett.* **2008**, *92*, 081502. [CrossRef]

52. Teschke, M.; Kedzierski, J.; Finantu-Dinu, E.G.; Korzec, D.; Engemann, J. High-speed photographs of a dielectric barrier at-mospheric pressure plasma jet. *IEEE Trans. Plasma Sci.* **2005**, *33*, 310–311. [CrossRef]

53. Lia, Q.; Li, J.-T.; Zhu, W.-C.; Zhu, X.-M.; Pu, Y.-K. Effects of gas flow rate on the length of atmospheric pressure nonequilib-rium plasma jets. *Appl. Phys. Lett.* **2009**, *95*, 141502. [CrossRef]

54. Sands, B.L.; Huang, S.K.; Ganguly, B.N. Current scaling in an atmospheric pressure capillary dielectric barrier discharge. *Appl. Phys. Lett.* **2009**, *95*, 51502. [CrossRef]

55. Laroussi, M.; Lu, X. Room-temperature atmospheric pressure plasma plume for biomedical applications. *Appl. Phys. Lett.* **2005**, *87*, 113902. [CrossRef]

56. Ito, T.; Gotoh, K.; Sekimoto, K.; Hamaguchi, S.; Gotou, K. Mass Spectrometry Analyses of Ions Generated by Atmospheric-Pressure Plasma Jets in Ambient Air. *Plasma Med.* **2015**, *5*, 283–298. [CrossRef]

57. Sharma, A.K.; Bhardwaj, P.; Dhawan, S.K.; Sharma, Y. Oxidative synthesis and electrochemical studies of poly(aniline-co-pyrrole)-hybrid carbon nanostructured composite electrode materials for supercapacitor. *Adv. Mater. Lett.* **2015**, *6*, 414–420. [CrossRef]

58. Srinivasan, P.; Gottam, R. Infrared Spectra: Useful technique to identify the conductivity level of emeraldine form of poly-aniline and indication of conductivity measurement either two or four probe technique. *Mat. Sci. Res. India* **2018**, *15*, 209–217. [CrossRef]

59. Botewad, S.N.; Pahurkar, V.G.; Muley, G.G. Fabrication and evaluation of evanescent wave absorption based polyani-line-cladding modified fiber optic urea biosensor. *Opt. Fiber Technol.* **2018**, *40*, 8–12. [CrossRef]

60. Wang, S.; Zhou, Y.; Liu, Y.; Wang, L.; Gao, C. Enhanced thermoelectric properties of polyaniline/polypyrrole/carbon nano-tube ternary composites by treatment with a secondary dopant using ferric chloride. *J. Mater. Chem. C* **2020**, *8*, 528–535. [CrossRef]
61. Su, N. Improving Electrical Conductivity, Thermal Stability, and Solubility of Polyaniline-Polypyrrole Nanocomposite by Doping with Anionic Spherical Polyelectrolyte Brushes. *Nanoscale Res. Lett.* **2015**, *10*, 1–9. [CrossRef]

Microfiltration Membranes Modified with Composition of Titanium Oxide and Silver Oxide by Magnetron Sputtering

Joanna Kacprzyńska-Gołacka [1],[*] , Monika Łożyńska [1], Wioletta Barszcz [1], Sylwia Sowa [1] , Piotr Wieciński [2] and Ewa Woskowicz [1]

[1] Łukasiewicz Research Networks—Institute for Sustainable Technology, 6/10 Pułaskiego St., 26-600 Radom, Poland; monika.lozynska@itee.lukasiewicz.gov.pl (M.Ł.); wioletta.barszcz@itee.lukasiewicz.gov.pl (W.B.); sylwia.sowa@itee.lukasiewicz.gov.pl (S.S.); ewa.woskowicz@itee.lukasiewicz.gov.pl (E.W.)
[2] Faculty of Materials Science and Engineering, Warsaw University of Technology, 141 Woloska St., 02-507 Warsaw, Poland; piotr.wiecinski@gmail.com
[*] Correspondence: joanna.kacprzynska-golacka@itee.lukasiewicz.gov.pl; Tel./Fax: +48-48-364-93-32

Abstract: In this work, the authors present the possibility of modification of polymer membranes by TiO_2 + AgO coating created by the magnetron sputtering method. The two-component TiO_2 + AgO coating can improve and shape new functional properties such as bactericidal and photocatalytic properties. The influence of magnetron power changes on the structure of the membrane was investigated as well. The structure and elemental composition of TiO_2 + AgO coatings were analyzed using SEM and EDS technique. All deposited coatings caused a total inhibition of the growth of two investigated colonies of *Escherichia coli* and *Bacillus subtilis* on the surface. The photocatalytic properties for membranes covered with oxide coatings were tested under UV irradiation and visible light. The filtration result show that polymer membranes covered with two-component TiO_2 + AgO coatings have a permeate flux similar to the non-coated membranes.

Keywords: polyamide membranes; surface modification; magnetron sputtering; TiO_2 + AgO coatings; low-pressure plasma; plasma treatment

1. Introduction

Microfiltration (MF) processes conducted with polymer membranes play an increasingly important role in many areas of the industry [1,2]. Due to their advantages, such as simplicity and application flexibility, these techniques are used in a variety of technological processes. However, membrane filtration processes also have disadvantages. The specificity of this process creates good conditions for the formation and deposition of biofilm on the active surfaces of membranes (biofouling). This requires membranes to be cleaned or replaced more frequently leading to a reduction in filtration efficiency and an increase in filtration costs [3–5]. Membranes made from polymers in many cases can be easily exposed to biofouling [6]. Microbial biofilm can form in both cases: living or non-living surfaces and are prevalent in natural, industrial and hospital settings [7]. The deposition of components from the feed solution and the growth of bacteria on the surface and inside the pores of the membrane causes malfunctions of devices or the increase in material and energy consumption [8,9].

Previous results evidenced an efficient modification of polymeric membrane surface by magnetron sputtering of metal oxide coatings that have the potential to prevent biofilm growth on the surface of the membranes [10,11]. This technology enables the production of thin coatings on the surface of the membrane providing various functional properties, which can improve the efficiency of membrane filtration and reduce the operating costs. The most extensively studied new material solutions (including membranes) concern hydrophilic and self-cleaning properties, which are based on metal oxides e.g., TiO_2 [12–14].

These coating are non-toxic and characterized by high thermal and chemical stability and resistance to unfavorable environmental factors. Photocatalytic properties also determine the wide area of application for TiO_2 as a self-cleaning coatings enabling the degradation of organic and inorganic compounds. In addition, these types of coating are characterized by a low water contact angle [15]. Nevertheless, the TiO_2 coating itself shows bactericidal activity only in the presence of UV radiation [16,17]. The state of the art shows that doping the TiO_2 coating with various metals, such as Cu, Zn, Cr or Ag, can contribute to the improvement of its functional properties [18–21]. As observed in our previous work, the best solution is to dope titanium oxide (TiO_2) with silver oxide (AgO), mainly due to the strong bactericidal activity of this material. The work carried out by the authors showed, that by using AgO coating for the modification of polymer membranes resulted in a 100% reduction of bacteria on its surface [11]. Moreover, it has been proved that the Ag doping expands the light absorption of TiO_2 in the visible light region [22–24]. It should contribute to the improvement of the efficiency of the degradation of organic and inorganic compounds on the membrane surface.

The study investigated how changes in the technological parameters of the TiO_2 + AgO coating deposition process influence the antibacterial effect as well as the structure and filtration efficiency of membranes. The application of magnetron sputtering technology is an innovative method, which generates functional thin films on the surface of the membrane. Herein, the authors have shown the possibility of using the magnetron sputtering technique to deposit of TiO_2 + AgO coatings on the surface of polymer microfiltration membranes in order to obtain antibacterial and photocatalytic properties. The influence of magnetron power changes on the structure of the membrane was also investigated. Structure and morphology of native and modified membranes were characterized. The bactericidal and photocatalytic properties of modified membranes, while retaining their filtration properties were confirmed as well.

2. Materials and Methods

2.1. Coatings Deposition

The TiO_2 + AgO coatings were deposited by reactive magnetron co-sputtering technology (MS-PVD) using a Standard 3 device produced by Ł-ITeE (Radom, Poland). The device was equipped with a two magnetron plasma sources located on the same wall in the chamber. Titanium and silver targets were used at the same time of the deposition process. The purity of both targets was 99.99%. The targets diameter was about 100 mm and the distance between the sample and the targets was 200 mm. The coatings were deposited with a reactive gas atmosphere composed of a mixture of 10% oxygen (99.9999% purity) and 90% argon (99.9999% purity). The TiO_2 + AgO coatings were prepared without the negative potential substrate polarization. The power of Ti magnetron source was variable in the range 650–1000 W. The power of Ag magnetron source was variable in the range 2580 W. The time of the MS-PVD process was 30 s.

2.2. Structure and Elemental Composition Characterization

The Hitachi Su-8000 scanning electron microscope (SEM; Tokyo, Japan) equipped with an electron gun with cold field emission was using for structure characterization of prepared coatings. The very good resolution with a relatively low beam current in this type of electron source is beneficial for observing materials sensitive to the electron beam, such as the analyzed membranes. The secondary electron signal (SE) was used for material observation but there was not deposited a conductive layer on the sample. The elemental composition of the tested material was determined by the EDX method.

2.3. Bactericidal Properties

Antibacterial properties of membranes modified with TiO_2 + AgO were examined for microorganisms that were representative of Gram-negative (*Escherichia coli*) and Gram-positive (*Bacillus subtilis*) bacteria. Before microbiological tests, the membranes were

sterilized with a UV-C lamp for t = 30 min. Microbiological tests were carried out using a vacuum filtration kit. An inoculum of the used bacteria was prepared in a saline buffer (KH_2PO_4, Chempur) from a 24-hour culture at a concentration of 1.5–3.0 * 10^5 CFU/cm^3. The obtained suspension was further diluted using the serial dilution method to achieve a countable number of colonies on the membranes. From the prepared dilutions, 0.04 cm^3 (for *Escherichia coli*) and 0.1 cm^3 (for *Bacillus subtilis*) of the suspension were taken and transferred to a sterile 1000 cm^3 phosphate buffer. Then 10 cm^3 of such prepared suspension, which was prepared in this way was filtered through the membranes under a pressure of 500 mbar using vacuum filtration kit. The membranes were placed on the plates containing Luria Bertani (LB, VWR) growth medium and incubated at 37 °C for 24 h. After this time, the bacterial colonies that had grown on the membranes were counted. The reference sample in the research was the unmodified membrane. Results of antibacterial activity of the membranes were expressed as the percentage (%) reduction in the colony (CFU) counts.

2.4. Photocatalytic Properties

Photocatalytic properties of the membranes were evaluated on the degree of methylene blue degradation (0.1% *v/v*, Science Company) under the UV and visible light. Polyamide membranes unmodified and modified with two-component TiO_2 + AgO coatings were placed in Petri dishes. A 20 cm^3 volume was applied to their surface. Both UV-A lamp and daylight were used to study the effect of the type of UV radiation on the photocatalytic properties. After 8, 24, 48 and 72 h of UV and visible light irradiation, spectrophotometric measurements were made at 665 nm using a Hach DR 6000 spectrophotometer (Hach Company, Loveland, CO, USA). The tests were repeated three times for each tested sample. In order to investigate the effect of doping TiO_2 coatings with AgO on the photocatalytic properties in visible light, one-component coatings were also tested according to the same methodology.

2.5. Filtration Properties

The permeate flux was determined by measuring the time required to filter deionized water (100 cm^3) through the membrane (8 cm^2) under defined transmembrane pressure (500 mbar). The deionized water was characterized by the conductivity and pH of 5.3 μS/cm and 6.5, respectively. For this purpose, the laboratory "dead-end" filtration set-up was used. The filtration properties of the membranes were evaluated based on the permeate flux (Equation (1)).

A "dead-end" vacuum system, operating at a pressure of 0.5 bar, was used to determine the permeate flux. The permeate flux (J_p) was calculated from the time (t) taken to filter 100 cm^3 (V_p) of deionized water through a membrane with an area of 8 cm^2 (A) in accordance with Equation (1).

$$J_P = \frac{V_p}{A \cdot t} \tag{1}$$

3. Results and Discussion

3.1. Structure and Elemental Composition Characterization

The SEM images of the membranes coated with TiO_2 + AgO were prepared for a different power of the magnetron source (P_{M-Ag} = 25 W, 50 W and 80 W, P_{M-Ti} = 650 W and 1000 W) used for modification were shown in Figures 1 and 2. The SEM analysis of the structure of membrane with TiO_2 + AgO coatings showed the comparison of the differences to non-coated membrane presented in Figure 3.
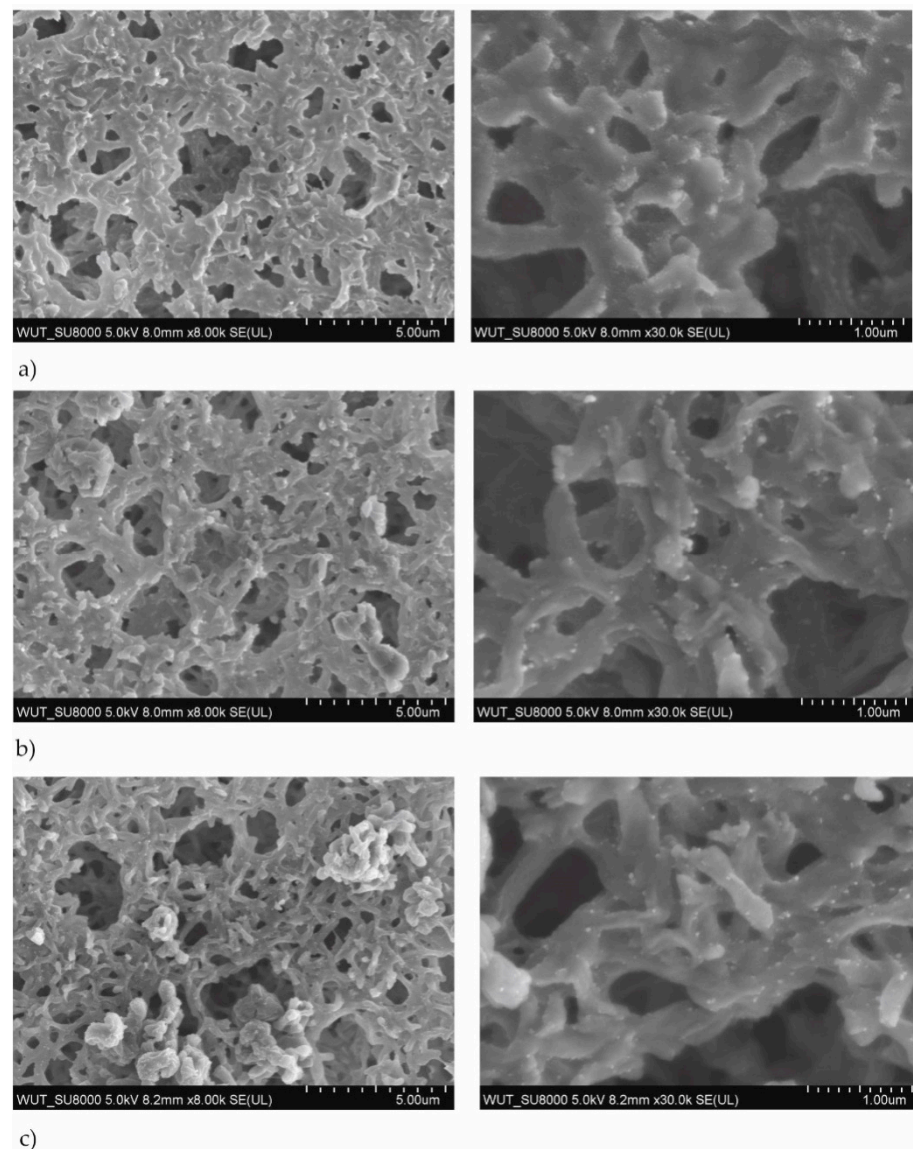
Figure 1. SEM images of the membranes with TiO_2 + AgO coatings deposited at the different magnetron powers P_M (**a**) P_{M-Ag} = 80 W, P_{M-Ti} = 1000 W, t = 30 s, (**b**) P_{M-Ag} = 50 W, P_{M-Ti} = 1000 W, t = 30 s, (**c**) P_{MAg} = 25 W, P_{M-Ti} = 1000 W, t = 30 s.

The SEM analysis showed that the structure of the membrane's surface changed depending on the magnetron power. In the case of coatings created with the magnetron power P_{MTi} = 1000 W (Figure 1), the multiple bright AgO particles smaller than 100 nm were observed in their structure. The proportion of these particles decreased as the power P_{M-Ag} of the magnetron decreased. In the case of coatings created with smaller magnetron power P_{M-Ti} = 650 W (Figure 2), much fewer light particles were observed on the surface. The particles were localized mainly inside the pores, as presented in Figure 3. The correlation between the magnetron power and the number of AgO particles on the membrane surface has remained unclear.

The elemental composition analysis included the assessment of the magnetron power effect on the percentage content for individual metallic elements in the elemental composition of the coating. The obtained results showed, that the TiO_2 + AgO coatings (Figure 4) created at the higher magnetron power P_{MTi} = 1000 W were characterized by a higher content of Ti compared to the coatings deposited at the power of P_{M-Ti} = 650 W. The increase of the magnetron power P_{M-Ag} resulted in the increase of Ag content in the elemental composition of the tested coatings.
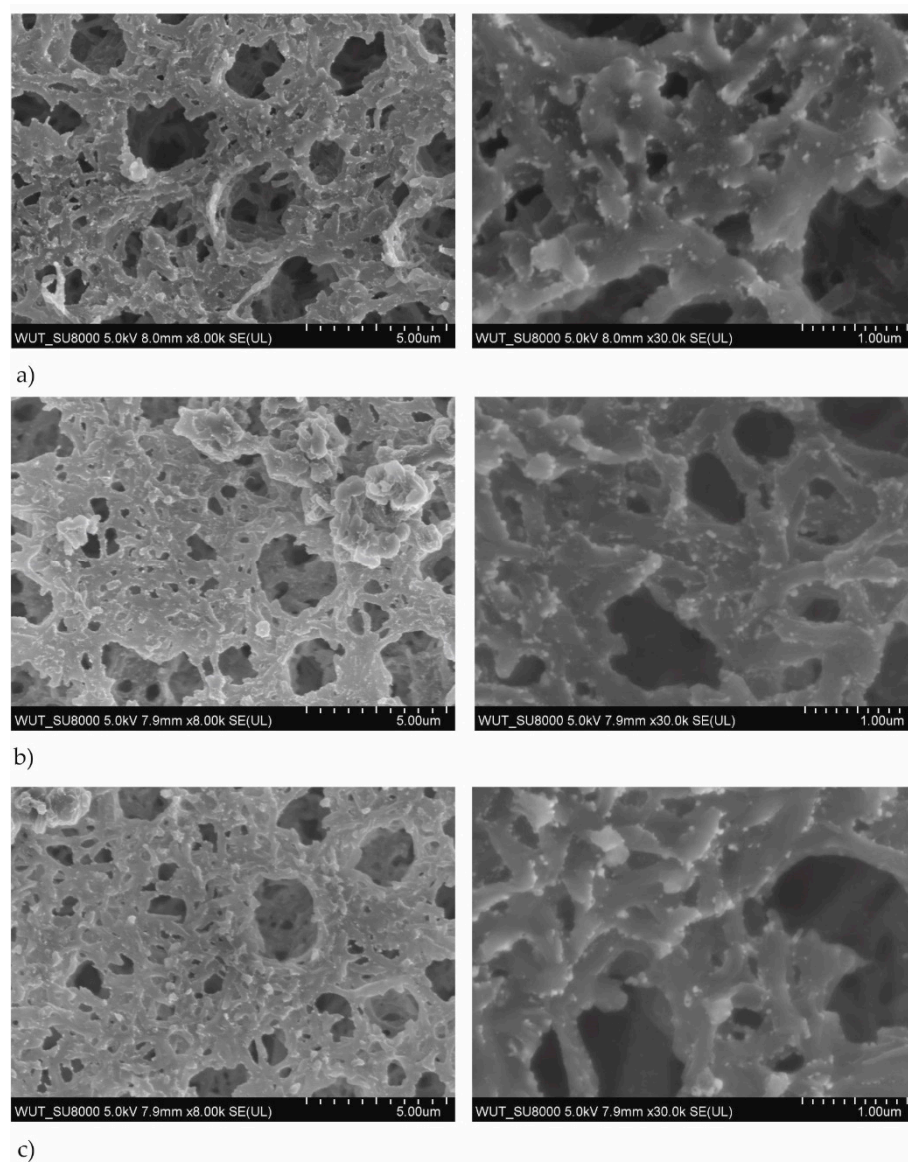
Figure 2. SEM images of the membranes with TiO_2 + AgO coatings deposited at the different magnetron powers P_M (**a**) P_{M-Ag} = 80 W, P_{M-Ti} = 650 W, t = 30 s, (**b**) P_{M-Ag} = 50 W, P_{M-Ti} = 650 W, t = 30 s, (**c**) P_{MAg} = 25 W, P_{M-Ti} = 650 W, t = 30 s.
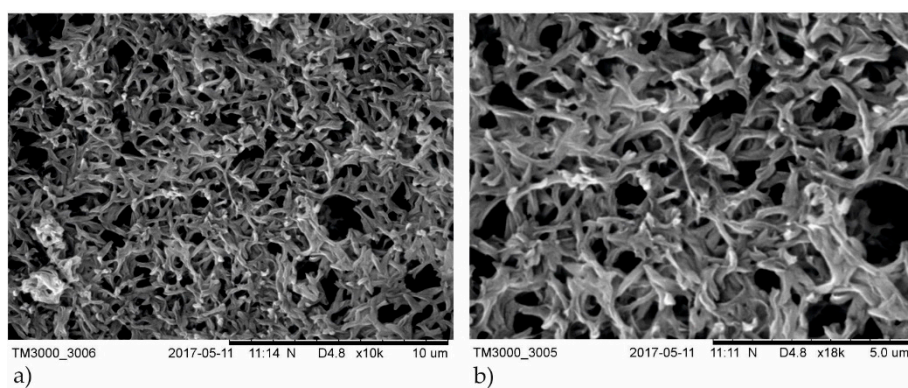
Figure 3. SEM images of the non-coated membranes: (**a**) magnification $10,000\times$, (**b**) magnification $18,000\times$.
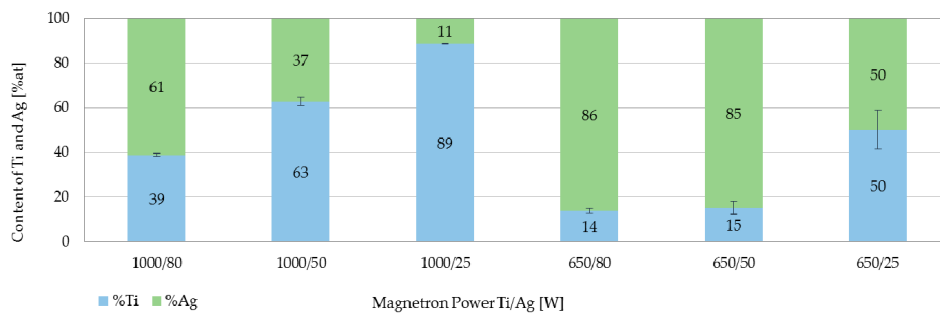
Figure 4. Elemental composition of TiO$_2$ + AgO coatings deposited at different magnetron powers.

3.2. Antibacterial Properties

The antibacterial activity of membranes modified by TiO$_2$ + AgO coatings was specified against two representative bacteria such as *Escherichia coli (E.coli)* and *Bacillus subtilis (B.subtilis)*, respectively. The coatings generated with the following power of magnetron source (P$_{M\text{-}Ag}$ = 25 W, 50 W and 80 W, P$_{MTi}$ = 650 W and 1000 W) lead to the complete growth inhibition of the colonies of *E.coli* and *B.subtilis* on the membranes which is shown in Figure 5. Both bacteria showed no growth on the agar plates after incubation.
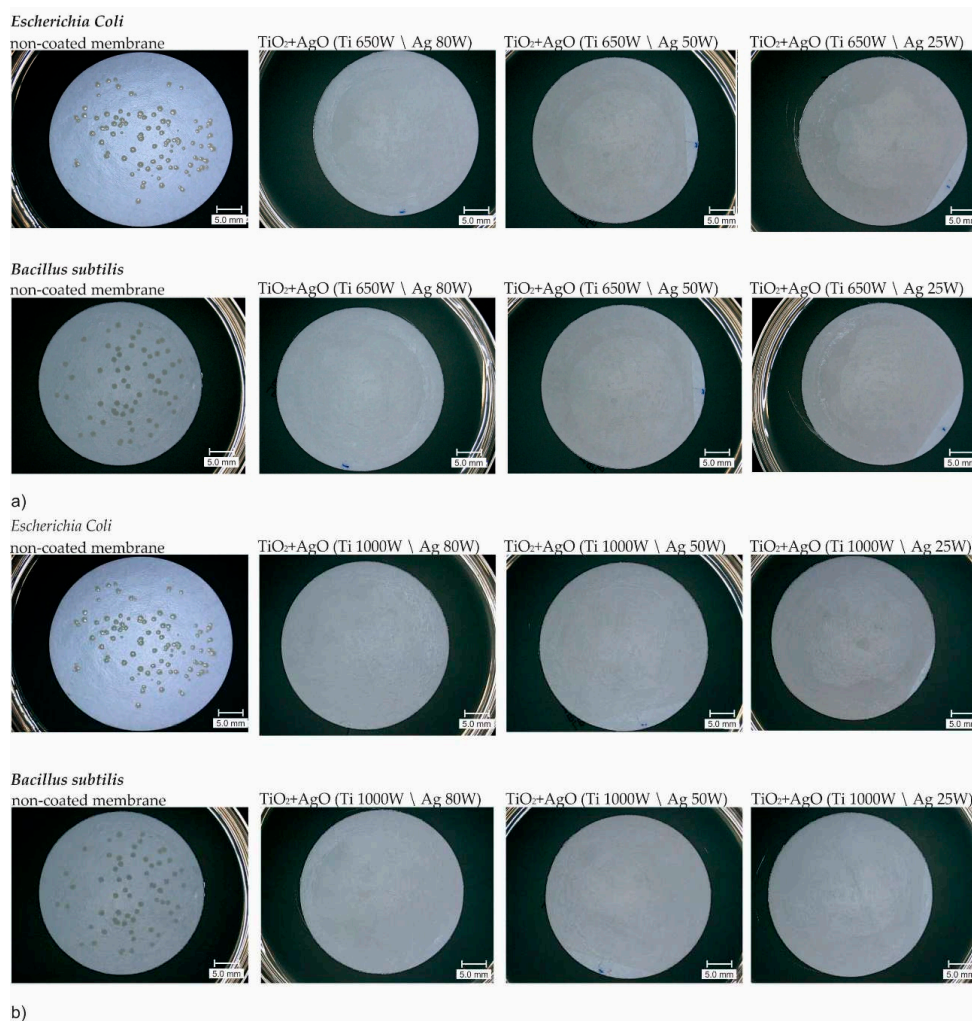
Figure 5. 3D microscope images of TiO$_2$ + AgO coated membranes after filtration of bacterial suspensions: (**a**) TiO$_2$ + AgO modified membranes (P$_{M\text{-}Ag}$ = 25 W, 50 W and 80 W; P$_{M\text{-}Ti}$ = 650 W); (**b**) TiO$_2$ + AgO modified membranes (P$_{M\text{-}Ag}$ = 25 W, 50 W and 80 W; P$_{M\text{-}Ti}$ = 1000 W).

These results were similar to those obtained in the previous study, where the AgO coated membranes with different power of magnetron source caused total growth inhibition of *E. coli* and *B. subtilis* [11]. The results of reduction (%) in CFU counts are presented in Figure 6. For each TiO$_2$ + AgO modified membranes the antibacterial activity of the membrane amounted to 100% compared to the no-coated membrane.
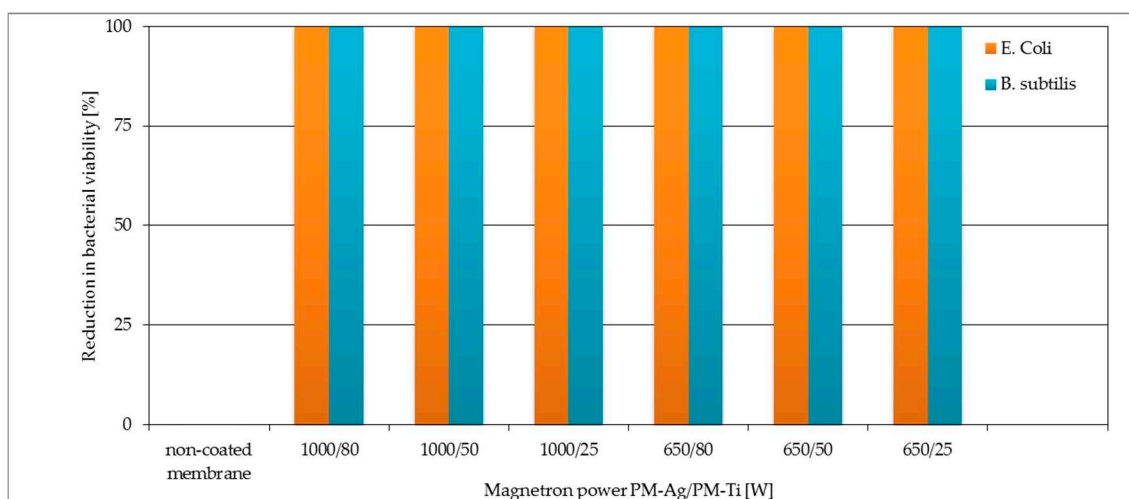
Figure 6. Reduction [%] CFU counts of *Escherichia coli* and *Bacillus subtilis* on no-coated membrane and membranes covered with TiO$_2$ + AgO coating deposited during 30 s at different magnetron powers P$_{M\text{-}Ti}$ and P$_{M\text{-}Ag}$.

The obtained results may be associated with the elemental composition of the coatings, which created with MS-PVD technique. The deposited coatings on the polymer membrane were in the form of a solid titanium oxide matrix where Ag/AgO nanoparticles were embedded, (Figures 2 and 3). The bactericidal properties of the TiO$_2$ + AgO composite coating were probably related to the presence of silver/silver oxide (Ag/AgO) nanoparticles in this coatings. Research by Thukkaram et al. confirmed that the enrichment of the titanium oxide coating with silver nanoparticles increases the antimicrobial activity against Gram-positive and Gram-negative bacteria [25]. Navabpour et al. proved that TiO$_2$ + AgO coatings formed by using the reactive magnetron sputtering have stronger bactericidal properties than TiO$_2$ coatings produced in the same ways [26]. The strong bactericidal properties of silver/silver oxide (Ag/AgO) nanoparticles were confirmed in many studies [27–29]. Silver and silver oxide nanoparticles have an affinity for functional groups included in cellular proteins and nucleic acids. The binding silver ions in the cytoplasmic membrane of the bacterial cell cause their accumulation and its destabilization and increase in membrane permeability. As a consequence, this leads to the uncontrolled transport of protons and depolarization of cell membrane, and death of microorganisms [30]. The antibacterial activity of silver and silver oxide nanoparticles can be associated with free radicals, which they generated. The free radicals cause oxidative stress in bacterial cells. Li et al. compared the relationship between the antimicrobial activity of nanoparticles of various metal oxides and oxidative stress. The viability of *E.coli* cells in solutions of metal oxide nanoparticles under the influence of UV radiation was reduced [31].

3.3. Photocatalytic Properties

The membranes with two-component coatings were subjected to photocatalytic tests. The results obtained for TiO$_2$ + AgO coatings after irradiation with a UV lamp and daylight are presented in Figures 7 and 8, respectively.
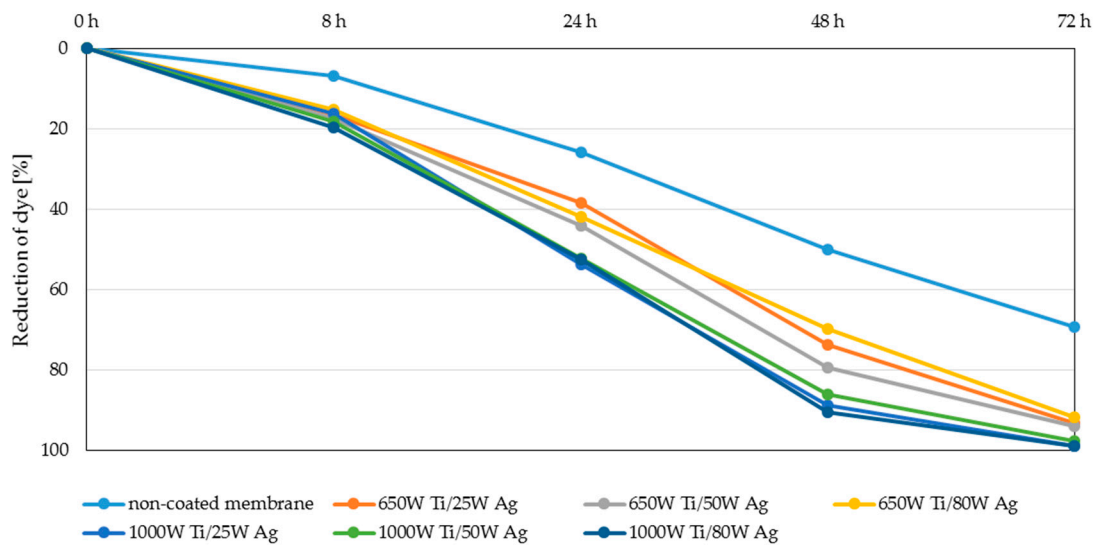
Figure 7. Reduction of the MB dye under the influence of UV-A light.
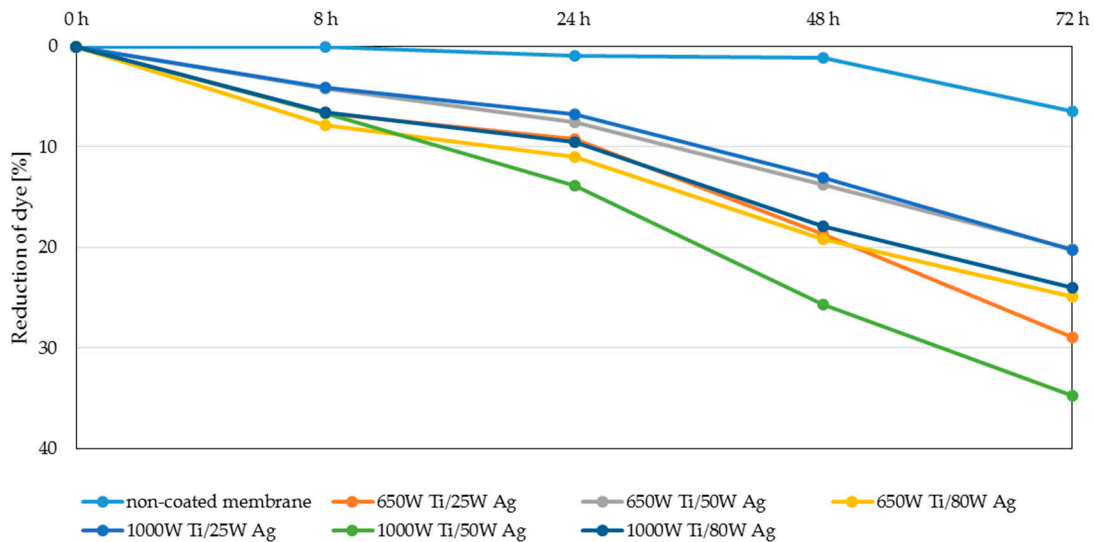
Figure 8. Reduction of the MB dye under the influence of visible light.

As shown in Figure 7 the membranes with TiO_2 + AgO coatings deposited with the magnetron power P_{M-Ti} = 1000 W showed better photocatalytic properties after irradiation UV lamp than the coatings deposited with the magnetron power P_{M-Ti} = 650 W (Figure 7). For all types of coatings with P_{M-Ti} = 1000 W over 90% reduction of the dye was achieved after 72 h. The literature and own research data show that titanium oxide is a substantial photocatalytic factor in UV light [32,33]. The doping of the coatings with silver oxide (AgO) for bactericidal and photocatalytic properties in visible light does not negatively influence photocatalytic properties under UV light.

The highest degree of dye reduction was achieved for membranes with magnetron power 1000 W Ti/50 W Ag and coatings with magnetron power 650 W Ti/25 W Ag (35 and 28% respectively) can be observed when two-component coatings are exposed to daylight. The achieved degree of dye reduction was much lower than that of UV irradiation. This is due to the fact that both TiO_2 and AgO do not have photocatalytic properties in visible light. Normally, with light irradiation UV for titanium oxide, an electron from the valence band can be promoted to the conduction band, leaving an electron. This deficiency is known as a hole in the valence band and is causing an excess of negative charge in the conduction band. These generated species can participate in surface redox reactions and generate

secondary reactive oxygen species. However, the excited reactive electron is unstable, and it can return to the valence band, to be stable again, provoking recombination. Studies revealed, that doping of silver improves the photocatalytic activity of TiO_2 inducing an efficient surface plasmon resonance effect under sunlight. That prevents the recombination of $e^- $-$h^+$ pairs, which is responsible for the decreasing process of the photocatalytic activity of TiO_2 [34–38]. In order to assess the effect of doping titanium oxide coating with silver oxide, additional experiments were conducted in visible light for one-component coatings. The results are presented in Figure 9.
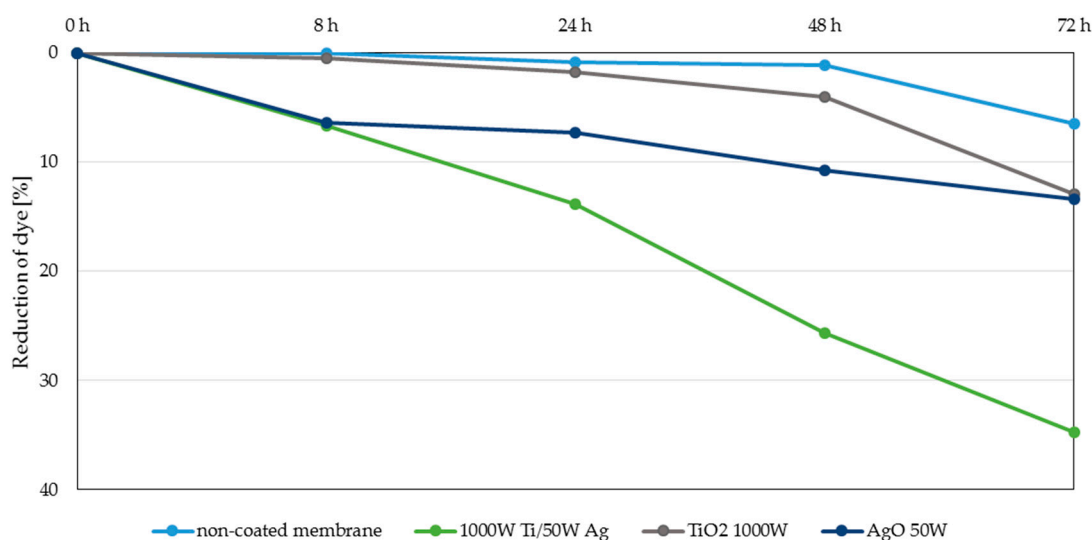
Figure 9. Reduction of the MB dye under the influence of visible light.

The obtained results showed that the tested one-component TiO_2 coating and AgO coatings have lower photocatalytic activity and yielded an approx. 10% reduction of the dye after 72 h. Doping the titanium oxide coating with silver oxide caused an even more than threefold increase in the photocatalytic properties of these membranes. The catalytic properties of such prepared membranes are influenced by many factors, including the quantity and size of the silver particles [35,36], which was confirmed during this study. In the case of the tested two-component coatings, the highest dye reduction was obtained for coatings with a silver content between 50 and 60% (Figure 2). The decomposition of MB dye in visible light was not as intense for the coating with the highest Ag content (90% for 1000 W Ti/80 W Ag coatings) or the lowest one (about 15% for 650 W Ti/50 W Ag and 650 W Ti/80 W coatings).

3.4. Filtration Properties and Stability of the Coatings

The results of the filtration and transport properties analysis for polymer membranes coated with two-component TiO_2 + AgO coatings showed an inconsiderable decrease in the permeate flux compared to the native membrane (Figures 10 and 11). The highest (27%) decrease in the permeate flux compared to the native membrane was recorded (Figure 10) in the case of the membrane with the coating deposited at the magnetron powers $P_{M-Ti} = 650$ W and $P_{M-Ag} = 80$ W. Reducing the power of the P_{M-Ag} magnetron resulted in an improvement of the permeate flux. After increasing the magnetron power to $P_{M-Ti} = 1000$ W, a significant improvement in the filtration properties was observed. The permeate flux was comparable to the non-coated membrane (Figure 11) for the membrane with the coating deposited at the magnetron powers $P_{M-Ag} = 25$ W and $P_{MAg} = 50$ W.
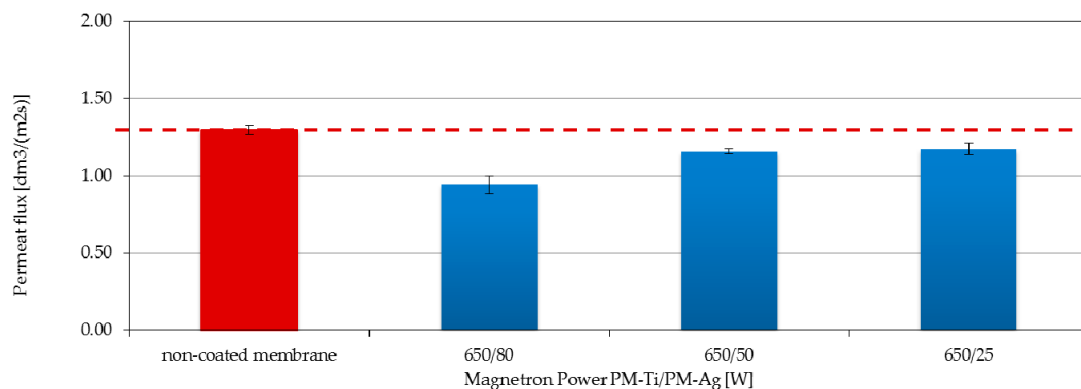
Figure 10. Effect of the P_{M-Ag} magnetron power on the permeate flux of membranes covered with TiO_2 + AgO coatings deposited at a constant power P_{M-Ti} = 650 W.
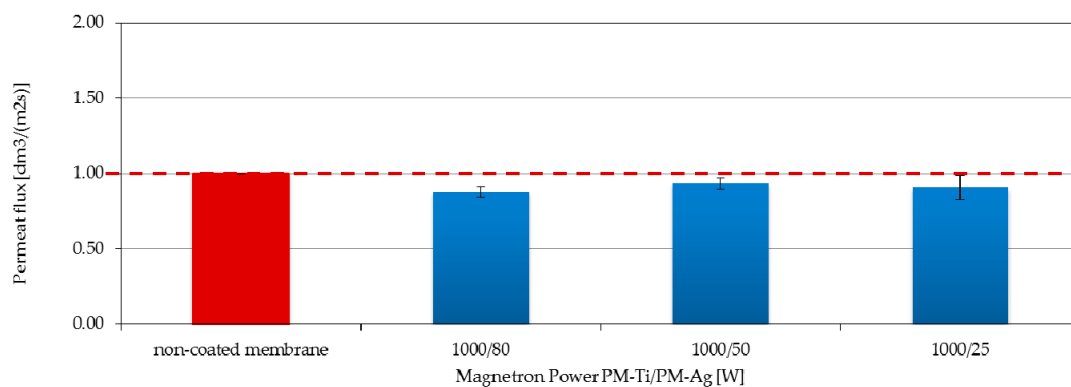
Figure 11. Effect of the P_{M-Ag} magnetron power on the permeate flux of membranes covered with TiO_2 + AgO coatings deposited at a constant power P_{M-Ti} = 1000 W.

The increasing of the magnetron power P_{M-Ti} caused the increase of the proportion of hydrophilic TiO_2 [15] in the coating structure and it can improve the hydrophilic properties of the whole coating, and consequently also the membrane surface. As a consequence, the filtration performance of the membrane will be most likely improved. The opposite situation was observed when the power P_{M-Ag} was increased. It caused an increase in the proportion of hydrophobic AgO in the coating structure. This can lead to a reduction in the hydrophilic properties of the membrane surface, which results in a decrease in its filtration properties.

4. Conclusions

In this study, the importance of an interdisciplinary approach was highlighted towards novel trends in the development of materials based on polymer membranes. Using the MS-PVD method can provide new functional properties for polymeric membranes. In the article, the different magnetron powers of Ti and Ag were used to create two-component coatings with new, common properties. Based on the surface analysis of the membrane the presence of AgO nanoparticles were observed. The size of these particles was smaller than 100 nm for magnetron power P_{M-Ti} = 1000 W. Research has shown that the magnetron power has effects on the percentage content for individual metallic elemental composition. The presence of AgO nanoparticles was related to the island nature of the AgO coating grown on a polymer substrate [11]. The antibacterial properties of TiO_2 + AgO coatings were determined for the two following bacteria: *Escherichia coli* and *Bacillus subtilis*. The TiO_2 + AgO coatings deposited at different magnetron powers resulted in complete reduction of growth of two representative bacteria. It was related to the presence of Ag/AgO nanoparticles in the coating structure, which exhibits strong antibacterial properties. All the tested membranes with TiO_2 + AgO coatings indicated very good photocatalytic properties

when irradiated with UV. The doping of TiO_2 coating with AgO led to an increase in photocatalytic properties in visible light compared to the one-component coating on the polymeric membranes. At the same time, the authors reported no negative influence of the coating on the filtration properties of the membrane. In the case of the membrane with the TiO_2 + AgO coating deposited on the membrane at the magnetron powers, P_{M-Ti} = 1000 W the permeate flux was similar to the no-coated membrane. The achieved results are very promising for polymeric material science, giving a prospect for potential application of thin film TiO_2 + AgO coatings onto the surface of polyamide membranes.

References

1. Kołtuniewicz, A.B.; Drioli, E. *Membranes in Clean Technologies. Theory and Practice, Vol. 1–2*; WILEY-VCH Verlag GmbH & Co: Weinheim, Germany, 2008.
2. Ursino, C.; Castro-Muñoz, R.; Drioli, E.; Gzara, L.; Albeirutty, M.H.; Figoli, A. Progress of Nanocomposite Membranes for Water Treatment. *Membranes* **2018**, *8*, 18. [CrossRef] [PubMed]
3. Nguyen, T.; Roddick, F.A.; Fan, L. Biofouling of Water Treatment Membranes: A Review of the Underlying Causes, Monitoring Techniques and Control Measures. *Membranes* **2012**, *2*, 804–840. [CrossRef] [PubMed]
4. Subramani, A.; Hoek, E.M.V. Direct observation of initial microbial deposition onto reverse osmosis and nanofiltration membranes. *J. Membr. Sci.* **2008**, *319*, 111–125. [CrossRef]
5. Boussu, K.; Belpaire, A.; Volodin, A.; van Haesendonck, C.; van der Meeren, P.; Vandecasteele, C.; van der Bruggen, B. Influence of membrane and colloid characteristics on fouling of nanofiltration membranes. *J. Membr. Sci.* **2007**, *289*, 220–230. [CrossRef]
6. Najjar, A.; Sabri, S.; Al-Gaashani, R.; Atieh, M.A.; Kochkodan, V. Antibiofouling Performance by Polyethersulfone Membranes Cast with Oxidized Multiwalled Carbon Nanotubes and Arabic Gum. *Membranes* **2019**, *9*, 32. [CrossRef] [PubMed]
7. Tilahun, A.; Haddis, S.; Hadush, A.T.T. Review on Biofilm and Microbial Adhesion. *Int. J. Microbiol. Res.* **2016**, *3*, 63–73. [CrossRef]
8. Garrett, T.R.; Bhakoo, M.; Zhang, Z. Bacterial adhesion and biofilms on surfaces. *Progr. Nat. Sci.* **2008**, *18*, 1049–1056. [CrossRef]
9. Vanysacker, L.; Denis, C.; Declerck, P.; Piasecka, A.; Vankelecom, I.F.J. Microbial Adhesion and Biofilm Formation on Microfiltration Membranes: A Detailed Characterization Using Model Organisms with Increasing Complexity. *BioMed Res. Int.* **2013**, *2013*, 470867. [CrossRef]
10. Kacprzyńska-Gołacka, J.; Kowalik-Klimczak, A.; Skowroński, J.; Rajewska, P.; Wieciński, P.; Smolik, J. Możliwości wykorzystania plazmowych technik inżynierii powierzchni do modyfikacji membran polimerowych. *Polimery* **2018**, *5*, 353–361.
11. Kacprzyńska-Gołacka, J.; Kowalik-Klimczak, A.; Woskowicz, E.; Wieciński, P.; Łożyńska, M.; Sowa, S.; Barszcz, W.; Kaźmierczak, B. Microfiltration Membranes Modified with Silver Oxide by Plasma Treatment. *Membranes* **2020**, *10*, 133. [CrossRef]
12. Yadav, H.M.; Kim, J.; Pawar, S.H. Developments in photocatalytic antibacterial activity of nano TiO_2: A review. *Korean J. Chem. Eng.* **2016**, *33*, 1989–1998. [CrossRef]
13. Vatanpoura, V.; Madaenia, S.S.; Khataeeb, A.R.; Salehia, E.; Zinadinia, S.; Monfareda, H.A. TiO_2 embedded mixed matrix PES nanocomposite membranes: Influence of different sizes and types of nanoparticles on antifouling and performance. *Desalination* **2012**, *292*, 19–29. [CrossRef]
14. Wafi, A.; Szabó-Bárdos, E.; Horváth, O.; Pósfai, M.; Makó, É.; Juzsakova, T.; Fónagy, O. The Photocatalytic and Antibacterial Performance of Nitrogen-Doped TiO2: Surface-Structure Dependence and Silver-Deposition Effect. *Nanomaterials* **2020**, *10*, 2261. [CrossRef] [PubMed]
15. Kacprzyńska-Gołacka, J.; Osuch-Słomka, E.; Wieciński, P.; Garbacz, H.; Skowroński, J.; Kowalik-Klimczak, A.; Smolik, J.; Mazurkiewicz, A. The impact of working gas atmosphere on phase composition and microstructure of TiO_2 coating prepared by reactive magnetron sputtering. In Proceedings of the 26th International Conference on Metallurgy and Materials, Brno, Czech Republic, 24–26 May 2017.

16. Kacprzyńska-Gołacka, J.; Sowa, S.; Kowalik-Klimczak, A.; Rajewska, P.; Stanisławek, E.; Wieciński, P. The Conception and Design of Polymeric Membranes Modification Technology Using Surface Engineering Techniques. In Proceedings of the 9th International Conference Nanomaterials: Applications & Properties (NAP), Odesa, Ukraine, 15–20 September 2019; pp. 01TFC31-1–01TFC31-3. [CrossRef]

17. Alotaibi, A.M.; Williamson, B.A.D.; Sathasivam, S.; Kafizas, A.; Alqahtani, M.; Sotelo-Vazquez, C.; Buckeridge, J.; Wu, J.; Nair, S.P.; Scanlon, D.O.; et al. Enhanced Photocatalytic and Antibacterial Ability of Cu-Doped Anatase TiO$_2$ Thin Films: Theory and Experiment. *ACS Appl. Mater. Interfaces* **2020**, *12*, 15348–15361. [CrossRef]

18. He, X.; Zhang, G.; Wang, X.; Hang, R.; Huang, X.; Qin, L.; Tang, B.; Zhang, X. Biocompatibility, corrosion resistance and antibacterial activity of TiO$_2$/CuO coating on titanium. *Ceram. Int.* **2017**, *43*, 16185–16195. [CrossRef]

19. Sethi, D.; Sakthivel, R. ZnO/TiO$_2$ composites for photocatalytic inactivation of Escherichia coli. *J. Photochem. Photobiol. B Biol.* **2017**, *168*, 17–123. [CrossRef]

20. Wysocka, I.; Kowalska, E.; Trzciński, K.; Łapiński, M.; Nowaczyk, G.; Zielińska-Jurek, A. UV–Vis-induced degradation of phenol over magnetic photocatalysts modified with Pt, Pd, Cu and Au nanoparticles. *Nanomaterials* **2018**, *8*, 28. [CrossRef]

21. Harikishore, M.; Sandhyarani, M.; Venkateswarlu, K.; Nellaippan, T.A.; Rameshbabu, N. Effect of Ag Doping on Antibacterial and Photocatalytic Activity of Nanocrystalline TiO$_2$. *Procedia Mater. Sci.* **2014**, *6*, 557–566. [CrossRef]

22. Al Suliman, N.; Awada, C.; Alshoaibi, A.; Shaalan, N.M. Simple Preparation of Ceramic-Like Materials Based on 1D-Agx(x=0, 5, 10, 20, 40 mM)/TiO$_2$ Nanostructures and Their Photocatalysis Performance. *Crystals* **2020**, *10*, 1024. [CrossRef]

23. Komaraiah, D.; Radha, E.; Sivakumar, J.; Ramana Reddy, M.V.; Sayanna, R. Photoluminescence and photocatalytic activity of spin coated Ag+ doped anatase TiO$_2$ thin films. *Opt. Mater.* **2020**, *108*, 110401. [CrossRef]

24. Spilarewicz-Stanek, K.; Jakimińska, A.; Kisielewska, A.; Batory, D.; Piwoński, I. Understanding the Role of Silver Nanostructures and Graphene Oxide Applied as Surface Modification of TiO$_2$ in Photocatalytic Transformations of Rhodamine B under UV and Vis Irradiation. *Materials* **2020**, *13*, 4653. [CrossRef] [PubMed]

25. Thukkaram, M.; Cools, P.; Nikiforov, A.; Rigole, P.; Coenye, T.; Van Der Voort, P.; Du Laing, G.; Vercruysse, C.; Declercq, H.; Morent, R.; et al. Antibacterial activity of a porous silver doped TiO$_2$ coating on titanium substrates synthesized by plasma electrolytic oxidation. *Appl. Surf. Sci.* **2020**, *500*, 144–235. [CrossRef]

26. Navabpour, P.; Ostovarpour, S.; Hampshire, J.; Kelly, P.; Verran, J.; Cooke, K. The effect of process parameters on the structure, photocatalytic and self-cleaning properties of TiO$_2$ and Ag-TiO$_2$ coatings deposited using reactive magnetron sputtering. *Thin Solid Film* **2014**, *571*, 75–83. [CrossRef]

27. Le Ouay, B.; Stellaci, F. Antibacterial activity of silver nanoparticles: A surface science insight. *Nano Today* **2015**, *10*, 339–354. [CrossRef]

28. Sri Devi, P.; Vijayalakshmi, K.A. Analysis of antibacterial activity and cytotoxicity of silver oxide doped hydroxyapatite exposed to DC glow discharge plasma. *Mater. Today Proc.* **2020**, *24*, 3604–3608. [CrossRef]

29. Duffy, L.L.; Osmond-McLeod, M.J.; Judy, J.; King, T. Investigation into the antibacterial activity of silver, zinc oxide and copper oxide nanoparticles against poultry-relevant isolates of Salmonella and Campylobacter. *Food Control* **2018**, *92*, 293–300. [CrossRef]

30. Slavin, S.N.; Asnis, J.; Häfeli, U.O.; Bach, H. Metal nanoparticles: Understanding the mechanisms behind antibacterial activity. *J. Nanobiotechnol.* **2017**, *15*. [CrossRef]

31. Li, Y.; Zhang, W.; Niu, J.; Chen, Y. Mechanism of Photogenerated Reactive Oxygen Species and Correlation with the Antibacterial Properties of Engineered Metal-Oxide Nanoparticles. *ACS Nano* **2012**, *6*, 5164–5173. [CrossRef]

32. Albiter, E.; Valenzuela, M.A.; Alfaro, S.; Valverde-Aguilar, G.; Martinez-Pallares, F.M. Photocatalytic deposition of Ag nanoparticles on TiO$_2$: Metal precursor effect on the structural and photoactivity properties. *J. Saudi Chem. Soc.* **2015**, *19*, 563–573. [CrossRef]

33. Mogal, S.I.; Gandhi, V.G.; Mishra, M.; Tripathi, S.; Shripathi, T.; Joshi, P.A.; Shah, D.O. Single-Step Synthesis of Silver-Doped Titanium Dioxide: Influence of Silver on Structural, Textural, and Photocatalytic Properties. *Ind. Eng. Chem. Res.* **2014**, *53*, 5749–5758. [CrossRef]

34. Din, M.I.; Khalid, R.; Hussain, Z. Minireview: Silver-Doped Titanium Dioxide and Silver-Doped Zinc Oxide Photocatalysts. *Anal. Lett.* **2018**, *51*, 892–907. [CrossRef]

35. Glez, V.R.; Hernandez-Gordillo, L. Silver-Based Photocatalysts: A Special Class. In *American Jewish Year Book*; Springer: Cham, Switzerland, 2018; Chapter 8, pp. 221–239.

36. Kodom, T.; Rusen, E.; Calinescu, I.; Mocanu, A.; Somoghi, R.; Dinescu, A.; Diacon, A.; Boscornea, C. Silver Nanoparticles Influence on Photocatalytic Activity of Hybrid Materials Based on TiO$_2$ P$_{25}$. *J. Nanomater.* **2015**, *2015*, 210734. [CrossRef]

37. Seery, M.K.; George, R.; Floris, P.; Pillai, S.C. Silver doped titanium dioxide nanomaterials for enhanced visible light photocatalysis. *J. Photochem. Photobiol. A Chem.* **2007**, *189*, 258–263. [CrossRef]

38. Xu, J.; Xiao, X.; Ren, F.; Wu, W.; Dai, Z.; Cai, G.; Zhang, S.; Zhou, J.; Mei, F.; Jaing, C. Enhanced photocatalysis by coupling of anatase TiO$_2$ film to triangular Ag nanoparticle island. *Nanoscale Res. Lett.* **2012**, *7*, 239–245. [CrossRef]

Surface Modification of Polyamides by Gaseous Plasma—Review and Scientific Challenges

Gregor Primc [ID]

Department of Surface Engineering, Jozef Stefan Institute, Jamova Cesta 39, 1000 Ljubljana, Slovenia;
gregor.primc@ijs.si

Abstract: A review of the most significant scientific achievements in the field of surface modification of polyamides by non-equilibrium plasma treatments is presented. Most authors employed atmospheric pressure discharges and reported improved wettability. The super-hydrophilic surface finish was only achieved using a low-pressure plasma reactor and prolonged treatment time, enabling both the nanostructuring and functionalization with polar functional groups. The average increase of the oxygen concentration as probed by XPS was about 10 at%, while the changes in nitrogen concentrations were marginal in almost all cases. The final static water contact angle decreased with the increasing treatment time, and the oxygen concentration decreased with the increasing discharge power. The need for plasma characterization for the interpretation of experimental results is stressed.

Keywords: polyamide; gaseous plasma; water contact angle; XPS

1. Introduction

Polyamides (PA) are thermoplastics of good thermal stability, high melting point, excellent durability and mechanical properties, and low permeability for oxygen. They are used as engineering plastics in the automotive industry, electrical industry and electronics, packaging, and synthesizing ropes, textiles and membranes. Polyamide is among the most promising materials for vehicle weight reduction by replacing metal parts in the automotive industry due to the ease of mass production and molding. The high demand from the automotive industry is currently the primary driving force of the global polyamide market. Despite its good dyeability, the printability or ability to adhere to other materials is limited due to the relatively poor wettability. Similar to most other polymers, the static contact angle of a water droplet is somehow below 90° for flat surfaces, therefore, the polar coatings do not adhere sufficiently. The surface properties should be altered to ensure better wettability. A typical method for improving the wettability of polymers is the treatment with non-equilibrium gaseous plasma. A product made from or containing polyamide is exposed to reactive gaseous particles and radiation from gaseous plasma. Depending on discharge parameters, the plasma contains various reactive gaseous species, as well as radiation in a broad range from visible to deep ultraviolet (UV) range. Furthermore, the polymer is also subject to bombardment with positively charged ions of kinetic energy from a few eV to several 100 or even 1000 eV, depending on the type of discharge used for sustaining gaseous plasma. The reactive species interact chemically with the surface of the polymer. The bombardment with ions adds to the intensity of chemical reactions, and the UV radiation causes bond scission on the surface and the sub-surface layer. The surface finish obtained upon the plasma treatment is the consequence of all these effects. Different authors reported plasma treatments using various experimental setups, and the results scatter significantly. This paper aims to review recent advances in the plasma treatment of polyamides, drawing correlations between the treatment parameters and surface finish, as well as the identification of future research that should be performed to achieve the desired surface finish in a highly predictable and repeatable manner.

2. Literature Survey

The surface modification of polymers is usually studied using smooth and flat samples. Such samples are useful due to the peculiarities of the most common technique for monitoring the evolution of surface functional groups—X-ray photoelectron spectroscopy (XPS). Namely, the XPS spectra are best interpreted if acquired from smooth surfaces. Mandolfino et al. [1] performed systematic research on the plasma activation of PA6 and PA6.6 using a low-pressure gaseous plasma. The plasma reactor was powered with a radiofrequency (RF) supply of adjustable powers up to about 200 W. The treatment was performed with a plasma sustained in air, argon, oxygen, and a mixture of 50% argon and 50% oxygen. Samples of polymer sheets were carefully cleaned with acetone to remove any organic surface contaminants before the plasma treatments. The initial water contact angles (WCAs) of pre-treated samples were 51° and 49° for PA6.6 and PA6, respectively. The plasma exposure time was varied up to 10 min. The evolution of the WCA versus plasma treatment time was studied in detail using air plasma. In the case of PA6 and discharge power of 50 W, the samples assumed a WCA of just about 20° after 1 min of plasma treatment. The prolonged treatment did not have any effect on the water contact angle. When the discharge power was 150 W, the WCA dropped to 32° after 10 s of plasma treatment and remained at about 23° up to 3 min. Then, the WCA started to decrease further until a super-hydrophilic surface finish was observed after 10 min. When the authors used 200 W, no plateau was observed on the curve, but the super-hydrophilic finish occurred even at 1 min of plasma treatment. The super-hydrophilic finish is usually explained by a combined effect of functionalization with polar functional groups and rich morphology on the sub-micrometer scale. The behavior of the WCA for different discharge powers, as reported by Mandolfino et al. [1], is explained by the extensive etching of PA6 at elevated powers. The treatment of smooth polymer surfaces with a low-pressure plasma often causes the formation of periodical structures on the surface, which has been explained by several different mechanisms [2–7]. The super-hydrophilic surface finish occurs within relatively narrow limits of experimental conditions [8]. Therefore, it is not surprising that the paper by Mandolfino et al. [1] is the only report on the super-hydrophilic surface finish of PA6.

Similar results were reported by Mandolfino et al. [1] for PA6.6, except that the initial functionalization was a bit more rapid than in the case of PA6. Adhesion of a bi-component acrylic adhesive was studied versus the discharge power and treatment times. Even a brief treatment by gaseous plasma caused a significant increase in the shear strength. Although the WCA for PA6 treated with plasma at 50 W for 10 s remained reasonably intact, the shear strength increased by a factor of 3. Longer treatment times caused even better adhesion of the glue. The best results in terms of shear strength were observed for moderate discharge powers and treatment times; two opposite effects often explain such a maximum in the shear strength versus the treatment parameters. The first one is an increase in surface wettability (functional groups and morphology) with increasing plasma treatment intensity. The second one is a decrease in wettability due to the thermal effects. Namely, the increased discharge power or treatment time (or both) causes heating of the polymer sample and thus rapid loss of the surface functional groups. The heating rate depends on the polymer materials' roughness and becomes large already at low discharge powers when a polymer is in the form of a powder [9].

Interestingly, the best shear strength at given experimental conditions was always observed for air plasma treatment, although the WCA was relatively moderate compared to other gases. For example, the WCA of PA6 treated with argon plasma at 150 W for 180 s was as low as 3°. At the same treatment time and air as the working gas, the WCA was still 21°.

A low-pressure plasma reactor was also used for the pre-treatment of PA6 discs to increase the adhesion properties [10]. The plasma was sustained in argon at the pressure of 40 Pa. The PA6 discs were washed in an ultrasonic bath with ethanol for 10 min, then dried thoroughly at 80 °C for one day. The authors did not reveal the plasma treatment time, but the WCA dropped from 64 to 31°. The XPS showed a small increase in both oxygen and nitrogen concentrations on the surface of the plasma-treated discs, and the peel strength remained practically intact. The plasma treatment, however, was found beneficial for the adhesion of a silane coupling agent, which assured excellent

joints between the PA6 and rubber discs. Namely, the peel strength increased from about 6 up to 80 N/cm. The adhesion mechanism and the reactions with the coupling agent are elaborated in [10]. The papers by Mandolfino et al. [1] and Sang et al. [10] are the only scientific documents on the application of low-pressure plasma reactors. Although the configurations vary, both groups applied the plasma reactors shown schematically in Figure 1. The energetic particles are concentrated next to the powered electrode, and the entire volume of the reactor is filled with a rather uniform diffusing plasma. The samples are placed away from the powered electrode to prevent overheating.
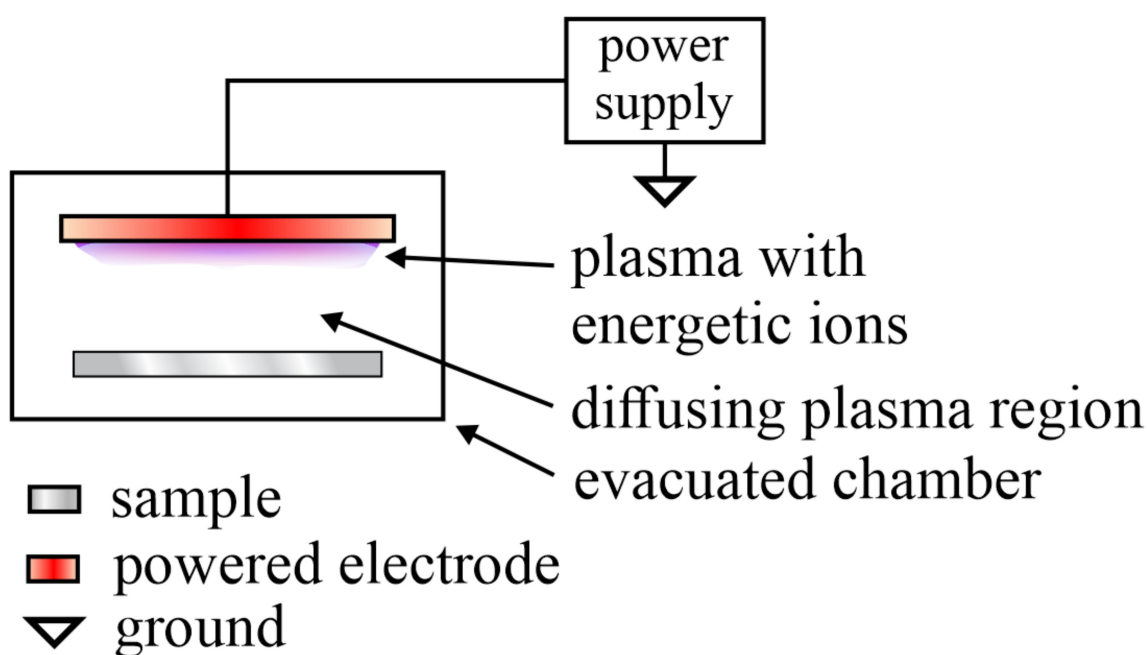
Figure 1. Schematic of the plasma reactor useful for the treatment of polyamide materials with a low-pressure gaseous plasma.

Due to the more straightforward configuration, atmospheric pressure plasmas are more popular for treating polyamide foils or textiles than the low-pressure ones. A recent review of such methods for treating packaging materials was prepared by Tyuftin and Kerry [11]. Various research groups have performed detailed studies. Hanusova et al. [12] used two atmospheric pressure plasma sources: A coplanar dielectric barrier discharge (DBD) and a corona discharge with air as the processing gas. The investigated foils were made of PA12. No pre-treatment of the foils was reported by Hanusova et al. [12]. The WCA of an untreated PA12 was 63°. Both plasma treatments caused a significant decrease in the WCA. The difference between the two plasma treatments was relatively marginal, and the WCA of about 30° was obtained already after 5 s of plasma treatment in both cases. XPS was used to detect the evolution of the surface composition. The samples were probed after 5, 10, and 15 s of plasma treatment. The oxygen concentration, as determined by XPS on the surface of virgin PA12, was 28 at%. The DBD discharge enabled an increase in the O concentration to 38 at% for 5 s, 36 at% for 10 s, and 40 at% for 15 s of plasma treatment. Interestingly, as revealed from WCA, the wettability did not follow the evolution of the oxygen concentration. A somehow better correlation between the concentration of oxygen on the surface of the PA12 film and the WCA was observed for the corona treatment. In this case, the oxygen concentration remained practically unchanged for all treatment times, the same as the WCA. The concentration of nitrogen was also probed by XPS. It was found to be about 3 at% for the untreated material and increased to 4 at% for the case of DBD treatment, and 5 at% for the corona discharge treatment. The hydrophobic recovery was also studied in detail both by WCA and XPS. The WCA started increasing soon after the plasma treatment and reached a value of roughly 50° after a few days. Interestingly, the oxygen concentration after 1 day of

aging dropped below the value of the untreated material, although the WCA revealed that a moderate hydrophilicity persisted. The oxygen concentration for the PA12 foil treated by the DBD plasma, on the other hand, remained fairly intact for the first few days of aging and persisted at 33 at% even after 14 days.

A similar diffuse coplanar DBD plasma sustained in the air was also used by Károly et al. [13]. The authors used PA6 foil to study adhesion properties using commercial glues. The polymer surface was first polished with a silicon carbide abrasive paper under wet conditions, followed by dry polishing. The final pre-treatment was performed with distilled water and ethanol. The DBD plasma was powered with a 15 kHz AC supply with a peak-to-peak voltage of approximately 20 kV and the plasma treatment time of 30 s was adopted. The adhesion between the plasma-treated polymer and other substrates was measured for the acrylic-based, two-component glue, and epoxy adhesive. The WCA of the pre-treated PA6 was 70°. A half-minute plasma treatment caused a drop to 28°, while a WCA of 21° was observed after 180 s of treatment. The initial oxygen concentration probed by XPS was about 13 at% and increased to 23 at% after 1 min of plasma treatment. The adhesive shear strength depended on the type of glue rather than on the surface finish. For example, the shear strength remained practically unchanged for glue type Loctite 406, but increased by a factor of two for Loctite 330.

A somehow different variety of DBD discharges in the random filamentary mode and sustained in the air was applied by Borcia et al. [14]. The discharge was powered at a frequency of 80 kHz and peak-to-peak voltage of about 15 kV. Several types of polyamide foils were probed. No pre-treatment of the foils was reported by Borcia et al. [14]. The original WCAs were 69, 80, and 102° for PA6, PA6.6, and PA12, respectively. The treatment time was varied between 0.1 and 5 s. Even a 0.1 s plasma treatment caused the WCA to decrease to 34, 48, and 67° for PA6, PA6.6, and PA12, respectively. The prolonged treatment time was beneficial, since the WCA decreased monotonously with the increasing treatment time. As probed by XPS, the concentration of oxygen increased monotonously with the increasing treatment time, but the exact behavior was different from the wettability investigated by WCA. Therefore, the results of Borcia et al. [14] indicate an extremely rapid functionalization of polyamide films using the DBD plasma, which consists of numerous stochastic plasma filaments.

The same authors also employed helium in order to treat polymeric foils with gaseous plasma. Commercial foils of PA6 were pre-treated to remove low molecular weight oligomers by rinsing in propanol for 10 min at room temperature, followed by vacuum drying [15]. In this paper, they used the discharge frequency of 13.5 kHz and peak-to-peak voltage of 28 kV. Helium was introduced into an inner electrode gap, therefore, a plasma plume expanded between the powered and grounded electrode. Despite using pure helium, the authors observed a significant increase in oxygen concentration as probed by XPS. The oxygen concentration of untreated samples was about 14 at% and increased to about 24 at% for both 10 and 30 s treatments. Fascinating, the oxygen concentration decreased to only 20 at% for the treatment time of 1 min. The wettability was expressed in terms of the adhesion work, which was about 100 mJ/m^2. Almost irrespective of the plasma treatment duration, the adhesion work increased to about 136 mJ/m^2 for the plasma-treated samples. However, differences were observed in the hydrophobic recovery. Borcia et al. [15] clearly showed that the hydrophobic recovery, in this particular case, was much more pronounced when polyamide foils were functionalized by short plasma treatments.

Either classical or coplanar dielectric barrier discharges (DBD) were used to treat PA materials at an atmospheric pressure. Unlike the low-pressure configuration where a rather uniform plasma occupies a large volume, as shown in Figure 1, the DBD produces temporally and spatially constrained streamers. The schematic of the experimental setups useful for the treatment of PA samples at an atmospheric pressure is shown in Figure 2. Numerous streamers (localized dense plasma of short duration) spread from the electrodes and influence the surface finish of polymer materials. The sample is placed between the electrodes (usually plane-parallel) in the classical mode, whereas in the coplanar mode the sample is above the plasma streamers.
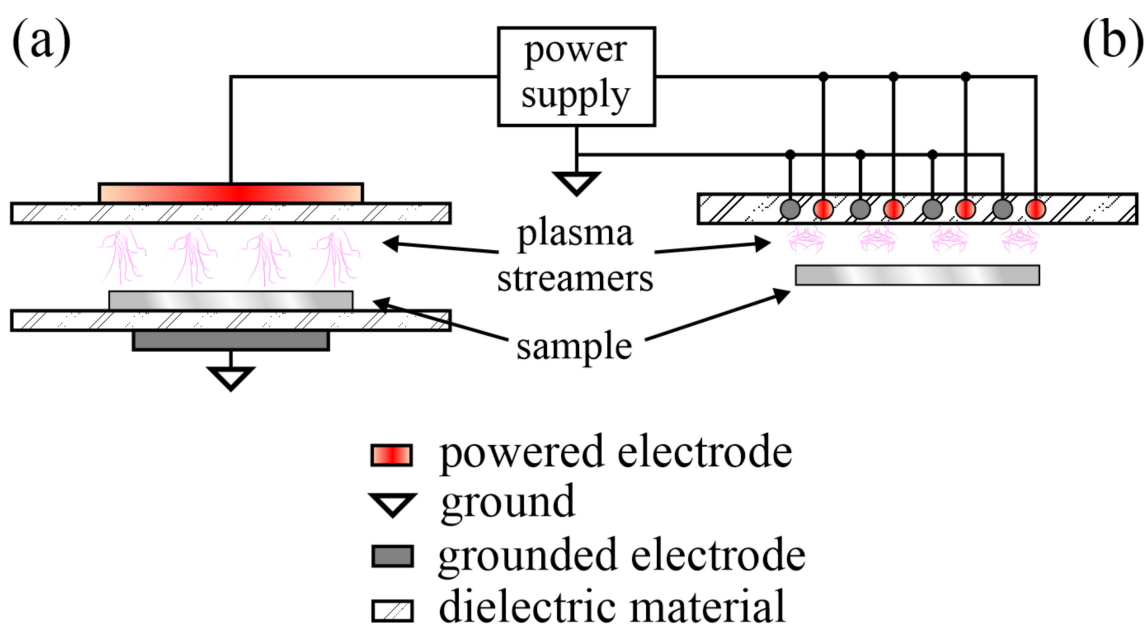
Figure 2. Schematic of atmospheric pressure dielectric barrier discharge in a classical (**a**) and coplanar (**b**) mode.

Gao et al. studied the behavior of PA6 films using atmospheric pressure plasma treatments. The specimens were soaked in acetone for 10 min and then dried in a desiccator for 24 h at room temperature to remove finishes and surface contamination. In one paper [16], they used helium discharge with oxygen admixture. The plasma was powered with a radiofrequency generator at the frequency of 13.56 MHz, therefore, the plasma was in a continuous mode. The plasma treatment time was 4 s. Pure helium and helium with 1 or 2% oxygen admixture were used as working gases. The initial WCA of the as-received PA6 foil was 76°, and it decreased slightly for the case of the treatment with pure helium and more intensively for the case of oxygen addition. Moreover, the morphology of the film changed with the increasing addition of oxygen into the gas mixture. The original oxygen and nitrogen concentrations, as probed by XPS, were 15 and 8 at%, respectively. Even the treatment with pure helium plasma caused a significant increase of both oxygen and nitrogen concentrations in the surface film. The nitrogen concentration increased by more than 5 at%, representing one of the highest reported increase among all cited authors. An addition of 1% of oxygen into the gas mixture resulted in a nitrogen concentration of 10 at%, therefore, it increased slightly compared to the untreated samples. In contrast, the further addition of oxygen caused a weaker functionalization with nitrogen, but the concentration remained higher than for the untreated sample. An intriguing behavior was also observed for the oxygen concentration in the surface film. Namely, pure helium plasma caused the O concentration of 26 at%. An admixture of 1% oxygen resulted in 33 at%, while in the case of 2% oxygen admixture to helium plasma, it was 36 at%. The authors also measured the weight loss of the films, which they ascribed to the plasma treatment. Even the pure helium plasma treatment caused a measurable loss of weight, and the loss increased with the increasing oxygen concentration. The peel strength was also measured versus plasma treatment time. In this case, the treatment times were up to 180 s. The original peel strength was 1.7 N/cm, and it increased for all gases, but the best results were observed after the prolonged treatment with helium and 2% oxygen admixture plasma, where the peel strength was the largest at the value of 3.8 N/cm.

Gao [17] also reported the plasma treatment of PA6 films using the same plasma source as in [16] and a plasma treatment time of 30 s. The etching rate, in this case, was expressed in nm/s and the value was about 1.85 for pure helium plasma and 2.65 for a mixture of helium with 1% of oxygen. In this case, the peel strength of an untreated material was 1.8 N/cm. Half a minute treatment with helium plasma resulted in the peel strength of about 2.25 N/cm, while the strength was 2.5 N/cm for the case of

helium plasma with 1% oxygen admixture. The reported results on the peel strength in [17] are almost the same as in [16]. The same applies to the chemical composition, as revealed by XPS.

The influence of moisture upon treatment of PA6 films with helium plasma with 1% oxygen at an atmospheric pressure using the same device as in [16,17] was published as in [18]. The etching rate was found as high as 8 nm/s in the case of 9% relative humidity in plasma sustained at the power of 80 W. The same discharge parameters with a relative humidity of 1.6% only resulted in the etching rate of approximately 5 nm/s. The discharge power was the crucial parameter for etching, as the reported rate at the power of 40 W was as low as about 0.5 nm/s, for the case of low relative humidity. The WCAs were also determined after the treatment time of 3 min. The hydrophilicity slightly increased for all treatment parameters. However, the best results with the WCA of 40° were observed for the case of high relative humidity and high discharge power. Similar, if not identical results, were also published in [19].

Moreover, Gao et al. [20] used a mixture of helium and CF_4 to treat PA6 films using the same experimental setup as in [16–19]. In this case, the etching rate depended significantly on the plasma treatment time. The reported etching rates are 3.0, 2.6, and 1.9 nm/s for the treatment times of 30, 60, and 90 s, respectively. The WCA dropped from the original 76° to about 27° for half a minute of the plasma treatment, but the prolonged treatment caused an increase of the WCA. At the treatment time of 90 s, the WCA was already about 100°. As the treatment time increased, the surface morphology developed as well. The average roughness, as deduced from AFM imaging, was 12 nm for the untreated material and as large as 36 nm for the material treated in the He/CF_4 plasma for 90 s. Fluorine was observed by XPS on the surface of the plasma-treated samples. The fluorine concentration was marginal for the treatment time of 30 s, but increased to approximately 10 at% for the treatment time of 90 s. Noteworthy, both oxygen and nitrogen concentrations, as revealed from the XPS survey spectra, were larger for plasma-treated samples than for the untreated sample. An interesting behavior was also reported for the peel strength.

Pappas et al. [21] treated both PA6 films and fibers using an atmospheric pressure glow discharge operating at the frequency of 90 kHz. Helium was used to ignite the discharge and nitrogen, or acetylene was added further on. The operating power was 850 W. The WCA on an untreated material was 76°, and it decreased to 58° upon treatment with the N_2/He plasma for 10 s. A rather interesting behavior of the WCA versus the treatment time is revealed in this paper and aging was also tackled. The slowest hydrophobic recovery was observed for PA6 foils treated for the most extended treatment time. The WCA increased to 55° after 1 month of aging at ambient conditions for the case of the 10 s plasma treatment. The same material treated by the plasma for 0.6 s only assumed the WCA of 65° after 1 month of aging. The WCA was still lower than for the original samples.

Polyamide 12 films were also treated by gaseous plasma sustained at an atmospheric pressure using a microwave (MW) plasma source [22]. The dense plasma was sustained within a discharge cavity using surface waves, and a plasma plume also expanded outside the cavity due to the continuous supply of argon. Different admixtures of oxygen and nitrogen were used to facilitate chemical reactions between the plasma jet and polymer samples. The treatment time was between 25 ms and 1 s. Although no pre-treatment was reported by Hnilica et al. [22], the WCA of untreated samples was about 80°. Even the shortest treatment time caused a decrease of the WCA to about 28°, while a further treatment resulted in a slightly lower contact angle. For example, at 1 s, the WCA was about 22°. Hnilica also provided lateral profiles and the diameter of the affected area was about 1 cm. The interface between the affected and original surface wettability was rather sharp. The oxygen concentration, as probed by XPS, marginally increased after 25 ms of plasma treatment. However, 1 s of plasma treatment caused the oxygen concentration to increase to 31 at% for a sample treated with argon, 34 at% for the treatment with argon mixed with 2% oxygen, and 36 at% for the treatment with argon mixed with 2% nitrogen. The concentration of nitrogen did not change significantly depending on the type of gas or the treatment time. The results presented by Hnilica, therefore, reveal extremely fast hydrophilization of PA12. The treatment times well below a second are very useful for industrial-scale modification of surface wettability, especially when the treatment is performed continuously.

The surface properties of polyamides can also be tailored using energetic ions. A useful device was applied by Kalácska et al. [23]. Samples of extruded PA6 of disc shape were polished with a silicon carbide abrasive paper and subsequently cleaned in an ultrasonic bath in distilled water and ethanol. The final stage of pre-treatment was drying in pure nitrogen at an atmospheric pressure. Samples were immersed into a high vacuum chamber, where the plasma was generated by a 27.13 MHz RF generator in relatively pure nitrogen. The estimated discharge power was 150 W, and the working pressure was 0.4 Pa. Samples were placed on the additionally biased electrode with the voltage of −30 kV and treated at conditions where the achieved fluence was 3×10^{13} ions/m^2. The oxygen concentration in the surface film increased by 24 at%, while the nitrogen content increased by 13 at% upon the nitrogen ion treatment. The WCA decreased from the original 60° down to 36°. The friction coefficient of the treated samples was fairly low at the beginning. Under dry sliding, the increased surface energy caused increased adhesion, associated with forming a transfer layer on the steel disc. A decreased friction was observed upon the run-out type lubrication test, explained by the increased oil retention on the treated surface.

PA66 foils were also treated by the atmospheric pressure DBD air plasma by Kuzminova et al. [24] using a semi-continuous mode. The power supply operated at the frequency of 22.5 kHz and discharge power of 30 W. The configuration was very similar to that adopted by Karoly et al. [13]. The treatment time ranged from 0.5 s to 0.5 min. The roughness, as determined by AFM, remained quite unchanged for the treatment time up to 15 s and increased significantly with the prolonged treatment times. The surface composition, as probed by XPS, was reasonably close to theoretical (C:O:N = 70:15:15) for untreated samples. Even 0.5 s of plasma treatment caused an increase of the oxygen concentration to 22 at%. The oxygen concentration increased rather monotonically with the increasing treatment time and reached 33 at% after half-a-minute of plasma treatment. The nitrogen concentration also increased with the increasing treatment time but only for a couple of at%. High-resolution XPS C1s peaks revealed a gradual increase of the carboxyl groups on the PA66 samples. The WCA dropped from the original 64° to about 30° even for the first 0.5 s treatment. With the increasing treatment time, it slowly decreased until about 25° was observed after half a minute of plasma treatment. The dispersive component of the surface energy remained practically unchanged during the plasma treatment. However, the polar component jumped to about 27 mJ/m^2 even for the shortest treatment time, indicating swift surface activation upon treatment by the DBD plasma. Hydrophobic recovery was marginal during the first 100 h. Optical, thermal, and mechanical properties remained practically intact, irrespective of the plasma treatment time.

Plasma treatments were also found useful for the modification of polyamide fibers, textiles, or membranes. The improved dyeing ability of PA66 fabrics was reported by Oliveira et al. [25]. Fabrics with a warp density of 42 threads/cm, weft density of 30 threads/cm, and mass per surface area of 95 g/m^2 were pre-washed with a 1 g/L of non-ionic detergent solution at 30 °C for 30 min and then rinsed in water for another 15 min. A commercial DBD plasma reactor was powered with a 10 kV source operating at 40 kHz. The fabric was treated in a continuous mode at the velocity of 4 m/min using 1 kW of discharge power. The corresponding treatment time was about 0.5 s. Such a short treatment time caused a significant modification of the surface composition. XPS spectra revealed that the oxygen concentration increased from 16 to 28 at% and the nitrogen concentration from 9 to 11 at%. The untreated fabric exhibited hydrophobic properties with WCA as large as 133°. The plasma treatment resulted in a WCA of 21° and moderate hydrophobic recovery upon aging. The WCA increased to about 23° after 1 day of aging at ambient conditions, 42° after 1 week, and 80° after a month. The plasma treatment caused a significant increase in the polar component of surface energy, from 1 to 73 mJ/m^2. In comparison, the dispersive component, as calculated using the Wu method [26,27], decreased from 10 to 7 mJ/m^2. The ability of dyeing was improved significantly, and the fastness properties persisted even after prolonged washing. Oliveira et al. also disclosed a comprehensive dyeing mechanism [25]. After the plasma treatment, the PA66 displayed a significant

amount of oxygen covalently bonded to the surface. The presence of microchannels promoted the diffusion of the dye into the fibers.

In another paper [28], Oliveira et al. described the influence of DBD plasma on the trichromic dyeing process of PA66 fabric and the reuse of the generated effluents for new dyeing processes. Fabric with a warp density of 40 threads/cm, weft density of 30 threads/cm, and mass per surface area of 95 g/m^2 was pre-washed and treated by DBD as in [25]. The static WCA of the untreated material was as high as 146°. The plasma treatment at a moderate discharge power density caused a rapid decrease of the static WCA until the power density of 2500 Wmin/m^2, at which it became immeasurable, since the plasma-activated fabric absorbed the water droplet before the measurement could be performed. In contrast to [25], the XPS results indicated only moderate functionalization of the fabric's surface as the oxygen content increased from 18 to 20 at% and nitrogen from 8 to 10 at%. The chemical composition was also probed by energy-dispersed X-ray spectroscopy (EDS). The method revealed an increase in the oxygen content from 23 to 25 at% and in nitrogen from 10 to 11 at%. The excellent agreement between XPS and EDS results was explained by the substantial incorporation of O and N atoms onto the fabric's surface. The difference in nitrogen content was explained by a surface cleaning effect that allowed the bulk material's fingerprint to appear on the spectra.

In yet another paper, Oliveira et al. focused on the whiteness degree and the tensile strength of polyamide fabric of various warp and weft densities [29]. The static WCA of untreated material was as high as 153° for the PA66 fabric of warp density of 8 threads/cm, weft density of 18 threads/cm, and mass per surface area of 95 g/m^2. The static WCA dropped to 75° after the treatment by the DBD plasma of 500 Wmin/m^2 power density. The plasma treatment with a power density of 1500 Wmin/m^2 caused a static WCA of 53°, while higher power densities caused an immediate absorption of a water droplet, therefore, no static WCA could be measured. The water absorption time was estimated to about 1 s for the well-activated PA66 samples. Both XPS and EDS were used to monitor the elemental composition. The XPS showed a significant increase in the oxygen content after treating different fabrics with a plasma sustained at the power density of 2500 Wmin/m^2—from 17 at% (for the untreated fabric) to about 28 at%. EDS showed a much smaller increase, i.e., from about 23 to 25 at%. A more considerable probing depth of EDS could explain such a discrepancy. The tensile strength and elongation remained unchanged after the plasma treatments.

A DBD plasma was also used for surface modification of PA66 by Bessada et al. [30]. A commercially available PA66 woven fabric of mass per surface area of 240 g/m^2 was treated in a continuous mode without any pre-treatment. The DBD was powered with a 40 kHz supply of peak voltage ~10 kV. The discharge power was varied between 500 and 1500 W, and the speed of fabric passed the DBD between 5 and 20 m/min. The DBD was operating in the filamentary mode, the same as many other DBDs operating at this frequency. Unlike Oliveira [25,28,29], Bessada et al. [30] found only modest wettability changes. The original static WCA was just below 80° and dropped to any value between 50 and 75°, depending on the treatment parameters. The slowest speed of fabric through the DBD caused the best wettability, which is explained by the prolonged plasma exposure time. Interestingly, no statistically significant difference was observed between discharge powers of 1000 and 1500 W. Three consecutive passages of fabric under the discharge caused no significant improvement of the surface wettability. The water droplets were absorbed fast after the plasma treatment—the WCA became immeasurable about 2 s after the droplet's deposition onto the activated fabric. A moderate hydrophobic recovery was also reported along with a marginal increase of the O and N concentrations as deduced from XPS. From this perspective, the results are similar to those reported by Oliveira [28], except for the absolute values.

Li et al. [31] also used an atmospheric-pressure DBD for treatment of the PA66 fabric with air plasma. However, they used a pulsed DC source to power the discharge, and the discharge chamber was cylindrical. The pulse rise-time was 30 ns only, and the peak voltage as high as 70 kV. The duration of plasma during each pulse was estimated at approximately 750 ns. The repetition time was variable between about 2 ms and 1 s. Samples were first sterilized by alcohol, then cleaned with deionized

water and dried before the plasma treatment. After a few seconds of plasma treatment, originally smooth fibers assumed rich morphology, and after 1 min of plasma treatment, a well-defined cone-like morphology appeared. XPS was used to study the surface composition. The untreated samples contained 14 at% O and 8 at% N. A 10-s plasma treatment caused an increase in oxygen concentration to about 16 at%, but nitrogen concentration dropped for about 1 at%. A 1-min plasma treatment resulted in 18 at% O and 9 at% N in the surface film of PA66 as probed by XPS. The same group published the same results on the surface characterization of PA66 in [32] and added a detailed study on the disinfection efficiency using *Escherichia coli* HT115 as model microorganisms.

All the above-cited authors used high impedance discharges for the plasma treatment of polyamide fabric at an atmospheric pressure. Pavlinak et al. [33], however, employed a microwave (MW) discharge, similar to that reported by Hnilica et al. [22]. PA6 nanofibers were synthesized by electrospinning and exposed to an MW plasma jet sustained in pure argon or a mixture of argon and 2 vol% oxygen at an atmospheric pressure. As expected, the nanofibers melted upon exposure to MW plasma sustained in the continuous mode. The samples passed the vicinity of the MW plasma jet at the speed of 12 mm/s. The surface composition, as determined from the XPS survey spectra, was studied versus the number of passes. The original O and N concentrations in the surface film were 11 at%. The concentrations changed after passing the vicinity of the MW plasma jet. One pass caused an increase in oxygen concentration in the surface film to 18 and 15 at% for the cases of pure Ar and Ar + 2 vol%O_2, respectively. Simultaneously, the N concentration decreased to 6 and 9 at%, respectively. The unanticipated result may be explained by the presence of water vapor in the effluent regime of the MW plasma jet. Pavlinak et al. [33] also showed that the O-concentration increased by increasing the number of plasma-passes. After about 10 passes, the O-concentration stabilized at about 22 at% for both Ar and Ar + 2 vol%O_2 treatments. Fibers have melted after such treatments. Some samples were also heated for 1 min to 300 °C, without being exposed to the plasma, to check whether the oxidation would occur merely due to thermal oxidation. Although the PA6 nanofibers, synthesized by electrospinning, melted at 300 °C, practically no oxidation was detected by XPS. Therefore, the extensive functionalization observed after the plasma treatment could not be attributed to the high sample temperature. Interestingly, the high concentration of functional groups remained on the surface even though the samples melted upon the plasma treatment. Namely, polar functional groups are usually unstable at high temperatures and decay spontaneously upon heating [34].

Polyamide is also an exciting material for the synthesis of membranes. Boulares-Pender et al. [35] treated nylon membranes of thickness of 0.15 mm and nominal pore sizes of 0.2 μm in a low-pressure plasma reactor using argon, nitrogen, and oxygen gases. The gas pressure was set to about 25 Pa and the flow rate to 20 sccm. The ultimate pressure was about 15 Pa, but the authors did not report the residual atmosphere's composition. The plasma treatment always caused an increased oxygen concentration as probed by XPS, almost irrespective of the gas or gas mixtures used. The original O-concentration was 12 at%, and it increased to about 18 at% after the plasma treatment. The nitrogen concentration remained somewhat intact at about 11 at%. No carboxyl or similar highly polar functional group was deduced from the high/resolution XPS C1s spectra. The peak attributed to the amide group remained intact irrespective of the type of gas or gas mixture used upon the plasma treatment. Plasma-treated membranes were further treated by electron beams using a home-made electron accelerator operating at about 170 kV. The adsorption of proteins on plasma-treated membranes was also studied by Boulares-Pender et al. [35]. The adsorption of albumin (BSA) was hardly affected by any plasma treatment. However, myoglobin adhered well on all plasma treated membranes, especially when the plasma was sustained in nitrogen or a nitrogen-argon gas mixture. The adsorbed quantity was doubled as compared to the pristine nylon membrane. Lysozyme, on the other hand, completely adhered to the membrane treated by the plasma containing oxygen. The authors found no correlation between the surface functionalities as probed by XPS and adhesion of blood proteins, which is slightly unexpected, considering the earlier works [36].

3. Correlations between Surface Finish and Treatment Parameters

The most relevant results reported by different authors are summarized in Table 1. Only the surface finish reported by a good number of authors is included in the summary. An interesting feature revealed by examining Table 1 is a large scattering of the original surface wettability. The WCA of the untreated samples spans from 49 to 153°. In general, the WCA does not depend only on the type of material but also its roughness. From the latter point of view, the WCA should be the highest for untreated samples of rich morphology on the sub-micrometer scale. Unusually, the water contact angles for the same material and morphology scatter significantly, as well. A feasible explanation is the purity of the material, both in terms of intentionally added blends and surface impurities. Unfortunately, not all authors reported details on the pre-cleaning of their samples. The surface impurities indeed influence the initial surface composition and thus the surface energy, but should not affect the final wettability after the plasma treatment, since they are likely to be removed upon the plasma treatment. Many authors did not report the evolution of surface morphology (usually studied by AFM or SEM). Therefore, it is impossible to draw a correlation between the roughness on the sub-micrometer scale and surface wettability.

Table 1. Summary of the reported results.

Ref.	Gas	P [W]	p [mbar]	f [MHz]	t [min]	O_2 [%]	ΔO [at%]	N [at%]	WCA_0 [°]	WCA_f [°]	Peculiarity	Polymer Type
[37]	O_2	40	0.5	N/A	0.2	N/A	N/A	N/A	N/A	N/A	N/A	PA
[38]	Air	900	1000	N/A	0.01	21	8	3	N/A	N/A	textile	N/A
[39]	Ar	N/A	1	N/A	0.5	0	N/A	N/A	80	18	tube	N/A
[39]	O_2	N/A	1	N/A	0.5	100	N/A	N/A	80	39	tube	N/A
[39]	N_2	N/A	1	N/A	0.5	0	N/A	N/A	80	30	tube	N/A
[39]	Air	N/A	1	N/A	0.5	21	N/A	N/A	80	42	tube	N/A
[40]	Air	900	1000	0.02	0.005	21	N/A	N/A	N/A	N/A	crystal	PA6
[41]	Ar	50	0.2	13.56	N/A	N/A	N/A	N/A	N/A	N/A	N/A	N/A
[42]	N_2	90	0.015	0.04	15	N/A	N/A	N/A	N/A	13	membrane	N/A
[43]	Air	1000	1000	0.04	1	21	2	−1	N/A	N/A	N/A	PA66
[44]	O_2	20	0.2	13.56	2	100	13	1	N/A	N/A	N/A	PA12
[44]	O_2	20	0.2	13.56	30	100	15	0	N/A	N/A	N/A	PA12
[24]	Air	30	1000	0.022	0.12	21	13	1	64	28	foil	PA66
[14]	Air	N/A	1000	0.08	0.002	21	5	N/A	69	34	foil	PA6
[14]	Air	N/A	1000	0.08	0.08	21	10	N/A	69	27	foil	PA6
[14]	Air	N/A	1000	0.08	0.002	21	7	N/A	81	48	foil	PA66
[14]	Air	N/A	1000	0.08	0.08	21	13	N/A	81	23	foil	PA66
[14]	Air	N/A	1000	0.08	0.002	21	2	N/A	102	67	foil	PA12
[14]	Air	N/A	1000	0.08	0.08	21	17	N/A	102	43	foil	PA12
[15]	He	N/A	1000	0.013	0.17	0	10	1	N/A	N/A	foil	PA6
[15]	He	N/A	1000	0.013	1	0	6	2	N/A	N/A	foil	PA6
[20]	He + 1% CF_4	N/A	1000	13.56	0.5	0	3	1	N/A	N/A	foil	N/A
[21]	N_2He	850	1000	0.09	0.16	0	N/A	N/A	76	34	foil	PA6
[21]	N_2He	850	1000	0.09	0.03	0	N/A	N/A	76	47	foil	PA6

Table 1. *Cont.*

Ref.	Gas	P [W]	p [mbar]	f [MHz]	t [min]	O_2 [%]	ΔO [at%]	N [at%]	WCA_0 [°]	WCA_f [°]	Peculiarity	Polymer Type
[22]	Ar	250	1000	2450	0.004	0	2	1	80	22	foil	PA12
[22]	Ar	250	1000	2450	0.017	0	7	1	80	N/A	foil	PA12
[22]	Ar	250	1000	2450	0.017	2	10	1	80	N/A	foil	PA12
[22]	Ar + 2% N$_2$	250	1000	2450	0.017	0	12	2	80	N/A	foil	PA12
[13]	Air	300	1000	0.015	0.5	21	11	4	70	28	foil	PA6
[32]	Air	N/A	1000	N/A	0.17	21	2	−1	N/A	N/A	textile	PA66
[32]	Air	N/A	1000	N/A	1	21	5	1	N/A	N/A	textile	PA66
[10]	Ar	N/A	0.4	N/A	N/A	0	4	−1	64	31	foil	PA6
[1]	Air	150	0.6	13.56	1	21	N/A	N/A	49	24	foil	PA6
[1]	Air	150	0.6	13.56	10	21	N/A	N/A	49	2	foil	PA6
[1]	Air	150	0.6	13.56	1	21	N/A	N/A	51	21	foil	PA66
[1]	Air	150	0.6	13.56	10	21	N/A	N/A	51	3	foil	PA66
[1]	Air	150	0.6	13.56	3	21	N/A	N/A	49	21	foil	PA6
[1]	Ar	150	0.6	13.56	3	0	N/A	N/A	49	3	foil	PA6
[1]	O$_2$	150	0.6	13.56	3	100	N/A	N/A	49	27	foil	PA6
[1]	ArO$_2$	150	0.6	13.56	3	50	N/A	N/A	49	15	foil	PA6
[1]	Air	150	0.6	13.56	5	21	N/A	N/A	49	5	foil	PA66
[1]	Ar	150	0.6	13.56	5	0	N/A	N/A	49	18	foil	PA66
[1]	O$_2$	150	0.6	13.56	5	100	N/A	N/A	49	11	foil	PA66
[1]	ArO$_2$	150	0.6	13.56	5	50	N/A	N/A	49	13	foil	PA66
[29]	Air	1000	1000	0.04	0.0002	21	N/A	N/A	153	75	textile	PA66
[29]	Air	1000	1000	0.04	0.0006	21	N/A	N/A	153	53	textile	PA66
[28]	Air	1000	1000	0.04	0.005	21	2	2	146	30	textile	PA66
[31]	Air	N/A	1000	N/A	0.17	21	3	−1	N/A	N/A	textile	PA66

Table 1. *Cont.*

Ref.	Gas	P [W]	p [mbar]	f [MHz]	t [min]	O_2 [%]	ΔO [at%]	N [at%]	WCA_0 [°]	WCA_f [°]	Peculiarity	Polymer Type
[31]	Air	N/A	1000	N/A	1	21	5	1	N/A	N/A	textile	PA66
[12]	Air	N/A	1000	N/A	0.08	21	10	0	63	32	foil	PA12
[12]	Air	N/A	1000	N/A	0.25	21	12	1	63	34	foil	PA12
[33]	Ar	140	1000	2450	0.5	0	11	−2	N/A	N/A	textile	PA6
[33]	Ar	140	1000	2450	0.5	2	12	−2	N/A	N/A	textile	PA6
[25]	Air	1000	1000	0.04	0.005	21	12	2	133	23	textile	PA66
[35]	N_2	100	0.1	13.56	5	0	5	1	56	34	membrane	N/A
[35]	Ar	100	0.1	13.56	5	0	6	−1	56	27	membrane	N/A
[35]	O_2	100	0.1	13.56	5	0	7	1	56	35	membrane	N/A
[23]	N_2	150	0.004	27.13	N/A	0	13	6	60	36	foil	PA6
[19]	HeH_2O	N/A	1000	13.56	N/A	1.2	11	1	76	48	foil	PA6
[19]	HeH_2O	N/A	1000	13.56	N/A	2	23	1	76	35	foil	PA6
[30]	Air	N/A	1000	N/A	0.017	21	2	−1	79	63	textile	PA66
[30]	Air	N/A	1000	N/A	0.05	21	N/A	N/A	79	48	textile	PA66
[16]	He	N/A	1000	13.56	0.07	0	12	5	76	58	foil	PA6
[16]	He	N/A	1000	13.56	0.07	1	19	2	76	47	foil	PA6
[16]	He	N/A	1000	13.56	0.07	2	21	1	76	29	foil	PA6
[17]	He	N/A	1000	13.56	0.5	0	12	5	76	58	foil	PA6
[17]	He	N/A	1000	13.56	0.5	1	21	1	76	29	foil	PA6
[18]	HeH_2O	80	1000	13.56	3	1	14	3	76	40	foil	PA6

The final WCA reported by the majority of authors is between 20 and 40°. Figure 3 reveals the final WCA versus the treatment time. Despite the large scattering of the reported results, there is an evident trend—a longer treatment time results in a lower WCA and thus better wettability. The super-hydrophilic effect (WCA below a few degrees) was reported only for treatment times of several minutes. This observation is explained due to the fact that the WCA on a smooth surface cannot be extremely low, but a nanostructured surface finish is needed for the super-hydrophilic effect [8]. Nanostructuring of polymers is a result of non-homogeneous etching. The etching at a reasonable temperature (preferably close to the room temperature) is a slow process since the etching rate is often the order of nanometers per second [45,46]. The combination of rich surface morphology and high concentration of polar functional groups is usually observed only for polymers treated by low-pressure plasma [46,47]. Surprisingly, most authors concentrated their research on atmospheric-pressure plasmas, although they rarely enable a super-hydrophilic surface finish.
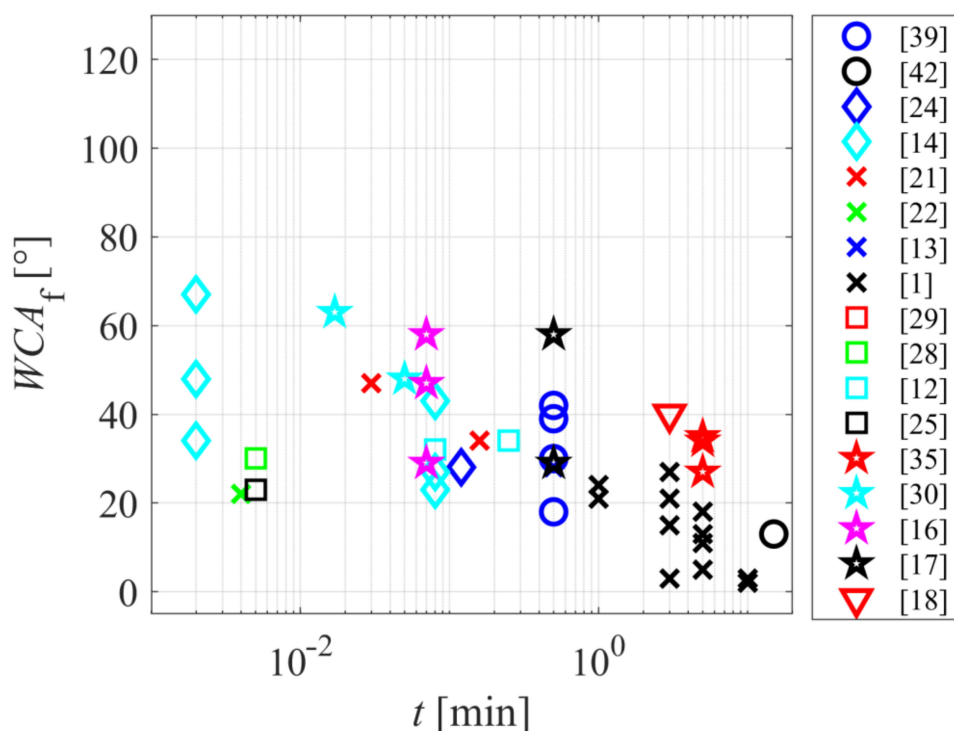

Figure 3. The final water contact angle versus the treatment time.

The relationship between the surface wettability and discharge power is shown in Figure 4. It seems that high discharge powers do not lead to highly wettable surfaces, but moderate powers around 100 W perform better. It should be stressed that the absolute value of the discharge power may not be the best parameter, since the processing parameters depend on numerous other parameters such as the size of the treatment device, the pressure, and many other peculiarities. A more appropriate parameter would be the power applied to the plasma and normalized to the surface area (in the case of one or two-dimensional discharges) or to the plasma volume (in the case of continuous discharges that create the homogeneous plasma in a particular volume).
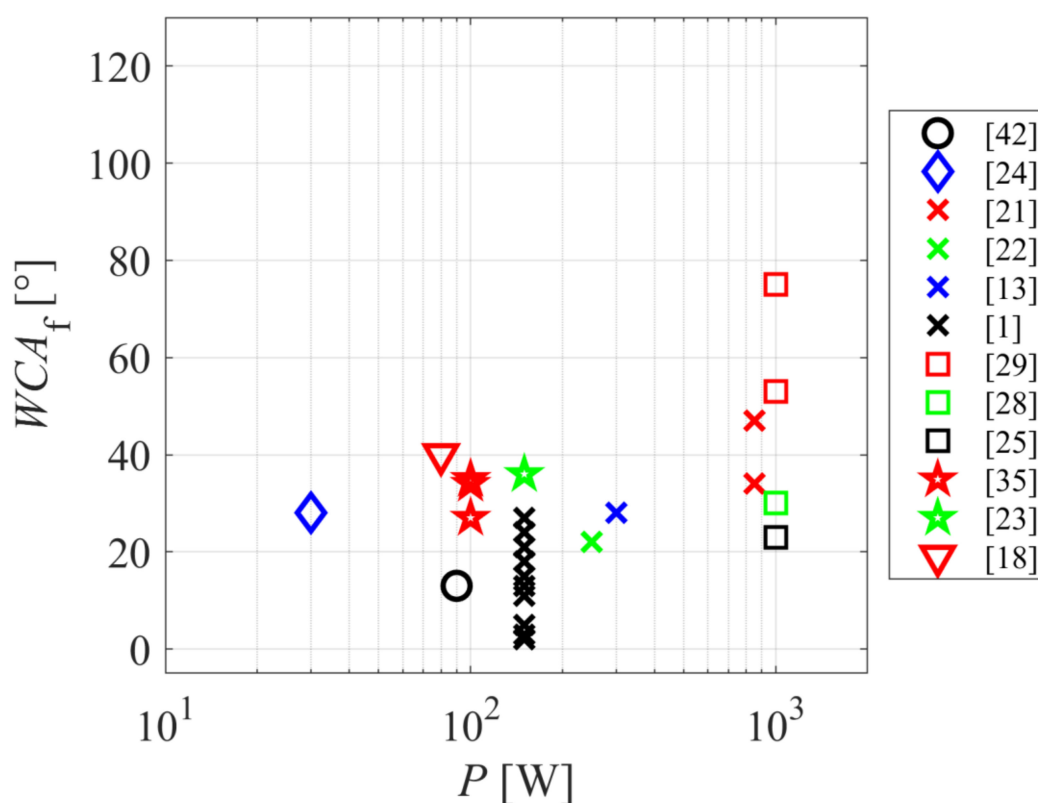
Figure 4. The final water contact angle versus the discharge power.

The majority of authors used XPS for monitoring the modification of surface chemistry. While the XPS survey spectra are acquired in a reasonable time, the acquisition and interpretation of high-resolution spectra may take time, therefore, most authors limited such investigations. Still, most authors represented the concentration of nitrogen, oxygen, and carbon versus the treatment parameters. Figure 5 represents the difference in N-concentration, as probed by XPS, versus the treatment time. Evidently, there is no trend, and the difference is rather small. Some authors reported enrichment in the N-concentration, but many a depletion despite using plasma sustained in the air or even "pure" nitrogen. The functionalization of polyamides with nitrogen functional groups (such as amino groups), therefore, remains a challenge. A feasible explanation for the lack of additional nitrogen on the PA surface is the preferential functionalization with oxygen. It is difficult to assure oxygen-free plasma due to the water vapor, which is likely to be present in low-pressure and atmospheric-pressure plasma reactors. Here, it should be stressed that even a 1 min concentration of water vapor in processing gas will cause the formation of OH radicals upon plasma conditions and the interaction of these radicals with the polymer surface. The effect of such water-vapor on the surface finish of a polymer upon treatment with "pure" argon was recently elaborated in [48].

The functionalization with oxygen functional groups is a common consequence of plasma treatment of polyamides. Figure 6 represents the increase of the oxygen content, as probed by XPS, versus the treatment time. Please note the logarithmic scale on the *x*-axis. Figure 6 reveals that all authors reported at least an increase of 2 at%. The average increase is about 10 at%, and it seems that the treatment time is not the factor dictating the concentration of oxygen on the surface of a polyamide sample. Such a rather unexpected fact is explained by the etching of polymer samples whose surfaces have been saturated with oxygen functional groups. The final concentration of oxygen is, therefore, a compromise of surface functionalization by the chemical interaction of reactive species such as O, OH, O_3, and positively charged ions, and the removal of surface functionalities by releasing CO, CO_2, and more complex molecules. The etching rate increases with increasing discharge power.
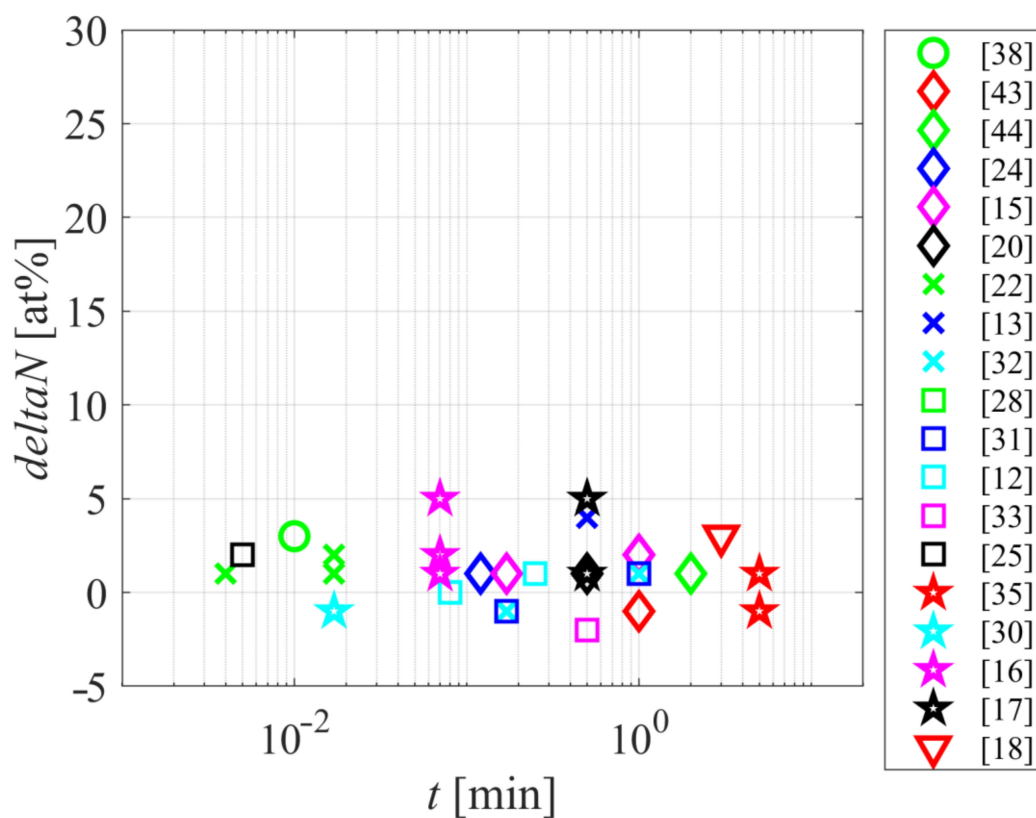
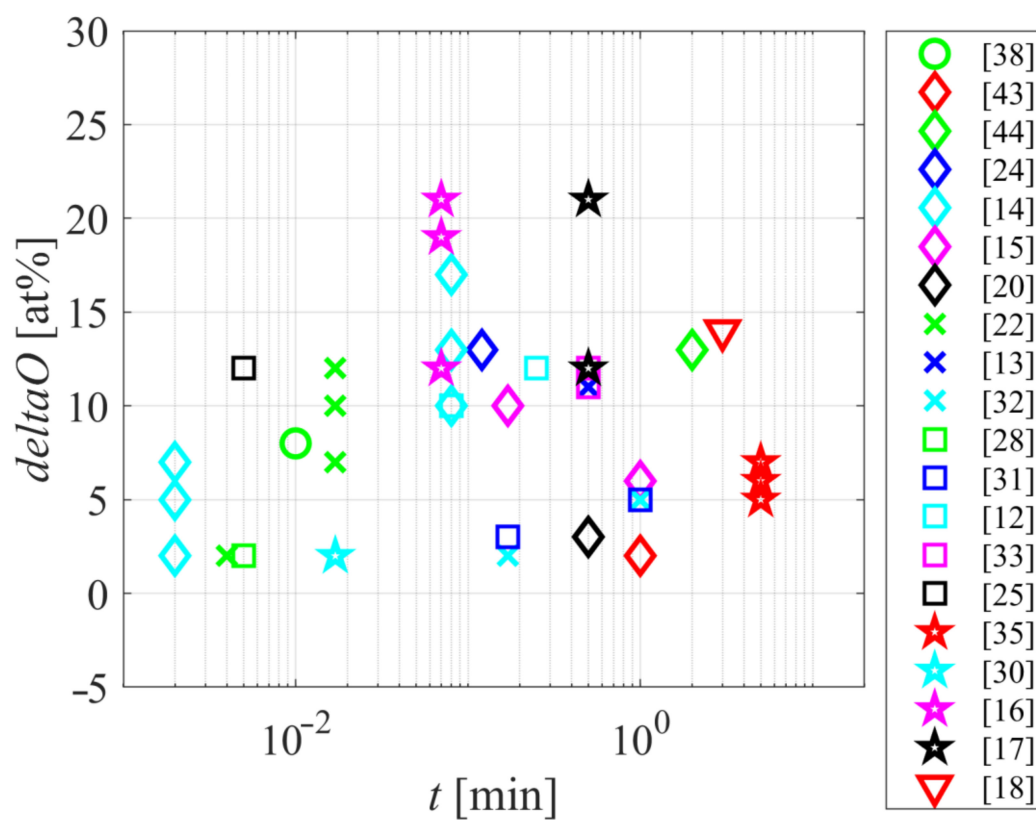**Figure 5.** The difference in nitrogen concentration as probed by XPS versus the plasma treatment time.

Figure 6. The difference in oxygen concentration as probed by XPS versus the treatment time.

Figure 7 shows the relationship between the oxygen concentration, as probed by XPS and the reported discharge power. The results are scattered due to the experimental setups' peculiarities, but a general trend is decreasing the O-concentration with the increasing discharge power. A feasible explanation is the extensive etching at elevated powers. The best functionalization should be obtained upon saturation with polar functional groups, as revealed recently, for the case of polystyrene [49]. Such studies have, however, not been performed for polyamides and represent a great scientific challenge.

Figure 7. The difference in oxygen concentration as probed by XPS versus the discharge power.

The concentration of oxygen in the original gas mixture does not seem to be a decisive factor for surface wettability. Figure 8 represents the final water contact angle versus oxygen concentration. Most authors used air as the source gas or a noble gas with a small oxygen admixture. Only a couple of authors employed almost pure oxygen for the plasma treatment of polyamides. The results summarized in Figure 8 show no correlation between the wettability and oxygen concentration in the gas mixture. Therefore, one can conclude that even a small admixture of oxygen in the gas mixture assures a highly wettable surface. This effect is explained by the preferential dissociation of oxygen and/or water vapor in the non-equilibrium gaseous plasma. The group of A. Ricard [50] showed that oxygen atoms extensively dissociate upon plasma conditions due to the rather low dissociation energy (as compared to the nitrogen dissociation energy or excitation energy of Ar or He metastables) and the existence of a couple of long-living molecular metastable states (the "a" and "b" states of neutral O_2 molecule). The long lifetime of such metastables enables a step-wise dissociation, therefore, the electron threshold energy for a dissociative collision is minimal. As a result, the density of O-atoms or OH radicals in a plasma sustained in other gases is large enough to cause the rapid functionalization of fabrics with oxygen functional groups [51]. Here, it is worth mentioning that the required fluence of oxygen atoms onto a smooth polymer surface for saturation with polar O-rich functional groups is close to 10^{21} m^{-2} [49]. Therefore, the surface is saturated in 1 s of the plasma treatment providing that

the O-atom density in the vicinity of the polymer sample being treated is about 10^{19} m^{-3}, which is a typical value in many industrial plasma reactors useful for surface activation of polymers [52].
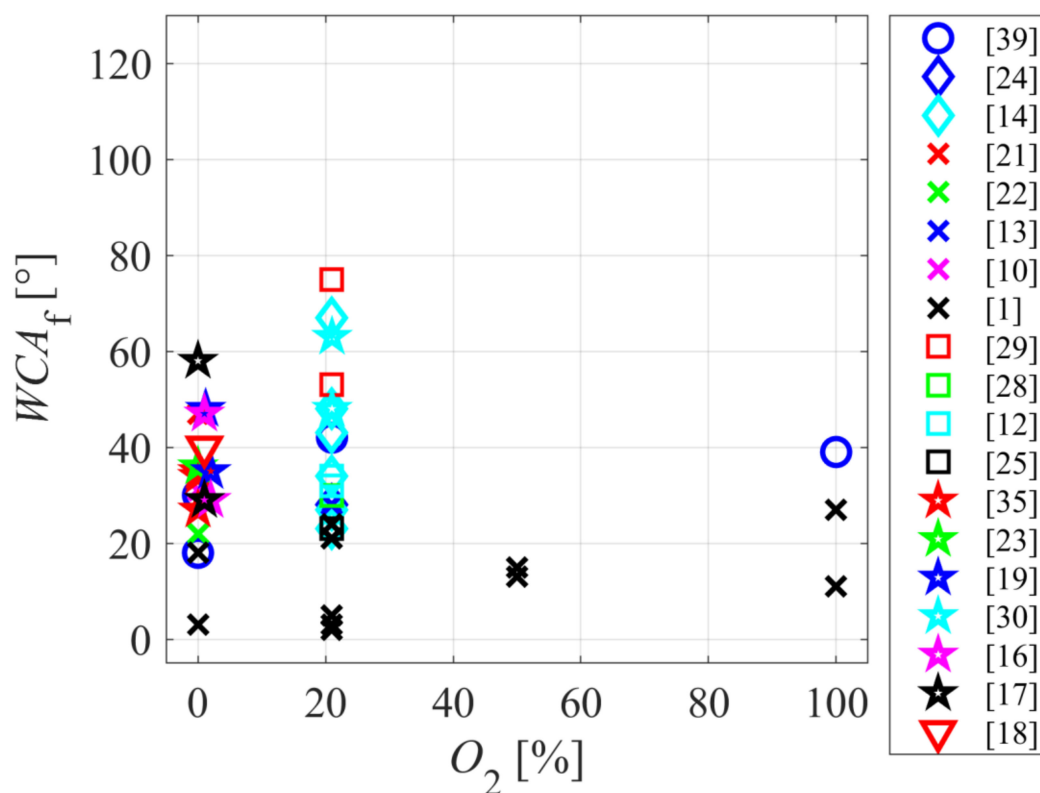

Figure 8. The final water contact angle versus the concentration of oxygen in the original gas mixture.

4. Conclusions and Roadmap

The survey of recent reports on the plasma functionalization of polyamides for the improved wettability indicates that the surface layer, as probed by XPS, is always enriched in oxygen functional groups irrespective of the type of gas used for plasma treatments. Useful results can be obtained at the treatment time as low as 1 s, providing that the discharge parameters are chosen carefully. Most authors, however, adopted longer treatment times lasting about 1 min. Such treatments cause an increase in oxygen concentration. However, the concentration of nitrogen in the surface film, as probed by XPS, remained relatively intact even when "pure" nitrogen or mixtures of nitrogen with other gases were used to sustain a non-equilibrium gaseous plasma. The concentration of oxygen in the surface film was found inversely proportional to the discharge power, which can be explained by the increased etching of the polymers upon powerful plasma conditions. Thermal effects may play a role in the final concentration of oxygen functional groups. However, only a few authors reported the increased surface temperature due to the exothermic surface reactions such as neutralization of charged particles, bombardment with positively charged ions, the heterogeneous surface association of radicals to stable molecules, and relaxation of any metastables that might appear in the plasma at moderate densities.

Only a handful of authors reported plasma parameters in papers disclosing the plasma activation of polyamides. In an analogy with other polymers, the surface finish should depend on the fluence of reactive gaseous species and ultraviolet radiation. Low fluences should cause functionalization, while higher fluences should cause etching of the already functionalized polymer surface and thus loss of some surface functionalities. Therefore, the scientifically spotless description of the surface phenomena upon the plasma treatment of polyamides should indicate the surface finish versus the fluences of reactive species. Numerous plasma characterization methods are available, and the authors are encouraged to report at least the most crucial parameters, such as densities of highly reactive

gaseous species that cause surface modification. Considering the results reviewed in this paper, the density of reactive oxygen species (O-atoms and OH radicals in particular) should be the critical parameter governing the surface finish.

Another scientific challenge is the functionalization of polyamide surfaces with functional groups other than oxygen. The literature survey clearly shows that even 1 min concentrations of oxygen or water vapor in the processing gas caused oxidation of the PA surfaces. The functionalization with other functional groups, therefore, requires an oxygen-free atmosphere, which can be achieved by the careful construction and preparation of experimental setups. Low-pressure plasma reactors should be hermetically tight and bakeable to elevated temperatures (to remove the water adsorbed on surfaces) and pumped with powerful high-vacuum pumps. The atmospheric pressure reactors should also be bakeable, and the diffusion of the surrounding atmosphere into the gaseous discharge should be prevented.

Conflicts of Interest: The author declares no conflict of interest.

References

1. Mandolfino, C.; Lertora, E.; Gambaro, C. Influence of cold plasma treatment parameters on the mechanical properties of polyamide homogeneous bonded joints. *Surf. Coat. Technol.* **2017**, *313*, 222–229. [CrossRef]
2. Bruce, R.L.; Weilnboeck, F.; Lin, T.; Phaneuf, R.J.; Oehrlein, G.S.; Long, B.K.; Willson, C.G.; Vegh, J.J.; Nest, D.; Graves, D.B. Relationship between nanoscale roughness and ion-damaged layer in argon plasma exposed polystyrene films. *J. Appl. Phys.* **2010**, *107*, 084310. [CrossRef]
3. Lin, T.-C.; Bruce, R.L.; Oehrlein, G.S.; Phaneuf, R.J.; Kan, H.-C. Direct and quantitative evidence for buckling instability as a mechanism for roughening of polymer during plasma etching. *Appl. Phys. Lett.* **2012**, *100*, 233113. [CrossRef]
4. Bernardelli, E.A.; Belmonte, T.; Duday, D.; Frache, G.; Poncin-Epaillard, F.; Noël, C.; Choquet, P.; Migeon, H.-N.; Maliska, A. Interaction Mechanisms Between Ar–O$_2$ Post-Discharge and Stearic Acid I: Behaviour of Thin Films. *Plasma Chem. Plasma Process.* **2011**, *31*, 189–203. [CrossRef]
5. Tsougeni, K.; Vourdas, N.; Tserepi, A.; Gogolides, E.; Cardinaud, C. Mechanisms of Oxygen Plasma Nanotexturing of Organic Polymer Surfaces: From Stable Super Hydrophilic to Super Hydrophobic Surfaces. *Langmuir* **2009**, *25*, 11748–11759. [CrossRef] [PubMed]
6. Gogolides, E.; Constantoudis, V.; Kokkoris, G.; Kontziampasis, D.; Tsougeni, K.; Boulousis, G.; Vlachopoulou, M.; Tserepi, A. Controlling roughness: From etching to nanotexturing and plasma-directed organization on organic and inorganic materials. *J. Phys. D Appl. Phys.* **2011**, *44*, 174021. [CrossRef]
7. Vourdas, N.; Kontziampasis, D.; Kokkoris, G.; Constantoudis, V.; Goodyear, A.; Tserepi, A.; Cooke, M.; Gogolides, E. Plasma directed assembly and organization: Bottom-up nanopatterning using top-down technology. *Nanotechnology* **2010**, *21*, 085302. [CrossRef]
8. Mozetič, M. Plasma-Stimulated Super-Hydrophilic Surface Finish of Polymers. *Polymers* **2020**, *12*, 2498. [CrossRef]
9. Šourková, H.; Špatenka, P. Plasma Activation of Polyethylene Powder. *Polymers* **2020**, *12*, 2099. [CrossRef]
10. Sang, J.; Sato, R.; Aisawa, S.; Hirahara, H.; Mori, K. Hybrid joining of polyamide and hydrogenated acrylonitrile butadiene rubber through heat-resistant functional layer of silane coupling agent. *Appl. Surf. Sci.* **2017**, *412*, 121–130. [CrossRef]
11. Tyuftin, A.A.; Kerry, J.P. Review of surface treatment methods for polyamide films for potential application as smart packaging materials: Surface structure, antimicrobial and spectral properties. *Food Packag. Shelf Life* **2020**, *24*, 100475. [CrossRef]
12. Hanusová, J.; Kováčik, D.; Stupavská, M.; Černák, M.; Novák, I. Atmospheric pressure plasma treatment of polyamide-12 foils. *Open Chem.* **2014**, *13*, 382–388. [CrossRef]

13. Károly, Z.; Kalácska, G.; Zsidai, L.; Mohai, M.; Klébert, S. Improvement of Adhesion Properties of Polyamide 6 and Polyoxymethylene-Copolymer by Atmospheric Cold Plasma Treatment. *Polymers* **2018**, *10*, 1380. [CrossRef]

14. Borcia, G.; Anderson, C.A.; Brown, N.M.D. Dielectric barrier discharge for surface treatment: Application to selected polymers in film and fibre form. *Plasma Sources Sci. Technol.* **2003**, *12*, 335–344. [CrossRef]

15. Borcia, G.; Dumitrascu, N.; Popa, G. Influence of helium-dielectric barrier discharge treatments on the adhesion properties of polyamide-6 surfaces. *Surf. Coat. Technol.* **2005**, *197*, 316–321. [CrossRef]

16. Gao, Z.; Sun, J.; Peng, S.; Yao, L.; Qiu, Y. Surface modification of nylon 6 films treated with an He/O$_2$ atmospheric pressure plasma jet. *J. Appl. Polym. Sci.* **2011**, *120*, 2201–2206. [CrossRef]

17. Gao, Z. Modification of surface properties of polyamide 6 films with atmospheric pressure plasma. *Appl. Surf. Sci.* **2011**, *257*, 6068–6072. [CrossRef]

18. Gao, Z.; Peng, S.; Sun, J.; Yao, L.; Qiu, Y. The influence of moisture on atmospheric pressure plasma etching of PA6 films. *Curr. Appl. Phys.* **2010**, *10*, 230–234. [CrossRef]

19. Gao, Z. Influence of environmental humidity on plasma etching polyamide 6 films. *Appl. Surf. Sci.* **2012**, *258*, 5574–5578. [CrossRef]

20. Gao, Z.; Sun, J.; Peng, S.; Yao, L.; Qiu, Y. Surface modification of a polyamide 6 film by He/CF$_4$ plasma using atmospheric pressure plasma jet. *Appl. Surf. Sci.* **2009**, *256*, 1496–1501. [CrossRef]

21. Pappas, D.; Bujanda, A.; Demaree, J.D.; Hirvonen, J.K.; Kosik, W.; Jensen, R.; McKnight, S. Surface modification of polyamide fibers and films using atmospheric plasmas. *Surf. Coat. Technol.* **2006**, *201*, 4384–4388. [CrossRef]

22. Hnilica, J.; Potočňáková, L.; Stupavská, M.; Kudrle, V. Rapid surface treatment of polyamide 12 by microwave plasma jet. *Appl. Surf. Sci.* **2014**, *288*, 251–257. [CrossRef]

23. Kalácska, G.; Zsidai, L.; Keresztes, R.; Tóth, A.; Mohai, M.; Szépvölgyi, J. Effect of nitrogen plasma immersion ion implantation of polyamide-6 on its sliding properties against steel surface. *Wear* **2012**, *290–291*, 66–73. [CrossRef]

24. Kuzminova, A.; Shelemin, A.; Kylián, O.; Choukourov, A.; Valentová, H.; Krakovský, I.; Nedbal, J.; Slavínská, D.; Biederman, H. Study of the effect of atmospheric pressure air dielectric barrier discharge on nylon 6,6 foils. *Polym. Degrad. Stab.* **2014**, *110*, 378–388. [CrossRef]

25. Oliveira, F.R.; Zille, A.; Souto, A.P. Dyeing mechanism and optimization of polyamide 6,6 functionalized with double barrier discharge (DBD) plasma in air. *Appl. Surf. Sci.* **2014**, *293*, 177–186. [CrossRef]

26. Wu, S. Calculation of interfacial tension in polymer systems. *J. Polym. Sci. Part C Polym. Symp.* **1971**, *34*, 19–30. [CrossRef]

27. Wu, S. Polar and Nonpolar Interactions in Adhesion. *J. Adhes.* **1973**, *5*, 39–55. [CrossRef]

28. Oliveira, F.R.; Steffens, F.; Souto, A.P.; Zille, A. Reuse of effluent from dyeing process of polyamide fibers modified by double barrier discharge (DBD) plasma. *Desalin. Water Treat.* **2016**, *57*, 2649–2656. [CrossRef]

29. Oliveira, F.R.; Steffens, F.; de Holanda, P.S.B.; do Nascimento, J.H.O.; Matsui, K.N.; Souto, A.P. Physical, Chemical and Morphological Characterization of Polyamide Fabrics Treated with Plasma Discharge. *Mater. Res.* **2017**, *20*, 60–68. [CrossRef]

30. Bessada, R.; Silva, G.; Paiva, M.C.; Machado, A.V. Functionalization of PET and PA6.6 woven fabrics. *Appl. Surf. Sci.* **2011**, *257*, 7944–7951. [CrossRef]

31. Li, L.; Peng, M.; Teng, Y.; Gao, G. Diffuse plasma treatment of polyamide 66 fabric in atmospheric pressure air. *Appl. Surf. Sci.* **2016**, *362*, 348–354. [CrossRef]

32. Peng, M.; Li, L.; Xiong, J.; Hua, K.; Wang, S.; Shao, T. Study on Surface Properties of Polyamide 66 Using Atmospheric Glow-Like Discharge Plasma Treatment. *Coatings* **2017**, *7*, 123. [CrossRef]

33. Pavliňák, D.; Hnilica, J.; Quade, A.; Schäfer, J.; Alberti, M.; Kudrle, V. Functionalisation and pore size control of electrospun PA6 nanofibres using a microwave jet plasma. *Polym. Degrad. Stab.* **2014**, *108*, 48–55. [CrossRef]

34. Mozetič, M.; Vesel, A. Thermal defunctionalization of an oxygen-plasma-treated polyethersulfone. *Mater. Technol.* **2013**, *47*, 89–92.

35. Boulares-Pender, A.; Thomas, I.; Prager, A.; Schulze, A. Surface modification of polyamide and poly(vinylidene fluoride) membranes. *J. Appl. Polym. Sci.* **2013**, *128*, 322–331. [CrossRef]

36. Recek, N.; Jaganjac, M.; Kolar, M.; Milkovic, L.; Mozetič, M.; Stana-Kleinschek, K.; Vesel, A. Protein Adsorption on Various Plasma-Treated Polyethylene Terephthalate Substrates. *Molecules* **2013**, *18*, 12441–12463. [CrossRef] [PubMed]

37. Rybkin, V.V.; Kuvaldina, E.V.; Smirnov, S.A.; Titov, V.A.; Ivanov, A.N. Kinetic features for the initial stages of interaction of oxygen plasma with the kapton h polyimide surface. *High Energy Chem.* **1999**, *33*, 409–412.

38. Ilić, V.; Šaponjić, Z.; Vodnik, V.; Molina, R.; Dimitrijević, S.; Jovančić, P.; Nedeljković, J.; Radetić, M. Antifungal efficiency of corona pre-treated polyester and polyamide fabrics loaded with Ag nanoparticles. *J. Mater. Sci.* **2009**, *44*, 3983–3990. [CrossRef]

39. Lin, N.H.; Kim, M.; Lewis, G.T.; Cohen, Y. Polymer surface nanostructuring of reverse osmosis membranes for fouling resistance and improved flux performance. *J. Mater. Chem.* **2010**, *20*, 4642–4652. [CrossRef]

40. Ben Salem, D.; Pulpytel, J.; Pillier, F.; Pailleret, A.; Arefi-Khonsari, F. Amorphization and Polymorphism Modification of Polyamide-6 Films via Open-Air Non-Equilibrium Atmospheric Pressure Plasma Jet Treatment. *Plasma Process. Polym.* **2014**, *11*, 961–973. [CrossRef]

41. Reis, R.; Dumée, L.F.; Tardy, B.L.; Dagastine, R.; Orbell, J.D.; Schutz, J.A.; Duke, M.C. Towards Enhanced Performance Thin-film Composite Membranes via Surface Plasma Modification. *Sci. Rep.* **2016**, *6*, 29206. [CrossRef] [PubMed]

42. Bagci, P.O.; Akbas, M.; Gulec, H.A.; Bagci, U. Coupling reverse osmosis and osmotic distillation for clarified pomegranate juice concentration: Use of plasma modified reverse osmosis membranes for improved performance. *Innov. Food Sci. Emerg. Technol.* **2019**, *52*, 213–220. [CrossRef]

43. Ribeiro, A.I.; Senturk, D.; Silva, K.K.; Modic, M.; Cvelbar, U.; Dinescu, G.; Mitu, B.; Nikiforov, A.; Leys, C.; Kuchakova, I.; et al. Antimicrobial Efficacy of Low Concentration PVP-Silver Nanoparticles Deposited on DBD Plasma-Treated Polyamide 6,6 Fabric. *Coatings* **2019**, *9*, 581. [CrossRef]

44. Holländer, A.; Cosemans, P. Surface technology for additive manufacturing. *Plasma Process. Polym.* **2020**, *17*, 1900155. [CrossRef]

45. Doliška, A.; Vesel, A.; Kolar, M.; Stana-Kleinschek, K.; Mozetič, M. Interaction between model poly(ethylene terephthalate) thin films and weakly ionised oxygen plasma. *Surf. Interface Anal.* **2012**, *44*, 56–61. [CrossRef]

46. Vesel, A.; Mozetic, M. New developments in surface functionalization of polymers using controlled plasma treatments. *J. Phys. D Appl. Phys.* **2017**, *50*, 293001. [CrossRef]

47. Vesel, A.; Primc, G.; Zaplotnik, R.; Mozetič, M. Applications of highly non-equilibrium low-pressure oxygen plasma for treatment of polymers and polymer composites on an industrial scale. *Plasma Phys. Control. Fusion* **2020**, *62*, 024008. [CrossRef]

48. Vesel, A.; Zaplotnik, R.; Primc, G.; Mozetič, M. Evolution of the Surface Wettability of PET Polymer upon Treatment with an Atmospheric-Pressure Plasma Jet. *Polymers* **2020**, *12*, 87. [CrossRef]

49. Vesel, A.; Zaplotnik, R.; Kovac, J.; Mozetic, M. Initial stages in functionalization of polystyrene upon treatment with oxygen plasma late flowing afterglow. *Plasma Sources Sci. Technol.* **2018**, *27*, 094005. [CrossRef]

50. Ricard, A.; Gaillard, M.; Monna, V.; Vesel, A.; Mozetic, M. Excited species in H_2, N_2, O_2 microwave flowing discharges and post-discharges. *Surf. Coat. Technol.* **2001**, *142*, 333–336. [CrossRef]

51. Vesel, A.; Mozetic, M.; Strnad, S.; Peršin, Z.; Stana-Kleinschek, K.; Hauptman, N. Plasma modification of viscose textile. *Vacuum* **2009**, *84*, 79–82. [CrossRef]

52. Primc, G.; Mozetič, M. Neutral reactive gaseous species in reactors suitable for plasma surface engineering. *Surf. Coat. Technol.* **2019**, *376*, 15–20. [CrossRef]

Defluorination of Polytetrafluoroethylene Surface by Hydrogen Plasma

Alenka Vesel [1,*] iD **, Dane Lojen** [1,2] **, Rok Zaplotnik** [1] iD **, Gregor Primc** [1] iD **, Miran Mozetič** [1] iD **,
Jernej Ekar** [1,2] **, Janez Kovač** [1] **, Marija Gorjanc** [3] iD **, Manja Kurečič** [4] **and Karin Stana-Kleinschek** [5] iD

1   Department of Surface Engineering, Jozef Stefan Institute, Jamova cesta 39, 1000 Ljubljana, Slovenia;
    dane.lojen@ijs.si (D.L.); rok.zaplotnik@ijs.si (R.Z.); gregor.primc@ijs.si (G.P.); miran.mozetic@ijs.si (M.M.);
    jernej.ekar@ijs.si (J.E.); janez.kovac@ijs.si (J.K.)
2   Jozef Stefan International Postgraduate School, Jamova cesta 39, 1000 Ljubljana, Slovenia
3   Faculty of Natural Sciences and Engineering, University of Ljubljana, Aškerčeva cesta 12,
    1000 Ljubljana, Slovenia; marija.gorjanc@ntf.uni-lj.si
4   Faculty of Mechanical Engineering, University of Maribor, Smetanova 17, 2000 Maribor, Slovenia;
    manja.kurecic@um.si
5   Institute of Chemistry and Technology of Biobased Systems, Graz University of Technology,
    Rechbauerstraße 12, 8010 Graz, Austria; karin.stanakleinschek@tugraz.at
*   Correspondence: alenka.vesel@guest.arnes.si

Abstract: Defluorination of polytetrafluoroethylene (PTFE) surface film is a suitable technique for tailoring its surface properties. The influence of discharge parameters on the surface chemistry was investigated systematically using radio-frequency inductively coupled H_2 plasma sustained in the E- and H-modes at various powers, pressures and treatment times. The surface finish was probed by X-ray photoelectron spectroscopy (XPS) and time-of-flight secondary ion mass spectrometry (ToF-SIMS). The measurements of water contact angles (WCA) showed increased wettability of the pristine PTFE; however, they did not reveal remarkable modification in the surface chemistry of the samples treated at various discharge parameters. By contrast, the combination of XPS and ToF-SIMS, however, revealed important differences in the surface chemistry between the E- and H-modes. A well-expressed minimum in the fluorine to carbon ratio F/C as low as 0.2 was observed at the treatment time as short as 1 s when plasma was in the H-mode. More gradual surface chemistry was observed when plasma was in the E-mode, and the minimal achievable F/C ratio was about 0.6. The results were explained by the synergistic effects of hydrogen atoms and vacuum ultraviolet radiation.

1. Introduction

Fluorinated polymers are used in various applications [1]. They are renowned for their chemical inertness and thermal stability [2]. The chemical inertness does not allow for reasonable adhesion of any coating deposited by numerous techniques [3,4]. Whatever material is deposited, the surface energy of the coating is much larger than the energy of the substrate; therefore, thin films tend to form 3D particles spontaneously rather than a uniform film. Coatings from liquid solutions also do not adhere well on the surface, especially when the liquid is polar, i.e., water. In order to improve the adhesion of coatings, methods for increasing the surface energy of fluorinated polymers have been invented [5–10]. Fluorinated polymers are usually treated with aggressive chemicals which

cause modification of the surface chemistry. Such techniques were invented in the 1960s, and some are still used nowadays. Common techniques include the application of sodium naphthalide [11], tetraalkylammonium radical anion salt, alkali metal vapours and amalgams [12], and electrochemical methods [13,14]. All these techniques represent an ecological hazard; therefore, researchers have been working on alternative techniques. A straightforward solution is irradiation of fluorinated polymers with beams of photons, electrons, or ions [15,16]. The insulating properties of fluorinated polymers make the techniques employing charged particles rather difficult, however.

A medium that contains both electrons, positively charged ions, and photons is gaseous plasma. Gaseous plasma is a state of gas also consisting of neutral particles (thereafter: radicals), which are chemically extremely reactive. For example, diatomic molecules are partially dissociated upon plasma conditions, and the atoms typically interact with most of the polymers even at room temperature. The atoms may bind to the surface of a polymer, thus forming functional groups of different polarity than those presented in fluorinated polymers. For example, oxygen plasma of a high density of oxygen atoms will cause functionalization of most polymers with various oxygen-containing functional groups [17]. While such treatments with oxygen plasma perform well for most types of polymers, they fail in the case of polytetrafluoroethylene (PTFE) for one simple reason: the binding energy of fluorine to carbon atoms is much larger than those of oxygen; therefore, a simple substitution of fluorine atoms on the surface of PTFE with oxygen atoms is energetically unfavourable. Treatment of fluorinated polymers by oxygen plasma will cause gradual etching of the polymer material rather than surface activation, as shown recently by Primc et al. [18].

Because classical plasma techniques fail in the case of PTFE, researchers have invented a variety of alternative methods. As early as 1987, Clark et al. [14] used a high vacuum plasma reactor to treat PTFE samples with hydrogen plasma. A radiofrequency (RF) generator coupled in a capacity mode was used for plasma generation. The maximum power was 10 W, and the treatment times were up to approximately 250 s. Upon such conditions, the surface film of PTFE was depleted of fluorine, which was proven by X-ray photoelectron spectroscopy (XPS). The water contact angle (WCA) showed moderate hydrophilicity of the treated samples after prolonged treatment. The minimum WCA was 50°. The authors explained the fluorine depletion by the interaction between hydrogen atoms and PTFE, causing the formation of HF molecules that were pumped away from the system.

About a decade later, Badey et al. [19] performed similar experiments, except that they used a powerful microwave (MW) generator for sustaining a dense plasma in a narrow quartz tube. PTFE samples were placed downstream from the centre of the discharge. The best results were observed at large gas flows and moderate discharge powers. The F/C ratio dropped from an original 2.45 to about 0.8. The WCA of water dropped from 115° to approximately 85° and diiodomethane from 84° to approximately 50°. The surface modifications were also monitored by secondary ion mass spectrometry (SIMS), and the authors found numerous C_xH_y peaks after accomplishing the remote plasma treatment. As by Clark et al. [14], Badey et al. [19] also explained the observed results by the interaction between the polymer surface and neutral hydrogen atoms, causing the formation of HF molecules. In the same year, Yamada et al. [20] also applied remote H_2 plasma treatment for the modification of PTFE samples. The plasma source was inductively coupled RF discharge. As by Badey et al. [19], the authors used a quartz tube for the discharge chamber and placed samples in the afterglow region. The authors reported similar results as Badey at large discharge powers. They also performed XPS characterization and found similar functional groups as Badey. The same group also used remote hydrogen plasma treatment to study the adhesion of Cu film on PTFE samples [21]. They obtained the minimum WCA of approximately 75° at the treatment time of approximately 2 min. In another paper, Inagaki et al. [22], used pulsed plasma treatment. An capacitiveRF discharge in the power range between 75 and 100 W was applied at the pressure of 13 Pa. The results and WCAs were slightly larger than in the case of using continuous plasma treatment. The same applied to the F/C ratio.

König et al. [23] used plasmas sustained in various gases for modification of a plasma-deposited fluorocarbon polymer with the structure close to PTFE. Plasma was sustained by a MW discharge in the

electron cyclotron resonance (ECR) mode. The working pressure was as low as 0.2 Pa. The maximum discharge power was 800 W. Samples were additionally biased using a capacitively coupled RF generator. The F/C ratio as deduced from the XPS survey spectra was 1.9 for the untreated material and dropped to 0.72 for plasma-treated samples. Simultaneously, the oxygen to carbon ratio O/C increased from 0.02 to 0.09. Such a surface finish enabled a slight decrease of WCA from the original 106° down to about 86°.

Tanaka et al. [24] investigated defluorination of PTFE by a combination of atmospheric pressure glow plasma treatment and a chemical transport method. Plasma was sustained in a mixture of He and H_2. The lowest F/C ratio reported for such plasma treatment was 0.4. The addition of oxygen in the gas mixture caused a further drop of the F/C concentration and appearance of a few atomic % of oxygen. More recently, Hunke et al. [25] performed direct treatment of PTFE powders in a low-pressure hydrogen plasma. They used a MW discharge and obtained a moderate decrease in the F/C ratio. The authors adopted the explanation provided previously by Inagaki et al. [22].

The review of the early work can be summarized as follows: the defluorination of PTFE surface occurs upon treatment with hydrogen plasma or its flowing afterglow and is explained by the interaction of hydrogen atoms with pristine material causing the formation of a dangling bond on one C atom. The dangling bond is quickly occupied with another H atom, forming the CHF group. This group may decompose by desorption of the HF molecule, and the result is the formation of the CF=CF group. The abundance of H atoms causes the gradual transformation of the polymer surface. A typical treatment time needed for observing a rather low F/C ratio is of the order of a minute.

In the present paper, we disclose experiments with hydrogen plasma performed in the same reactor at different conditions. Gaseous plasma was created in different discharge modes; therefore, some plasma parameters depended enormously on discharge conditions.

2. Materials and Methods

PTFE foils were purchased from Goodfellow Ltd. (Huntingdon, UK). The foils with a thickness of 0.5 mm were cut to pieces of 10×10 mm^2 and cleaned with ethanol, followed by drying at ambient conditions.

PTFE was treated in a glass discharge chamber using an electrodeless radio-frequency (RF) discharge. A schematic of the discharge chamber is shown in Figure 1. The discharge chamber was a long glass tube with a diameter of 4 cm. It was pumped on one side, and on the other side, H_2 gas was introduced through the flow controller. The vacuum system was sealed with rubber gaskets. It was pumped with a two-stage rotary pump of a nominal pumping speed of 80 m^3/h. The experimental conditions, therefore, enabled achieving the ultimate pressure just below 1 Pa after pumping for a reasonable time. Optical emission spectroscopy (OES) was used to check any gaseous impurities in the discharge chamber. Spectral features of any trace gases were below the detection limit of the spectrometer; therefore, the system was hermetically tight, and the residual atmosphere contained water vapour only. Plasma was sustained within the coil, as shown in Figure 1 and diffusing plasma expanded far away from the coil. The coil was connected to the RF generator via a matching network. The matching network allowed for coupling optimization to run the plasma mostly in the H-mode, depending on the power. The generator operated at the standard frequency of 13.56 MHz and adjustable output power up to 1000 W. The samples were treated at various conditions, i.e., various powers from 100 to 1000 W, hydrogen pressures from 10 to 60 Pa, and treatment times from 0.5 to 12 s.

The surface wettability of samples was measured using a Drop Shape Analyser DSA-100 (Krüss GmbH, Hamburg, Germany). A static contact angle was measured using a sessile drop method. The volume of a drop was 1 μL. MiliQ water was used for determination of the wettability.

Surface modifications were probed by XPS and time-of-flight secondary ion mass spectrometry (ToF-SIMS). The XPS characterization was performed using an XPS instrument (model TFA XPS from Physical Electronics, Münich, Germany). The samples were irradiated with monochromatic Al K$\alpha_{1,2}$ radiation with the photon energy of 1486.6 eV. Spectra were measured at an electron take-off angle

(TOA) of 45°. Selected samples were also measured at various TOAs to manipulate the detection depth of XPS. Survey spectra were acquired at a pass-energy of 187 eV using an energy step of 0.4 eV. High-resolution carbon C1s spectra were measured at a pass-energy of 23.5 eV using an energy step of 0.1 eV. An additional electron gun was used for compensation of the surface charge. Spectra were calibrated by adjusting the C1s peak corresponding to CF_2 groups to 292 eV. The measured spectra were analyzed using MultiPak v8.1c software (Ulvac-Phi Inc., Kanagawa, Japan, 2006) from Physical Electronics, which was supplied with the spectrometer. Linear background subtraction was used.
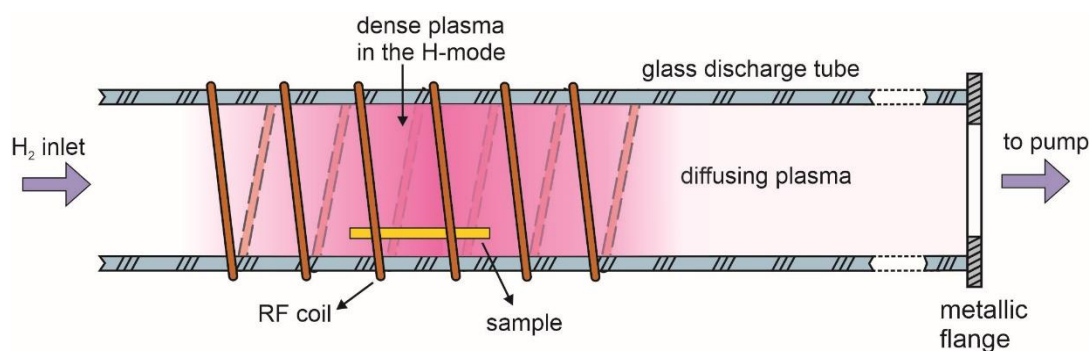
Figure 1. Schematic of the plasma set-up.

ToF-SIMS analyses were performed using a ToF-SIMS 5 instrument (ION-TOF, Münster, Germany) equipped with a bismuth liquid metal ion gun with a kinetic energy of 30 keV. The analyses were performed in an ultra-high vacuum of approximately 10^{-7} Pa. The ToF-SIMS spectra were measured by scanning a Bi^{3+} cluster ion beam over the surface spot of approximately 100×100 μm^2. An electron gun was used to allow for charge compensation on the sample surfaces during the analysis. Positive and negative ion spectra were measured

3. Results and Discussion

3.1. Modification of the Surface Wettability

Samples were placed at different positions along the discharge tube to measure the gradient in the surface wettability. Some of them were placed inside the RF coil, and many were placed away from the coil, in the direction of the pump duct. The water contact angle was measured for all these samples, and the result is presented in Figure 2. Plasma treatment time in all cases was 1 s, the hydrogen pressure was 25 Pa, and the discharge power was 400 W. The WCA for the untreated sample was approximately 110°. One can observe a gradual increase in the WCA with the increasing distance from the RF coil. The samples treated within the coil assume the WCA of approximately 83°, which is the value already reported by previously cited authors. This value is typical for oxygen-free polymers such as polyolefins. Such a rather low WCA extends a few cm away from the coil, which is explained by the simple fact that a dense plasma in the H-mode was not limited to the coil only, but also stretched outside of the coil as shown schematically in Figure 1. Away from the coil, the WCA increases to approximately 100° within a distance of several cm. Thereafter, the WCA increases rather linearly with increasing distance, and at large distances approaches the value typical for the untreated sample. The measured points scatter somehow, but the trend is obvious and is presented by straight lines. The results summarized in Figure 2, therefore, suggest almost complete defluorination of the PTFE samples upon treatment with a dense, glowing hydrogen plasma, and a more gradual activation upon treatment with a diffusing plasma, which in our case is a result of a weak capacitive coupling between the coil and the metallic pump duct.
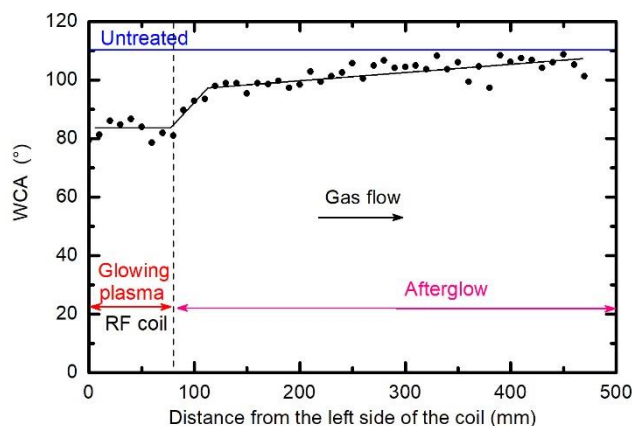
Figure 2. Variation of water contact angle (WCA) on the polytetrafluoroethylene (PTFE) surface of the samples arranged along the discharge tube. The treatment time was 1 s, the hydrogen pressure was 25 Pa, and the discharge power was 400 W.

As already reported by numerous authors, the WCA depends on numerous treatment parameters, including the treatment time, the pressure, and the power absorbed by the gaseous plasma [20–22,26,27]. To get additional information about the evolution of the surface wettability, we treated several samples inside the RF coil at various conditions. Figure 3 represents the WCA versus plasma treatment time. We adopted the same parameters as in Figure 2, i.e., the pressure of 25 Pa and the power of 400 W. It seems that the WCA in Figure 3 does not really depend on treatment time at these particular discharge conditions. All values lay at approximately 90°, with the exception of the first measurement corresponding to the lowest treatment time of 0.5 s where the standard deviation is rather large. The almost constant WCA, as revealed from Figure 3, is explained by the saturated defluorination of the surface. This effect will be further discussed later. Figure 4 is a plot of the WCA versus the discharge power for the treatment time of 1 s and the pressure of 25 Pa. Again, one can observe a rather constant WCA, except for the measurement performed at the lowest power of 100 W. The WCA also does not depend much on the H_2 pressure in the discharge tube, as shown in Figure 5. Figures 3–5, therefore indicate that the surface activation is accomplished within the second of plasma treatment providing the discharge power is reasonably large, and the pressure is in the range between 10 and 60 Pa.
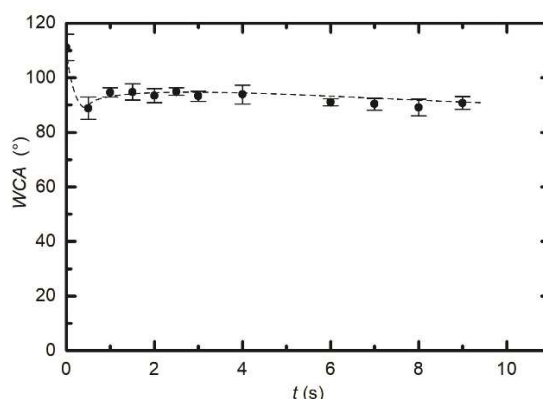
Figure 3. Variation of surface wettability with treatment time. The samples were inside the radiofrequency (RF) coil. Discharge power and hydrogen pressure were constant at 400 W and 25 Pa, respectively.
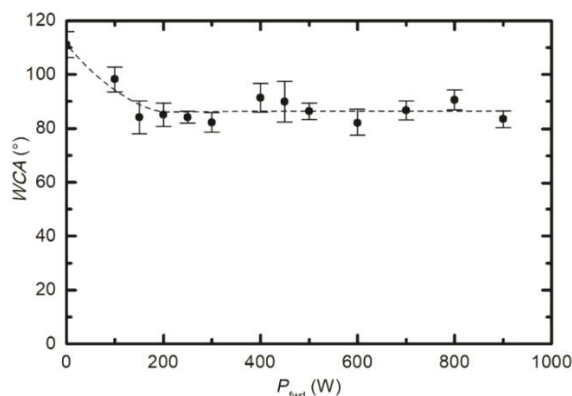
Figure 4. Variation of surface wettability with the forward discharge power. Treatment time and hydrogen pressure were constant at 1 s and 25 Pa, respectively.
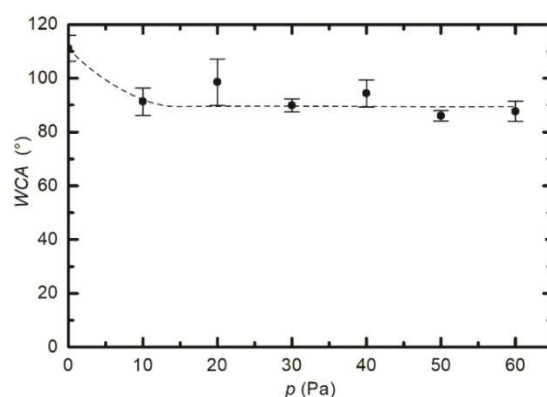
Figure 5. Variation of surface wettability with hydrogen pressure. Treatment time and discharge power were constant at 1 s and 400 W, respectively.

The water contact angles, as observed from Figures 2–5, indicate a rather marginal increase of the PTFE wettability, i.e., the WCA remained above 80°. Such a WCA was reported already by Badey at al. [4] and Konig at al. [8]. Somehow lower WCA of 75° was reported by Yamada et al. [5], and the WCA of about 50° was found by Clark et al. [2]. The discrepancy was explained recently by Primc [3] who showed that the WCA on the surface of fluorinated polymers depends on the concentration of other elements. Even a small concentration of oxygen, for example, caused a decrease of the WCA below the values typical for polyolefins (about 80°).

The results of the surface wettability as probed by the WCA do not show any obvious trend. Because this technique does not reveal the chemical modifications taking place on the sample surface upon plasma treatment, we additionally performed research on the composition and structure of the surface film as probed by XPS and ToF-SIMS to further elaborate details about the surface chemistry.

3.2. Chemical Modifications as Determined by X-ray Photoelectron Spectroscopy (XPS)

Figure 6 shows the XPS F/C ratio versus the treatment time when plasma was sustained at a large power of 400 W (lower curve) and at low power of 100 W (upper curve). See also supplementary Figures S1 and S2 showing individual survey spectra and elemental composition versus treatment time. The upper curve of Figure 6 corresponds to the same experimental conditions as the WCA measurement at the discharge power of 100 W in Figure 4, which reveals incomplete activation of the surface at 100 W after the treatment for 1 s. Examining Figure 6, it is obvious that incomplete surface activation is a consequence of the insufficient removal of fluorine from the surface of PTFE, because the F/C concentration after the treatment for 1 is still about 1.25, thus far from complete defluorination.
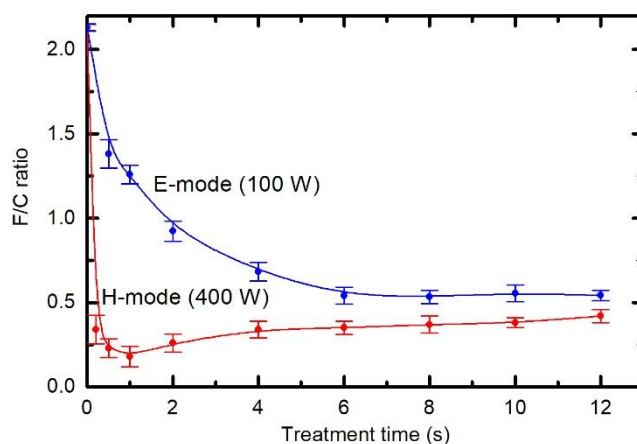
Figure 6. Variation of the X-ray photoelectron spectroscopy (XPS) F/C ratio versus treatment time for two different powers. Hydrogen pressure was constant at 25 Pa.

The upper curve in Figure 6 shows a gradual decrease of the F/C ratio with increasing treatment time. Gaseous plasma at the pressure of 25 Pa and RF power of 100 W is sustained in the E-mode. Because the matching network was optimized for coupling in the H-mode, a significant fraction of the RF power was reflected and thus not absorbed by the gaseous plasma. The power absorbed in plasma for the case of the upper curve of Figure 6 is, therefore, well below 100 W. Still, the surface film as probed by XPS is depleted of fluorine even after several seconds of plasma treatment and approaches a value of approximately 0.6. It seems that such a concentration of fluorine is about all one can achieve upon treatment of PTFE in hydrogen plasma sustained in the E-mode.

The mechanism is completely different when plasma is sustained in the H-mode (lower curve). In this case, the surface film is depleted of fluorine even after approximately 0.2 s of plasma treatment. The F/C ratio further decreases with increasing treatment time until a minimum at approximately 1 s appears. Thereafter, a gradual but slow increase in the F/C ratio is observed. After approximately 10 s, the F/C ratio assumes a value of approximately 0.4. This value is lower than what is achievable in the E-mode.

A huge difference in the surface composition between the E- and H-modes, as evident from Figure 6, should be explained by different mechanisms. Gaseous plasma in the H-mode is an extensive source of vacuum ultraviolet (VUV) radiation [28]. Recently, Fantz et al. investigated the details regarding the radiation arising from H_2 plasma sustained by an inductively coupled RF discharge in the H-mode [29]. The discharge configuration was almost identical to the one shown in Figure 1. Fantz et al. showed that approximately 10% of the available discharge power is transformed into radiation in the VUV range. This radiation causes bond scission in the surface film of a thickness of the order of a penetration depth for VUV photons. The penetration depth depends on the wavelength (i.e., photon energy) but is definitely larger than the escape depth of photoelectrons. By considering this fact, one can assume a rather homogenous treatment of the surface film with the VUV. The bond scission enables further reactions, including the interaction with H atoms. The H atoms attack the dangling bonds as already reported by Badey et al. [19]. Furthermore, they interact with F atoms forming HF molecules, which are desorbed upon vacuum conditions and pumped away. The combination of bond scission caused by absorption of VUV radiation and chemical interaction with H atoms should, therefore, ensure an F-free surface. Such an effect cannot be confirmed from XPS measurements because of the final escape depth of photoelectrons. It will be shown later in this paper that the best technique to prove the F-free surface is ToF-SIMS.

After prolonged treatment of PTFE samples in the H-mode, the F/C ratio does not remain constant but increases slowly with increasing treatment time. Such an increase may be explained by a different thickness of the F-depleted surface film rather than by incomplete defluorination. This effect will be explained later by using angular-resolved XPS characterization (AR-XPS).

When plasma is in the E-mode, the minimum in the F/C ratio is not observed, which may be a consequence of the fact that such plasma is not a significant source of VUV radiation. The luminosity of plasma in the E-mode is typically 3–4 orders of magnitude lower than in the H-mode at this pressure, i.e., 25 Pa. The difference in plasma luminosities between the E- and H-modes normally increases with increasing pressure, as shown by Fantz et al. [29]. The F/C ratio, however, does not deviate for orders of magnitude but is comparable for long treatment times. The comparison of the two curves in Figure 6, therefore, indicate that the intensive VUV radiation only accelerates defluorination of the surface film. A rather low F/C ratio observed after the treatment in the E-mode should be because of other mechanisms. It was already mentioned that H atoms attack the polymer surface and dangling bonds, causing the formation of the volatile HF molecule. Badey et al. [19], as well as Yamada et al. [20], investigated the evolution of the F/C ratio in the flowing afterglow where VUV radiation is negligible, but the density of H atoms is still significant. They found moderate F/C ratios of approximately 0.8. Somehow, lower F/C ratio was also reported by König et al. [23]. Unlike VUV radiation, the H atoms do not penetrate into the solid polymer; therefore, the chemical modification should be limited to a thinner film in the E-mode as compared to the H-mode. Such a difference in the thickness of the well-affected film can explain the fact that the achievable F/C ratio in the E-mode is lower than in the H-mode. A confirmation for the statement about the F-free surface for the H-mode is provided in Figure 7, which shows the F/C ratios as deduced from AR-XPS. The lower curve is for the sample treated for 1 s in the H-mode, whereas the upper for the sample treated for the same time in the E-mode. The F/C ratio in the H-mode gradually increases with increasing take-off angle θ (TOA). Detection depth (d) is given by the following relation, $d = 3\lambda \cdot \sin(\theta)$, where λ is the inelastic mean free path of photoelectrons. The detection depth thus increases with increasing TOA. The gradual increase in the F/C ratio is explained by the formation of the almost F-free surface as well as a subsurface layer with a thickness close to the detection depth of XPS. Extrapolation of the lower curve to the TOA $\theta = 0°$ reveals the F/C ratio is practically zero on the surface. Unfortunately, measurements at extremely low TOA are not feasible.
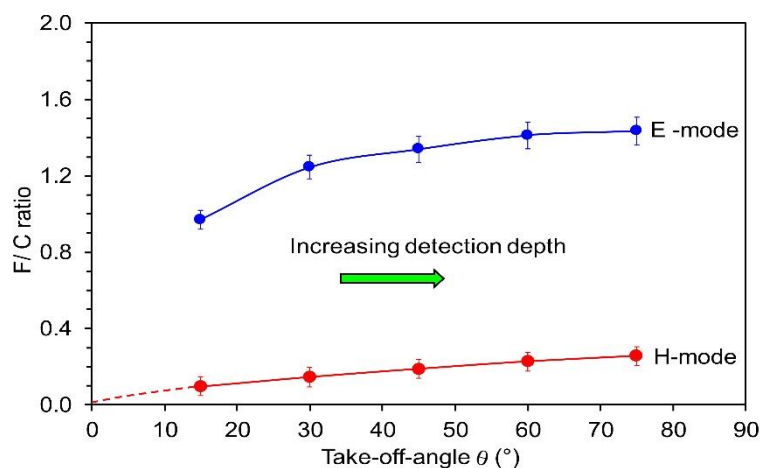
Figure 7. Variation of the AR-XPS F/C ratio versus the photoelectron take-off angle for two different powers and the same pressures of 25 Pa and treatment times of 1 s.

As shown before in Figure 6, a defluorination is incomplete when plasma is in the E-mode for 1 s. The upper curve in Figure 7 confirms this. However, it is interesting that the F/C ratio in Figure 7 increases by a factor of approximately 1.5 when the TOA is increased from $\theta = 15$ to $75°$. Obviously, the surface film contains much less fluorine than the subsurface one, and there is a significant gradient in F concentration. Any extrapolation of the curve towards the TOA $\theta = 0°$ would be speculation; therefore, it is not shown in Figure 7.

Figures 6 and 7 indicate large differences in surface chemistry, depending on the type of discharge. The differences can be further elaborated by performing measurements at a fixed treatment time and

pressure, but different RF powers. The result is plotted in Figure 8. Here, the F/C ratio reaches the minimum at 400 W. At larger powers, the F/C is somehow slightly larger. The behaviour of the curve for powers between 400 and 900 W is similar to the lower curve in Figure 6. In both cases, the fluence of VUV radiation increases with increasing value at the abscissa. More interesting is the behaviour at lower powers. One can observe a gradual and rather linear decrease of the F/C ratio with increasing power. The discharge power of 300 W results in the F/C ratio of approximately 0.5, similar to what is observed in Figure 6 for the upper curve after prolonged plasma treatment. Comparison of Figures 6 and 8, therefore, indicates that the key parameter governing the surface chemistry is the fluence of reactive species and/or VUV radiation rather than discharge power or treatment times. Nonetheless, it is important that the surface finish in the E-mode as deduced from XPS is different to that in the H-mode. In addition to Figure 8, see also supplementary Figures S3 and S4 showing individual survey spectra and elemental composition versus the discharge power.
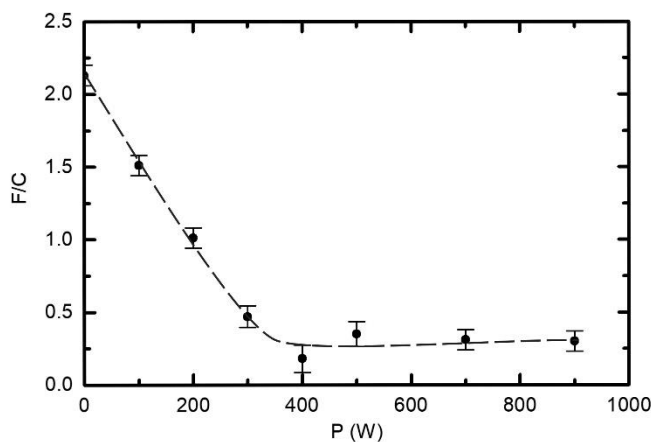
Figure 8. Variation of the F/C ratio versus the discharge power. Treatment time and H_2 pressure were constant at 1 s and 25 Pa, respectively.

The variation of the F/C ratio versus the discharge power (Figure 8) is different to the behaviour of WCA (Figure 4). Comparison of Figures 4 and 8 indicates that even an incomplete defluorination causes the drop of the water contact angle to values typical for polyolefins.

Figure 9 reveals the high-resolution C1s spectra for the untreated sample and samples treated in the H-mode for 1 and 12 s. There is a huge difference between the untreated and treated samples. The untreated sample contains only carbon bonded in CF_2 groups. The C1s peak, therefore, appears at a binding energy of approximately 292 eV. There is also a small peak at approximately 285 eV, which corresponds to surface impurities. The treated samples exhibit the opposite behaviour—the major peak is at about 285 eV, whereas some features also persist at higher binding energies up to approximately 294 eV. Taking into account Figure 7, and the discussion thereafter, it can be concluded that the features correspond to degraded PTFE-like film, whereas the main peak at 285 eV corresponds to F-depleted surface film. Therefore, we can conclude that the surface film of samples treated in H_2 plasma in the H-mode contains olefin-like carbon. It is interesting that the intensity in the range of binding energies from about 287 and 294 eV is slightly larger for the case of 12 s than for 1s of plasma treatment. The reasons for this have already been elaborated when explaining the behaviour of the lower curve in Figures 6 and 7.

By considering the upper discussion, the C1s peak of samples treated in the E-mode should differ from those in the H-mode. Figure 10 represents solid proof of the evolution of the surface chemistry upon treatment of PTFE samples in the E- and H-modes. The behaviour of the two curves at 400 and 800 W was already explained. Interesting, and sound with the previous discussion, is the behaviour of the curves acquired after the treatment at discharge powers of 100 and 200 W. In both cases, plasma was in the E-mode. The curve at 100 W indicates that the rather intact PTFE still persists, but a fraction is

already modified enough to form various carbon chemistries including intermediate ones, as already reported by Badey et al. [19]. A well-expressed peak is observed at approximately 292 eV, as well as a broad feature between 292 and 285 eV. This indicates that CH groups have already appeared on the surface, but the thin surface film also contains other groups with binding energies between 292 and 285 eV. The spectrum corresponding to treatment at 200 W shows a gradual deviation from the untreated PTFE to a surface film of polyolefin-like structure. As discussed above and in keeping with the observations in Figures 6 and 7, the thickness of the F-free surface film in the E-mode is much lower than the escape depth of photoelectrons, so the significant contribution of photoelectrons with binding energies of 292 eV still persists. In between the two well-defined peaks at 292 and 285 eV, there is a rich structure, which could be deconvoluted almost arbitrarily taking into account a variety of functional groups as well as peculiarities of XPS regarding the interpretation of F-containing functional groups [30]. For this reason, we made no attempt to deconvolute C1s peaks shown in Figure 10.
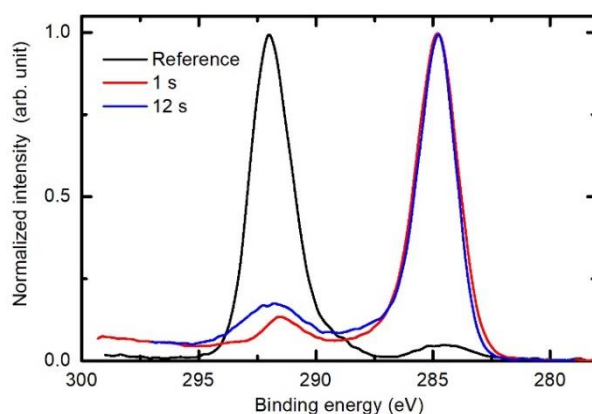
Figure 9. Comparison of XPS high-resolution C1s spectra of the untreated PTFE, and PTFE exposed to H_2 plasma for 1 and 12 s. The discharge power and the pressure were constant at 400 W and 25 Pa, respectively.
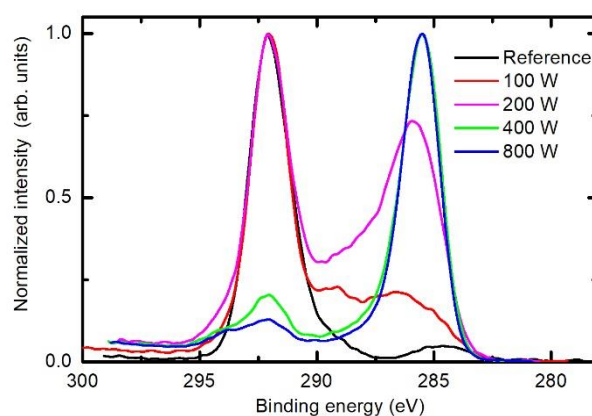
Figure 10. Comparison of the selected XPS high-resolution C1s spectra of the PTFE samples treated for various powers. The treatment time and the pressure were constant at 1 s and 25 Pa, respectively.

3.3. Chemical Modifications as Determined by Time-of-Flight Secondary Ion Mass Spectrometry (ToF-SIMS)

Deconvolution of C1s XPS spectra of fluorinated samples definitely represents a scientific challenge. Therefore, it is useful to characterize selected samples also with an alternative technique, such as ToF-SIMS. The evolution of the ToF-SIMS spectral features was investigated systematically for the treatment time of 1 s and hydrogen pressure of 25 Pa. We varied the discharge power to obtain further insight into the surface chemistry. Some examples of the selected positive in negative ion spectra of the samples are shown in Supplementary Figures S5–S8. Figure 11 shows the selective negative ion

intensities and Figure 12 positive ion intensities. One can observe a gradual decreasing of the F^{2-} intensity versus the discharge power. This behaviour indicates depletion of the surface film as probed by ToF-SIMS. It should be noted that the surface sensitivity of ToF-SIMS is superior in comparison to XPS. Simultaneous to decreasing of the F^{2-} intensity, a number of fluorine-free ions appear in the ToF-SIMS negative ion spectra. All of them keep increasing with increasing discharge power up to the power of 400 W. Thereafter, the intensity of fluorine-free ions in ToF-SIMS spectra remains constant. This observation is in keeping with results presented in Figure 11, where exactly the same effect was observed. Unfortunately, ToF-SIMS does not allow for reliable quantification of the measured spectra. The drop of the intensity of F^{2-} for more than a factor of 50 indicates practically F-free surface.
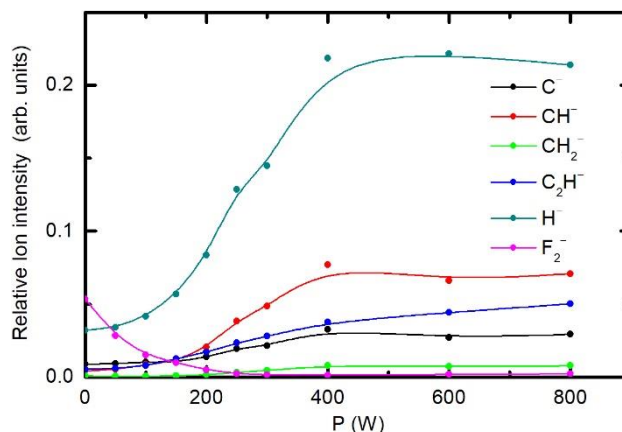
Figure 11. Variation of time-of-flight secondary ion mass spectrometry (ToF-SIMS) intensities of selected negative ions. The pressure was 25 Pa and treatment time 1 s.
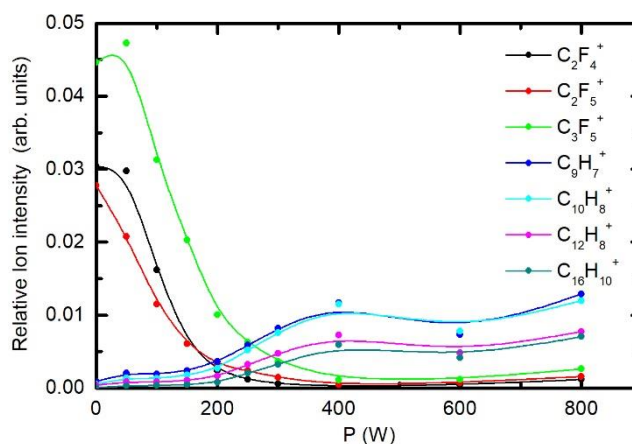
Figure 12. Variation of ToF-SIMS intensities of selected positive ions. The pressure was 25 Pa and treatment time 1 s.

Figure 12 shows the behaviour of positive ion fragments. The intensities of F-containing ions decreases monotonously with increasing discharge power, and the minimum is observed at the power of 400 W. By contrast, the ions containing hydrogen increase gradually up to the power of 400 W and remain fairly intact thereafter. The ToF-SIMS results are, therefore, in keeping with those obtained by XPS.

4. Conclusions

Systematic characterization of PTFE was performed to reveal the kinetics of fluorine depletion of the surface film of this polymer upon treatment with hydrogen plasma at various conditions. Unlike previous authors, we concentrated on rather short treatment times of the order of a second.

Such short times are attractive for any application of gaseous plasma technology for surface processing of products made from fluorinated polymers. A broad range of parameters was found useful for the depletion of the surface film. Nominal discharge powers of the RF generator of as low as 100 W are capable of depletion of the surface film within several seconds of plasma treatment. The intensity of surface chemical reactions increases with increasing discharge power, and the reactions become almost instant once the discharge is in the H-mode. A significant difference in the surface finish between the discharge modes was observed. In the case the discharge is in the E-mode, the F concentration decreases monotonously with increasing treatment time, and the minimal achievable F/C ratio is just above 0.5. By contrast, when the plasma is in the H-mode, a well-defined minimum in the F concentration occurs at rather short treatment times. The minimal F/C ratio as deduced from the XPS spectra acquired at standard take-off angle is about 0.2. The surface layer of the polymer, however, is almost free from fluorine, which is proved by ARXPS as well as by the behaviour of specific ion fragments acquired by ToF-SIMS. Experiments performed at different discharge conditions qualitatively indicate that the key parameter governing the surface finish is the fluence of reactive plasma species. Unfortunately, our experimental set-up did not allow for reliable determination of the radiation in the VUV range. The surface finish versus the fluence of VUV radiation upon treatment of fluorinated polymers with hydrogen plasma, therefore, remains a scientific challenge.

References

1. Améduri, B. The promising future of fluoropolymers. *Macromol. Chem. Phys.* **2020**, *221*, 1900573. [CrossRef]
2. McKeen, L.W. Chapter 11—Fluoropolymers. In *Fatigue and Tribological Properties of Plastics and Elastomers*, 2nd ed.; McKeen, L.W., Ed.; William Andrew Publishing: Oxford, UK, 2010; pp. 249–264. [CrossRef]
3. Ohkubo, Y.; Shibahara, M.; Nagatani, A.; Honda, K.; Endo, K.; Yamamura, K. Comparison between adhesion properties of adhesive bonding and adhesive-free adhesion for heat-assisted plasma-treated polytetrafluoroethylene (PTFE). *J. Adhes.* **2020**, *96*, 776–796. [CrossRef]
4. Badey, J.P.; Espuche, E.; Jugnet, Y.; Chabert, B.; Duct, T.M. Influence of chemical and plasma treatments on the adhesive properties of PTFE with an epoxy resin. *Int. J. Adhes. Adhes.* **1996**, *16*, 173–178. [CrossRef]

5. Lee, S.W.; Hong, J.W.; Wye, M.Y.; Kim, J.H.; Kang, H.J.; Lee, Y.S. Surface modification and adhesion improvement of PTFE film by ion beam irradiation. *Nucl. Instrum. Methods Phys. Res. B* **2004**, *219*, 963–967. [CrossRef]

6. Baumgärtner, K.M.; Schneider, J.; Schulz, A.; Feichtinger, J.; Walker, M. Short-time plasma pre-treatment of polytetrafluoroethylene for improved adhesion. *Surf. Coat. Technol.* **2001**, *142*, 501–506. [CrossRef]

7. Koh, S.-K.; Park, S.-C.; Kim, S.-R.; Choi, W.-K.; Jung, H.-J.; Pae, K.D. Surface modification of polytetrafluoroethylene by Ar+ irradiation for improved adhesion to other materials. *J. Appl. Polym. Sci.* **1997**, *64*, 1913–1921. [CrossRef]

8. Hopp, B.; Kresz, N.; Kokavecz, J.; Smausz, T.; Schieferdecker, H.; Döring, A.; Marti, O.; Bor, Z. Adhesive and morphological characteristics of surface chemically modified polytetrafluoroethylene films. *Appl. Surf. Sci.* **2004**, *221*, 437–443. [CrossRef]

9. Ohkubo, Y.; Ishihara, K.; Shibahara, M.; Nagatani, A.; Honda, K.; Endo, K.; Yamamura, K. Drastic improvement in adhesion property of polytetrafluoroethylene (PTFE) via heat-assisted plasma treatment using a heater. *Sci. Rep.* **2017**, *7*, 9476. [CrossRef]

10. Gilman, A.; Piskarev, M.; Yablokov, M.; Kechek'Yan, A.; Kuznetsov, A.A. Adhesive properties of PTFE modified by DC discharge. *J. Phys. Conf. Ser.* **2014**, *516*, 012012. [CrossRef]

11. Marchesi, J.T.; Ha, K.; Garton, A.; Swei, G.S.; Kristal, K.W. Adhesion to sodium naphthalenide treated fluoropolymers. Part II. Effects of treatment conditions and fluoropolymer structure. *J. Adhes.* **1991**, *36*, 55–69. [CrossRef]

12. Kavan, L.; Dousek, F.P.; Janda, P.; Weber, J. Carbonization of highly oriented poly(tetrafluoroethylene). *Chem. Mater.* **1999**, *11*, 329–335. [CrossRef]

13. Ha, K.; McClain, S.; Suib, S.L.; Garton, A. Adhesion to sodium naphthalenide treated fluoropolymers Part I-Analytical methodology. *J. Adhes.* **1991**, *33*, 169–184. [CrossRef]

14. Clark, D.T.; Hutton, D.R. Surface modification by plasma techniques. 1. The interactions of a hydrogen plasma with fluoropolymer surfaces. *J. Polym. Sci. Part A Polym. Chem.* **1987**, *25*, 2643–2664. [CrossRef]

15. Wang, L.; Angert, N.; Trautmann, C.; Vetter, J. Effect of ion irradiation and heat treatment on adhesion in the Cu / Teflon system. *J. Adhes. Sci. Technol.* **1995**, *9*, 1523–1529. [CrossRef]

16. Takata, R.; Iwao, T.; Yumoto, M. Surface modification of PTFE using low-energy nitrogen ion irradiation: Improvement in adhesive strength on modification of deep modifying layer. *Electron. Commun. Jpn.* **2016**, *99*, 93–99. [CrossRef]

17. Vesel, A.; Mozetic, M. New developments in surface functionalization of polymers using controlled plasma treatments. *J. Phys. D Appl. Phys.* **2017**, *50*, 293001. [CrossRef]

18. Primc, G. Recent advances in surface activation of polytetrafluoroethylene (PTFE) by gaseous plasma treatments. *Polymers* **2020**, *12*, 2295. [CrossRef]

19. Badey, J.P.; Espuche, E.; Sage, D.; Chabert, B.; Jugnet, Y.; Batier, C.; Duc, T.M. A comparative study of the effects of ammonia and hydrogen plasma downstream treatment on the surface modification of polytetrafluoroethylene. *Polymer* **1996**, *37*, 1377–1386. [CrossRef]

20. Yamada, Y.; Yamada, T.; Tasaka, S.; Inagaki, N. Surface modification of poly(tetrafluoroethylene) by remote hydrogen plasma. *Macromolecules* **1996**, *29*, 4331–4339. [CrossRef]

21. Inagaki, N.; Tasaka, S.; Umehara, T. Effects of surface modification by remote hydrogen plasma on adhesion in poly(tetrafluoroethylene)/copper composites. *J. Appl. Polym. Sci.* **1999**, *71*, 2191–2200. [CrossRef]

22. Inagaki, N.; Tasaka, S.; Narushima, K.; Teranishi, K. Surface modification of poly(tetrafluoroethylene) with pulsed hydrogen plasma. *J. Appl. Polym. Sci.* **2002**, *83*, 340–348. [CrossRef]

23. König, U.; Nitschke, M.; Pilz, M.; Simon, F.; Arnhold, C.; Werner, C. Stability and ageing of plasma treated poly(tetrafluoroethylene) surfaces. *Colloid. Surf. B* **2002**, *25*, 313–324. [CrossRef]

24. Tanaka, K.; Takahashi, K.; Kogoma, M. Defluorination of polytetrafluoroethylene by combination of atmospheric pressure glow plasma treatment and chemical transport method. In Proceedings of the 20th International Symposium on Plasma Chemistry, Philadelphia, PA, USA, 24–29 July 2011.

25. Hunke, H.; Soin, N.; Shah, T.; Kramer, E.; Pascual, A.; Karuna, M.; Siores, E. Low-pressure H_2, NH_3 microwave plasma treatment of polytetrafluoroethylene (PTFE) powders: Chemical, thermal and wettability analysis. *Materials* **2015**, *8*, 2258–2275. [CrossRef]

26. Zanini, S.; Barni, R.; Pergola, R.D.; Riccardi, C. Modification of the PTFE wettability by oxygen plasma treatments: Influence of the operating parameters and investigation of the ageing behaviour. *J. Phys. D Appl. Phys.* **2014**, *47*, 325202. [CrossRef]

27. Abourayana, H.M.; Dowling, D.P. Plasma Processing for Tailoring the Surface Properties of Polymers. In *Surface Energy*; Aliofkhazraei, M., Ed.; Intech Open: Rijeka, Croatia, 2015.

28. Wilken, R.; Holländer, A.; Behnisch, J. Quantitative comparison between vacuum-ultraviolet irradiation and remote hydrogen plasma treatment of hydrocarbon polymers. *Plasmas Polym.* **1998**, *3*, 165–175. [CrossRef]

29. Fantz, U.; Briefi, S.; Rauner, D.; Wünderlich, D. Quantification of the VUV radiation in low pressure hydrogen and nitrogen plasmas. *Plasma Sources Sci. Technol.* **2016**, *25*, 045006. [CrossRef]

30. Ferraria, A.M.; Lopes da Silva, J.D.; Botelho do Rego, A.M. XPS studies of directly fluorinated HDPE: Problems and solutions. *Polymer* **2003**, *44*, 7241–7249. [CrossRef]